Lecture Notes in Electrical Engineering 1303

Hemender Pal Singh
Ishak B. Aris
Anwar Shahzad Siddiqui *Editors*

Recent Developments in Control, Automation and Power Engineering

Select Proceedings of the 5th International Conference, RDCAPE-2023, Volume 2

Springer

Lecture Notes in Electrical Engineering

Volume 1303

Series Editors

Leopoldo Angrisani, Department of Electrical and Information Technologies Engineering, University of Napoli Federico II, Napoli, Italy
Marco Arteaga, Departament de Control y Robótica, Universidad Nacional Autónoma de México, Coyoacán, Mexico
Samarjit Chakraborty, Fakultät für Elektrotechnik und Informationstechnik, TU München, Munich, Germany
Shanben Chen, School of Materials Science and Engineering, Shanghai Jiao Tong University, Shanghai, China
Tan Kay Chen, Department of Electrical and Computer Engineering, National University of Singapore, Singapore, Singapore
Rüdiger Dillmann, University of Karlsruhe (TH) IAIM, Karlsruhe, Germany
Haibin Duan, Beijing University of Aeronautics and Astronautics, Beijing, China
Gianluigi Ferrari, Dipartimento di Ingegneria dell'Informazione, Sede Scientifica Università degli Studi di Parma, Parma, Italy
Manuel Ferre, Centre for Automation and Robotics CAR (UPM-CSIC), Universidad Politécnica de Madrid, Madrid, Spain
Faryar Jabbari, Department of Mechanical and Aerospace Engineering, University of California, Irvine, USA
Limin Jia, State Key Laboratory of Rail Traffic Control and Safety, Beijing Jiaotong University, Beijing, China
Janusz Kacprzyk, Intelligent Systems Laboratory, Systems Research Institute, Polish Academy of Sciences, Warsaw, Poland
Alaa Khamis, Department of Mechatronics Engineering, German University in Egypt El Tagamoa El Khames, New Cairo City, Egypt
Torsten Kroeger, Intrinsic Innovation, Mountain View, USA
Yong Li, College of Electrical and Information Engineering, Hunan University, Changsha, China
Qilian Liang, Department of Electrical Engineering, University of Texas at Arlington, Arlington, USA
Ferran Martín, Departament d'Enginyeria Electrònica, Universitat Autònoma de Barcelona, Bellaterra, Spain
Tan Cher Ming, College of Engineering, Nanyang Technological University, Singapore, Singapore
Wolfgang Minker, Institute of Information Technology, University of Ulm, Ulm, Germany
Pradeep Misra, Department of Electrical Engineering, Wright State University, Dayton, USA
Subhas Mukhopadhyay, School of Engineering, Macquarie University, Sydney, NSW, Australia
Cun-Zheng Ning, Department of Electrical Engineering, Arizona State University, Tempe, AZ, USA
Toyoaki Nishida, Department of Intelligence Science and Technology, Kyoto University, Kyoto, Japan
Luca Oneto, Department of Informatics, Bioengineering, Robotics and Systems Engineering, University of Genova, Genova, Italy
Bijaya Ketan Panigrahi, Department of Electrical Engineering, Indian Institute of Technology Delhi, New Delhi, India
Federica Pascucci, Department di Ingegneria, Università degli Studi Roma Tre, Rome, Italy
Yong Qin, State Key Laboratory of Rail Traffic Control and Safety, Beijing Jiaotong University, Beijing, China
Gan Woon Seng, School of Electrical and Electronic Engineering, Nanyang Technological University, Singapore, Singapore
Joachim Speidel, Institute of Telecommunications, University of Stuttgart, Stuttgart, Germany
Germano Veiga, FEUP Campus, INESC Porto, Porto, Portugal
Haitao Wu, Academy of Opto-electronics, Chinese Academy of Sciences, Beijing, China
Walter Zamboni, Department of Computer Engineering, Electrical Engineering and Applied Mathematics, DIEM—Università degli studi di Salerno, Fisciano, Italy
Kay Chen Tan, Department of Computing, Hong Kong Polytechnic University, Hong Kong, Hong Kong

The book series *Lecture Notes in Electrical Engineering* (LNEE) publishes the latest developments in Electrical Engineering—quickly, informally and in high quality. While original research reported in proceedings and monographs has traditionally formed the core of LNEE, we also encourage authors to submit books devoted to supporting student education and professional training in the various fields and applications areas of electrical engineering. The series cover classical and emerging topics concerning:

- Communication Engineering, Information Theory and Networks
- Electronics Engineering and Microelectronics
- Signal, Image and Speech Processing
- Wireless and Mobile Communication
- Circuits and Systems
- Energy Systems, Power Electronics and Electrical Machines
- Electro-optical Engineering
- Instrumentation Engineering
- Avionics Engineering
- Control Systems
- Internet-of-Things and Cybersecurity
- Biomedical Devices, MEMS and NEMS

For general information about this book series, comments or suggestions, please contact leontina.dicecco@springer.com.

To submit a proposal or request further information, please contact the Publishing Editor in your country:

China

Jasmine Dou, Editor (jasmine.dou@springer.com)

India, Japan, Rest of Asia

Swati Meherishi, Editorial Director (Swati.Meherishi@springer.com)

Southeast Asia, Australia, New Zealand

Ramesh Nath Premnath, Editor (ramesh.premnath@springernature.com)

USA, Canada

Michael Luby, Senior Editor (michael.luby@springer.com)

All other Countries

Leontina Di Cecco, Senior Editor (leontina.dicecco@springer.com)

**** This series is indexed by EI Compendex and Scopus databases. ****

Hemender Pal Singh · Ishak B. Aris ·
Anwar Shahzad Siddiqui
Editors

Recent Developments in Control, Automation and Power Engineering

Select Proceedings of the 5th International Conference, RDCAPE-2023, Volume 2

Springer

Editors
Hemender Pal Singh
Department of Electrical and Electronics Engineering
Amity School of Engineering and Technology
Amity University
Noida, Uttar Pradesh, India

Ishak B. Aris
Department of Electrical and Electronic Engineering
Faculty of Engineering
Universiti Putra Malaysia
Serdang, Malaysia

Anwar Shahzad Siddiqui
Department of Electrical Engineering
Jamia Millia Islamia University
New Delhi, Delhi, India

ISSN 1876-1100 ISSN 1876-1119 (electronic)
Lecture Notes in Electrical Engineering
ISBN 978-981-96-0046-5 ISBN 978-981-96-0047-2 (eBook)
https://doi.org/10.1007/978-981-96-0047-2

© The Editor(s) (if applicable) and The Author(s), under exclusive license to Springer Nature Singapore Pte Ltd. 2025

This work is subject to copyright. All rights are solely and exclusively licensed by the Publisher, whether the whole or part of the material is concerned, specifically the rights of translation, reprinting, reuse of illustrations, recitation, broadcasting, reproduction on microfilms or in any other physical way, and transmission or information storage and retrieval, electronic adaptation, computer software, or by similar or dissimilar methodology now known or hereafter developed.
The use of general descriptive names, registered names, trademarks, service marks, etc. in this publication does not imply, even in the absence of a specific statement, that such names are exempt from the relevant protective laws and regulations and therefore free for general use.
The publisher, the authors and the editors are safe to assume that the advice and information in this book are believed to be true and accurate at the date of publication. Neither the publisher nor the authors or the editors give a warranty, expressed or implied, with respect to the material contained herein or for any errors or omissions that may have been made. The publisher remains neutral with regard to jurisdictional claims in published maps and institutional affiliations.

This Springer imprint is published by the registered company Springer Nature Singapore Pte Ltd.
The registered company address is: 152 Beach Road, #21-01/04 Gateway East, Singapore 189721, Singapore

If disposing of this product, please recycle the paper.

Preface

This book compiles the research presented at the 5th International Conference on Recent Developments in Control Automation and Power Engineering (RDCAPE-2023) held from 12th–13th October 2023. The conference, technically co-sponsored by Springer, was organized by the Department of Electrical and Electronics Engineering, Amity School of Engineering and Technology, Amity University Uttar Pradesh, India.

RDCAPE-2023 aimed to bring together academicians, scientists, industrialists, and researchers under one roof to discuss the recent developments in the field of power system, control, and automation engineering. The event focused on contemporary challenges in renewable energy, new control paradigms for efficient automation and decentralized power systems, and the evolving economics of open auction-based electricity generation, transmission, and distribution markets. RDCAPE-2023 played a pivotal role in setting up a bridge between academia and industry.

This book is divided into two volumes with total of 72 chapters. Volume 1 includes 34 chapters and primarily focused on power system technology, power electronics drives, and its applications with particular attention to recent advancements in renewable energy which is discussed here. The volume 2 presents 38 chapters discussing soft computing and its applications for electrical and other emerging areas of science and technology.

The chapters in this book reflect the recent findings in the area of power system technology, control system, and renewable energy. This book is designed to serve as a valuable reference for researchers and practitioners promoting better connections between academic and industrial sectors.

We extend our heartful thanks to all the participants and reviewers who contributed to this volume. We are profoundly grateful for the unwavering support from Amity University Uttar Pradesh, Noida, our university partner, the University of Tamaulipas, and industry partner, DesignTech Systems, India. We would also like to express our gratitude to the publisher. Special thanks are due to Dr. Ashok K. Chauhan, Founder

and President of Amity University, for his indispensable support and blessings, without which this book was not possible.

Noida, India
May 2024

Dr. Hemender Pal Singh
Dr. Ishak B. Aris
Dr. Anwar Shahzad Siddiqui

Contents

Automatic Parallel Parking Car 1
Tanooj Sreesailam, Nagireddy Ranga Rao, Ram Bhushan Singh, Anirudh Nawani, and Javed Dhillon

Analysis of Hand Shapes with Convolutional Neural Networks for Sign Language Recognition 11
Sandeep Bhatia, Bharat Bhushan Naib, Amit Kumar Goel, Anurag Verma, Sachin Gangwar, and Neha Goel

Performance Evaluation of Load Balancer in Storage Level Service Offering Applications 23
Maria Manuel Vianny, Rajat Bhardwaj, Vivek Bhardwaj, Vikrant Sharma, Virender, and S. Manikandan

A Comparative Study of Poisson Algorithm and Other Surface Reconstruction Techniques for 3D Modeling from 2D Images 33
Vaibhav Sharma, Dipin Garg, Rohit Sharma, and Palak Girdhar

Optimal Scheduling of Vehicle-to-Grid Power Exchange Using Hybrid BPSO and GSA Approach 45
Vikas Kumar Badhan and Shelly Vadhera

Smooth Imaging System Using Learning Generative Adversarial Network 55
Shipra Saraswat, Kajal Rani, Ishita Kanotra, and Aditya Kumar Singh

Encoding Data Using Slayer Exciter Circuits with Simultaneous Power and Information Transmission 67
Eshaan Yadav and Chaudhary Indra Kumar

Design and Analysis of Dual-Band Rectenna for Internet of Things Applications 79
Asmita Rajawat, Kushagra M. Agrawal, and Raghav Tola

A Study of an Efficient Edge Detection Approach with Machine Learning Techniques 93
Faiza Mushtaq and Harpreet Singh Bedi

Wireless EV Charging Station Using Weight Sensor 105
Sourav Kumar Singh, Jayesh Kumar, Seikh Atif Aslam, and Suresh Kumar Sudabattula

Universal Filters Based on Bulk-Driven CCII for Low-Voltage Analog Applications 113
Anu Tonk, Vandana Khanna, and Neelofer Afzal

Neural Networks-Based Control Framework for Teleoperation System 129
Anirudh Anand and Rohit Singla

Reinforcement Learning in Simultaneous Localization and Mapping 143
Abhik Kumar, Sudarshan K. Valluru, and M. M. Rayguru

Comparative Performance Analysis of PV System in Island Mode Using MPPT Fuzzy Logic Controller and Perturb and Observe Algorithm 155
Sagnik Ghosh and Shivam

Comparative Analysis of SOC Prediction Using Machine Learning Algorithms 165
Utsab Bhattacharya and Pradeep Kumar

PLC-SCADA-Based Automation System for Remote and Sensitive Areas 179
Udit Mittal, Gaurav Kaushal, Ankit Gupta, Lokesh, Abhishek, and Subhash Yadav

Analyzing the Performance of Fuzzy Tunned PID Control of Antilock Braking System 191
Pritish Sharma and Jyoti Ohri

Design and Implementation of an Automated Conveyor Belt System with Speed Control, Size Sortation, and IoT Data Publication 205
Aryan Thakur, Devraj Gautam, Sandeep Bhatia, and Surender Kumar

Investigating Quantum-Inspired Evolutionary Algorithm with Restarts for Solving IEEE CEC 2022 Benchmark Problems 219
Lubna Siddiqui, Ashish Mani, and Jaspal Singh

ANN Based Control Strategy for Automatic Generation Control of an Interconnected Power Systems 231
Omveer Singh and Shreya Chaudhary

Discrete-Time Realization of Fractional-Order Proportional Integral Controller for First-Order Plus Time Delay Plant 243
Bhanita Adhikary and Jaydeep Swarnakar

Energy Management System for Sustainable Energy Sources Using Hybrid Approaches 253
Mahesh Palavalasa, Shamik Chatterjee, and R. S. R. Krishnam Naidu

ANFIS-Controlled Hybrid Renewable Source System for Optimal Power Sharing 271
Ravikant, Asha Rani, and Vijander Singh

Robust Sliding Mode Controller for Flyback Converter in Continuous Conduction Mode 287
Mukund Kumar Choudhary, G. L. Pahuja, and Rahul Sharma

An Employment of PID Controller-Based Genetic Algorithm for the Load Frequency Control of Two-Area Power System Network 305
Arun Singh Rana, Omveer Singh, and C. B. Vishwakarma

Order Reduction of Linear Dynamic System Using Recursive Pole Array Technique and Pade Approximation 319
Deepa Kumari, Kirti Pal, and C. B. Vishwakarma

Power Generation from Food and Garden Waste in Educational Institute 335
Amit Atri, Anita Khosla, and Shashank Gaur

Modeling and Performance Analysis of a Model Predictive and Feedback Linearization Controlled UAV Autonomous Quadcopter Drone in 3D Dynamics 343
Ahsan Kabir Nuhel, Md. Nursari Hasan Sheham, Mir Mohibullah Sazid, Riad Mollik Babu, Hossain Md. Arif Shah, Bishal Saha, and Diva Bhatia

GA Optimization Methods for Charging of Electric Vehicles by Scheduling the Load of Home Appliances 357
Madhavi Nerkar, Aniruddha Mukherjee, and Bhanu Pratap Soni

Design of Type Compensators Using *K*-factor Method 369
Adnan Mukhtar and Arghya Chakravarty

Placement and Sizing of Distributed Generation Using MELGWO Algorithm in Distribution Networks 385
Priyanka Maurya and Prabhakar Tiwari

Stability Preservation Technique for Order Reduction of *z*-Domain Interval Structure 399
Shweta Kumari and Amit Kumar Choudhary

Pregnancy, Postpartum Hemorrhage Management System Using IoT 411
Amit Kumar Singh, M. Kavin, M. Thamaraiselvan, M. Periyasamy, M. Kiruthik Rosan, and Pyare Mohan Tiwari

Analyzing the Link Lifetime and Doppler Shift Between Connected Vehicles in VANET 423
Vishvendra Pal Singh Nagar and Anil Kumar Sagar

Comparative Analysis of Short-Term Load Forecasting Techniques: Conventional Deep Learning Models Versus Proposed LSTM with Attention Layers 433
Ravi Shekhar Tiwari, D. Lakshmi, Pragya Jha, Shubh Sharma, Neelu Nagpal, and Pierlugi Siano

Colourization of Greyscale Images Using GAN with ResNet as the Backbone 443
Shikhar Gaur, Md Salman, Anshu Khurana, and Seema Kalonia

Development of Electrical Power Train for Conversion of Motorcycle with an Internal Combustion (IC) Engine to an Electric Bike 461
Sachin Chavhan and Mahesh Kumbhar

Belief Reliability Evaluation of F-18 LLF System by Disjoint Method 473
Roopshi Gupta and G. L. Pahuja

Author Index 483

About the Editors

Dr. Hemender Pal Singh is the professor and head of the Department of EEE at Amity University, Noida. His areas of interest are control systems, instrumentation, and optical communication.

Dr. Ishak B. Aris is a professor in the Department of Electrical and Electronics Engineering at Universiti Putra Malaysia. He has 34 years of teaching and administrative experience in various positions. He was also an adjunct professor at the Faculty of Science, Engineering, and Technology at Swinburne University of Technology, Australia (15 August 2017–14 August 2020). He received an Honorary Professorship from the School of Engineering and Technology at Amity University, Uttar Pradesh, India, on 26 October 2017. Before this appointment, he was an army officer at the Electrical and Mechanical Engineering Corps, Malaysia Army. He graduated from the George Washington University, USA, with a B.Sc. in Electrical Engineering (1988). He obtained his M.Sc. in Power Electronics Engineering and Ph.D. from the University of Bradford, UK, in 1991 and 1995, respectively.

Dr. Anwar Shahzad Siddiqui is a Professor in the Department of Electrical Engineering at the Faculty of Engineering and Technology, Jamia Millia Islamia (JMI), and has 27 years of teaching and research experience in the field of power systems. He was a faculty member at the Department of Electrical Engineering, Z. H. College of Engineering and Technology, AMU, Aligarh, before joining Jamia. He also served at BITS, Pilani Dubai Campus as an associate professor in Electrical and Electronics Engineering and as an officiating registrar from 2003 to 2008. He obtained his B.Tech. (Electrical Engineering) and M.Tech. (Power System and Drives), both from the Department of Electrical Engineering, Z. H. College of Engineering and Technology, AMU, Aligarh, with Honors. He earned his Ph.D. degree from the Department of Electrical Engineering, Faculty of Engineering and Technology, Jamia Millia Islamia (JMI), in 2001.

Automatic Parallel Parking Car

Tanooj Sreesailam, Nagireddy Ranga Rao, Ram Bhushan Singh, Anirudh Nawani, and Javed Dhillon

Abstract In this paper, an algorithm was developed for a new self/automatic parking system based on a reverse parking with vehicle attitude as input and steering rate as output. The algorithm applied on a prototype electrical vehicle consists of ultrasonic-based sensors. Using this if–then based algorithm, vehicle follows the given instruction to perform the reverse parking after receiving the parking command from the user. After receiving the command, it detects green zones to verify either car is ready to reverse or not, and only if it is in reverse can it stop. In the paper, from the results it has been analyzed that the design prototype is successfully following the step-by-step instruction as given by the reverse parking algorithm to perform reverse parking.

Keywords Electric vehicle · Self-parking system · Arduino

1 Introduction

Most cars with self-driving parking capabilities cannot handle the parking process 100% on their own. The driver must be present to control the brakes for the accurate movement of the car. Commonly, new drivers waste lots of time in parking the vehicle due to the fears from crashing of car with other vehicle. On other hand, skilled drivers also take few minutes to perform parking accurately. Self-parking system automatically transforms the car into a parallel or perpendicular parking space. Self-parking can reduce stress, but it can also save money by reducing the risk of expensive wheels and tires causing damage to sidewalks. Repairing a flat tire can cost $150 or more, and with many newer models, even the cheapest tire can cost $200 or more. Front and rear bumper scratches are another part of the story, especially if you hit another car. Mostly the average priced car can't offer this automated self-parking system due to its high-cost technology. These automatic self-parking systems have been found in many new cars, SUVs, and minivans since their introduction in

T. Sreesailam (✉) · N. R. Rao · R. B. Singh · A. Nawani · J. Dhillon
Lovely Professional University, Phagwara, Punjab, India
e-mail: tanooj.sreessailam@gmail.com

© The Author(s), under exclusive license to Springer Nature Singapore Pte Ltd. 2025

H. P. Singh et al. (eds.), *Recent Developments in Control, Automation and Power Engineering*, Lecture Notes in Electrical Engineering 1303,
https://doi.org/10.1007/978-981-96-0047-2_1

Table 1 Car with automatic parking feature

Year	Car Model
2022	Cadillac Escalade
2022	Ford Escape
2022	Hyundai Sonata
2022	Nissan Rogue
2022	Volkswagen Atlas
2022	Chrysler Pacifica
2022	Genesis GV70
2022	Kia EV6
2022	Tesla Model Y
2022	Volvo XC602

the Lexus LS 460 in 2007. Each automaker's system has a unique brand name. For example, Nissan (NSANY) calls it Pro Pilot Park, and Ford calls it Ford Active Park Assist [1]. But the car without any self-parking assistant systems requires the driver to adjust the accelerator and brake pedals. The beep from the parking sensors hidden behind the bumper gets louder and faster as you get closer to the obstacle. In these cars, driver requires to press the brakes to avoid colliding with other cars. A rear-view camera display on the dash can also provide the help in parking. In most of these features, once the machine is in place, the system prompts to manually switch between forward and reverse [2]. Many new models can park themselves with or without driver intervention. In Table 1, top 10 self-parking car list has been provided with automatic parking system. However, in some cases, parking assistance may be optional. Car manufacture company recommends that the owner carefully read the standard and optional features for their model to determine if the vehicle you are purchasing has auto-park. Some of the several advantages and disadvantages of automatic parking system has been given below.

1.1 Advantages of Self-parking Mechanism

There is high parking efficiency. A self-parking car can fit into smaller spaces than most drivers can manage on their own. This makes it easier for people to find parking spaces, and allows the same number of cars to take up fewer spaces. Additionaly, it reduces the stress experienced by new drives when parking manually. There is no need for driving while looking for an available space, as it is feasible to park the car in the small parking lots.

1.2 Drawback of Self-parking Mechanism

As the mechanism is involved with high technology, so it also has high cost too. The parking systems are usually automated, but they require regular maintenance to ensure everything is working smoothly.

2 Literature Review

The main reason behind the lack of parking spaces in the urban areas is mainly due to the huge usage of private vehicles, that leads to inappropriate management of available space. This not only consumed the timing but also caused the air pollution due to more wastage of gas during the vehicle parking [3–5]. So it would be very difficult for any person to find a suitable parking space in the crowded areas. As per the survey it is analyzed that there is about 30% of traffic congestion due to drivers cruising for the parking space. In this paper, main aim is to sort out the parallel parking issue of non-holonomic vehicles under certain conditions. In recent paper, various authors present a shortest path planning algorithm to park the vehicle under the limited parking space [6–9]. By improving the shortest path planning algorithm, a feasible model of iterative parking in a narrow space is developed.

This paper presents a new approach for parallel path tracking and providing the control of automated parking systems for electric car. This includes optimizing the output wheel position of the car, validating the trajectory following designed parking algorithm, and performing reverse parking on physical electric car. Proposal for a parking lane monitoring planning and control model: The purposed parallel parking system is developed based on the identification of parking barrier, tracking the parallel spacing in between the parking barrier and control the wheel position. It is not only very intelligent, but also leads to a good accuracy with recommended parking efficiency. This shows that it offers reliability and stability for the manager. The main goal of this work is first the establishment of an algorithm for vehicle parking and the analysis of the various constraints creating the parking obstacle. A rational and workable planning scheme for parallel parking lanes is proposed and a simulation analysis is performed. In addition, an optimization procedure was performed for the simulation analysis.

In addition, a procedure for optimizing the outliers of the trajectory curve is studied based on insight theory. Finally, the parking lane is optimized. A simplified parking path detection model is developed to reflect the movement of the vehicle accurately. In order to provide better route following accuracy for a given parallel parking route following controller based on variable structure multiple sensor-based control algorithm is designed. Establish the test vehicle model based on EV and predefine the controller input and output parameters. Design and optimize parallel parking lane planning and tracking control models on the platform. In addition, the

performance of the designed model is verified by performing multiple experiments on different routes.

3 Methodology

3.1 Parallel Parking Using Arduino

Parallel parking using the Arduino microcontroller requires some key components including sensors, a motor driver and a microcontroller board such as the Arduino Uno. In Fig. 1, a basic overview of how to build a parallel parking system with an Arduino is presented for automated marking system. A parking algorithm as shown in Fig. 2, also has been designed to communicate the control command to the motor drives circuit based on the data received from the various position sensors on certain assumptions. In this project, some of the assumptions are as follows. In this scene, the left side of the road will consist of the wall and the park area. As you can see in Fig. 3 there are 4 sensors, 2 on the left side of the car and 1 on the front and rear of the car. Two sensors on the left side of the cart learned that the wall was 15 cm smaller than the measurement and moved forward. It is saved in memory. The two sensors on the side measure continuously, and when these values are the same as the resulting value, you decide how to stop the car.

3.2 Parallel Parking Algorithm

In the case, Arduino received the command. The car drives through the parking lot and stops when both side sensors see the wall again. He turned around a bit and turned 45° to the right. When reversing, rear sensors measure entry into parking bays and initiation of left turns. During the movement to the left, the sensor on the edge continues to measure and both sensors continue to rotate to the left until the measured values are equal. Stop when balanced. Front sensor measures and continues to measure until it is 10 cm short and it stops, when it is 10 cm short.

3.3 Select and Install Sensors

Parking algorithm needs the sensors to measure the distance between the car and the cars parked in front and behind it. Ultrasonic sensors are often used for this purpose, but other options include an infrared sensor and a laser rangefinder. Mount the sensors to the front and rear of the car, placing them carefully so they can detect the edges of other cars.

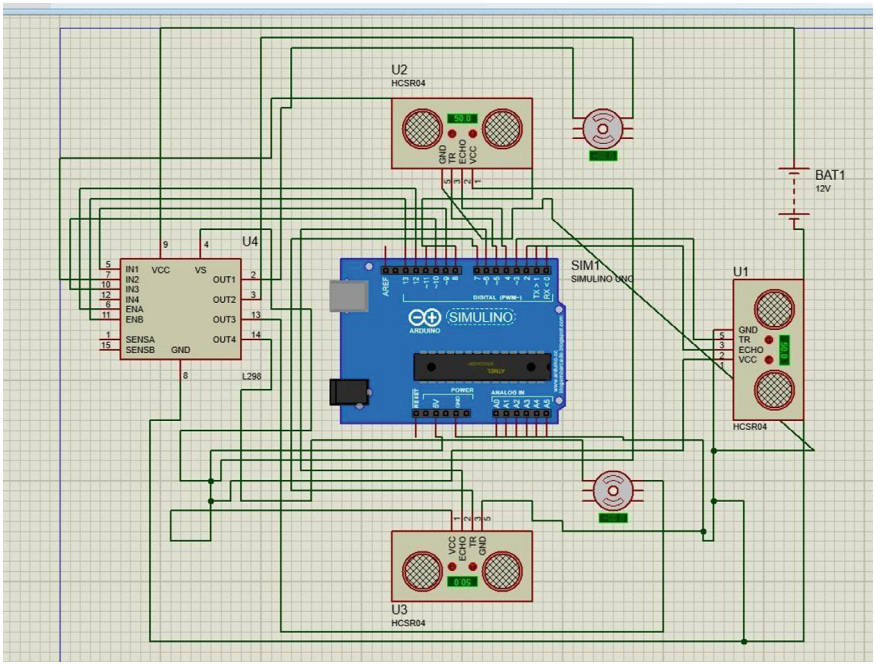

Fig. 1 Circuit diagram

3.4 Connect the Sensor to the Arduino

Connect the sensor to the Arduino using jumper wires. Depending on the type of sensor you are using, a voltage divider or other circuit is required to ensure that the sensor output is within a range that the Arduino can read.

3.5 Arduino Programming

In this paper, program is designed for an Arduino that reads sensor data and uses it to control the motion of a motor. This program required the car driver to control the speed and direction of the car wheels to reach toward the parking lots. But during the parking, program used the sensor data to determine when to start and stop the car, and how much to turn the wheels to get the car to the desired location.

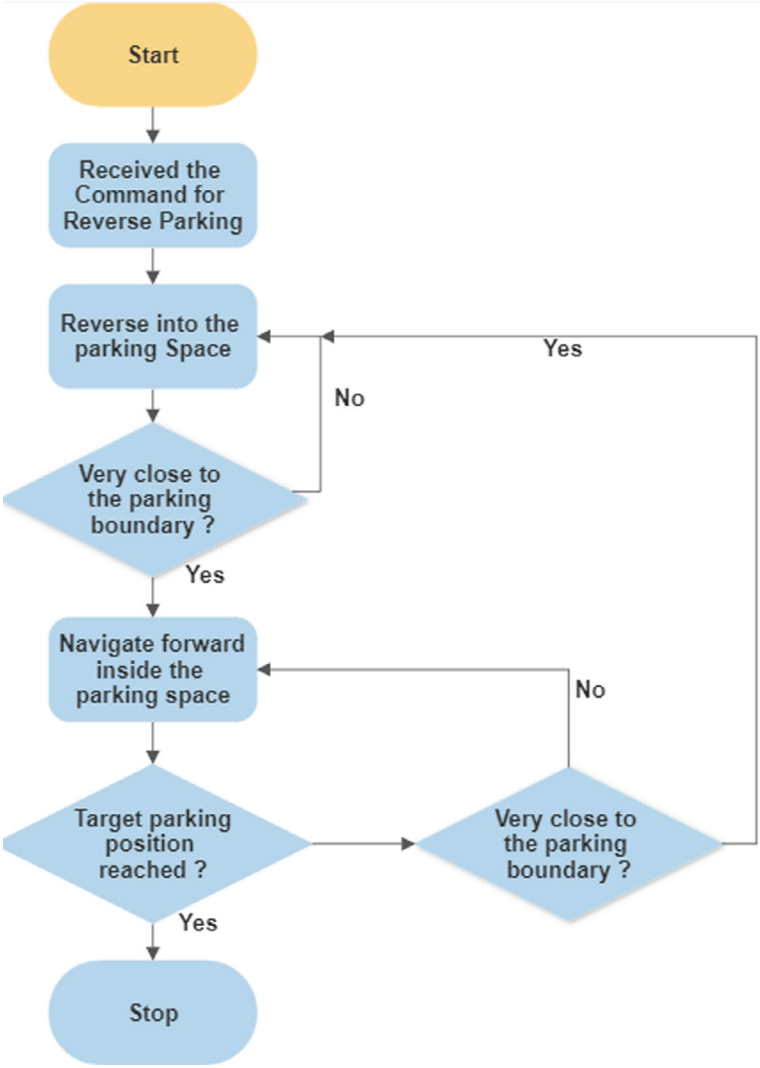

Fig. 2 Self-parking algorithm

3.6 Testing and Fine-Tuning Systems

Once the basic system is working, test it in a safe, controlled environment to make sure it works as expected. It may need to adjust the program or the location of the sensors to improve the accuracy of the system. It should be noted that creating a parallel parking system using an Arduino is a complex project that requires extensive knowledge of electrical engineering and programming. For a person, very new to electronics or

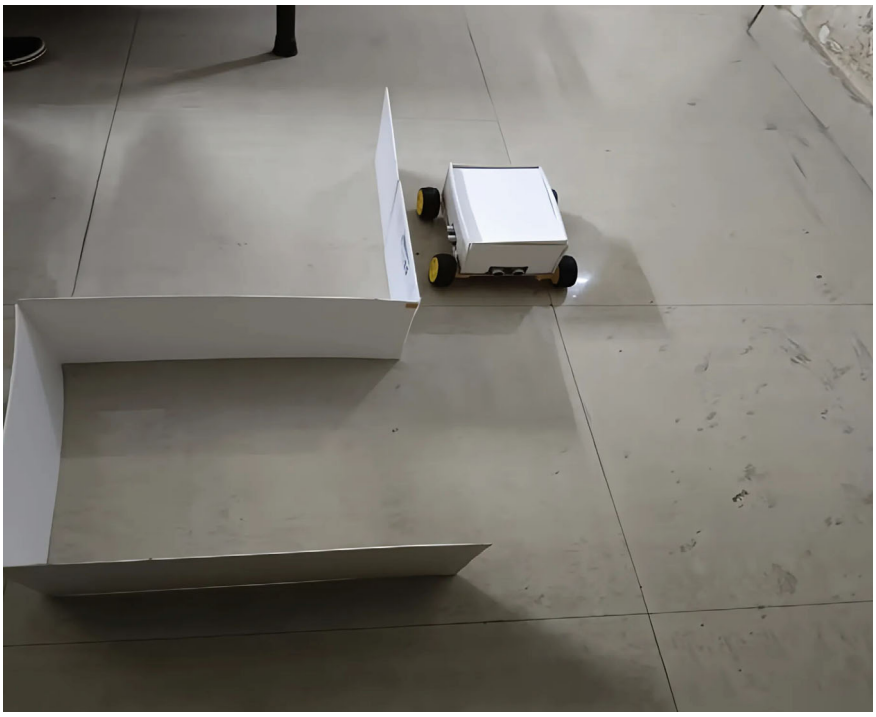

Fig. 3 Car prototype with the parking lots

programming, it is best to start for him with simple projects before building more complex projects, such as a parallel parking system.

3.7 Circuit Diagram and Operation

As seen in the circuit diagram, the design of automatic parking system designed model consists of various parts: first is sensing unit, second is operational unit that creates the control command and third one is motor control unit. An Arduino Mega 2560 board is attached with four ultrasonic sensors (HC-SR04) to detect the parking barrier. These devices provide the data to the operational unit for further processing. Arduino is a microcontroller that can be programmed with an open-source software Arduino IDE. It has 54 digital input/output pins, 16 analog inputs and 4 communication ports. The ultrasonic sensors are used in this prototype using SONAR to detect the distance of an object. The basic role of the ultrasonic sensor is to detect the obstacles during the reverse parking. An algorithm as shown in Fig. 2 is evaluated on Arduino board to fulfill the defined goal. Four geared DC motors are used in getting the control input from the motor driver circuit named as L293D IC, used to move the chaises to

given direction. The given driver circuit acts as an H-bridge controller used to control the direction of DC motor. It controls the directions of motor in both the directions (forward or reverse). The detailed circuit diagram has been given in Fig. 1.

4 Results and Discussions

A prototype car has been designed in this paper that automatically determines parking spaces and performs the parallel parking. The car used the manual control to find a parking space on the right and drive along the road. Once the vehicle recognizes a specific location, the algorithm starts to work after receiving the command from the drivers. If the algorithm determines that there is enough space, the car will parallel park there. It uses information from the vehicle's front, right and rear sensors to guide the vehicle into a parking space. Once a vehicle is parked, it will stay in that position until it is repaired. Once it received the paring command, it will move to ready-to-reverse position, if it reaches the position with an obstacle then it reverses into the parking space and after that it checks whether it is very close to the boundary or not and moves a bit forward if it is close to it. And after placing itself in a parking space it will stop the execution.

5 Conclusion

This paper describes our project to set up automatic parallel parking for cars. The prototype of our system involves an automotive system that performs a parallel parking procedure to find an empty parking space and then the station in parallel. We also used an RC motor in our system, to which we added hardware components such as a microcontroller, DC motor, servo motor, 2 infrared sensors and an ultrasonic sensor. In the system, the car searches for a free space to park, and if the space found is less than the required space, the car continues the search using the parking algorithm. However, if the length of the empty slot is greater than a certain size, the motor stops. After the system is simulated, implemented and tested, the results show that the car can successfully perform all the above tasks.

References

1. Andrew, G.: How does a car park itself, and which models offer self-parking? Market Watch. https://www.marketwatch.com/story/how-does-a-car-park-itself-and-which-models-offer-self-parking-11654288626?mod=autotrader. Last accessed 26 Mar 2023
2. Andrew, G.: Self-parking cars: what you need to know. Market Watch. https://www.autotrader.com/car-shopping/self-parking-cars#-text-Self-parking. Last accessed 26 Mar 2023

3. Aneez Z (2010) Parking Space in Kochi: Issues and Solutions, pp. 1–40. Centre for Public Policy Research (2010)
4. Lin, T., Rivano, H., Le Mouël, F.: A survey of smart parking solutions. IEEE Trans. Intell. Transp. Syst. **18**(12), 3229–3253 (2017)
5. Chandana, M., Aniruddh, M.C., Fathima, A., Chandan, G., Kumari, H.A.C.: A study on smart parking solutions using IoT. In: 2019 International Conference on Intelligent Sustainable Systems (ICISS), pp. 542–548. Palladam, India (2019)
6. Kanteti, D., Srikar, D.V.S., Ramesh, T.K.: Intelligent smart parking algorithm. IEEE FLEX Chip Signal Processor (MC68175/D), Motorola (1996)
7. Kaur, G., Joshi, S., Kaur, J., Kaur, S.: Going driverless with sensors. Int. J. Sci. Eng. Technol. **2**(5), 298–305 (2014)
8. Ashwini, H.Y., Mala, T., Yamuna, N., Vanitha, K.S.: A smart parallel parking by rotating wheels of vehicles. Int. J. Eng. Res. Technol. **8**(11), 221–224 (2020)
9. Mohate, G.A., Bawankude, S., Sonule, S., Wachhani, H., Wasnik, P.C., Patil, V.: Design and fabrication of parallel parking system in four wheel drive. Int. J. Adv. Res. Innov. Ideas Educ. **4**(2), 2533–2537 (2018)

Analysis of Hand Shapes with Convolutional Neural Networks for Sign Language Recognition

Sandeep Bhatia, Bharat Bhushan Naib, Amit Kumar Goel, Anurag Verma, Sachin Gangwar, and Neha Goel

Abstract According to the late theoretical physicist Stephen Hawking, having a disability need not prevent you from succeeding. People with talents should always work to make the lives of disabled people better. The deaf and dumb benefit from a variety of technological developments and studies. Numerous message boards are used by people to spread their message. Text messages can now be sent using rewritable pads, however doing so requires time and isn't always successful. Technologies like machine learning and open CV can be employed to progress the situation. These can be created into automatic editors for anyone with limitations like as speech or hearing loss. Hand gestures can be used to convey messages. With the aid of open CV and machine learning, we can capture their hand motions and translate them into a language that we can all comprehend. This study article will look at how to implement a model that will assist the disabled with this problem and challenges associated with sign language recognition.

Keywords Gesture recognition · Language translation · Image processing · Convolution neural network

S. Bhatia (✉) · B. B. Naib · A. Verma · S. Gangwar
School of Computing Science and Engineering, Galgotias University, Greater Noida, Uttar Pradesh, India
e-mail: sandeep.bhatia@galgotiasuniversity.edu.in

B. B. Naib
e-mail: bharat.bhushan@galgotiasuniversity.edu.in

A. K. Goel
School of Engineering and Technology, Apeejay Stya University Sohna, Gurugram, India
e-mail: amit.goel@galgotiasuniversity.edu.in

N. Goel
Department of Electronics and Communication Engineering, RKGIT Ghaziabad, Ghaziabad, Uttar Pradesh, India

Department of ECE, RKGIT, Ghaziabad, India

© The Author(s), under exclusive license to Springer Nature Singapore Pte Ltd. 2025

H. P. Singh et al. (eds.), *Recent Developments in Control, Automation and Power Engineering*, Lecture Notes in Electrical Engineering 1303,
https://doi.org/10.1007/978-981-96-0047-2_2

1 Introduction

The rise in public interest and financial support for international efforts highlights the necessity of sign language. An increasingly common choice for deaf persons in modern times is a laptop-based solution. The outcomes, however, are beginning to appear good as a result of the regular research into the problem. There is currently no commercially accessible signal recognition solution, despite the fact that cutting-edge technology has arisen for voice recognition. In order to interpret human language, there is a need for a user-friendly interface. Coaching a program for a technology that can read and learn human faces, human speech, and other hand signals; the nonverbal exchanged data are gestures [1]. Gesture reputation is a teaching tool that illustrates a human-to-computer contact and is essential to spreading the idea that people may communicate with one another. Additionally, there should be a precise and effective link between the user and the equipment. This will make it easier to study the hand movements. There is a specific science section that approves of the motion of the arms, head motions, hand gestures, and any other movement that can convey a message while analyzing human gestures [2]. After a successful installation, one can use hand motions for documentation and finish tasks that take time and effort in less time. A variety of techniques have been developed to process gesture outputs in real time using computer vision algorithms [3]. The computer vision study employs the Python programming language and focuses on gesture detection within the open CV framework [4]. Language is heavily used in communication. Language is useless to a person with a disability. For the visibly disabled person, movement is a crucial and important form of communication. To solve this issue, we developed a completely computer-based system that enables regular people to comprehend what impaired persons are trying to communicate [5]. For monitoring, we have a large number of algorithms and item popularity structures. It is now possible to recognize gestures, circumventing the drawbacks of pre-existing structures, thanks to a number of reliable algorithms for gesture detection that are believed to operate well. A robot that is controlled by gestures is seen. Neural networks, adaptive boosting, and the assist vector device are the techniques that are employed in the reconnaissance. To apply hand motions for better fingertip detection, the convex hull is used. In comparison with other existing structures, the associated paper has a greater accuracy result. The focus is on broadly effective techniques for capturing gestures that have become increasingly important in recent years [6]. The study also describes how to detect skin color for form identity using the YCbCr coloring space transformation and the convex hull approach. Ten clients provide 330 separate examples of different hand movements for precisely molded results. Describing a hand movement ubiquitous device that is primarily built on Linux and uses Python. The algorithm employed is independent of the circumstances and uses hidden Markov model [7]. It is aware of the user's fingertip range and even the task carried out in relation to the requirement. According to an Indian study from 2022, over 1. 3 million people are hearing-impaired. On the other hand, according to the national association for the deaf, there are 18 million deaf persons in India, or 1% of the entire population [8]. Those numbers

inspired our endeavor. Thus, there is a need for a framework since those who are deaf or hard of hearing need the best means to communicate with hearing individuals. The sign language used by the disabled is no longer understood by everyone. As a result, we are building this project with regular people and the deaf in mind so that they can converse with no restrictions [9].

2 Organization of the Paper

The paper is organized into 5 sections, Sect. 3 belongs to literature review, Sect. 4 represents proposed system, Sect. 5 shows methodology, Sect. 6 mentions algorithm design, and Sect. 7 demonstrates output and conclusion.

3 Literature Survey

Before considering any novel ideas, we studied several outstanding works that have been completed in recent years and gathered all relevant information. These are some of those.

Signal Sign Recognition Technique Survey on Language Recognition: We learned about various technologies utilized in this industry after reading this survey. HMM-based techniques have become the most used technology in recent years. The most often used modern technologies are convolutional neural networks and machine learning. Research is being done on the convolution neural network and HMM combination, and the findings support further study. Clusters and high computational demands, however, impede their adoption. To obtain great performance with a little CPU, we must build a basic network and learn how to use multi-layer networks. This network won't be helpful until it is not a mobile device. To suggest for, we need to manage several little gadget prototypes [10].

Interaction Between Deaf-Mutes and Hearing People: The general movement task is to encourage daily interaction among deaf-mutes by accurately translating sign language into sound or text. The sign language used by the deaf-mutes is difficult to understand by non-native speakers. Therefore, a tool that can understand the message and translate it into other languages is required so that everyone may understand it, independent of their native tongue [11]. For those who are deaf or mute, being able to speak with the wider public can be a huge accomplishment [12].

OTSU Algorithm-Based Device to Promote Indian Sign Language for the Deaf [13]: By creating methods that turn hand movements photographed with a webcam into a grayscale image, the proposed work aims to increase the use of sign language. The OTSU threshold technique is used to segment the grayscale image and distinguish the hand movement from the background. After that, the image is split into two

categories—hand and background—by figuring out an upper threshold value based on the sum of all class variances and the proportion of class variance. Edge-based segmentation and threshold-based segmentation are combined to create a region detection technique that locates the limits of the hand movement in the image. The OTSU algorithm is used because it is straightforward and stable, even when the target's global distribution and history diverge significantly.

Intelligent Sign Language Recognition Using Photo Processing: Finally, we have a special remark for the outstanding work in this area; because of their peculiar time-varying nature, HMMs perfectly match the reputation of ASL signals. Because a chain of several of the 38 primary hand shapes can be used to gesture for the majority of ASL signals [14]. The most crucial hand forms can be retrieved by separating the non-stop warning indications and feeding them into the HMM processor. The methods outlined in this article can be used to identify the fundamental hand shapes and combine them into ASL phrase outputs. These techniques can be used to the device to make it a better sign language communication tool [15].

4 Proposed System

Our proposed system as shown in Fig. 1 has users and a shared system or can have a single user and system. The user can show words there with hand gestures on the OpenCV screen and it will be reflected in the meaning of the screen [7], the other user will understand the use of these screen messages and help the user convey the message. UML diagram for our proposed system is below. The user interface of our system has two screens, one for inputs and one for outputs. One screen is OpenCV [16] which records hand gestures and other screen response messages, meanwhile our system performs several functions. The system captures a video and extracts a gesture from the video, and then translates that gesture, combines that gesture and recognizes the gesture, and finally displays the result [3].

4.1 Ease of Use

The ease of use is the most important consideration in the design of a sign language recognition equipment because if it is difficult for most people to use, people will not accept its availability. One benefit of the suggested system is its interface, which is merely a screen with a message to display. Once the system is created, it can be easily linked with other small devices and put to widespread usage. Since our system has a multilingual translator, there won't be a language barrier in communication, and it provides real-time experience and very high accuracy compared to other solutions on the market as shown in Fig. 4.

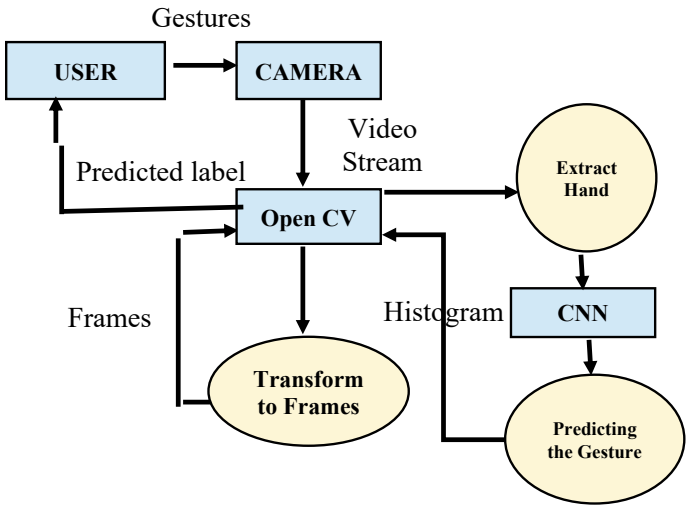

Fig.1 Sequence of data flow

5 Methodology

Figure 2 shows the system execution start from webcam capture video and gestures to extracting, matching, and organizing images.

6 Algorithm Design

Our solution includes two stages: the first stage is data collection and model training, and the second step is real-time OpenCV testing. We gather datasets for various signals in a variety of contexts at the first stage since, when the model is being used, the hands and background can vary greatly. To train our model, we are utilizing a lot of data. This is being captured in various settings and recording modes. These data will be used to train the model. We train the model using supervised learning, first instructing the computer that this is the sign for this word and this is the sign for this word. After the model has been trained on a large amount of data, we can expect to receive accurate results in a variety of backgrounds or runtime environments.

We utilize CNNs to train our model because they are good at differentiating between different types of data and optimizing objective functions [17], like the loss function,

$$f_j(z) = \frac{e^{z_j}}{\sum_{k=1}^{C} e^{z_k}}$$

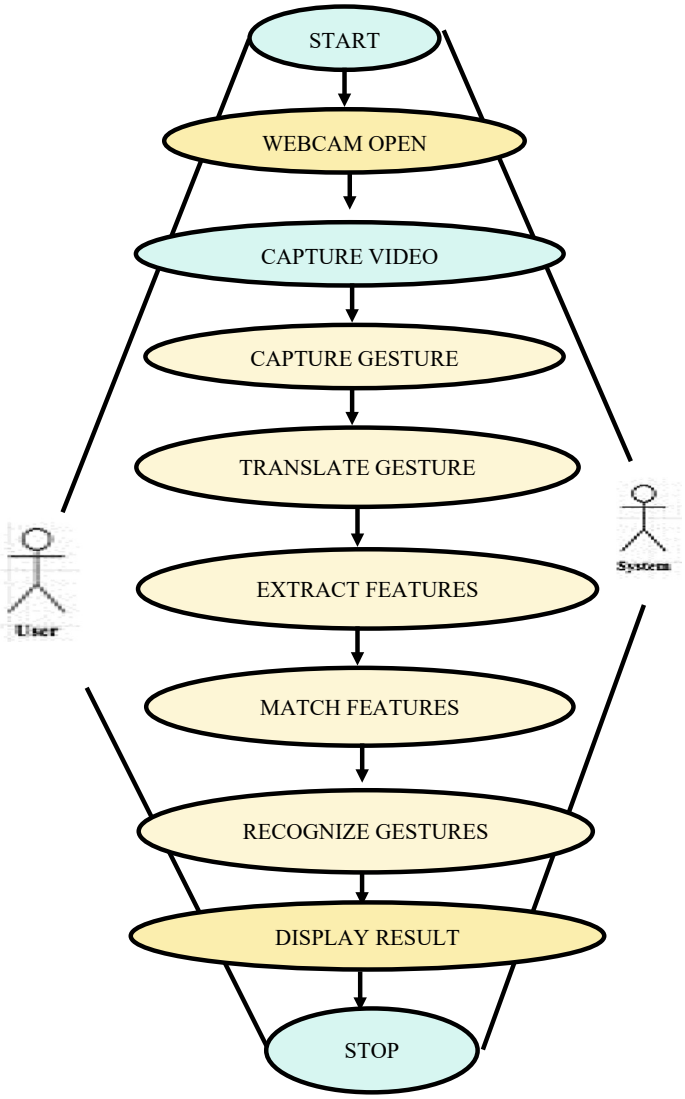

Fig. 2 System execution

$$Loss = \frac{1}{N}\sum_{i=1}^{N} -\log\left(\frac{e^{f_i,y_i}}{\sum_{k=1}^{C} e^{f_i,y}}\right)$$
$$\mathrm{N} = \text{total number of training examples}$$
$$\mathrm{C} = \text{total number of classes} \quad (1)$$

which is crucial. The aforementioned function computes the loss and maximizes the model's accuracy. To create such a system, we use a variety of machine learning and programming tools, including Numpy, Scikit Learn, Sklearn, TensorFlow, Keras, and a few supporting Python libraries. These libraries aid with a variety of calculations and extractions. The model is trained using Tensor Flow as the primary software library. For classifications and closeting algorithms, use Sklearn and Scikit Learn. Following model training, we go on to the second stage of system design, where computer vision is used to collect input and forecast output. The model's operation is depicted in the diagram below. OpenCV takes the user's input, turns it into frames, creates a histogram, finds the sign by separating the hands, and then, using the CNN algorithm, displays the message in response.

7 Output

A table called a confusion matrix as shown in Fig. 3 and Fig. 4 is frequently used to assess how well a machine learning classification model is performing. By comparing the predicted labels with the actual labels in a dataset, it is used to condense the prediction outcomes of a classification model. Each of the four cells in the matrix represents the number of data that the model classified correctly or erroneously. True positive, false positive, true negative, and false negative are the names of these cells. False positives indicate success when failure was anticipated, while true positives indicate success when it was needed. False negatives show failure when success was anticipated, while genuine negatives show failure when success was anticipated. Accuracy, precision, recall, and F1-score are just a few of the metrics for the model that may be calculated using the matrix. These metrics show how well the model is working and can be used to adjust the model's settings or evaluate it in comparison with other models as shown in Fig. 5.

A graph that displays accuracy versus epoch is also available. During the training of a machine learning model, an epoch represents a whole iteration through a given dataset. The complete dataset is fed to the model in smaller chunks throughout each epoch in order to change its parameters and enhance performance. The model fits better when there are fewer epochs, while the model may overfit if there are too many epochs. The resulting graph, which is given below, gives the model the least amount of loss.

8 Result Discussion

Modern programs demand a large number of photo types as storage media for analysis and evaluation. To act in diverse duties, you need to look for a variety of traits. The image may degrade to some extent as the input obtained with the open CV is subjected to various forms of scanning and modifications [18]. As a result, the

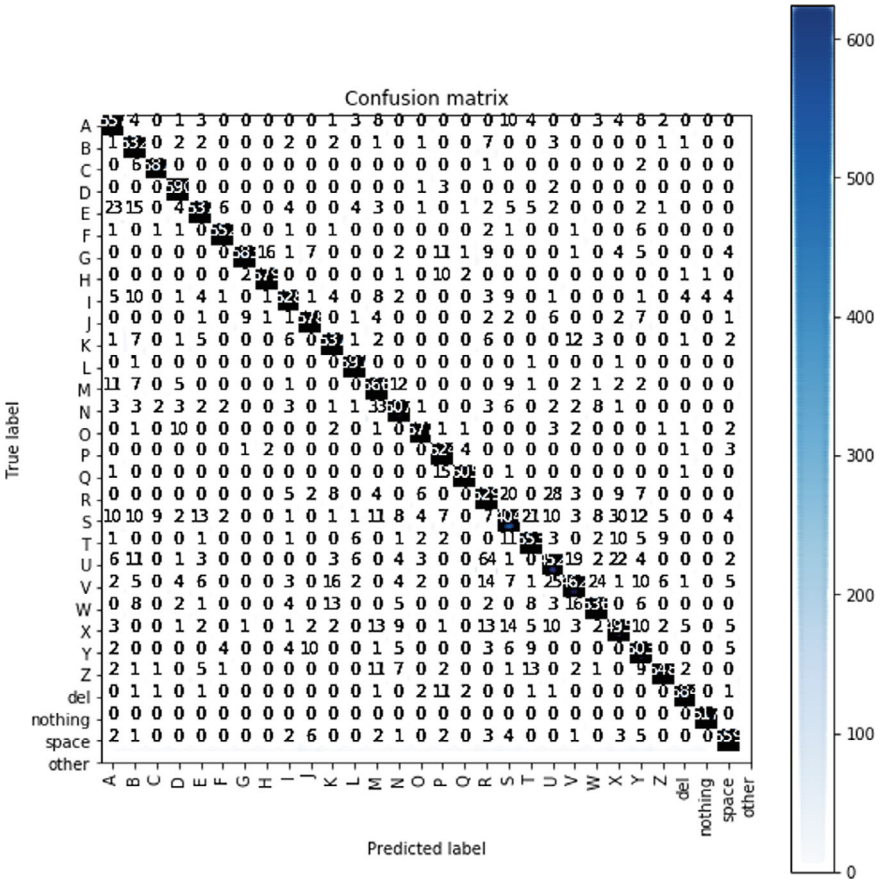

Fig. 3 Confusion matrix

output image must go through a system known as image enhancement, which uses a number of techniques to try to boost the visibility of the picture as shown in Fig. 5. The interpretability or understanding of image statistics for humans is improved via photo enhancement. Different methods are used to perform extraction operations on an image when you wish to generate one reads better on a laptop, a potent technique for producing expert knowledge, spotting edges, and combining erroneous data from several sources.

	precision	recall	f1-score	support
A	0.88	0.92	0.90	608
B	0.85	0.96	0.90	555
C	0.98	0.98	0.98	590
D	0.94	0.99	0.96	596
E	0.92	0.87	0.89	615
F	0.97	0.97	0.97	567
G	0.98	0.91	0.94	644
H	0.97	0.97	0.97	596
I	0.93	0.89	0.91	591
J	0.95	0.94	0.95	615
K	0.91	0.92	0.91	578
L	0.96	0.99	0.98	594
M	0.85	0.91	0.88	619
N	0.89	0.87	0.88	583
O	0.96	0.96	0.96	602
P	0.91	0.98	0.94	635
Q	0.98	0.97	0.98	623
R	0.79	0.85	0.82	621
S	0.79	0.69	0.74	583
T	0.89	0.91	0.90	607
U	0.82	0.75	0.78	603
V	0.87	0.77	0.82	600
W	0.91	0.89	0.90	604
X	0.85	0.83	0.84	599
Y	0.83	0.91	0.87	552
Z	0.95	0.90	0.93	606
del	0.97	0.96	0.97	606
nothing	0.99	1.00	1.00	617
space	0.94	0.95	0.94	591
avg / total	0.91	0.91	0.91	17400

Fig. 4 Table of precision, recall, f1-score for alphabets

9 Conclusion and Future Scope

The suggested method successfully converts hand motions into texts. Although this content is made up of brief word combinations and uses neural networks to ensure accuracy, short words are difficult to understand. Combining short words may result in a delayed communication process, thus we can create models for lengthy phrases. That may foretell the entire meaning from a few phrases. There are also feelings in the message that we are unable to communicate by hand. To capture these emotions, we may also incorporate a facial expression detecting tool. We can now add some

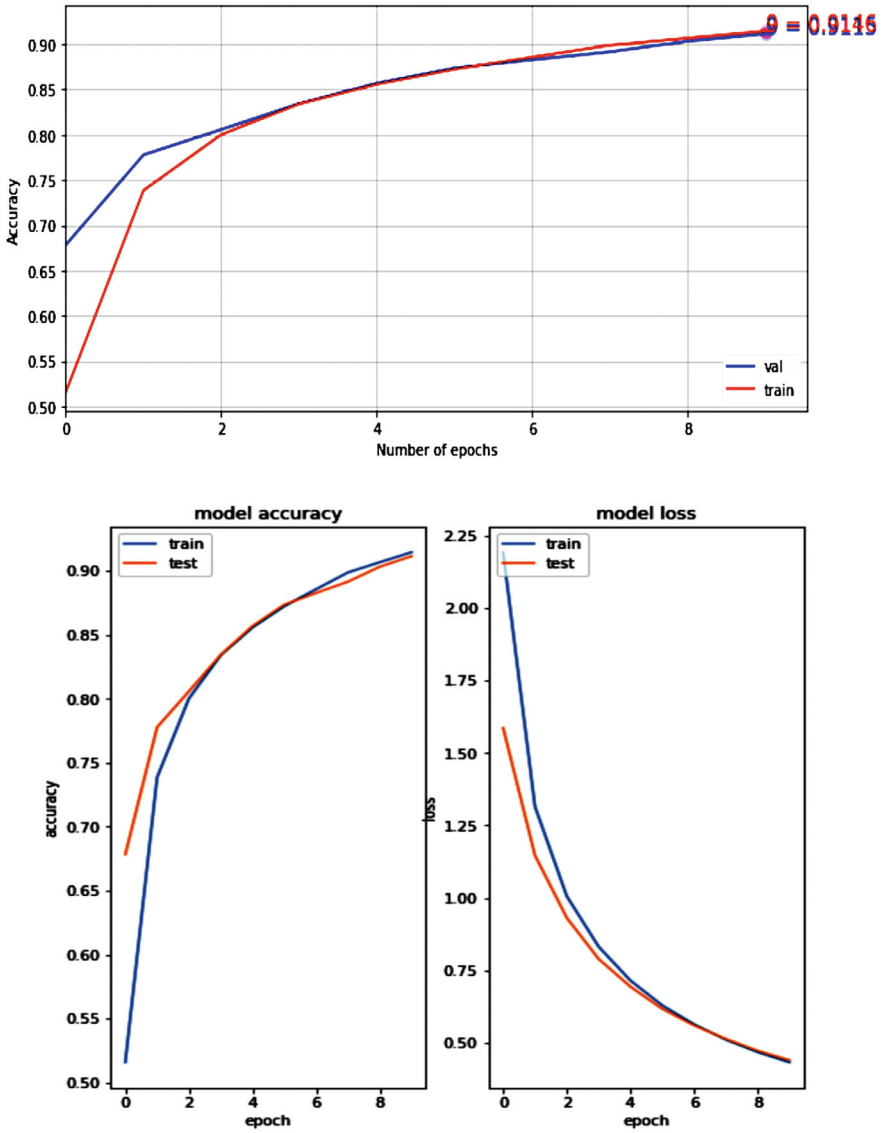

Fig. 5 **a** Accuracy versus epochs, **b** model accuracy and model loss

routines to export the screen output to a text file since we have output to display while the system is running as well. It may be integrated with the APIs to translate across languages, which will reduce the dependence on a single language. We can also incorporate an API to voice the displayed message, which improves the experience, and make it as simple and intuitive to use as possible [16, 19].

Acknowledgements We would like to sincerely thank Galgotias University, our university, for giving us the chance to work on this project. We would want to take this opportunity to thank everyone who has supported us wholeheartedly at every level of this project. No project is made by a single person. We are appreciative and lucky to have our parents, friends, and teachers provide us with ongoing motivation and support

References

1. Verma, A., Gupta, V., Singh, A.K.: An automated irrigation system: an IoT application. In: 2022 3rd International Conference on Intelligent Engineering and Management (ICIEM), pp. 648–651. IEEE, 27 Apr (2022)
2. Athavale, S., Deshmukh, M.: Dynamic hand gesture recognition for human computer interaction; a comparative study. Int. J. Eng. Res. Gen. Sci. **2**(2), 38–55 (2014)
3. Bhatia, S., Gautam, D., Kumar, S., Verma, S.: Automatic seat identification system in smart transport using IoT and image processing. In: 2023 3rd International Conference on Intelligent Communication and Computational Techniques (ICCT), pp. 1–6. IEEE, Jan 19 (2023)
4. Bhatia, S., Mallikarjuna, B., Gautam, D., Gupta, U., Kumar, S., Verma, S.: The future IoT: the current generation 5G and next generation 6G and 7G technologies. In: 2023 International Conference on Device Intelligence, Computing and Communication Technologies, (DICCT), pp. 212–217. IEEE, 17 Mar (2023)
5. Starner, T., Pentland, A.: Real-time American sign language recognition from video using hidden Markov models. In: Proceedings of International Symposium on Computer Vision-ISCV, pp. 265–270. IEEE, 21 Nov (1995)
6. Ganai, P.T., Bag, A., Sable, A., Abdullah, K.H., Bhatia, S., Pant, B.: A detailed investigation of implementation of Internet of Things (IOT) in cyber security in healthcare sector. In: 2022 2nd International Conference on Advance Computing and Innovative Technologies in Engineering (ICACITE), pp. 1571–1575. IEEE, 28 Apr (2022)
7. Jebali, M., Dalle, P., Jemni, M.: Extension of hidden Markov model for recognizing large vocabulary of sign language. arXiv preprint arXiv:1304.3265 (2013)
8. Kuo, C.C.: Understanding convolutional neural networks with a mathematical model. J. Vis. Commun. Image Represent. **1**(41), 406–413 (2016)
9. Srivastava, M.K., Bhatia, S., Dwivedi, M., Pandey, K., Ragini, K.: Solar based E-Uniform for Soldiers. Int. J. Res. Appl. Sci. Eng. Technol. **8**(5), 728–733 (2020)
10. Bhatia, S., Gautam, D., Tomar, R., Bhandari, M., Chaubey, S.: IoT Enabled Smart Irrigation Techniques with Leaf Disease Detection. Available at SSRN 4157558, 14 Jul (2022)
11. https://nhm.gov.in/index1.php. Content Owned & Provided by National Health Mission Department of Health & Family Welfare, Ministry of Health & Family Welfare, Government of India
12. Bhatia, S., Malik, P., Kumar, D.: Face recognition door unlocking and monitoring system. In: Futuristic Sustainable Energy and Technology, pp. 455–466. CRC Press, 7 Jun (2022)
13. Vishwakarma, D.K., Kapoor, R.: Simple and intelligent system to recognize the expression of speech-disabled person. In: 2012 4th International Conference on Intelligent Human Computer Interaction (IHCI), pp. 1–6. IEEE, 27 Dec (2012).
14. Bhatia, S., Ahlawat, V., Verma, S.: An IoT Enabled Smart Garbage Management System for Effective Waste Utilization Strategy in Cities. Available at SSRN 4211518 (2022)
15. Jeet, V., Dhillon, H.S., Bhatia, S.: Radio frequency home appliance control based on head tracking and voice control for disabled person. In: 2015 Fifth International Conference on Communication Systems and Network Technologies, pp. 559–563. IEEE, 4 Apr 2015
16. Srinivasan, R., Kavita, R., Kavitha, M., Mallikarjuna, B., Bhatia, S., Agarwal, B., Ahlawat, V., Goel, A.: Python and Opencv for sign language recognition. In: 2023 International Conference

on Device Intelligence, Computing and Communication Technologies (DICCT), pp. 1–5. IEEE, 17 Mar (2023)
17. Cheok, M.J., Omar, Z., Jaward, M.H.: A review of hand gesture and sign language recognition techniques. Int. J. Mach. Learn. Cybern. **31**(10), 131–153 (2019)
18. Jia, Y., Shelhamer, E., Donahue, J., Karayev, S., Long, J., Girshick, R., Guadarrama, S., Darrell, T.C.: Convolutional architecture for fast feature embedding. In: Proceedings of the 22nd ACM International Conference on Multimedia, pp. 675–678 (2014)
19. Bhatia, S., Sharma, P., Verma, S., Ansari, M.T., Kumar, U., Singh, S.P.: Automatic Window Curtain System. Available at SSRN 4157347, 14 Jul (2022)

Performance Evaluation of Load Balancer in Storage Level Service Offering Applications

Maria Manuel Vianny, Rajat Bhardwaj, Vivek Bhardwaj, Vikrant Sharma, Virender, and S. Manikandan

Abstract Cloud computing is a world view appropriately characterized for IT contributions where data and resources are aggregated by web-based cloud administration organizations using planned hardware and packages, primarily based on the web. People could use at a reasonable cost. Combining resources may affect the ease with which those resources are accessed, which might result in an issue. Load control is the process of distributing network traffic among several servers. No server will be overburdened as a result of this. In order to increase user responsiveness, load regulation equitably distributes the tasks. Additionally, it improves client accessibility to projects and websites. This archive is being kept in order to better understand charge control. It is connected to other structures via correspondence bodies like the Internet. Load balancing is an important distributed computing space to stay away from work beyond the workload and provide equally important support. Different calculations are used to determine the complexity of the system. Our suggested technique selects

M. M. Vianny (✉)
Department of Artificial Intelligence and Data Science, Panimalar Engineering College, Chennai, Tamilnadu, India
e-mail: viannycse@gmail.com

R. Bhardwaj
Department of Computer Science and Engineering, ASET, Amity University, Bengaluru, Karnataka, India

V. Bhardwaj
School of Computer Science and Engineering, Manipal University Jaipur, Jaipur, India

V. Sharma
Department of Computer Science and Engineering, Graphic Era Hill University, Dehradun, India
e-mail: vsharma@gehu.ac.in

Virender
Chandigarh University, Mohali, Punjab, India
e-mail: virender.t1729@cumail.in

S. Manikandan
Department of Information Technology, E.G.S. Pillay Engineering College, Nagapattinam, Tamil Nadu, India

© The Author(s), under exclusive license to Springer Nature Singapore Pte Ltd. 2025

H. P. Singh et al. (eds.), *Recent Developments in Control, Automation and Power Engineering*, Lecture Notes in Electrical Engineering 1303,
https://doi.org/10.1007/978-981-96-0047-2_3

100 virtual computers and, with 92% accuracy, determines where an ideal storage facility is for use in real time.

Keywords Cloud computing · Load balancer · Service offering · Virtualization · Scheduling

1 Introduction

Furthermore, cloud load tuning with various load balancer types enables us to improve application execution and unwavering quality [1]. Reduced expenses and increased or decreased interest to satisfy demand are two benefits of distributing resources from common local sources [2]. A complicated IT workforce is needed to input, modify, and maintain data for regular load balancing agreements, which rely on data entry into devices. Better outcomes and excellent, unflappable quality may only be attained by sizable partnerships and organizations with significant IT spending plans; cloud-based basic suppliers, on the other hand, often do not permit their know-how to own their own content [3]. Load balancing planning only accounts for a little portion of the cost and may give team leaders and consistency. They are available to independent firms as well because they utilize necessary equipment.

Load balancing can handle the cloud like any other program, and they are also excellent for maximizing cloud load. Distributed computing can be an infinite and versatile framework in every asset unit of the organization [4]. All of the framework's assets must work together to meet customer needs. Distributed computing is the dissemination of various contributions such as capacity, servers, organizations, programming, knowledge, and research over the Internet in order to transfer faster progress, adapt more sources, and scale website cost reserves. Funds Open to all Countless customers can have a website or one at any time Visit web-based application. The ability of a web application to address these customer demands in a second becomes a single extreme opportunity for the program to reduce PC usage in a number of incidents [5].

Section 2 explains background study of load balancing. The suggested load balancing strategies addressed in Sect. 3. Section 4 covers the details of result and discussion analyzed with AWS ninja simulation. The article is concluded with a brief conclusion.

2 Background Study

With the heap balancer, you can isolate and distribute responsibility between at least two servers in the cloud. This allows you to organize your base to expand the movement, update the asset designation, and achieve negligible response time [6].

Suggested in all cases, regardless of whether you want at least one companion: By using a stack balancer under all circumstances [7].

We can address at least one of the accompanying needs, administration consistency guaranteed, high handling traffic, and planning Abrupt peaks in the application for adapting jobs are required in the configuration and information mode, e.g., two indistinguishable cloud servers [8]. Cloud load tuning is the way in which process resources and responsibilities are distributed across at least one server. The dispatch guarantees the most extreme execution with the shortest lead time. At least two servers, hard drives, organizational interfaces or other PC assets are isolated in order to enable better asset utilization and the expected response time for system tasks [9]. Cloud load adjusting is an interaction that circulates jobs and ascertains assets in a distributed computing climate. With load adjusting, associations can deal with the application or required responsibility by dispensing assets to various PCs, organizations, or servers [10]. The field of cloud computing has experienced significant growth. However, because of its importance, Intense scientific research has been done on the relationship between the cloud computing participants, i.e., cloud service provider and the cloud resource user. One of the explanations given, based on an examination of the available review literature, is the lack of accurate categorization among the many methods. This section provides a comprehensive overview of the relevant prior literature [11–15].

An overview of cloud computing load balancing algorithms was presented by Ghomi et al. [16, 17]. Some of the load balancing and scheduling algorithms that the researchers have categorized into different agents models. The algorithms are organized by kind, and their benefits and drawbacks are compared and contrasted. In the meanwhile, Milani et al. [18] using the results of the survey, the authors examined the state of the art in load balancing and divided the different load balancing methods into static, dynamic, and hybrid categories. They also explicitly submitted significant issues regarding load balancing. Quality Evaluation Criteria (QEC), Boolean operations in search strings were utilized to perform a thorough search and gather the most pertinent data from a number of publishing sources. However, only a small sample of QoS metrics—including response time, makespan, capacity, utilization of resources, relocation time, speed, and energy savings—were examined in the two studies [19, 20]. Several significant QoS indicators were not taken into account, including migration costs, service-level violations, measure of balancing, task refusal ratio, etc. In our work, we address this gap by methodically deciding which indicators to analyze [21] (Fig. 1).

3 Load Balancing Strategies

A functioning university website could completely fail during any statement of results due to the possibility of receiving strong inquiries. Cloud load balancers reduce response time to customer needs which significantly improve the rate of asset utilization. Improve the performance of execution time and maintain a robust framework.

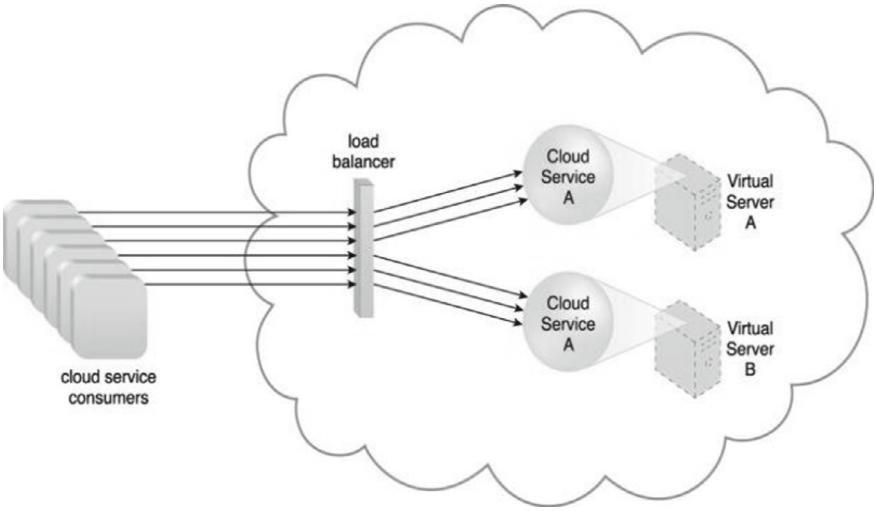

Fig. 1 Cloud service offering with load balancer

Increase the adaptability of the framework to respond to changes Heap Balancer. When a hub fails, responsibility can shift to a more dynamic one. The hub can be relocated when it is distributed to different servers or drives in the organization [23].

3.1 Objectives of Load Balancing

Load balancing is classified as follows:

- Manage and control traffic peaks on a server
- Reduce response times to user requests
- Increase the rate of resource utilization
- Significant improvement in performance
- Maintain system stability
- Increase the flexibility of the system.

Figure 2 show the objectives of load balancer.

3.1.1 Balancing System

The explanations behind this are as follows: Limited power consumption—Load tuning can reduce power consumption by limiting unnecessary liability to essential hubs or virtual machines [23] (Fig. 3; Table 1).

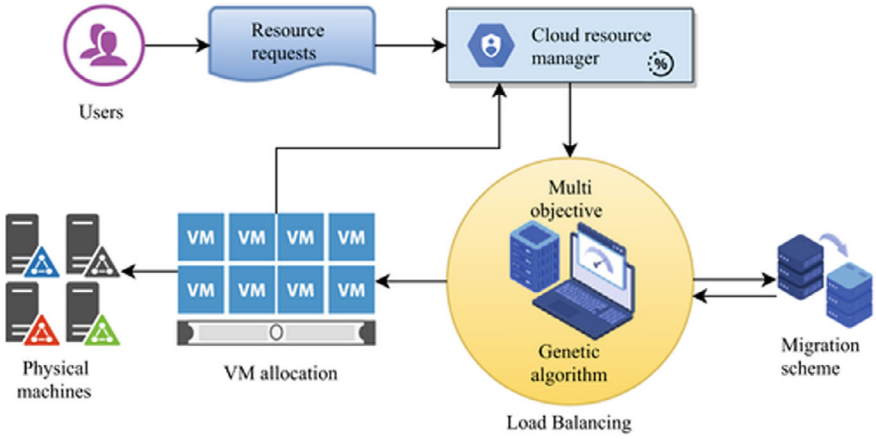

Fig. 2 Objectives of load balancer

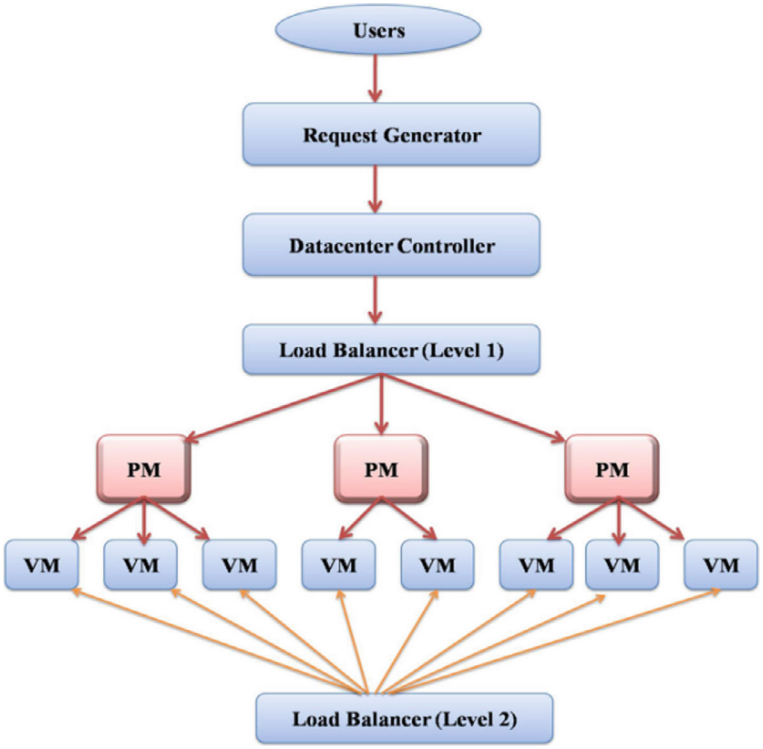

Fig. 3 Load balancer operations in VM level

Table 1 Load balancer inputs

Software defined network	Load balancing in server	Virtualization	Computing services
This enables you to arrange various task balances. Additionally, it facilitates the network's ability to act as storage for both version and virtualization	Utilizing a variety of load balancing approaches, it provides connectivity as well as content distribution services	In the virtual machine, maintain the real-world devices	For organizations adopting private cloud infrastructure, load balancing technologies to satisfy increasing load as well as application needs
Improved effectiveness	Maintain the Website Traffic Increased	Deal with an abrupt traffic increase	Versatility
Compared to its alternatives, load balancing techniques are simpler and more compact	Organizations can handle consumer applications more quickly and provide greater performance at a lower cost	Capability for handling traffic is offered through cloud balancing. It can be selected by managed and network peripherals with effective load balancing	It demonstrates adaptability, versatility, and traffic handling capacity

4 Operational-Level Service as Load Balancer

Load balancers are categorized as follows.

4.1 Static Load Balancing

With regards to stack adjusting, a heap adjusting approach is "static" assuming it disregards the circumstance of the framework. The circumstance of the framework includes sports just like the degree of heap of the distinct processors. The numbers, energy, and correspondence velocities of the CPUs are moreover known [18–20]. Static burden adjusting is for this reason deliberate to sign up for a given association of jobs with the on hand processors so one the exhibition paintings is limited. This lower may recollect statistics approximately the assignments to be scattered and a ordinary execution time. The advantage of static calculations is that without a doubt non-stop undertakings aren't hard to install and staggeringly proficient [18–21].

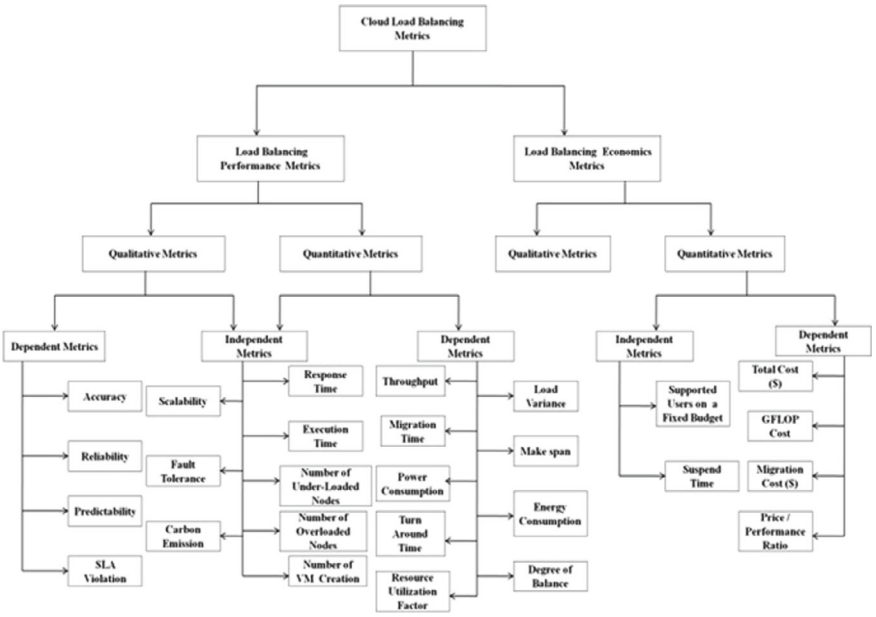

Fig. 4 Load balancer input and parameters

4.2 Load Balancing at Dynamic Level

Dynamic calculations take into account the current heap of each IT unit (also known as hubs) instead of static load tuning methods. Organizations could then move from an overload hub to a stacked hub for better handling, which are more difficult to build. Overall, they can produce amazing results, especially when execution times vary widely from message to message. Since you don't need a different center for task balancing, the powerful load balancing configuration can make it more adaptable [22]. It's a unique job when businesses have a processor be allocated according to their respective status. The dynamic task, on the other hand, alludes to the ability to rearrange assignments on a continuous premise as indicated by the framework, and it apparently involves a heap-fit calculation that requires exorbitant correspondence to arrive at its conclusions, the risk. to deviate from the general aim of the problem [23] (Fig. 4).

5 Experimental Result and Analysis

The proposed systems are evaluated based on cloud load balancer activities, features, and application specifications. The simulation results and values are shown in Fig. 5 (Table 2).

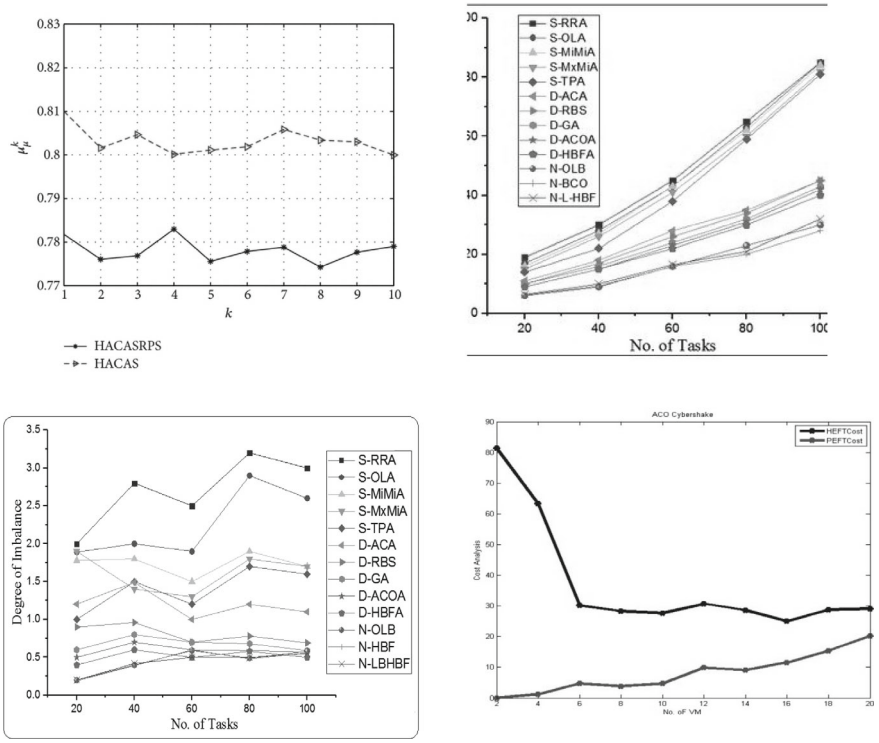

Fig. 5 Simulation results from AWS code Ninja representation

Table 2 Simulation results and test values

Virtual machines	Balancing loads	Weighted count	Each Hop count	% of Accuracy
5	2, 5, 10, 20	50, 50, 50, 50	10, 10, 10, 10	87, 88, 89, 88
10	2, 5, 10, 20	50, 50, 50, 50	10, 10, 10, 10	91, 92, 90, 92
20	2, 5, 10, 20	50, 50, 50, 50	10, 10, 10, 10	92, 92, 91, 93
50	2, 5, 10, 20	50, 50, 50, 50	10,10,10,10	89, 88, 90, 91
100	2, 5, 10, 20	50, 50, 50, 50	10, 10, 10, 10	92, 92, 91, 92

6 Conclusion

We examined the causes that lead to demand unbalancing in the cloud. The procedure of load balancing services and an abstract load balanced paradigm were extensively examined. Cloud computing is a strategy by which various customers can access various resources on the web according to their needs. However, there are huge barriers to distributed computing. Load regulation is a major obstacle in distributed computing. Numerous static and dynamic calculations are examined in this dossier.

The cloud is known to be heterogeneous in nature. Static calculations make it easier to demonstrate and screen the climate, but do not recreate the mixed idea of the cloud. The dynamic load adjustment calculations are difficult to show, but they all fit the different idea of cloudy conditions. Distributed computing adjusts expenses related to head reduction, further developing framework execution, framework increase, administration time, and governance. In order to propose more effective load balancing strategies for the future, essential QoS measurements, including movement duration, migration expense, energy use, service-level agreement violation, activity denial ratio, and level of balancing, are briefly mentioned in the studies. Our contributions are evaluating different load balancing effectiveness.

References

1. Khan, Z., Singh, R., Alam, J., Saxena, S.: Classification of load balancing conditions for parallel and distributed systems. Int. J. Comput. Sci. Issue **8**, 411–419 (2020)
2. Gulati, A., Chopra, R.K.: Dynamic round robin for load balancing in a cloud computing. Int. J. Comput. Sci. Mob. Comput. 274–278 (2019)
3. Afzal, S., Kavitha, G.: Load balancing in cloud computing—a hierarchical taxonomical classification. J. Cloud Comput. **8** (2019). Article number 22. https://doi.org/10.1186/s13677-019-0146-7
4. Kumawat, B., Kumawat, R.: A comparative study of load balancing algorithms in cloud computing environment using cloud analyst. IJESC **7**(3)
5. Joshi, S., Kumari, U.: Load balancing in cloud computing: challenges & issues. In: 2016 2nd International Conference on Contemporary Computing and Informatics. https://doi.org/10.1109/IC3I.2016.7917945 (2016)
6. Manikandan, S., Chinnadurai, M., Maria Manuel Vianny, D., Sivabalaselvamani, D.: Real time traffic flow prediction and ıntelligent traffic control from remote location for large-scale heterogeneous networking using TensorFlow. Int. J. Fut. Gener. Commun. Netw. **13**(1), 1006–1012 (2020). ISSN: 2233-7857
7. Manikandan, S., Chinnadurai, M.: Effective energy adaptive and consumption in wireless sensor network using distributed source coding and sampling techniques. Wirel. Pers. Commun. **118**, 1393–1404 (2021)
8. Yi, H., Jung, H., Bae, S.: Deep neural networks for traffic flow prediciton. In: IEEE Conference on BigComp 2017, pp. 328–331 (2017). ISBN: 971-5090-3015-6/17
9. Abadi, M., et al.: TensorFlow: Large-Scale Machine Learning on Heterogeneous Distributed Systems. arXiv:1603.04467v2 (2015)
10. Kato, N., et al.: The deep learning vision for heterogeneous network traffic control: proposal, challenges, and future perspective. IEEE Wirel. Commun. **24**(3), 146–153 (2017)
11. Ghomi, E.J., Rahmani, A.M., Qader, N.N.: Load-balancing algorithms in cloud computing: a survey. J. Netw. Comput. Appl. **88**, 50–71 (2017)
12. Javadpour, A., Sangaiah, A.K., Pinto, P., Ja'fari, F., Zhang, W., Abadi, A.M.H., Ahmadi, H.: An energy-optimized embedded load balancing using DVFS computing in cloud data centers. Comput. Commun. **197**, 255–266 (2023)
13. Abdi, M., Ginzburg, S., Lin, X.C., Faleiro, J., Chaudhry, G.I., Goiri, I., ... Fonseca, R.: Palette load balancing: locality hints for serverless functions. In: Proceedings of the Eighteenth European Conference on Computer Systems, pp. 365–380 (2023)
14. Shahid, M.A., Alam, M.M., Su'ud, M.M.: Performance evaluation of load-balancing algorithms with different service broker policies for cloud computing. Appl. Sci. **13**(3), 1586 (2023)

15. Latchoumi, T.P., Parthiban, L.: Quasi oppositional dragonfly algorithm for load balancing in cloud computing environment. Wirel. Pers. Commun. **122**(3), 2639–2656 (2022)
16. Jena, U.K., Das, P.K., Kabat, M.R.: Hybridization of meta-heuristic algorithm for load balancing in cloud computing environment. J. King Saud Univ.-Comput. Inf. Sci. **34**(6), 2332–2342 (2022)
17. Yu, D., Ma, Z., Wang, R.: Efficient smart grid load balancing via fog and cloud computing. Math. Probl. Eng. **2022**, 1–11 (2022)
18. Shakambhari Raj, J.S., Anantha Babu, S.: Smart cyberbullying detection with machine learning. In: Disruptive Technologies for Big Data and Cloud Applications: Proceedings of ICBDCC 2021, pp. 237–248. Springer Nature Singapore, Singapore (2022)
19. Babu, S.A., Basha, M.J., Arvind, K.S., Sivakumar, N.: Analysis of hate tweets using cbow-based optimization word embedding methods using deep neural networks. In: Proceedings of International Conference on Computational Intelligence and Data Engineering: ICCIDE 2022, vol. 163, p. 373. Springer Nature (2023)
20. Babu, S.A., James, J.W., Vedaiyan, R.: ARIMA based time series analysis: forecast COVID-19 most vaccinated process and active cases classify using probability distribution curve rates (ARIMAPDC). In: 2021 2nd International Conference on Smart Electronics and Communication (ICOSEC), pp. 546–551. IEEE (2021)
21. Angurala, M., Bala, M., Bamber, S.S.: A novel technique for energy replenishment and load balancing in wireless sensor networks. Optik **248**, 168136 (2021)
22. Jarraya, M., Elloumi, S.: Load balancing scheduling algorithms for virtual computing laboratories in a desktop-as-a-service cloud computing services. Comput. Commun. **192**, 343–354 (2022)
23. Shafiq, D.A., Jhanjhi, N.Z., Abdullah, A.: Load balancing techniques in cloud computing environment: a review. J. King Saud Univ.-Comput. Inf. Sci. **34**(7), 3910–3933 (2022)

A Comparative Study of Poisson Algorithm and Other Surface Reconstruction Techniques for 3D Modeling from 2D Images

Vaibhav Sharma, Dipin Garg, Rohit Sharma, and Palak Girdhar

Abstract Three-dimensional modeling, which involves creating representations of objects and surfaces, is commonly referred to as 3D modeling. In this study, a new method for generating 3D models from color images using point cloud generation is presented. In a three-dimensional context, a point cloud is a set of individual points. By using surface reconstruction algorithms, we demonstrate the ability to generate mesh structures from point clouds. This technique has the potential to improve the efficiency and accuracy of 3D modeling methods. Furthermore, this research includes a comparative assessment of various surface reconstruction algorithms and their performance in contrast to the established Poisson algorithm.

Keywords 3D modeling · Point clouds · Surface reconstruction · Poisson

1 Introduction

A 3D model made from multiple polygons is structurally sustained by a mesh in three dimensions. The mesh outlines the shape by utilizing reference points on the X, Y, and Z plane. The vertices, edges, and faces that constitute an individual polygon mesh is what provides a 3D object its shape. Because it makes the rendering process more straightforward, the faces are usually composed of convex polygons like triangles, quadrilateral, although they can also consist of concave polygons or polygons with holes.

Generally, 3D data can be exhibited in several styles, including depth images, volumetric grids, point clouds, meshes. Point cloud modeling is a frequently employed technique which preserve the unique geometric information in a 3D space with no division. In this strategy, we were able to obtain a color photograph and transform it into 3D meshes through the point cloud generation.

V. Sharma (✉) · D. Garg · R. Sharma · P. Girdhar
Bhagwan Parshuram Institute of Technology, New Delhi, India

© The Author(s), under exclusive license to Springer Nature Singapore Pte Ltd. 2025

H. P. Singh et al. (eds.), *Recent Developments in Control, Automation and Power Engineering*, Lecture Notes in Electrical Engineering 1303,
https://doi.org/10.1007/978-981-96-0047-2_4

First, we used an image to convert into a point cloud of 1K points using a pretrained model, then upsample it to 4K points. The generated point cloud goes through a further process of vertex normal estimation. Further, 3D mesh is generated from point clouds (aim of this research paper) using Poisson surface reconstruction. We tried and compared different surface reconstruction algorithms like alpha shapes, ball pivoting, SDF regression (Marching Cubes), and Poisson, where Poisson found to be the best among all.

2 Literature Survey

The technique used to convert 2D images to point clouds in Alex Nichol's academic work is "Point-E: A System for Generating 3D Point Clouds from Complex Prompts." To create 3D RGB point clouds, this technique employs point cloud diffusion, and it is a hierarchy-based method. By initially generating 1000 points utilizing a large base model and subsequently increasing the number to 4000 points through the utilization of a smaller upsampling model.

This technique efficiently creates point clouds from a color image by utilizing a GLIDE model with 3 billion parameters, which has been fine-tuned using 3D models generated from the Point-E dataset. It utilizes a restrictive, permutation invariant diffusion model to generate point cloud with 1024 points. Furthermore, a smaller model is also employed, on the base point cloud to enhance the resolution of these point clouds.

Further, our survey delved into the importance of vertex normal estimation as it is necessary for generating 3D meshes from point clouds. Accurate surface orientation determination is crucial for reconstructing the 3D shape of objects using point clouds. By calculating the normal for each distinct point in the point cloud, it can be as certain as the orientation of the surfaces and reconstruct the 3D shape of the item. Normals, being vectors perpendicular to surfaces, play a vital role in producing watertight meshes.

In [1], Principal Component Analysis (PCA) method is used for vertex normal estimation. PCA is a method of statistics that is commonly used for calculating the normal of a set of points by exploring its covariance matrix. The eigenvectors in the covariance matrix correspond to the main directions of the point cloud, and the eigenvector with the lowest eigenvalue matches the normal direction.

Due to its capability to process big point clouds quickly and its capacity to be used in real-time applications, this method is highly advantageous. Moreover, the PCA approach can be applied to determine the normal of a triangular mesh by carrying out the PCA of the points around the vertices.

The point cloud that was normal estimated further goes through a surface reconstruction algorithm to generate a point cloud. There are several types of surface reconstruction algorithms such as ball pivoting, alpha shapes, SDF regression (Marching Cubes), and Poisson.

2.1 Alpha Shapes

Alpha Shapes [2] is a technique used to rebuild the given surface from a collection of data points. The common approach is to obtain a point cloud and extract the surface as a polygon mesh. It shows that surfaces that are either bounded or unbounded can be successfully constructed even when alpha shapes are complicated internal structures with generalized polytopes. These surfaces accurately display the shapes that are perceivable from outside.

2.2 Ball Pivoting

In [3], ball pivoting algorithm is used to build a triangle mesh from a given set of points. The points typically come from a series of range scans which measure the surface of an object. The main idea behind the BPA is straightforward: If a ball of a specific size can touch three points without any other points being in the way, then these three points will form a triangle. The process begins with a seed triangle and the ball which will then pivot around the edge of the triangle, while in contact with the endpoints, until it bumps into another point and forms a new triangle. This continues until each reachable edge has been tried, then the cycle begins again until all points have been included with a new seed triangle. This process can be repeated with a bigger ball in case of uneven sampling densities.

2.3 SDF Regression

In [4], it takes SDF regression model in utilization for converting point clouds into meshes. The approach involves using a regression model to forecast the SDF of the target based on its point cloud data. Subsequently, the generated SDF is processed using the marching cubes algorithm [5] to extract a mesh representation.

2.4 Poisson SRA (Surface Reconstruction Algorithm)

A technique [6] used for creating a 3D shape from an unordered group of 3D points has been proposed. The system is constructed on the Poisson equation, which explains the arrangement of a scalar quantity across an area in terms of the gradient of the field and its origins and terminations. The PSR algorithm employs the Poisson equation to construct a 3D surface that most accurately matches the provided point cloud.

Compared to alpha shapes, ball pivoting, and SDF regression, PSR is seen to be the superior algorithm due to its ability to generate high-quality reconstructions.

It manages unstructured data, takes on large datasets, is resilient against noise and outliers, processes multiple regions and closed surfaces, and reconstructs surfaces with holes and indentations.

3 Materials Used

A picture is a portrayal of something, for example, a person, object, or scene. It can either be caught or produced by a camera, scanner, or programming, and it can be put away in different configurations, including JPEG, PNG, and GIF. Pictures can likewise be sorted as indicated by their resolution. An image with high resolution has more pixels and thus provides more detail than one with low resolution. Resolution is regularly gauged in pixels per inch (PPI) or dots per inch (DPI).

3.1 Bitmap Image

A bitmap image, also referred to as a raster image, constitute a grid of tiny blocks called pixels. Every pixel is allocated a higher resolution image having more pixels. These types of images are mainly used for photographs and illustrations that need to be printed, like books and magazines.

In contrast to other types of images, a vector picture is composed of numerical equations that define its shapes, lines, and colors. They are specified by their starting and finishing points, as well as the equations that link them. This means that vector images can be enlarged or reduced without a drop in quality. They are regularly used for logos, illustrations, and design elements that must be resized frequently, such as symbols and graphs.

3.2 RGB Image

A color image also known as (RGB) image has intensity information that is associated with the three primary colors (RGB) that is, red, blue, and green. We pick these three colors because the cone cells in the human eye, which are responsible for color vision, can detect red, blue, and green light.

In our approach, we are using a raster-colored image to convert it into a 3D mesh.

3.3 PLY File

PLY format represents each side of a 3D figure by a group of vertices and their associated customary vectors. The file structure is a header followed by data outlining the 3D model. The header communicates information about the layout of the file and the type of data that ensues. It is made up of numerous keywords that identify the components and properties of the 3D object.

The vertex data section of the PLY file involves the coordinates of every vertex in the 3D model. Every line of this section contains three or more values indicating the (x, y, z) coordinates of a vertex, along with additional details such as color or other elements if desired. The normal vector has a certain spot in the grid, as well as a certain color. The resolution of the image is based on the number of pixels in the grid, which is a unit vector which is perpendicular to the face and is used to generate lighting and shading effects.

4 Method Used

See Fig. 1.

4.1 Input Image

At first, a colored image is taken from the user to pass it on to the large pretrained model for point cloud generation of low resolution.

4.2 Low-Resolution Point Cloud

A low-resolution point cloud (LRPC) is a three-dimensional representation of an entity or environment, composed of a cluster of points that are placed over the object or scene's surface. The resolution of a point cloud is based on the number of points it contains, with a low-resolution point cloud having fewer points, while a higher resolution point cloud has more points.

These low-resolution point clouds are regularly utilized in 3D modeling and mapping projects. For 3D modeling, a low-resolution point cloud can be the point of

Fig. 1 Flowchart

commencement for the development of a comprehensive 3D model of the scene or item. This is done by either manually or automatically inserting more points to the cloud to raise its resolution.

In mapping applications, low-resolution point clouds are used to make 3D maps of external environments, such as terrain and buildings. These maps can be utilized for various purposes, including navigation and planning. Low-resolution point clouds can also be used to create 3D models of indoor environments.

4.3 Point Cloud Upsampler

For creating point clouds utilizing diffusion, RGB hues are integrated with each point in the cloud, which is an extension of the framework by [7]. A point cloud can be described as a tensor with a dimension of $P \times 6$, where P represents the total points. Within this tensor, each point is represented by its (x, y, z) coordinates and (R, G, B) colors. All points and their colors are standardized to fall within -1 to 1. The process of generating these tensors involves starting with random irregularities of size $P \times 6$ and constantly refining it through diffusion-based denoising techniques.

When it comes to image diffusion models, a hierarchical structure is usually adopted to attain the best results. In this approach, the initial output is produced by a base model of lower resolution, and then it is upsampled by a different model [8–11]. To generate a point cloud, the method utilized is to initially create 1024 points using a larger foundational model and then increase the count to 4024 points using a support model. It is important to note that as the number of points increases, so does the computational requirement, making it four times costlier to generate 4024 points compared to 1024 points for a constant model size. The upsampler used in this process has the same framework as the foundation model but includes additional tokens for the foundational point cloud. To reach 4024 points, the upsampler takes 1024 points as input and creates an additional 3000 points, which are then combined with the foundational point cloud. To distinguish between conditioning information and new points, the extracted points are passed through a different linear embedding layer, eliminating the need for positional embeddings.

4.4 Point Cloud Generation

Initially, the point cloud is generally exported in a polygon file (.ply) format, which is then applied to generate 3D surfaces using surface reconstruction algorithms (Fig. 2).

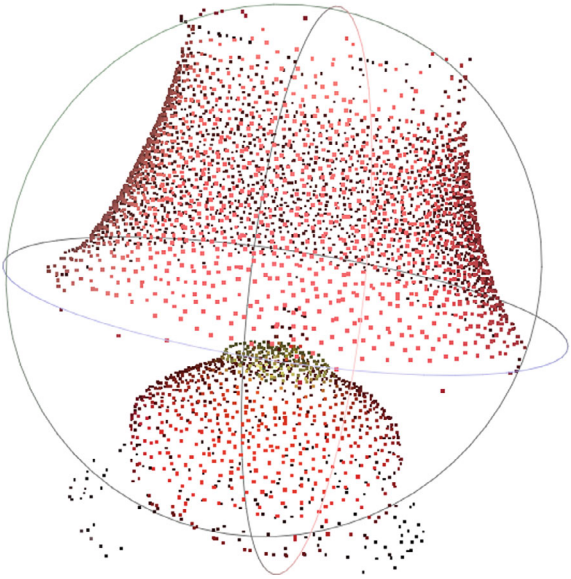

Fig. 2 Generated point cloud of lamp

4.5 Vertex Normal Estimation

A function is employed to determine the normal at each distinct point in the point cloud. This operation identifies the nearby points and applies covariance analysis to find the main axis of the neighboring Cartesian points. The point's nearby region (which is also referred to as k-neighborhood) is used to decide the normal at a point. The two main variables RADIUS = 0.1 and MAXN = 30 are used to specify the search radius and maximum nearest neighbor. For cutting down computation time, only the closest 30 neighbors are considered, and the search radius is fixed at 10 cm (Fig. 3).

The normal estimated point cloud is then passed to the surface reconstruction algorithm for the mesh generation.

4.6 Poisson Surface Reconstruction

Instead of rendering generated point clouds directly, this approach opted to take the less complicated approach for converting them into 3D meshes and render them. Creating meshes from point clouds can be a complex task, often resulting in issues such as cavity, deviation, or other forms of irregularities that further complicate the process. To transform point clouds into meshes, we employed the surface reconstruction algorithm, which enables us to generate meshes based on the given point cloud data. Through analysis, we determined that Poisson SRA is the most suitable

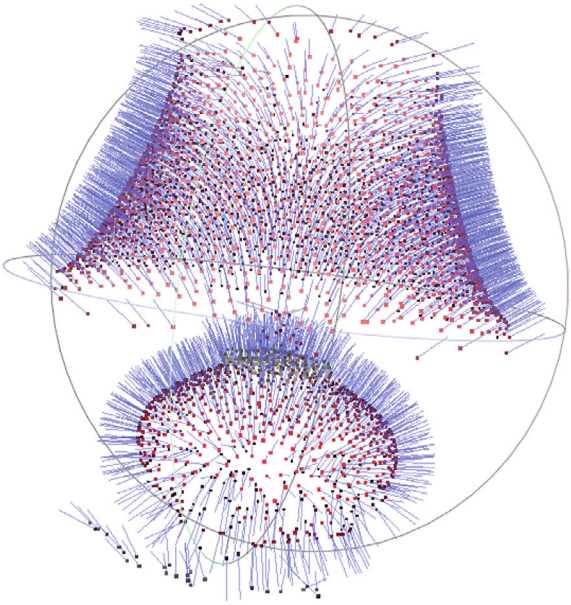

Fig. 3 Normal estimated point cloud

algorithm among the major surface reconstruction methods like alpha shapes, ball pivoting, SDF regression, and Poisson [6]. Additionally, in our approach, we assigned colors to each vertex of the mesh by matching them with the closest point's color in the original point cloud.

4.7 Mesh Generation

The 3D mesh that was produced with the help of Poisson surface reconstruction algorithm used on normal estimated point clouds is then exported (Fig. 4).

5 Comparison to Other Methods

Generating a 3D model of a scene or item can be done also through RGB-D imaging (also known as 3D modeling from color and depth images) which involves a few stages. Firstly, in this method, we acquire the color and depth image via a device such as a Kinect camera or a stereo camera. Afterward, the color and depth images must be aligned so that the pixels in each image represent the same 3D point. To generate a point cloud, which are 3D points in space replicating the item or scene, the depth image is used. Following that, the point cloud is then utilized to reconstruct the surface of the object or scene through methods such as Marching Cubes or Poisson

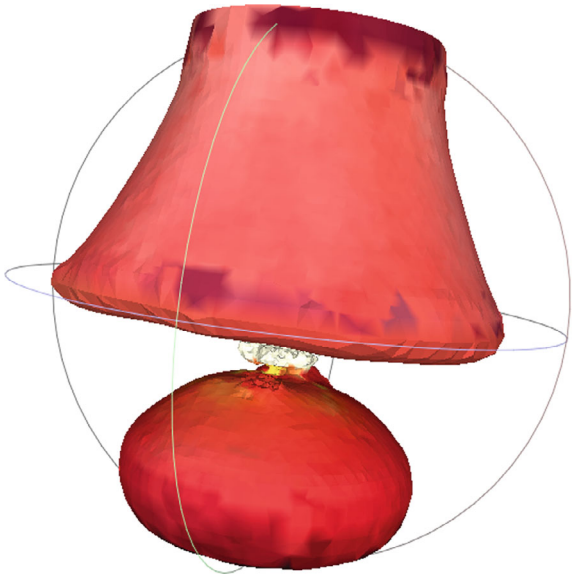

Fig. 4. 3D lamp generated from Poisson surface reconstruction

Surface Reconstruction (PSR). Finally, once the mesh is created, it is then tweaked and adjusted to minimize the number of vertices and enhance the general standard of the 3D model.

However, this method makes it possible to gather precise data concerning the depth and color of real-world objects, which can be employed for a variety range of purposes, such as VR and AR (virtual and augmented reality), robotics, archeology, and more. Still, 3D modeling from deep learning considered to be better approach because of its ability to handle more complicated scenarios, obstructions, variations in illumination, objects without texture, partial detections, ample datasets, and images of high resolution with more precision.

6 Result

In this research, numerous comparisons were conducted to evaluate the performance and effectiveness of different algorithms.

Lamp generated from a point cloud with different algorithms.

6.1 Comparison Between Different Algorithms on a 3D Lamp

See Table 1, Figs. 5 and 6.

Table 1 Surface reconstruction algorithm comparison

Algorithm	Size	Time	Vertices	Faces
SDF	21.2	577.9	620	940
Alpha shapes	158	79.8	2236	3676
Ball pivoting	297	69.21	4096	7303
Poisson	819	1077	10,920	21,690

The unit of size taken is Kilobytes (Kb)
The unit of time taken is in Milliseconds (ms)

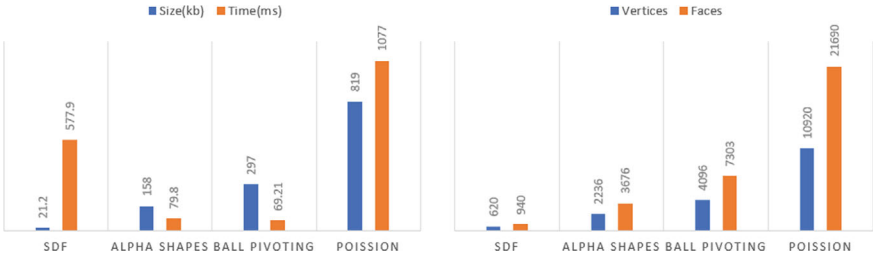

Fig. 5 Graphical comparison of different algorithms

6.2 Comparison Between Different Algorithms on Multiple Objects

Different objects including Vase, Laptop, and Tree images are used to generate meshes with different algorithms (Fig. 7).

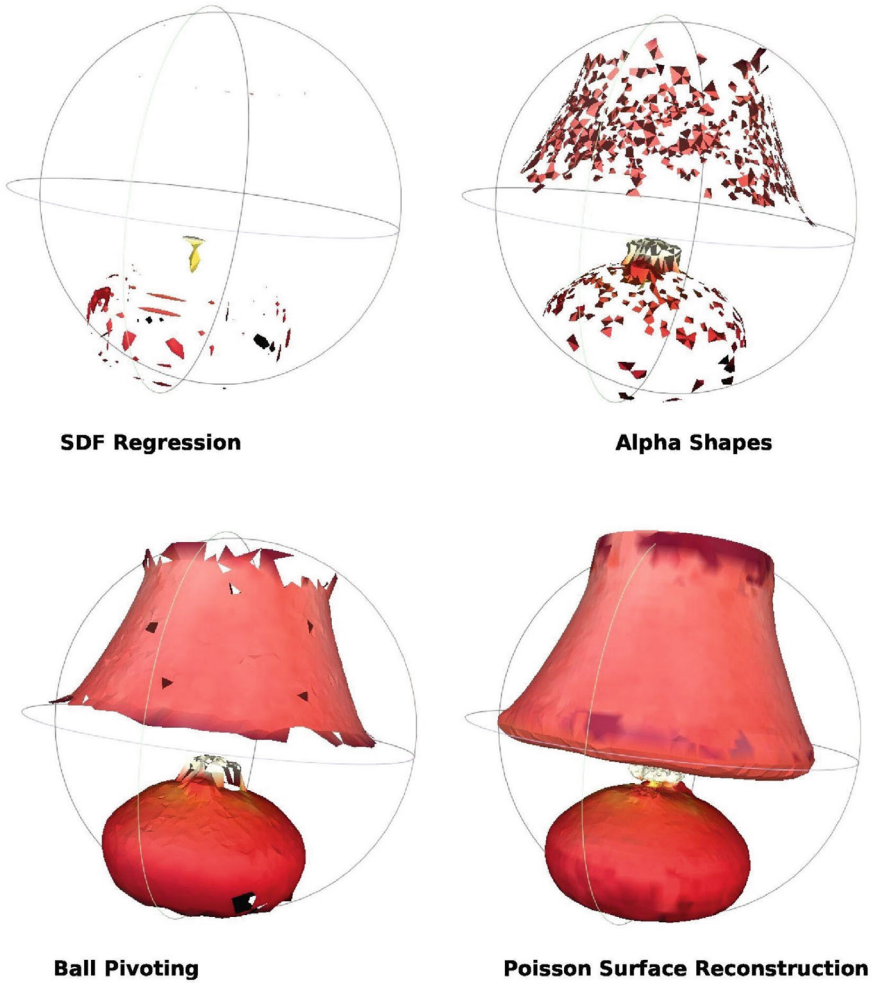

Fig. 6 Mesh generated with different SRA

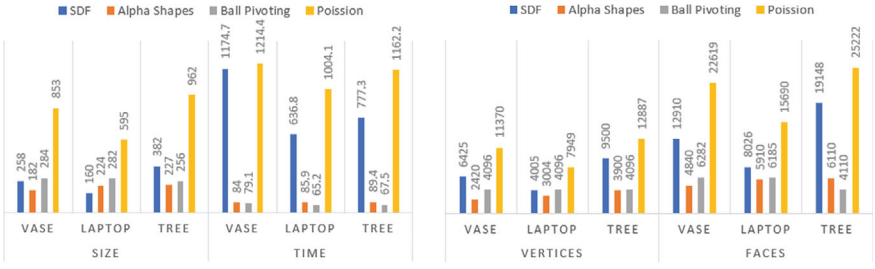

Fig. 7 Graphical comparison between SRAs on different objects

7 Conclusion

In conclusion, our research employed the Poisson algorithm to construct meshes and then compared their output with the SDF, alpha shapes, and ball pivoting techniques. The outcomes of our study strongly indicate that the meshes generated from the Poisson algorithm are highly efficient and can generate a wide range of intricate 3D models. Therefore, our findings present a compelling case for considering the Poisson algorithm as an excellent starting point for future endeavors in image-to-3D modeling.

References

1. Sanchez, J., Denis, F., Coeurjolly, D., Dupont, F., Trassoudaine, L., Checchin, P.: Robust Normal Vector Estimation in 3D Point Clouds through Iterative Principal Component Analysis. Elsevier (2020)
2. Guo, B., Menon, J., Willette, B.: Surface reconstruction using alpha shapes. In: Computer Graphics Forum (2008)
3. Bernardini, F., Mittleman, J., Rushmeier, H., Silva, C., Taubin, G.: The ball-pivoting algorithm for surface reconstruction. IEEE Trans. Visual. Comput. Graph. (1999)
4. Nichol, A., Jun, H., Dhariwal, P., Mishkin, P., Chen, M.: Point·E: A System for Generating 3D Point Clouds from Complex Prompts (2022)
5. Lorensen, W., Cline, H.: Marching cubes: a high resolution 3D surface construction algorithm. In: ACM SIGGRAPH Computer Graphics (1987)
6. Kazhdan, M., Bolitho, M., Hoppe, H.: Poisson surface reconstruction. In: Eurographics Symposium on Geometry Processing (2006)
7. Zhou, L., Du, Y., Wu, J.: 3D Shape Generation and Completion Through Point-Voxel Diffusion. arXiv:2104.03670 (2021)
8. Rombach, R., Blattmann, A., Lorenz, D., Esser, P., Ommer, B.:. High-Resolution Image Synthesis with Latent Diffusion Models. arXiv:2112.10752 (2021)
9. Saharia, C., Ho, J., Chan, W., Salimans, T., Fleet, D.J., Norouzi, M.: Image Super-Resolution Via Iterative Refinement. arXiv:2104.07636 (2021)
10. Ho, J., Saharia, C., Chan, W., Fleet, D.J., Norouzi, M., Salimans, T.: Cascaded Diffusion Models for High Fidelity Image Generation. arXiv:2106.15282 (2021)
11. Nichol, A. and Dhariwal, P (2021). Improved Denoising Diffusion Probabilistic Models. arXiv: 2102.09672 (2021)

Optimal Scheduling of Vehicle-to-Grid Power Exchange Using Hybrid BPSO and GSA Approach

Vikas Kumar Badhan and Shelly Vadhera

Abstract Electric vehicles (EVs) are set to revolutionize the transportation industry due to their benefits and incentives. Because of their onboard battery power, they have the distinct feature of being a distributed energy storage device. This function enables them to offer essential ancillary services such as load variance minimization on grid via vehicle-to-grid (V2G) operation. However, issues such as unsure EV availability and constantly evolving state of charge (SOC) preempted practical V2G implementation. By investigating the stochastic nature of EV grid connection, this article suggests a scheduling approach for V2G power exchange which tackles these obstacles. In this article, we propose a novel method for optimizing V2G power exchange scheduling using binary particle swarm optimization with Gravitational Search Algorithm. This hybrid optimization algorithm of BPSO and GSA has a faster convergence rate than either PSO or GSA alone, making it a much efficient method for optimizing V2G power exchange scheduling. As per statistical analysis of data, the proposed V2G scheduling approach might substantially flatter load profile. In order to concern the results and validate the recommended strategy, contrasts were made among the conductivity of suggested method's best-case situation and greatest performance of methods proposed in previous work on an associated subject.

Keywords Electric vehicle · Vehicle-to-grid · Binary particle swarm optimization · Gravitational search algorithm

V. K. Badhan (✉) · S. Vadhera
Department of Electrical Engineering, NIT Kurukshetra, Kurukshetra, India
e-mail: vikas_32114323@nitkkr.ac.in

S. Vadhera
e-mail: shelly_vadhera@nitkkr.ac.in

© The Author(s), under exclusive license to Springer Nature Singapore Pte Ltd. 2025

H. P. Singh et al. (eds.), *Recent Developments in Control, Automation and Power Engineering*, Lecture Notes in Electrical Engineering 1303,
https://doi.org/10.1007/978-981-96-0047-2_5

1 Introduction

Environmental advantages are highlighted when contrasting electric vehicles (EVs) to conventional gasoline-powered automobiles. They enhanced energy stability whereas lowering air pollution and emissions of greenhouse gases by reducing oil imports.

According to projections, EV market penetration will skyrocket in the coming years. The limited onboard battery backup and electric driving scale of plug-in EVs are major concerns [1]. A vehicle movement optimization method along with battery advances in technology are required for vehicle's battery to utilize its stored energy as effectively as possible [2].

As traditional gasoline car invention has nearly reached the saturation point, the focus has shifted on effectiveness. Several optimization algorithms are being examined for rapid driving on various routes. Several techniques have been developed for HEVs to efficiently control energy flow between gasoline source and batteries. This raises the issue whether or not plug-in electric vehicles might represent an identical ideal driving style, incorporating into consideration how vehicle movement affects SOC of batteries [3]. SOC is defined as the percentage of remaining battery charge instead of a full charge. One requirement for establishing optimal control is to have an accurate SOC value. Regardless of the fact that it is unorganized, the SOC control approach for EVs has been investigated in a few works [4].

The factor that drives features all through a trip, such as battery SOC, vehicle acceleration, electrical consumption of key components, drivers' conduct, etc., has an important effect on the range of a plug-in EV. Outside parameters like road condition, slope, rolling resistance, and aerodynamics also influence distance while driving [5]. The articles describe systems for anticipating, sustaining, or increasing the driving scale. Some articles describe an optimization approach for finding the best solution to a set of problems that considers batteries autonomy, ergonomics of driving indicators, and journey time [6]. Also, many researchers provide an assessment of the driving situation. While certain techniques monitor operations in real time, others depend on prior forecasts of future driving conditions. In paper [7], authors describe a few specifically designed operating modes for various purposes.

This article is organized as follows: Hybrid BPSO-GSA is depicted in Sect. 2. Objective function and input data are shown in Sect. 3, Sect. 4, respectively. Section 5 contains summary of modeling results for different scenarios. In the final section, this article offers the conclusion.

2 Hybrid BPSO-GSA

PSO-HPGSA had been introduced to maximize the benefits of PSO social optimization algorithm called HPSO-GSA integrates two widely used optimization methods GSA and BPSO. The search field in BPSO is specified as a collection of binary strings.

Every particle within the swarm reflects a potential solution, and each one modifies its speed and place in area of search on the basis of its own ideal circumstance and best location for the entire swarm [8]. BPSO is able to deal with discrete optimization issues thanks to binary representation of solution. On the other hand, the inspiration for GSA came from law of gravity and motion of celestial bodies in space [9]. Every solution in GSA is viewed as a celestial body that pulls on other solutions through gravity. The mass and separation among solutions produce the force and greater mass regions that relate to superior solutions. By employing BPSO to produce binary solutions and GSA to optimize continuous variables of solution, HBPSO-GSA integrates the advantages of BPSO and GSA. Binary elements are modified employing traditional BPSO technique, while the retained constant is modified using gravitational effect as estimated by GSA coordination and the exploratory capabilities of GSA. Over all, the BPSO-GSA algorithm can be better optimization technique for V2G power exchange, as it can effectively handle the complex and dynamic nature of the optimization problem and provide more accurate and robust solutions [10].

3 Objective Function

The goal of the V2G optimization approach in this study is to decrease grid load variability by properly using the charging and discharging power of grid-linked EVs. This may be accomplished by completing the valley filling (when going to charge) and peak demand shaving (while discharging) procedures. To carry out these operations, a targeted load (Pt) is set, around which the algorithm will try to flatter the load profile. When the targeted load is exceeded, the algorithm will direct all accessible EVs to deliver power into the network. When the true load (pl) falls below the intended load, the EVs are commanded to draw electricity from the power network by charging the internal batteries.

When the true load matches the targeted load, no electricity is transferred between the EV and the power network. This goal function is stated mathematically by Eq. (1)

$$\min \Delta p = pt(t) - pl(t) - \mathrm{PEV}(t) \tag{1}$$

$$\mathrm{PEV}(t) = \sum_{i=1}^{N} \mathrm{pev}^i(t) \tag{2}$$

In Eq. (1), Δp is the change in grid load relative to the goal load, and PEV is the power shared by all ($N = 2200$) EVs, as shown in Eq. (2).whereas the output contributed by the ith vehicle is referred to as pev^i.

By dissolving Eq. (1) on the basis of just one vehicle, we obtain

$$\min \ \Delta p = \frac{pt(t)}{K} - \frac{pl(t)}{K} - \mathrm{pev}^i(t) \tag{3}$$

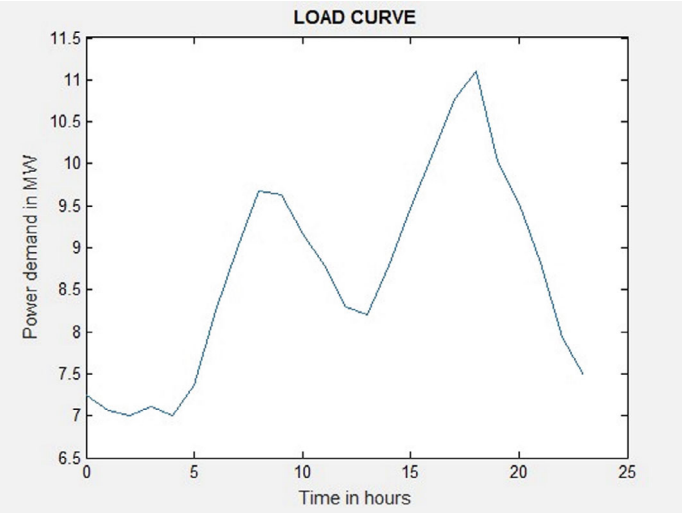

Fig. 1 Load curve

K is a term in Eq. (3) that simply represents the total population of EVs that are grid-tied while meeting the SOC limit [11, 12].

4 Input Data

4.1 Load Curve

For modeling purposes, a regional grid's 24-h load curve, as shown in Fig. 1, was created. In the actual world, the V2G power exchange could be scheduled in real time or a day in advance using load curve forecasting [13].

4.2 EV Availability

Only when EVs are linked to the grid, the V2G power exchange is feasible. Because to their mobility and stochastic nature, each EV's accessibility, however, cannot be guaranteed.

For the computational analysis of proposed V2G approach, it is feasible to develop a preliminary collectively driving concept for EVs, as shown in Fig. 2. Assume that there are V2G bidirectional chargers available in parking lots in an ordinary town with about 2000 EVs. Residence and commercial parking lots are two categories into which parking lots are divided. Mostly EVs are available in residential parking lots

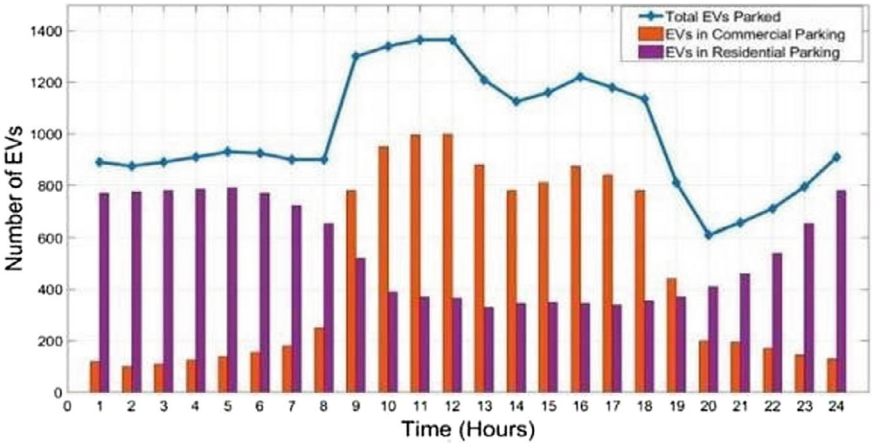

Fig. 2 EV grid connection probability

Table 1 Input data of EV designs for computation

EV design	Battery capacity (kWh)	Power exchange rate (KW)
Model 1 (Tesla Model S)	75	100
Model (Chevrolet Bolt EV)	66	150
Model 3 (Volkswagen ID.4)	82	150
Model 4 (Hyundai Kona Electric)	64	150

at night time and until six in the early hours of the day. After that, EVs in residential parking declines as people leave for work and other locations. In contrast to common belief, between the hours of 9:00 am and 6:00 pm, commercial parking spaces have higher concentration of EVs but are rarely occupied at night [13].

4.3 EV Specification

In this methodology's simulation analysis, four distinct EV models are used. Their specifications, which include the battery's capacity and power exchange rate, are listed in Table 1.

4.4 EV SOC Limit

The highest as well as lowest SOC values have been set at 90% and 50%, respectively, to account for overcharging problems and avoid potential battery pack destruction.

Enable discharging only if SOC > SOCmin.
Enable charging only if SOC < SOCmax.

5 Results and Discussion

The suggested V2G algorithm-achieved improved load curves are shown beside the actual load curve. The chart in the illustration probably depicts two different curves, one of which represents the actual load curve and the other the optimal load curve attained by implementing the hybrid BPSO-GSA. This hybrid optimization algorithm of BPSO and GSA has a faster convergence rate than either PSO or GSA alone, making it a much efficient method for optimizing V2G power exchange scheduling.

The target load in the best situation depicted in Fig. 3 was set at 8 MW, and the V2G method is effective in maintaining this goal load all day. This indicates that the method was successful in controlling the energy usage and redistribution because the optimized load curve closely resembled the goal load curve. Minimization of load variations on the grid improves overall stability and efficiency of the electrical system, leading to reduced power disruptions and optimized energy utilization. By minimizing load variations, grid operators can accurately forecast future demand trends and make informed decisions regarding the expansion, upgrade, or maintenance of grid infrastructure. This promotes a more reliable and resilient power system, ensuring it can meet the evolving needs of consumers.

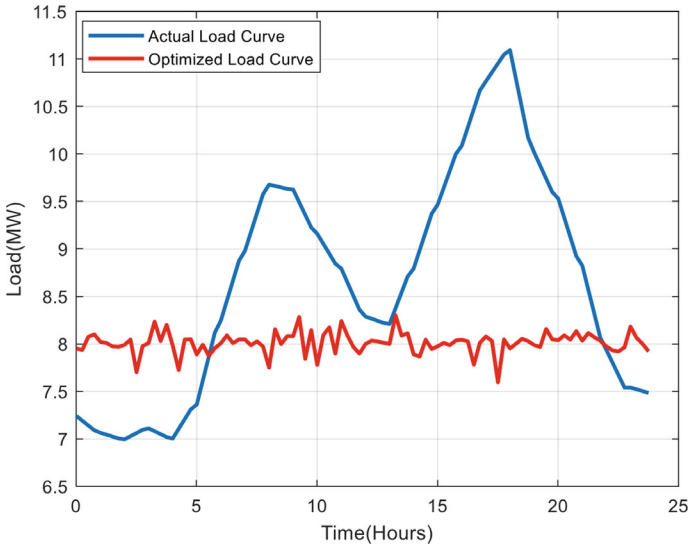

Fig. 3 Optimized load curve with targeted load 8 MW

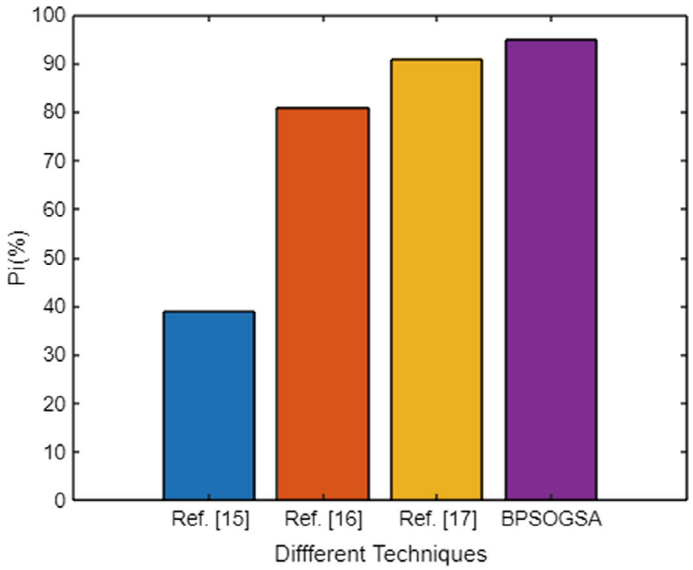

Fig. 4 Comparison of the suggested V2G algorithm

All things considered, Fig. 3 shows how well the V2G algorithms optimized the load curve to reach a certain target load. It draws attention to the potential advantages of these technology in improving energy efficiency and sustainability and stresses the significance of ongoing research and development in this field.

A suggested optimization technique is shown in Fig. 4 along with a comparison of the peak and valley load variations percentage improvements before and after optimization.

The peak and valley prior to and after optimization, accordingly, are the parameters utilized to characterize this enhancement and Pi is the comparison factor. A graph or chart that displays the improvement in peak and valley load differences as a percentage over a given time period is most usually included in the Fig. 4. Other details may also be included, such as the precise algorithm that was utilized, the desired load or energy consumption objective, as well as any pertinent data points or annotations. Comparisons were made between the production of the suggested technique best-case phase and the accurate performance of approach suggested in earlier work on a related topic in order to concern the outcomes and verified the suggested approach [14–17]. Finally, Fig. 4 illustrates how well the suggested optimization approach works to lessen the disparity between peak and valley loads. This measure can save costs and advance sustainability.

6 Conclusion

An optimal scheduling method for V2G action is suggested in this study to reduce load fluctuations in the power grid around a certain targeted load. The accessibility of EVs for V2G function, the regularly shifting SOC of EV batteries, and other issues make the efficient deployment of V2G power exchange difficult. Through examining the unpredictable nature of EV grid connection and continuously shifting the variables at certain intervals, the proposed optimization technique addresses these issues. By assessing the outcomes of all cases, it is shown that the suggested technique may considerably and successfully flatten the load curve.

Comparisons were made between the production of the suggested technique best-case phase and the accurate performance of approach suggested in earlier work on a related topic in order to concern the outcomes and validate the suggested approach.

References

1. Nazaripouya, H., Wang, B., Black, D.: Electric vehicles and climate change: additional contribution and improved economic justification. IEEE Electrif. Mag. **7**(2), 33–39 (2019)
2. Yilmaz, M., Krein, P.T.: Review of the impact of vehicle-to-grid technologies on distribution systems and utility interfaces. IEEE Trans. Power Electron. **28**(12), 5673–5689 (2013)
3. Richardson, D.B.: Electric vehicles and the electric grid: a review of modeling approaches, impacts, and renewable energy integration. Renew. Sustain. Energy Rev. **19**, 247–254 (2013)
4. Liu, H., Qi, J., Wang, J., et al.: EV dispatch control for supplementary frequency regulation considering the expectation of EV owners. IEEE Trans. Smart-Grid. **9**(4), 3763–3772 (2018)
5. Wang, X., He, Z.Y., Yang, J.W.: Unified strategy for electric vehicles participate in voltage and frequency regulation with active power in city grid. IET Gener. Transm. Distrib. **13**(15), 3281–3291 (2019)
6. Huang, Q., Wang, X., Fan, J., et al.: V2g optimal scheduling of multiple EV aggregator based on TOU electricity price. In: Proceedings of 2019 IEEE International Conference on Environmental and Electrical Engineering, 2019 IEEE Industrial and Commercial Power Systems Eur. EEEIC/I CPS (1), pp 1–6 (2019)
7. Tan, K.M., Ramachandaramurthy, V.K., Yong, J.Y., Padmanaban, S., Mihet-Popa, L., Blaabjerg, F.: Minimization of load variance in power grids—investigation on optimal vehicle-to-grid scheduling. Energies **10**(11), 1880 (2017). https://doi.org/10.3390/en10111880
8. Higgs, B., Abbas, M.: Segmentation and clustering of car-following behavior: recognition of driving patterns. IEEE Trans. Intell. Transp. Syst. (2015)
9. Wang, B., Hu, Y., Xiao, Y., et al.: An EV charging scheduling mechanism based on price negotiation. Futur Internet (2018)
10. Mulla, A., Jadhav, H.T.: Optimal scheduling of vehicle-to-Grid power exchange using particle swarm optimization technique. Int. J. Comput. Appl. **44**(7), 687–704 (2022)
11. Gupta, V., Reddy K.S., Panwar, L., Kumar, R., Panigrahi, B.: Optimal V2G and G2V operation of electric vehicles using binary hybrid particle swarm optimization and gravitational search algorithm. In: IEEE International WIE Conference on Electrical and Computer Engineering (WIECON-ECE) (2017). https://doi.org/10.1109/wieconece.2017.8468892
12. Liu, B.C., Chau, K.T., et al.: Opportunities and challenges of vehicle-to-home, vehicle-to-grid technologies. Proc. IEEE (2013)
13. Mirjalili, S., Wang, G.-G., Coelho, L.S.: Binary optimization using hybrid particle swarm optimization and gravitational search algorithm. Neural Comput. Appl. (2014)

14. Cho, H., Goude, Y., Brossat, X., et al.: Modeling and forecasting daily electricity load curves: a hybrid approach. J. Am. Stat. Assoc. (2013)
15. Alam, M.J.E., Muttaqi, K.M., Sutanto: Controllable local peak shaving strategy for effective utilization of PEV battery capacity for distribution network support. IEEE Trans. Ind. Appl. **51**(3), 2030–2037 (2014)
16. Tan, K.M., Ramachandaramurthy, V.K., Yong, J.Y., Padmanaban, S., Mihet Popam, L., Blaabjerg, F.: Minimization of load variance in power grids—investigation on optimal vehicle-to-grid scheduling. Energies **10**(11), 1880 (2017)
17. Jian, L., Zheng, Y., Xiao, X., Chan, C.C.: Optimal scheduling for vehicle-to grid operation with stochastic connection of plug-in electric vehicles to smart grid. Appl. Energy **146**, 150–161 (2015)

Smooth Imaging System Using Learning Generative Adversarial Network

Shipra Saraswat, Kajal Rani, Ishita Kanotra, and Aditya Kumar Singh

Abstract A method for smoothing the blur images by deblurring them using GAN is discussed in the paper. The method includes learning techniques to detect the type of filters applied to the image, all possible edges present in the image and counting all those details into account. This method makes assumptions about the filters on the image and uses techniques to de-filter all the affected pixels. This method can also handle the unconstrained blurs caused due to overexposure, underexposure, shaking of the camera lens, zooming of pixels and optical noise. Due to these unconstrained measures of the photograph, the image becomes blurred or semi-blur. The proposed method also focuses on constrains of prior information about blurring filters and parametric definitions of filters used. This method detects all possible blurred edges in its own way using the contrast of all blurry areas. The colour contrasts of blurred images are different from that of deblurred images. Also, it can work on both single-frame and multi-frame scenarios. The constrained parameters of the blurry areas in multi-frames are used in achieving improved quality images.

Keywords Generative adversarial network · Image deblurring · Generator · Discriminator

1 Introduction

The goal of the inverse issue known as "IMAGE deblurring" is to restore an image from a form of the image that has undergone linear degradation, either with or without noise. Hand-held camera images or movies with low frame rates that include moving things frequently have motion blur. Blurs reduce the quality of human perception and

S. Saraswat (✉)
Amity School of Engineering and Technology, Amity University Noida, Noida, India
e-mail: sshipra1510@gmail.com

K. Rani · I. Kanotra · A. K. Singh
Department of Computer Science and Engineering, ABES Institute of Technology, Affiliated to AKTU, Ghaziabad, Lucknow, Uttar Pradesh, India

© The Author(s), under exclusive license to Springer Nature Singapore Pte Ltd. 2025

H. P. Singh et al. (eds.), *Recent Developments in Control, Automation and Power Engineering*, Lecture Notes in Electrical Engineering 1303,
https://doi.org/10.1007/978-981-96-0047-2_6

impair later computer vision analyses. Image deconvolution techniques can be broken down into two categories: blind and non-blind. A well-known inverse problem, non-blind deconvolution [1] requires knowledge of the blur kernel but is difficult to solve without some picture priors. Blind deconvolution, then again, infers that the portion is mysterious. Due to its weakly posed nature and lack of image and kernel information, the blind deconvolution problem is extremely challenging to solve. This work presents a novel contribution in image deblurring using Generative Adversarial Networks (GANs). The suggested method uses progressive training, which entails a number of stages and is intended to enhance the outcomes of picture restoration. Following stages deal with high-frequency detail recovery and artefact reduction. The first stage concentrates on recreating the sharp image from the hazy input. On the basis of widely used benchmark datasets, extensive tests are carried out to assess the effectiveness of the technique. The outcomes show enhanced image quality, preserved detail and less artefacts. This work contributes to the field of image deblurring and could improve a number of applications that rely on image restoration. In this paper, a neural network will be used to deblur images. This neural network, known as a Generative Adversarial Network, is typically used for picture analysis [2].

This paper includes the following sections: Sect. 1 is Introduction, Sect. 2 is Related Work, Sect. 3 is Methodology which is followed by Sect. 4, i.e. Training and Testing of GAN, then Results are depicted in Sect. 5, Scope of Future is mentioned in Sect. 6 then Conclusion is given in Sect. 7, followed by References.

A learning-to-DeBlur GAN algorithm is specifically suggested as a method in. The DeBlurry-GAN module learns to recover sharp images from blurry images, both real and artificially produced [3]. Additionally, relativistic blur loss can be used to predict whether a genuine blurry image is more realistic than a synthetic one. In the context of image processing, the following equation describes deconvolution in two dimensions:

$$u = l \otimes k + m \tag{1}$$

where in (1), u and l respectively represent the original and obscured latent pictures. The blur kernel and added noise are denoted by k and m, correspondingly.

Goodfellow et al. first put forth the idea of GAN machine learning systems in 2014 with a method of using adversarial methods in generative network training. A two-player min–max game is formed by two networks, a discriminator D and a generator G [4]. The generator takes the input of noise z and outputs a sample. A discriminator attempts to differentiate between a genuine and produced sample after receiving one from each. By producing perceptually compelling samples that cannot be differentiated from the actual one, the generator aims to deceive the discriminator. The formula for the mini-max game with the value function V (D, G) is as follows:

$$\min\ G\ \max\ \mathrm{DE}\tilde{x}\,\mathrm{Pr}\big[\log(D(x))\big] + E\tilde{x}\mathrm{Pg}\big[\log(1 - D(x))\big] \tag{2}$$

where in (2), Pr is the data distribution, Pg is the model distribution and input z is a selection from a straightforward noise distribution, as specified by $x = G(z)$, z $P(z)$. Three categories are used to describe P contributions:

- To accelerate deblurring, GAN is combined with an encoder-decoder framework.
- The generator introduces perceptual loss to lessen ringing and blocking effects while preserving the deblurred image's details.
- GoPro large files to recover the original, blurry pictures.

2 Related Work

In recent years, image deblurring has made significant use of Generative Adversarial Networks (GANs). The following are a few noteworthy connected efforts in this field: A GAN-based method for deblurring single images is proposed [5], which implies a discriminator network that evaluates the veracity of the generated images and trains the generator network to produce sharp images from blurry inputs. A prior distribution of sharp images is incorporated into the generator network extending the previous method and improving the network's ability to handle challenging image deblurring scenarios.

In addition to the above work, an attention-based GAN method is suggested for deblurring images [6]. In this method, the generator network gains the ability to carefully attend to various regions of the picture. A conditional GAN-based method for deblurring blind motion uses a generator network that receives a blurred picture and a motion kernel as inputs and outputs a crisp image [7].

In one another approach the ill-posed and non-linear blind pictures are deconvoluted using deep generative networks as prior [8]. The model here employs two pre-trained distinct generative neural networks: one sample from the distribution of sharps images, while the other samples from the distribution of blur kernels. These samples are Gaussian vectors of lower-dimensions. A clear image and a blur kernel in the range of the respective generators are used to examine the blurred image in the deblurring process. This model produces convincing deblurred outcomes on images even when there are significant blurs and noise. Overall, these linked works show how effective GANs are at deblurring pictures and emphasize how crucial it is to include prior information and attention processes in order to enhance the quality of the output.

3 Methodology

3.1 Architecture of GAN

A generator network and a discriminator network usually make up the design of a generative adversarial network (GAN).

Generator Network: The generator network creates a new output picture that is meant to resemble the training data by using a random noise vector as its input. The generator network usually has several convolutional, deconvolutional and/or completely connected layers that gradually convert the input noise into the output picture. The generator network has been taught to generate images that look exactly like the originals.

Discriminator Network: The discriminator network attempts to differentiate between two inputs by using either a real picture from the training data or a generated image from the generator network. Convolutional layers are frequently used in discriminator networks to categorize incoming images as either genuine or fake. The discriminator network is taught to distinguish between authentic and fake input pictures.

As depicted in Fig. 1, in an antagonistic manner, the generator and discriminator networks are trained simultaneously. The generator network attempts to generate images that can deceive the discriminator network into believing they are real, while the discriminator network attempts to distinguish between the produced images and the real ones from the image provided. As the two networks are taught iteratively, the generator network tries to increase its output based on the input from the discriminator network.

Depending on the particular application and data type being used, the design of a GAN can be altered and tailored. For instance, a Conditional GAN (CGAN) augments the discriminator and generator networks with additional conditioning factors to produce pictures that meet predetermined criteria. There are also multiple types of GANs, including Deep Convolutional GANs (DCGANs), Wasserstein GANs (WGANs) and StyleGANs, which have various architectural characteristics and learning goals (Fig. 2).

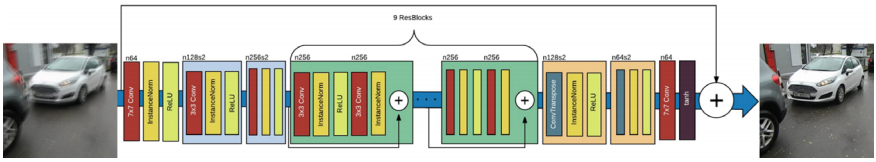

Fig. 1 Model architecture of GAN

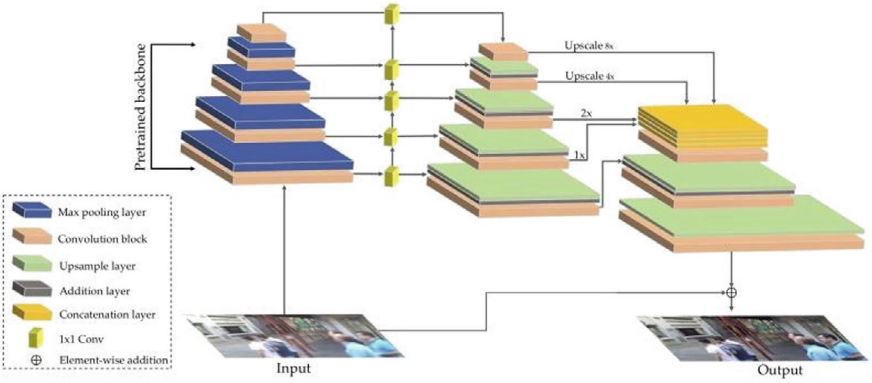

Fig. 2 Architecture of GAN-based deblurring model

3.2 GAN Module Design

The methodology of using a Generative Adversarial Network (GAN) for image deblurring typically involves the following steps.

Data preparation involves gathering and preparing a collection of blurred pictures and the ground truth clear images that go with them. Any sort of picture can be used as the training data.

Generator Network: A generator network is created and given arbitrary weights at the beginning. A blurry picture is fed into the generator network, which outputs a matching clear image.

Discriminator Network: A discriminator network is created and given arbitrary weights at the beginning. The discriminator network attempts to differentiate between two inputs, either a generated clear image from the generator network or an actual clear image from the training data.

Adversarial Training: Iteratively and in an adversarial fashion, the creator and discriminator networks are taught. The discriminator network attempts to differentiate between the generated clear images and the actual clear images, while the generator network attempts to create clear images that can trick the discriminator network into believing they are real. The generator network tries to better its output based on the input from the discriminator network as the two networks are trained alternately.

Evaluation: By creating new clear images from blurred pictures and contrasting them with the original clear images, the performance of the taught GAN is assessed. Metrics like the Peak Signal-to-Noise Ratio (PSNR), Structural Similarity Index (SSIM) and Mean Squared Error (MSE) can be used to evaluate the clarity of the clear images that are produced.

Deployment: The GAN can be used to deblur new images in real-time or offline after being taught and assessed.

A diagram illustrating the stages involved in the deblurring process of a blurred picture is shown in Fig. 3 for a better grasp of the suggested model and the operation of GAN.

Depending on the particular application and sort of data being used, the technique for using a GAN for image deblurring can be altered and customized. For instance, a Deep Convolutional GAN (DCGAN) [9] can be used for quicker and more effective training, or a Conditional GAN (CGAN) [10] can be used to produce clear images that meet particular criteria.

Fig. 3 Flowchart of GAN working

4 Training and Testing of GAN

4.1 Algorithm of Generator

Input: A random noise vector z of dimension (n), where n is the size of the input noise space.
Output: A generated sample x_hat of the same shape as the training data.
Step 1. Define the generator function G(z) which takes as input a random noise vector z and outputs a generated sample x_hat.
Step 2. Generate a batch of noise vectors {z_1, z_2, …, z_m} of size (n), where m is the batch size.
Step 3. Pass each noise vector z_i through the generator G to obtain a generated sample x_hat_i.
Step 4. Calculate the loss L_G as the negative log-likelihood of the discriminator's output on the generated samples. Step 5. Compute the gradients of L_G with respect to the generator's parameters using back propagation.
Step 6. Update the generator's parameters using an optimization algorithm (such as Adam) with the computed gradients.
Step 7. Repeat Steps 2–6 until the generator produces samples that are similar to the training data.

Keep in mind that the generator makes an effort to generate samples that are indistinguishable from the actual ones in order to make it harder for the discriminator to tell the difference between the generated samples and the real ones. By taking part in a course of ill-disposed preparation with the discriminator, the generator builds its ability to create exact models.

4.2 Algorithm of Discriminator

The discriminator in a Generative Adversarial Network (GAN) aims to distinguish between real and generated data. Here's an algorithm in point form:

Input:
Real data x or Generated data G(z).
Output:
Scalar value D(x) or D(G(z)).

Algorithm

Step 1. Initialize the discriminator parameters.
Step 2. Loop until convergence:

A. Sample a mini-batch of noise samples z from a prior distribution.
B. Generate a mini-batch of fake examples G(z) using the generator.

C. Compute the discriminator loss on real data D(x) and fake data D(G(z)).
D. Compute the gradients of the discriminator loss w.r.t. its parameters.
E. Update the discriminator parameters using the gradients.

Step 3. Output the discriminator parameters.

4.3 Training of the Model

Training the GAN model for image deblurring is one of the main tasks that is done before deblurring an image using the system. To train our model we are using GOPRO Large Dataset and a loss function is introduced during training which is crucial to the success of the GAN. This loss function includes perceptual (pixel-wise) loss and Wasserstein GAN loss [11]. During training, the generator and the discriminator are trained in recursive fashion [12]. The generator tries to minimize the loss function by creating a more realistic image, while the discriminator tries to maximize it by comparing the generated image to the given target image. The goal is to find a balance between generating realistic images and accurately deblurring the input images. Function of both generator and discriminator is summed up in Fig. 4, as a component of GAN training component.

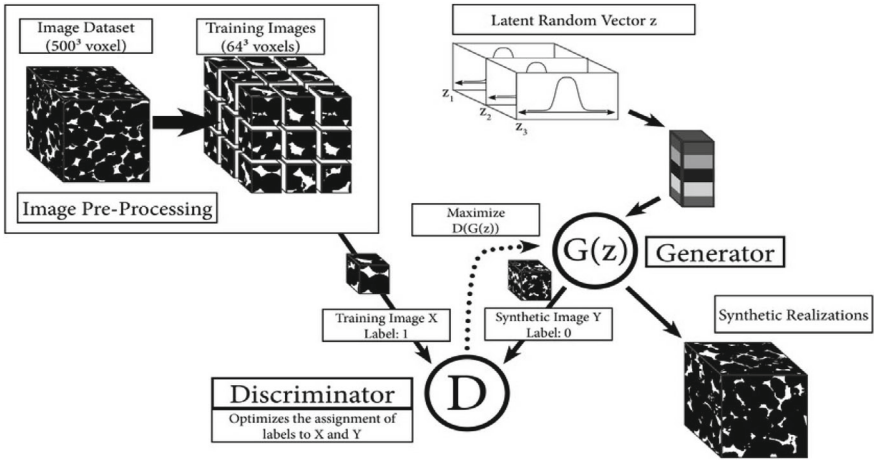

Fig. 4 Workflow of GAN training

5 Results

Generative Adversarial Networks (GANs) have been used for image deblurring with promising results. GANs are a type of neural network that can generate new images by learning from existing ones. In image deblurring, a GAN is trained to generate sharp and clear images from blurry ones.

Even in cases of the severe blur, the system still generates GAN deblurred output with convincing outcomes shown in Fig. 5, including sharper tree edges, improved number plate visibility and clearer vehicle headlights. The model in this case lowers the blur by individually adjusting each pixel's values before adding them all together. Due to the inclusion, of Wasserstein loss in the model, deblurring has some restrictions.

5.1 Architectural Performance of Model

Several levels of completely connected or Convolutional Neural Networks makes up the architecture of a GAN. The discriminator takes the sample and outputs a binary classification, whereas the generator usually begins with a random noise vector as input and creates a new sample (real or fake) [13]. It contains two stridden convolution blocks, two transposed convolution blocks and nine residual blocks and depicts the performance of model in below Table 1.

- The Instance Norm layer and LeakyReLU layer, both with $\boldsymbol{\alpha} = 0.2$, are placed after every convolutional layer but the final one.
- We used 200 training epochs to train this model.
- Matrices.
  - PSNR.

Fig. 5 Left to Right: Blurred image, deblurred image and target image

Table 1 Performance table for the model

PSNR	SSIM
25.4	0.8208

Table 2 Comparison of different datasets used for testing and training the GAN model

Validation dataset		Train dataset				
		GoPro	DVD	NFS	HIDE	Custom
GoPro	PSNR	30.09	28.54	27.95	30.15	30.50
	SSIM	0.9383	0.9080	0.8988	0.9398	0.9433
DVD	PSNR	27.77	31.28	29.68	27.81	30.27
	SSIM	0.8781	0.9244	0.9022	0.8828	0.9222
NFS	PSNR	31.72	34.10	34.01	30.42	34.06
	SSIM	0.9492	0.9630	0.9610	0.9499	0.9644
HIDE	PSNR	27.60	26.91	26.07	28.80	29.00
	SSIM	0.9134	0.8889	0.8775	0.9321	0.9340

– SSIM.

The model includes the image similarity measurements SSIM and PSNR. They are employed to assess image quality loss during the deblurring procedure. The Peak Signal-to-Noise Ratio is referred to as PSNR in engineering. The Structural Similarity Index, or SSIM, is a more sophisticated measure designed to identify perceptible differences between two images.

5.2 Dependence of Model on Type of Dataset Used in Training

The GAN image deblurring model is affected by training with different datasets. To demonstrate this, we used different types of datasets namely GoPro, DVD, NFS and HIDE datasets for training and testing the model in the same conditions. After seeing the results of PSNR and SSIM from different datasets it is concluded that the results achieved using the DVD dataset are the worst. The dependency of GAN on the type of dataset is shown in Table 2. Here, each column in Table 2 represents the dataset used for training and each row of the table represents the dataset used for testing [11].

6 Scope of Future Work

Using Generative Adversarial Networks (GANs), image deblurring has a bright future. Deblurring is just one of several image-related tasks for which GANs have demonstrated their enormous potential. The development of more sophisticated GAN networks designed specifically for image deblurring applications can be the subject

of future study. These models could provide clearer and more realistic deblurred photos by better capturing the underlying blur patterns.

- Satellite imaging and military applications are regarded as future trends in the field of image processing.
- Techniques for GAN-based deblurring can be adapted to certain fields, including surveillance or medical imaging.
- The deblurring procedure can be improved using interactive methods that require user guidance. In the future, improvements might incorporate user inputs like scribbles or sparse annotations to direct the deblurring models as they reconstruct images according to human intents.

7 Conclusion

In conclusion, GAN-based image deblurring modules offer a powerful and effective approach to address the challenge of image deblurring. By using a generator network to produce high-resolution and sharp images and a discriminator network to distinguish between the generated image and the ground truth sharp image, GAN-based models can produce high-quality deblurred images. Additionally, by using adversarial loss, perceptual loss and L1/L2 loss functions, the generated image can maintain the same structure and features as the ground truth sharp image, while also being similar to the ground truth image in terms of pixel values. GAN-based image deblurring modules are applicable in many fields, including medical imaging, astronomy and computer vision, and have the potential to significantly improve the quality of images in a variety of fields. The use of GANs for image deblurring has demonstrated outstanding results in bringing back the clarity of blurry photos. We may anticipate continuing development in this area, which will lead to more dependable and aesthetically acceptable image deblurring solutions in a variety of practical applications, as long as GAN architectures, training methods and the availability of high-quality datasets continue to increase.

In summary, GAN-based image deblurring modules offer a promising avenue for addressing image blurring challenges. With their ability to generate high-quality and sharp images, they hold great potential for improving image restoration in various fields, ultimately enhancing visual perception and aiding in critical decision-making processes. Continued research and development in this area are expected to drive further improvements and open up new possibilities for image deblurring using GANs.

References

1. Chen, M., Quan, Y., Pang, T., Ji, H.: Non-blind image deconvolution via leveraging model uncertainty in an untrained deep neural network. Int. J. Comput. Vision **130**(7), 1770–1789 (2022)
2. Zhang, Y., Tao, L., Qun, L., Xianbin, F., Tao, K.: Image motion deblurring via attention generative adversarial network. Comput. Graph. (2023)
3. Lu, W., Meng, Z.: Image deblurring based on generative adversarial networks. In: 2022 7th International Conference on Intelligent Computing and Signal Processing (ICSP), pp. 1555–1559. IEEE (2022)
4. Wu, C., Du, H., Wu, Q., Zhang, S.: Image text deblurring method based on generative adversarial network. Electronics **9**(2) (2020)
5. Kupyn, O., Budzan, V., Mykhailych, M., Mishkin, D., Matas, J.: Deblurgan: Blind motion deblurring using conditional adversarial networks. In: Proceedings of the IEEE Conference on Computer Vision and Pattern Recognition, pp. 8183–8192 (2018)
6. Xiang, X., Yu, Z., Lv, N., Kong, X., Saddik, A.E.: Attention-based generative adversarial network for semi-supervised image classification. Neural Process. Lett. **51** (2020)
7. Su, K., Li, X., Li, X.: Blind motion deblurring based on generative adversarial networks. In: Proceedings of the 2019 International Conference on Video, Signal and Image Processing, pp. 15–20 (2019)
8. Asim, M., Shamshad, F., Ahmed, A.: Blind image deconvolution using deep generative priors. IEEE Trans. Comput. Imaging **6**, 1493–1506 (2020)
9. Devakumar, S., Sarath, G.: Forensic sketch to real image using DCGAN. Procedia Comput. Sci. **218**, 1612–1620 (2023)
10. Zhao, H., Wu, D., Su, H., Zheng, S., Chen, J.: Gradient-based conditional generative adversarial network for non-uniform blind deblurring via Dense ResNet. J. Vis. Commun. Image Represent. **74**, 102921 (2021)
11. Tomosada, H.H., Kudo, T., Fujisawa, T., Ikehara, M.: GAN-based image deblurring using DCT loss with customized datasets. IEEE Access **9**, 135224–135233 (2021)
12. Zhang, X., Jiang, R., Wang, T., Wang, J.: Recursive neural network for video deblurring. IEEE Trans. Circuits Syst. Video Technol. **31**(8), 3025–3036 (2020)
13. Ganesan, P., Xue, Z., Singh, S., Long, R., Ghoraani, B., Antani, S.: Performance evaluation of a generative adversarial network for deblurring mobile-phone cervical images. In: 2019 41st Annual International Conference of the IEEE Engineering in Medicine and Biology Society (EMBC), pp. 4487–4490. IEEE (2019)

Encoding Data Using Slayer Exciter Circuits with Simultaneous Power and Information Transmission

Eshaan Yadav and Chaudhary Indra Kumar

Abstract This paper proposes a novel approach to wireless power transmission using a Slayer exciter circuit that generates high-voltage AC signals. The primary goal of the proposed system is to transmit both power and information simultaneously without the need for any conduction. However, wireless power transmission is often subject to environmental noise, which can lead to data transmission errors. To overcome this challenge, a simple encoding scheme based on Hamming(7,4) is employed to enhance the system's resilience to noise. The proposed system uses digital bits to transmit data, which are modified to include parity bits for error detection and correction. The addition of these parity bits ensures that any demodulator can accurately retrieve the transmitted data, even in the presence of noise. This paper shows that the proposed system is capable of both power transmission and data communication, making it a suitable candidate for various applications, including wireless charging, remote sensing, wireless communication, and Li-Fi. The paper also discusses the design and implementation of the proposed system, providing detailed information on the circuit components and their functions.

Keywords Slayer exciter · Tesla coil · Wireless transmission · Digital signals · Encoding · Parity · Li-Fi

1 Introduction

A Slayer exciter comprises an air-cored transformer and inputs a relatively low DC input voltage. It takes advantage of the switching property of bipolar junction transistors (BJTs) and switches this DC voltage into a high-frequency, high-voltage AC output. This setup can be compared to Nikola Tesla's spark-gap Tesla coil, which

E. Yadav (✉) · C. I. Kumar
Delhi Technological University, Rohini, Delhi 110042, India
e-mail: eshaanyadav24@gmail.com

C. I. Kumar
e-mail: indrachaudhry@dtu.ac.in

© The Author(s), under exclusive license to Springer Nature Singapore Pte Ltd. 2025

H. P. Singh et al. (eds.), *Recent Developments in Control, Automation and Power Engineering*, Lecture Notes in Electrical Engineering 1303,
https://doi.org/10.1007/978-981-96-0047-2_7

uses spark-gap switches, capacitors, and a resonant circuit to create wireless energy devices, with sparks emanating at the top load that are grounded via parasitic capacitance. It should be noted that iron cores are not used within such transformers, since high-frequency currents can induce eddy currents within the ferromagnetic core, which can lead to overheating.

When an electron is in motion, it creates EM waves around it. In such high-frequency circuits, radio waves are produced. These can be used as carrier waves and modulated to send information.

Hamming code was developed by Richard Wesley Hamming in 1950 as a linear error correction code for reliable data transmission in binary. The Hamming(7,4) uses three redundant bits (error correction bits) and four message bits. Although the code itself cannot remove errors, it can be processed and used reliably to retrieve erred data, in case of wrongful transmission due to noise in the channel.

Universal Asynchronous Receiver-Transmitter (UART) is a hardware system that facilitates the exchange of information without the need for a clock signal. Although unreliable due to susceptibility to electromagnetic interference and slow transmission, it still provides the easiest and cheapest methods of setting up transmission-reception networks. It sends the data as bits, one by one, with constant speed configured at both ends, i.e., the transmitter and receiver.

This paper is organized into six sections. It begins with an introduction providing an overview of wireless power transmission and the use of Slayer exciter circuits, along with the objective of achieving simultaneous power and information transmission. The encoding scheme based on Hamming(7,4) for error detection and correction is also introduced. The subsequent section presents a literature review, discussing previous research on wireless power transmission, gas discharge lamps, Tesla coil circuits, and Slayer exciter circuits, as well as the applications of Li-Fi and its limitations. The construction section delves into the details of transistors, coils, functioning of the Slayer exciter circuit, modulation techniques, and the implementation of Hamming code. The paper then explores the system's working, including the Tesla coil's power transmission capabilities, the modulating circuit, and the Raspberry Pi microcomputer program. Results from experimental testing are presented, showcasing electromagnetic wave measurements and the visualization of modulated messages. The paper concludes by summarizing the proposed system, highlighting potential applications, and emphasizing key findings and contributions. Finally, a list of references is provided.

2 Literature Review

Wireless power transmission has been a topic of interest for researchers due to its potential for practical applications in various fields. Gokulprasath and Rishi Kesan [1] explored the concept of wireless power conduction, which allows the transfer of power from a transmitter to a receiver through the use of electromagnetic fields. The

authors presented a wireless power transmission circuit that utilized the principles of magnetic resonance coupling to transfer power wirelessly.

The use of gas discharge lamps has also been a subject of interest for researchers in electrical engineering. Luković et al. [2] presented a simple electrical circuit that can be used to light up a gas discharge lamp. The circuit is composed of a capacitor, a ballast resistor, and a gas discharge tube. The authors showed that by applying a high voltage to the circuit, the gas discharge tube can be ionized, leading to the emission of light.

Tesla coil circuits have also been studied by researchers, particularly concerning their ability to generate high-frequency electrical fields. Moura [3] presented a Tesla coil circuit project that included an FIR audio filter. The filter was designed to improve the quality of the audio output from the circuit, which is typically distorted due to the high-frequency electrical fields generated by the Tesla coil.

Another circuit that generates high-frequency electrical fields is the Slayer exciter circuit. Kuriakose et al. [4] analyzed the Slayer exciter circuit and presented a mathematical model that can be used to predict its behavior. The Slayer exciter circuit is composed of a resonant LC tank circuit and a transistor that acts as a switch. The authors showed that the circuit can generate high-frequency electrical fields that can be used for various applications, such as wireless power transmission and lighting.

In addition, Shirodkar and Wadyalkar [5] explored the concept of a plasma speaker audio-modulated solid-state Tesla coil. The authors presented a circuit that utilizes a plasma arc to generate high-frequency electrical fields that are modulated by an audio signal. The result is an audio output that can be heard through the ionization of the air by the plasma arc.

Li-Fi technology, utilizing visible light for wireless communication, has gained significant research attention due to its potential applications. Wu et al. [6] provided a comprehensive overview, discussing Li-Fi principles, applications, and future directions. They highlighted its advantages such as high-speed data transmission and energy efficiency, while addressing challenges and paving the way for further advancements. Gupta et al. [7], in their review, focused on Li-Fi's features, advancements, and emerging trends. They analyzed its potential to revolutionize wireless communication, emphasizing the need to address challenges for widespread adoption.

Haq et al. [8] presented an overview of Li-Fi, highlighting challenges and proposing solutions. Zheng et al. [9] conducted a survey, discussing Li-Fi principles, integration, and diverse application areas analyzing research trends and challenges.

The literature on Li-Fi provides insights into its principles, applications, and challenges. These studies contribute valuable knowledge, fostering further research and development in this promising field, whereas researchers have explored various circuits that generate high-frequency electrical fields for applications such as wireless power transmission, lighting, and audio output.

3 Construction

The Tesla coil works on the Slayer exciter circuit (Fig. 1). It uses an NPN bipolar junction transistor (BJT) as a switch. A current limiting base resistance is used. A coil with a low number of turns acts as a primary coil and is electrically insulated and wrapped around a secondary coil, which is wrapped around an air core. One end of this secondary is free and can be thought of as being grounded via a parasitic capacitance. The other end of this coil is connected to the base of the transistor.

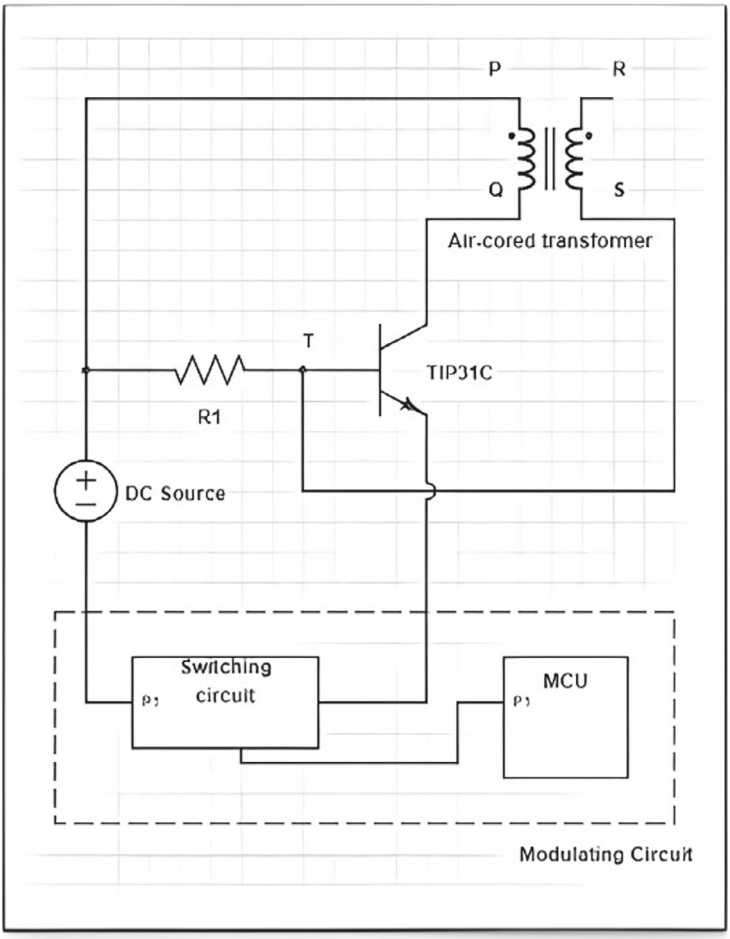

Fig. 1 Schematic for the Slayer exciter transmitter

3.1 Transistor

A bipolar junction transistor is an electrical device, which essentially controls a relatively larger current using a small current at one of the terminals. When the emitter and the collector are both forward-biased, the transistor operates in the saturation region, acting like a switch in the ON position. But if both the emitter and collector regions are reverse-biased, the transistor goes into the cut-off region, acting like an open switch. An NPN transistor, the TIP-31C was chosen for this Slayer exciter, due to its low leakage current. It was necessary to use a heatsink with it, to avoid overheating.

3.2 Coils

The primary coil was made from a 20-AWG stranded wire, having 2 turns, and galvanically insulated using electrical tape. The secondary coil tower is made using 30-AWG insulated copper wire, having 320 turns, wrapped tightly around a glass jar. The base is insulated by tightly wrapping electrical insulation. The primary rests on this insulation. The primary is capable of inducing a current in the secondary through electromagnetic induction.

3.3 Functioning

The transistor conducts current initially since the base of the transistor is at a voltage greater than the threshold. Current flows through the primary in P to Q (Fig. 1) direction and by electromagnetic induction, a potential difference occurs between R and S (Fig. 1) in the secondary. This creates a very low potential at the base of the transistor, thus putting it in the cut-off region. The flow of current through the primary stops. To oppose this change in current, by Lenz's law, an opposite potential occurs between R and S, creating a large voltage at Tnear the base of the transistor, again putting it in the saturation region. This conducts the current again and this cycle repeats very quickly. Thus, a high-frequency current is produced, and due to the turn ratio of coils, a high AC voltage source is produced. The voltage at R is grounded to the earth via parasitic capacitance.

3.4 Modulation

The EM-wave generated due to the high-frequency AC current can act as a carrier wave, and information can be encoded within it. To achieve it, modulation must be

employed. It is the process of varying one or more properties (amplitude, frequency) of the carrier wave, so that information can be transmitted.

The simplest way of digital modulation would be employing non-constant envelope techniques, particularly Amplitude Shift Keying, using a MOSFET or relay in accordance with an encoding scheme, where the ON position will denote the 1 and the OFF position will denote 0, thus effectively transmitting binary data. Thus, data will be transmitted as pulses of bursts of EM waves. These could be visualized with a digital storage oscilloscope. Although a relay will provide better Galvanic Isolation, a MOSFET can switch much faster.

The signal for the switching of MOSFET or relay comes from a microcomputer, which has been programmed in accordance with one of the encoding schemes, and accepts input through the serial bus.

MOSFET: A metal–oxide–semiconductor field-effect transistor MOSFET is an electrical device that can be used to control a current flow, by subjecting a voltage at one of its terminals. It can be used as a switch. An Enhancement MOSFET, particularly the IRFZ44 n-channel MOSFET, was used, due to its thermal stability and low power loss during high-frequency switching.

PNP Transistor: The IRFZ44 N-channel MOSFET requires at least 5 V to drive itself. The GPIO pins of the Raspberry Pi are capable of outputting only 3V3. Hence, the 5 V pin is used to drive the MOSFET, but cannot be logically operated. Therefore, a BJT is used as a switch to convert the 3V3 signal to a 5 V signal. It is important to note that the signal will be inverted due to the presence of a PNP BJT, and hence the program logic must send inverted signals, taking this into account (Fig. 2).

3.5 Hamming Code

When the message travels through any media, there is a possibility of it getting tampered due to noise in the media. Any kind of switching and electromagnetic noise can change the bits in the message. Hamming code is an error-correcting code that comprises redundant bits along with message bits. The code in itself cannot correct errors, but the receiver can be programmed to comprehend the encoded message and check for errors.

The Hamming(7,4) code comprises 3 parity bits for every 4 message bits. These parity bits may be odd or even parity.

In Table 1, $p1$, $p2$, and $p3$ are the parity bits, whereas $d1$, $d2$, $d3$, and $d4$ are message bits. The placement fashion of these bits is necessary. Considering the case of even parity, the $p1$ bit will be zero or one depending on the $d1$, $d2$, and $d4$ bits. Similarly, the other parity bits assume 0 or 1 in accordance with the value of their corresponding message bits, as shown in Fig. 3.

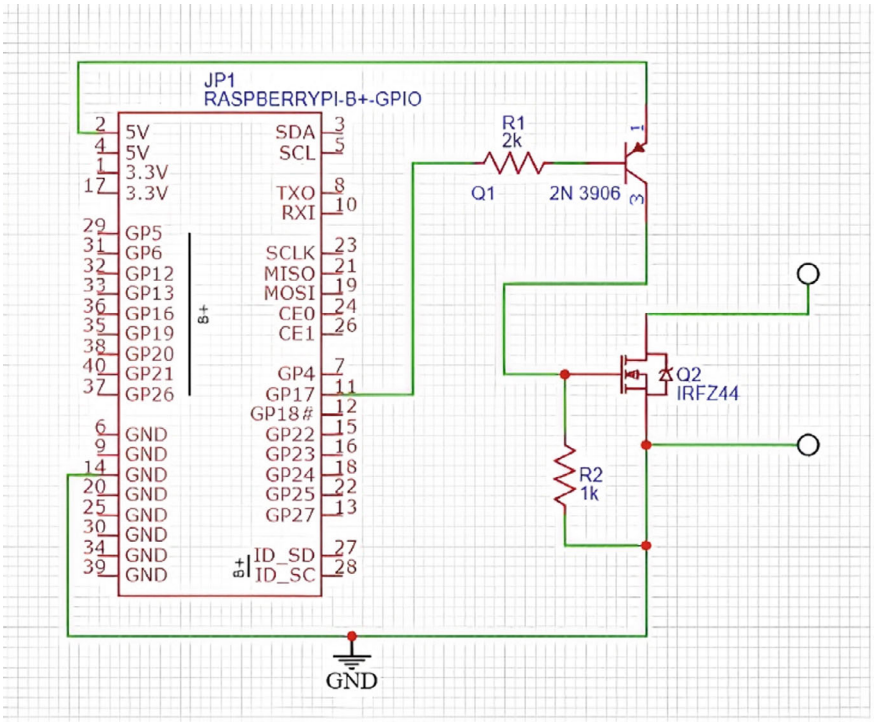

Fig. 2 Schematic for the modulating circuit

Table 1 Placement of parity bits

1	2	3	4	5	6	7
$p1$	$p2$	$d1$	$p3$	$d2$	$d3$	$d4$

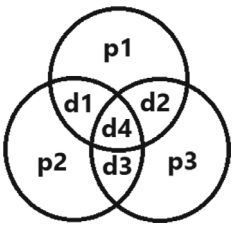

Fig. 3 Parity bits' inter-relation

4 Working

4.1 Working of the System

The Tesla coil excites the low DC voltage to a high-frequency high-voltage AC output. This creates electromagnetic waves, around the top load of the coil tower. These are potent enough to light a fluorescent lamp. The lamp contains mercury atoms, which get excited due to this EM radiation and emanate light as they reach their ground state. Thus, bringing a fluorescent lamp near the coil tower makes it light up. Without manipulating the modulating circuit, the Tesla coil transfers power wirelessly.

When we power up the modulating circuit, the Raspberry Pi microcomputer asks for input from the keyboard. Any number from 0 through 63 will act as valid input. The microcomputer drives the MOSFET following a pre-programmed algorithm. It converts the input from decimal to binary and rightly adds parity bits. This bit stream of 7 bits translated to a digital signal at the gate of the MOSFET, turning it ON and OFF. A bit denoting 1 will switch it on and a 0 will switch it off. The speed of switching can be controlled by reprogramming the microcomputer.

By employing amplitude shift keying, the sinusoidal signal can be modulated with ON–OFF keying. Every time the MOSFET goes into the ON state, it conducts and allows current to pass through the Slayer exciter circuit. This allows an AC signal to be generated around the secondary, creating EM waves around it. A loop of wire connected to the probes of an oscilloscope can harness this energy through mutual induction and show this bit stream as a waveform.

4.2 Program and Logic

The Raspberry Pi microcomputer is pre-programmed in accordance with the encoding scheme. The microcomputer waits for the input from the serial monitor. A program encodes this value under the Hamming(7,4). Thus 3 redundant bits are added to the 4 message bits following the parity (Fig. 4).

5 Results

A loop of wire is used to harness the EM radiations generated around the coil tower. The ends of the loop are connected to a digital storage oscilloscope. The DSO-138 served as a cheap and effective instrument for the measurement of bit pulses (Fig. 5).

Simultaneously, an incandescent fluorescent bulb was used to visualize these bursts of EM radiation. Every time a ‘1’ bit was encountered, the bulb flashed ON, and a ‘0’ bit would switch it back off (Fig. 6).

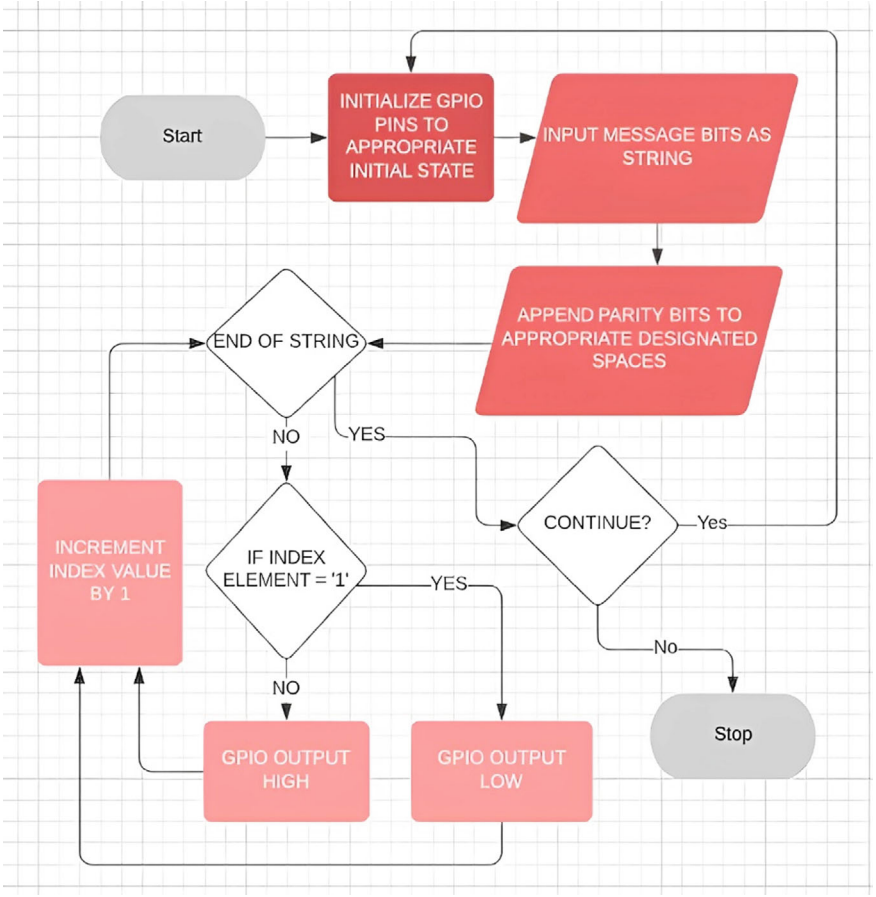

Fig. 4 Logic flow for the program

On quick succession, fluctuations are invisible to the human eye, and hence long streams of data can be transmitted, thus allowing this device to be used as Li-Fi setup. Several studies have reviewed the technology, its potential, and its limitations [10, 10]. Yadav and Mehta [12] conducted a performance analysis of Li-Fi technology using different modulation techniques. They found that the performance of the system is significantly affected by the modulation technique used. Pradhan et al. [13] analyzed the performance of a Li-Fi system under ambient light conditions and found that the signal-to-noise ratio and bit error rate were affected by the ambient light level. Islim and Haas [6] explored different modulation techniques for Li-Fi and identified the benefits and drawbacks of each, including that of amplitude shift keying. The thus build Tesla coil is capable of transmitting fast streams of data and powering the devices simultaneously. As Li-Fi technology continues to develop, it is expected to

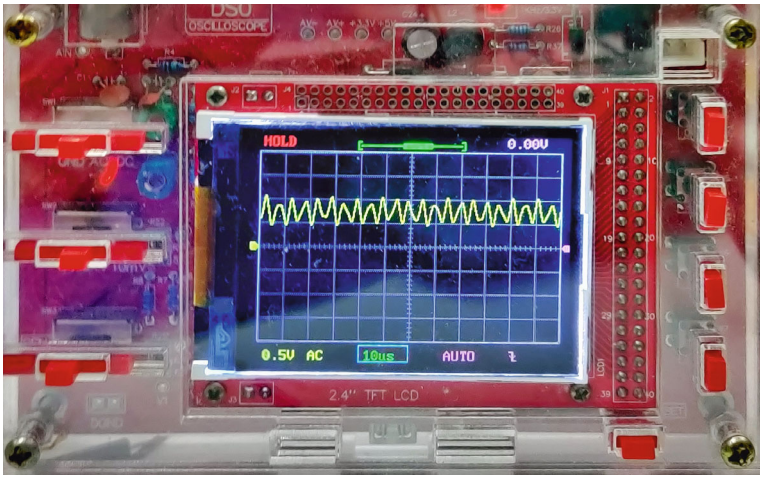

Fig. 5 Carrier wave oscilloscope output

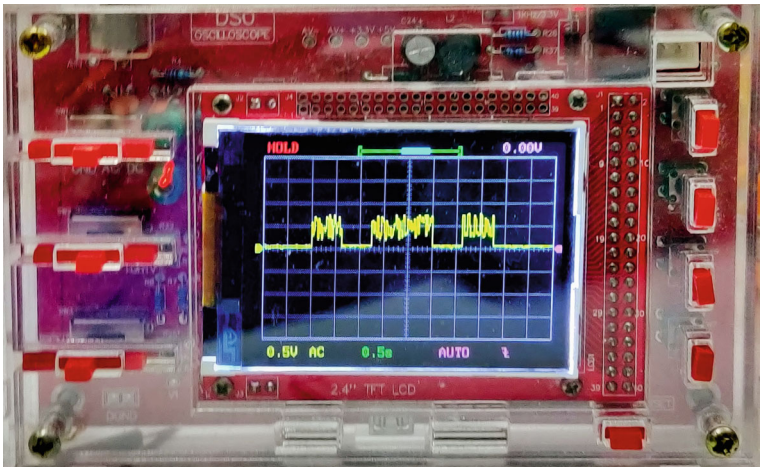

Fig. 6 Modulated message for input as 1010, with parity bits

find applications in areas such as healthcare, defense, and indoor positioning systems [10].

6 Conclusion

The Slayer exciter circuit thus built produces a high-voltage output, with an extremely small current magnitude. The EM waves thus generated are capable of lighting incandescent bulbs within the vicinity of the device, by exciting the mercury atoms within. These EM waves can act as carrier waves of our signal and allow simultaneous power and data transmission. By employing amplitude shift keying, we encode our message in this carrier wave. We have successfully minimized the effect of noise on the system, by utilizing the encoding scheme of Hamming(7,4) and added parity bits to the message. When the bits are fired in quick succession, the human eye cannot see the flickering of the lamp, due to the persistence of vision, and thus it appears, to glow consistently. This allows us to modulate the daily household lamp into a functioning Li-fi device, powering it wirelessly and using it as a communication device as well. The use of Li-Fi technology for wireless communication has gained significant attention in recent years. Li-Fi offers advantages over traditional radio frequency-based wireless communication technologies, such as higher data rates and improved security.

References

1. Gokulprasath, K., Rishi Kesan, A.P.: Wireless power conduction. Int. J. Res. Eng. (2019)
2. Luković, M., Antić, S., Luković, V.: Simple electrical circuit to light up a gas discharge lamp. In: Proceedings of Technics and Informatics in Education (2016)
3. Moura, M.G.L.: Tesla coil circuit Project with FIR audio filter. In: Brazilian Applied Science Review, pp. 329–341 (2022)
4. Kuriakose, A., Solanki, K., Tom, M.S.: An Analysis of the Slayer Exciter Circuit. arXiv preprint arXiv:2104.12092 (2021)
5. Shirodkar, A.K., Wadyalkar, S.: Plasma speaker audio modulated solid state tesla coil. Res. J. Eng. Technol. **9**, 293–296 (2018)
6. Wu, Z., Yang, C., Wu, M., Wang, S.: Li-Fi technology: principles and applications. J. Commun. **15**(4), 363–372 (2020)
7. Gupta, A., Gupta, P., Gupta, R.: Li-Fi technology: a review. In: 5th International Conference on Communication Systems and Network Technologies (CSNT), pp. 11–16. IEEE (2020)
8. Haq, M.M., Imran, M., Ali, S., Anwar, K.: Li-Fi technology: an overview, challenges, and future directions. In: 2020 International Conference on Communication, Computing and Digital systems (C-CODE). IEEE (2020)
9. Zheng, H., Zhou, W., Zhang, Z., Zhang, S.: A survey on Li-Fi technology and its applications. Wirel. Commun. Mob. Comput. (2020)
10. Swami, K.T., Moghe, A.A.: A review of LiFi technology. In: 2020 5th IEEE International Conference on Recent Advances and Innovations in Engineering (ICRAIE). IEEE (2020)
11. Karthika, R., Balakrishnan, S.: Wireless communication using Li-Fi technology. SSRG Int. J. Electron. Commun. Eng. (SSRG-IJECE) **2**(3), 32–40 (2015)
12. Islim, M.S., Haas, H.: Modulation techniques for li-fi. ZTE Commun. **14**(2), 29–40 (2016)
13. Pradhan, J., Kappala, V.K., Das, S.K.: Performance analysis of a Li-Fi system under ambient light conditions. In: National Conference on Communications (NCC). IEEE (2020)

Design and Analysis of Dual-Band Rectenna for Internet of Things Applications

Asmita Rajawat, Kushagra M. Agrawal, and Raghav Tola

Abstract The paper focuses on the designing of dual-band microstrip rectenna with the purpose of harvesting RF energy for the Wi-Fi frequency range. Rectenna can convert the RF energy present in the environment into direct current (DC) which is used to power various low energy-consuming devices. The proposed rectenna is supposed to be used as an alternate to conventional energy source for low power devices involved in IoT systems. The microstrip rectenna resonates at 900 MHz frequency and 2.45 GHz frequency which are the operating frequency of Wi-Fi HaLow technology and conventional Wi-Fi technology which is advantageous for IoT applications. Air is used as a substrate with dielectric permittivity of 1.0 for the development of antenna. The design and simulation of the antenna were conducted using Computer Simulation Technology (CST) Studio Suite The rectifier circuit employed in this study utilized an HSMS-285C Schottky diode in conjunction with a Greinacher voltage doubler circuit. Advanced Design System (ADS) was used for the simulation purpose of rectifier. The antenna operates at 900 MHz with gain of 8.84 dB and at 2.45 GHz with the gain of 8.82 dB and S11 below −10 dB. The proposed rectifier achieves peak output voltage of 3.269 V with a conversion efficiency of 71.235% for 900 MHz and maximum output of 3.142 V that has conversion efficiency of 65.801% for 2.45 GHz which can be used for powering low power IoT devices operating on Wi-Fi HaLow as well as conventional Wi-Fi.

Keywords Wi-Fi HaLow · Energy harvesting · Conversion efficiency · Wide band rectenna

A. Rajawat · K. M. Agrawal (✉)
Acropolis Institute of Technology and Research, Indore, India
e-mail: kushagraagrawal265@gmail.com

R. Tola
Amity University, Noida, Uttar Pradesh, India

© The Author(s), under exclusive license to Springer Nature Singapore Pte Ltd. 2025

H. P. Singh et al. (eds.), *Recent Developments in Control, Automation and Power Engineering*, Lecture Notes in Electrical Engineering 1303,
https://doi.org/10.1007/978-981-96-0047-2_8

1 Introduction

Radiofrequency (RF) energy harvesting is a method in which harnessing RF energy from the surrounding environment by utilizing an antenna. This energy is subsequently converted into direct current (DC) power, which can be used then to operate low power electronic devices. A rectenna is a device designed to capture and convert RF energy into DC. It typically consists of an antenna to capture RF energy from the environment and a rectifier that converts the RF energy into DC power. To improve efficiency and enable compact design, a microstrip antenna is often used in rectenna. This makes them well-suited for use in portable electronic devices. A block diagram illustrating the process of energy harvesting is presented in Fig. 1.

In [1], rectenna operating at 2.45 GHz is designed and two rectifier topologies were compared to verify the benefits rectifier circuit without matching network. In [2], a WPT system is suggested which is connected to a current doubler rectifier circuit which incorporates an autotransformer. The rectifier has low voltage high current producing capabilities and by the use of autotransformer, losses are reduced. Reference [3] describes a rectenna consisting of a dipole antenna and a rectifier circuit for rectification which achieves high gain and works on 5.8 GHz frequency. Conversion efficiency was improved by removing lossy component between the antenna and rectifier. In [4], design of a dual-band rectenna is proposed which is compact in size and focuses on ISM frequency band and UHF band. Two Schottky diode voltage doubler rectifiers are used for rectification process. For both frequencies, the proposed design achieves conversion efficiency of about 60% for −5 dBm signal. In [5], design of a dual-band rectifier is presented which is resonant at 0.915 GHz and 2.45 GHz, the efficient rectifier design achieves compact 21.47 mm × 18.93 mm dimensions. The conversion efficiency achieved for the 0.915 GHz is 74% and for 2.45 GHz is 73%. In reference [6], a wireless power transfer system is described that achieves a conversion efficiency of 35% and enables wireless communication of a sensor node at a maximum distance of 0.15 metres. Reference [7] presents a rectifier design to be employed in a rectenna for a wireless energy transfer system, the use of phase multitone input signal is explained to improve efficiency. In [8], design of a dual-band rectifier is presented with resonating frequency at 915 MHz and 2.45 GHz. An improvised T section is being used for the improvement of rectifier efficiency. The rectifier when simulated achieves a peak conversion efficiency of 75 and 65% at two frequencies, respectively. Reference [9] presents the design for a miniature dual-band rectifier with good conversion efficiency. T type network is used to improve the efficiency while maintaining a compact form factor. For 12

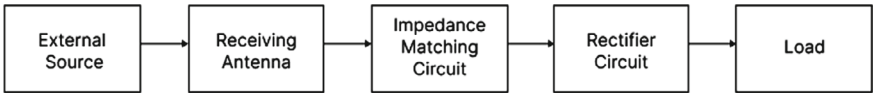

Fig. 1 Block diagram for RF energy harvesting device

dBm of input power, conversion efficiency measures are 81.7 and 73.1% for the two frequencies, respectively.

Reference [10] presents design of an energy harvesting device capable of being used at wireless sensor node which converts RF energy in DC voltage. The designed system focuses on 4G and 5G frequency band, at an input power 6 dBm, the two-toned signal achieves a conversion efficiency of 78.1%. Work in [11] proposes a dual-band antenna design which is developed on defected ground structure technique to get the dual-band operation in the ISM frequency band. Using FR4 as substrate reduces the cost of the antenna significantly. Reference [12] describes a dual-band rectenna at 2.45 GHz and 5.8 GHz, with conversion efficiency of 63% and 54.8%, respectively. Reference [13] presents an examination of a rectifier circuit designed for wireless energy transfer. This circuit achieves a conversion efficiency of 66% when operating at 100mW power and 5.8 GHz.

In [14], a dual-band rectenna design was presented for harvesting energy in small IoT, a metal-rimmed antenna was constructed for capturing RF energy. Moreover, the size of rectifier circuit is reduced by combining two different resonant structures while attaining an overall conversion efficiency of 60%. Reference [15] presents a detailed survey on Wi-Fi HaLow technology, and it is a Wi-Fi network protocol IEEE 802.11ah which was published in 2017 that uses sub gigahertz spectrum hence providing greater range of Wi-Fi networks while using low power consumption. Reference [16] introduces a rectifier circuitry of a voltage doubler which consists of a Schottky diode that yields a conversion efficiency greater than 50%.

To facilitate a clear presentation, this paper is structured as follows: Sect. 2 consists design of proposed rectenna that is further described in two subsections. Subsection 2.1 shows the design of microstrip antenna, and Subsection 2.2 has the voltage doubler design for rectifier. Section 3 contains the simulated results of the proposed design. Section 4 contains the conclusion of the paper.

2 Antenna Design with Defected Ground Structure (DGS)

2.1 Microstrip Antenna

In this study, a microstrip antenna is designed using air as the substrate material with a dielectric permittivity of 1.0. The height of the substrate is selected as 1.6 mm. Typically, substrates for microstrip antennas have dielectric constants ranging from 2.2 to 12. Choosing a substrate with a low dielectric constant is advantageous because it can improve the antenna's efficiency and widen its operational bandwidth. Air is chosen as the dielectric substrate because it provides advantages such as low cost and high gain capabilities as a dielectric substance. The substrate has dimensions of 321 mm $\times$ 362 mm.

The rectangular-shaped patch antenna is designed with a hexagonal slot in the middle to make the antenna resonate at dual frequencies. The rectangular patch has dimensions of 160.5 mm × 181 mm. Thickness of the patch is taken as 0.1 mm.

Inset feeding is used for feeding the microstrip antenna as inset feed is easy to fabricate and impedance matching provided is also simple as inset feed position can be adjusted. Table 1 contains the dimension detail of the proposed microstrip antenna.

The structure of the patch and the substrate for the dual-band microstrip patch antenna is shown below (see Fig. 2).

Anneal copper is used as the ground, patch material and feed line. The thickness of the ground has been kept 0.1 mm. While designing this antenna, rectangular patch comprising of a hexagonal slot in the centre of the patch has been designed. Radius of the hexagonal slot is 10 mm (see in Fig. 3).

Table 1 Geometrical parameters of antenna

S. No.	Dimensions	Micro strip patch (mm)	Substrate (mm)
1	Length	160.5	321
2	Width	181	362
3	Thickness	0.1	1.6

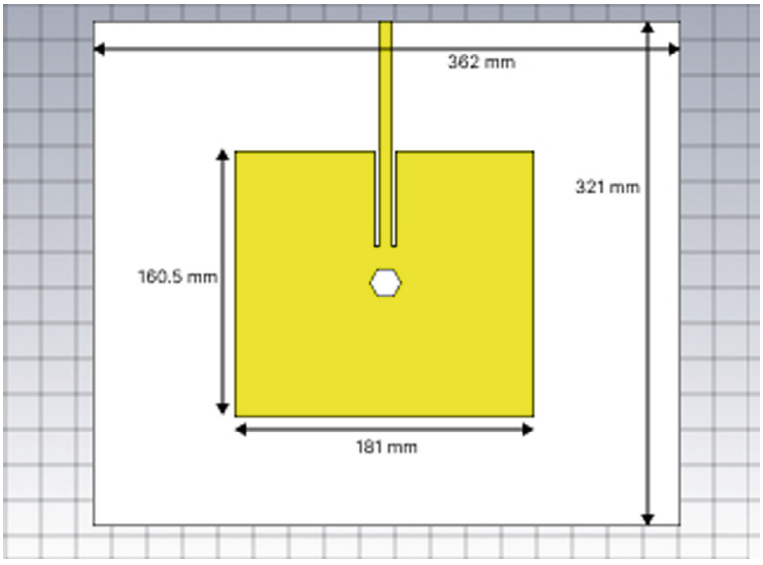

Fig. 2 Microstrip patch antenna design

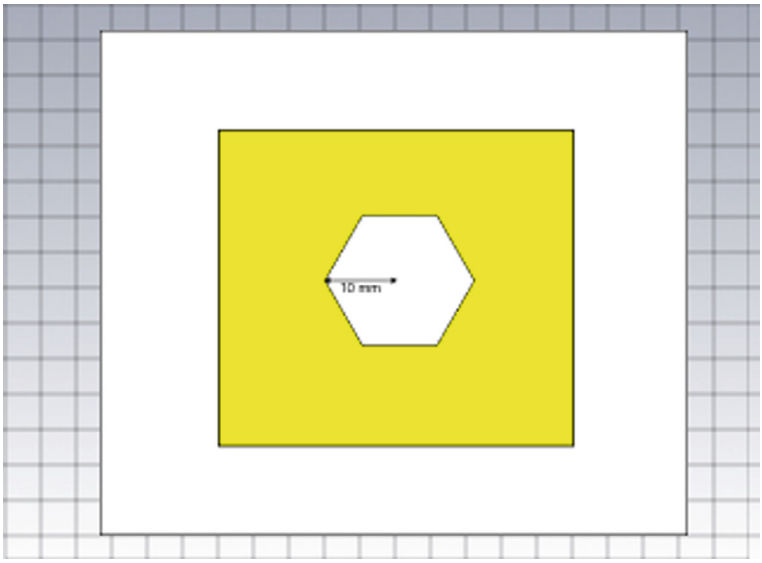

Fig. 3 Slotted hexagon on patch

2.2 Voltage Doubler for the Rectifier

Voltage doubler is a circuit that provides twice the output voltage in comparison to input voltage. Greinacher voltage doubler circuit is used in the following design because this circuit practically removes the ripple present in the energy signal coming from the antenna, and it does not use any transformer making it cheap and less bulky. Greinacher voltage doubler has a capability to provide high output voltage relative to low input voltage. Use of zero bias HSMS-285C Schottky diode makes the effective rectification possible as the forward voltage of this diode in low. The simulated rectifier operates at 900 MHz and 2.45 GHz.

When the rectifier circuit has a direct coupling from the power source, output voltage of the circuit designed is low. Impedance matching is required to effectively transfer power from source to load and for device protection. This is done for the improvement of the rectifier circuit efficiency. Hence, for the impedance matching purpose, a resistor of 1500 ohms is connected across which the voltage is calculated. You can find the values of capacitors and inductor below (see Fig. 4).

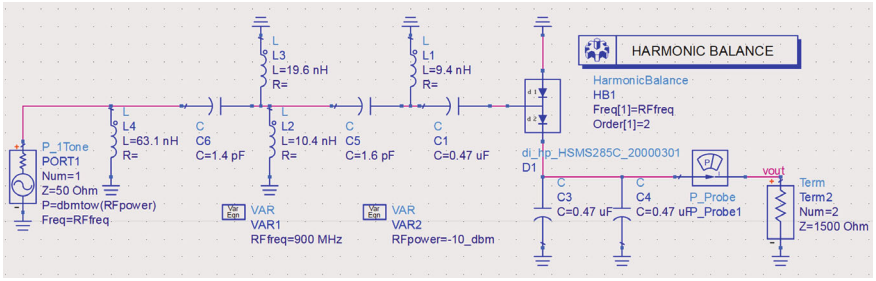

Fig. 4 Impedance matched rectifier circuit

3 Results and Discussions

3.1 Results for Antenna with Defected Ground Structure (DGS)

RF energy harvesting process requires a dual-band antenna that can perform energy harvesting at two different frequencies. The frequencies considered are 900 MHz and 2.45 GHz. To investigate the current flow on the surface of the patch, the current distribution is analysed. Figures 5 and 6 display the current movement on the patch surface at both 900 MHz and 2.45 GHz, respectively. The current movement is more around the hexagonal slot (see Fig. 6).

S-parameter stands for scattering parameters, by scattering it means that, effect on currents and voltages that are travelling in a transmission line whenever an abrupt discontinuity is encountered. It gives the relationship between reflected power wave

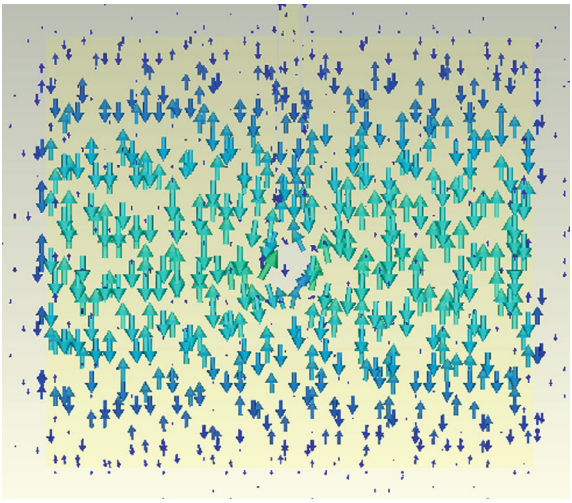

Fig. 5 Surface current distribution at 900 MHz

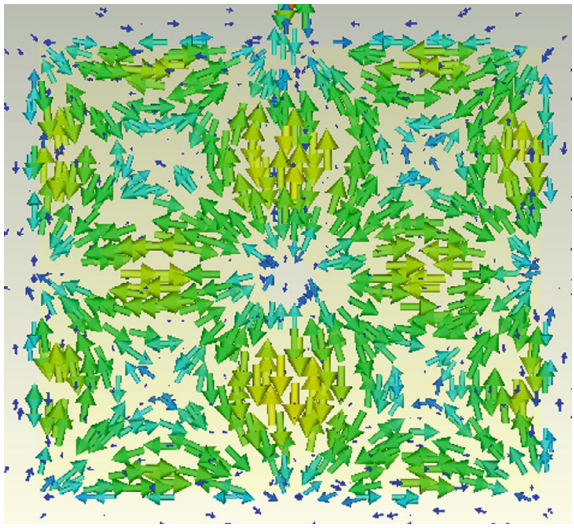

Fig. 6 Surface current distribution at 2.45 GHz

and incident power. Return loss refers to the portion of a signal that is reflected due to impedance mismatch, resulting in a loss of power. It is a positive value that is calculated as the ratio of the input power to the power that is reflected back. Return loss of −10 dB is the minimum acceptable value; it means 10% of the incident power or radiation would be reflected back from the antenna. Minimum value of −23.009 dB was observed for 0.9003 GHz, and value of −10.764 dB is observed for 2.4507 GHz. The simulation results of S_{11} can be seen in Fig. 7. The simulation results show that plot falls below −10 dB for two frequencies, 900 MHz and 2.45 GHz that is desirable for Wi-Fi HaLow and conventional Wi-Fi frequency range.

Farfield radiation pattern is generally represented as 3D graph in vertical and horizontal planes. Figures 8 and 9 show the farfield plots at 900 MHz and 2.45 GHz.

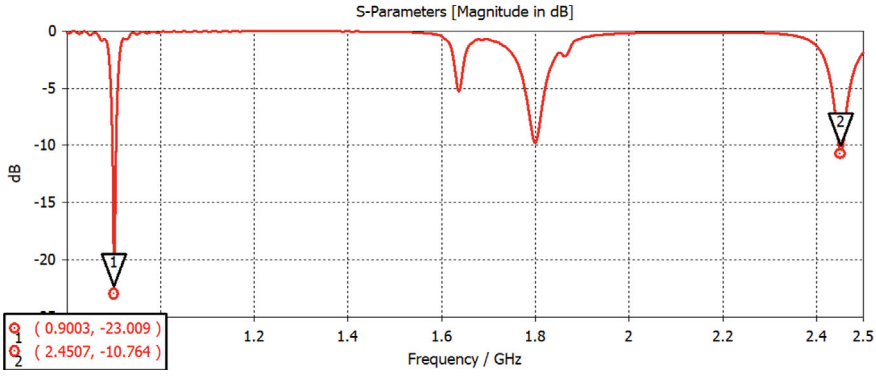

Fig. 7 Simulated results for S-parameter

The plots clearly show that gain of 8.797 dB for 900 MHz and gain of 8.852 dB for 2.45 GHz frequency.

An antenna's radiation pattern is nothing but the graph depicting the variation or distribution of field intensity at the vicinity of an antenna or it is calculated at a specific distance from the antenna, it is a particularly important characteristic of an antenna which is generally calculated after the input impedance is known. The 2D polar plot of radiation pattern can be seen in Fig. 10 and Fig. 11 for proposed antenna at two frequencies, 900 MHz and 2.45 GHz, respectively.

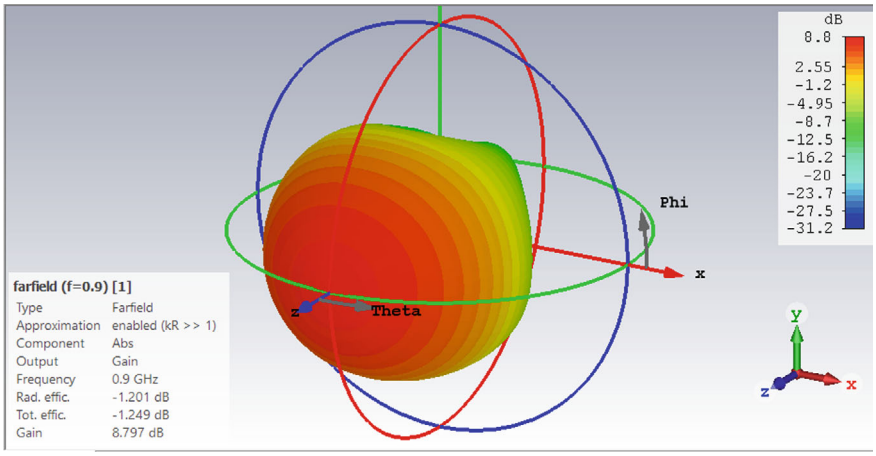

Fig. 8 Farfield plot at 900 MHz

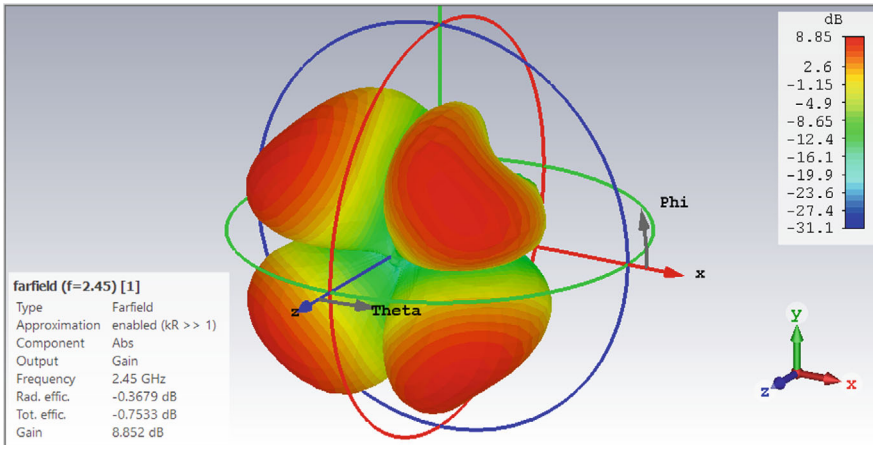

Fig. 9 Farfield plot at 2.45 GHz

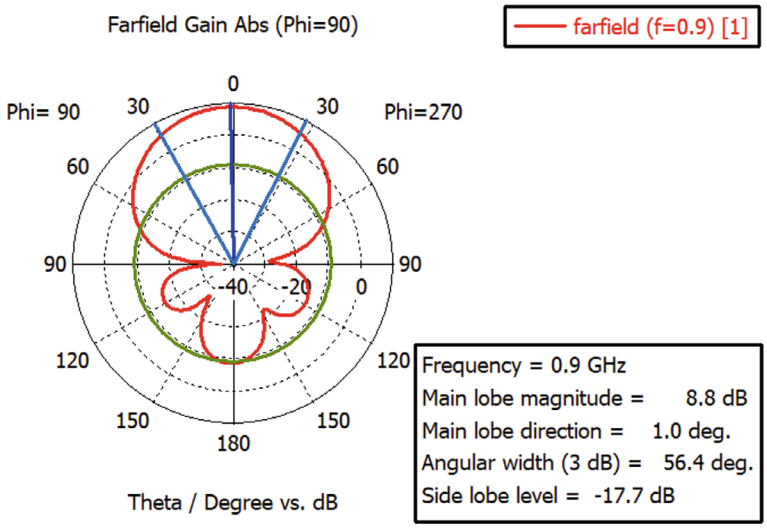

Fig. 10 2D polar plot of the radiation pattern at 900 MHz

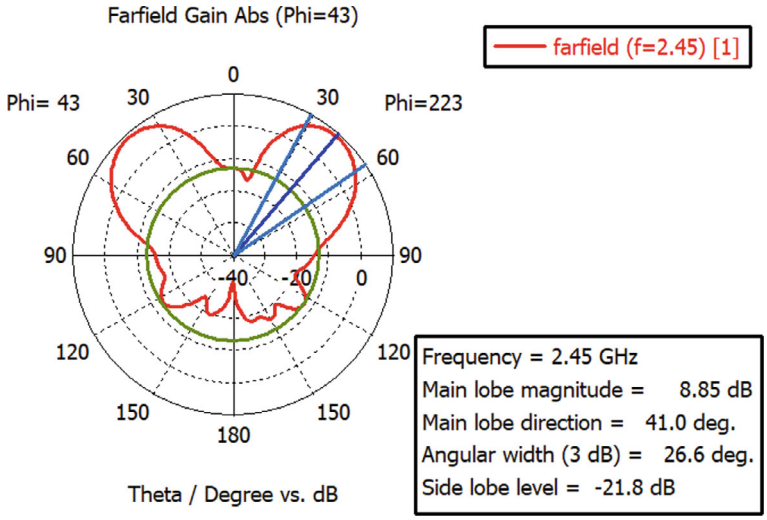

Fig. 11 2D polar plot of the radiation pattern at 2.45 MHz

3.2 Results for Voltage Doubler for Rectification

Rectifier circuit results were optimized for 900 MHz and 2.45 GHz frequencies. For each frequency, the graph for output voltage along with conversion efficiency was noticed for a range of −10 to 10 dBm of input power. The impedance of 1500

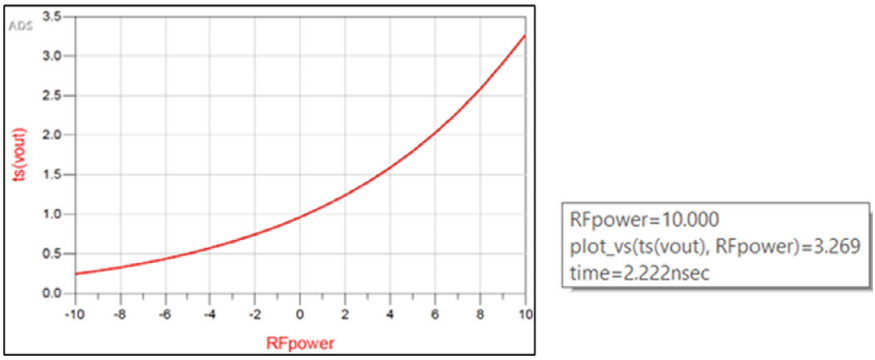

Fig. 12 Output voltage of rectifier at 900 MHz

ohms is been taken, across which the output is obtained. The conversion efficiency is determined using:

$$P_{\text{out}} = (V_{\text{out}})^2/R_L \tag{1}$$

$$\eta = P_{\text{out}}/P_{\text{in}} \tag{2}$$

where

P_{out} denotes output power
P_{in} denotes input power
R_L denotes load resistance
V_{out} denotes output voltage.

Figure 12 illustrates the output voltage versus input power plot for impedance matched rectifier circuit at 900 MHz frequency. The graph depicts that when compared to unmatched rectifier, the output voltage attained is improved to 3.269 V.

Figure 13 illustrates the efficiency versus input power plot for impedance matched rectifier circuit at 900 MHz frequency. The plot tells us that conversion efficiency achieved is 71.235% which is due to the increased voltage output generated by the matched circuit.

Figure 14 illustrates the output voltage versus input power plot for impedance matched rectifier circuit at 2.45 GHz frequency. Similar to the 900 MHz results of rectifier, the output voltage has improved to 3.142 V.

Figure 15 illustrates the efficiency versus input power plot for impedance matched rectifier circuit at 2.45 GHz. The plot tells us that, conversion efficiency realized is 65.801% which is due to the increased voltage output generated by the matched circuit.

Table 2 encapsulates the results of gain and conversion efficiency at 900 MHz and 2.45 GHz operating frequencies.

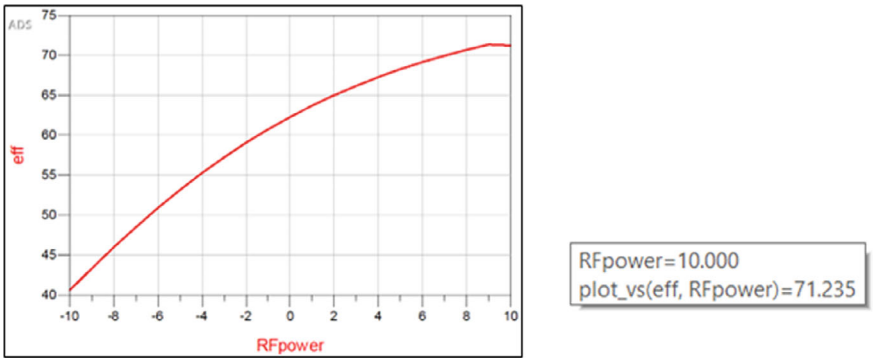

Fig. 13 Efficiency versus input power plot for impedance matched rectifier at 900 MHz

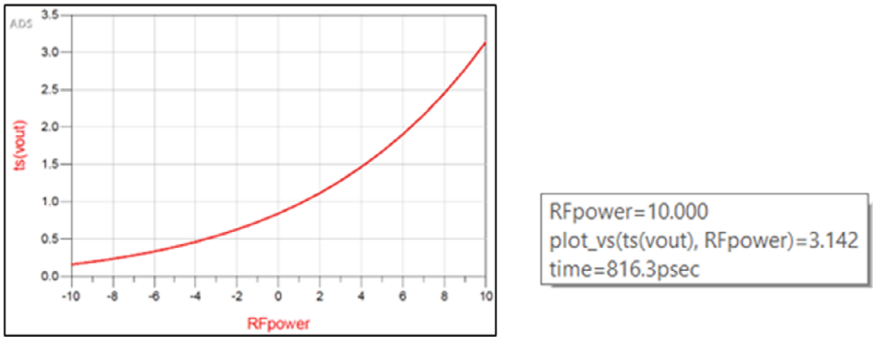

Fig. 14 Output voltage of rectifier at 2.45 GHz

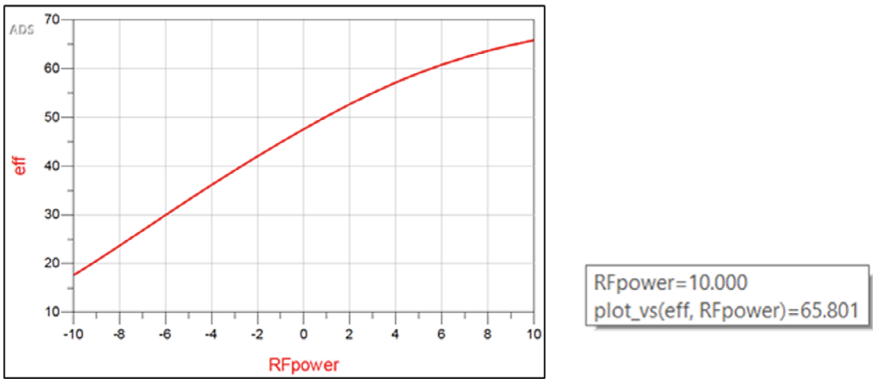

Fig. 15 Efficiency versus input power plot for impedance matched rectifier at 2.45 GHz

Table 2 Gain and conversion efficiency at 900 MHz and 2.45 GHz frequency

Operating frequency	Gain (dB)	Conversion efficiency (%)
900 MHz	8.797	71.232
2.45 GHz	8.852	65.801

4 Conclusion

The proposed rectenna achieves a gain of 8.797 dB at 900 MHz frequency and 8.852 dB at 2.45 GHz frequency which are suitable for energy harvesting in IoT applications as IoT systems use Wi-Fi HaLow technology conventional Wi-Fi technology. The rectifier has maximum conversion efficiency of 71.232% at 900 MHz and 65.801% at 2.45 GHz frequencies. Hence, the antenna is suitable as alternate to conventional power source for low power, and portable devices are used in IoT systems.

References

1. Maher, R., Allam, A., Kanaya, H., Abdelrahman, A.B.: Integrated compact-size rectenna with enhanced RF to DC power conversion efficiency and high-gain antenna. In: IEEE 22nd Annual Wireless and Microwave Technology Conference (2022). https://doi.org/10.1109/WAMICON53991.2022.9786182
2. Shi, L., Delgado, A., Ramos, R., Alou, P.: A wireless power transfer system with inverse coupled current doubler rectifier for high output current applications. IEEE Trans. Ind Electron. https://doi.org/10.1109/TIE.2021.3078350
3. Sakai, N., Noguchi, K., Itoh, K.: A 5.8-GHz band highly efficient 1-W rectenna with short-stub-connected high-impedance dipole antenna. IEEE Trans. Microw. Theory Tech. https://doi.org/10.1109/TMTT.2021.3074592 (2021)
4. Quddious, Zahid, S., Tahir, F.A., Antoniades, M.A., Vryonides, P., Nikolaou, S.: Dual-band compact rectenna for UHF and ISM wireless power transfer systems. IEEE Trans. Antennas Propag. **69**(4), 2392–2397 (2021). https://doi.org/10.1109/TAP.2020.3025299
5. Li, S., Cheng, F., Gu, C., Yu, S., Huang, K.: Efficient dual-band rectifier using stepped impedance stub matching network for wireless energy harvesting. IEEE Microw. Wirel. Compon. Lett. https://doi.org/10.1109/LMWC.2021.3078546 (2021)
6. Malik, T., Doychinov, V., Hayajneh, A.M., Zaidi, S.A.R., Robertson, I.D., Somjit, N.: Wireless power transfer system for battery-less sensor nodes. IEEE Access **8**, 95878–95887 (2020). https://doi.org/10.1109/ACCESS.2020.2995783
7. Rotenberg, S.A., Podilchak, S.K., Re, P.D.H., Mateo-Segura, C., Goussetis, G., Lee, J.: Efficient rectifier for wireless power transmission systems. IEEE Trans. Microw. Theory Tech. **68**(5), 1921–1932 (2020). https://doi.org/10.1109/TMTT.2020.2968055
8. Liu, Qin, Y., Chen, Y., Wei, R.: A dual-band rectifier with improved T-section matching network for RF energy harvester. In: 2020 International Conference on Microwave and Millimeter Wave Technology (ICMMT), pp. 1–3 (2020). https://doi.org/10.1109/ICMMT49418.2020.9386721
9. Liu, J., Huang, M., Du, Z.: Design of compact dual-band RF rectifiers for wireless power transfer and energy harvesting. IEEE Access **8**, 184901–184908 (2020). https://doi.org/10.1109/ACCESS.2020.3029603

10. Papadopoulou, M.S., Boursianis, A.D., Goudos, S.K., Psannis, K.: Dual-band rectifier design for ambient RF energy harvesting. In: 2020 3rd World Symposium on Communication Engineering (WSCE), pp. 7–11 (2020). https://doi.org/10.1109/WSCE51339.2020.9275569
11. Ghaffar, A., Jun Li, X., Awan, W.A., Hussain, N.: A compact dual-band antenna based on defected ground structure for ISM band applications. In: WSA 2020; 24th International ITG Workshop on Smart Antennas (2020)
12. Bhatt, K., Kumar, S., Kumar, P., Tripathi, C.C.: Highly efficient 2.4 and 5.8 GHz dual-band rectenna for energy harvesting applications. IEEE Antennas Wirel. Propag. Lett. **18**(12), 2637–2641 (2019). https://doi.org/10.1109/LAWP.2019.2946911
13. Wang, M., Fan, Y., Yang, L., Li, Y., Feng, J., Shi, Y.: Compact dual-band rectenna for RF energy harvest based on a tree-like antenna. IET Microw. Antennas Propag. **13**(9), 1350–1357 (2019). https://doi.org/10.1049/iet-map.2018.5704
14. Trinh, L.H.: Design of a dual-band rectenna for small IoT terminal. In: 2019 International Symposium on Electrical and Electronics Engineering (ISEE) (2019)
15. Qiao, L., Zheng, Z., Cui, W., Wang, L.: A survey on Wi-Fi HaLow technology for Internet of Things. In: 2018 2nd IEEE Conference on Energy Internet and Energy System Integration (EI2), pp. 1–5. Beijing (2018). https://doi.org/10.1109/EI2.2018.8582141
16. Aboualalaa, M., et al.: Dual-band rectenna using voltage doubler rectifier and four-section matching network. In: 2018 IEEE Wireless Power Transfer Conference (WPTC), pp. 1–4. Montreal, QC, Canada (2018). https://doi.org/10.1109/WPT.2018.8639451

A Study of an Efficient Edge Detection Approach with Machine Learning Techniques

Faiza Mushtaq and Harpreet Singh Bedi

Abstract The daily traffic volume is increasing, and there is insufficient infrastructure to manage it effectively. This study aims to improve traffic identification outcomes by conducting a comparative analysis between the Sobel and Canny edge detection techniques using image processing. The analysis is performed across various parameters to determine the superior approach and subsequently develop an advanced technique for data abstraction in the context of the traffic system. Only an edge map with accurate edges can provide useful information. Edge detection is a highly challenging process, and our goal is to achieve precise edge location of the vehicle, which further aids in detecting the vehicle. The primary objective of our proposed research is to enhance the accuracy and speed of vehicle detection by developing an efficient algorithm. We aim to exceed the performance of existing algorithms in the field and provide a more precise and reliable solution for vehicle detection. The proposed algorithm will assist in managing traffic congestion by utilizing edge gradient direction and magnitude images. Our study aims to contribute to the field of traffic management by providing an effective solution for detecting vehicles.

Keywords Image processing edge detection · Canny edge detection · Sobel algorithm · Gradient direction · Gradient magnitude

F. Mushtaq (✉)
School of Electronics and Electrical Engineering, Lovely Professional University, Punjab, India
e-mail: faizabeigh7@gmail.com

H. S. Bedi
School of Electronics and Electrical Engineering, Lovely Professional University, Punjab, India
e-mail: harpreet.17377@lpu.co.in

© The Author(s), under exclusive license to Springer Nature Singapore Pte Ltd. 2025

H. P. Singh et al. (eds.), *Recent Developments in Control, Automation and Power Engineering*, Lecture Notes in Electrical Engineering 1303,
https://doi.org/10.1007/978-981-96-0047-2_9

1 Introduction

In intelligent traffic systems, images are an essential means of conveying information. Digital images are composed of pixels and can be manipulated through image processing techniques. The resolution of a digital image is determined by its dimensions, expressed in pixels that correspond to its height and width. Digital images are interpreted by computers as functions, denoted by $I(x, y)$ or $I(x, y, z)$ for binary/grayscale or RGB images, respectively, where "I" represents pixel intensity and (x, y) or (x, y, z) represents the pixel coordinates in the image. Detecting edges in the images is a crucial task in image processing and segmentation [1].

The present research study aims to conduct a comparative analysis of two widely employed edge detection methods, i.e., Canny edge detection and Sobel algorithm. The primary objective of this study analyze and evaluate the performance of these two techniques in terms of accurately detecting edges in digital images while minimizing computational time. The study proposes an approach that combines the strengths of both algorithms, resulting in improved outcomes. Edge detection's goal is to considerably reduce an image's data content while maintaining the structural integrity of the image for subsequent image processing. The identification of edges can be achieved through two methods: the gradient method and the Laplacian method [2] (Fig. 1).

The basic approach for detecting edges in an image involves analyzing the gradient's magnitude and orientation at each pixel. The gradient is represented as a vector, referred to as "grad," for every pixel location (x, y) within an image (f) [3].

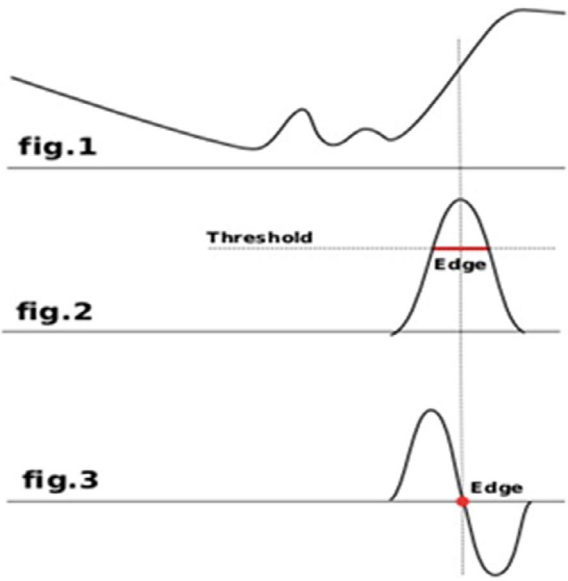

Fig. 1 **a** An image signal, **b** Gradient edge signal, **c** Laplacian edge signal

$$\text{grad}(f) = \left[\frac{Gx}{Gy}\right] \tag{1}$$

where Gx = df/dx and Gy = df/dx

The gradient magnitude is determined by:

$$|G| = \sqrt{(Gx)^2 + (Gy)^2}. \tag{2}$$

The gradient vector's angle of direction is:

$$\tan^{-1}(\text{Gy} / \text{Gx}). \tag{3}$$

Image processing improves the visual quality of an image and extracts relevant information from it. The image processing toolbox can process, visualize, and analyze images in various data formats, such as single-precision and double-precision floating-point numbers, as well as 8-, 16-, and 32-bit signed or unsigned integers simultaneously removing impulsive noise from the image [4].

2 Literature Survey

Algorithms are a set of instructions that solve a particular problem or perform a specific task. In the literature survey, we will explore some research articles based on algorithms and analyze their performance.

2.1 Analysis of Image Processing Approach

Mohan et al. examined the effectiveness of segmentation and edge detection methods in identifying the number and density of vehicles within designated lanes with the aim of improving traffic management in India [5]. Uddin et al. proposed a traffic density estimation by analyzing the road traffic, utilizing image processing, applying an algorithm, and ultimately making decisions. The proposed method is suitable for integration into intelligent traffic control systems, particularly in densely populated countries [6]. The study by Shaikat et al. proposes a solution to address traffic congestion by using artificial intelligence and image processing techniques to control traffic signals. The proposed system utilizes the Haar cascade method to detect the number of vehicles and AI to adjust the timing of traffic signals accurately. The paper concludes that the system is highly efficient and can serve as a self-contained traffic control device [7].

2.2 Performance of Edge Detection Algorithm

Ansari et al. analyzed Prewitt, Sobel, Canny, Roberts, and Laplacian of Gaussian. Canny and Log outperformed first-order techniques, but Log was less effective due to noise susceptibility. Canny is the most effective for detecting both inner and outer lines, while Sobel is better for detecting outer lines [8]. Ganesan et al. study is a thorough analysis of edge detection methods in image processing and finds that the Canny edge detector works well in noisy conditions, while wavelet-based methods are more accurate than other techniques [9].

2.3 Efficient Edge Detection Algorithm

Mittal et al. proposed a new edge detection technique called B-Edge that aims to overcome the limitations of existing edge detection methods. B-Edge utilizes simulated triple thresholds to offer better edge continuity, detect robust and thin edges with low noise, and provide a higher entropy value. The proposed technique has potential applications in object recognition and security in computer vision [10]. Yuan et al. paper proposes a method to identify edges in an image using a combination of local and global edge detection techniques. The method uses a localized approach for detecting edges in a specific area and a global edge detection algorithm that employs the Canny operator. The combination of these techniques results in higher resolution, more precise positioning, and better noise resistance compared to the Canny edge detection approach [11].

2.4 Satellite Traffic Monitoring

The study by Eslami et al. proposes a method to detect cars and roads in high-resolution satellite images for accurate traffic management and density determination by using an artificial immune mechanism to extract vehicle targets and feature extraction and image processing techniques, including Hough transform, gradient, and thresholding, to recognize roads [12].

3 Methodology

This study compares the Canny and Sobel algorithms in order to assess their strengths and hence proposes an improved edge detection algorithm which will surpass the limitation of both the traditional algorithms.

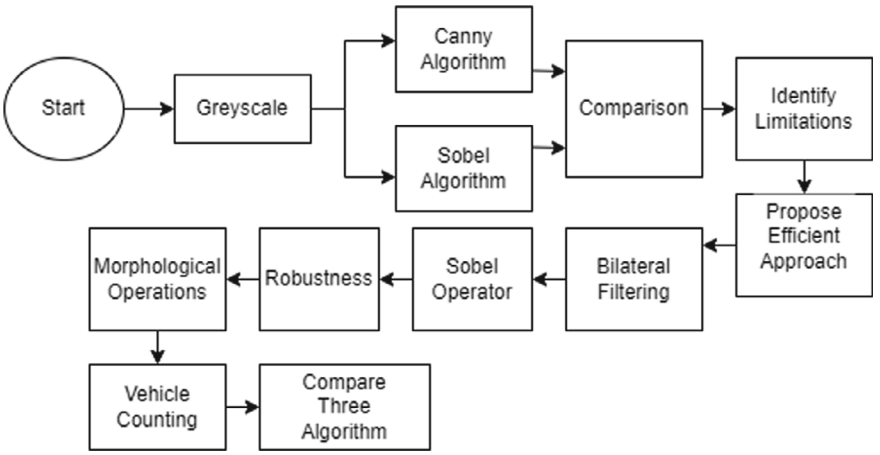

Fig. 2 Steps toward the efficient algorithm approach

Dataset of vehicle images was gathered and preprocessed into gray scale. The preprocessed photos were then subjected to the Sobel and Canny edge detection algorithms. Visual evaluation and comparison were done on the edges, robustness, and vehicle count that resulted. Execution time was another way to gauge computational effectiveness. The Canny edge detection method is combined with a number of image processing methods, such as bilateral filtering, Gaussian smoothing, morphological operations, and the Sobel operator, in our enhanced improved algorithm proposal. A Gaussian blur filter was used before Canny edge detection to enhance image quality and lower noise. Morphological procedures were used to better improve the edges that were already detected. The gradient magnitude and direction were computed using the Sobel operator, which provided important edge information. These results underline how crucial it is to take into account the order and mix of image processing steps in order to maximize edge detection efficiency (Fig. 2).

3.1 Canny Edge Detection

The Canny edge detector was designed to detect precise edges of high intensity [13]. The Canny operator is effective in controlling the level of detail in the edge image and suppressing noise. It employs two threshold values, namely T1 and T2 [8]. Canny algorithm is adjustable, extracts features without disturbing the image, and is noise-resistant [14] (Fig. 3).

Gx and *Gy* represent horizontal and vertical patterns while *Gxy* is the pixel value of an image. The central pixel's gradient direction and magnitude are determined as follows [16]:

Fig. 3 3 × 3 mask for Canny edge detection

$$p_x = (a_6 + 2a_7 + a_8) - (a_0 + 2a_3 + a_6) \tag{4}$$

$$p_y = (a_6 + 2a_7 + a_8) - (a_0 + a_1 + a_2) \tag{5}$$

3.2 Sobel Algorithm

The Sobel method employs two 3 × 3 masks to detect edges, with the central pixel given priority as it relies on central differences. One of the masks can detect edges at a 45-degree angle, as it is a 90-degree rotation of the other. The Sobel operator's fast detection speed is a significant advantage [8]. However, it detects edges in the horizontal and vertical directions, ignoring other directions [15] (Fig. 4).

$$|G| = \sqrt[2]{Gx^2 + Gy^2} \tag{6}$$

To measure orientation angle

$$\Delta = \arctan\left(\frac{Gx}{Gy}\right) - \frac{3\pi}{4} \tag{7}$$

Fig. 4 3 × 3 mask for Sobel algorithm

3.3 Improved Algorithm

The proposed algorithm outperforms the established Sobel and Canny edge detection techniques in terms of accuracy and reliability. By integrating bilateral filtering, the algorithm gains resilience and effectively reduces noise, producing a cleaner input. The improved method exhibits enhanced edge recognition accuracy by mitigating false positives. Additionally, the algorithm produces an orientation histogram based on the edge data, offering valuable insights into edge orientations. As a result, the algorithm achieves significantly improved accuracy in determining the direction of edges within the image. The overall precision and dependability of the method are greatly enhanced by these improved edge detection outcomes.

4 Results and Analysis

Our experiment is done on Spyder (Python 3.9). We evaluated the outcome of Canny edge algorithm and Sobel algorithm and obtained the following results:

The improved algorithm performed well in terms of scalability and efficiency. However, Canny produced finer and Sobel algorithm produced thicker edges, resulting in reduced precision. While the Sobel algorithm had edge disconnections, the Canny algorithm displayed edge connectedness. As opposed to Canny and Sobel, our suggested better approach demonstrated increased edge continuity, resulting in a finer edge representation. The enhanced algorithm performed remarkably well in terms of robustness by precisely highlighting vehicles in the image. Vehicles were also recognized by Canny; however, it occasionally added extra edges, whereas the Sobel method had detection issues. The Sobel method produced inaccurate findings when it came to vehicle counting, whereas the upgraded algorithm and Canny both offered precise counts. The enhanced algorithm outperformed the Sobel and Canny algorithms in terms of execution time. The Canny algorithm had the longest execution time, whereas the Sobel algorithm took a little less time than Canny. In light of these results, we found that our modified algorithm surpassed the Canny and Sobel algorithms in terms of every parameter that was tested. These enhanced results have a great deal of promise to improve traffic-related applications and progress the science.

Table 1 presents the analysis of time execution using a dataset of vehicle images, revealing that the Canny algorithm exhibits higher time consumption compared to the Sobel algorithm and our proposed improved algorithm. While Canny is regarded as an advanced technique, its disadvantage is that it takes longer to execute. In contrast, our proposed algorithm demonstrates superior performance in terms of time execution, robustness, edge detection, and vehicle count, surpassing both Canny and Sobel algorithms (Figs. 5 and 6; Table 2).

Table 1 Time execution

Image	Canny edge detection (s)	Sobel algorithm (s)	Improved algorithm (s)
1	0.0126	0.0030	0.00
2	0.2025	0.0381	0.02
3	0.0354	0.0010	0.00
4	1.0199	0.0010	0.00
5	1.0892	0.0363	0.02

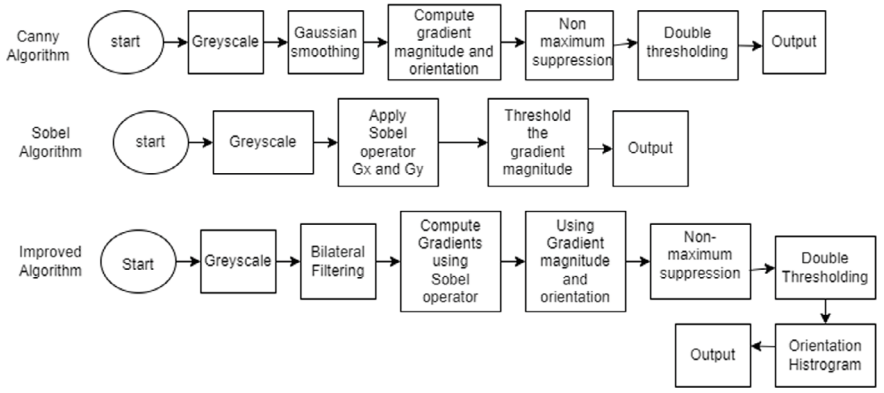

Fig. 5 Flowchart of the Canny, Sobel, and improved algorithm

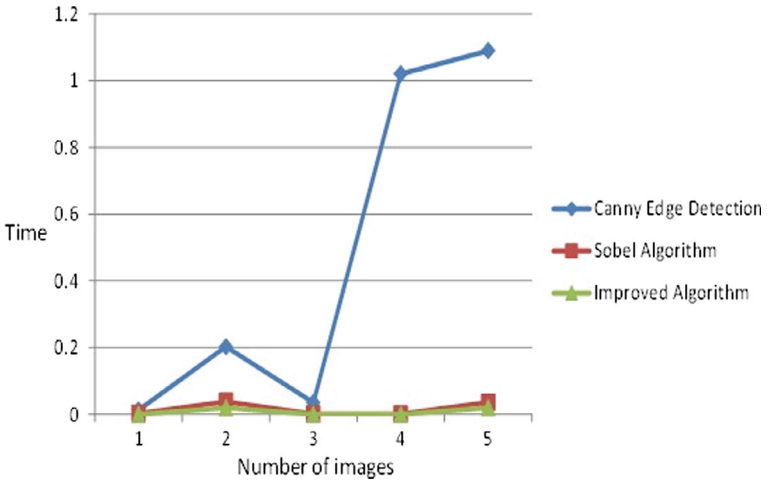

Fig. 6 Comparison graph of time execution

Table 2 Comparison between Canny and Sobel Algorithm

Method name	Canny algorithm	Sobel algorithm	Improved algorithm
Original image			
Edge detection			

(continued)

Table 2 (continued)

Method name	Canny algorithm	Sobel algorithm	Improved algorithm
Robustness	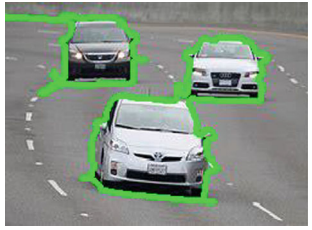		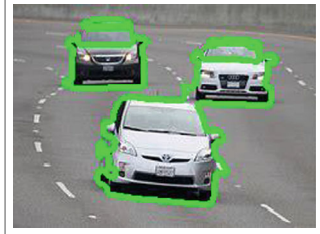
Vehicle count	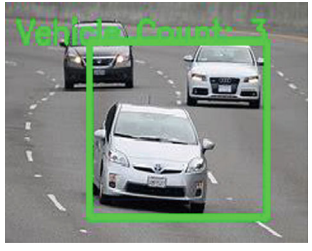	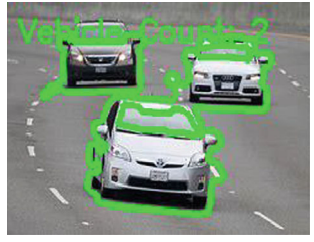	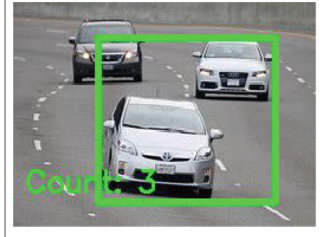

5 Conclusion

This study conducts in-depth research on the edge detection technique used in digital image processing for Canny and Sobel edge detection algorithm and proposes an improved algorithm which surpasses the limitations of traditional algorithms. Our research focuses on improving edge detection techniques in digital image processing with the help of machine learning. Through the integration of bilateral filtering, Gaussian blur, Canny edge detection, the Sobel operator, morphological operations, and precise vehicle counting, our proposed algorithm outperforms traditional methods.

References

1. Sharma, A., Ansari, M.D., Kumar, R.: A comparative study of edge detectors in digital image processing. In: Proceedings of the 4th IEEE International Conference on Signal Processing, Computing and Control, p. 5. Solan, India (2017)
2. Phueakjeen, W., Jindapetch, N., Kuburat, L., Suvanvorn, N.: A study of the edge detection for road lane. In: Proceedings of the 8th Electrical Engineering/Electronics, Computer, Telecommunications and Information Technology Association of Thailand Conference 2011, p. 4 (2011)
3. Sharma, T., Shokeen, V., Mathur, S.: Performance comparison of edge detection algorithms for satellite images using bigdata platform spark. In: Proceedings of the 2016 1st India International Conference on Information Processing, p. 5. IEEE, Delhi (2016)
4. Kour, A., Yadav, V.K., Maheshwari, V., Prashar, D.: A review on image processing. Int. J. Electron. Commun. Comput. Eng. **6** (2012)
5. Mohan, N., Mishra, G.: Density based traffic control using image processing methods: a review. Int. J. Innov. Sci. Res. Technol. **4** (2022)
6. Uddin, M.S., Das, A.K., Taleb, M.A.: Real-time area based traffic density estimation by image processing for traffic signal control system: Bangladesh perspective. In: 2nd International Conference on Electrical Engineering and Information & Communication Technology (ICEEICT), p. 5. IEEE, Savar, Bangladesh (2015)
7. Shaikat, A.S., Tasnim, R., Mahbub, F., Saleheen, R.U., Mahmud, R., Islam, T.: An image processing and artificial intelligence based traffic signal control system of Dhaka. In: Asia Pacific Conference on Research in Industrial and Systems Engineering, p. 6. IEEE, Depok (2019)
8. Ansari, M.A., Kurchaniya, D., Dixit, M.: A comprehensive analysis of image edge detection techniques. Int. J. Multimedia Ubiq. Eng. **13** (2017)
9. Ganesan, P., Sajiv, G.: A comprehensive study of edge detection for image processing applications. In: 2017 International Conference on Innovations in Information, Embedded and Communication Systems (ICIIECS), p. 6. Chennai, India (2017)
10. Mittal, M., Verma, A., Kaur, I., Kaur, B., Sharma, M., Goyal, L.M., Roy, S., Kim, T.-H.: An efficient edge detection approach to provide better edge connectivity for image analysis. IEEE Access **16** (2019)
11. Yuan, L., Xu, X.: Adaptive image edge detection algorithm based on canny operator. In: 4th International Conference on Advanced Information Technology and Sensor Application, p. 4 (2015)
12. Eslami, M., Faez, K.: Automatic Traffic Monitoring from Satellite Images Using Artificial Immune System, p. 10. Springer, Berlin (2010)
13. Kumar, S., Upadhyay, A.K., Dubey, P., Varshney, S.: Comparative analysis for edge detection techniques. In: International Conference on Computing, Communication, and Intelligent Systems (ICCCIS), p. 7. Springer (2021)

14. Dhankhar, P., Sahu, N.: A review and research of edge detection techniques for image segmentation. Int. J. Comput. Sci. Mob. Comput. **7** (2013)
15. Jain, A., Gupta, M., Tazi, S.N., Deepika: Comparison of edge detectors. In 2014 International Conference on Medical Imaging, m-Health and Emerging Communication Systems (MedCom), 6. Springer (2014)
16. Xuan, L., Hong, Z.: An improved canny edge detection algorithm. In: 2017 8th IEEE International Conference on Software Engineering and Service Science (ICSESS), p. 4. Springer, Beijing, China (2017)

Wireless EV Charging Station Using Weight Sensor

Sourav Kumar Singh, Jayesh Kumar, Seikh Atif Aslam, and Suresh Kumar Sudabattula

Abstract Wireless charging has become a practical method for EVs due to its effectiveness and portability. In this study, we introduce a novel wireless charging station for electric vehicles that utilizes a weight sensor to improve charging effectiveness. The charging station is set up to automatically change the charging power based on the weight of the EV, providing information about the battery state of charge (SOC) and charging efficiency. A weight sensor built into the charging station measures the mass of the electric vehicle when it is parked there to recharge. The vehicle's mass information is used by an advanced charge control system to determine the most effective charging current. The charging power is managed in real time to avoid overcharging or undercharging, which can be damaging to a battery's performance and lifespan. The charging station is adaptable in that it may be used to accept a variety of electric vehicle types as a standalone device or as part of an existing charging network. Experimental findings show that weight-based charge optimization significantly increases charging efficiency and reduces charging time when compared to conventional fixed-power charging stations.

Keywords Electric vehicles (EVs) · State of charge (SOC) · Internal combustion engine (ICE)

List of Abbreviations and Variables

EVs	Electric vehicles
EMF	Electromagnetic field
ICE	Internal combustion engine
WCS	Wireless charging station
SOC	State of charge

S. K. Singh · J. Kumar · S. A. Aslam · S. K. Sudabattula (✉)
School of Electronics and Electrical Engineering, Lovely Professional University, Phagwara, Punjab 144411, India
e-mail: suresh.21628@lpu.co.in

© The Author(s), under exclusive license to Springer Nature Singapore Pte Ltd. 2025

H. P. Singh et al. (eds.), *Recent Developments in Control, Automation and Power Engineering*, Lecture Notes in Electrical Engineering 1303,
https://doi.org/10.1007/978-981-96-0047-2_10

ICPT Inductively coupled power transfer

1 Introduction

The tremendous advancement of technology over the last few decades has caused a significant transformation of the planet. The growth of technology has changed every aspect of existence. Technology advancements have caused a rapid shift of the automotive industry as well. Although transportation is crucial to our everyday lives, internal combustion engines (ICEs) are being phased out in favor of electric motors and batteries as the globe works to minimize carbon emissions. Electric cars require an energy supply, which can come from a variety of sources. Electric vehicles often use batteries to power their motors. Due to the growing usage of batteries as a form of energy storage, there is an immediate need for charging stations that would be used to replenish the batteries of electric vehicles [1]. Installing charging stations is a long-term investment in sustainable transportation that benefits the economy, environment, and both. The installation of charging stations for EVs would require collaboration between the government, industry, and individuals in order to accomplish a seamless transition to the use of electric cars. To make the transition easier, charging stations should be placed in high-traffic areas including parking lots, commercial districts, and residential neighborhoods. Making our transportation system more environmentally friendly and less dependent on fossil fuels requires installing charging stations for electric vehicles. The demand for quick and dependable charging options has increased as electric vehicles become more and more popular as a green transportation choice [2, 3]. Due to the necessity to physically connect and unhook cables and connectors, EV drivers may find it inconvenient to utilize conventional wired charging stations. Wireless charging systems offer a potential substitute for utilizing wires to power electric automobiles. The creation of a weight-sensing wireless electric vehicle charging station prototype is described in this project report [4–7]. Further, in Sect. 2 literature survey is given, In Sect. 3 scope and objective of the study is explained. In Sect. 4 methodology followed by system study and design is explained. In Sects. 5 and 6 results and discussion followed by conclusion of the article are explained.

2 Literature Survey

2.1 Two Receiver Coils Being Used in a Novel Wireless Charging System for Electric Automobiles

This research looks at the pros and cons of using dual receiver coils in comparison with the tried-and-true single-coil approach. A new mathematical model of the wireless power transmission system is used as the basis for this inquiry. In order to assess how the proposed model's parameters (resistance, inductance, pitch angle, coil size, distance between coils, and receiver coil displacement speed) affected the recharge tool's efficiency, extensive research was conducted [8–12]. This new model will help you determine how many wireless coils you will need to properly charge your vehicle if the road you are driving on is capable of being recharged.

Inductively Coupled Power Transfer (ICPT) for Electric Vehicle Charging

In this research, we examine the development of inductively coupled power transfer (ICPT) for recharging EVs. The authors emphasize the need for efficient and easy charging options for EVs, as well as the potential benefits of ICPT technology, such as reduced charging time and greater safety. They explain how an ICPT works and what components it needs to function properly. The several charging topologies now used in the field are also discussed, and a comparison is offered with previously reported ICPT systems. Consequences of misalignment, the high cost of setting up the necessary infrastructure, and the need for increased charging efficiency are only a few of the issues with ICPT technology that are explored.

3 Scope of the Study

3.1 Problem Statement

One of the most crucial components of driving an electric car is plugging it in to charge. Currently, there is a lack of clarity about how to properly charge an electric vehicle at a charging station. While charging stations are being installed at a rapid rate, the information being made available to the public regarding how these stations work is falling short of expectations. As a result, the driver won't have to do a thing once he pulls up to the charging station and parks his car on the platform. The goal of developing a smart charging station for EVs based 'on a weight sensor is to minimize the amount of time and effort required by the user. As soon as the system recognizes the vehicle, the charging process will begin, and the user will be provided with all the information, including the battery's current status, the time it will take to fully charge the vehicle, and the total cost to the customer.

3.2 *Objective and Hypothesis of the Study*

The objective of this project is to design and implement a wireless EV charging station that uses a weight sensor to automatically detect the presence of an EV and initiate the charging process. The weight sensor will be integrated into the charging pad, which will be installed on the platform. When an EV parks on the charging pad, the weight sensor will detect the presence of the EV, and the charging process will start wirelessly, eliminating the need for physical connections.

4 Research Methodology

The wireless EV charging station will be designed and implemented using the following methodology shown in the Fig. 1 given below.

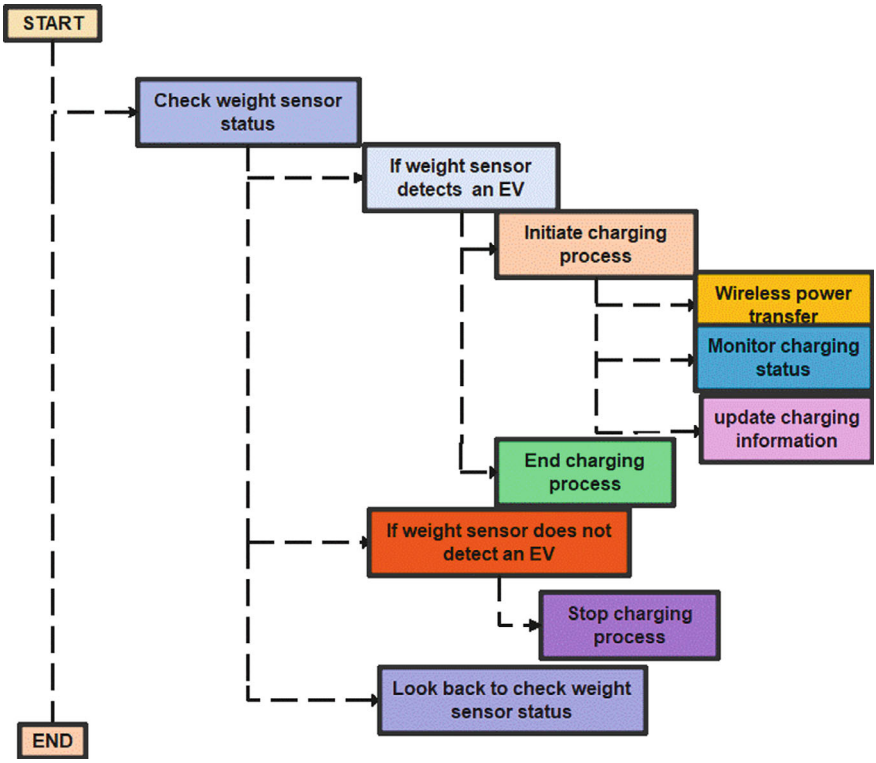

Fig. 1 Graphical representation of the work

Table 1 Overview of different components used and their specifications

Components	Specifications 1	Specifications 2	Specifications 3
Transformer	Input voltage (V): 230–240 V	Current (A): 2 A	Frequency: 50 Hz
IN4007 diode	Reverse voltage: 1000 V	Forwards current: 1A	Maximum surge current: 30 A;
Bridge rectifier	Maximum DC output current—100A	Maximum threshold voltage (VFO)—0.8 V	Maximum peak forward voltage—1.3 V
IC7805 voltage regulator	Min input voltage: − 7 V Min	Max input voltage: − 25 V Max	Maximum 125 °C junction temperature
Weight sensor	5–15 V Excitation voltage operating window	1055 ± 15-Ω input impedance	1000 ± 5-Ω output impedance
HX711 amplifier	24 Bit resolution	Excitation voltage 5–10 V	Normal operating state—1.5 Ma
Arduino	Operating voltage—5 V	SRAM—2 KB	Flash memory 32 KB
LCD display	Aspect ratio 16:5 and 4:3	Operating voltage 4.7–5.3	Operating current 1.3 mA

4.1 System Design

There will be an EV receiving coil, a charging pad, a weight sensor, and a power electronics unit. To facilitate cordless power delivery, the charging pad will be wired with coils. When an EV is present, the charging pad's weight sensor, which is coupled to a microcontroller, will register the difference in mass. The magnetic field will be captured by the EV receiver coil, converted into electrical energy, and then used to charge the EV's battery, all under the direction of the power electronics unit. The specifications of components are given in Table 1.

4.2 System Implementation

A non-conductive substance will be used to build the charging pad, and the coils will be wound and wired to the power electronics module. The microcontroller will be wired to the weight sensor embedded in the charging pad, and its software will be set to recognize the presence of an electric vehicle and begin the charging process automatically. A power supply, a resonant converter, and a control unit will make up the power electronics unit, which will manage the flow of energy. Aligning the EV's undercarriage with the charging pad will maximize energy transfer from the charging pad to the EV's receiver coil.

5 Results and Discussion

We have used weight sensor implanted in the charging pad of 50 kg in which our system will operate when the weight is more than 10 kg and less than 50 kg, the charging process will be triggered within the specified limit. The hardware implementation results are represented in below figures. Figure 2 depicts that when light weight is placed on the charging pad, the system does not start the charging process. In Fig. 3 illustrating light weight vehicles are not allowed by the system so it signals the vehicle to move forward. System recognizes that vehicle parked on the charging pad, battery status is displayed and charging process starts and the same represented in Fig. 4. In Fig. 5 charging process is displayed and charging process has started and need to wait until fully charging will be done. Finally Fig. 6 shows that EV placed on the charging pad is completely charged and after complete charging the system is turned off. There was an average of less than 5% error in detecting both the presence and weight of the vehicles when using the weight sensor. A vehicle's weight sensor provides for more precise billing and reduces the likelihood of either over-or undercharging. It is more convenient for drivers of electric vehicles because the weight sensor is built in and they no longer have to guess how long it will take to charge.

Fig. 2 Light weight placed on the charging pad

Fig. 3 LCD status

Fig. 4 Vehicle placed on the charging pad

Fig. 5 LCD status displaying charging process

Fig. 6 Constant output of 4.9 V

6 Conclusion and Future Scope

A weight sensor-based wireless EV charging station offers a practical and efficient solution for the charging of electric vehicles. Wireless EV charging systems are a cutting-edge innovation that could dramatically alter the charging process for electric vehicles. The technological hurdles of increasing efficiency, guaranteeing interoperability, and addressing safety issues remain, notwithstanding the substantial progress made in recent years. However, inductive dynamic charging and static charging for homes, offices, and public spaces are just a few of the promising uses for wireless EV charging systems. Break through is needed. Additionally, the wireless charging eliminates the need for traditional charging cords and reduces clutter from the charging station area. Moreover, this technology can be easily integrated into existing infrastructure with minimal modifications. Overall, the weight sensor-based wireless EV

charging station is a promising and innovative technology that can help accelerate the adoption of electric vehicles and contribute to a cleaner future.

In future, this paper aspires to implement a wireless charging facility for EVs, which would cut down on the price of the wires needed for charging while also providing an efficient means of charging for the vehicles, in which the user is relieved of all responsibility once the vehicle is parked on the platform; the system handles everything from the charging to billing, resulting in higher customer satisfaction.

References

1. Dharavat, N., Sudabattula, S.K., Velamuri, S.: Review on the integration of distributed generations (solar, wind) and electric vehicles connected to the distribution system to minimize power loss and voltage profile enhancement. In: AIP Conference Proceedings, p. 020001 (2022)
2. Dharavat, N., et al.: Optimal allocation of renewable distributed generators and electric vehicles in a distribution system using the political optimization algorithm. Energies **15**, 6698 (2022)
3. Dai, J., Ludois, D.C.: Wireless electric vehicle charging via capacitive power transfer through a conformal bumper. In: 2015 IEEE Applied Power Electronics Conference and Exposition (APEC), pp. 3307–3313 (2015)
4. Bojarski, M., Asa, E., Colak, K., Czarkowski, D.: A 25 kW industrial prototype wireless electric vehicle charger. In: 2016 IEEE Applied Power Electronics Conference and Exposition (APEC), pp. 1756–1761 (2016)
5. Niu, S., Xu, H., Sun, Z., Shao, Z.Y., Jian, L.: The state-of-the-arts of wireless electric vehicle charging via magnetic resonance: principles, standards and core technologies. Renew. Sustain. Energy Rev. **114**, 109302 (2019)
6. Yang, G., et al.: Interoperability improvement for wireless electric vehicle charging system using adaptive phase-control transmitter. IEEE Access **7**, 41365–41379 (2019)
7. ElGhanam, E.A., Hassan, M.S., Osman, A.: Design and finite element modeling of the inductive link in wireless electric vehicle charging systems. In: 2020 IEEE Transportation Electrification Conference and Expo (ITEC), pp. 389–394 (2020)
8. ElGhanam, E.A., Hassan, M.S., Osman, A.H.: Deployment optimization of dynamic wireless electric vehicle charging systems: a review. In: 2020 IEEE International IOT, Electronics and Mechatronics Conference (IEMTRONICS), pp. 1–7 (2020)
9. Liang, C., et al.: Modeling and analysis of thermal characteristics of magnetic coupler for wireless electric vehicle charging system. IEEE Access **8**, 173177–173185 (2020)
10. Song, K., et al.: Design of DD coil with high misalignment tolerance and low EMF emissions for wireless electric vehicle charging systems. IEEE Trans. Power Electron. **35**, 9034–9045 (2020)
11. ElGhanam, E., Hassan, M., Osman, A.: Design of a high power, LCC-compensated, dynamic, wireless electric vehicle charging system with improved misalignment tolerance. Energies **14**, 885 (2021)
12. ElGhanam, E., Hassan, M., Osman, A., Kabalan, H.: Design and performance analysis of misalignment tolerant charging coils for wireless electric vehicle charging systems. World Electr. Veh. J. **12**, 89 (2021)

Universal Filters Based on Bulk-Driven CCII for Low-Voltage Analog Applications

Anu Tonk, Vandana Khanna, and Neelofer Afzal

Abstract This study presents four universal filter implementations employing second-generation current conveyors designed utilizing bulk-driven technique (BDCCIIs) that enable filter operations at considerably low voltage-supply levels. Current-conveyor-based low-and ultra-low-voltage analog signal processing circuits have been rarely investigated. However, they have been subjected to further discussions by design engineers because such modules continue to find wide applications in the emerging fields of portable and wearable electronics, smart environmental monitoring, implantable medical devices, and ambient power harvesting systems. In this study, a detailed circuit analysis of four multi-input single-output (MISO) topologies along with a brief discussion on their component count, tuning feature, and hardware complexity has been discussed. These filters operate at a voltage supply of $\pm$ 0.5 V and exhibit all standard filter responses in voltage mode. Furthermore, PSPICE simulation results obtained with 180-nm CMOS TSMC technology illustrate the operability of each application.

Keywords Low-voltage · BDCCII · MISO · UF · Voltage mode

1 Introduction

In this era of digital electronics, analog signal processing (ASP) circuits continue to evolve because of their considerable applicability for various purposes, including the study of different linear or nonlinear time-varying modules and the simulation of complex mathematical and engineering problems. This stems from the fact that it is fairly easy to compress signals of large dynamic range to one that is manageable in transistor-level design. Often, analog designs consume lesser power than their digital

A. Tonk (✉) · V. Khanna
Department of Multidisciplinary Engineering, The NorthCap University, Gurugram 122017, India
e-mail: anutonk@ncuindia.edu

N. Afzal
Department of Electronics and Communication Engineering, JMI, New Delhi 110025, India

© The Author(s), under exclusive license to Springer Nature Singapore Pte Ltd. 2025

H. P. Singh et al. (eds.), *Recent Developments in Control, Automation and Power Engineering*, Lecture Notes in Electrical Engineering 1303,
https://doi.org/10.1007/978-981-96-0047-2_11

counterparts. A suitable example would be log-domain filtering, which uses the square law in the strong inversion zone of both CMOS and bipolar devices and follows an exponential relationship between current–voltage (I–V) in the subthreshold zone.

Currently, special attention is being devoted to ASP in low-power embedded systems, such as heart or brain implants, biomedical sensors, convertors, and body area monitors [1]. This increasing demand for analog computing combined with the increasing concern for portable and battery powered gadgets has garnered interest toward building circuits that can operate at very low voltage-supply levels. The application of such design techniques [2] is apparently growing, specifically in current conveyors (CCs), because of its success in building other active blocks [3–6]. Previously, based on historic technology trends, analog engineers had anticipated that the MOSFET threshold voltage VT will not decrease at the same pace in the future. Therefore, the development of some nonconventional design techniques that permit existing MOSFETs to implement analog circuits at power supply levels of as low as ≤ 1 V became important. The bulk-driven (BD) method is one such method. In case of a bulk-driven MOS transistor (BDMOST), body/bulk/substrate is the terminal at which the signal input is applied, unlike that in the traditional transistor, which significantly minimizes the threshold voltage constraint [7, 8] or may eliminate it from the signal path. A detailed account of the equivalents of large and small signal BDMOST-based common source amplifier models analyzed at high frequency as published in [2, 9] can be referred by the readers for in-depth explanations.

2 Bulk-Driven Current Conveyor

The most adaptable active building block is thought to be a second-generation current conveyor (CCII). The relation appearing on the three ports of a plus-type CCII is presented below. Further, in a minus-type CCII, the current polarities are opposite, i.e., $Iz = -Ix$.

$$\begin{bmatrix} V_X \\ I_Z \\ I_Y \end{bmatrix} = \begin{bmatrix} 0\ 0\ 1 \\ 1\ 0\ 0 \\ 0\ 0\ 0 \end{bmatrix} \begin{bmatrix} I_X \\ I_Z \\ I_Y \end{bmatrix} \tag{1}$$

In this section, a minus-type BDCCII (BDCCII $-$) implementation is suggested utilizing the plus-type cell recently introduced in previous study [10]. Schematics of the two CMOS implementations are presented (Fig. 1a and b) for reference purposes. There are only 14 transistors in plus-type BDCCII (BDCCII $+$) and 18 in the minus-type bulk-driven CCII (BDCCII $-$) structure. The gate terminals of transistors M4–M5 and M8–M9 have been proposed to operate under a fixed voltage that is necessary for the formation of a channel. Based on the BD concept of driving a MOSFET in its own well rather than the gate, the substrates of transistors M8 and M9 are connected to the input signals X and Y, respectively. The bulk of the remaining PMOS and

NMOS are wired to the positive and negative supply voltages. Current transfer can be obtained from terminal X to $Z+$ via transistors M1–M2, M4–M5, and M6–M7. Subsequently, a stack of four transistors, i.e., M1P–M2P and M1N–M2N, inverts the current polarity of $IZ+$ at the $Z-$ terminal. The voltage-conveying action from the Y terminal to the X terminal is completed by the transistors M8–M9 and M3. The X terminal to the Z+/Z—terminal and the Y terminal to the X terminal are the simulated responses of the current-copying and voltage-copying actions of BDCCII+ and BDCCII−, respectively, and are shown in Figs. 2 and 3. The − 3 db current bandwidth is 72 MHz for BDCCII+ (with 2 kΩ resistors each at X and Z+ terminals), whereas the − 3 db current bandwidth is 66 MHz for BDCCII − (with 2 kΩ resistors each at X and Z+ terminals). Further, the − 3 db voltage bandwidth at port X is 114 MHz (with 2 kΩ resistors each at X and Z+ terminals). The simulated parameters for BDCCIIs are shown in Table 1. The validation of the specified settings using PSPICE simulations is shown in Figs. 2, 3, and 4.

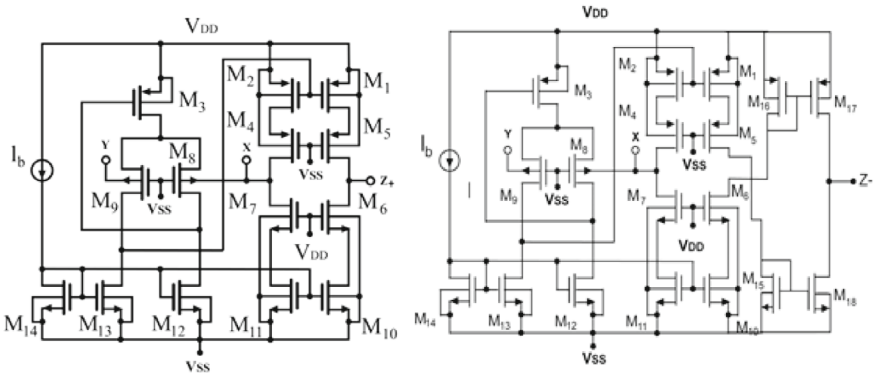

(a) BDCCII+ (b) BDCCII-

Fig. 1 Schematic of (**a**) BDCCII + (**b**) BDCCII −

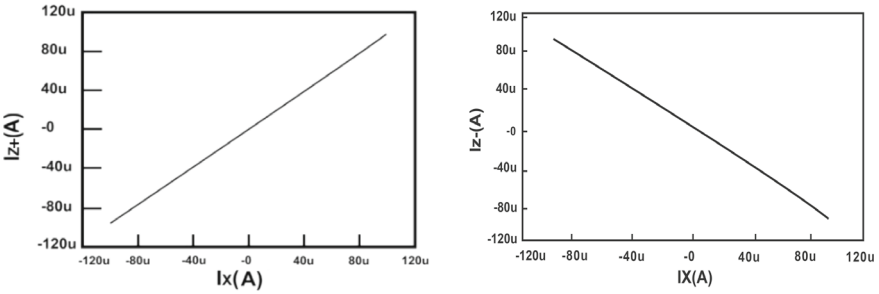

(a) (b)

Fig. 2 Simulated plot of current (**a**) $IZ+$ against IX (**b**) $IZ-$ against IX

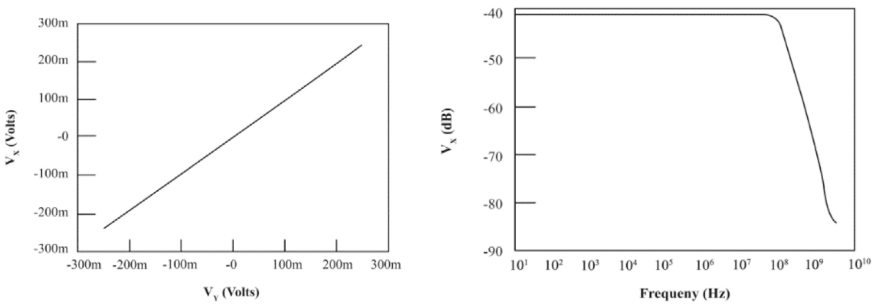

Fig. 3 Simulated (**a**) DC response of *Y* to *X* voltage transfer (**b**) response of the AC voltage at port *X*

Table 1 Main properties of bulk-driven CCII

Characteristics	Simulated results
Ibias	28 μA
Transistor count	14 + , 18 −
DC voltage range	− 250–250 mV
DC current range	− 100–100 μA
BDCCII + bandwidth (current follower)	72 MHz
BDCCII − bandwidth (current follower)	66 MHz
Bandwidth (voltage follower)	114 MHz

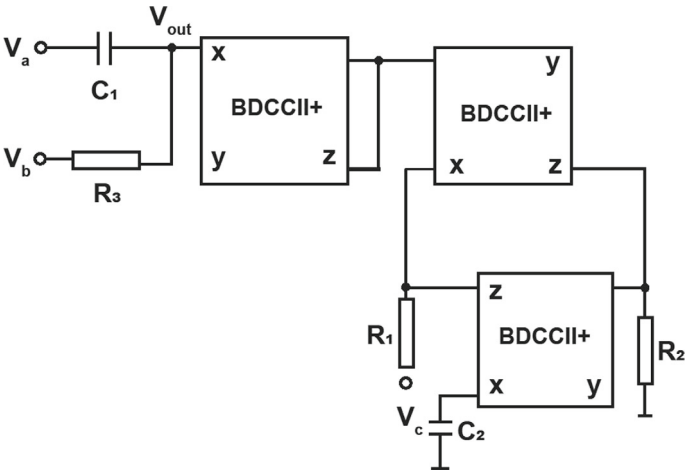

Fig. 4 UF I employing three BDCCII +

3 Universal Filters

Recently, a current-mode (CM) UF based on BDCCII was introduced by Khateb et al. [11]. However, voltage-mode (VM) UFs based on BDCCII have not yet been investigated. In this section, four such biquads exhibiting multifunctional capability are realized. The configuration in Fig. 4 is derived from the study by Çiçekoğlu [12], whereas the topologies in Figs. 5 and 6 are derived from the study by Horng [13]. The fourth one is entirely novel. The UF I employs three BDCCIIs in its structure. The application of only plus-type active blocks simplifies the configuration as given in Ozoguz and Gunes [14]. The UFs II–IV employ just two BDCCIIs, i.e., plus-type and minus-type, in their structure. However, for realizing the AP function, an additional BDCCII will be required for ensuring the unity-gain inversion of one input. In UFs I–III, the signal inputs *Va* and *Vb* are connected to C_1 and R_3, respectively, whereas *Vc* is applied at R_1 (in UFs I and III) and R_2 (in UF II). By connecting all inputs as summarized in Table 2, which presents the operation of every design for different input combinations, an all-pass (AP) response can be obtained. All topologies require only three resistors (3R) and two capacitors (2C), which may be of the floating type in some cases. Currently, advanced IC technologies implement floating capacitors as double poly (poly1–poly2) capacitors and have become a standard [15].

3.1 Transfer Functions

Network analysis yielded the following input–output response. For the topologies presented in Figs. 4, 5, 6 and 7, we obtain

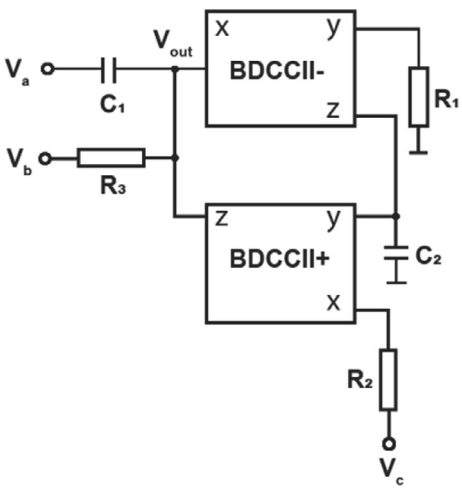

Fig. 5 UF II employing one BDCCII + and BDCCII −

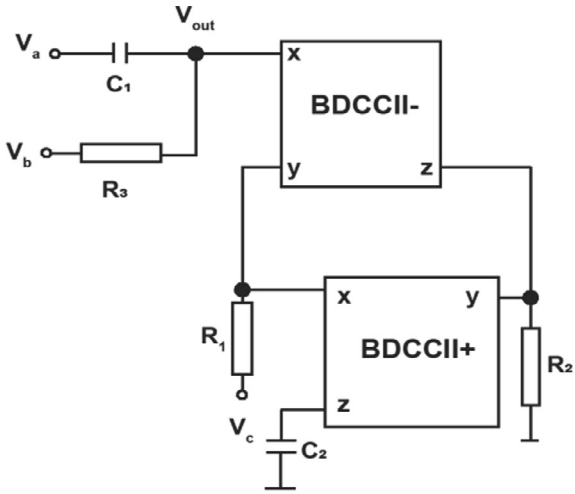

Fig. 6 UF III employing one BDCCII + and BDCCII −

Table 2 Input combinations for implementing different filtering functions of UFs I–IV

Filter	LP	HP	BP	NH	AP
I	$Vc = Vin$ $Va = 0$ $Vb = 0$	$Va = Vin$ $Vb = 0$ $Vc = 0$	$Vb = Vin$ $Va = 0$ $Vc = 0$	$Va = Vin$ $Vc = Vin$ $Vb = 0$	$Va = Vin$ $Vc = Vin$ $Vb = -Vin$
II	$Vc = Vin$ $Va = 0$ $Vb = 0$	$Va = Vin$ $Vb = 0$ $Vc = 0$	$Vb = Vin$ $Va = 0$ $Vc = 0$	$Va = Vin$ $Vc = Vin$ $Vb = 0$	$Va = Vin$ $Vc = Vin$ $Vb = -Vin$
III	$Vc = Vin$ $Va = 0$ $Vb = 0$	$Va = Vin$ $Vb = 0$ $Vc = 0$	$Vb = Vin$ $Va = 0$ $Vc = 0$	$Va = Vin$ $Vc = Vin$ $Vb = 0$	$Va = Vin$ $Vc = Vin$ $Vb = -Vin$
IV	$Vb = Vin$ $Va = 0$ $Vc = 0$ $Vd = 0$	$Vc = Vin$ $Va = 0$ $Vb = 0$ $Vd = 0$	$Vd = Vin$ $Va = 0$ $Vb = 0$ $Vc = 0$	$Vb = Vin$ $Vc = Vin$ $Va = 0$ $Vd = 0$	$Va = Vin$ $Vb = Vin$ $Vc = Vin$ $Vd = 0$

$$Vo = \frac{s^2 V_a + \frac{sC_2V_b}{C_1R_3} + \frac{V_c}{R_1R_2C_1C_2}}{s^2 + \frac{sC_2}{C_1R_3} + \frac{1}{R_1R_2C_1C_2}} \tag{2}$$

$$\omega_o = \frac{1}{\sqrt{R_1R_2C_1C_2}}; Q = R_3\sqrt{\frac{C_1}{R_1R_2C_2}} \tag{3}$$

For the topology presented in Fig. 8, we obtain

$$V_o = \frac{s^2 V_C + \frac{sV_d}{R_5C_4} - \frac{sV_a}{R_1C_4} + \frac{V_b}{R_1R_3C_2C_4}}{s^2 + \frac{s}{R_5C_4} + \frac{1}{R_1R_3C_2C_4}} \tag{4}$$

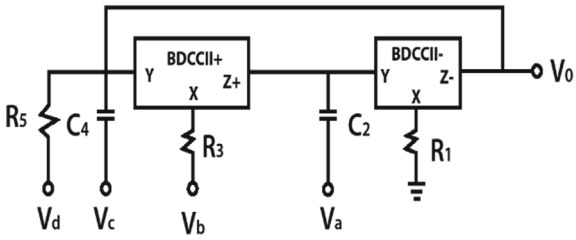

Fig. 7 UF IV employing one BDCCII + and BDCCII −

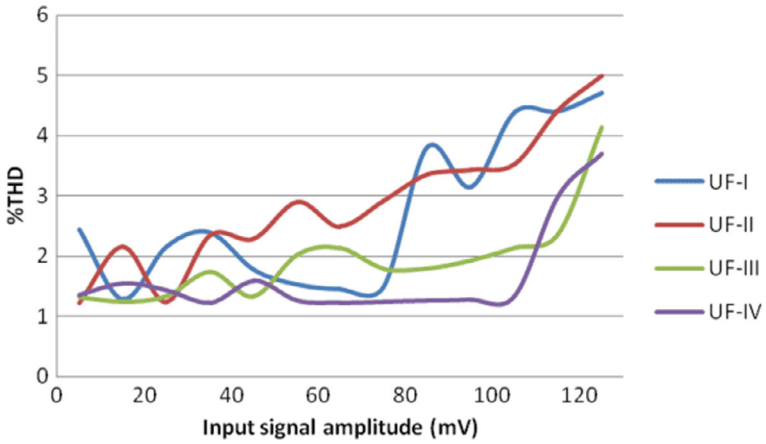

Fig. 8 Total harmonic distortion variation (in %) in the LP output with an input signal of one Kilo Hertz

$$\omega_o = \frac{1}{\sqrt{R_1 R_3 C_2 C_4}}; Q = R_5 \sqrt{\frac{C_4}{R_1 R_3 C_2}} \tag{5}$$

where ω_o is the natural/resonance frequency (in radians) and Q is the quality factor. From Eqs. (3) and (5), it is clear that by carefully choosing the component values, it is possible to control the pole-frequency and pole-Q separately. Furthermore, the simulation results presented in Sect. 4 better explain the above equations.

3.2 Non-ideal Gains

When the non-unity transfer gains (αn and βn) are considered toward evaluation of the non-idealities of BDCCII, then the expression of VX and IZ become as follows: $VX = \beta n VY$ and $IZ = \pm \alpha n IX$. Here, n is the number of block (1st, 2nd, etc.). Further, αn and βn can be expressed as: $\alpha n = 1 - \varepsilon i$, $\beta n = 1 - \varepsilon v$. Here, εi and εv denote the current and voltage gain tracking errors, respectively.

$$Vo = \frac{s^2 V_a + \frac{sC_2V_b}{C_1R_3} + \frac{V_c\alpha_1\alpha_2}{R_1R_2C_1C_2}}{s^2 + \frac{sC_2}{C_1R_3} + \frac{\alpha_1\alpha_2\beta_1\beta_2}{R_1R_2C_1C_2}} \tag{6}$$

$$\omega_o = \frac{\sqrt{\alpha_1\alpha_2\beta_1\beta_2}}{\sqrt{R_1R_2C_1C_2}}; Q = R_3\sqrt{\frac{\alpha_1\alpha_2\beta_1\beta_2}{R_1R_2C_1C_2}} \tag{7}$$

Equations (4) and (5) respectively will modify as follows:

$$V_o = \frac{s^2 V_C + \frac{sV_d}{R_5C_4} - \frac{s\alpha_1\alpha_2\beta_1V_a}{R_1C_4} + \frac{\alpha_1\alpha_2\beta_1V_b}{R_1R_3C_2C_4}}{s^2 + \frac{s}{R_5C_4} + \frac{\alpha_1\alpha_2\beta_1\beta_2}{R_1R_3C_2C_4}} \tag{8}$$

$$\omega_o = \frac{\sqrt{\alpha_1\alpha_2\beta_1\beta_2}}{\sqrt{R_1R_3C_2C_4}}; Q = R_3\sqrt{\frac{\alpha_1\alpha_2\beta_1\beta_2C_4}{R_1R_3C_2}} \tag{9}$$

Using Eqs. (6)–(9), the active and passive sensitivities of UFs I–IV are presented in Table 3. All these values are within unity in terms of magnitude [−1, 1]. Thus, all topologies enjoy low active and passive sensitivity figures. As inferred from Eqs. (3) and (5), the value of ω_o is inversely proportional to $(R_1)^{-1/2}$. For UFs I–III, $R1$ or $R2$ can be changed to change ω_o, while $R3$ can be changed to independently regulate Q. Similar to UF IV, Q can be independently tuned using $R5$, whereas ω_o can be changed by altering $R1$ or $R3$.

Table 3 Sensitivity of UFs I–IV

Sensitivity w.r.t	UFs I–III ωo	UFs I–III Q	UF IV ωo	UF IV Q
$R1$	− 1/2	− 1/2	− 1/2	1/2
$R2$	− 1/2	− 1/2	–	–
$R3$	–	1	− 1/2	1/2
$R5$	–	–	–	1
$C1$	− 1/2	1/2	–	–
$C2$	− 1/2	− 1/2	− 1/2	− 1/2
$C4$	–	–	− 1/2	1/2
$\alpha1$	1/2	1/2	1/2	1/2
$\alpha2$	1/2	1/2	1/2	1/2
$\beta1$	1/2	1/2	1/2	1/2
$\beta2$	1/2	1/2	1/2	1/2

Table 4 Aspect ratio for each MOS transistor M_i

i	*W*/*L*
1, 2	100/0.3 μm
3	18/0.3 μm
4, 5	100/2 μm
6, 7	50/2 μm
8, 9	10/0.3 μm
10, 11	40/0.3 μm
12, 13, 14	4/0.3 μm
1P, 2P	100/0.5 μm
1N, 2N	50/0.5 μm

4 Result

BD CCs utilizing a ± 0.5 V symmetrical DC power voltage supply and $I_b = 21$ μA are constructed based on the implementation presented in Fig. 1 to accomplish the UFs I–IV simulations presented in Sect. 3. Further, the aspect ratios of the transistors are presented in Table 4. All common filter functions, such as high-pass (HP), band-pass (BP), low-pass (LP), notch (NH), and all-pass (AP), can be realized in each configuration. Note that UFs I–III need no critical passive-component matching, unlike UF IV, for obtaining an AP response. To achieve an AP response, they need an additional active device in relation to the unity-gain inverting input ($-Vb$). To illustrate the viability of all circuits, the universal filters in Figs. 4, 5, 6 and 7 have been designed for $Q = 1$ and $fo = \sim 159$ kHz by selecting appropriate passive-component values as follows: (1) for UF I, $R_1 = R_2 = R_3 = 2$ kΩ and $C_1 = C_2 = 0.5$ nF; (2) for UF II, $R_1 = R_2 = R_3 = 1$ kΩ and $C_1 = C_2 = 1$ nF; (3) for UF III, $R_1 = R_2 = R_3 = 3.3$ kΩ and $C_1 = C_2 = 0.3$ nF, and (4) for UF IV, $R_1 = R_3 = R_5 = 1$ kΩ and $C_2 = C_5 = 1$ nF. The filters are applied to an input of a sine waveform V in with a frequency of 1 kHz and an amplitude of 10 mV. The simulation results that are presented in Figs. 9, 10, 11 and 12 agree well with the results of the theoretical analysis. However, a slight difference among them may arise because of the non-ideal gain and parasitic effects. To assess the output's quality, the total harmonic distortion (%THD) for UFs I–IV with respect to the varying input signal amplitude is obtained, as shown in Fig. 8. The THD was considerably lower than 5% up to 125 mV amplitude of the input signal.

5 Discussion

The topologies introduced in previous studies [11–14, 16–40] are universal in their designs and operate either with high (≥1 V) or very-high (≥5 V) voltage supplies. We have mainly concentrated on MISO implementations and have proposed four

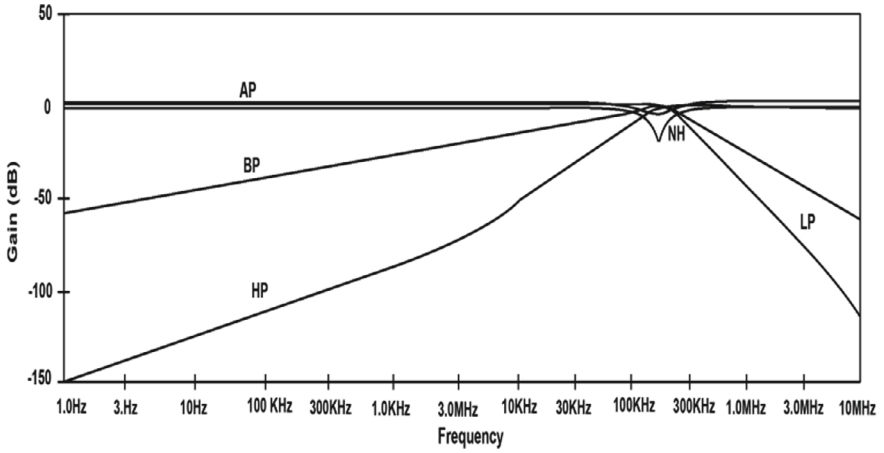

Fig. 9 Frequency response of UF I for $R1 = R2 = R3 = 2\ \text{k}\Omega$, $C1 = C2 = 0.5$ nF

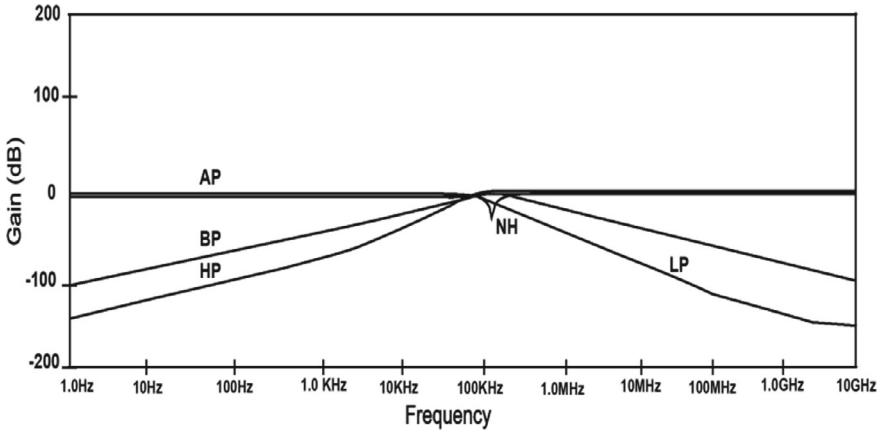

Fig. 10 Frequency response of UF II for $R1 = R2 = R3 = 1\ \text{k}\Omega$, $C1 = C2 = 1$ nF

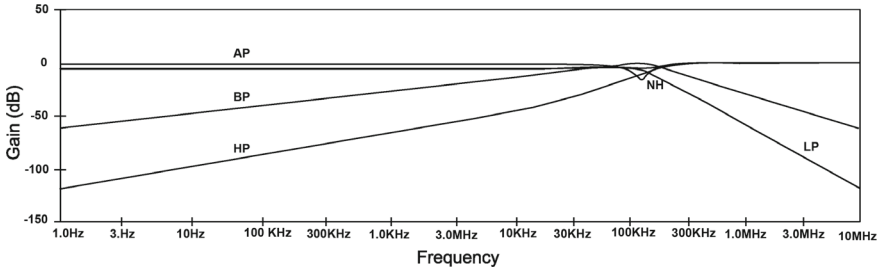

Fig. 11 Frequency response of UF III $R1 = R2 = R3 = 3.3\ \text{k}\Omega$, $C1 = C2 = 0.3$ nF

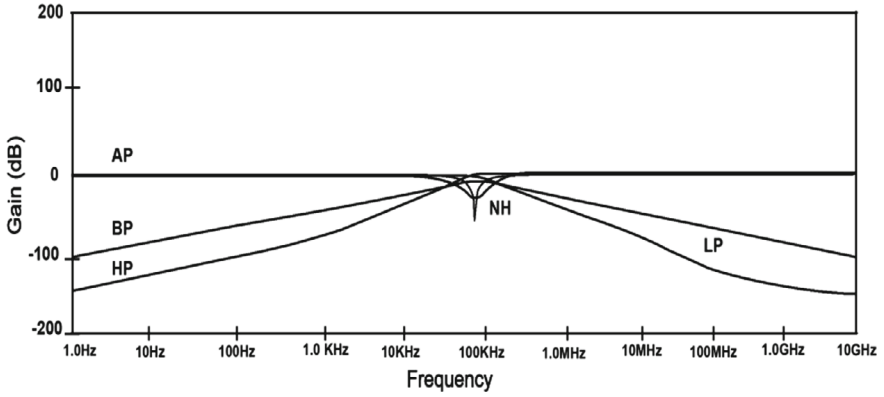

Fig. 12 Frequency response of UF IV $R1 = R3 = R5 = 1$ kΩ, $C2 = C5 = 1$ nF

MISO UFs in our study. In addition, the filters reported in previous studies [14, 18, 19, 28, 32, 33, 36, 38] suffer from a large active component count. The UFs in previously conducted studies [11, 18, 22, 32, 36, 38, 40] involve the usage of excessive passive components. Moreover, some lack the ability of independently tuning the quality factor, i.e., Q [16, 19, 21–23, 25–30, 32, 33, 35–37] indicating the need for designing more circuits that exhibit better topologies and are operable at very low voltage levels. The filters presented in this study have been designed to overcome all the shortcomings of the UFs presented previously [11–14, 16–40]. Furthermore, this study extends the potential for designing ASP applications based on BDCCs. These circuits are best suited for LV, low-power, and low-frequency applications such as portable devices, body monitors, and biological signal processors. This is because the biological/bioelectric signals have low amplitude and limited frequency range (upto a few kHz). Table 5 presents the main features of the proposed UFs as well as their comparison with some important existing filters based on seven criteria, i.e., (A) technology and voltage supply, (B) number of inputs, (C) count of active elements, (D) type and count of passive elements, (E) control on Q, (F) matching condition required, and (G) whether operable at LV levels.

Table 5 Comparison of proposed design with some previously reported MISO configurations

Criteria Ref.	A	B	C	D	E	F	G
[13]	AD844, ~	3	2CCII	$3R + 2C$	I	N	N
[14]	LM30TOA, ~	3	3CCII	$3R + 2C$	I	Y(HP NH AP)	N
[16]	AD844,20 V	3	2CCII	$2R + 2C$	D	N	N
[17]	AD844, ~	3	2CCII	$3R + 2C$	I	Y(AP)	N
[18]	AD844, ~	3	4CCII	$5R + 2C$	I	N	N
[19]	AD844, ~	3	3CCII	$2R + 2C$	D	N	N
[20]	AD844, ~	4	1CFOA	$3R + 2C$	I	Y(LP NH AP)	N
[21]	AD844, ~	3	2CCII	$2R + 2C$	D	N	N
[22]	0.5 µm, 6.6 V	3	2DDCC	$2R + 2C$	D	N	N
[23]	AD844, 20 V	3	3CCII	$2R + 3C$ $3R + 3C$	D	Y(NH AP)	N
[24]	0.25 µm, 2.5 V	3	1FDCCII	$3R + 2C$	I	N	N
[25]	BJT, 5 V	3	2CCCII	$2C$	D	N	N
[26]	BJT, 5 V	3	1CCII	$2R + 2C$	D	Y(LP HP)	N
[27]	0.5 µm, 6.6 V	3	2CCII	$2C$	D	Y(LP NH AP)	N
[28]	0.35 µm, 3.3 V	3	3DDCC	$2R + 2C$	D	N	N
[29]	0.35 µm, 3.3 V	3	2FDCCII	$2R + 2C$	D	N	N
[30]	BJT, 4 V	4	1CCTA	$2R + 2C$	D	N	N
[31]	AD844, 10 V	4	4CFOA	$5R + 2C$	I	Y(AP)	N
[32]	0.5 µm, 6 V	3	6OTA	$2C$	D	N	N
[33]	0.35 µm, 3.3 V	3	1DXCCII	$4R + 2C$	I	N	N
[34]	0.35 µm, 5 V	4	1CCCII + 1DOCCII	$2C$	D	N	N
[35]	0.18 µm, 2.5 V	3	3DVCC	$4R + 2C$	D	Y(AP)	N
[36]	0.35 µm, 4 V	3	1VDTA	$2C$	D	Y(LP NH AP)	N
[37]	AD844, 24 V	3	2CDBA	$4R + 2C$	I	Y(NH AP)	N
[38]	0.25 µm, 2.5 V	3	1VDTA	$1R + 2C$	I	N	N
[39]	LT1288, 10 V	3	1LT1228	$1R + 2C$	D	N	N
[40]	1.2 µm, 5 V	3	1OTRA	$4R + 4C$	D	Y(LP HP NH AP)	N
UF I	0.18 µm, 1 V	3	3CCII (+1 for AP)	$3R + 2C$	I	N	Y
UF II	0.18 µm, 1 V	3	2CCII (+1 for AP)	$3R + 2C$	I	N	Y
UF III	0.18 µm, 1 V	3	2CCII (+1 for AP)	$3R + 2C$	I	N	Y
UF IV	0.18 µm, 1 V	4	2CCII	$3R + 2C$	I	Y(AP)	Y

Acronyms: CFOA: current feedback amplifier; D/I: dependent/independent; CDBA: current differencing buffered amplifier; Y/N: yes/no; VDTA: voltage differencing transconductance amplifier; DDCC: differential difference CC; CCCII: current controlled CCII; DO–CCCII: dual output-CCCII; FDCCII: fully differential CCII; OTA/OTRA: operational transconductance/transresistance amplifier; DXCCII: dual-X current conveyor; DVCC: differential voltage CC; BJT: bipolar junction transistor; R/C: resistance/capacitance; CDTA/CCTA: current differencing/conveyor transconductance amplifier

6 Conclusion

LV analog circuit design is an active research area in electronics. Therefore, CC-based LV circuits are also under review. Four new circuits employing BD second-generation CCs for realizing second-order filtering functions (LP, HP, BP, AP, and NH) are proposed. Furthermore, the filters implemented in this study are some of the handful of CC-based circuits capable of working at as low as 0.5 V supply levels, exhibiting excellent behavior at sufficiently low frequencies. PSPICE simulations were conducted using the TSMC 0.18-μm CMOS technology. The simulation results agree very well with theoretical characteristics. This research is a valuable addition to the existing repository and provides important context for future research on ultra-LV ASP applications with CC.

Acknowledgements We thank The NorthCap University and Jamia Millia Islamia for their continuous support during writing this research article.

References

1. Rajput, S.S., Jamuar, S.S.: Low voltage analog circuit design techniques. Circuits Syst. Mag. **2**(1), 24–42 (2002)
2. Khateb, F., Biolek, D., Khatib, N., Vávra, J.: Utilizing the bulk-driven technique in analog circuit design. In: Proceedings of IEEE Symposium on Design and Diagnostics of Electronic Circuits and Systems, Vienna, Austria, pp. 16–19 (2010)
3. Raikos, G., Vlassis, S., Psychalinos, C.: 0.5 V bulk-driven analog building blocks. AEU-Int. J. Electron. Commun. **66**(11), 920–927 (2012)
4. Kumngern, M., Khateb, F., Kulej, T.: 0.5 V bulk-driven CMOS fully differential current feedback operational amplifier. IET Circuits Devices Syst. **13**(3), 314–320 (2019)
5. Raikos, G., Vlassis, S.: 0.8 V bulk-driven operational amplifier. Analog Integr. Circuits Signal Process. **63**, 425–432 (2010)
6. Khateb, F., Biolek, D.: Bulk-driven current differencing transconductance amplifier. Circuits Syst. Signal Process. **30**(5), 1071–1089 (2011)
7. Tonk, A., Goyal, S.: A literature review on leakage and power reduction techniques in CMOS VLSI design. Int. J. Adv. Res. Comput. Commun. Eng. **3**(2), 554–558 (2015)
8. Khateb, F., Dabbous, S.B.A., Vlassis, S.: A survey of non-conventional techniques for low-voltage low-power analog circuit design. Radioengineering **22**(2), 415–427 (2013)
9. Tonk, A., Afzal, N.: Bulk driven second generation current conveyor based all-pass section for low voltage operation. In: Proceedings of IEEE International Conference on Computing, Power and Communication Technologies, Greater Noida, UP, pp. 946–949 (2018)
10. Tonk, A., Afzal, N.: Ultra-low voltage operable bulk-driven second generation current conveyor based filters with single-input and single-output. J. Eng. Sci. Technol. **14**(1), 216–226 (2019)
11. Khateb, F., Khatib, N., Kubanek, D.: Novel low-voltage low-power high-precision CCII± based on bulk-driven folded cascode OTA. Microelectron. J. **42**(5), 622–631 (2011)
12. Çiçekoğlu, O.: New current conveyor based active-gyrator implementation. Microelectron. J. **29**(8), 525–528 (1998)
13. Horng, J.W., Tsai, C.C., Lee, M.H.: Novel universal voltage-mode biquad filter with three inputs and one output using only two current conveyors. Int. J. Electron. **80**(4), 543–546 (1996)
14. Özoğuz, S., Güneş, E.O.: Universal filter with three inputs using CCII+. Electron. Lett. **32**(23), 2134–2135 (1996)

15. Tonk, A., Afzal, N.: Second generation fully differential current conveyor based analog circuits. J. Semicond. **40**(4), 042401 (2019)
16. Horng, J.W., Lee, M.H., Cheng, H.C., Chang, C.W.: New CCII-based voltage-mode universal biquadratic filter. Int. J. Electron. **82**(2), 151–156 (1997)
17. Liu, S.I., Lee, J.L.: Voltage-mode universal filters using two current conveyors. Int. J. Electron. **82**(2), 145–150 (1997)
18. Chang, C.M.: Multifunction biquadratic filters using current conveyors. IEEE Trans. Circuits Syst. II: Analog. Digit. Signal Process. **44**(11), 956–958 (1997)
19. Horng, J.W.: High-input impedance voltage-mode universal biquadratic filter using three plus-type CCIIs. IEEE Trans. Circuits Syst. II: Analog. Digit. Signal Process. **48**(10), 996–997 (2001)
20. Horng, J.W., Chang, C.K., Chu, J.M.: Voltage-mode universal biquadratic filter using single current-feedback amplifier. IEICE Trans. Fundam. Electron. Commun. Comput. Sci. **85**(8), 1970–1973 (2002)
21. Chang, C.M., Chen, H.P.: Universal capacitor-grounded voltage-mode filter with three inputs and a single output. Int. J. Electron. **90**(6), 401–406 (2003)
22. Horng, J.W.: Voltage-mode universal biquadratic filters using CCIIs. IEICE Trans. Fundam. Electron. Commun. Comput. Sci. **87**(2), 406–409 (2004)
23. Horng, J.W.: High input impedance voltage-mode universal biquadratic filters with three inputs using plus-type CCIIs. Int. J. Electron. **91**(8), 465–475 (2004)
24. Chang, C.M., Chen, H.P.: Single FDCCII-based tunable universal voltage-mode filter. Circuits Syst. Signal Process. **24**, 221–227 (2005)
25. Minaei, S., Yuce, E., Cicekoglu, O.: Electronically tunable multi-input single-output voltage-mode filter. In: Proceedings of IEEE European Conference on Circuit Theory and Design, 3, pp. III-401 (2005)
26. Sagbas, M., Koksal, M.: Voltage-mode three-input single-output multifunction filters employing minimum number of components. Frequenz **61**(3–4), 87–93 (2007)
27. Paul, S.K., Pandey, N., Jain, S.B.: Realization of plus-type CCCIIs based voltage mode universal filter. In: Proceedings of IEEE International Symposium on Integrated Circuits, pp. 119–122 (2007)
28. Chiu, W.Y., Horng, J.W.: High-input and low-output impedance voltage-mode universal biquadratic filter using DDCCs. IEEE Trans. Circuits Syst. II Express Briefs **54**(8), 649–652 (2007)
29. Chen, H.P., Liao, Y.Z.: High-input and low-output impedance voltage-mode universal biquadratic filter using FDCCIIs. In: Proceedings of IEEE Conference on Solid-State and Integrated-Circuit Technology, pp. 1794–1798 (2008)
30. Herencsar, N., Koton, J., Vrba, K.: Single CCTA-based universal biquadratic filters employing minimum components. Int. J. Comput. Electr. Eng. **1**(3), 307 (2009)
31. Nikoloudis, S., Psychalinos, C.: Multiple input single output universal biquad filter with current feedback operational amplifiers. Circuits Syst. Signal Process. **29**, 1167–1180 (2010)
32. Kumngern, M., Knobnob, B., Dejhan, K.: Electronically tunable high-input impedance voltage-mode universal biquadratic filter based on simple CMOS OTAs. AEU-Int. J. Electron. Commun. **64**(10), 934–939 (2010)
33. Myderrizi, I., Minaei, S., Yuce, E.: DXCCII-based grounded inductance simulators and filter applications. Microelectron. J. **42**(9), 1074–1081 (2011)
34. Ranjan, A., Paul, S.K.: Voltage mode universal biquad using CCCII. Act. Passiv. Electron. Compon. **2011**, 1–5 (2011)
35. Horng, J.W., Hsu, C.H., Tseng, C.Y.: High input impedance voltage-mode universal biquadratic filters with three inputs using three CCs and grounding capacitors. Radioengineering **21**(1), 290–296 (2012)
36. Satansup, J., Tangsrirat, W.: Single VDTA-based voltage-mode electronically tunable universal filter. In: Proceedings of 27th International Technical Conference on Circuits/Systems, Computers and Communications, pp. 1–4 (2012)

37. Pathak, J.K., Singh, A.K., Senani, R.: New voltage mode universal filters using only two CDBAs. Int. Sch. Res. Not. (2013)
38. Mekhum, W., Jaikla, W.: Three input single output voltage-mode multifunction filter with independent control of pole frequency and quality factor. Adv. Electr. Electron. Eng. **11**(6), 494–500 (2013)
39. Klungtong, S., Thanapatay, D., Jaikla, W.: Three-input single-output voltage-mode multifunction filter with electronic controllability based on single commercially available IC. Act. Passiv. Electron. Compon. (2017)
40. Kılınç, S., Keskin, A.Ü., Çam, U.: Cascadable voltage-mode multifunction biquad employing single OTRA. Frequenz **61**(3–4), 84–86 (2007)

Neural Networks-Based Control Framework for Teleoperation System

Anirudh Anand and Rohit Singla

Abstract Teleoperation is a crucial aspect of robotics, which enables humans to control objects from a remote location by simulating the conditions of the object's actual location. In bilateral teleoperation, force feedback is necessary for the master operator to ensure accurate work, but the transmission delay in communication can cause instability and difficulty. Despite the development of various methods to alleviate the effects of time delay in signal transmission, it remains a significant challenge for ensuring stability and transparency in bilateral teleoperation systems. One potential solution to address this challenge is the utilization of neural networks (NN). These networks are adaptable to system uncertainties and disturbances as they are model-free and can be utilized for predicting teleoperation signals. This study focuses mainly on developing a deep neural network-based control framework for the considered bilateral teleoperation system, with the presence of TOP delay and other disturbances. Long short-term memory (LSTM), a specialized variant of recurrent neural network (RNN), was driven due to its capacity to handle more intricate scenarios in contrast to traditional CNN strategies, hence it was adopted for this application. The system is modeled using Lyapunov functions and an LSTM-based controller is developed to counter the effects of TOP delay and random perturbation and measurement noises in the system. The model was developed in Python, with the use of the Keras API module of Tensorflow to use the pre-trained LSTM model.

Keywords Bilateral teleoperation · Robot manipulator · Teleoperation delay · Long short-term memory · Python

A. Anand · R. Singla (✉)
Mechanical Engineering Department, Amity University Uttar Pradesh, Noida, India
e-mail: rsingla1@amity.edu

© The Author(s), under exclusive license to Springer Nature Singapore Pte Ltd. 2025

H. P. Singh et al. (eds.), *Recent Developments in Control, Automation and Power Engineering*, Lecture Notes in Electrical Engineering 1303,
https://doi.org/10.1007/978-981-96-0047-2_12

1 Introduction

Teleoperation is the method of remotely controlling a robot, through a master–slave architecture. It can be observed that time delay in the communication channel is a problem that always induces difficulty in effective control of the bilateral teleoperation system. Physically, this problem can be rectified by decreasing the number of individual channels (depending on the number of control variables used and the DOF of the manipulator) [1] or by making the system isolated to reduce interactions with external disturbances, but with the emergence and advancements in neural networks and deep learning techniques, an efficient control framework could be built without much changes to the physical system.

I have employed the use of Lyapunov energy functions for modeling the TOP system. The usual modeling approaches for modeling any dynamical system result in a rapid increase in the DOF of the energy function for storing and approximating the system, along with the dimensions of the state space. This is commonly termed as the 'curse of dimensionality'. Recently, ample research is done on solving higher-order PDEs through deep learning methodologies. Since a Lyapunov function can also be represented as a PDE, a suitably constructed deep neural network can compute approximations on compositional Lyapunov functions using only a few layers of neurons to achieve the required accuracy and system response. This can very well eradicate the curse of dimensionality [2] (Fig. 1).

The bilateral TOP system considered in this study consists of a master robot communicating with a slave robot. Because of the environment, the slave robot experiences a torque that changes its position when compared with the case of no environmental torque. This change should be communicated to the master robot through a feedback mechanism to ensure that the master realizes this change and acts accordingly to perform the required task. It is assumed that the time delay 'T' exists in the communication, referring to the time taken for the propagation of the

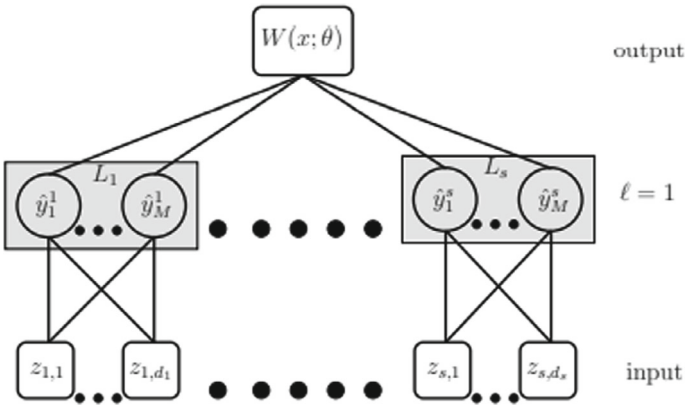

Fig. 1 Neural network model for Lyapunov functions

force feedback signals between the master and slave controllers [3, 4]. This delay is called the teleoperation delay and it is essential in producing the error signals to control the master and slave robots. This study analyzes the TOP system in presence of random feedback errors and disturbances produced by the environment to determine the approximate correlation between the angular position of master and slave robots.

2 Literature Survey

Hokayem and Spong [5] present an extensive examination of bilateral teleoperation, a research field spanning over 70 years and remaining an active domain for both theoretical exploration and various applications. The paper primarily delves into the realm of control theory, specifically addressing inherent control challenges like delays and information loss.

In the work by Arcara and Melchiorri [6], various control strategies for teleoperation over packetized (TOP) systems are explored, considering factors such as passivity and compliance. Each strategy grapples with significant issues, notably stability, especially when confronted with time delays in communication channels, and the telepresence of the overall system. The article conducts a comparative analysis of the prominent control schemes found in the literature. It initially outlines the conditions set for the comparative study and subsequently presents and discusses the obtained results.

R. Singla et al. [7] proposed a TOP system model with nonlinear feedback fluctuations, external disturbances, and random noises and employs the use of perturbation theory, much like the calculations used in this paper, to effectively manage the stability and perform the cost functional analysis of the entire system. The results presented a very low noise-to-signal ratio and joint tracking errors, hence validating the method employed.

In traditional telesurgery control design, there is a limitation on the upper boundary of time delay which makes it infeasible for telesurgery to be performed across regions. Overcoming time-delay hurdles in telesurgery, Bacha et al. [8] utilize DDPG and Kalman filters to restore surgeon control and interaction. This ground-breaking framework ensures synchronization and transparency, even without delay knowledge. Their work represents a significant step forward in applying deep learning to delicate telesurgery practices, opening doors for improved surgical outcomes and patient care.

The significant challenge in bilateral teleoperation systems lies in the time delay during signal transmission, impacting both stability and transparency. Despite the existence of numerous proposed methods to mitigate these effects, the approach based on neural networks (NN) stands out for being model-free and capable of adapting to system uncertainties and disturbances. This characteristic renders the NN-based method highly promising for predicting teleoperation signals. Zhou et al. [9] proposed a bilateral active estimation model of teleoperation based on neural networks, the specific approach being long short-term memory (LTSM), estimating the time delay

in both directions of the teleoperation system, and the condition and proof of the model stability are provided. On top of that, the study also explained the concepts of active and passive predictors based on neural networks to elucidate the selection of appropriate deep networks for the required control framework [10–12]. The presented model integrates an active predictor based on long short-term memory (LSTM), effectively forecasting teleoperation signals with anticipation while accounting for the estimated time delay in signal transmission. This predictive approach is not reliant on the dynamics of the teleoperation system, demonstrating its applicability to diverse teleoperation scenarios.

Through the literature survey, a key takeaway was that by using a deep learning-based control algorithm, the thus-developed controller would operate independently of system dynamics and would produce accurate and effective results irrespective of various other physical parameters. Robustness of this kind is very much favorable when tackling a complex control problem like bilateral teleoperation.

The model was developed in Python, with the use of the Keras API module of Tensorflow to use the pre-trained LSTM model. The code developed is a simulation of a state-space model of the teleoperation system and an LSTM network used for control. The simulated response is corrupted by a random delay and measurement noise. The goal is to train an LSTM network to estimate the delayed and noisy response and generate a control signal that minimizes the difference between the desired response and the estimated response. The system response of the bilateral teleoperated robot with the LSTM controller was almost identical to the ideal response, along with the slave position being identical to the desired trajectory (of the master). The parameters of the manipulators (stiffness and damping coefficients) along with slave positional and torque error were considered for parametric error estimation, which were also quite low considering the disturbances provided to the model.

With daily advancements in the field of neural networks, artificial intelligence (AI) and other advanced control methods, there are ample resources available to withstand much more complicated scenarios in this field. Incorporating LSTM with other strategies like model-based predictive control (MPC) can further optimize the algorithm, irrespective of the dynamics of the system or the environment [13, 14]. Therefore, future scope of this study with respect to robotics is plentiful. Also, to further validate the results, practical implementation of the network model in loop with the physical teleoperated robot can be considered for further research to gain more understanding and exposure to more complex problems in the actual field.

Gupta et al. [15, 16] studied the steepening of waves in non-ideal magnetogasdynamics and examined the effect of the magnetic field on an unstable, inviscid non-ideal gas.

3 Approach

3.1 LSTM-Based Neural Network

LSTM represents a distinctive form of RNN architecture specifically engineered to mitigate the vanishing gradient issue encountered in conventional RNNs. In a conventional RNN, the output at each time step is influenced by both the past outputs and the current input. Nonetheless, as time progresses, the gradient backpropagated through the network can diminish significantly, posing challenges in learning long-term dependencies. LSTM addresses this concern by incorporating a memory cell capable of retaining information over extended periods. The memory cell is regulated by three gates: the input gate determines what information is accepted, the forget gate determines what information is retained, and the output gate determines what information is outputted.

The input gate manages the information flow from the current input into the memory cell, employing a sigmoid function to determine the proportion to be stored. Similarly, the forget gate utilizes a sigmoid function to decide the proportion of the prior memory to retain, essentially determining what to forget. The output gate dictates the extent to which the current memory should serve as the output of the LSTM. During the training process, the weights of the LSTM are adjusted to minimize the disparity between the predicted output and the actual output. This adjustment is achieved through backpropagation through time, where the gradient is backpropagated across the time steps, as illustrated in Fig. 2.

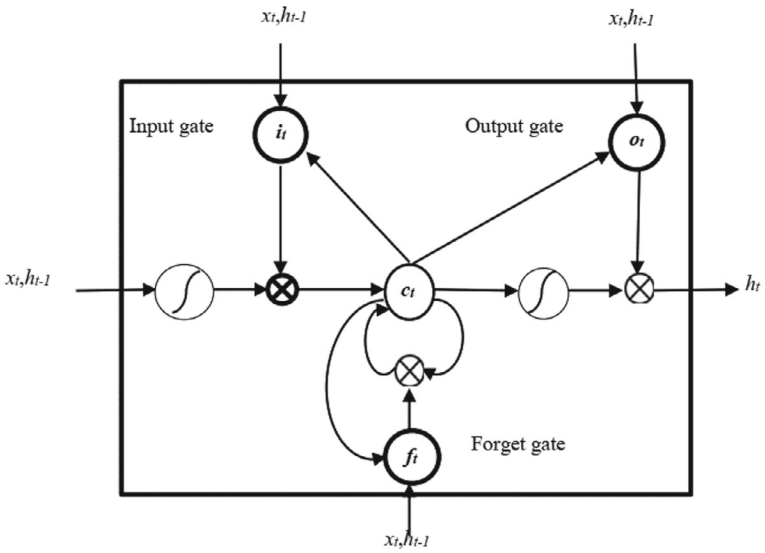

Fig. 2 Structural architecture of LSTM

In essence, LSTM proves to be a potent tool for modeling sequential data and mastering long-term dependencies. Its applications span diverse domains, including speech recognition, natural language processing, and time series forecasting.

In a teleoperated robotics system, LSTM can be trained on a sequence of input data, such as the robot's previous movements, to predict its future behavior [10, 17]. This prediction can then be used to adjust the robot's control commands, ensuring that it stays on track and avoids obstacles. In a teleoperated robotics system, an operator remotely controls a robot using a human–machine interface (HMI) such as a joystick or a computer mouse. The HMI sends control commands to the robot, which then executes them to perform a specific task.

However, teleoperated robotics systems face several challenges, such as communication delays, network disruptions, and operator fatigue, which can affect the system's performance and safety. LSTM can help mitigate some of these issues by predicting the robot's future behavior and adjusting its control commands accordingly. It has the capability to anticipate the robot's forthcoming position, speed, or trajectory by analyzing its present and past movements. Utilizing this information, adjustments can be made to the robot's control commands, ensuring it remains on course and navigates around obstacles effectively.

Furthermore, LSTM can also be used to detect anomalies or unexpected behavior in the robot's movements, which can help identify potential safety risks and prevent accidents. Overall, LSTM can be a valuable tool in teleoperated robotics systems, helping to improve their performance, reliability, and safety.

3.2 Dynamic Modeling of the System

The notation used throughout the paper is as follows:

The symbols with subscripts 'm' and 's' indicate the master and slave modules, respectively.

M_m and M_s—Inertial matrix.

C_m—Centrifugal vector.

C_s—Coriolis vector.

τ_m and τ_s—Input torque.

F_{op}—represents the force exerted by the human operator on the master robot.

F_{env}—denotes the environmental force acting on the slave robot.

q_m and q_s—joint angular displacements.

K_m, K_s—Stiffness of master and slave modules, respectively.

B_m, B_s—Damping coefficient of master and slave modules, respectively.

m_m, m_s—Mass of master and slave manipulators.

W_k—Random Gaussian noises applied to the system.

V_k—Random measurement noises from the output.

For a TOP system, the system dynamics are modeled as a Lagrangian system and use the Lyapunov energy function to include the stability of the overall system in the analysis.

The basic dynamical equation of the master and slave dynamics can be expressed as [11]:

$$M_m(q_m)\ddot{q}_m(t) + C_m(q_m, \dot{q}_m)\dot{q}_m(t) = \tau_m(t) + F_{\text{op}}(t) \tag{1a}$$

$$M_s(q_s)\ddot{q}_s(t) + C_s(q_s, \dot{q}_s)\dot{q}_s(t) = \tau_s(t) - F_{\text{env}}(t) \tag{1b}$$

The developed TOP system with an LSTM-based control algorithm is shown in Fig. 3. The only difference from a standard bilateral teleoperated manipulator is that the master and slave controllers have deep learning-based control frameworks embedded in them. This is done through modeling of controller equations for the TOP system.

The predictor is trained offline using raw data, represented as sequences of joint velocities $\dot{q}_m$. This forecaster predicts signals for the upcoming step by forecasting $x(t)$ with a lead of $u(t)$, symbolized as the estimated value $\hat{x}(t + u(t))$.

Following this, the expected outcome following the delay is anticipated to align with the original data $x(t)$, expressed as:

$$\hat{x}(t - \tau(t) + u(t - \tau(t))) = x(t) \tag{2}$$

Under the assumption of minimal error between $\hat{x}(t)$ and the ground truth $x(t)$, the correlation between the estimated time delay $\hat{\tau}(t)$ and $u(t)$ is given by:

$$\hat{\tau}(t) = u(t - \tau(t)) \tag{3}$$

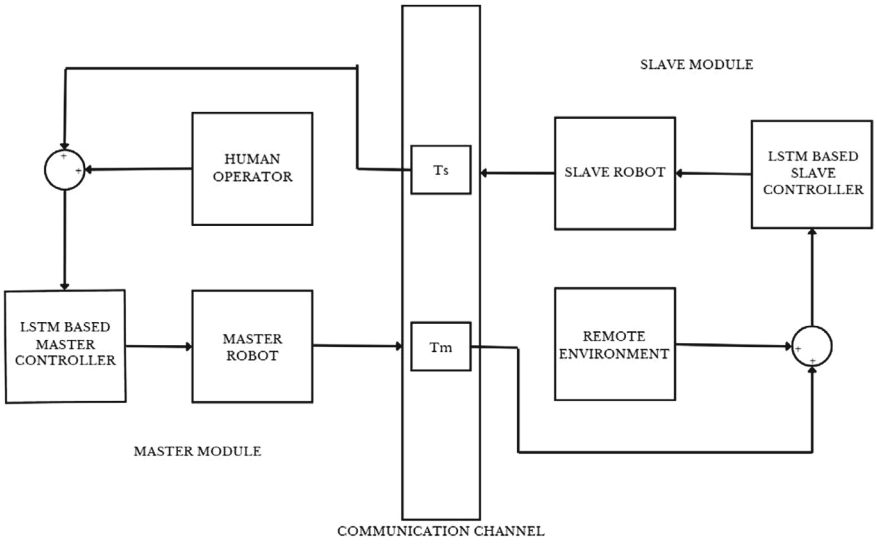

Fig. 3 Block diagram of LSTM-based bilateral TOP system

In the general scenario, the time delay in both directions can be expressed as:

$$\tau ms(t) = t_T - t_{ds} \tag{4a}$$

$$\tau sm(t) = t_T - t_{dm} \tag{4b}$$

The dynamical equation of the entire TOP system can be represented in state space as follows:

$$A_{11} = \begin{bmatrix} 0 & 1 \\ 0 & 0 \end{bmatrix}, A_{12} = \begin{bmatrix} \frac{-K_s}{m_s} & \frac{-B_s}{m_s} \\ 0 & 0 \end{bmatrix}, A_{21} = \begin{bmatrix} 0 & 0 \\ 0 & 1 \end{bmatrix}, A_{22} = \begin{bmatrix} \frac{K_m}{m_m} & \frac{-B_m}{m_m} \\ 0 & 0 \end{bmatrix}$$

$$A = \begin{bmatrix} A_{11} & A_{12} \\ A_{21} & A_{22} \end{bmatrix}, B = \begin{bmatrix} 0 & 1/m_s \\ 0 & 0 \end{bmatrix}, C = \begin{bmatrix} 1 & 0 & 0 & 0 \\ 0 & 0 & 1 & 0 \end{bmatrix}, D = \begin{bmatrix} 0 & 0 \end{bmatrix}$$

$$\dot{x}_s = Ax + Bu + W_k \tag{5}$$

$$\dot{x}_m = Cx + Du + V_k \tag{6}$$

3.3 Simulation

The system was modeled in Python for performing tracking analysis and parametric error estimation. The Tensorflow-based API known as Keras library was used to model the pre-trained LSTM network. The sequential LSTM model is mostly used for speech recognition and language training models. The reason for using the same pre-trained model is due to the similarity in the operation of teleoperation system, where the model acts like a predictor/estimator function to determine the future state of physical parameters of the system and provide control signals to the slave manipulator accordingly so as to reduce the error and stabilize the signal much sooner.

The TOP time delay is modeled as a randomly varying time signal, along with random white Gaussian noise signal as well with the dynamic model of the system. The physical parameters used for initializing and training the LSTM network is listed in Table 1. The loss function of the LSTM network is estimated through mean squared error method and the network is optimized through adaptive moment estimator (ADAM) optimizer.

In the realm of neural networks, the term ‘loss’ denotes the disparity between the anticipated output of the network and the actual output. Throughout the training phase, the network endeavors to diminish this disparity by fine-tuning its parameters, namely weights and biases, employing optimization algorithms like stochastic

Table 1 Parameters for training the LSTM network

Network parameters	Values
Number of samples (N)	1000
Number of layers (L)	200
Number of epochs	100
Sampling time (dT)	0.01
Simulation time (T_f)	10.0
Loss compensation (estimation)	Mean squared error (MSE)
Optimizer	Adaptive moment estimator (ADAM)

gradient descent. The loss function functions as a metric for evaluating the effectiveness of the network on the training data, aiming to minimize it. The selection of a suitable loss function is contingent upon the nature of the specific problem, offering alternatives such as mean squared error (MSE) for regression tasks or categorical cross-entropy for classification challenges.

After completing each epoch, the loss is computed by passing the training data through the network and assessing the disparity between the predicted and actual outputs using the selected loss function. Subsequently, the optimizer adjusts the network parameters according to the determined loss, and this cycle repeats for the subsequent epoch. The expectation is that the loss diminishes with each epoch, signifying that the network is acquiring knowledge and enhancing its proficiency in the given task.

Adam, short for adaptive moment estimation, is a widely utilized optimization algorithm in the training of neural networks. It serves as an extension of stochastic gradient descent (SGD) and amalgamates the advantageous features of two other SGD variants—AdaGrad and RMSProp. Adam computes adaptive learning rates for individual parameters by relying on estimates of the first and second moments of the gradients, providing a dynamic approach to the optimization process. The learning rate for each parameter undergoes personalized adaptation grounded in the historical momentum, historical gradient, and current gradient of that specific parameter. This approach enhances the efficiency of optimization, facilitating a quicker convergence of the model.

4 Results and Discussions

The system response of the model and network were calculated through Euler's method of numerical simulation. The plot has two components, namely 'Desired' and 'Actual'. Desired response is the system response without the use of the LSTM network, without the inclusion of noise and measurement disturbances, hence it was the ideal response expected out of the system. Actual response is obtained after including noise parameters in the dynamical model, and using LSTM-based control

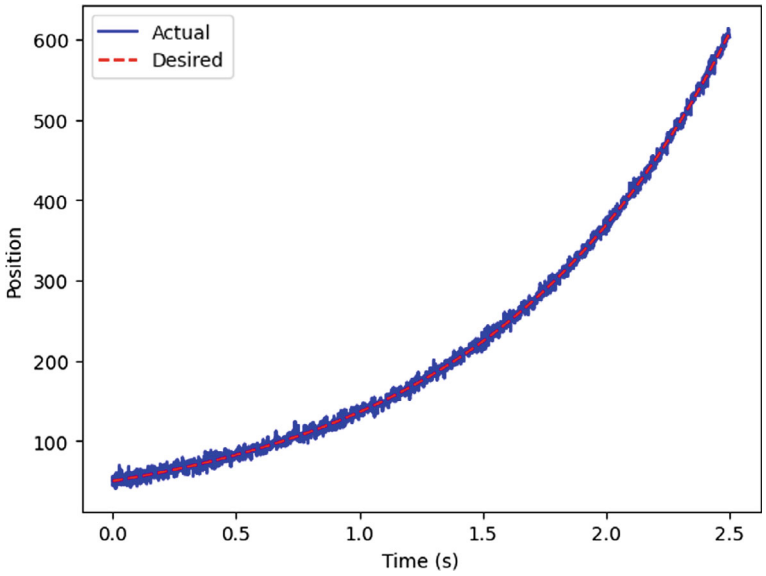

Fig. 4 System response of the model

framework to counter the effect and stabilize the system. From Fig. 4, it can be observed that even in spite of external disturbances in the system, the actual response was able to track the desired response quite well without much oscillations produced. This can attribute to the fact that the system behavior is stable and optimal.

The required trajectory was initialized as a simple sinusoidal signal as input to the model. Practically, this is the command signal given through the master module to the slave manipulator. This is our 'desired' signal. From the output of Fig. 5, the positional error is very low, and the slave trajectory is very optimal, forming the 'actual' signal. The error has significantly reduced though, when compared with the previously adopted control algorithm of the PD controller as shown in Fig. 6.

The result of the model is validated through three analyses. First one being a simple analysis of system response of the dynamic model with and without the implementation of LSTM model. Second analysis is the trajectory tracking of the master and slave joint angles. Last one is a more of an analytical analysis, where parametric error estimation was performed on various physical parameters like stiffness, damping coefficient, torque, and positional error.

The physical parameters considered for the error estimation are stiffness and damping coefficient of master and slave modules, positional error and slave torque. The stiffness and damping coefficients are analyzed to estimate the compensation of measurement noise at both master and slave ends. All these parameters are estimated through the predictor algorithm of the LSTM model. The magnitudes of error values are very low, signifying that our system has been substantial in countering TOP

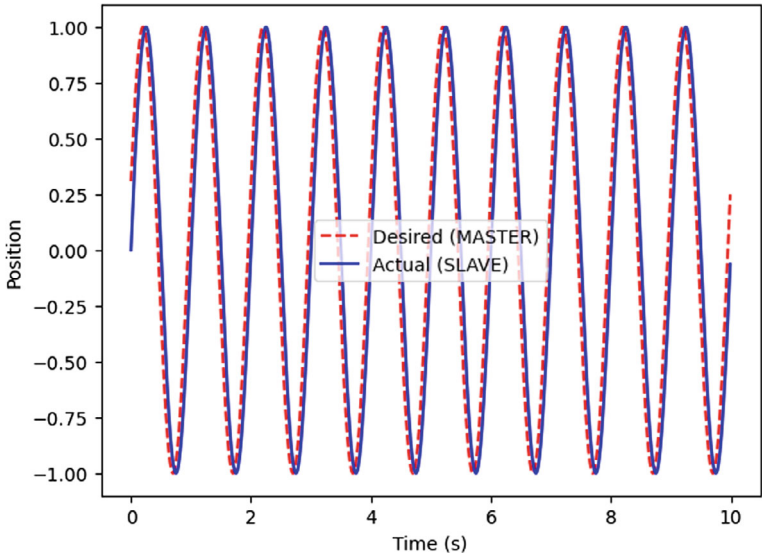

Fig. 5 Trajectory tracking response

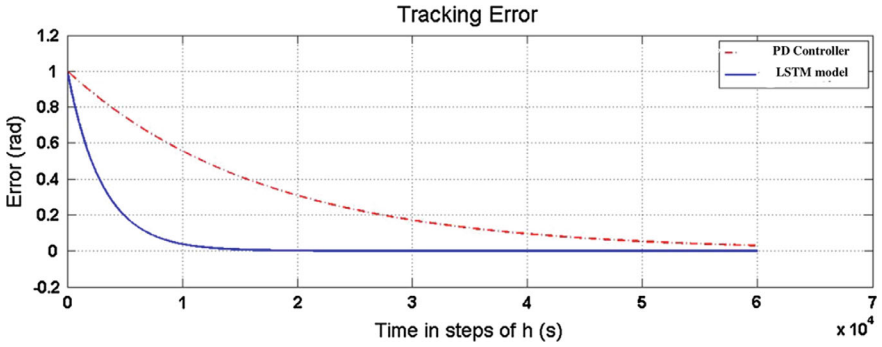

Fig. 6 PD versus LSTM-based model controller

delay and disturbance noises provided to the system. The results of parametric error estimation are stated in Table 2.

Table 2 Parametric error estimation

Physical parameters	Error estimated
Master stiffness (K_m)	0.00056052
Slave stiffness (K_s)	0.00079894
Master damping coefficient (B_m)	0.00027355
Slave damping coefficient (B_s)	0.00075347
Position (q_s)	0.00298214
Torque (τ_s)	0.00185704

5 Conclusion

After modeling the dynamics of a bilaterally teleoperated system, the next challenging task is adopting a suitable control strategy to effectively manage the system parameters and reduce error while countering the disturbances presented to the system. Time delay of communication channels is already an established problem in teleoperation; hence it has been explored in the course of this study.

The primary emphasis of this research was on formulating a control framework for the bilateral teleoperation system, leveraging a deep neural network. The framework addressed challenges such as TOP delay and various disturbances. In this context, LSTM, a specialized variant of RNN, was driven due to its capacity to handle more intricate scenarios in contrast to traditional CNN strategies.

References

1. Srikar, A., Kumar, P.V., Thondiyath, A.: Enhancement of stability and transparency in teleoperated robots through isotropy-based design. IEEE Access **8** (2020)
2. Grune, L.: Computing Lyapunov functions using deep neural networks. Cornell University "arXivLabs" Optimization and Control edition (2020)
3. Singla, R., Agarwal, V., Parthasarathy, H.: Statistical analysis of tracking and parametric estimation errors in a 2-link robot based on Lyapunov function. Nonlinear Dyn. **82**, 217–238 (2015)
4. Singla, R., Parthasarathy, H., Agarwal, V., et al.: Feedback optimization problem for master–slave teleoperation tracking in the presence of random noise in dynamics and feedback. Nonlinear Dyn. **86**, 559–586 (2016)
5. Hokayem, P.F., Spong, M.W.: Bilateral teleoperation: an historical survey. Automatica **42** (2006)
6. Arcara, P., Melchiorri, C.: Control schemes for teleoperation with time delay: a comparative study. Robot. Auton. Syst. **38** (2002)
7. Singla, R., Agarwal, V., Parthasarathy, H.: Nonlinear robot teleoperation with random fluctuations in the feedback controller. In: IEEE International Conference on Computer, Communication, and Control (IC4-2015) (2015)
8. Bacha, S.C., Bai, W., Wang, Z., Xiao B., Yeatman, E.M.: Deep reinforcement learning-based control framework for multilateral telesurgery. IEEE Trans. Med. Robot. Bionics **4** (2022)

9. Zhou, X., Bai, W., Ren, Y., Yang, Z., Wang, Z., Lo, B., Yeatman, E.M.: An LSTM-based bilateral active estimation model for robotic teleoperation with varying time delay. In: 7th IEEE International Conference on Advanced Robotics and Mechatronics (2022)
10. Cursi, F., Bai, W., Li, W., Yeatman, E.M., Kormushev, P.: Augmented neural network for full robot kinematic modelling in SE(3). IEEE Robot. Autom. Lett. **7** (2022)
11. Chopra, N., Spong, M.W., Lozano, R.: Adaptive coordination control of bilateral teleoperators with time delay. In: 43rd IEEE Conference on Decision and Control (2004)
12. Hou, Y., Luecke, G.R.: Time delayed teleoperation system control, a passivity-based method. IEEE Trans. Robot. Autom. (2015)
13. Ghavifekr, A.A., Ghiasi, A.R., Badamchizadeh, M.A., Hashemzadeh, F., Fiorini, P.: Stability analysis of the linear discrete teleoperation systems with stochastic sampling and data dropout. Eur. J. Control (2018)
14. Liu, S., Zhang, X., Zheng, W., Yang, B.: Adaptive neural network control for time-delay teleoperation with uncertainties. In: 2017 11th Asian Control Conference (ASCC), Gold Coast Convention Centre, Australia (2017)
15. Gupta, B., Singla, R.: On singular surface theory to study steepening of waves in non-ideal magnetogasdynamics. Ricerche mat. **71**, 253–263 (2022)
16. Gupta, B., Jena, J., Singla, R.: Propagation and interaction of waves in non-ideal magnetogasdynamics. Ric. Di Mat. (2022)
17. Stefano Peluchetti, Stefano Favaro. "Neural Stochastic Differential Equations". Cornell University "arXivLabs" Machine Learning edition (May 2019). https://doi.org/10.48550/arXiv.1905.11065.

Reinforcement Learning in Simultaneous Localization and Mapping

Abhik Kumar, Sudarshan K. Valluru, and M. M. Rayguru

Abstract The primary objective of this research work is to investigate model-free path planning for reconfigurable robots using value and policy iterations. The focus is on developing and evaluating an autonomous algorithm for robot path planning. Initially, the A-Star algorithm was modified to incorporate model-based learning. Subsequently, model-free reinforced learning was incorporated through value iteration and policy iteration. The experimental validations of modified A-Star algorithm is conducted in python virtual environment.

Keywords Model-free reinforcement learning · Path planning · Value iteration · Policy iteration · A-Star · Modified A-Star

1 Introduction

Robot has become an integral part of human life from medical to automotive industry which revolutionized the performance and efficiency of human society. The work puts into practice an improved version of the A* algorithm for tracking the course of a mobile robot that can be reconfigured. Reinforcement learning with value and policy iteration was one of the modifications suggested to improve the robustness of path planning. And the second modification suggested is the penalty cost modification while taking diagonal path. For a reconfigurable robot, effective control approach is just as important as an ideal path-finding strategy. Although many different control

A. Kumar (✉) · S. K. Valluru · M. M. Rayguru
Control of Dynamical Systems, Computation Laboratory, Department of Electrical Engineering, Delhi Technological University, Delhi, India
e-mail: abhikkum@seas.upenn.edu

S. K. Valluru
e-mail: sudarshanvalluru@dce.ac.in

M. M. Rayguru
e-mail: mmrayguru@dtu.ac.in

© The Author(s), under exclusive license to Springer Nature Singapore Pte Ltd. 2025

H. P. Singh et al. (eds.), *Recent Developments in Control, Automation and Power Engineering*, Lecture Notes in Electrical Engineering 1303,
https://doi.org/10.1007/978-981-96-0047-2_13

frameworks have been employed, shape-changing mobile robots have not made use of a flexible technique with benefits like backstepping.

This research article organized in six sections with starting from introduction as sect. 1. Sect. 2 frames the literature review with problem formulation. Sect. 3 explains the traditional Dijkstra and A* path planning algorithms and proposes the modified A* algorithm with experimental validation. The value and policy iteration of reinforcement learning for optimal path planning is proposed in sect. 4. The results, observations made in this research article are given in sects. 5, 6, and end with references.

2 Mapping and Planning

2.1 Literature Review

Authors [1, 2, 3] propose different approaches for trajectory control in autonomous mobile robots: a favorable controller, neural network control, fuzzy-logic controller, and backstepping-based trajectory tracking control. Efficient motion planning is crucial for robot movement, addressing challenges like uncertainty [3], multiple robots [4], and dynamics [5]. Quantitative concepts like MDP [6], strategic equilibrium [7], and partial state learning methods [8] aid in planning. While motion planning focuses on translation, rotation, and uncertainty, path planning in regard to autonomous robots is a complex area with many different techniques [9], differential constraints [10], and optimality [7, 8, 11].

Mobile robots face the challenge of seamless navigation in complex interiors. They perform tasks like mapping [11], self-localization [12], and collision-free maneuvering. Simultaneous localization and mapping (SLAM) integrates mapping and localization [13–15]. It constructs environment representation while estimating the robot's position, enhancing spatial awareness and navigation.

With precise environment scanning, a mobile robot gains strategic navigation options. It analyzes spatial information, identifies obstacles, and chooses the best route. It optimizes for factors like time, energy, and safety. Real-time adaptability allows it to navigate around changes and obstacles, reaching destinations efficiently. Intelligent path planning ensures seamless interactions in complex indoor settings.

2.2 Problem Statement—Path Planning

Reconfigurable robots are currently required in a number of industries to execute increasingly complex jobs due to advancements in intelligent control systems. Extensive study and development have gone into obstacle avoidance, trajectory tracking, navigation, and IOT-connected parking systems. Autonomous robots can move and

learn about their environment with the aid of sensors and controllers. In order to enable the robotic vehicle to carry out a variety of tasks, it must be carefully managed in the proper position and route by carefully choosing the best stabilizing strategy. The aforementioned special characteristics make it difficult to create the best path-searching architecture for a mobile robot.

3 Path Planning

3.1 Dijkstra Algorithm

An incremental method called Dijkstra's algorithm finds the optimum route between a given source-destination and every other destination in a graph. During execution, it adds the edge weights to determine the shortest path. Due to its reliance on the idea that longer paths have higher costs, this technique is only useful when all edge weights are positive. Dijkstra's algorithm would not work properly if the graph's edges had negative weights.

The relaxation principle is typically followed by Dijkstra's algorithm, which finds the shortest path by progressively updating an initial distance estimate with more precise data.

3.2 A Algorithm*

The A* approach, which is commonly used for path planning, allows the use of both metric and topological configuration spaces. This method combines shortest path exploration with heuristics. Due to its capacity to analyze each node in the coordinate space, the A* algorithm is frequently regarded as one of the best path-searching algorithms.

$$f(v) = h(v) + g(v)\,. \tag{1}$$

In this context, $h(v)$ is the heuristic distance, which can be calculated using various methods like Manhattan, Minkowski, Euclidean, or Chebyshev, from the node to the desired state. On the other hand, $g(v)$ is the course distance of the pathway from the beginning state to the target state via the selected network of nodes. This sequence comes to an end at the node that is being evaluated. The data $f(v)$ is added to every node that is a neighbor of a visited node. The next node in the chain is selected based on which node has the lowest $f(v)$ value. This method enables the adoption, modification, or insertion of new methodology into the function $f(v)$ as distance measures, such as time, safety, and energy usage.

Table 1 A* algorithm

Algorithm used	Disadvantage	Advantage
A*	In its simplest form, does not account for reconfiguration time and is unable to fully search from all angles	Simple to change, uncomplicated, quick, and efficient

In [4], researchers successfully developed and validated a path planning system for a mobile robot using the A* algorithm. This work builds upon the advancements made in [4] and further refines the methodology. To provide a comprehensive overview, Table 1 outlines the disadvantage and advantage associated with the conventional A* path-finding algorithm, offering insights into its limitations and benefits.

3.3 Modified A Algorithm*

The A* algorithm was enhanced for mobile robot path planning by enabling diagonal movement, which is essential for faster navigation. Traditional A* algorithm limits connections to 8, but in our case, diagonal movement is crucial. Figure 1 presents pseudocodes for both traditional and improved A* algorithms. However, incorporating diagonal movement increases computational requirements as the robot must account for the additional cost of diagonal travel. To ensure minimal computational cost while selecting the optimal path, the improved A* algorithm incorporates a conditional statement. This statement increases the heuristic reward of a diagonal neighboring node by one unit, as depicted in the equation below.

$$f(v) = h(v) + g(v) + c\,. \tag{2}$$

The constant term, c, is tuned to improve performance by penalizing configuration changes in the cost function. Each configuration change increases energy consumption, adding to the cost. The heuristic score is periodically calculated using the traditional A* approach Equation (2), except when the neighboring node is not positioned diagonally adjacent to its current node, in which case it is not considered.

3.4 Modified A Algorithm Performance*

In infinite search spaces, the perplexity of Temporal A* algorithm increases exponentially with the heuristic dependency. The constant term c in the algorithm has a time complexity of c: $O(b^i)$, where i represents the divergence factor, which is the median number of descendants per state. This exponential increase in perplexity can pose challenges in terms of computational resources and time required for the search process.

(a) A* algorithm

```
Input: Grid_World
Input: Start_Node
Input: Target_Node
Output: Trajectory

for node in grid do
    node score: = Infinity;
    node.heuristic_Score: = Infinity;
    node.visited: = false;
end for
Start_Node score: = Infinity;
Start_Node.heuristic_Score: = Infinity;

while true do
    Current_Node score: = node_With_Lowest_Score(grid);
    Current_Node.visited: = true;

    for next_Node in Current_Node.neighbours do
        if next_Node.visited = False then
            new_Score: = calculate_Score(current_Node,
                  Next_Node);
            if new_Score < next_Node.Score then
            next_Node.Score = new_Score;
                next_Node.heuristic_Score = new_Score +
                Calculate.heuristic_Score(Next_Node,
                      Target_Node);
            end if
            next_Node.route_To_Node = current_Node;

        end if

end for

if current_Node = Target_Node then
    return Build_Path(Target_Node);
end if
if node_With_Lowest_Grid_Score = Infinity then
    return No_Path_Found;
end if
end while
```

(b) Modified A* algorithm

```
Input: Grid_World
Input: Start_Node
Input: Target_Node
Output: Trajectory
for node in grid do
    node score:= Infinity;
    node.heuristic_Score:= Inf;
    node.visited:= false;
end for
Start_Node score:= Infinity;
start_Node.heuristic_Score:= Infinity;
while true do
    Current_Node score:= node_With_Lowest_Score(grid);
    Current_Node.visited:= true;
    for next_Node in Current_Node.neighbours do
        if next_Node.visited=False then
          new_Score:=calculate_Score(current_Node,Next_Node
                );
           if new_Score < next_Node.Score then
            next_Node.Score=new_Score;
           if next_Node=diagonal.neighbour then
             next_Node.heuristic_Score=new_Score +
                    Calculate.heuristic_Score(Next_Node,
                    Target_Node)+1;
           else
             next_Node.heuristic_Score=new_Score+
             Calculate.heuristicScore(Next_Node,
                    Target_Node);
           end if
              next_Node.route_To_Node=current_Node;
           end if
        end if
    end for
    if current_Node=Target_Node then
        return Build_Path(Target_Node);
    end if
    if node_With_Lowest_Grid_Score=Infinity then
        return No_Path_Found;
    end if
end while
```

Fig. 1 Pseudocodes for A-Star and Modified A-Star

If the state space is perpetual, hence no reachable goal state from its initial state, then temporal A* algorithm may fail to terminate. To address this issue, additional constraints or stopping criteria may need to be implemented to ensure termination or determine when to halt the algorithm's execution. These constraints can help prevent the algorithm from running indefinitely in search of a goal state that may never be reachable.

The heuristic function employed in the A* search algorithm plays a crucial role in its practical performance. By guiding the search process, the heuristic function assists in eliminating many of the b^d nodes that would be generated in an unguided or unqualified search. This reduction in the number of expanded nodes leads to improved efficiency and faster convergence toward the goal state.

Therefore, selecting an effective and well-designed heuristic function is essential to optimize the practical performance of the A* search algorithm.

3.5 Path-Finding Goal

While path-finding algorithms can effectively solve certain problems, it is important to acknowledge that not all problems can be adequately addressed by these algorithms alone. In light of this, our objective is to develop an algorithm that can effectively

handle a broader range of problems, specifically targeting scenarios where diagonal movement is essential for achieving faster travel.

Incorporating diagonal movement into the algorithm introduces additional complexities, primarily due to the increased computational requirements. The robot must dynamically adjust its configuration and carefully consider the cost associated with diagonal travel when determining the optimal path. This means that the algorithm needs to account for the trade-off between the potential benefits of diagonal movement and the additional costs incurred. This process demands extensive computational power and efficient algorithms to find the most efficient and feasible path considering these factors.

By addressing these challenges and developing an algorithm that accommodates diagonal movement, hence it aims to enhance the robot's ability to navigate efficiently and effectively in diverse environments. This advancement enables the robot to take advantage of diagonal paths, which can significantly reduce travel time and improve overall performance in situations where faster movement is crucial.

3.6 Analysis

The A* and modified A* algorithm outcomes are demonstrated in Fig. 2a and b. Figure 2b evidenced the exploration approach of modified A* algorithm with entire traversal area to be pre-mapped to identify the optimal path. The modified A* approach proves most effective in environments where the topography is known in advance. However, to overcome this limitation, model-free path planning techniques are employed.

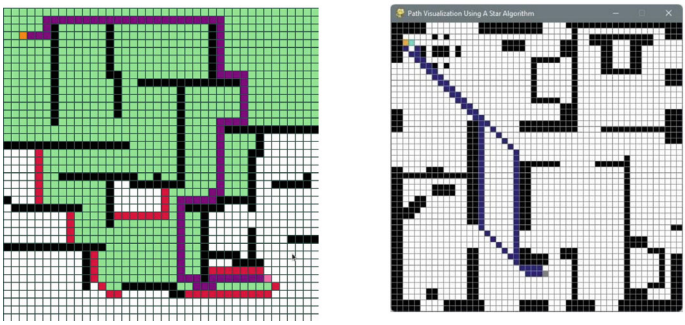

(a) A* algorithm **(b)** Modified A* algorithm

Fig. 2 Optimal path planning

4 Reinforcement Learning

The reinforcement learning utilizes a machine-based learning technique that operates using the framework of the Markov decision process (MDP). An MDP states a sequential-based decision problem in which the environment is completely observable and stochastic, and follows a Markovian-based transition model. The MDP is identified by a collection of transition models, states, actions, and a reward-based function that is additive in nature. The mathematical model of the robot is expressed by an MDP.

4.1 Value Iteration

$$U(s) = R(s) + \gamma \max_{a \in A(s)} \sum_{s'} P\left(s' | s, a\right) U\left(s'\right). \tag{3}$$

This is a result of the Bellman equation. For instance, the utility associated with the state (1, 1) in the aforementioned MDP example is:

$$U(1,1) = -0.04 + \gamma \max \left\{ \begin{array}{ll} 0.8U(1,2) + 0.1U(2,1) + 0.1U(1,1), & \text{(North)} \\ 0.9U(1,1) + 0.1U(1,2), & \text{(West)} \\ 0.9U(1,1) + 0.1U(2,1), & \text{(South)} \\ 0.8U(2,1) + 0.1U(1,2) + 0.1U(1,1), & \text{(East)} \end{array} \right\}. \tag{4}$$

Value iteration updates the utilities of n states using an iterative method, starting from zero and continuing until convergence (equilibrium) is attained. The iteration of the step that is represented by Bellman update is:

$$U_{i+1}(s) \leftarrow R(s) + \gamma \max_{a \in A(s)} \sum_{s'} P\left(s' | s, a\right) U_i\left(s'\right). \tag{5}$$

The following pseudocode is for figuring out every state's utility.

```
returns utility for function Value Iteration (mdp, ϵ)
inputs: mdp, an Markov decision process with actions A(s), states S, rewards R(s),
     discount factor γ
     ϵ, transition-based model P(s′|s, a), the highest amount of inaccuracy permitted in a
          state's utilities
initial variables: U, U′, utility vectors for the states in S, starting at zero
               δ, the greatest variation in a state's utility during a possible iteration
loop:
  U ← U′; δ ← 0
  for every state s in S do
     U′[s] ← R(s) + γ max_{a∈A(s)} Σ_{s′} P(s′|s, a)U[s′]
     if |U′[s] − U[s]| > δ then δ ← |U′[s] − U[s]|
until δ < ϵ(1 − γ)/γ
return U
```

The optimum course of action for each state can then be decided after considering the utilities of each state. As shown in Table 2, after each iteration the utility state converges drastically. The biggest change per iteration is decreasing in nature which is shown in Fig. 3, hence verifying the optimization in each state.

4.2 Policy Iteration

The policy $\pi(s)$ is a solution to a Markov decision process that states an action for every states. The MDP seeks to determine the optimum course of action to maximize expected utility. Policy iteration is another method for resolving MDPs. The procedure starts with an arbitrarily chosen policy and then alternates between the following rules until the policy enhancement stage fails to make any change:

- Policy evaluation: computes each state's utility $U(s)$ based on a policy, assuming the policy is followed;
- Policy improvement: adjusts the policy related to the utility's current condition, indicated by the symbol $U(s)$.

$$\pi^*(s) = \arg\max_{a \in A(s)} \sum_{s'} P\left(s' | s, a\right) U\left(s'\right). \tag{6}$$

Using a shortened version of the Bellman equation, we determine each state's utility for the policy evaluation phase.

$$U_i(s) = R(s) + \gamma \sum_{s'} P\left(s' | s, \pi_i\left(s\right)\right) U_i\left(s'\right). \tag{7}$$

To determine the utility of states, a common approach is to represent them as a set of n equations with n unknowns in a linear system. However, solving this system exactly can be computationally expensive, requiring $O(n^3)$ time for n states. As an alternative, an approximation of the utilities can be obtained by employing a condensed Bellman update approach.

The policy iteration pseudocode is for optimizing the policy.

```
returns a policy for function Policy Iteration(mdp)
  inputs: mdp, an markov decision process with transition-based model P(s|s, a), actions
       A(s), states S
  initial variables: U, a utility vector for states in S, starting at zero
                  π, a state-indexed policy vector, starting at random

  loop:
    U ← PolicyEvaluation(π, U, mdp)
    stable? ← true
    for every state s in S do
        if max_{a∈A(s)} Σ_{s'} P(s'|s, a)U[s'] > Σ_{s'} P(s'|s, π[s])U[s'] then do
        π[s] ← arg max_{a∈A(s)} Σ_{s'} P(s'|s, a)U[s']
        stable? ← false
  until stable?
  return π
```

Table 2 Value convergence table with final value

Initial state				Intermediate state				Final state			
VI iteration 0:				VI iteration 3:				VI iteration 6:			
0.79	0.19	0.28	0.00	0.89	0.99	1.10	0.00	0.89	0.99	1.10	0.00
0.96	0.00	0.62	0.00	0.80	0.00	0.99	0.00	0.80	0.00	0.99	0.00
0.78	0.44	0.80	0.27	0.72	0.70	0.89	0.63	0.72	0.80	0.89	0.80
biggest change is: 0.823536				biggest change is: 0.173265				biggest change is: 0.000000			

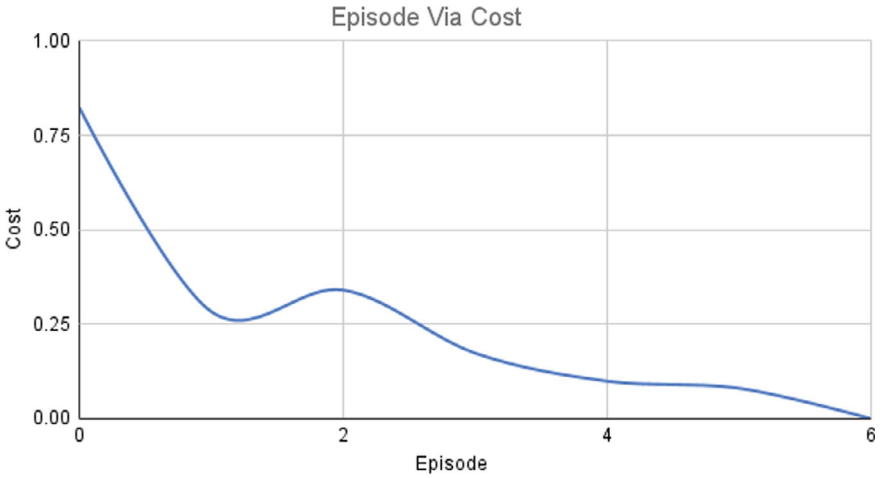

Fig. 3 Episode via cost analysis

Instead of aiming for precise solutions, condensed Bellman updates provide a more efficient approximation by considering the stagnate policy. The process involves iterative updating of the utility values of states based on the current estimates and the expected rewards and transition probabilities associated with each state-action pair. These updates help refine the utility values by gradually incorporating information from neighboring states.

By repeatedly applying condensed Bellman updates, the algorithm converges toward an approximation of the utilities that captures the overall value and characteristics of the states. Although this approach may not yield exact solutions, it significantly reduces the computational complexity compared to solving the entire linear system.

The condensed Bellman update approach strikes a balance between accuracy and computational efficiency, making it a practical choice when precise solutions are not essential. By utilizing this approximation technique, the algorithm can efficiently estimate the utilities of states, offering valuable perspectives and streamlining decision-making across different fields.

$$U_{i+1}(s) \leftarrow R(s) + \gamma \sum_{s'} P\left(s' | s, \pi_i(s)\right) U_i\left(s'\right). \tag{8}$$

In Table 3, the algorithm comprises dual phases: first (policy evaluation) and second (policy improvement). At the time of evaluating the policy, the value function is updated. During the policy improvement stage, the supplied policy is updated using Eq. (7). Iterations continue until convergence.

Table 3 Policy convergence table with final policy

Initial state				Intermediate state				Final state			
Values (iteration 0):				*Values (iteration 7):*				*Values (iteration 15):*			
0.79	0.19	0.28	0	0.01	0.01	1.1	0	0.89	0.99	1.1	0
0.96	0	0.62	0	0.01	0	0.99	0	0.8	0	0.99	0
0.78	0.44	0.8	0.27	0.01	0.01	0.89	0.01	0.72	0.8	0.89	0.8
Policy (iteration 0):				*Policy (iteration 7):*				*Policy (iteration 15):*			
R	R	U	N/A	R	R	R	N/A	R	R	R	N/A
U	N/A	D	N/A	U	N/A	U	N/A	U	N/A	U	N/A
D	R	R	R	R	R	U	L	U	U	U	L

5 Result

This work investigates value and policy iteration-based reinforcement learning for model-free path planning. We built our foundation by researching model-based algorithms.

- A greedy-based algorithm is the Dijkstra algorithm.
- The A-Star algorithm is built upon the foundation of the Dijkstra algorithm.
- Modified A-Star, although A-Star is only capable of moving in four directions, can move in eight.

To overcome the limitation of requiring prior environment information, we adopt model-free learning using reinforcement learning, which involves advanced exploration. Value iteration computes state utilities in an MDP, representing anticipated discounted rewards. It has fast convergence and low processing power requirements, making it ideal for solving MDPs.

Policy iteration is a strategy for solving MDPs. It iteratively evaluates and improves a policy until no further modifications are made. It produces an optimal policy and corresponding value function. Model-based path planning relies on predefined models of the robot and environment, assuming fixed kinematics.

6 Observation

Model-free path planning algorithms adapt to the robot's shape and current environment, without relying on predefined models. They dynamically select feasible and efficient paths. Policy iteration outperforms value iteration by iteratively modifying the policy for faster convergence. However, for large-scale problems, additional computational resources may be impractical for policy evaluation.

The choice between value iteration and policy iteration depends on limitations and requirements. Value iteration suits limited resources and approximate optimal policies. Policy iteration suits faster convergence and accurate optimal policies, despite higher computing costs.

References

1. Hemami, A., Mehrabi, M., Cheng, R.: Synthesis of an optimal control law for path tracking in mobile robots. Automatica **28**(2), 383–387 (1992)
2. Parween, R., Vega-Heredia, M., Rayguru, M., Abdulkader, R., Mohan, R.E.: Autonomous self-reconfigurable floor cleaning robot. IEEE Access **8**, 1–1 (2020)
3. van den Berg, J., Abbeel, P., Goldberg, K.: LQG-MP: Optimized path planning for robots with motion uncertainty and imperfect state information. Int. J. Robot. Res. **30**, 895–913 (2011)
4. Liu, S., Sun, D., Zhu, C.: Coordinated motion planning for multiple mobile robots along designed paths with formation requirement. IEEE/ASME Trans. Mechatron. **16**, 1021–1031 (2011)
5. Plaku, E., Kavraki, L., Vardi, M.: Motion planning with dynamics by a synergistic combination of layers of planning. IEEE Trans. Robot. **26**, 469–482 (2010)
6. Al-Sabban, W.H., Gonzalez, L.F., Smith, R.N., Wyeth, G.: Wind energy- based path planning for electric unmanned aerial vehicles using Markov decision processes. In: IROS 2012 (2012)
7. Le, A., Prabakaran, V., Sivanantham, V., Mohan, R.: ModifiedA-Star algorithm for efficient coverage path planning in tetris inspired self- reconfigurable robot with integrated laser sensor. Sensors **18**(8), 2585 (2018)
8. Konar, A., Goswami, I., Singh, S.J., Jain, L.C., Nagar, A.K.: A deterministic improved q-learning for path planning of a mobile robot. IEEE Trans. Syst., Man, Cybern. Syst. **43**, 1141–1153 (2013)
9. Bry, A., Roym, N.: Rapidly-exploring random belief trees for motion planning under uncertainty. In: 2011 IEEE International Conference on Robotics and Automation, pp. 723–730 (2011)
10. Plaku, E., Hager, G.: Sampling-based motion and symbolic action planning with geometric and differential constraints. In: 2010 IEEE International Conference on Robotics and Automation, pp. 5002– 5008 (2010)
11. Wiemann, T., Lingemann, K., Hertzberg, J.: Automatic map creation for environment modelling in robotic simulators. In: ECMS (2013)
12. Raja, P., Pugazhenthi, S.: Optimal path planning of mobile robots: a review. Int. J. Phys. Sci. **7**, 02 (2012)
13. Cetin, H., Durdu, A.: Path planning of mobile robots with Q-learning. In: 22nd Signal Processing Conference, pp. 2162–2165 (2014)
14. Landgraf C, Meese B, Pabst M, Martius G, Huber MF. A reinforcement learning approach to view planning for automated inspection tasks. Sensors (Basel). **21**(6), 2030 (2021). PMID: 33805587; PMCID: PMC7998553. https://doi.org/10.3390/s21062030
15. Lu, W., Yang, J., Chu, H.: Playing mastermind game by using reinforcement learning. In: 2017 1st IEEE International Conference on Robotic Computing (IRC), pp. 418–421 (2017)

Comparative Performance Analysis of PV System in Island Mode Using MPPT Fuzzy Logic Controller and Perturb and Observe Algorithm

Sagnik Ghosh and Shivam

Abstract This paper analyzes the performance of a PV system under different irradiance using a fuzzy logic controller and P&O algorithm. The PV system is established by using a converter and a maximum power point (MPPT)-based controller. PV array shows no linear VI curve voltage–current character-tracking characteristic feature and shows contrasting results under different irradiances. The boost converter increases the voltage to operate at the MPPT. The fuzzy logic and P&O controller has the capability to control nonlinear irregularity and obtain the appropriate result. In this paper, a comparative performance analysis is done based on fuzzy logic and P&O controller under island mode for the specified resistive load range in order to achieve a better response. The performance analysis is verified in MATLAB/Simulink environment.

Keywords Boost converter · Fuzzy logic · Perturb and observe · MPPT

1 Introduction

Energy is a matter which is found in nature in one form or other and is converted into different forms according to our needs. Electrical energy is found in nature in different forms, but the most convenient method of extracting electricity from nature is the burning of coal and fossil fuels. But with changing of times, people are looking toward a replacement in renewable forms of energy. Solar energy doesn't cause any kind of hazardous effect on the environment, and the form is also inexhaustible. Solar energy can also be used for other purposes also especially in heating objects for different purposes [1]. Solar cells can produce electricity when there is an abundant source of solar rays on the panels. Again due to climatic conditions, the production of electricity also varies. In hot climatic zones like deserts, the amount of solar radiation obtained is more, and in cold climatic zones, the solar radiation received is less [2].

S. Ghosh (✉) · Shivam
Department of Electrical Engineering, National Institute of Technology, Kurukshetra, India
e-mail: sagnikg98@gmail.com

© The Author(s), under exclusive license to Springer Nature Singapore Pte Ltd. 2025

H. P. Singh et al. (eds.), *Recent Developments in Control, Automation and Power Engineering*, Lecture Notes in Electrical Engineering 1303,
https://doi.org/10.1007/978-981-96-0047-2_14

For this reason, we use the MPPT method. There are various power point tracking methods, and the most modern technique is the introduction of automation in the process. Machine learning algorithms are one of the most used techniques in the automation industry to get the most accurate results.

A fuzzy logic controller is used for MPP at various irradiance using a boost converter [3]. Comparative studies have been made between the various algorithmic techniques for extracting maximum power [4]. In [5], variable temperature and irradiance are the PV input, and peak power is affected by exterior factors. The SEPIC converter is used to extract maximum power under varying irradiance and charge the battery [6]. In [7], the cleansing technique of PV is discussed to extract maximum power under different climatic conditions. Artificial intelligence-based method of extracting MPP like fuzzy, ANN, and P&O is discussed [8]. Fuzzy logic controller is used to get power and charge a battery at a constant voltage by passing through a Buck–Boost converter [9].

In this paper, the comparative performance analysis of PV system based on two methods is demonstrated for extracting maximum power in island mode to achieve a better response.

This paper discusses about the different components of PV system in Island mode. These components are put together to perform comparative performance analysis using two algorithms to track maximum power. A conclusion is made after analyzing the results of the two algorithms.

2 PV System in Islanded

2.1 PV Array

Solar PV array is a vital part for the extraction of solar energy. PV array produces electricity when sunlight falls on the panels. So an advanced system is constructed to achieve maximum power [10]. The climatic condition and temperature have a huge influence on the power generated by the PV panels.

2.2 Power Converter

When power transfer in PV array occurs, some power is lost and this reduces the efficiency; to counter this problem, we have to increase the voltage. The circuit consists of a boost converter, inductance, capacitance, and power MOSFET which is controlled by the PWM technique. The control of this system helps in the controlling of output voltage and power [3] (Fig. 1).

When the switch is off,

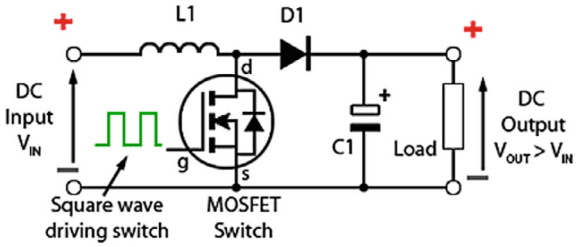

Fig. 1 Schematic circuit of boost converter

$$V_{in} + V_L - V_0 = 0. \tag{1}$$

The voltage across the inductor,

$$V_l = L\frac{di}{dt}, \tag{2}$$

the average inductor current in on and off time is the, therefore;

$$T_{ON} * V_{in} = (T - T_{ON})(V_0 - V_{in}). \tag{3}$$

Substituting $T_{ON} = DT$ and $T_{OFF} = (1 - D)T$ in (3),
where D is the duty cycle.
From (4)

$$D = (V_0 - V_{in})/V_0 \tag{4}$$

The output voltage V_o is simplified as

$$V_o = V_{in}/(1 - D). \tag{5}$$

Applying Laplace transform and solving,

$$\frac{V_{out}(s)}{a(s)} = \frac{\{(1-D)V_{OUT} - L * I_L S\}}{\left\{LC * S^2 + \frac{L}{R} * S + (1-D)^2\right\}}. \tag{6}$$

2.3 *Fuzzy Logic Controller*

This is an advanced automated system to bring out the maximum efficiency of a model [4].

The MPPT algorithm is designed based on fuzzy logic so that it can track the maximum power at different irradiance. The input parameters of the controller

$\Delta P/\Delta V$ are arranged as one is the change in error and the other is the measurement of the error itself. If the ratio of change of power to voltage is less than zero, the controller changes the duty ratio to lower the voltage so that the power becomes maximum. Otherwise, the duty ratio increases the voltage so that power becomes maximum.

$$E(\mathrm{k}) = \frac{p(k) - p(k-1)}{E(\mathrm{K}) - V(k-1)}. \tag{7}$$

The change in error is,

$$\Delta e = e(k) - e(k-1). \tag{8}$$

The duty cycle function is:

$$\Delta D = D(K) - D(k-1). \tag{9}$$

Seven logic levels are considered for input and output to get output.

The range of membership functions in Fig. 2 shows the range of error between [–12, 10], the range of change of error is between [–2, 2], and the duty cycle in [–1, 1]. The nature of all the membership functions is triangular. Table 1 shows the fuzzy logic and it is developed to track maximum power points at different irradiance. The rules are summarized in Table 2.

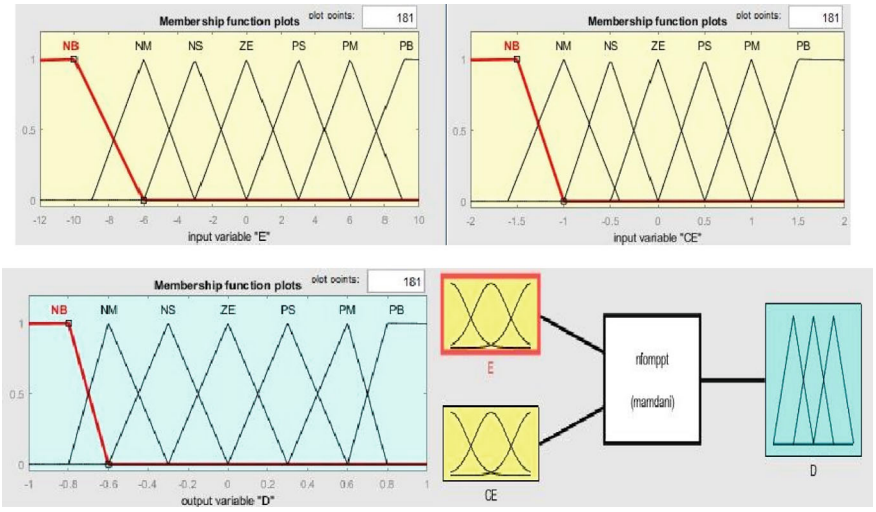

Fig. 2 Range of membership functions for the fuzzy logic controller

Table 1 Rules for fuzzy logic controller

E/CE	PB	PM	PS	ZE	NS	NM	NB
PB	ZE	ZE	ZE	NB	NB	NB	NB
PM	ZE	ZE	ZE	NB	NM	NM	NM
PS	ZE	ZE	ZE	NS	NS	NM	NM
ZE	NS	NS	ZE	ZE	ZE	PS	PS
NS	PM	PM	PS	NS	ZE	PS	ZE
NM	PM	PM	PM	PB	ZE	ZE	NS
NB	PB	PM	PM	PB	ZE	ZE	ZE

Table 2 System parameters

Parameters	Rating
Number of cells	60
Maximum power	255 W
Current during short circuit condition	8.8 A
Voltage during open-circuit condition	38 V
Resistive loads	19–20 Ω
Capacitor	1734 μF
Inductor	162 mH

2.4 P&O MPPT Algorithm

The P&O is a conventional method of tracking MPP. The algorithm controls the voltage to achieve MPPT. Voltage increases if the $\frac{\Delta p}{\Delta v}$ ratio is positive, while voltage decreases if the $\frac{\Delta p}{\Delta v}$ ratio is negative. The step size is fixed at first but is changed accordingly to get the duty cycle to achieve MPP [11].

3 Simulation Results and Discussion

The Simulink model is developed according to the system block diagram as shown in Fig. 3. At first fuzzy logic method is used for tracking maximum power. Two variables are treated in the fuzzy logic controller function to obtain the desired result. The performance of the system based on the methods is compared.

The system based on fuzzy logic is, performed under a constant temperature of 25°C, and the input irradiance is considered 600, 700 and 800 W/m^2, respectively. The output results are shown in Figs. 4, 5, and 6, and for variable irradiation, the output results are given in Fig. 7.

The output readings are obtained 109 W and 44.82 V, respectively, at 600 W/m^2 irradiance. The power increases to 157 W and voltage build-up occurs 54.40 V when

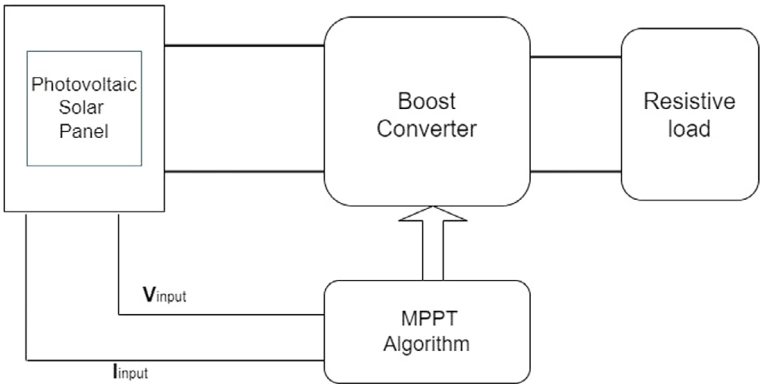

Fig. 3 Block model of PV array system having fuzzy logic controller

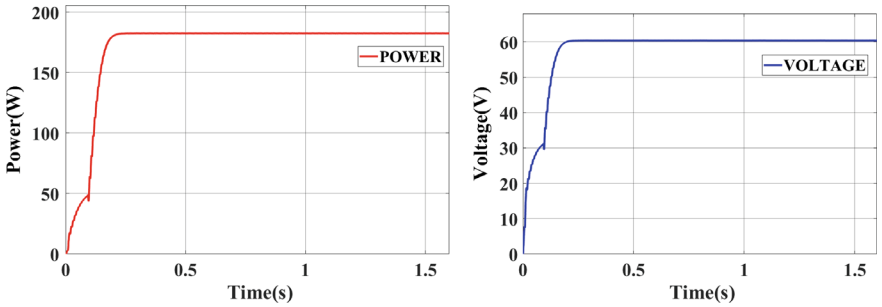

Fig. 4 Output power and voltage at 800 W/m^2 irradiance using fuzzy logic

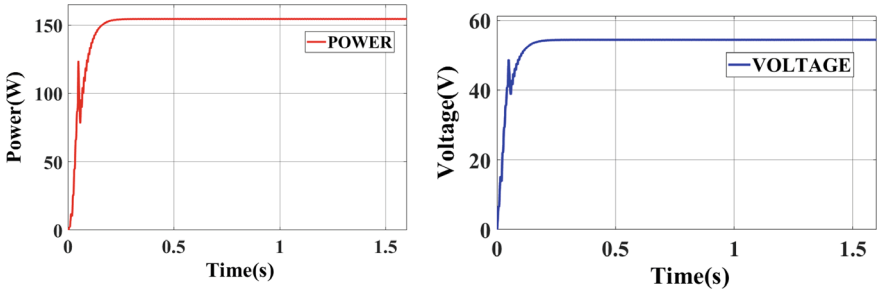

Fig. 5 Output power and voltage at 700 W/m^2 irradiance using fuzzy logic

the value is increased to 700 W/m^2. When irradiance reaches 800 W/m^2, the power reaches 186 W and the voltage settled at 60.24 V.

The system based on the algorithm is performed for MPPT under a constant temperature of 25 °C and 600, 700, and 800 W/m^2 irradiances. The maximum power

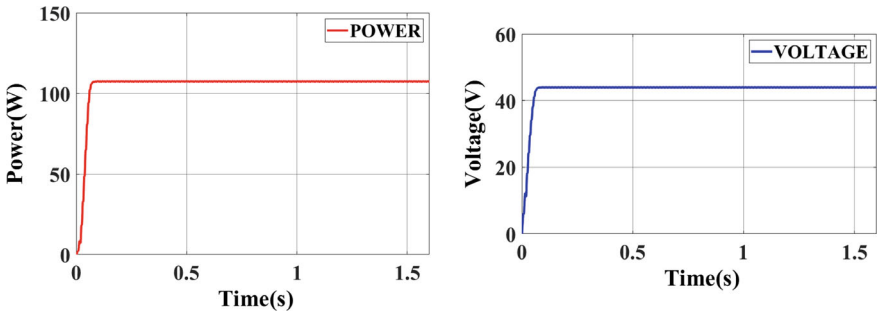

Fig. 6 Output power and voltage at 600 W/m^2 irradiance using fuzzy logic

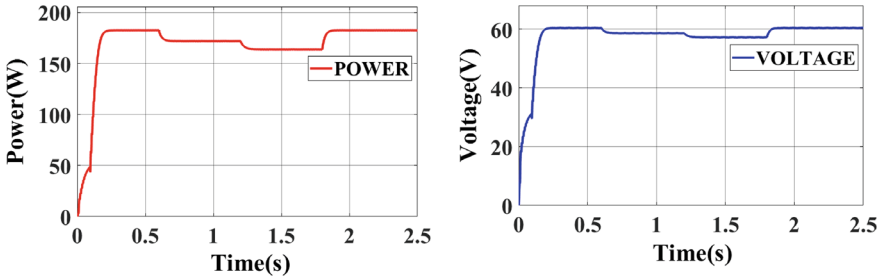

Fig. 7 Change in output power and voltage for changing irradiance using fuzzy logic

corresponding to the irradiance is extracted and is shown in Figs. 8, 9, and 10, and change in output readings for varying radiation is given in Fig. 11.

In Fig. 8, the power and the voltage are obtained 106 W and 44.52 V at 600 W/m^2. When the value is increased at 700 W/m^2, the power is increased to 154 W and voltage builds up to 53.90 V in Fig. 9. Finally, these values are obtained 184 W and 59.84 V for 800 W/m^2.

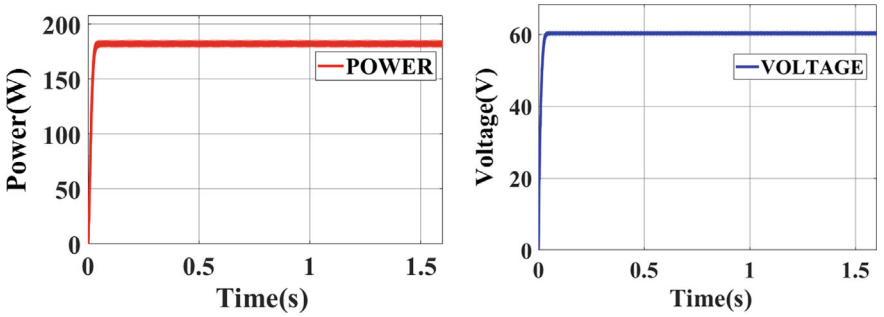

Fig. 8 Output power and voltage at 800 W/m^2 irradiance using P&O logic

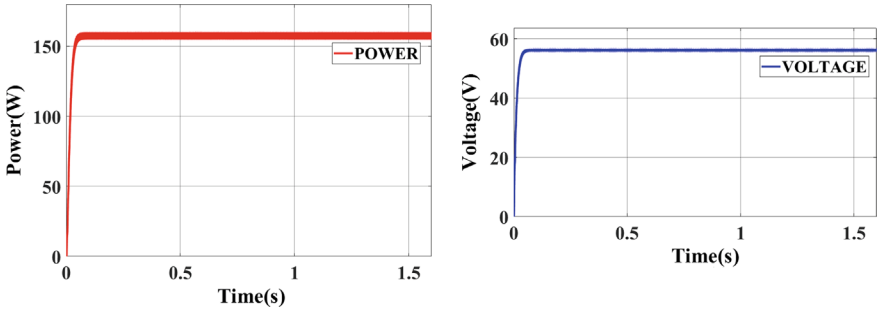

Fig. 9 Output power and voltage at 700 W/m^2 irradiance using P&O logic

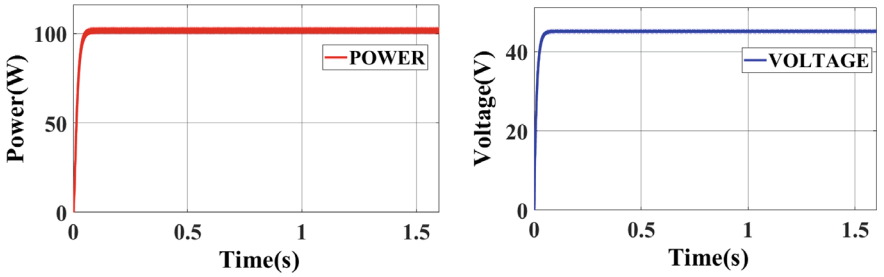

Fig. 10 Output power and voltage at 600 W/m^2 irradiance using P&O logic

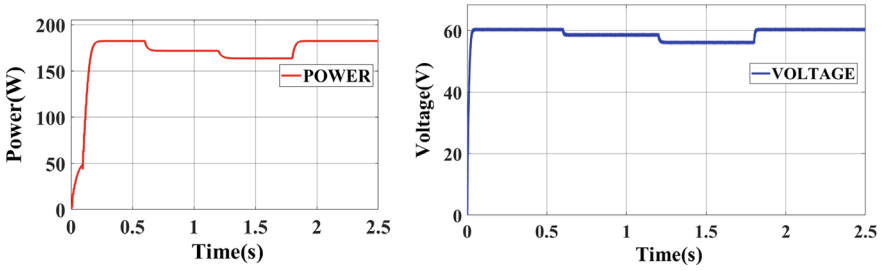

Fig. 11 Change in output power and voltage for changing irradiance P&O logic

Comparing the output parameters as summarized in Tables 3 and 4, it is observed that fuzzy logic extracts more power and voltage. The mean efficiency of the algorithm using the fuzzy controller is around 93% and that of P&O is 91%.

Table 3 Power comparison table for fuzzy logic

Irradiance (W/m^2)	Voltage (V)	Input power (W)	Output power (W)	Efficiency (%)
800	60.24	192	186	96.83
700	54.40	165	157	95.15
600	44.82	127	109	85.82

Table 4 Power comparison table for P&O logic

Irradiance (W/m^2)	Voltage(V)	Input power (W)	Output power (W)	Efficiency (%)
800	59.84	192	184	95.13
700	53.90	165	154	93.33
600	44.52	127	106	83.46

4 Conclusion

A comparative performance analysis is done on PV system based on fuzzy logic and P&O controller in Island mode. The analysis is verified based on both algorithms. Results of the fuzzy algorithm show maximum output power tracked at every irradiance over P&O MPPT. The results are compared and the overall efficiency of Fuzzy controller is found 2% more than P&O algorithm due to converter parameters [12–14].

This work may integrate with energy storage system and electric vehicle charging station in future.

References

1. Delucchi, M.A., Jacobson, M.Z.: Providing all global energy with wind, water, and solar power, Part II: Reliability, system and transmission costs, and policies. Energy policy 39, no 3 (2011): 1170–1190. Ministry of Energy, Renewable and alternative energy, Renewable and Alternative Energy Development Plan 2015–2036, **1**(1), (2015).
2. Putri, R. I., Setiawan, H., Irawan, B., Yunus, Y., Patma, T.S., Pradani, E.R.K.: Fuzzy maximum power point tracking (MPPT) controller for photovoltaic system on mini greenhouse. In J Phys: Conf Series, **1402**(3), p. 033109. IOP Publishing, (2019).
3. Aganah, A.K., Leedy A.W.: A constant voltage maximum power point tracking method for solar powered systems. In 2011 IEEE 43rd Southeastern Symposium on System Theory, pp. 125–130. IEEE (2011)
4. Atia, Y.: Photovoltaic maximum power point tracking using SEPIC converter. ERJ. Engineering Research Journal **32**(4), 437–445 (2009)
5. Raj, M.P., Joshua, A.M.: Design, implementation and performance analysis of a LabVIEW based fuzzy logic MPPT controller for stand-alone PV systems. In *2017* IEEE International Conference on Power, Control, Signals and Instrumentation Engineering (ICPCSI) pp. 1012–1017. IEEE, (2017)

6. Boonraksa, P., Chaisa-Ard, T., Sommat, S., Pimpru, P., Booraksa, T., Marungsri, B.: Design and simulation of fuzzy logic controller based MPPT of PV module using Matlab Simulink. In 2022 International Electrical Engineering Congress (*iEECON)*, pp. 1–4. IEEE, (2022)
7. Sasi, M.A.: Fuzzy logic control of MPPT controller for PV systems. PhD diss., Memorial University of Newfoundland, (2017)
8. Mohammed, Z.: Design and simulation of the MPPT control based on a fuzzy logic controller for a photovoltaic system. 1st International conference on embedded systems and artificial intelligence, ESAI'19, At: Fez Morocco,. Jomyut's House, General working principle of solar cells,"baanjomyut.com(2019)
9. Afshan, I., Rizwan Khan, M., Ayyub, M.: FPGA based real-time implementation of fuzzy logic controller for maximum power point tracking of solar photovoltaic system. Optik 213: 164668. (2020)
10. Ozdemir, S., Altin, N., Sefa, I.: Fuzzy logic based MPPT controller for high conversion ratio quadratic boost converter. Int J Hydr Energy 42, (28) 17748–17759 (2017) Selvan, S., Mohammed, D., feros, J., Khan, J., Umayal, V., Indumathi, M., Simulation of fuzzy logic control based MPPT technique for photo- voltaic system. 2nd international conference on innovations in engineering and technology, ICCET 2014, pp.10–14. At Penang (2014)
11. Messai, A., Mellit, A., Massi Pavan, A., Guessoum, A., Mekki, H.: FPGA-based implementation of a fuzzy controller (MPPT) for photovoltaic module. Energy conversion and management 52, (7) 2695–2704 (2011)
12. Laxman, B., Annamraju, A., Srikanth N.V.: A grey wolf opti- mized fuzzy logic based MPPT for shaded solar photovoltaic systems in microgrids. Int J Hydr Energy 46(18), 10653–10665 (2021)
13. Podder, A.K., Roy, N.K., Pota H.R.: MPPT methods for solar PV systems: A critical review based on tracking nature. IET renewable power generation 13(10), 1615–1632 (2019)
14. Madhusudhana, J., Puttaswamy, P.S., Chapparband, M.R.: Design and simulation of boost converters suitable for photo voltaic applications, IJRET: Int J Res Eng Tech eISSN: 2319–1163 | pISSN: 2321–7308(2018)
15. Baramadeh, M.Y., Almonem Abouelela, M.A., Alghuwainem. S.M.: Maximum power point tracker controller using fuzzy logic control with battery load for photovoltaics systems. Smart Grid and Renewable Energy **12**(10), 163–181 (2021)
16. Saravanan, S., Ramesh Babu, N.: Maximum power point tracking algorithms for photovoltaic system–a review. Renewable and sustainable energy reviews 57, 192–204 (2016)

Comparative Analysis of SOC Prediction Using Machine Learning Algorithms

Utsab Bhattacharya and Pradeep Kumar

Abstract Li-ion batteries are an essential and vital component of Electric Vehicles (EVs). SOC estimation of these batteries is critical to ensure optimal vehicle performance and avoid potential safety hazards. SOC variation is highly nonlinear, where machine learning (ML) algorithms are suitable for estimation. This paper presents a comparative analysis of seven different ML algorithms for predicting SOC. The performance of the algorithms is evaluated using Mean Squared Logarithmic Error (MSLE), Adjusted R2 score, Pearson Correlation Coefficient, Geometric Mean Absolute Error, and Theil U Statistic. The results show that random forest regression (RFR), support vector regression (SVR), and K-nearest neighbor (KNN) regression provide better results, with much effort to tuning the algorithm.

Keywords State-of-charge · Machine learning · Prediction · Artificial intelligence

1 Introduction

The rising demand for Electric Vehicles (EVs) to address climatic and energy issues has brought significant battery development [1]. Li-ion batteries are preferred for these applications for their long cycle life, high energy density, and low self-discharge rates [2]. However, the production and disposal of Li-ion cells have significant environmental impacts, like the extraction and processing of raw materials, high energy requirements for manufacturing, and hazardous waste disposal [3]. The available batteries must be utilized effectively to minimize the environmental impact [4]. Therefore, it is essential to develop efficient methods for predicting these batteries'

U. Bhattacharya (✉) · P. Kumar
Department of Electrical Engineering, National Institute of Technology, Kurukshetra, India
e-mail: utsabbhattacharya71@gmail.com

P. Kumar
e-mail: pradeepkumar@ieee.org

© The Author(s), under exclusive license to Springer Nature Singapore Pte Ltd. 2025

H. P. Singh et al. (eds.), *Recent Developments in Control, Automation and Power Engineering*, Lecture Notes in Electrical Engineering 1303,
https://doi.org/10.1007/978-981-96-0047-2_15

SOC [5]. The battery SOC reflects the amount of charge remaining. Accurate prediction of SOC is crucial to extend the battery life and ensure its safe and efficient operation [6]. The SOC depends on various factors like the voltage, current, temperature, and battery arrangement [7].

Research studies have been conducted to develop accurate and reliable models that predict the SOC of Li-ion batteries [8–13]. Machine learning (ML) algorithms have also been used, such as decision trees [7], support vector regression (SVR) [10], long short-term memory (LSTM) [11], and Artificial Neural Networks (ANNs) [12], to predict the SOC. An optimized support vector machine has been proposed to predict SOC [10]. MSE and error sum are used for performance evaluation. The SOC prediction for LiFePO4 battery using decision tree is presented in [8] with 3319 samples' data from BTSDA, and accuracy is evaluated with mean error. SOC prediction for Li-ion batteries is performed in [9] with ML algorithms using an experimental setup with a multi-sine load profile to collect data. LSTM, Auto ARIMA, Prophet, and decision trees are used. Mean Percentage Error (MPE) and Normalized Root Mean Squared Error (NRMSE) are used to describe the performance [10]. SOC is predicted using SVM and optimized by Genetic Algorithm with voltage, current, and temperature as input variables [14]. An overview of ML methods for controlling, monitoring, and estimating battery management systems, including the SOC, SOH, and remaining usable life, is presented in [13]. A passive cell balancing is presented in [16]. The performance is evaluated using radial basis neural network, backpropagation neural network, and LSTM. In [15], SVM, RF, and the GBRT algorithm are used for cell balancing. MSE and MAE are used for error value comparison. A review and classification of different ML algorithms have been presented in [17] for RUL prediction of Li-ion cells and compared for accuracy and complexity. When considering computational complexity, SVM, GPR, and ELM are preferred due to their simple characteristics and structures requiring fewer calculations. However, the LSTM training approach is complex and needs time for training.

Different performance measurements are employed to rate the efficiency of algorithms. The performance matrices help in various ways like:

- Selection of best model.
- Improvement of model performance while identifying weaknesses in the model.
- Understanding of the model's behavior.
- Comparison of different algorithms.

This paper presents a comparative performance analysis to identify more accurate and efficient ML approaches that predict Li-ion batteries' SOC. The ML algorithms used are Linear Regression, DTR, KNN, RFR, SVR, LSTM, and ANN. The models were trained and tested using the output of the battery model in MATLAB/Simulink, and a dataset was obtained from it. The algorithms are used to develop the model for prediction of SOC, and the above-mentioned performance metrics are used for evaluation. The predicted results of ML algorithms are thoroughly analyzed, showing that the ML algorithms and AI techniques can effectively predict

the SOC of Li-ion cells. The performance is evaluated using Mean Squared Logarithmic Error (MSLE), Adjusted R2 score, Pearson Correlation Coefficient (PCC), Geometric Mean Absolute Error (GMAE), and Theil U Statistic.

The remaining paper is structured as follows: Sect. 2 describes various ML algorithms used in this paper. Section 3 presents the performance matrices used for performance evaluation of the algorithms. Results and discussions are presented in Sect. 4, while the conclusions are drawn in Sect. 5.

2 Machine Learning Algorithms

This section describes the various ML algorithms used for predicting SOC.

2.1 Linear Regression

LR is used for regression analysis [18]. Its presumption relies on the linear connection among independent variables current, voltage, and temperature and dependent variable SOC. It is given as

$$y = \beta_0 + \beta_1 x_1 + \beta_2 x_2 + \beta_3 x_3 + \ldots + \beta_k x_k + \varepsilon, \tag{1}$$

where $\beta_0, \beta_1, \beta_2, \beta_3, \ldots, \beta_k$ are regression coefficients, independent variables are x_1, x_2, x_3, …., x_k, while dependent variable is y and the error term is denoted by ε.

2.2 Decision Tree Regression

DTR is a non-parametric regression analysis method [19]. Meanwhile, each branch and leaf node stands for the test's results and the accompanying prediction, while each internal node relates to a test performed on an attribute. The DTR can be presented as:

$$y = \frac{1}{N} \sum_{i=1}^{N_x} y_i, \tag{2}$$

where N_x is number of data points in the subset to which x belongs, N is total number of data points, and y_i is i-th data value in the subset.

2.3 K-Nearest Neighbors Regression

KNN is a non-parametric regression analysis method [20]. It uses the average of k-nearest neighbors of a data point to make a prediction. The KNN can be given as:

$$y = \frac{1}{N} \sum_{h=1}^{N_x} y_{nn,h}, \tag{3}$$

where $y_{nn,h}$ is the value of y in h-th neighbor and n is the number of nearest neighbors.

2.4 Random Forest Regression

It is an ensemble learning, classification, and regression analysis method. It uses the concept of a decision tree, where several decision trees are employed for prediction [21]. The RFR is given as:

$$y = \frac{1}{N} \sum_{i=1}^{N_x} y_i, \tag{4}$$

$$\theta_i = (\omega_i, b_i, T_i), \tag{5}$$

$$T(x, \theta_i) = \sum_{i=1}^{N} \omega_{ij} I\left(x \in T_{ij}\right) + b_i, \tag{6}$$

where θ_i is the parameter vector of i-th tree, ω_{ij} is weight of the j-th leaf in the i-th tree, I(x ε T_{ij}) is the indicator function which returns 1 if x falls in the j-th leaf of the i-th tree, and 0 otherwise, T_i is the set of all leaves in the i-th tree, J is number of leaves one tree, N is number of trees in forest, and b_i is bias term.

2.5 Support Vector Regression

A regression algorithm that maps input features to higher-dimensional space using kernel function and tries to find a linear function that maximizes the margin between values that were predicted and actual values [22]. The SVR is given as

$$y = \frac{\lambda}{N} \sum_{k=1}^{N} \left(\sigma_k + \sigma_k^*\right) K(l_k, l) + b, \tag{7}$$

where λ is the regularization parameter, N is number of training samples, σ_k and σ_k^* are dual variables, K(l_i,l) is Kernel function evaluated at the k-th training sample, and b is the bias term

2.6 Long Short-Term Memory

A specific recurrent neural network called LSTM is used to process and examine input data. A gating mechanism is built into LSTMs, making them capable of successfully handling long-term dependencies and suitable for jobs like speech recognition, time series analysis, and so on [23]. It is given as

$$fr_t = \emptyset_g\left(M_f\left[x_t, k_{t-1}\right] + \beta_{fr}\right), \tag{8}$$

$$o_t = \emptyset_g\left(M_o\left[x_t, k_{t-1}\right] + \beta_m\right), \tag{9}$$

$$in_t = \emptyset_g\left(M_t\left[x_t, k_{t-1}\right] + \beta_m\right), \tag{10}$$

$$c_t = fr_t * c_{t+1} + in_t * \emptyset_c\left(M_c\left[x_t, k_{t-1}\right] + \beta_c\right), \tag{11}$$

$$h_t = \emptyset_h(c_t), \tag{12}$$

where, at time t, in_t is input gates, k_t is hidden state, c_t is state of the cell, fr_t is forget gates, g_t is the output gates, M is weight matrices, and β is bias vectors.

2.7 Artificial Neural Network

ANN is motivated by human brain, its structure, and working. ANNs consist of interconnected nodes that process and transmit information [24]. It is given as

$$z^{(t)} = M^{(t)} h^{(t-1)} + b^{(t)}, \tag{13}$$

$$h^{(t)} = \sigma\left(z^{(t)}\right), \tag{14}$$

$$\hat{y} = h^{(t)}, \tag{15}$$

where $z^{(t)}$ is the weighted sum of inputs to t-th layer of neural network, and $M^{(t)}$ is weight matrix that is connected to the (t-1)th layer to the t-th layer. After the input has been through activation function, the output of t-th layer is represented by $h^{(t)}$,

$b^{(t)}$ is bias term, σ is activation function used in neural network, like *tanh*, *ReLU*, or sigmoid functions, and $\hat{y}$ is the predicted output of the last layer.

3 Performance Metrics

The performance of the different ML algorithms for predicting the SOC of Li-ion cells is evaluated using the performance matrices below.

3.1 MSLE

The MSLE handles outliers and significant differences in target variable values better than MSE. MSLE adds logarithmic scaling, making large errors less significant, resulting in a balanced and accurate performance measure. It is given as

$$\frac{1}{n}\sum_{i=1}^{n}\left(\left(\log(1+t_s)-\log\left(1+\widehat{y_s}\right)\right)\right)^2,$$

where $\widehat{y_s}$ is predicted value of s-th observation, t_s is true value of the s-th observation, and n is number of observations.

3.2 Adjusted R-squared

Adjusted R2 is an essential improvement over R2 as it considers how many independent variables are included in the model. It adjusts R2 to penalize adding useless variables that do not improve the model's predictive power. It is given as

$$1-\left[\frac{n-1}{n-p-1}*0(1-R2)\right],$$

where p is predictors' value, R2 is the R2 score, and n is number of observations.

3.3 Pearson Correlation Coefficient

PCC identifies the direction and strength between the variables. It is given as

$$\frac{\sum_{s=1}^{n}(x_s-\overline{x_s})(o_s-\overline{o_s})}{\sqrt{\sum_{s=1}^{n}(x_s-\overline{x_s})^2}\sqrt{\sum_{s=1}^{n}(o_s-\overline{o_s})^2}}.$$

Here, the first variable's s-th value is represented by x_s, the second variable's s-th value is represented by o_s, the mean of the first variable is represented by $\overline{x}$, and the second variable's mean is represented by $\overline{o}$.

3.4 Geometric Mean Absolute Error

GMAE is a metric that provides more balanced view of the error across the entire range of values in the data and is useful for cases with outliers in the data, as it is less sensitive to outliers than other error metrics like RMSE or MAE. It is given as

$$e^{\frac{1}{n}\sum_{s=1}^{n}\log\left(t_s-\widehat{y_s}\right)},$$

where t_s is true value of s-th observation, n is number of observations, while $\widehat{y_s}$ is the s-th observation's predicted value.

3.5 Theil U Statistic

Theil's U Statistic accounts for trend and seasonality, offers a comprehensive evaluation, and can be used to compare different models and accuracy assessment. It is given as

$$\sqrt{\frac{1}{n}\sum_{j=1}^{n}\frac{\left(o_j-\widehat{y_j}\right)^2}{o_j^2}},$$

where o_j is true value of the j-th observations, n is number of observations, and $\widehat{y_j}$ is j-th observation's predicted value.

4 Results and Discussion

Various ML algorithms were developed and evaluated using voltage, current, temperature, and SOC measurements' dataset using battery model, as shown in Fig. 1. The test system is simulated using MATLAB, and the ML algorithms are implemented using Python on a CORE i5 8th Gen with 8 GB RAM Laptop. With a sampling rate of 64 Hz, the total data has 230,400 samples. Using current, voltage, and temperature as inputs, SOC is predicted. $\text{Current}_{\text{in}}$ is input current, found using summation of DC offset and two frequency signals. The model takes into account the rate capacity impact. SOC is computed based on the capacity of the dischargeable cell, which fluctuates the operational current. The real-time voltage of cell is Vcell which the model produces in response to a real-time input of current and SOC [25]. This system produces the real-time SOC given as SOC_{out} is presented as

$$\text{SOC}_{\text{out}} = \text{SOC}_{\text{in}} - \int \frac{\text{Current}_{\text{in}} * 100}{Q * 3600} dt, \tag{16}$$

where the cell's nominal capacity (Ah) is Q.

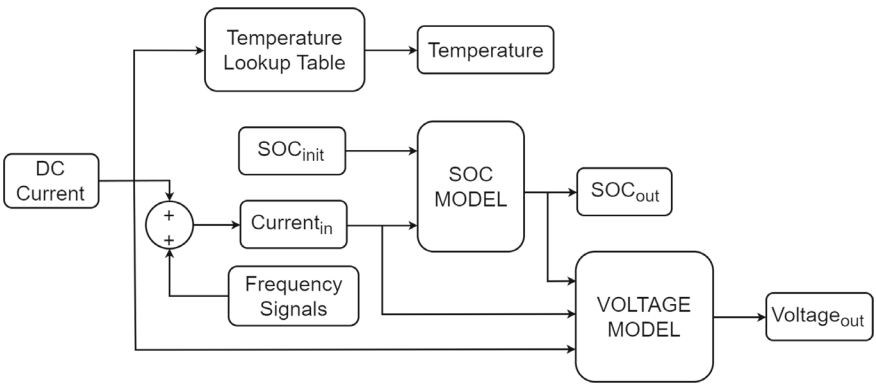

Fig. 1 Block diagram of battery model

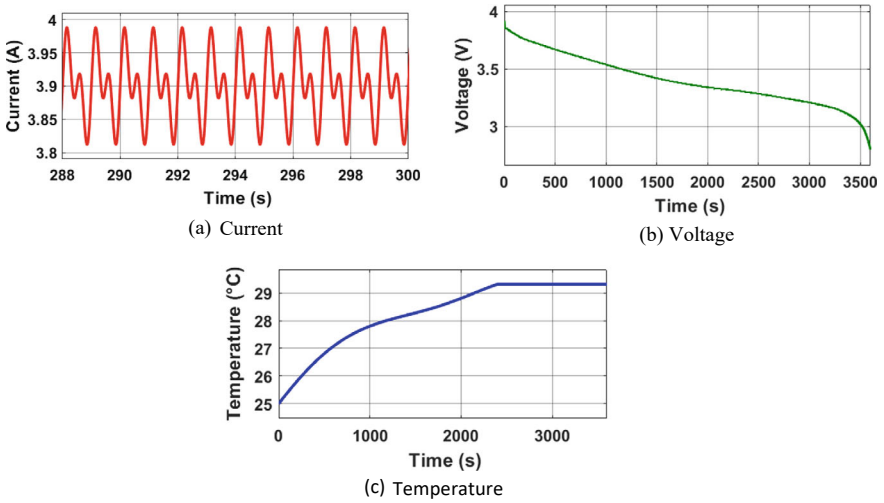

Fig. 2 Preview of data collected from the simulation

The models are trained using 80% of available data, and the rest 20% is used for testing and evaluating the model's performance. The preview of data collected from simulation is shown in Fig. 2. An overview of the ML algorithms' performance using the chosen performance metrics is given in Table 1, and predictions of various ML algorithms are shown in Figs 3 and 4. The results show that RFR, KNN, and SVR with a sigmoid kernel perform better. RFR shows the lowest MSLE and highest PCC, while KNN has the lowest GMAE and Theil U Statistic. SVR with the sigmoid kernel has the lowest Adjusted R2 score. LSTM and ANN also perform well but do not provide more accurate results. Also, it is found that LR has high errors due to SOC's nonlinear nature (Fig. 5)

Table 1 Error comparison of different ML algorithms

Algorithm	MSLE	Adjusted R2	PCC	GMAE	Theil U Statistic
LR	0.061629983121026	1.005959886490060	0.989366010374540	2.931582162220260	0.062699674553793
DTR	0.006703028596800	1.000260118056410	0.999479718156615	0.999479718156615	0.016061161643498
KNN	0.000001427949257	1.000000069674920	0.999999724331888	0.000142712518509	0.000262102008827
RFR	0.000001055211723	1.000000054941090	0.999999890118145	0.000864925373811	0.000864925373811
SVR	0.000001089752513	1.000000054017520	0.999999782680580	0.000864099846744	0.000864099846744
LSTM	0.000094788178107	1.000004886726170	0.999996587391651	0.075139541741645	0.002205957798307
ANN	0.000030166556524	1.000003051779460	0.999998445324867	0.060133988529896	0.001740547899890

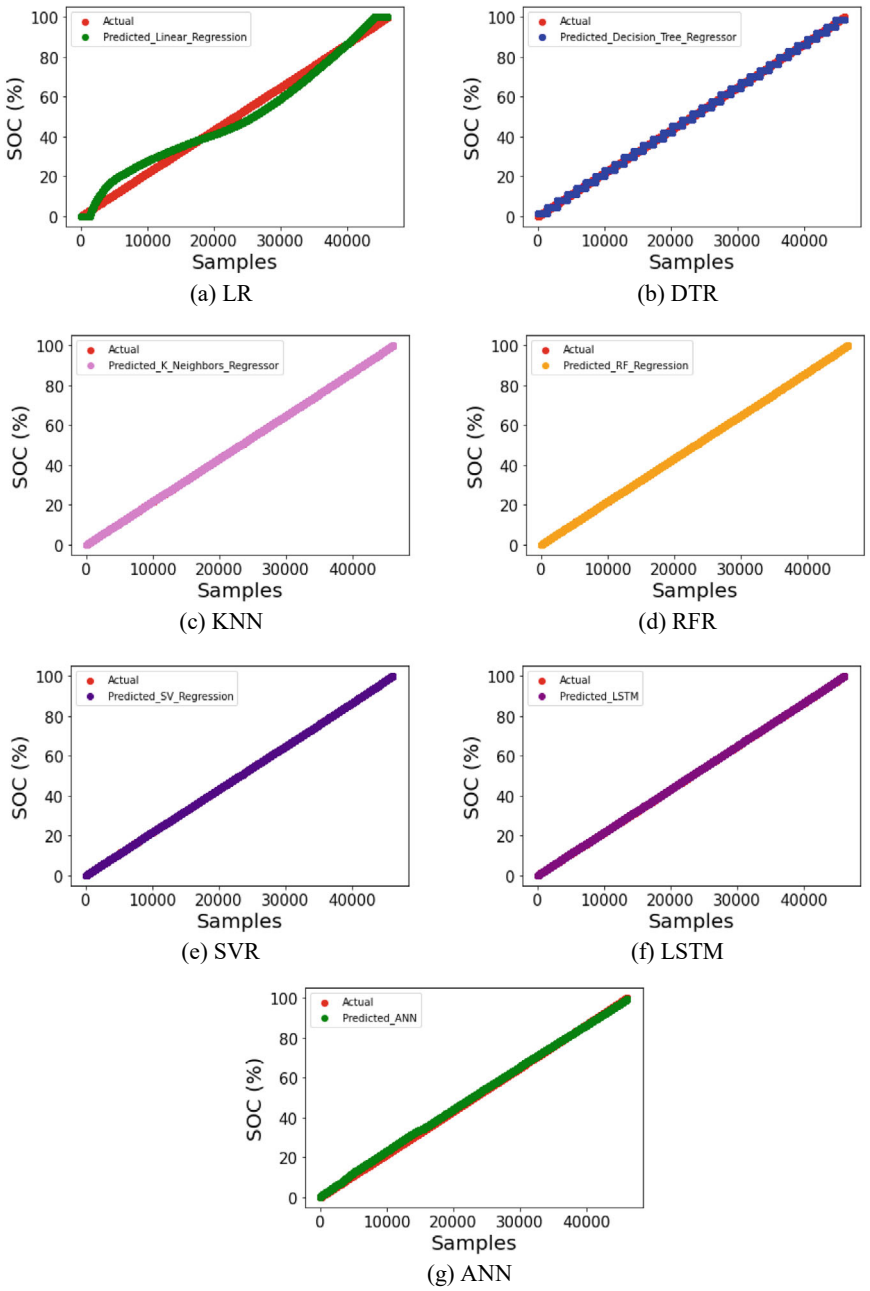

Fig. 3 Performance of SOC prediction

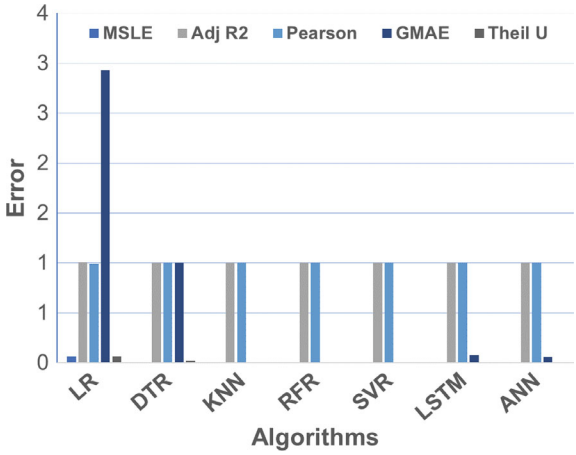

Fig. 4 Comparison of various algorithms

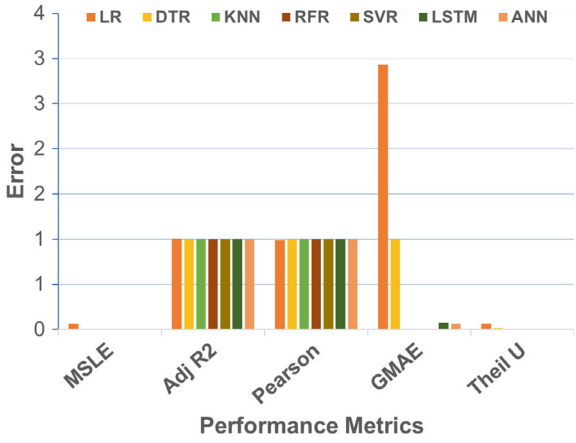

Fig. 5 Comparison of performance metrics

5 Conclusion

This study compares different ML algorithms, namely, Linear Regression, DTR, KNN, RFR, SVR, LSTM, and ANN, to estimate SOC of Li-ion batteries. The algorithms' performance is evaluated using various performance metrics, including MSLE, Adjusted R2 score, PCC, GMAE, and Theil U Statistic. Based on the results, it is inferred that the RFR, KNN, and SVR with a sigmoid kernel outperform the other algorithms. They improve performance and accuracy without modifying the algorithm. Although LSTM and ANN function well, they do not deliver more accurate solutions, as they depend highly on the settings. These algorithms must be modified specifically for the application. Furthermore, because of the nonlinear structure of the SOC, it is found that LR exhibits significant errors.

References

1. Zhang, J.B., Lu, L.G., Li, Z.: Key technologies and fundamental academic issues for traction battery system. J. Automot. Saf. Energy **3**(2), 87–104 (2012)
2. Nitta, N., Wu, F., Lee, J.T., Yushin, G.: Li-ion battery materials: Present and future. Mater. Today **18**(5), 252–264 (2015). https://doi.org/10.1016/j.mattod.2014.10.040
3. Scrosati, J.G.B.: Lithium batteries: Status, prospects and future. J. Power. Sources **195**(9), 2419–2430 (2010)
4. Jenu, S., Deviatkin, I., Hentunen, A., Myllysilta, M., Viik, S., Pihlatie, M.: Reducing the climate change impacts of lithium-ion batteries by their cautious management through integration of stress factors and life cycle assessment. J. Energy Storage **27**, 101023 (2020). https://doi.org/10.1016/j.est.2019.101023
5. Liu, Y., Shu, X., Yu, H., Shen, J., Zhang, Y., Liu, Y., Chen, Z.: State of charge prediction framework for lithium-ion batteries incorporating long short-term memory network and transfer learning. J. Energy Storage **37**(102494), 2021 (2021). https://doi.org/10.1016/j.est.2021.102494
6. Carkhuff, B.G., Demirev, P.A., Srinivasan, R.: Impedance-based battery management system for safety monitoring of lithium-ion batteries. IEEE Trans. Industr. Electron. **65**(8), 6497–6504 (2018)
7. Li, R., Wang, H., Dai, H., Hong, J., Tong, G., Chen, X.: Accurate state of charge prediction for real-world battery systems using a novel dual-dropout-based neural network. Energy **250**, 123853 (2022). https://doi.org/10.1016/j.energy.2022.123853
8. Ng, M., Zhao, J., Yan, Q., Conduit, G.J., Seh, Z.W.: Predicting the state of charge and health of batteries using data-driven machine learning. Nature Machine Intelligence, 2(3), 161–170.Zhou, W., Zheng, Y., Pan, Z., Lu, Q.: Review on the battery model and SOC estimation method. Processes **9**, 1685 (2021) (2020)https://doi.org/10.3390/pr9091685
9. Nizam, M., Mujianto, A., Waloyo, H. T., Purwanto, A., Inayati. Decision tree for state of charge (SOC) prediction of LiFePO4 battery. In Proceedings of the Joint International Conference on Electric Vehicular Technology and Industrial, Mechanical, Electrical and Chemical Engineering (ICEVT & IMECE) pp. 359–361. Surakarta, Indonesia. https://doi.org/10.1109/ICEVTIMECE.2015.7496687 (2015)
10. Hu, J.N., Hu, J.J., Lin, H.B., Li, X.P., Jiang, C.L., Qiu, X.H., Li, W.S.: State-of-charge estimation for battery management system using optimized support vector machine for regression. J Power Sources **269**, 682–693. ISSN 0378–7753. (2014)
11. Dineva, A.: Advanced machine learning approaches for state-of-charge prediction of Li-ion batteries under multisine excitation. In 17th Conference on Electrical Machines, Drives and Power Systems (ELMA) pp. 1–5. Sofia, Bulgaria. https://doi.org/10.1109/ELMA52514.2021.9502962. (2021)
12. Yan, Q.: SOC prediction of power battery based on SVM. In: 2020 Chinese control and decision conference (CCDC) pp. 2425–2429. Hefei, China (2020) https://doi.org/10.1109/CCDC49329.2020.9164245.
13. Ardeshiri, R.R., Balagopal, B., Alsabbagh, A., Ma, C., Chow, M.Y.: Machine learning approaches in battery management systems: State of the Art: Remaining useful life and fault detection. In 2020 2nd IEEE International Conference on Industrial Electronics for Sustainable Energy Systems (IESES) pp. 61–66. Cagliari, Italy (2020)https://doi.org/10.1109/IESES45645.2020.9210642
14. Mehta, C., Sharma, P., Sant, A.V.A.: Comprehensive study of machine learning techniques used for estimating state of charge for Li-ion battery. In: 2021 International Conference on Artificial Intelligence and Machine Vision (AIMV) pp. 1–6. Gandhinagar, India (2021) https://doi.org/10.1109/AIMV53313.2021.9671010
15. Karthic, K.M.P., Babu, R.S., Patil, B.H., Chandan, P.R., Hemavathi, R.R.: Machine learning model for the prediction of an E-Vehicle's battery life cycle. In: 2022 International Conference on Edge Computing and Applications (ICECAA) (pp. 717–722). Tamilnadu, India. https://doi.org/10.1109/ICECAA55415.2022.9936343. (2022).

16. Stock, S., Pohlmann, S., Guenter, F.J., Hille, L., Hagemeister, J., Reinhart, G. Early quality classification and prediction of battery cycle life in production using machine learning. J. Energy. Storage **50**, 104144. (2022) https://www.sciencedirect.com/science/article/pii/S2352152X22001785S.
17. Pohlmann, A., Mashayekh, A., Karnehm, D., Kuder, M., Gieraths, A., Weyh, T.: State of charge prediction of lithium-ion batteries based on artificial neural networks and reduced data. In: 2022 24th European Conference on Power Electronics and Applications (EPE'22 ECCE Europe) pp. 1–10. Hanover, Germany (2022)
18. Dinata, I.B.P.P., Hardian, B.: Predicting smart home lighting behavior from sensors and user input using very fast decision tree with kernel density estimation and improved Laplace correction. ICACSIS 2014. (2014)
19. Sidhu, M.S., Ronanki, D., Williamson, S.: Hybrid state of charge estimation approach for lithium-ion batteries using k-nearest neighbour and Gaussian filter-based error cancellation. In: 2019 IEEE 28th International Symposium on Industrial Electronics (ISIE) pp. 1506–1511. Vancouver, BC, Canada. https://doi.org/10.1109/ISIE.2019.8781330. (2019).
20. Kumari, N., Namrata, K., Kumar, M., Gupta, R.P.: Random forest algorithm for solar forecasting in Jamshedpur—India. In 2022 4th Intl. Conf. on Energy, Power and environment (ICEPE) pp. 1–6. https://doi.org/10.1109/ICEPE55035.2022.9797975. (2022).
21. Ben Ali, J., Saidi, L.: A new suitable feature selection and regression procedure for lithium-ion battery prognostics. Intl. J. Comp. App. in Tech. **58**(2), 102–115 (2018)
22. Zhou, H., Zhou, Y., Hu, J., Yang, G., Xie, D., Xue, Y., Nordstrom, L.: LSTM-based energy management for electric vehicle charging in commercial-building prosumers. J. Mod. Power Syst. Clean Energy **9**(5), 1205–1216 (2021)
23. Chaoui, H., Ibe-Ekeocha, C.C.: State of charge and state of health estimation for Lithium batteries using recurrent neural networks. IEEE Trans. Veh. Technol. **66**(10), 8773–8783 (2017). https://doi.org/10.1109/TVT.2017.2715333
24. Kim, J., Kowal, J.: Development of a Matlab/Simulink Model for monitoring cell state-of-health and state-of-charge via impedance of Lithium-Ion battery cells. Batteries **8**(2), 8 (2022). https://doi.org/10.3390/batteries8020008

PLC-SCADA-Based Automation System for Remote and Sensitive Areas

Udit Mittal, Gaurav Kaushal, Ankit Gupta, Lokesh, Abhishek, and Subhash Yadav

Abstract In this study, a PLC-SCADA system is proposed for secure automation of remote and sensitive locations in industrial and home automation. The system consists of a PLC connected to a central SCADA system for secure real-time monitoring and control. Multiple security protocols, including authentication and authorization, are used to ensure data confidentiality and integrity during network transmission. The system is designed to address the challenges of managing critical infrastructure in hard-to-reach or environmentally sensitive areas. It uses sensors, actuators, and comprehensive SCADA software to collect data, monitor asset health, detect anomalies, and enable remote control of actuators from a central location. Security and privacy are prioritized, with strict access control mechanisms and SCADA security features protecting sensitive data from unauthorized access and cyber threats. The system demonstrates fast response times, maintaining stability and enabling ongoing operations in various test scenarios.

Keywords PLC · SCADA · Home automation · Sensor · Ladder logic

1 Introduction and Literature Review

Modern industrial processes can now be improved in terms of productivity, efficiency, and safety thanks to industrial automation. Automation in sensitive and remote locations, such as military outposts, power plants, and oil rigs, poses particular security and dependability problems. A security compromise in these areas might have disastrous effects on both human life and the economy. Therefore, it is essential to create an automation system that is trustworthy and secure for these sectors.

U. Mittal · G. Kaushal (✉) · A. Gupta · Lokesh · Abhishek · S. Yadav
JSS Academy of Technical Education, Noida, India
e-mail: gauravkaushal.kaushal@gmail.com

U. Mittal
e-mail: udit.mittal27@gmail.com

© The Author(s), under exclusive license to Springer Nature Singapore Pte Ltd. 2025

H. P. Singh et al. (eds.), *Recent Developments in Control, Automation and Power Engineering*, Lecture Notes in Electrical Engineering 1303,
https://doi.org/10.1007/978-981-96-0047-2_16

PLC and SCADA control systems are frequently used in industrial automation because of their dependability and flexibility in managing intricate processes. The integrity and confidentiality of data carried over the network may be jeopardized by cyberattacks, which frequently target the communication between PLCs and SCADA systems. Therefore, creating a safe communication pathway between PLCs and SCADA systems is crucial.

The PLC-SCADA-based system for secure automation of remote and sensitive locations is proposed in this study. A PLC that is connected to a central SCADA system allows for real-time monitoring and control of remote locations over a secure communication channel in the proposed system. To guarantee the confidentiality and integrity of data communicated over the network, the system employs multiple layers of security protocols, including authentication and authorization. The system's efficiency in offering secure automation in remote and delicate places has been shown through implementation and testing in a simulated environment.

Due to its potential to improve energy efficiency, convenience, and security in residential settings, smart home automation systems have attracted a lot of interest recently. This study of the literature looks at several prestigious publications that advance the topic of smart home automation by emphasizing energy efficiency, task scheduling, system development, security, and control technologies. The chosen articles provide insight into the developments and difficulties involved in putting intelligent automation systems in residential settings.

Mukkawar and Sawant emphasize development of energy-efficient smart homes by addressing the task scheduling challenges [1]. Pawlenka and Škuta explore the implementation of intelligent systems for family houses using programmable logic controllers (PLC) and PIC microcontrollers. Their work highlights the potential of providing insights into the practical aspects of implementing intelligent systems in residential settings [2]. Sam et al. focus on the development of PLCs based in smart homes, including monitoring and controlling devices, managing energy consumption, and enhancing security. The study contributes to the understanding of how PLCs can be effectively utilized in smart home automation [3]. Majeed et al. research addresses the challenges related to data privacy, device authentication, and secure communication in smart homes along with data integration [4]. Baraka et al. introduced a significantly lower cost automation system that integrates Arduino and Android platforms to achieve energy efficiency scheduling to manage energy usage [5]. Alimi and Ouahada propose a scheduling method for balancing user comfort and energy efficiency by intelligently scheduling appliance usage, thereby contributing significantly to energy management strategies in smart homes [6]. Zhang's doctoral dissertation explores the concept of smart houses and their potential impact on future housing. It serves as a foundational work for understanding the long-term implications of integrating automation technologies into residential environments [7]. Jo et al. present a scheduling method that considers customer convenience in optimizing HVAC user-centric approaches for energy management in smart homes [8]. Bingol et al. discuss a web-based smart home automation system that utilizes PLC technology for controlling various aspects of a smart home, offering insights into the integration of web technologies and PLCs for home automation [9]. Gomez

and Paradells provide an overview of wireless communication protocols, network topologies, and associated challenges. It contributes to understanding the wireless networking aspects of smart home automation systems [10]. Barz et al. explore the use of program PLCs in smart home systems. Their research highlights the advantages and implementation aspects of using PLCs for intelligent control of various home automation tasks [11].

Collectively, the papers that have been examined advance the technology behind automated smart homes. They cover a variety of topics, including job scheduling, system development, security, and control technologies, as well as energy efficiency. The research discussed in these publications provides insightful information about the problems and potential remedies for designing intelligent and energy-efficient residential environments. The results advance the development of sustainable and user-centered smart homes by advancing ongoing research and development activities in the field of smart home automation.

This paper elaborates on the software used to construct the PLC-SCADA system and includes a detailed overview of all the parts used in the system. Various automation procedures are extensively described in the system. Additionally, the layout of the SCADA system is shown, along with a description of its design and operation. The study utilizes visual representations of the physical configuration of the system through snapshots of the generated hardware model. The ladder logic implemented in the PLC is visually displayed, providing insights into the programming logic employed for system control and management.

2 Components Description

2.1 PIR Sensor

An electronic device called a passive infrared (PIR) sensor uses variations in infrared radiation to measure motion or the presence of objects within its field of view. It is frequently utilized in many different applications, including energy-saving gadgets, automatic lighting, occupancy detection, and security systems. PIR sensors function by sensing the infrared radiation that objects emit. They have a sensing component that can pick up changes in the environment's heat signature. The sensor is activated when an object moves inside the sensor's detection range and creates a change in the infrared radiation. Figure 1 depicts a PIR sensor.

2.2 Smoke Detector

A smoke detector is a crucial safety tool used to find smoke in the surrounding area. In the event of a fire, it plays a key part in protecting lives and property by giving

Fig. 1 PIR sensor

Fig. 2 Smoke detector

an early warning. Ionization detectors monitor changes in electrical conductivity as smoke particles reach the sensor chamber using a tiny radioactive source. A light source and a photosensitive sensor are employed in photoelectric detectors to track variations in light scattering brought on by smoke particles. A smoke detector is shown in Fig. 2.

2.3 Proximity IR Sensor

A proximity infrared (IR) sensor is a device that uses infrared technology to detect the presence or closeness of objects within a specific range. The reflection or disruption of infrared light is the basis for how proximity IR sensors operate. They emit infrared light, and they measure how much of it is reflected back or received by a receiver. The received signal is altered when an object enters the range of the sensor because it scatters or blocks the infrared light. A proximity IR sensor is shown in Fig. 3.

Fig. 3 Proximity IR sensor

Fig. 4 GIC programmable logic controller

2.4 PLC

A dedicated industrial computer system termed a Programmable Logic Controller (PLC) is used to automate and control machinery and processes in manufacturing and industrial settings. The major functions of PLCs include monitoring and controlling electromechanical in-nature operations. They take in signals from a variety of sensors and devices, process the data using preprogrammed logic, and provide output signals that are used to operate actuators, motors, and other devices. In our automation system, we are using GIC PLC Model No. G7TDD11. A GIC PLC is shown in Fig. 4.

3 Methodology

Figure 5 depicts the working of an automation system with PLC as a central control unit. The automation system comprises the PLC, sensors, and actuators which are connected through a wired network which eliminates cyber threats. The PLC has two analog input and six digital inputs which are connected with different analog and digital sensors.

3.1 System Block Diagram Description

The connections between a Programmable Logic Controller (PLC), input devices, output devices, and a programming device are shown in the block diagram. It illustrates how data move across the PLC system. The different parts of the block diagram are described below.

Input Devices. These are actual objects that send data or signals to the PLC so it can process them. Switches, sensors, push buttons, and limit switches are a few examples. The input modules of the PLC are coupled with input devices.

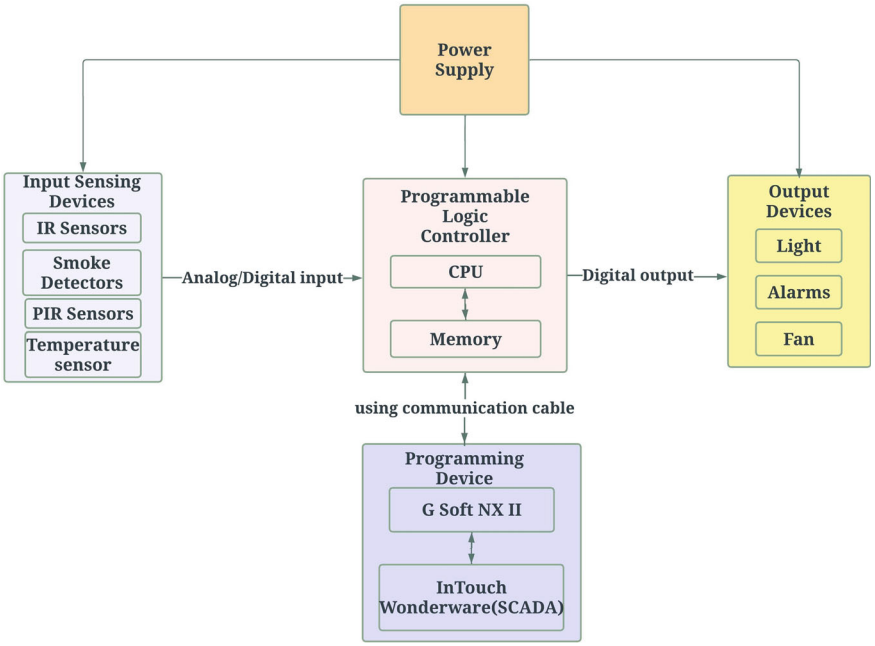

Fig. 5 System block diagram for home automation

PLC. Based on the inputs it receives, the PLC, which serves as the central control unit, executes logic and control operations. It consists of an input/output module, a processor, and memory. Based on its preprogrammed instructions, the PLC analyzes the input signals and produces the appropriate output signals.

Output Devices. These are actual objects that carry out particular tasks after receiving control signals from the PLC. Examples include relays, valves, lamps, solenoids, and motors. The output modules of the PLC are coupled with output devices.

Programming Interface. The programming tool generates, edits, and downloads the PLC's program logic. You can use a personal computer (PC) or a specialized PLC programming tool. A communication channel like Ethernet, USB, or serial connection connects the programming device to the PLC.

3.2 Flowcharts for Various Automation Processes

The flowchart showing process of automation of fan and lighting is given in Fig. 6.

For the automation of fan, we have used temperature sensor module which is set to a predetermined temperature limit. After crossing the threshold, it sends a digital signal to the PLC. Along with this we have connected a PIR sensor for motion

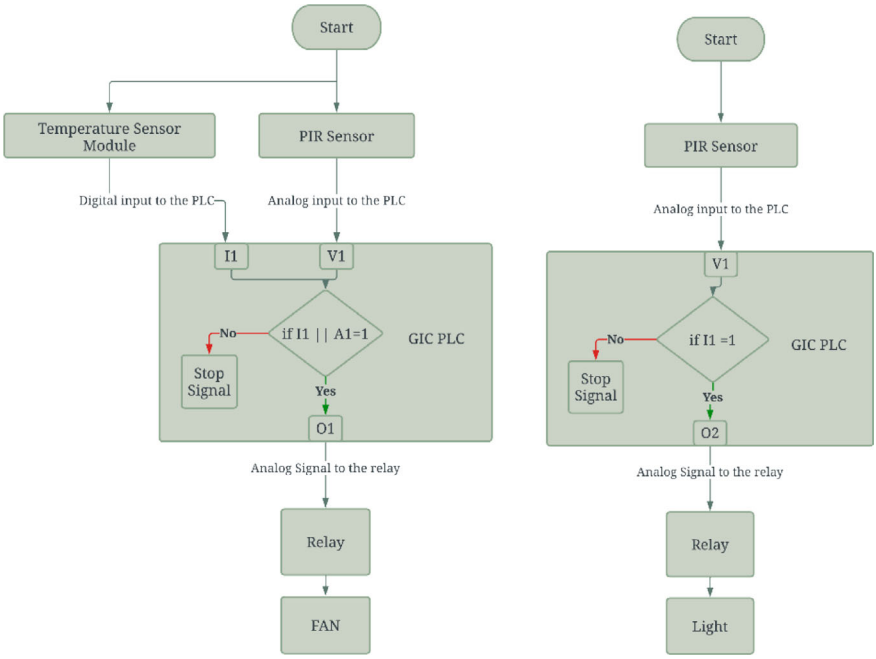

Fig. 6 Flowchart for automation of fan and lighting

detection. When both of these sensors send signals to the PLC, then the fan is turned on for a certain period of time.

The flowchart showing automation of fire and security alarm is given in Fig. 7. For the automation of fire alarm and security alarm, we have taken the use of smoke sensor for fire alarm and proximity IR sensor for security or burglar alarm. When there is a fire, smoke sensor detects the fire and triggers the fire alarm giving time to occupants to get out of the area and call the fire station. When there is an intruder in the property, proximity sensor triggers the security alarm and alerts the occupants of any intruders.

4 Software Implementation

4.1 Software Description

GENIE NX II. This software is used for programming the PLC and also used to establish communication between PLC and programming device.

Intouch Wonderware. This is the SCADA software which is used for monitoring and controlling the system through a secure communication channel.

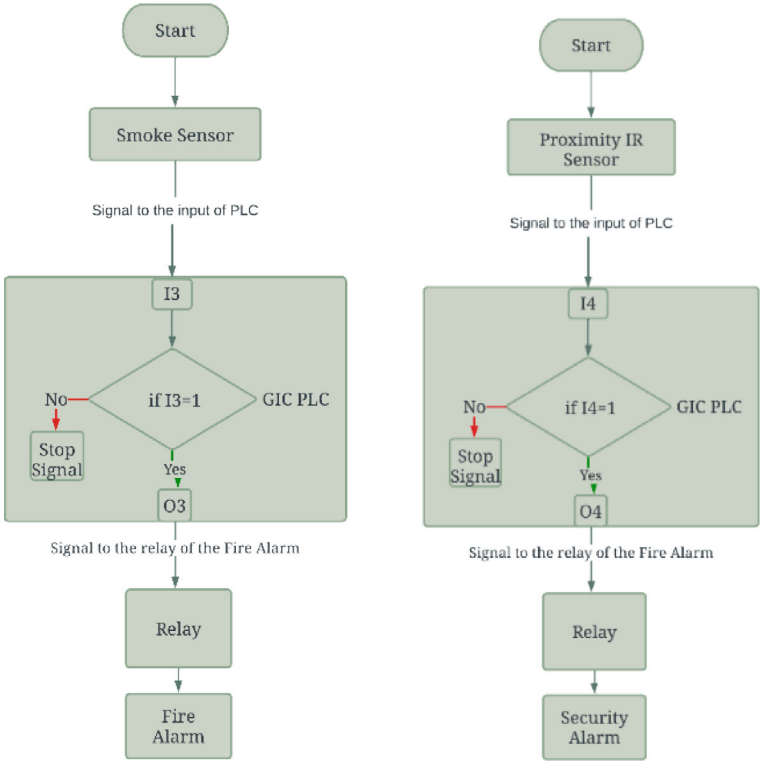

Fig. 7 Flowchart for automation of fire alarm and security alarm

4.2 Ladder Logic Program

Figure 8 depicts the ladder diagram of the system.

4.3 Developed SCADA System

The SCADA layout of the home automation system is shown in Fig. 9.

5 Hardware Implementation

5.1 Circuit Diagram of the Automation System

Diagram of the home automation system's circuit is depicted in Fig. 10.

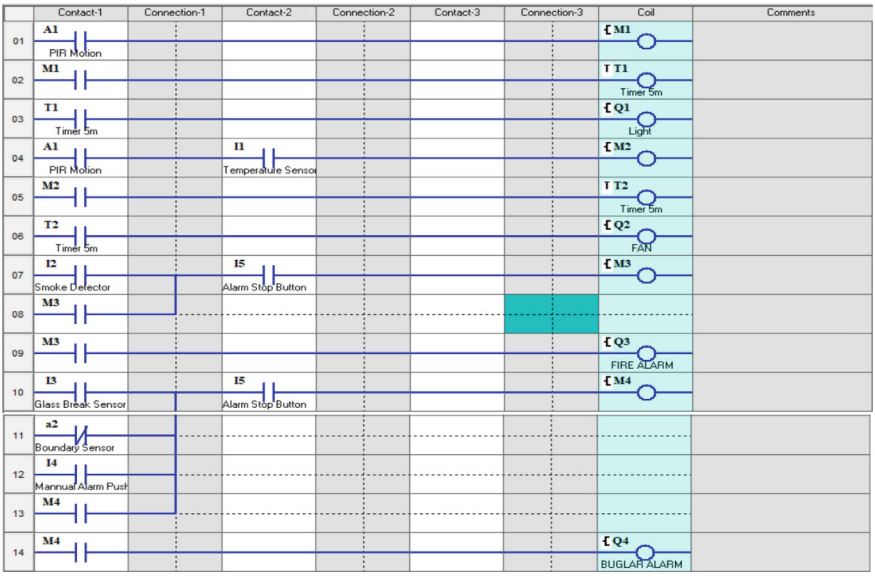

Fig. 8 Ladder logic of automation system

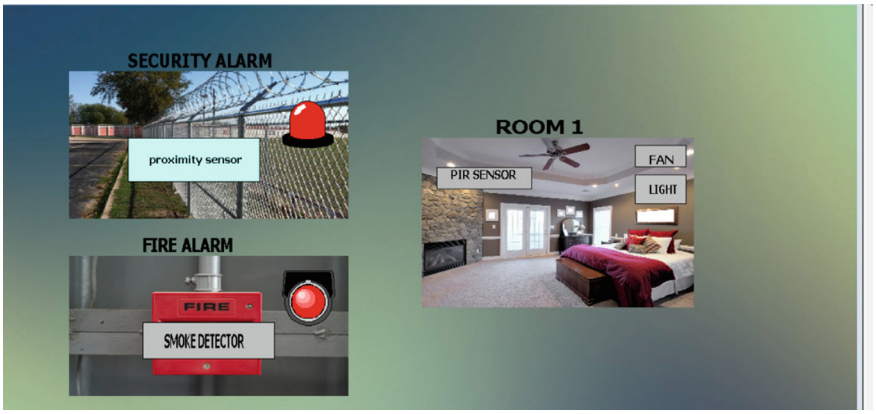

Fig. 9 Developed SCADA program

5.2 Photo of the Hardware Model

An image of the hardware model developed is shown in Fig. 11.

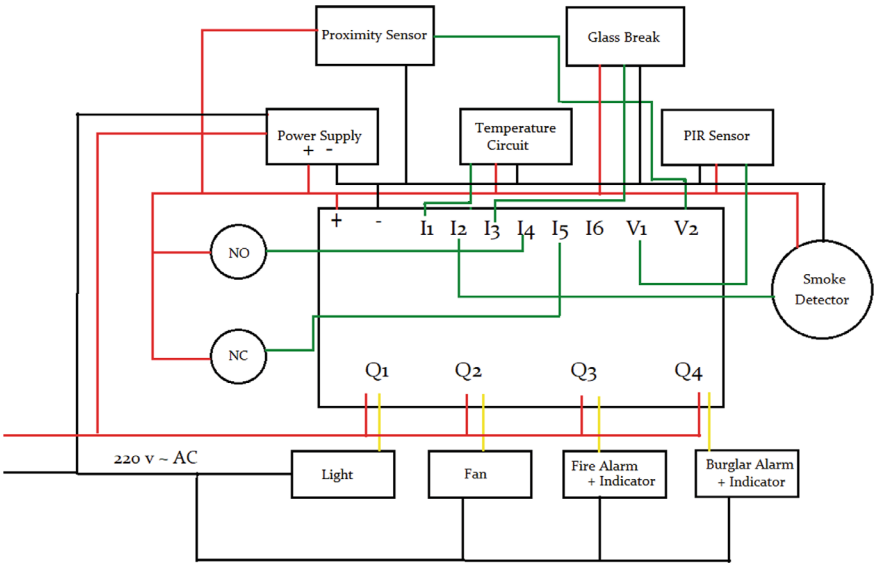

Fig. 10 Circuit diagram for home automation system

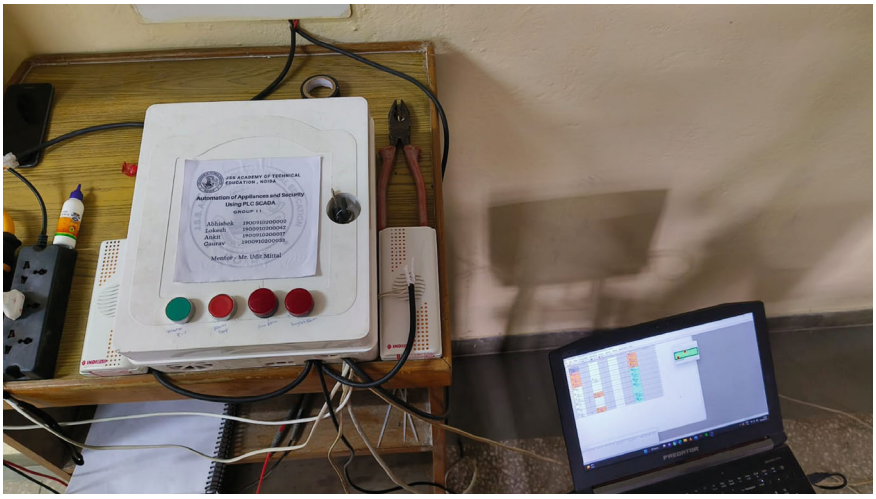

Fig. 11 Snapshots of the hardware model

6 Results and Discussions

The system was created to handle the difficulties in monitoring and managing crucial infrastructure in places that are hard to reach or subject to environmental threats. The system used a variety of sensors and actuators to gather data and communicate with

the outside world. PLC configuration and programming, SCADA software creation, and component integration were all parts of the implementation process. Operators were able to monitor equipment status, spot anomalies, and make deft judgements thanks to the SCADA system's full picture of the sites. The technology additionally permitted remote control of actuators, allowing operators to make appropriate modifications and interventions from a centralized location.

Any automation system must take security and privacy concerns seriously, especially in remote and sensitive locations. Strong security measures were incorporated by the PLC-SCADA-based automation system to guard against unauthorized access and data breaches. The system's access was restricted to authorized personnel exclusively thanks to access control mechanisms. The SCADA security elements of the system successfully protected sensitive data and shielded it from any cyber threats.

Because of its quick reaction times, the system was able to monitor and control operations in real time. System stability was maintained under various test scenarios, ensuring uninterrupted operation.

7 Conclusion

In conclusion, the automation system based on PLC-SCADA successfully handled the difficulties of monitoring and regulating crucial infrastructure in remote and delicate places. The system collected data and interacted with the physical world using sensors and actuators. It gave a thorough understanding of remote sites, allowing for remote actuator control, anomaly detection, and real-time monitoring. Protection from unauthorized access and data breaches was secured by robust security measures. The system demonstrated quick response times and kept stability under a variety of circumstances. Overall, the system provides dependable and effective monitoring and control capabilities for remote and sensitive locations, with room for additional development in anomaly detection and predictive maintenance.

References

1. Mukkawar, M.R., Sawant, S.D.: Energy efficient automation system with smart task scheduling. In: 2015 international conference on computing communication control and automation pp. 1003–1007 IEEE (2015)
2. Pawlenka, M., Škuta, J.: Use of PLC and PIC for realization of intelligent family house. Proceedings of the 2015 16th International Carpathian Control Conference (ICCC). IEEE, (2015)
3. Sam, R., Wahab, N.H.A., Sunar, N., Ahsan, M.A. and Wong, K.Y.: Development of smart home automation system based on PLC. In: 2022 IEEE 12th Symposium on Computer Applications and Industrial Electronics (ISCAIE) pp. 196–200. IEEE (2022)
4. Majeed, R., Abdullah, N.A., Ashraf, I., Zikria, Y.B., Mushtaq, M.F. and Umer, M.: 2020. An intelligent, secure, and smart home automation system. Scientific Programming, 2020.

5. Baraka, K., Ghobril, M., Malek, S., Kanj, R. and Kayssi, A.: Low cost arduino/android-based energy-efficient home automation system with smart task scheduling. In 2013 Fifth international conference on computational intelligence, communication systems and networks pp. 296–301. IEEE (2013)
6. Alimi, O.A., Ouahada, K.: Smart home appliances scheduling to manage energy usage. In: 2018 IEEE 7th International Conference on Adaptive Science and Technology (ICAST) (pp. 1–5). IEEE 2018
7. Zhang, P.: Smart house: home automation and housing for the future (Doctoral dissertation, Carleton University) (2003)
8. Jo, H.-C., Kim, S., Joo, S.-K.: Smart heating and air conditioning scheduling method incorporating customer convenience for home energy management system. IEEE Trans. Consum. Electron. **59**(2), 316–322 (2013)
9. Bingol, O., Tasdelen, K., Keskin, Z., Kocaturk, Y.E.: Web- based smart home automation: PLC-controlled imple- mentation. Acta PolytechnicaHungarica **11**(3), 51–63 (2014)
10. Gomez, C., Paradells, J.: Wireless home automation networks: A survey of architectures and technologies. IEEE Commun. Mag. **48**(6), 92–101 (2010)
11. Barz, C., Deaconu, S.I., Latinovic, T., Berdie, A., Pop-Vadean, A. and Horgos, M.: PLCs used in smart home control. In: IOP Conference Series: Materials science and engineering **106**, (1),012036 IOP Publishing (2016)

Analyzing the Performance of Fuzzy Tunned PID Control of Antilock Braking System

Pritish Sharma and Jyoti Ohri

Abstract In this era of modern vehicle, antilock braking system (ABS) becomes very important for significantly improving safety by preventing wheel lock-up during braking. It provides safe protection and minimizes stopping distance. This paper focuses on the control techniques and their comparison specifically conventional PID control and fuzzy-based gain scheduling in PID control of ABS systems to enhance their performance. Fuzzy linguistic variables help in maintaining the desired slip ratio and wheel speed. This approach is better in terms of performance and stability gain by vehicle after applying brakes. The integration of fuzzy-based PID control technique with ABS systems offers several advantages over simple PID control. The paper concludes by emphasizing the importance of further research and development in optimizing fuzzy logic-based PID tunning control algorithm for ABS systems and comparing it with conventional PID control technique.

Keywords Antilock braking system · Fuzzy logic control · PID control · Slip control · Gain scheduling

1 Introduction

A braking system is important for the performance and safety of a vehicle. Thus, it is essential to maintain the vehicle speed and stopping distance while applying the brakes. The ABS prevents from locking of wheel after applying the brakes. Performance of ABS depends on wheel brakes and different ABS methods [1]. The braking action depends on the parameters like distance between vehicle and obstacle, road surface [2]. This system is used for braking and hence prevents from slipping and reduces stopping distance and reduces stopping time [3]. The primary purpose

P. Sharma (✉) · J. Ohri
Electrical Engineering Department, National Institute of Technology, Kurukshetra, Haryana, India
e-mail: pritish.umri@gmail.com

J. Ohri
e-mail: ohrijyoti@nitkkr.ac.in

© The Author(s), under exclusive license to Springer Nature Singapore Pte Ltd. 2025

H. P. Singh et al. (eds.), *Recent Developments in Control, Automation and Power Engineering*, Lecture Notes in Electrical Engineering 1303,
https://doi.org/10.1007/978-981-96-0047-2_17

of ABS is to minimize slipping and control unpredictable slip under braking [4]. ABS receives the lower-level speed signal from the sensor and then it forwards this command to braking control unit (BCU) which further reduces the braking force. In this modern, it is very important to implement safety-based components in automotive [5]. The major concern is the wheel slip control [6].

The unpredictability and nonlinearities that happen in the mathematical model of ABS make it hard to design its parameters according to the condition. Robust fuzzy sliding mode control was suggested for the implementation of ABS in their research [7]. The nonlinear PID control has smaller stopping distance and less time for stopping than the conventional PID controller [8]. The performance of ABS with Bang–Bang controller is described in [9]. Two types of control are defined [5]: first one is wheel deceleration control, which depends upon the road surface and is difficult to analyze and estimate the road surface. Another one is control of slip, which is easy to get the set points of all types of roads. From the above discussion, we can conclude the main objective of ABS: reducing of stopping distance, boosting the rigidity of the automobile during brakes, and improving the steerability.

Initially, this paper will analyze ABS control without any controller; for this kind of control operation, the slip ratio is used as a variable that is controlled. A simple linear PID system is created that produces the best brake torque output and the required slip variable. Ziegler and Nichols (Z-N) provide a better tuning method of PID [10]. A PID controller considers the past, present, and future errors which helps in the calculation of the gain parameters and all benefits, and drawback is discussed in [11].

Another control method is being used is Fuzzy gain scheduling of PID control in ABS. On the basis of error signal and its initial difference, the controller parameters are determined online using fuzzy rules and reasoning. The theory of fuzzy logic is discussed by Professor L.A in [12]. Fuzzy works on a basic rule where we can ask to human about if–then rule and in accordance with that we can tune the desired parameters. Mamdani type is ordinary used fuzzy inference system. The defuzzification method transforms linguistic variables into a crisp set in the fuzzy inference system created and edited with the help of the fuzzy logic toolkit [13].

If compared to Ziegler–Nichols controllers and Kitamori's PID controllers, better performance can be attained. The tunning of parameters of PID of controller makes use of human expertise and knowledge in the design of control systems [14]. To counteract these impacts of nonlinear dynamics of road and friction, a self-tuning scheme appears to be necessary. The self-tuning tool can monitor operational changes in the system and account for parameter uncertainty and nonlinear drift as proved in [3]. These problems can be solved by using fuzzy gain scheduled PID control in ABS system [15].

As discussed above, there are different control strategies for ABS control. First there is discussion of only ABS control, which is further modified by using PID control with it. Further, there is discussion of fuzzy gain scheduling of PID control in ABS control, which has more benefits in the presence of nonlinearities and unpredictability. The working and comparison of these control strategies are discussed in this paper.

2 Working and Modeling

2.1 Antilock Braking System Modeling

The dynamic of vehicle is described into three parts: vehicle dynamics, wheel dynamics, and braking dynamics [16].

For vehicle, dynamic equation can be expressed by the second law of Newton:

$$mV = -F_t - F_a \tag{1}$$

where V = vehicle velocity, F_a = aerodynamic force on vehicle, F_t = friction force, and

m = total vehicle mass.

Friction force by road is defined as:

$$F_t = \mu N' \tag{2}$$

where overall normal load is N' and μ is frictional force coefficient.

Overall vehicle mass is:

$$m = m_t + \frac{1}{4} m_c \tag{3}$$

where m_t is tire mass and m_c is defined as vehicle mass.

Overall load that is normal to vehicle is written as:

$$N' = mg - F_l \tag{4}$$

where F_l = braking load transfer and g = gravitational constant.

The aerodynamical force depends on the square of speed and vehicle dynamics as follows:

$$F_a = \frac{1}{4} \rho C_d A_f V^2 \tag{5}$$

where ρ = density of vehicle mass, C_d = drag coefficient, and A_f = frontal vehicle area.

For wheel dynamic motion equation is given as:

$$J_w \omega = -T_b + F_t R \tag{6}$$

where J_w = wheel moment of inertia, ω = wheel speed, R = wheel radius,

T_b= braking torque, and F_t = Friction force of road.

The combined speed dynamic and wheel dynamic equations are

$$(m_t - \mu(s))V = -\mu(s)m_t g - \frac{1}{4}\rho C_d A_f V^2 \tag{7}$$

$$J_w \omega = -T_b + \mu(s)(m_t g - m_e V)R \tag{8}$$

where m_e = effective mass.

In ABS, a sensor provides information to the control unit by tracking the result, which is the relative slip ratio. The control unit will make the necessary adjustments to manage the pressure in the brake modulator in order to maintain the desired system result, whether it matches the required relative slip value or the value used as a reference for the wheel slip ratio. So, slip equation reads as follows:

$$s = 1 - \frac{\omega_w}{\omega_v} \tag{9}$$

where ω_w = vehicle angular velocity and ω_v = wheel angular velocity

$$\omega_w = \frac{T_t - B_t}{I} \tag{10}$$

where T_t = tire torque, B_t = braking torque, and I = wheel rotational inertia

$$\mathrm{T_t} = \mathrm{NR} \tag{11}$$

Normal force per wheel,

$$N = \frac{1}{4}mg \tag{12}$$

The transfer function (TB) of hydraulic lag [17] is:

$$\mathrm{TF} = \frac{K}{(\mathrm{TB})s + 1} \tag{13}$$

$$\omega_\mathrm{w} = \frac{v0}{R} \tag{14}$$

The simulation of ABS model is developed based on the above calculations as shown in Fig. 1, (Table 1).

3 Controller Design

The objective of controller design is to keep slip ratio approx. 0.2 and also to maintain the minimum stopping distance as much as possible. So, proposed control actions taken on ABS control are discussed.

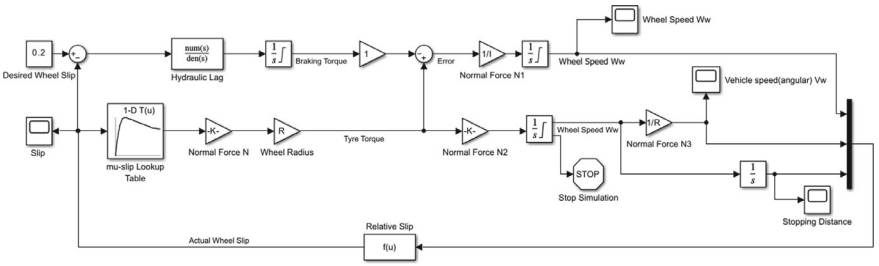

Fig. 1 Simulation of model of ABS

Table 1 Parameters used and their values

Parameters	Value
Proportional gain (K)	1200
Mass	50 lbs
Wheel radius ®	1.25 ft
Gravitational constant (g)	32.18 ft/s^2
Initial velocity (v0)	80.64 ft/s
Moment of Inertia (J)	5 ft^4
Hydraulic lag (TB)	3.25 s

3.1 PID Controller Design

This controller sends the gains values of k_p, k_i, and k_d to the ABS (P.E. Wellstead 1997) [16]. The tunning of PID is done by Ziegler–Nichols which gives the better values of k_p, $\mathrm{k_{i,}}$ and k_d.

The obtained values of parameters are $K_\mathrm{u} = 178.5$ and $T_\mathrm{u} = 4.68$, which gives $k_p = 105$, $k_\mathrm{i} = 75$, and $k_d = 102.66$.

3.2 Fuzzy Gained Scheduling of PID Controller in ABS Control

Figure 2 depicts a proposed PID control system with fuzzy gain scheduling (Table 2).

Further, k_p and k_d are normalized by between one and zero by following linear transformation.

$$k_p\prime = \frac{\left(K_p - k_p\mathrm{min}\right)}{k_p\,\mathrm{max} - k_P\mathrm{min}} \tag{15}$$

$$k_d\prime = \frac{(k_d - k_{\mathrm{dmin}})}{k_{\mathrm{d\,max}} - k_{\mathrm{dmin}}} \tag{16}$$

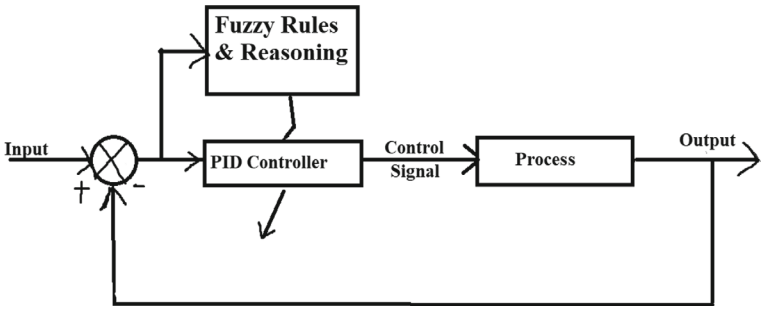

Fig. 2 PID with fuzzy gain scheduling

Table 2 Ziegler–Nichols parameters

Control action	k_p	k_i	k_a
P	K_u 12		
PI	K_u 12.2	1.2 Kd / T_u	
PID	0.6 K_u	2 K_u / T_u	K_u * T_u/8

$$k_i = \frac{k_p^2}{\alpha k_d} \tag{17}$$

The PID parameters are found by error e (k) and its first derivative Δe (k), Also, the parameters $k_p\prime$, $k_d\prime$, and α are calculated by a set of fuzzy tunning rules as defined in the given following tables (Tables 3, 4, and 5).

Here, triangular membership function (trimf) for e (k) and Δ e (k) has been taken from fuzzy logic toolbox, while Gaussian membership function (gaussmf) for $k_d\prime$ and $k_p\prime$ and membership function of α is a singleton value function. The corresponding abbreviations are—BN: negative big, MN: medium negative, SN: small negative, Z: zero, SP: small positive, MP: medium positive, BP: big positive, s: small, b: big.

Table 3 Fuzzy tunning rules for $k_p\prime$

$e(k)/\Delta e(k)$	BN	MN	*SN*	*Z*	*SP*	*MP*	*BP*
BN	*b*	*b*	*b*	*b*	*b*	*b*	*b*
MN	*s*	*b*	*b*	*b*	*b*	*b*	*s*
SN	*S*	*s*	*b*	*b*	*b*	*s*	*s*
Z	*s*	*s*	*s*	*b*	*s*	*s*	*s*
SP	*S*	*s*	*b*	*b*	*b*	*s*	*s*
MP	*s*	*b*	*b*	*b*	*b*	*b*	*s*
BP	*b*	*b*	*b*	*b*	*b*	*b*	*b*

Table 4 Fuzzy tunning rules for $k_d{}'$

$e(k)/\Delta e(k)$ $Zle(k)$	*BN*	*MN*	*SN*	*Z*	*SP*	*MP*	*BP*
BN	*s*	*s*	*s*	*s*	*s*	*s*	*s*
MN	*b*	*b*	*s*	*S*	*s*	*b*	b
SN	*b*	*b*	*b*	*S*	*b*	*b*	b
Z	*b*	*b*	*b*	*b*	*b*	*b*	b
SP	*b*	*b*	*b*	*s*	*b*	*b*	b
MP	*b*	*b*	*s*	*s*	*s*	*b*	b
BP	*s*	*s*	*s*	*s*	*s*	*s*	*s*

Table 5 Fuzzy tunning rules for α

$e(k)/\Delta e(k)$	BN	MN	SN	Z	SP	MP	BP
BN	2	2	2	2	2	2	2
MN	3	3	2	2	2	3	3
SN	4	3	3	2	3	3	4
Z	5	4	3	3	3	4	5
SP	4	3	3	2	3	3	4
MP	3	3	2	2	2	3	3
BP	2	2	2	2	2	2	2

A general guideline for figuring out the values of k_p and the values of k_d is given as follows, which is based on a thorough simulation study on numerous processes [16].

$$k_{\text{pmin}} = 0.32k_u, k_{p\text{max}} = 0.6k_u, k_{\text{dmin}} = 0.8k_uT_u, k_{\text{dmax}} = 0.15k_uT_u, \quad (18)$$

After the calculations, the obtained values of parameters are $k_u = 75$, $T_u = 4.66$. Also, we can obtain the values of remaining parameters using Eqs. 15, 16, and 17.

4 Results and Discussion

The simulation results for ABS system using simple PID controller and fuzzy gain scheduled PID controller and without any controller are produced as follows:

4.1 ABS Without Controller

We can see that stopping distance with time is excessive when the ABS is not attached with any controller. Fig. 4 shows that the slip variations are too high from desired slip of 0.2. The stopping distance is 669.5ft which is very high value (Figs. 3, 5, and 6).

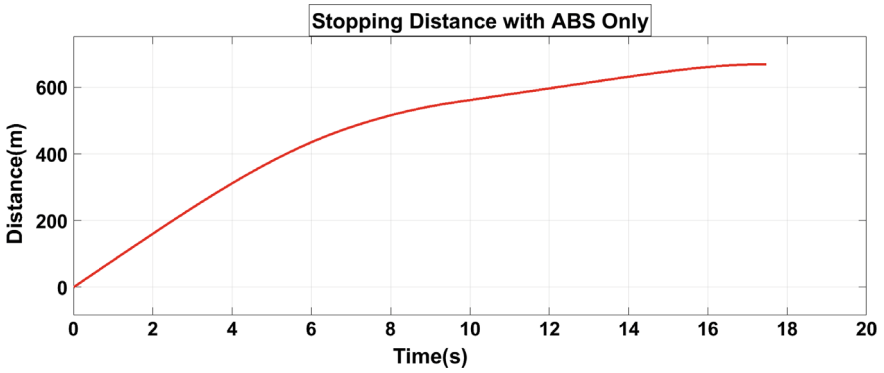

Fig. 3 Distance plot for only ABS control

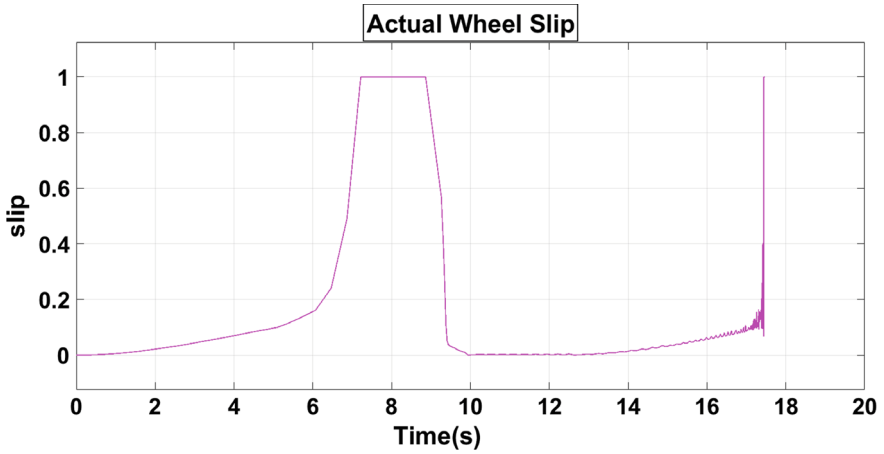

Fig. 4 Slip plot for only ABS control

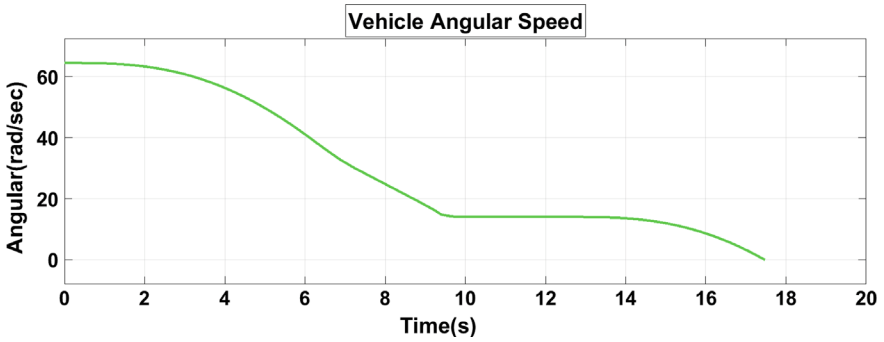

Fig. 5 Vehicle speed plot for only ABS

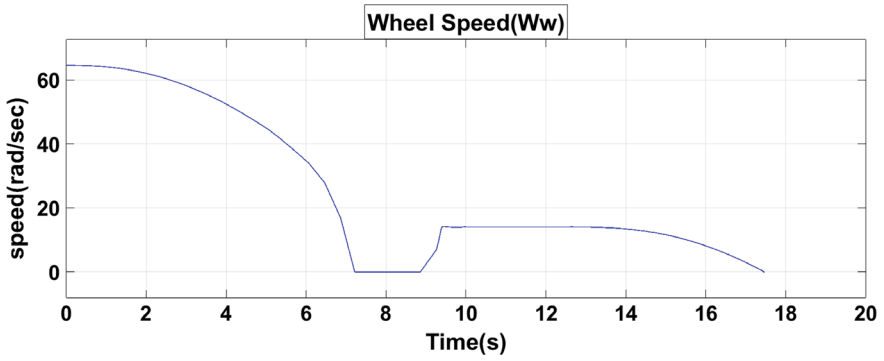

Fig. 6 Wheel speed plot for only ABS

4.2 ABS with PID Controller

The value of K_p is 105, K_i value is 75, and K_d value is 102.66. In this case, stopping distance and stopping time are 379.6ft (Fig. 7) and 7.344 s, respectively, which are very lesser values as compared to parameters of only ABS control. But still there are some variations in slip (Fig. 8) with respect to desired slip, whereas the fluctuations in vehicle speed are present, which is further solved by using fuzzy-based system (Figs. 9 and 10).

4.3 ABS with Fuzzy Gain Scheduled PID Controller

Here, the stopping distance is 298.2ft (Fig. 11) which is much lesser than PID control, and stopping time is at 7.171 s. Also, slip values (Fig. 12) are closer to 0.2 and comparatively better than PID control (Figs. 13 and 14).

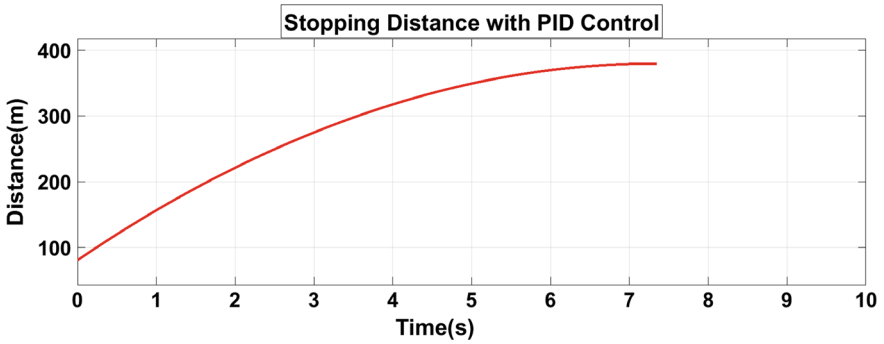

Fig. 7 Distance plot for PID ABS

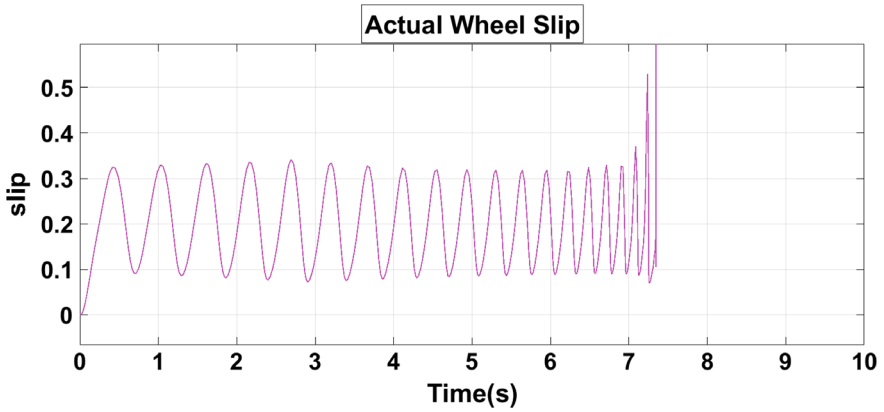

Fig. 8 Slip plot for PID ABS

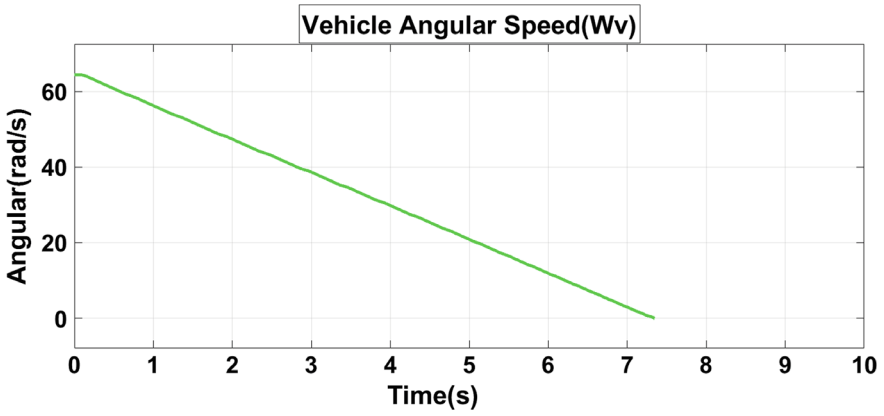

Fig. 9 Vehicle speed plot for PID

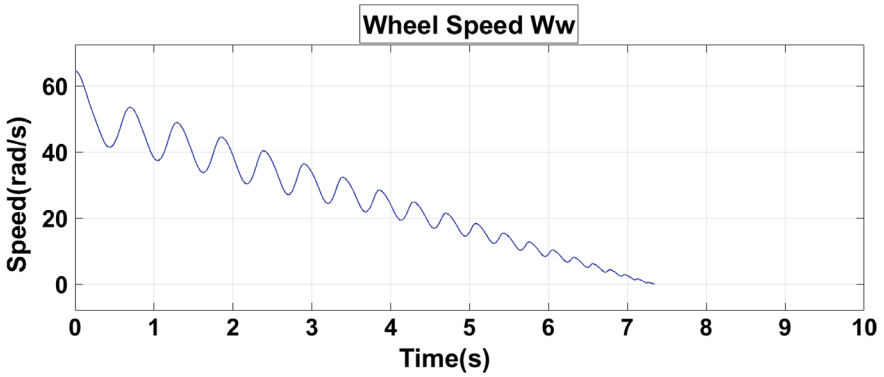

Fig. 10 Wheel speed plot for PID

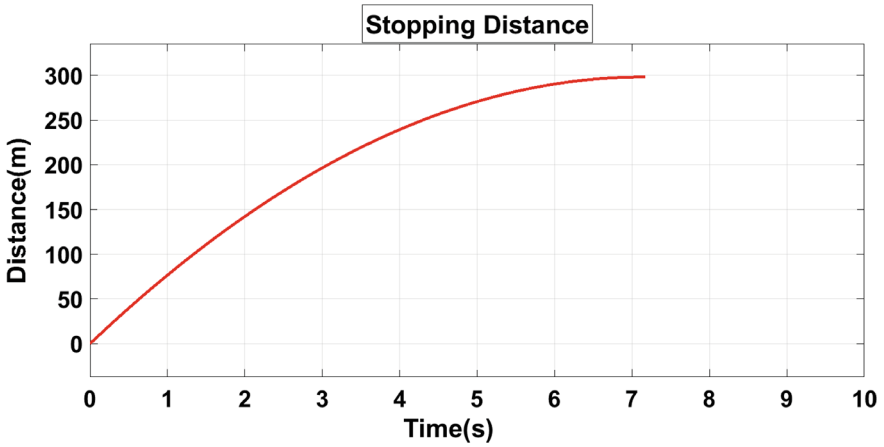

Fig. 11 Distance plot (fuzzy-based PID)

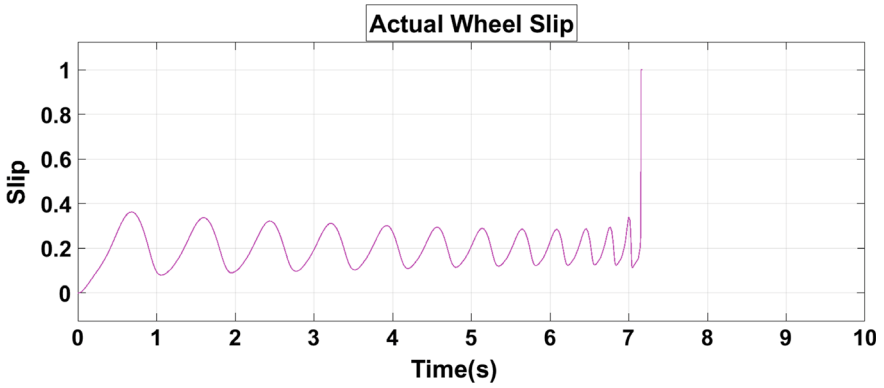

Fig. 12 Slip plot (fuzzy-based PID)

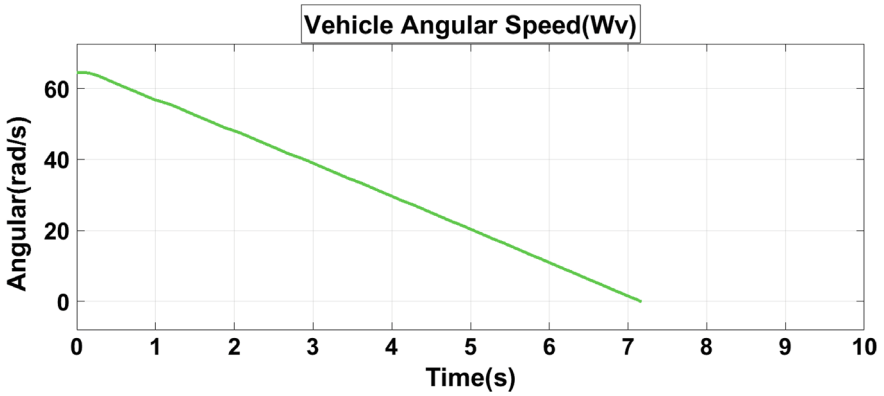

Fig. 13 Vehicle speed plot (fuzzy-based PID)

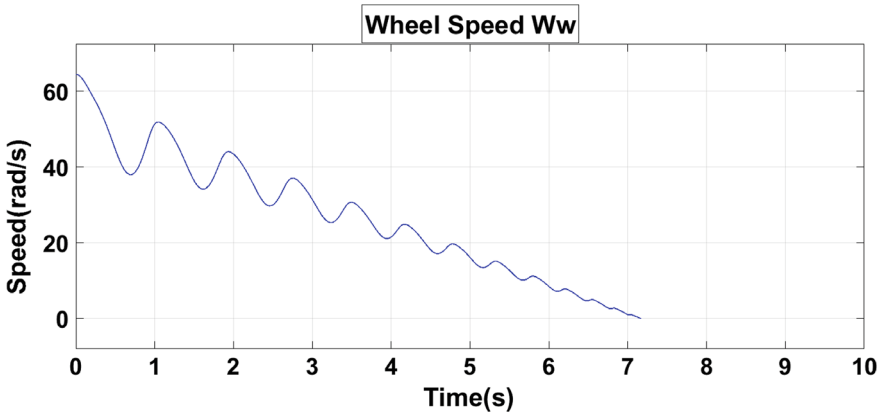

Fig. 14 Wheel speed plot (fuzzy-based PID)

As we have compared the stopping distance is very less (298.2ft) in fuzzy-based control with PID-based control and only ABS control. The slip value is closer to 0.2 in fuzzy-based PID control, while slip variations in PID and only ABS are higher (Table 6).

Table 6 Comparison of performance of different controllers

Parameters	Only ABS	PID	Fuzzy gain scheduled PID
Stopping distance (ft)	669.5	379.6	298.2
Stopping time (s)	17.471	7.344	7.171

5 Conclusions

This paper explains the relevance of the controller used for the ABS system and the control techniques of the ABS in a car. We may conclude that PID controller perform better than only ABS system, but the addition of fuzzy logic control in PID controllers makes system more stable and more steerable. The mathematical modeling and simulation are done with the help of MATLAB/Simulink. This paper showed how the ABS performs better with fuzzy logic by lowering halting time and keeping slip ratio close to 0.2. Thus, ABS with fuzzy logic in PID tuning will aid in steering when the driver applies the brakes. Further optimization work can be done by adding more input parameters to controller.

References

1. Th. Fraichard∗, Ph. Garnier.: Fuzzy control to drive car-like vehicles. Robot. Auton. Syst. **34**, 1–22 (2001)
2. Lakhemaru, P., Adhikari, S.P.: Design and analysis of vehicle anti-lock braking system with fuzzy logic, Bang-Bang and PID Controllers. Himal J. Appl. Sci. Eng. 8–17 (2022)
3. Oudghiri, M., Chadli, M., El Hajjaji, A.: Robust fuzzy sliding mode control for antilock braking system. International. J. sci. tech. automatic control **1**(1), 13–28 (2007)
4. Sharkawy, A.B.: Genetic fuzzy self-tuning PID controllers for antilock braking systems. Engineering applications of Artificial Intelligence 1041–1052 (2010)
5. Listiyono, L., Nurhadi, N., Khambali, K.:Compressor air pressure and brake shield distance brake to braking accuracy on brakes anti-lock braking system. Asian J. Sci. Eng. Politekhnik Negeri Malang, Indonesia. **1**(1), 37–47 (2022)
6. Ćirović, V., Aleksendrić, D.: Adaptive neuro-fuzzy wheel slip control. Expert Syst. Appl. **40**, 5197–5209 (2013)
7. Harshal, R., Aniket, D.: Linear PID control technique for single wheel ABS (anti-lock braking system) of motorcycle. 2nd international conference for convergence in technology (i2ct). IEEE. 277–281 (2017)
8. Jiang, F., Zhiqiang, G.: An application of nonlinear PID control to a class of truck ABS problems. 40th IEEE conference on decision and control (Cat. No. 01CH37228), **1** IEEE. 516–521. (2001)
9. Listiyono, L., Nurhadi, N., Khambali, K.: Compressor air pressure and brake shield distance brake to braking accuracy on brakes anti-lock braking system. Asian J S Eng **1**(1), 37–47 (2022)
10. Kushwah, M., Patra, A.: PID controller tuning using Ziegler-Nichol's method for speed control of DC motor. Int J Sci Eng Technol Res **3**(13), 2924–2929 (2014)
11. Astrom, K.J.: PID controllers: theory, design, and tuning. The international society of measurement and control (1995)
12. Tippannavar, S.S., Yashwanth, S.D., Sudan, M.P.M., Puneeth, K.M., Chandrashekar Murthy, BN., Vinay Prasad, MS.: Analysis of performance of different control techniques on anti-lock braking system. International conference on disruptive technologies for multi-disciplinary research and ap-plications (CENTCON), IEEE. (2), 35–40 (2022)
13. Wellstead, P.E., Pettit, N.B.O.L.: Analysis and redesign of an antilock brake system controller. IEE Proc.-Control. Theory Appl. **144**(5), 413–426 (1997)
14. Wayse, A., Digras, A.: Uncertainty and disturbance estimation using inertial delay observer with integral-sliding mode control. International conference on intelligent computing and control systems (ICICCS). IEEE. 771–775 (2017)

15. Sharkawy, A.B.: Genetic fuzzy self-tuning PID controllers for antilock braking systems. Alexandria Eng. J. (2006)
16. ohedi, F.N., Rahmat, M.A., Kasdirin, H.A.: A critical analysis of fuzzy logic controller for slip control in antilock braking system (ABS). International J Eng Technol (7), 3.28 116–123 (2018)
17. Zadeh, L.A.: Fuzzy sets. Intl J. Inf. Control. (1965)
18. More, H.R., Digrase A.A, Wayse, A.V.: Linear PID control technique for single wheel ABS (anti-lock braking system) of motorcycle. 2nd international conference for convergence in technology (i2ct). IEEE. 277–281 (2017)
19. Xue, X., Cheng, K.W.E.: Electric antilock braking systems for electric vehicles. 8th International conference on power electronics systems and applications (PESA). IEEE (2020)
20. Zhao, Z., Tomizuka, M., Isaka, S.: Fuzzy gain scheduling of PID controllers. IEEE transactions on systems, man, and cybernetics 23. IEEE. 1392–1398 (1993)

Design and Implementation of an Automated Conveyor Belt System with Speed Control, Size Sortation, and IoT Data Publication

Aryan Thakur, Devraj Gautam, Sandeep Bhatia, and Surender Kumar

Abstract In this research work, an automated conveyor belt system with a speed controller and a size sorting mechanism is designed and put into operation. The system aims to optimize the efficiency of material handling processes by dynamically adjusting the conveyor belt speed and accurately sorting items based on their dimensions. Furthermore, the system leverages the power of Internet of Things (IoT) technology by seamlessly publishing real-time data to the ThingSpeak IoT platform. The paper discusses the system's architecture, the integration of speed control and size sortation mechanisms, and the communication protocols used for data publication. Experimental results demonstrate the effectiveness of the proposed system in enhancing productivity, reducing errors, and providing valuable insights for process optimization. The research contributes to the field of automation and IoT-based solutions for industrial applications.

Keywords Automated conveyor belt system · Speed control · Size sortation mechanism · ThingSpeak IoT · Real-time data publication · Material handling · Process optimization

A. Thakur · D. Gautam · S. Kumar
Department of ECE, ADGIPS, Shastri Park, New Delhi, Delhi 110053, India
e-mail: aryanthakur0600@gmail.com

D. Gautam
e-mail: devrajgautam10@gmail.com

S. Kumar
e-mail: drsurenderkdhiman@gmail.com

S. Bhatia (✉)
Department of Computer Science and Engineering, Galgotias University, Greater Noida, Uttar Pradesh 201310, India
e-mail: sandeep.bhatia@galgotiasuniversity.edu.in

© The Author(s), under exclusive license to Springer Nature Singapore Pte Ltd. 2025

H. P. Singh et al. (eds.), *Recent Developments in Control, Automation and Power Engineering*, Lecture Notes in Electrical Engineering 1303,
https://doi.org/10.1007/978-981-96-0047-2_18

1 Introduction

With several benefits like higher productivity, reduced labor costs, and improved operational efficiency, conveyor belt systems have revolutionized material handling and product transportation in numerous sectors. There is a rising need for sophisticated conveyor belt systems that include automation components like speed control and size sortation as industries continue to develop. These features are essential for streamlining manual errors, increasing the speed and accuracy of product delivery, and optimizing material handling procedures.

This study aims to investigate the difficulties faced by industries that use conveyor belt systems and how contemporary developments, such as OpenCV and other cutting-edge technologies, are incorporated into these systems to resolve these difficulties. We'll also delve into the benefits of these developments and how they've revolutionized industrial processes.

We have responded to the increasing application of Internet of Things (IoT) technology in industrial settings by enhancing our automated conveyor belt system through its integration with the ThingsTalk IoT platform. Through this integration, we are able to upload real-time data to the ThingSpeak server, enabling remote access to crucial data like the location of the conveyor belt system at the moment. We can track and analyze system performance, make wise decisions, and promote ongoing development of material handling procedures by utilizing the power of the Internet of Things. We will talk about the IoT integration in our automated conveyor belt system throughout this paper, emphasizing the advantages and implications of ThingSpeak real-time data publishing. We hope to offer a comprehensive solution that uses IoT technology to enable remote monitoring and data-driven decision-making in addition to speed control and size sortation for effective and optimized material handling operations.

2 Organization of the Paper

Literature Survey: This section aims to present an extensive overview of the current literature on conveyor belt systems, with a particular emphasis on automation, image processing, speed control, size sorting, and the incorporation of Internet of Things (IoT) technology.

Approach to Investigating Industry Challenges and Using OpenCV and IoT in Our Better Automated Conveyor Belt System: In this section, we will describe the methodology that we used for our study.

Operations of the Project: We will go into detail in this section about how our automated conveyor belt system is connected to the ThingSpeak IoT platform. We'll go through how remote access to important data is made possible by uploading data in real time to the ThingSpeak server.

Discussion of the Study's Results: In this section, we'll examine and talk about the findings, emphasizing the performance gains made possible by integrating OpenCV, IoT, and other cutting-edge technology.

Final Thoughts and Prospects Scope: We will talk about possible future developments and uses for conveyor belt systems in industrial settings as well as present the findings from our additional research. We will also point out areas that require more investigation and development.

References: In order to give due credit to all the sources that helped shape this paper, we will conclude with a thorough list of all the references that are relevant to our research.

3 Literature Survey

Recent studies focusing on the integration of Raspberry Pi, OpenCV, and image processing methods have drawn a lot of attention to the field of object detection and separation. Numerous researchers have looked into how these technologies might be used to create novel solutions for various applications. There has been a lot of study done on the integration of IoT technology in conveyor belt systems for industrial automation. Various research has been mentioned regarding the development and application of IoT-based conveyor belt systems, emphasizing how these systems can enhance data publication, control, and monitoring capabilities.

An approach for object separation and detection using Raspberry Pi was put forth by Walam et al. [1]. Using Raspberry Pi, based on the color, categorization can be implemented on three colors and the detection of specific colors can be carried out by a light intensity camera.

Dabade [2] presented a demonstration of an automatic sorting device based on conveyor belts. After passing through a set of sensors with varying sizes of objects, the objects with the designated size are sorted. A driver circuit that is managed by a drive controller drives the belt. Yeole and Vardhan (2015) developed an automated monitoring and control system for goods on a conveyor belt [3]. This system makes use of feedback sensors to monitor the objects and an Allen Bradley MicroLogix PLC to control them. The program allows for the easy adjustment of the system's production capacity, which satisfies seasonal demand. Janagam et al. [4] focused on real-time object counting using a Raspberry Pi. By incorporating OpenCV, the authors created an algorithm for accurate object counting. Object sorting is typically done by humans, and it requires a lot of time and work. In their 2018 paper, R. V. Soans, G. R. Pradyumna, and Y. Fukumizu [5] suggested utilizing conveyor belts and computer vision techniques to create a system that employs mechanical structures, stepper motors, and servo motors to identify and sort different objects. This saves time and human labor while increasing the amount of time available to market the products. The applicability of working object detection on the Raspberry Pi 3 is examined by Sai et al. [6]. It takes a lot of processing power to detect objects in real time, and it is challenging to achieve real-time speed in a system with limited performance. An

improved method for identifying objects and calculating their measurements in real time from video streams is presented by N. A. OTHMAN et al. [7]. Using OpenCV libraries, we proposed an object measurement method for real-time video that incorporates erosion, dilation, and canny edge detection algorithms. The four steps of the proposed technique are as follows: (1) identifying an object to be measured using a clever edge detection algorithm; (2) closing gaps between edges using morphological operators, such as the dilation and erosion algorithms; (3) locating and sorting contours; and (4) measuring object dimensions. P. Yadav et al. [8] suggest a low-cost automated system that uses a conveyor belt system, a Raspberry Pi 3 module B, and deep learning to sort various common products. Sorting of objects is done according to their features. F. Montañez, J. J. [9] Python and an open computer vision library are used for image processing in the defect detection process. The corn is manually loaded onto the roller conveyor, where it passes in front of a camera to capture a real-time picture. The idea presented by Narzary and Ashok [10] aims to monitor and control the conveyor belt in real time using Internet of Things technology, as well as arrange different objects in the conveyor belt based on differences: color, size and shape differences by computer low-resolution vision and camera. The Raspberry Pi serves as the central processing unit for tasks such as image processing, data acquisition, parallel data sorting, and updating. N. Hakami and R. Dhakshyani [11]. This search system can distinguish transparent, opaque, opaque, and others by using photoconductor or sensor and laser beam by emission method Shows shape based on open CV classification. R.R. Mhaski et al. [12] examined tomato quality based on their shape, size, and ripeness. Tomato size and shape were estimated using an edge detection algorithm, and ripeness was evaluated using a color detection algorithm. Sandeep et al. [13] presented IoT application in smart waste management system. V. Sachan et al. [14] aimed to identify defects in shape, size, and color and thereby find them. Raspberry Pi and image processing are used to detect product defects. Currently, industrial inspection systems most often rely on very simple elementary features, which most often require human labor, which means that advanced image analysis techniques are not widely applied. Al-Shahethi et al. [15] presented a remote monitoring system for a direct current (DC) motor based on Internet of Things (IoT) for safe and economic data communication in industrial fields. Using a single sensor that tracks the speed of a DC motor, the data is transmitted to the Raspberry Pi microcontroller, which in turn uploads the data to the cloud database which can then be monitored remotely. A rescue robot for detecting live human bodies in debris was developed by Sandeep et al. [16]. By adjusting the stepper motor speed with the microprocessor, M. Kalamalakannan et al. [17] demonstrated that RP 3B + can be used to generate sequences of control signals on the GPIO pins of RP 3B + K in order to control the conveyor belt speed using the Raspberry Pi 3B + 's (RP 3B +) General-Purpose Input Output (GPIOs). This paper proposes a conveyor design using IoT based on a barcode scanner-based mail sorting system as proposed by Venusamy et al. [18]. The main goal of this job is to estimate weight, scan barcodes, and track products using a conveyor system powered by the Internet of Things. Sandeep et al. [19] presented automatic seat identification system in smart transport using IoT as one of the applications. The article published by C. Ulices et al.

(20) focuses on the introduction of an electronic coupling device to make Industrial Internet of Things (IIoT) connections within a conventional programmable logic controller (PLC), aiming at updating the design and construction of an electronic coupling device It was proposed by T. P. Tho et al. [21] that the sorting system could be utilized by the use of a high-resolution camera affixed on the surface of the mechanical conveyor belt. Using the camera's captured images, the software will run algorithms to determine the attributes of the object (such as tomatoes or passion fruits), sort the objects, and store the locations of the sorted objects in a database. The data from the objects can then be utilized for pick-and-place operations that are in sync with the actuator controllers. It was suggested by R. Sahu et al. [22] to arrange the pencils according to color. For this procedure, a conveyor-driven system has been employed. It merely illustrates how an intelligent conveyor belt works by sorting items based on color. Y. Li et al. [23] presented a computer vision-based method in which it proposed to recognize the congestion on conveyor belts. Sandeep et al. [24] developed automatic window curtain system using conveyor belt. These investigations highlight the variety of uses and the effectiveness of using Raspberry Pi, OpenCV, and image processing techniques for object detection, separation, sorting, and counting tasks. They highlight the potential of these technologies in various fields, including industrial automation, agriculture, transportation, quality control, waste management, and surveillance. By leveraging the capabilities of Raspberry Pi and image processing algorithms, researchers have developed innovative solutions for real-world problems. As shown in Fig. 1, we proposed a flowchart of the methodology adopted.

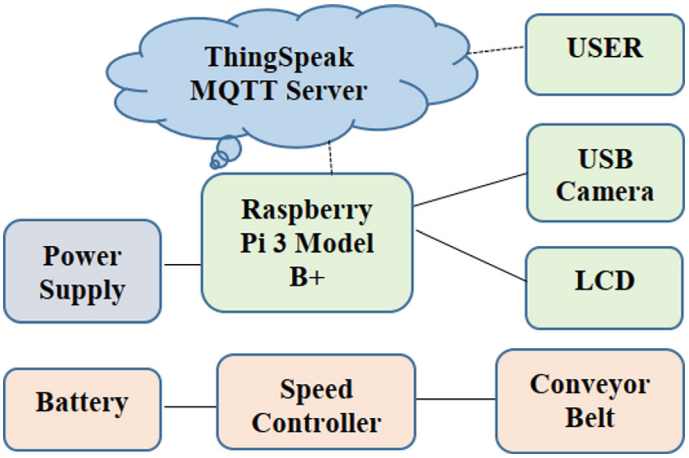

Fig. 1 A flowchart illustrating the employed methodology

4 Methodology

Following is the explanation of components used in our system.

Power Supply: A crucial part of the system, the power supply, is in charge of supplying electricity to various parts. It guarantees that the Raspberry Pi and the monitor get the power they require to work properly. The conveyor belt is also powered by a separate 12 V power supply, ensuring the conveyor belt's smooth operation. The power supply unit has regulation mechanisms to guarantee stability and dependability throughout the system and is connected to a regular electrical outlet.

OpenCV: The system's image processing and estimation of object size heavily rely on OpenCV. The system employs backend and contour area calculations to precisely detect and measure the size of objects by utilizing OpenCV's capabilities. This method enables precise and effective object recognition, adding to the system's overall effectiveness.

Speed Controller: A speed controller is built into the system to improve control over the conveyor belt's motion. By connecting the power source to the motor through the speed controller, the system is able to precisely control the speed of the conveyor belt. Due to the consistent and dependable performance it enables, this level of control is essential for precise object detection and measurement.

USB Camera: A USB camera is used to perform object detection while taking pictures of the conveyor belt. The Raspberry Pi then employs OpenCV to process these images. The system can successfully detect and analyze objects by utilizing the capabilities of the USB camera and the Raspberry Pi, allowing for additional processing and measurement.

LCD Display: The system includes an LCD display that is connected to the GPIO pins of the Raspberry Pi. This display acts as an interface to convey information about the detected objects and visual feedback. The system's OpenCV-based processing is used to determine the calculated area of the objects, which is displayed on the LCD display along with other pertinent data. Real-time observation and analysis of the items moving along the conveyor belt are made possible by this feature.

IoT Integration: To enable real-time data publication and remote access, an IoT integration has been added to the list of system components already in place. The ThingSpeak IoT platform receives the area that the Raspberry Pi processed, as determined by OpenCV calculations. Utilizing the Raspberry Pi's network connectivity abilities, this integration is made possible. This makes it possible for users to remotely access the data of the conveyor belt system, keep an eye on the processing area, and learn more about the functionality and productivity of the system.

Overall, Hardware Layout: The Raspberry Pi, the dedicated 12 V power supply for the conveyor belt, the speed controller, and the LCD display are all connected to the power supply in the system's hardware layout. To make image capture and processing easier, a USB port on the Raspberry Pi is also used to connect the USB

camera. The seamless automation of the process made possible by the components' harmonious integration reduces the need for manual labor while providing financial advantages to the organizations where the system is used.

5 Working

The conveyor belt system is powered on by a power source that provides the necessary voltage for it to function, as seen in Fig. 2. In order to regulate the conveyor belt's speed, a pulse width modulation (PWM) speed controller essentially adjusts the voltage applied to the conveyor belt's 12 V gear motor. A USB camera is strategically positioned above the conveyor belt to capture the area of interest, with a set frame size to concentrate on this particular area. Utilizing a power source, which supplies the required voltage to enable the conveyor belt system's operation, turns it on. A pulse width modulation (PWM) speed controller controls the conveyor belt's speed by altering the voltage delivered to the 12 V gear motor that powers the belt. A USB camera is positioned above the conveyor belt with a designated frame size set to focus on this particular area in order to carefully capture the area of interest. The camera is positioned at a constant height, and a calibration object is used to translate the pixel values into tangible units, like centimeters, in order to obtain measurements that are simple to interpret. This calibration procedure makes sure that the system can easily comprehend the size of the objects passing through it and sort them accordingly. A visual depiction of the sorting procedure is provided by an LCD display that is positioned next to the conveyor belt. This allows observers to monitor the setup and promptly identify any possible issues that may arise. The Raspberry Pi's OpenCV software diligently processes the images that are captured as objects move through the area of interest, subsequently identifying each object's contour area and translating it into units that people can understand. The system successfully establishes the necessity of considering an object's size in the sorting process using predefined sorting criteria. If an object doesn't fit the requirements for size, a bounding box is indicated in red; if it does, it's indicated in blue. This practical implementation allows the system to classify objects according to their size, reducing the need for time-consuming manual sorting activities. The system successfully establishes the necessity of considering an object's size in the sorting process using predefined sorting criteria. If an object doesn't fit the requirements for size, a bounding box is indicated in red; if it does, it's indicated in blue. This practical implementation allows the system to classify objects according to their size, reducing the need for time-consuming manual sorting activities. The system also includes an IoT integration in addition to the object classification based on the color of the bounding box. The data, including the object's size and classification, is uploaded to the ThingSpeak IoT platform concurrently with the object classification process. Users can log in and remotely access the system to check on its performance thanks to this real-time data upload. Users can gain insightful knowledge into the

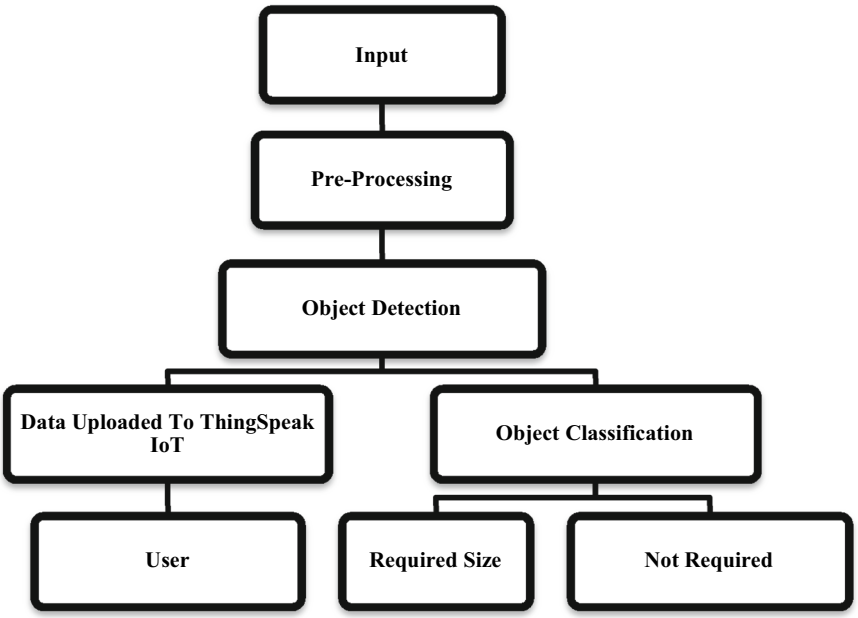

Fig. 2 Flowchart of working

sorting process and make wise decisions based on the real-time data by utilizing the ThingSpeak IoT platform.

In conclusion, this automated system offers a practical method for streamlining the sorting procedure by fusing hardware elements with OpenCV software to accurately process and classify objects according to their size. The data is simultaneously uploaded to the ThingSpeak IoT platform, where it can be accessed by the user in real time, along with the classification based on the color of the bounding box. This system significantly boosts productivity and operational effectiveness by reducing the need for manual labor, and by integrating IoT, it also offers remote monitoring capabilities.

6 Result Discussion

Conveyor belt, USB camera, Raspberry Pi, and OpenCV software were used to successfully design and implement the automated sorting system. According to the predetermined sorting criteria, the system was able to precisely detect and classify objects based on their size as shown in Fig. 3. The USB camera's images could be processed by the object detection algorithm, which was able to recognize the contour area of objects passing through the region of interest (Figs. 4 and 5).

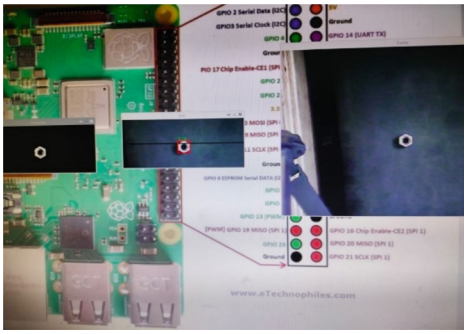

Fig. 3 An image of a not required case (Left)

Fig. 4 Top view (Right)

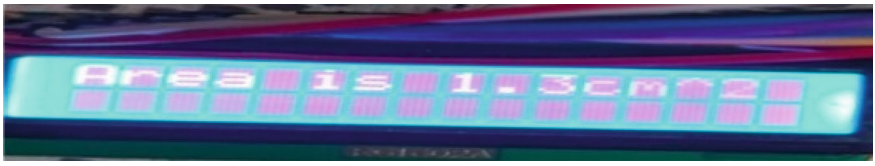

Fig. 5 LCD connected to raspberry PI showing area

With a precision of up to 1 decimal place, the system was able to precisely calculate the objects' surface areas. Figure 4 represents a top view of the conveyor belt system.

The size classification algorithm was able to distinguish between objects that did and did not fit the size specification. The system made it simple to identify and sort the objects by drawing a bounding box around them in either red or blue depending on whether they were required or not. The sorting process could be easily monitored, and any mistakes or problems could be quickly found and fixed thanks to the use of an LCD display, as shown in Fig. 5. Additionally, the system significantly reduced the amount of manual labor needed for sorting, increasing productivity and decreasing labor costs.

The object detection algorithm was able to process images from the USB camera and identify the contour area of the objects passing through the region of interest.

The object detection algorithm was able to process images from the USB camera and identify the contour area of the objects passing through the region of interest. The system was able to accurately calculate the area of the objects, with a precision of up to 1 decimal place. The accuracy of the object area calculations was evaluated using a test dataset, and the results are depicted in the graph shown in Fig. 6. The graph shows how well the system performs in terms of the precision of the object area calculations. A high level of accuracy was consistently attained by the system, with an average accuracy rate of over 95% as displayed in Fig. 7. The size classification algorithm can distinguish between objects that adhere to the size requirement and those that do not with this level of accuracy. The system's functionality is further improved by the incorporation of IoT, as shown in Fig. 8. The system seamlessly uploads the data, including the object's size and classification, to the ThingSpeak IoT platform in tandem with the object detection and size classification process.

By merging precise object identification with size through this integration, users can remotely access real-time data, allowing them to keep an eye on the sorting process and make decisions based on the state of the system at the time. Classification along with IoT integration, the automated sorting system presented in our proposed framework offers a comprehensive solution for efficient and reliable object sorting. The system's high accuracy in calculating object area, as evidenced by the graph, ensures precise size classification, minimizing errors in the sorting process. The IoT integration provides real-time data access, enabling remote monitoring and facilitating data-driven decision-making. Overall, this automated sorting system holds great potential for industrial applications, where it can significantly improve efficiency, reduce labor costs, and enhance operational productivity.

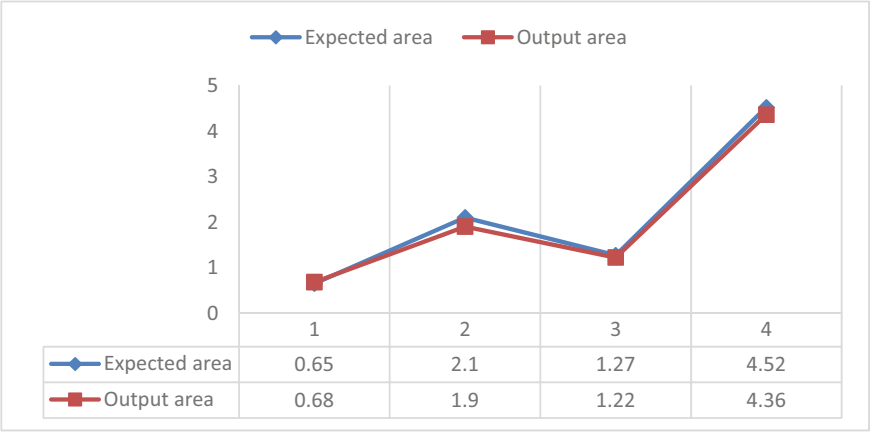

	1	2	3	4
Expected area	0.65	2.1	1.27	4.52
Output area	0.68	1.9	1.22	4.36

Fig. 6 Area output

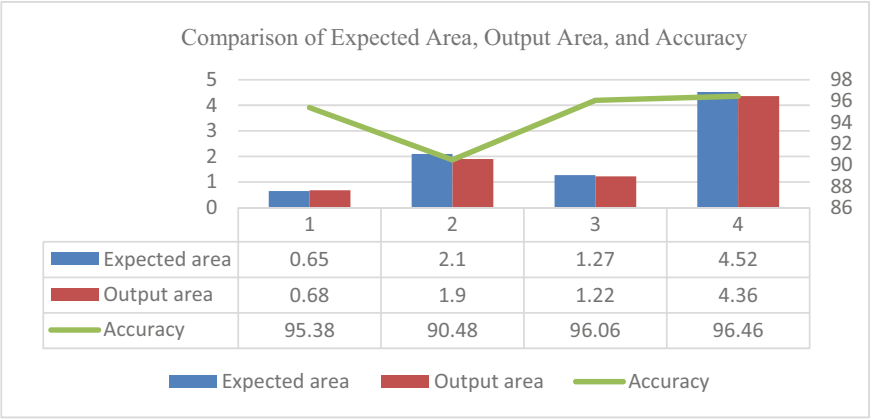

Fig. 7 Accuracy plot

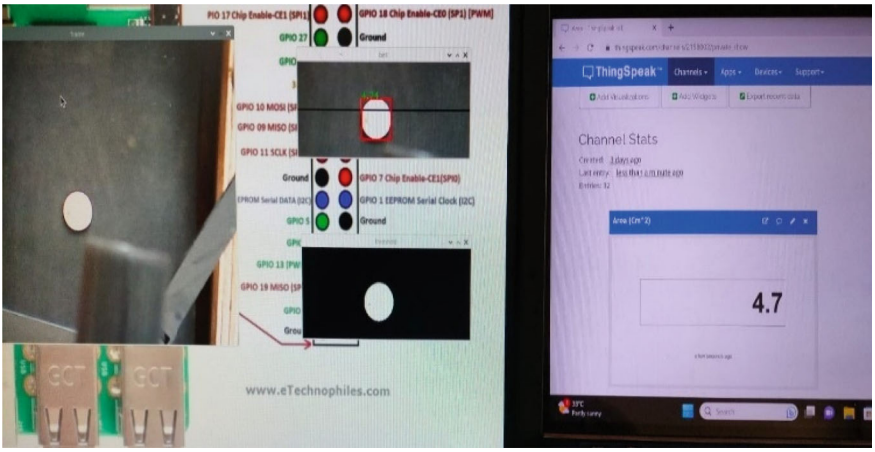

Fig. 8 ThingSpeak IoT channel

7 Conclusion

Using a Raspberry Pi, PWM speed controller, DC gear motor, and OpenCV, this system was successful in creating an automated conveyor belt system with speed control and size sorting. Through accurate object classification based on size, the system reduced the need for manual labor and increased productivity. The outcomes demonstrated that the system could detect the area of objects with an accuracy of up to 1 decimal place. The system's capabilities have also been increased by the addition of IoT. The ThingSpeak IoT platform and the Raspberry Pi are connected, allowing for remote real-time data access and monitoring. Users can follow the

sorting procedure, keep track of the object classifications, and base their decisions on the most recent data provided by the system thanks to this IoT integration. A wide range of industries, including manufacturing, aviation, warehousing, the food and beverage, mining, pharmaceutical, e-commerce, logistics, automotive, and medical equipment and device sectors, could make use of this system. Small adjustments to the system can result in material increases in revenue for these businesses depending on the needs of each industry.

Overall, the system shows the viability and efficiency of creating an automated conveyor belt system using a Raspberry Pi, OpenCV, and IoT integration. The system is a valuable addition to many industries because it can significantly reduce manual labor, boost productivity, improve efficiency, and offer real-time monitoring capabilities. Companies can optimize their operations, streamline their processes, and experience greater levels of success in the quick-paced and cutthroat business environment by embracing technological and automated advancements.

8 Future Scope

The following points in our paper can be updated as a future scope:

- Enhanced sorting algorithms.
- Real-time analytics and decision support.
- Automated fault detection and maintenance.
- Modular and scalable design.
- Supply chain management system integration.

To sum up, there are a number of future directions that the research will pursue. These include refining the sorting algorithms, utilizing machine learning techniques, growing IoT integration for real-time analytics and decision support, automating fault detection and maintenance, building for scalability and modularity, and connecting the system to more comprehensive supply chain management systems. These developments have the potential to unlock new levels of productivity, efficiency, and operational excellence in industries where material handling and sorting operations rely on conveyor belt systems.

References

1. Walam, SS., Teli, SP., Thakur, BS., Nevarekar, RR., Patil, SM.: Object detection and seperation using raspberry pi. In: 2018 Second International Conference on Inventive Communication and Computational Technologies (ICICCT) **20,** 214–217. IEEE 2018
2. Dabade, S.P., Chumble, R.P.: Automatic Sorting Machine Using Conveyor Belt. Int J Innov Emer Res Eng. **2**(5), 66–70 (2015)

3. Vardhan, DS., Narayan, YS.: Development of an automatic monitoring and control system for the objects on the conveyor belt. In: 2015 International Conference on Man and Machine Interfacing (MAMI) IEEE **17**, 1–6 (2015)
4. Manasa, J., Pramod, J.T., Jilani, S.A., Hussain, M.S.: Real time object counting using Raspberry pi. Int. J. Adv. Res. Comp Commun Eng. **4**(7), 540–544 (2015)
5. Soans, RV., Pradyumna, GR., Fukumizu, Y.: Object sorting using image processing. In: 2018 3rd IEEE International Conference on Recent Trends in Electronics, Information and Communication Technology (RTEICT) IEEE **18**, 814–818 (2018)
6. Sai, TV., Aditya, B., Reddy, AM., Srinivasulu, Y.: Real time object detection using raspberry Pi. International J. Res. Appl. Sci. Eng. Technol. **11**, 834–838 (2023). https://doi.org/10.22214/ijraset.2023.48549
7. Othman, NA., Salur, MU., Karakose, M., Aydin, I.: An embedded real-time object detection and measurement of its size. In2018 International Conference on Artificial Intelligence and Data Processing (IDAP) IEEE **28**, 1–4 2018
8. Yadav, P., Uikey, M., Lonkar, P., Kayande, S., Maurya A.: Sorting of objects using image processing. In: 2020 IEEE International Conference for Innovation in Technology (INOCON) IEEE **6**, 1–6. (2020)
9. Montañez, JJ.: Smart defect detection and sortation through image processing for corn. In: 2020 IEEE Region 10 Conference (TENCON) IEEE **16**, 1233–1237 (2020)
10. Narzary, A., Ashok, S.: Real-time monitoring of conveyor using computer vision and IoT. In: 2019 2nd International Conference on Intelligent Computing, Instrumentation and Control Technologies (ICICICT) IEEE **5** (1), 73–78 (2019)
11. Hakami, N., Dhakshyani, R.: IoT-based Automatic sorting of objects that are transparent translucent and opaque using the effect of light. In:2022 3rd International Conference on Smart Electronics and Communication (ICOSEC) IEEE **20,** 458–463 (2022)
12. Mhaski, RR., Chopade, PB., Dale, MP.: Determination of ripeness and grading of tomato using image analysis on Raspberry Pi. In: 2015 Communication, Control and Intelligent Systems (CCIS) IEEE **7**, 214–220 (2015)
13. Bhatia, S., Ahlawat, V., Verma, S.: An IoT enabled smart garbage management system for effective waste utilization strategy in cities. Available at SSRN 4211518 5 (2022)
14. Sachan, V., Deb, PS., Sharma, S., Thakur, H., Dubey, GK.: Product quality inspector. In: 2020 9th International Conference System Modeling and Advancement in Research Trends (SMART) IEEE **4**, 212–215 2020
15. Al-Shahethi, MG., Muneer, A., Ghaleb, EA., Darshi, S., Almohammedi, AA.: Real life monitoring of conveyor line speed using IoT and raspberry Pi. In: 2021 International Conference on Intelligent Technology. System and service for internet of everything (ITSS-IoE) IEEE **1**, 1–5 (2021)
16. Bhatia, S., Dhillon, HS., Kumar, N.: Alive human body detection system using an autonomous mobile rescue robot. In2011 Annual IEEE India Conference IEEE **16,** 1–5 (2011)
17. Kamalakannan, M., Devadharshini, K.: Controlling the speed of conveyor belt using python–raspberry Pi 3B+. Oriental j comput sci technol. 25, **12**(2), 57–64. 2019
18. Venusamy, K., Hafeel, A., Kamal, M., Muthukkaruppan, S., Chandramohan, P.: Study on conveyor belt system enabled with IoT in postal and courier services. In: 2023 Second International Conference on Electronics and Renewable Systems (ICEARS) IEEE **2,** 511–515 (2023)
19. Bhatia, S., Gautam, D., Kumar, S., Verma, S.: Automatic seat identification system in smart transport using IoT and image processing. In: 2023 3rd International Conference on Intelligent Communication and Computational Techniques (ICCT) IEEE **19,** 1–6 (2023)
20. Ulices, C., Irma, M., Carlos, J.: Design of an electronic coupling to control speed of motor on a conveyor belt using IoT. In: 2020 International Conference on mechatronics, electronics and automotive engineering (ICMEAE) **16,** 115–121 IEEE (2020)
21. Tho, TP., Thinh, NT., Bich, NH.: Design and development of the vision sorting system. In: 2016 3rd International Conference on green technology and sustainable development (GTSD) **24** 217–223. IEEE. (2016)

22. Sahu, R., Swain, MK., Swain, KB., Patnaik, RK.: Productive and economical sorting of objects by low resolution camera. In: 2017 IEEE international conference on smart technologies and management for computing, communication, controls, energy and materials (ICSTM) **2**, 290–294. IEEE. 2017
23. Li, Y., Niu, Y., Liu, Y., Zheng, L., Wang, Z., Zhe, W.: Computer vision based conveyor belt congestion recognition in logistics industrial parks. In: 2021 26th IEEE international conference on emerging technologies and factory automation (ETFA) **7,** 1–8. IEEE 2021
24. Bhatia, S., Sharma, P., Verma, S., Ansari, MT., Kumar, U., Singh, SP.: Automatic window curtain system. Available at SSRN 4157347. **14** 2022

Investigating Quantum-Inspired Evolutionary Algorithm with Restarts for Solving IEEE CEC 2022 Benchmark Problems

Lubna Siddiqui, Ashish Mani, and Jaspal Singh

Abstract This paper investigates the effectiveness of two restart methods, local and global restarts, in enhancing the performance of the quantum-inspired evolutionary algorithm (QiEA) to solve optimization problems. The study compares the result of these modifications by testing their performance against the widely recognized and challenging IEEE CEC 2022 benchmark functions. The objective is to analyze the impact of the restart methods on the convergence and optimization outcomes of the QiEA. Through experimental evaluation, it was sought to determine whether the inclusion of restart methods in the QiEA framework would lead to improved convergence toward the optimal solution. Also, a novel Greedy Local Restart algorithm is proposed. The results demonstrate that the QiEA variants consistently outperform the basic QiEA, achieving superior optimization results in terms of convergence and accuracy. Restart approaches are thus observed as an indispensable asset in handling complex optimization problems, greatly enhancing the effectiveness and applicability of evolutionary algorithms.

Keywords IEEE CEC 2022 benchmark functions · Quantum-inspired evolutionary algorithm · Optimization method · Global and local restarts

L. Siddiqui
Amity School of Engineering and Technology, Amity University, Noida, India
e-mail: lub.sid@gmail.com

A. Mani (✉)
Amity Innovation and Design Centre, Amity University, Noida, India
e-mail: amani@amity.edu

J. Singh
Centre for Development of Advanced Computing, Chandigarh, India
e-mail: jaspal@cdac.in

© The Author(s), under exclusive license to Springer Nature Singapore Pte Ltd. 2025

H. P. Singh et al. (eds.), *Recent Developments in Control, Automation and Power Engineering*, Lecture Notes in Electrical Engineering 1303,
https://doi.org/10.1007/978-981-96-0047-2_19

1 Introduction

Evolutionary algorithms are optimization techniques for solving complex problems. Quantum-inspired evolutionary algorithms (QiEAs) combine the principles of quantum computing with evolutionary computation. However, they face obstacles such as noise and error correction issues in quantum computing. Another obstacle is limited accessibility to a broader range of researchers and practitioners due to requirement of specialized knowledge. QiEAs differ from quantum evolutionary algorithm (QEAs). While QEAs require quantum computing resources, QiEAs are classical algorithms that are built on quantum-inspired concepts. This paper focuses on QiEAs.

Quantum-inspired evolutionary algorithms have their limitations, but they indeed offer astounding advantages that are impossible to overlook when compared to their classical counterparts. They exploit quantum mechanics to efficiently search complex solution spaces by representing solutions as quantum states. This parallel exploration enables faster convergence. Additionally, QiEAs benefit from quantum computing power, allowing them to tackle difficult problems that classical algorithms struggle with. Quantum computers can solve certain problems exponentially faster than classical computers, such as integer factorization and database search [1, 2]. These competitive advantages of QiEAs can be further enhanced by incorporating restart strategies.

Restart strategies play a crucial role in overcoming local optima, maintaining diversity, and rejuvenating the search process. They provide a mechanism to explore new regions of the search space and prevent the algorithm from getting trapped in suboptimal solutions. The aim of this paper was to evaluate the impact of restart methods on the performance of QiEAs and whether the inclusion of restart methods would enhance the convergence of QiEA toward optimal solutions. Also, a simple novel Greedy Local Restart algorithm is introduced. This algorithm is vetted against the benchmark functions of IEEE Congress on Evolutionary Computation (CEC) Competition of 2022.

The paper is organized as follows: Sect. 2 provides an overview of related work in QiEAs. Section 3 describes the QiEA algorithm. Section 4 describes restarts followed by testing and results in Sect. 5. Section 6 showcases the conclusions and discussions followed by future scope in the last section.

2 Related Work

Quantum-inspired evolutionary algorithms (QiEAs) are a class of algorithms that combine the principles of evolutionary computation and quantum mechanics to solve complex optimization problems. QiEAs were first proposed in the late 1990s, and since then, they have undergone significant development.

In 1977, MIT colleagues Ronald Rivest, Adi Shamir, and Leonard Adleman [3] known as RAS, by the initials of their surnames, laid out a notable challenge regarding intractable prime factors of 129 digit number, commonly called RAS-129 challenge. This was also the basis of encryption methods widely employed called data encryption standard (DES) thus, in turn making fail-safe systems. This challenge was left undisputed for many years until in 1994, 1600 computers were linked together with the help of the Internet, to determine the factors of a 129-digit factorization in 8 months[4]. Also, in the same year, Peter Shor [5] proved that the same could happen in a matter of a few seconds by changing the paradigm from classical to quantum.

Narayanan and Moore's [4] extension to Shor's method can be said to be the initial introduction of QiEAs. In their paper, they showed how the quantum-inspired method increased the efficiency of sorting a list from $\frac{1}{2N(N-1)}$ to $\sqrt{N}\left(N + 2\sqrt{N} - 1\right)$ selections; i.e., for 16 numbers, this value is 88 selections considerably lower than 120 which is for the "classical" method. However, QiEAs did not receive substantial attention until a practical algorithm was proposed by Han and Kim (2002) [6].

Another promising paper by Zhang, [7] in 2011, discusses the principles of quantum computing and the applications of QiEAs in solving optimization problems. The empirical study compares the performance of various QiEAs with traditional evolutionary algorithms on benchmark problems like the traveling salesman problem and the knapsack problem. The results showed that QiEAs outperformed traditional evolutionary algorithms in terms of convergence speed and solution quality. QiEA has been successfully applied to a variety of optimization problems, including combinatorial, continuous, and multi-objective optimization [8, 9]. The algorithm has also been extended to distributed and parallel settings [10] to further improve its efficiency.

The work presented in this paper is to test the efficiency of QiEA on the challenging benchmark suite of IEEE CEC 2022. Additionally, a short analysis was also made of the winners of this competition [11]. One of the best-ranked algorithms was the NL-SHADE RSP-MID algorithm [12], which is an extension of NL-SHADE RSP algorithm [13]. It stands for nonlinear self-adaptive differential evolution with restart strategy and parameter control. The NL-SHADE-RSP-MID extends its predecessor by adding four components: [12] the concept of midpoint; restarts; resampling as bound constraint handling; k-means grouping. The drawback of this algorithm was its high complexity. It was observed that the k-means component strongly increases the algorithm's complexity. This speed can be easily gained by using alternative versions of k-means and alternative initialization methods [12]. One such initialization method is the quantum-inspired technique and thus a motivation behind this work.

The proposition of this work is that a simpler algorithm can be made by changing the paradigm: from classical EA to quantum EA. For better understanding, the basic concepts of quantum computing are outlined.

3 Quantum-Inspired Evolutionary Algorithm

The quantum-inspired evolutionary algorithm is a type of optimization algorithm inspired by quantum mechanics and evolutionary biology. It uses a probabilistic approach to search for the optimal solution to a given problem. The key feature of QiEA is its ability to leverage quantum mechanics principles, such as superposition (existence of more than 2 states at a single time), entanglement (one state related to the other state even if apart), and quantum measurement (collapse operation), to improve the search process.

The algorithm begins with initializing the population randomly. Each chromosome (also called individual) in the population denotes a solution of the objective function. More specifically, each chromosome is represented by the Qbit representation first.

The rotation lookup table outlines eight combinations of rotation angles determined by the fitness of the current bit (Ri) and the chosen attractor, referred to as the best bit (Bi). In this paper, four more angles termed as Θ_{2a}, Θ_{4a}, Θ_{6a}, and Θ_{8a} are explored when the fitness values of the current individual and best individual are equal. Table 1 is a lookup rotation table implemented in this work. Also, in the context of minimization problems, the best bit corresponds to the individual with the lowest fitness observed in the current generation.

The angle of rotation (theta) of the qubit depends on the sign, given by $\alpha_i{}^* \beta_i$. When the qubit is anywhere in the first or third quadrant (positive sign), a positive theta value is required to reach the basis state $|1>$, as can be seen from Table 1. Conversely, when aiming to reach the basis state $|0>$, theta takes on a negative value. Similarly, if the qubit is located in the second or fourth quadrant, a negative theta is needed to reach the basis state $|1>$, while a positive delta theta is necessary to reach the basis state $|0>$.

The offspring Qbits are collapsed into binary bits and converted into real coded strings. This conversion of binary bits to real numbers is done using the IEEE 754:2008 standard convention. The fitness of the offspring solutions is evaluated. The iteration continues until a convergence criterion is met. Here, the algorithm sometimes suffers from convergence to suboptimal solutions or stagnation in the optimization process. To address this, the incorporation of restart strategies has gained attention as an effective means to enhance the performance of QiEAs.

4 Restarts in QiEA

Restart methods in evolutionary algorithms have undergone significant evolution and refinement since their first usage. The early usage of restarts can be traced back to the 1970s and 1980s when evolutionary algorithms were first developed. While not explicitly referred to as "restarts," researchers recognized the need for rejuvenation or diversification in optimization algorithms. Several restart strategies can be employed

Table 1 Lookup rotation table

Condition	R_i	B_i	$\Delta\theta_i$	Sign $\alpha_i{}^*\beta_i$	Han and Kim [6]	Experimental	R_i	B_i	$\Delta\theta_i$	Sign $\alpha_i{}^*\beta_i$	Han and Kim [6]	Experimental
Fr > Fb	0	0	Θ_1	+	0	0	1	0	Θ_5	+	0.01*P*i	−ve
				−						−		
Fr < Fb			Θ_2	+	0	0			Θ_6	+	0	0
				−						−		
Fr = Fb			Θ_{2a}	+	N.A	−ve			Θ_{6a}	+	N.A	0
				−						−		
Fr > Fb	0	1	Θ_3	+	0.01Pi	+ ve	1	1	Θ_7	+	0	0
				−		−ve				−		0
Fr < Fb			Θ_4	+	0	0			Θ_8	+	0	0
				−						−		
Fr = Fb			Θ_{4a}	+	N.A	0			Θ_{8a}	+	N.A	0
				−						−		

in QiEAs, each with its own characteristics and advantages. These strategies include global restart, local restart, fitness-based restart, convergence detection restart, adaptive restart, and hybrid restart. Global restart discards the entire population and starts with a fresh one, allowing for a new exploration of the search space [10]. Local restart focuses on restarting a subset of the population to refine the search in the current region [14]. Fitness-based restart triggers a restart based on specific fitness criteria, while convergence detection restart initiates a restart when convergence criteria are met [15, 16]. On the other hand, adaptive restart dynamically adjusts the restart behavior based on performance indicators, and hybrid restart combines multiple strategies to strike a balance between exploration and exploitation [17–21]. For the sake of simplicity, a comparison will be drawn out between global and local restart methods in this paper along with a novel technique in the local restart domain.

The choice of restart strategy depends on the problem's characteristics, optimization goals, and the desired trade-off between exploration and exploitation.

Two restart strategies are investigated in this work, with comparisons with the basic no restart QiEA (QiEA-NR). The first variation is introduced by incorporating a global restart strategy, called QiEA-global restart. The second, a novel QiEA-Greedy Local Restart method is proposed. They both start similar to the basic QiEA algorithm, with the initialization of the random quantum population, measurement, conversion to real numbers and evaluation of fitness for the objective function. However, a key difference is introduced when fitness fails to improve over several generations.

4.1 QiEA with Global Restart (QiEA-Global R)

In QiEA with global restart, when the fitness stagnates and fails to improve a variation is introduced. At this point, the restart operation is triggered. It involves completely resetting or rejuvenating the population of Qbit chromosomes globally, in sync with its name, introducing randomness to explore different regions of the search space, and overcoming stagnation.

4.2 QiEA with Greedy Local Restart (QiEA- Greedy LR)

This paper proposes a novel quantum-inspired evolutionary algorithm with Greedy Local Restart (QiEA—Greedy LR). The pseudocode for this strategy is given below:

- Initialize population of random Qbits.
- Measurement of quantum population.
- Convert binary bits to a real coded solution string P.
- Evaluate the fitness of P.
- Repeat until convergence:

- Generate new offspring using a quantum rotation gate operator on Qbits.
- Collapse the offspring Qbits into binary bits and then to a subsequent offspring real coded string.
- Evaluate the fitness of real coded offspring.
- Restart operation is initiated:

  Restart qubits randomly by including a subsetbest solution of previous generations.

The algorithm begins by initializing random Qbits, followed by measuring them to obtain binary bits. The binary bits are converted into a real coded solution string which is tested against the fitness function. In subsequent generations, new qubits are generated through a quantum rotation gate operation on the previous qubits. These new qubits are then collapsed into binary bits and further into real coded strings. The fitness of the offspring solutions is evaluated, and a counter tracks any lack of improvement. When the fitness of the population remains stagnant, indicating that the algorithm is trapped in a local optima, a restart is initiated. That is, re-initializing the population with a new quantum population while also incorporating a subset of the previous best solutions. This strategy aims to strike a balance between retaining promising solutions and exploring new regions of the search space. The flowchart for this algorithm is shown in Fig. 1.

The QiEA-Greedy Local Restart approach offers flexibility in selecting the subset of the previous best solutions to include in the new population. The two strategy parameters evaluated are:

1. Variant–A: Including the top three best solutions: In this greedy method, the new population upon restart includes the top three solutions that performed the best in the previous generation. By retaining these top-performing solutions, the algorithm focuses on refining and potentially improving their quality in subsequent iterations, while still exploring untouched search spaces.
2. Variant–B: Including only one best solution: This greedy strategy involves saving only the single best solution from the previous generation in the new population. This approach allows for greater exploration by incorporating a fresh set of candidate solutions while maintaining a reference to the most promising solution found (Fig. 1)

The specific choice between these two conditions depends on the optimization problem and the desired trade-off between exploitation (refining known good solutions) and exploration (searching for new solutions). This approach can help prevent premature convergence and increase the likelihood of finding better solutions in subsequent iterations. The algorithm continues to iterate through these steps until the optimal solution is found or a termination criterion is met.

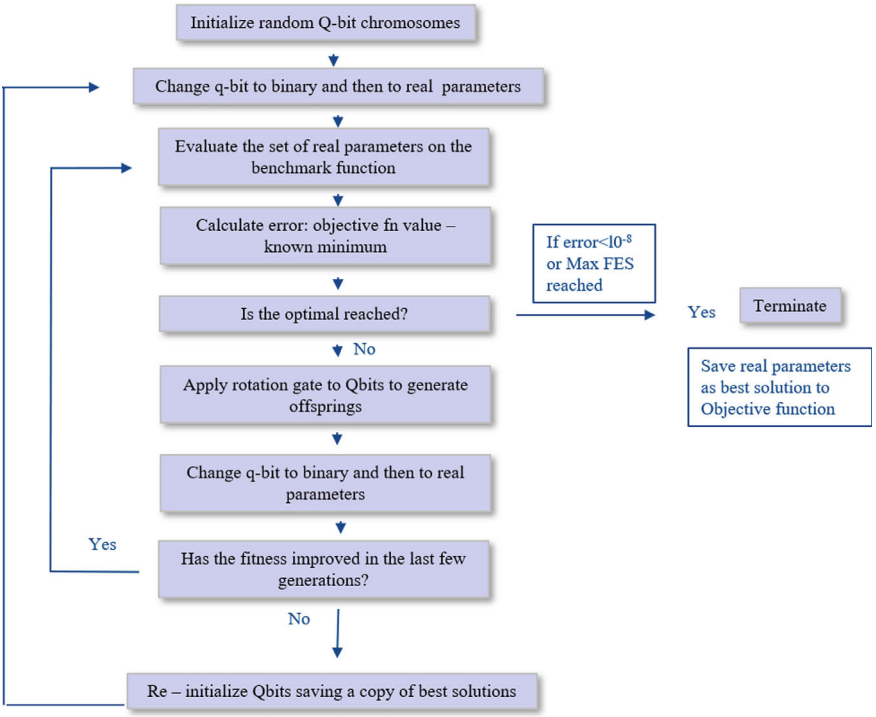

Fig. 1 Flowchart of QiEA—Greedy Local Restart

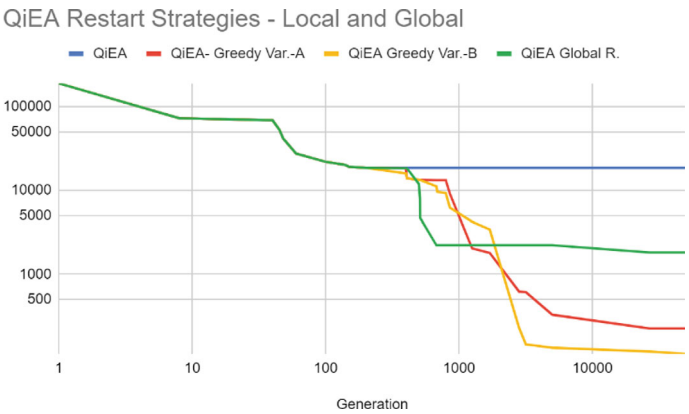

Fig. 2 Comparing best reached value for three algorithms

5 Testing and Results

In this study, the performance of quantum-inspired evolutionary algorithms (QiEAs) with restarts on the IEEE CEC (Single Output Bound Constrained) benchmark suite is evaluated. The suite comprises 12 optimization problems, including 5 basic functions, 3 hybrid functions, and 4 composition functions, all with a fixed search space of [–100, 100] and dimension of 10 as mentioned in the Technical Report [22].

Parameters

Problems: 12 minimization problems.
Dimensions: D = 10.
Runs/problem: 5.
MaxFES: 5000.
Search Range: [–100,100].
Restart Trigger: 100 generations of no improvement.
Environment: Python, Visual Studio Code, Windows 10.
Server Specifications: 11th Gen Intel(R) Core(TM) i7-11800H @ 2.30 GHz.

Experiments were conducted with termination criteria set as reaching the optimal value or reaching MaxFES. A population size of 100 individuals was taken across all problems. The environment was Python on a system specifications.

The three algorithms (QEA-NR, QEA-Global R, and QEA-Greedy LR) were evaluated on the 12 benchmark functions, and the corresponding results were presented in Table 2. The evaluation of the Greedy Local Restart strategy and the global restart strategy in this study reveals that the Greedy LR tends to yield results that are closer to the optimal solution. This indicates the effectiveness of the Greedy Local Restart strategy in improving the performance of the algorithm winning 7 out of 12 times (Table 2).

Furthermore, within the Greedy Local Restart strategy, there are two variants, Variant-A: save top three solutions, and Variant-B: save 1 best solution only. The second variant demonstrates competitive results when compared to the first variant. For instance, the fitness value of function 2 dropped from 12.01 in basic no restart algorithm to 7.04 in Greedy Local Restart Variant-A and further lower to 5.66 for Variant-B. However, it is important to note that there are instances where the Variant-A outperforms the other strategies.

The variations in performance across different functions can be attributed to the characteristics of the optimization problem and the specific search landscape. Each variant of the Greedy Local Restart strategy has its own strengths and limitations. Saving the top three best solutions, Variant-A, allows for exploration of multiple promising regions in the search space, which can be advantageous in certain scenarios along with exploration. Variant-B is saving a single best solution from the previous generations. It helps the algorithm to focus on exploiting promising areas of the search space while still allowing for more exploration.

Global restart shows superior performance in three test cases where local optima hinder progress, allowing for a fresh start and exploration of new, promising regions.

Table 2 Best values obtained

Func	Best			
	QiEA- No Restart	QiEA-Global R	QiEA-Greedy Local R	
			Variant-A	Variant-B
1	4153.38	840.66	328.58	**131.99**
2	12.01	9.46	7.04	**5.66**
3	6.6	5.03	**0.65**	1.08
4	36.65	**13.95**	28.58	14.99
5	59.79	20.16	99.76	**10.46**
6	17,149.15	**250.31**	1032.40	294.25
7	28.92	13.96	24.03	**7.56**
8	25.82	**12.44**	21.56	19.56
9	258.21	239.22	**231.93**	243.81
10	111.94	100.82	101.03	**10.21**
11	147.42	146.05	160.81	**73.16**
12	169.58	165.87	165.93	**162.82**

Evaluating and comparing restart strategies in QiEAs is crucial, considering problem domains and the exploration–exploitation trade-off. The most suitable restart strategy depends on the specific problem and optimization process.

Figure 2 provides further evidence to support the significance of integrating restart strategies into evolutionary algorithms, highlighting their ability to improve performance and explore a broader range of solutions within the search space. The figure demonstrates that, initially, the QiEA algorithm makes progress in finding better solutions for the objective functions. However, when it encounters stagnation or becomes stuck, the implementation of various restart strategies becomes crucial. These restart strategies depicted in the figure play a vital role in enabling the algorithm to overcome local optima and move closer to the optimal solution.

In this specific study, the QiEA-Greedy LR algorithm, implemented with two variants—Variant-A and Variant-B—has demonstrated superior performance compared to other restart strategies. The results indicate that both variants of QiEA-Greedy LR approach the optimal solution more closely.

The QiEA-Greedy LR Variant-B notably achieved the best fitness across most of the benchmark functions evaluated winning 7 out of 12 times. This finding suggests that by selectively incorporating and preserving the single best solution from the previous generation, the algorithm is able to focus on exploiting promising areas of the search space while still allowing for exploration.

6 Conclusion

The performance of a quantum-inspired evolutionary algorithm (QiEA) with global and local restart methods was investigated. It was hypothesized that these restart methods could enhance the algorithm's ability to escape local optima and explore unexplored regions of the search space, ultimately resulting in a closer approximation of the optimal value. The results of this study have provided confirmation for the initial hypothesis, demonstrating that the variants of QiEAs with restart methods consistently outperformed the basic QiEA approach on the IEEE CEC 2022 benchmark functions. Notably, this novel approach of QiEA-Greedy Local Restart strategy exhibited remarkable success by achieving a lowest fitness value of 0.65, outperforming the global restart strategy, which could only reach a fitness value of 5, making it a winner 9 out of 12 times across the benchmark functions. Furthermore, within the Greedy Local Restart strategy, Variant-B consistently demonstrated remarkable results in most cases winning 7 out of 12 times, along with Variant-A winning 2 times, making the total wins to 9 out of 12. By demonstrating the superiority of the QiEA variants with restart methods, this research highlights the significance of incorporating effective exploration strategies in evolutionary optimization algorithms.

7 Future Scope

The future scope of this work is to further fine-tune the parameters to improve their performance in the restart methods. Also, the combination of restart methods with other optimization techniques or metaheuristics may harness the complementary strengths of different approaches and improve overall optimization outcomes.

References

1. Shor, P.W.: Polynomial-time algorithms for prime factorization and discrete logarithms on a quantum computer. In: AT and T Research. IEEE Computer Society Press (1995)
2. Jiang, S., Britt, K.A., McCaskey, A.J., Humble, T.S., Kais, S.: Quantum annealing for prime factorization. Sci. Rep. **8**(1), 17667 (2018). https://doi.org/10.1038/s41598-018-36058-z
3. Adleman, L., Rivest, R. The use of public key cryptography in communication system design. IEEE Communications society magazine. **16**(6), 20–23. (1978) https://doi.org/10.1109/MCOM.1978.1089778
4. Moore, M., Narayanan, A.: Quantum-inspired computing. technical report, department of computer science. (1995)
5. Shor, P.W.: Algorithms for quantum computation: discrete logarithms and factoring. Proceedings 35th Annual Symposium on Foundations of Computer Science, 124–134. (1994) https://doi.org/10.1109/SFCS.1994.365700

6. Han, K.-H., Kim, J.-H.: Quantum-inspired evolutionary algorithm for a class of combinatorial optimization. IEEE Trans. Evol. Comput. **6**(6), 580–593 (2002). https://doi.org/10.1109/TEVC.2002.804320
7. Zhang, G.: Quantum-inspired evolutionary algorithms: a survey and empirical study. J. Heuristics **17**(3), 303–351 (2011). https://doi.org/10.1007/s10732-010-9136-0
8. Chen, S.: Quantum-Behaved Particle Swarm Optimization with Weighted Mean Personal Best Position and Adaptive Local Attractor. Information **10**(1), 22 (2019). https://doi.org/10.3390/info10010022
9. Talbi, H., Draa, A.: A new real-coded quantum-inspired evolutionary algorithm for continuous optimization. Appl. Soft Comput. **61**, 765–791 (2017). https://doi.org/10.1016/j.asoc.2017.07.046
10. Zhang, G., Ma, W., Xing, K., Xing, L., Wang, K.: Quantum-inspired distributed memetic algorithm. Complex System Modeling and Simulation. **2**(4), 334–353. (2022) https://doi.org/10.23919/CSMS.2022.0021
11. Bujok, P., Kolenovsky, P.: Eigen crossover in cooperative model of evolutionary algorithms applied to CEC 2022 Single Objective Numerical Optimisation (2022)
12. Biedrzycki, R., Arabas, J., Warchulski, E.: A Version of NL-SHADE-RSP Algorithm with Midpoint for CEC 2022 Single Objective Bound Constrained Problems. IEEE Congr Evol Comput (CEC) **2022**, 1–8 (2022). https://doi.org/10.1109/CEC55065.2022.9870220
13. Stanovov, V., Akhmedova, S., Semenkin, E.: NL-SHADE-RSP Algorithm with Adaptive Archive and Selective Pressure for CEC 2021 Numerical Optimization. IEEE Congress on Evolutionary Computation (CEC) **2021**, 809–816 (2021). https://doi.org/10.1109/CEC45853.2021.9504959
14. Di Carlo, M., Vasile, M., Minisci, E.: Multi-population inflationary differential evolution algorithm with Adaptive Local Restart. IEEE Congr Evol Comput (CEC) **2015**, 632–639 (2015). https://doi.org/10.1109/CEC.2015.7256950
15. Cuccu, G., Gomez, F., Glasmachers, T.: Novelty-based restarts for evolution strategies. IEEE Congr Evol Comput (CEC) **2011**, 158–163 (2011). https://doi.org/10.1109/CEC.2011.5949613
16. Jansen, T.: On the analysis of dynamic restart strategies for evolutionary algorithms 33–43 (2002) https://doi.org/10.1007/3-540-45712-7_4
17. Zhang, Y.-X., Gou, J.: Adaptive differential evolution algorithm based on restart mechanism and direction information. IEEE Access **7**, 166803–166814 (2019). https://doi.org/10.1109/ACCESS.2019.2953776
18. Dubois, A., Dehos, J., Teytaud, F.: Improving multi-modal optimization restart strategy through multi-armed bandit. 2018 17th IEEE International Conference on Machine Learning and Applications (ICMLA), 338–343. (2018) https://doi.org/10.1109/ICMLA.2018.00057
19. Zhang, Y., Wu, L.: A robust hybrid restarted simulated annealing particle swarm optimization technique. In: advances in computer science and its applications **5**, (1) (2012). www.worldsciencepublisher.org
20. El-Mihoub, T.A., Nolle, L., Tholen, C., Aref, I., Paulenz, I.: Multi-start, random reselection of algorithms or both? 2022 IEEE 2nd International Maghreb Meeting of the Conference on Sciences and Techniques of Automatic Control and Computer Engineering (MI-STA), 21–26. (2022) https://doi.org/10.1109/MI-STA54861.2022.9837625
21. Wang, J., Li, C., Zeng, S., Yang, S. History-guided hill exploration for evolutionary computation. IEEE transactions on evolutionary computation, 1–1. (2023) https://doi.org/10.1109/TEVC.2023.3250347
22. Kumar, A., Price Kenneth, V., Mohamed, A.W., Hadi Anas, A., Suganthan, P.N.: Problem definitions and evaluation criteria for the CEC 2022 special session and competition on single objective bound constrained numerical optimization. (2021)

ANN Based Control Strategy for Automatic Generation Control of an Interconnected Power Systems

Omveer Singh and Shreya Chaudhary

Abstract Automatic generation control of a two-area power network in an interconnection system is considered. The most effective controller is determined by comparing the performance of three controllers: Proportional-Integral (PI), Proportional-Integral-Derivative (PID), and Artificial Neural Network (ANN) controllers. For the analysis and evaluation of system frequency and tie-line power deviations, MATLAB/Simulink is utilized. Rise time, settling time, overshoot, undershoot, and slew rate are evaluated and compared for both frequency deviation and tie-line power responses. The comprehensive simulation results, supported by tables and bar graphs, indicate that the ANN controller outperforms the classical controllers in terms of faster response, enhanced damping of system oscillations, reduced settling time, enhanced accuracy, and efficient power transfer. The bar graphs further emphasize the superiority of the ANN controller in terms of frequency deviation and tie-line power response parameters by providing visual representations of the data. This study contributes to the comprehension and advancement of AGC control strategies in interconnected power networks by highlighting the potential of ANN controllers to achieve greater stability and faster, more precise regulation. For further improvement, future research directions include optimizing the ANN controller's hyperparameters and investigating advanced neural network approaches such as ReLU activation functions. The combination of quantitative analysis and visual representations provides a comprehensive evaluation of controller performance in AGC applications, thereby facilitating well-informed power system control decisions.

Keywords AGC · ANN · Controller · MATLAB/Simulink · System frequency deviation · Tie-line power deviation

O. Singh (✉) · S. Chaudhary
Department of Electrical Engineering, Gautam Buddha University, Greater Noida 201312, India
e-mail: omveers@gmail.com

© The Author(s), under exclusive license to Springer Nature Singapore Pte Ltd. 2025

H. P. Singh et al. (eds.), *Recent Developments in Control, Automation and Power Engineering*, Lecture Notes in Electrical Engineering 1303,
https://doi.org/10.1007/978-981-96-0047-2_20

1 Introduction

As the complexity of interconnected power systems has increased over time, automatic generation control (AGC) mechanisms have become more essential than ever [1]. In real-world power systems, load demands are in a constant state of flux and can change at any time. Power system disturbances, such as sudden shifts in the amount of load, can cause variations in the amount of power that is interchanged between tie-lines and the area frequency. There is frequently a disparity between the amount of power that is actually generated and the amount that was planned to be generated [2]. This is because physical limitations make it difficult for generators to respond quickly to changes in load. An AGC system must be installed in order to reduce frequency deviations and maintain power transfer between different regions [3]. This is necessary in order to ensure that power systems that are interconnected operate with a constant frequency and a consistent power supply. The scheduling method known as automatic generation control, or AGC, modifies the power outputs of generators within a given region in response to changes in network frequency and tie-line power [4, 5].

The network frequency and tie-line power are kept within the limits using this technique. Numerous control strategies had to be developed in order to maintain network frequency and tie-line power transfer. This called for a wide range of control methods. Conventional control theory underpins the AGC that commands the largest share of the market. These traditional methods of control have been the subject of extensive investigation in a number of research studies [6–9]. Integral controllers that are effective at removing steady-state deviations have been found to be ones that can be implemented with a relatively low degree of complexity. On the other hand, their dynamic response properties are frequently below average. One of the drawbacks of these controllers is that, despite the fact that power systems can function in a wide variety of operating conditions; the gain values they provide are always the same. Due to this disparity, conventional controllers are rendered ineffective across a wide range of operational conditions. AGC also works to ensure that the behavior of the network during transitions is stable and that errors do not occur during steady-state operations. Control systems that are based on artificial intelligence (AI) have demonstrated that they have the potential to overcome these challenges.

A number of AI-based techniques for improving AGC performance have been presented in recent publications. Neural networks [3], fuzzy control methods [6], and optimization techniques based on bacterial foraging [7] are some examples of the techniques that fall under this category. The effectiveness of ANN-based techniques for automatic generation control is investigated in this study. These control techniques are contrasted with more traditional methods to assess their efficacy [5]. In this study, we explore whether an ANN-based control system can enhance an AGC's functionality. It evaluates using MATLAB/Simulink. You can review results and assess control strategies using this software. This study examined the potential advantages and effectiveness of implementing artificial intelligence (AI) in AGC for networked power systems. The benefits and effectiveness of these techniques are

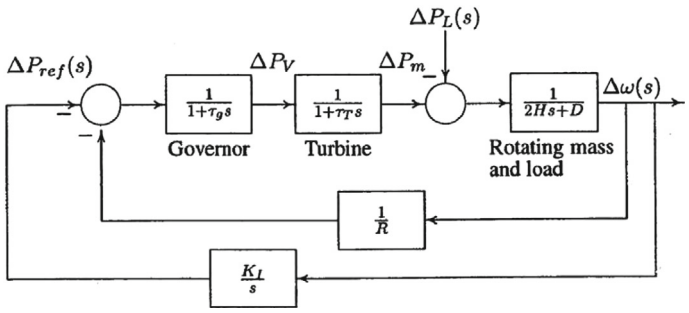

Fig. 1 Single-area power system model

both examined in this study. Authors contrasted the PI, PID, and ANN-based control strategies in order to achieve this goal. The effectiveness and potential advantages of using AI techniques for automatic generation control, or AGC, are assessed in this study.

2 Frequency Response Modeling

It is necessary to mathematically model each component of power systems in order to investigate their dynamics. Transfer functions are used in this model [4].

Figure 1 depicts the complete block diagram for load frequency control (LFC) of a power supply, which can be created by combining the block diagrams of each component. The speed of turbines in power systems can vary based on the system's load. To maintain system speed, the governor can adjust the input to the turbine. It is essential to remember that sporadic changes will occur, so constant speed updates are unnecessary. Consequently, it is essential to implement a control mechanism to precisely manage the generator and set its speed or frequency to a standard value. Figure 1 provides a visual representation of this control configuration.

3 Automatic Generation Control of an Interconnected Power System

The recommended control model for a power system that serves two areas is depicted in Fig. 2. This model makes use of two-area conventional energy generation sources, and distributes them across the two locations. The areas are connected to one another through a tie-line, which enables power sharing between Area 1 and Area 2 in order to more effectively meet the load demands of consumers.

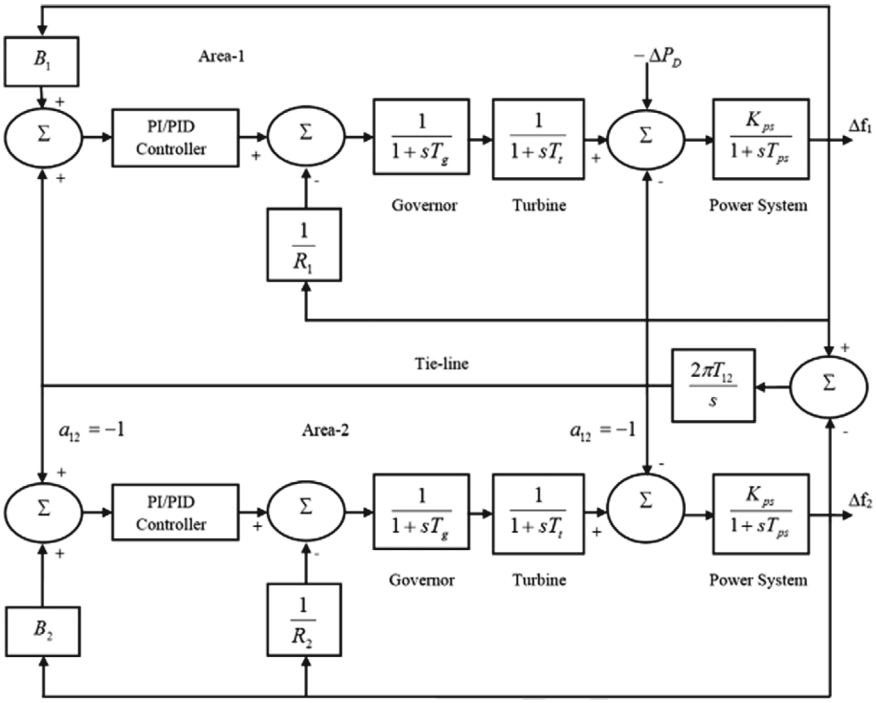

Fig. 2 Two-area power system model block diagram

In Area 1, the thermal unit generates energy by using geothermal heat. A distribution pattern analogous to the one in Area 2 can be found with the corresponding energy sources. The tie-line acts as a connecting element, bringing together and integrating the two distinct regions. This tie-line makes it possible to trade power with the other location, which maintains a consistent level of power delivery to both locations. When there is a shift in the load that is being carried by one of the regions, it is the responsibility of the respective power system to make the necessary adjustments. Adjustments are made to the flow of power through the tie-line in situations where the power system serving the respective area is unable to adequately handle the change in load. These adjustments are made in order to maintain load balance and stability. The model that has been proposed for the two-area power system can be seen in Fig. 2. This model includes a secondary control loop. This model takes into account the varying loads in each section and attempts to regulate and optimize the flow of power in accordance with those changes so that the system continues to function effectively.

4 ANN-Based Controller

Artificial neural networks, also known as ANNs, are highly effective computing systems that simulate the way in which the human brain works. Neurons are interconnected nodes in a network that carry out data processing and analysis. ANN-based controller structure is in Fig. 3.

Control is being provided by ANNs within the framework of this research work. This investigation makes use of a particular form of ANN control known as the NARMA L2 controller, which stands for Nonlinear Autoregressive Moving Average, Level 2. The nonlinearities and dynamic behaviors exhibited by nonlinear systems inspired the development of the NARMA L2 controller, which was designed to address these issues. The trajectory of the system can be successfully controlled by the controller if the complex systems being used are first translated into implicit algebraic models. f and g are the names of the two sub-networks that make up the structure of the NARMA L2 controller.

When developing a precise neural controller model, it is essential to pay careful attention to all of the components, including inputs, delayed inputs, outputs, and hidden layers. It is imperative that the size of the neural network's hidden layers be optimized if it is to provide an accurate approximation of the nonlinearity of the system. Estimating the nonlinear functions f and g, which are then used to train the NARMA L2 controller, requires a set of input–output data pairs, which are used in the estimation process. In order to produce a control system that is both effective and efficient, the controller will rearrange the plant model sub-networks. Figure 4 is a diagram of a closed-loop system that illustrates the interactions that take place between the NARMA L2 controller and the system or plant that is being controlled.

In this particular investigation, the inputs for the ANN control are the system frequency deviation, the tie-line transfer power deviations, and the load disturbances. These parameters are required in order to achieve a level of control that is both precise and effective. The NARMA L2 controller is able to effectively regulate the system and ensure stable, optimal performance because it monitors and adjusts these inputs. MATLAB/Simulink model of the complete system is presented in Fig. 5.

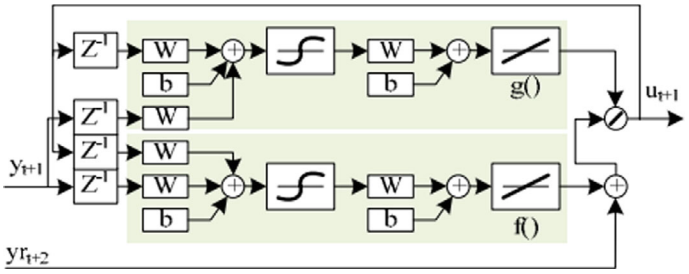

Fig. 3 ANN-based controller structure

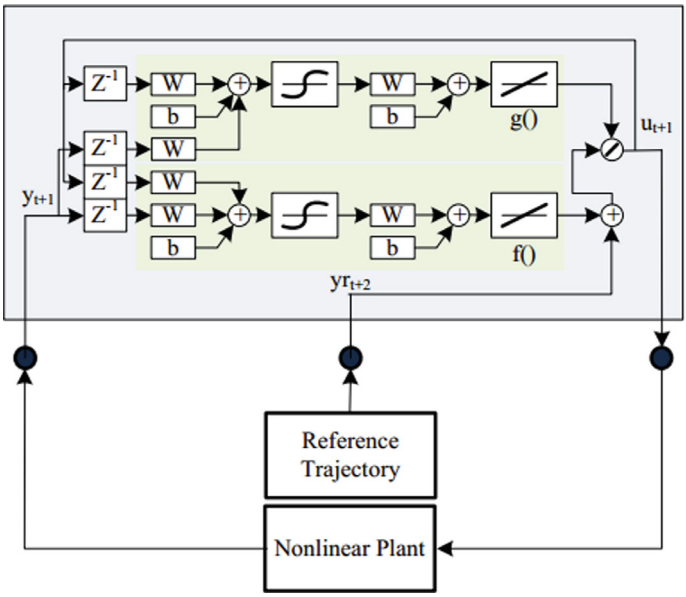

Fig. 4 Closed-loop system of ANN controller structure

5 Simulation Results and Discussions

This study focuses on the AGC of a two-area power network in an interconnection system. Three different controllers, namely PI, PID, and ANN controllers, are implemented for AGC control. The objective is to compare the performance of these controllers. To analyze the results from Figs. 6, 7, 8, and 9, the MATLAB/Simulink software is utilized. For each scenario, the study evaluates the responses of the system frequency and tie-line transfer power deviations. These parameters provide valuable insights into the effectiveness and efficiency of the implemented controllers. Through careful examination and comparison, the study aims to identify the controller that exhibits the most desirable performance in regulating system frequency and managing power deviations in the tie-line (Tables 1, 2 3, and 4).

These figures provide a clear visualization of the superior performance of the ANN controller in terms of faster response, reduced settling time, improved damping, and more accurate regulation of frequency and power deviations. In conclusion, the comprehensive analysis and comparison of the results, as supported by tables confirm that the ANN controller surpasses the classical PI and PID controllers in the AGC of the two-area power network. The ANN controller exhibits faster response, improved damping of system oscillations, reduced settling time, enhanced accuracy, and efficient power transfer. The visual representations provided by the bar graphs further emphasize the superiority of the ANN controller.

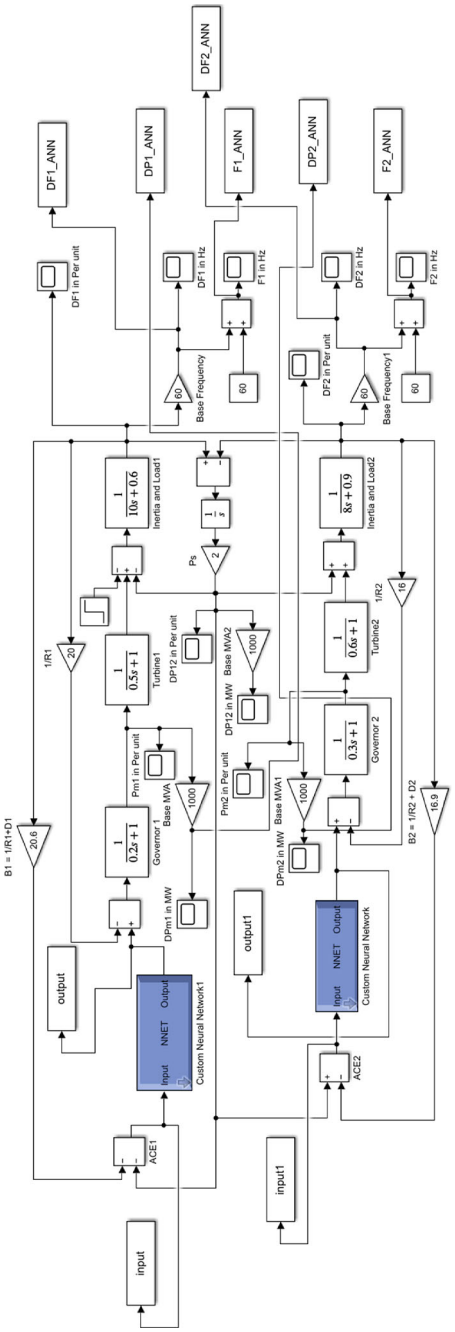

Fig. 5 MATLAB/Simulink model of the complete system

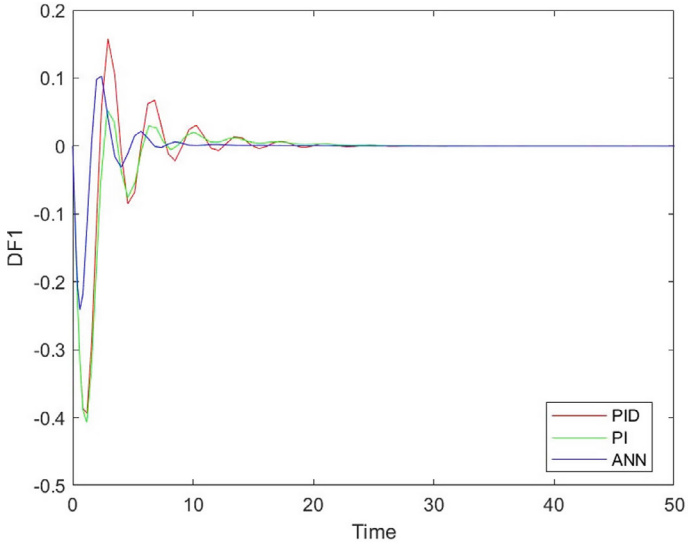

Fig. 6 Change in frequency response for Area-1

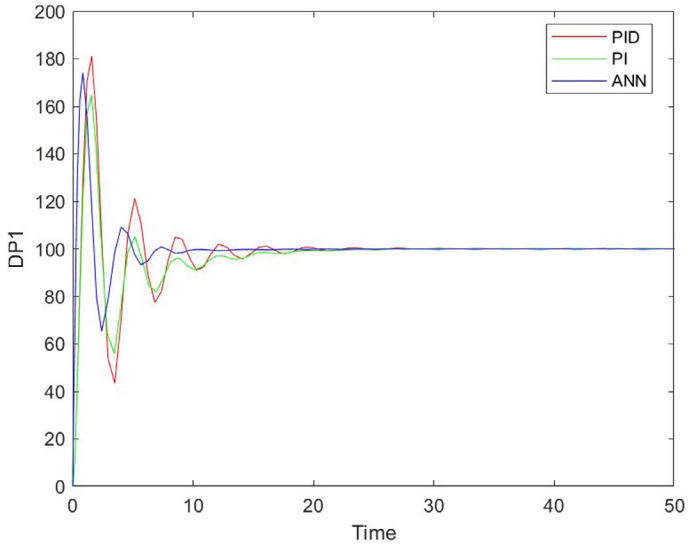

Fig. 7 Tie-line power flow (DP1) for Area-1

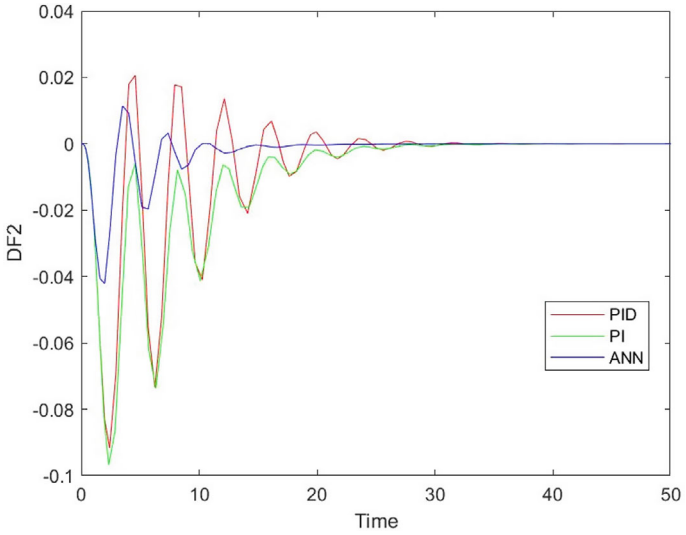

Fig. 8 Change in frequency response (DF2) for Area-2

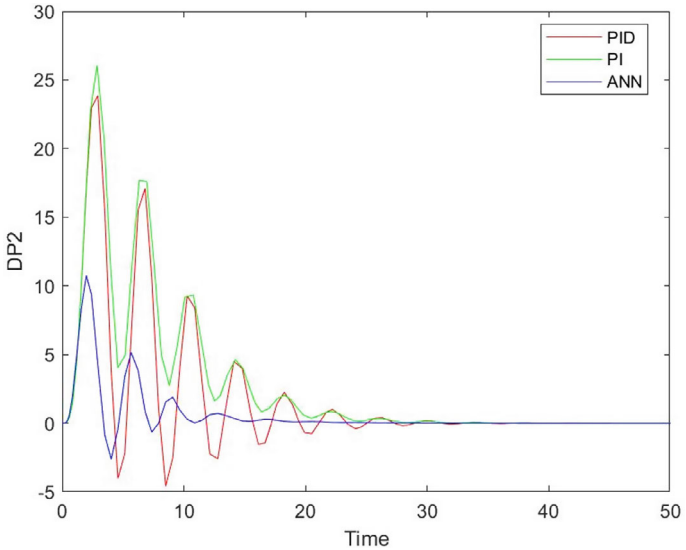

Fig. 9 Tie-line power flow (DP2) for Area-2

Table 1 Frequency deviation response for Area-1

Controllers	Rise time (ms)	Settling time	Overshoot (%)	Undershoot (%)	Slew rate (per sec)
PI	1012	33.240	13.068	18.728	5.335
PID	819.103	33.371	40.141	21.951	382.60
ANN	655.553	24.626	0.42143	0.02469	294.069

Table 2 Frequency deviation response for Area-2

Controllers	Rise time (ms)	Settling time	Overshoot (%)	Undershoot (%)	Slew rate (per sec)
PI	1336	48.521	0.88	3.614	56.082
PID	1011	53.149	22.84	80.535	71.997
ANN	854.744	38.369	27.564	45.306	39.103

Table 3 Tie-line power response of Area-1

Controllers	Rise time (ms)	Settling Time	Overshoot (%)	Undershoot (%)	Slew rate (per sec)
PI	485.652	38.213	65.833	20.622	162.828
PID	466.084	39.108	80.9	28.493	170.943
ANN	224.552	20.712	63.237	1.88	353.394

Table 4 Tie-line power response of Area-2

Controllers	Rise time (ms)	Settling Time	Overshoot (%)	Undershoot (%)	Slew rate (per sec)
PI	1001	48.733	48.507	77.646	13.963
PID	844.865	48.184	27.46	5.386	14.689
ANN	605.63	39.048	86.058	37.882	5.656

6 Conclusion

Based on the results obtained and the comparative analysis conducted, it can be concluded that the ANN controller outperforms the classical PI and PID controllers in the AGC of the two-area power network. The ANN controller exhibits several advantages that make it a superior choice:

i. Faster response: The ANN controller demonstrates faster rise time and settling time compared to the PI and PID controllers. It quickly adjusts and stabilizes the system frequency and tie-line power deviations.

ii. Improved damping of system oscillations: The ANN controller effectively dampens system oscillations, resulting in lower overshoots and undershoots. It provides more stable and precise regulation of frequency and power transfer.
iii. Reduced settling time: The ANN controller achieves the shortest settling time among the three controllers, indicating its ability to rapidly reach the desired steady-state operation.
iv. Enhanced accuracy: The ANN controller shows cases of minimal overshoot and undershoot, ensuring accurate control of system parameters and reducing the risk of instability.
v. Efficient power transfer: The ANN controller effectively manages tie-line power deviations, maintaining smooth power transfer between areas with reduced fluctuations.
vi. Promising adaptability: The ANN controller's adaptability allows it to handle complex and nonlinear control scenarios. It has the potential for further optimization and exploration of advanced techniques, such as ReLU activation functions.

References

1. Kundur, P.: Power system stability and control. McGraw-Hill Education, New York (1994)
2. Prakash, S., Sinha, S.K., Pandey, A.S., Singh, B. Impact of slider gain on load frequency control using fuzzy logic controller. ARPN J Eng and Appl Sci, **4**(7) (2009)
3. Patel, N., Jain, B.B.: Automatic Generation control of four area power systems using ANN controllers. Int. J. Elect. Electro. Comput. Eng **3**(1), 62–68 (2014)
4. Saadat, H.: Power system analysis. 6th edition, Tata McGraw-Hilledition. IEEE Committee Report. (1970). IEEE standard definitions of terms for automatic generation control of electric power system. IEEE transactions on power apparatus and systems, PAS-89, 1358–1364 (2002)
5. Prakash, S., Sinha, S.K.: Artificial intelligent and PI in load frequency control of interconnected power system. Int. J. Comput. Sci. Emerg. Technol **1**(4), 377–384 (2010)
6. Khan, C.M., Konar, S.C., Chanda, C.K.: Study of thermal generating units of multi-area power system connected to grid and its stability. Int. J. Recent Dev Eng Technol **2**(2), 55–65 (2014)
7. Kumar, A., Singh, O.: Recent strategies for automatic generation control of power systems with diverse energy sources. Int. J. Syst. Dynam. Appl. 10, Online: **26**, (2021) https://doi.org/10.4018/IJSDA.20211001.oa8.
8. Li, B., Chen, J.: Automatic generation control strategy based on deep forest. IEEE Access, **11**, 23495–23504. Online: (2023) https://doi.org/10.1109/ACCESS.2023.3254501.
9. Chen, J., Ding, D., Yuan, X, Liu, K. and Zhang, Y.: A fully non-interactive automatic generation control strategy for multi-area interconnected power systems. IEEE transactions on power systems. 1–1. Online: (2023) https://doi.org/10.1080/15325008.2023.2207572.

Discrete-Time Realization of Fractional-Order Proportional Integral Controller for First-Order Plus Time Delay Plant

Bhanita Adhikary and Jaydeep Swarnakar

Abstract This work focuses on discrete-time realization of fractional-order proportional integral (FOPI) controller for a class of first-order plus time delay (FOPTD) plant. The designing has been accomplished in three stages. The initial stage involves designing of the fractional-order controller in *s*-domain through an analytical method considering frequency domain design criteria. In the next stage, FOPI controller has been approximated in *s*-domain using Oustaloup method. At the final stage, Al-Alaoui approximation method has been employed to discretize the FOPI controller. The efficacy of the controller realization method has been examined by analyzing the frequency responses of the approximated system through simulation results.

Keywords Fractional-order controller (FOC) · First-order plus time delay (FOPTD) · Oustaloup approximation · Al-Alaoui approximation

1 Introduction

Physical phenomena often exhibit complex behavior which is not feasible to accurately describe using traditional integer-order models. As a result, there was a need of more flexible and comprehensive modeling framework. The non-integer-order calculus theory emerged as a powerful tool for such kind of modeling since seventeenth century [1, 2]. Fractional calculus still remains an effective field of research in many areas [3–5]. In control theory, there has been significant exploration for tuning of fractional-order controller (FOC) ever since the first proposal given by Podlubny [1, 6]. The FOCs are tuned in frequency domain based on certain design specifications namely phase crossover frequency, phase margin, gain crossover frequency, etc., so as to obtain a robust system [7, 8]. In literature [9–12], some of the analytical approaches of controller design are highlighted. The dynamics of many industrial

B. Adhikary · J. Swarnakar (✉)
Department of Electronics and Communication Engineering, School of Technology, North-Eastern Hill University, Shillong, Meghalaya 793022, India
e-mail: jaydeepswarnakar@gmail.com

© The Author(s), under exclusive license to Springer Nature Singapore Pte Ltd. 2025

H. P. Singh et al. (eds.), *Recent Developments in Control, Automation and Power Engineering*, Lecture Notes in Electrical Engineering 1303,
https://doi.org/10.1007/978-981-96-0047-2_22

plants can be approximately modeled using FOPTD system [10, 13]. The controlling of the FOPTD plant model is considered to be a challenging task in terms of maintaining the stability and robustness of the overall system. In this work, a frequency domain design approach has been presented to tune FOPI controller for a FOPTD plant model which aims at achieving a flat phase without computing any complex phase derivative expression equated to zero at specific frequency, unlike other analytical approach [13, 14]. Nevertheless, the FOC involves non-integer-order term, s^{β} which requires suitable approximation. There are several continuous-time domain approximation techniques which provide precise fitting of FOC within a frequency limit, and the Oustaloup approximation is a popular approach in this regard [12, 15]. Additionally, for digital execution of FOC, discrete-time approximation is essential. Discretization rules are primarily s-domain to z-domain mapping [16, 17]. One of the most preferred operators is the Al-Alaoui operator. It is a hybrid scheme that involves linear combination of Tustin and Euler rule [18]. The preliminary objective of this work is to realize a discrete-time FOC and then analyze the simulation outcomes to establish the efficiency of the approximation method.

The paper has been well organized into four sections. Section 1 begins with the outline of FOC. Section 2 includes the entire design procedure to realize a discrete-time controller followed by simulations and results in Sect. 3. The final work is summarized in Sect. 4.

2 Designing Methodology of FOPI Controller

A typical first-order plus time delay plant is considered as below:

$$P(s) = \frac{K}{1 + Ts} e^{-\tau s}. \tag{1}$$

The transfer function of FOPI controller is given as follows:

$$C(s) = K_p + \frac{K_i}{s^{\beta}}. \tag{2}$$

On combining fractional-order controller with the plant model, the following open-loop transfer function (OLTF) is obtained:

$$G(s) = P(s) \times C(s) = \frac{Ke^{-\tau s}}{1 + Ts} \times \left(K_p + \frac{K_i}{s^{\beta}} \right). \tag{3}$$

The plant model requires fulfilling the following four frequency design criteria:

- Gain crossover frequency criterion:

$$|G(j\omega)|_{\omega=\omega_g} = |P(j\omega)C(j\omega)|_{\omega=\omega_g} = 1. \tag{4}$$

- Phase margin criterion:

$$\angle G(j\omega)|_{\omega=\omega_g} = \angle P(j\omega)C(j\omega)|_{\omega=\omega_g} = -\pi + \varphi_m. \tag{5}$$

- Gain margin criterion:

$$|G(j\omega)|_{\omega=\omega_p} = |P(j\omega)C(j\omega)|_{\omega=\omega_p} = 10^{|\mathrm{GM}|/20}. \tag{6}$$

- Phase crossover frequency criterion:

$$\angle G(j\omega)|_{\omega=\omega_p} = \angle P(j\omega)C(j\omega)|_{\omega=\omega_p} = -\pi. \tag{7}$$

The tuning procedure is based on loop shaping approach known as frequency frame method [13, 14]. It gets its name from the rectangular frame that is created on considering the four constituents, namely gain cross over frequency (ω_g), phase cross over frequency (ω_p), phase margin at a desired ω_g, and gain margin at desired ω_p. The prime objective of this work is to maintain a flat phase characteristics so as to retain system's robustness despite any variations in the plant gain. Unlike other analytical method, it does not use phase derivative expression equated to zero at a specific frequency in order to obtain the flat phase. Rather, it uses four basic criterions that make the calculation comparatively easier without affecting the robustness. The criterions can be described mathematically as given below:

$$|G(j\omega)|_{\omega=\omega_g} = \sqrt{\left.\frac{K^2\left\{\left(K_p + K_i\omega^{-\beta}\cos(\beta\pi/2)\right)^2 + \left(K_i\omega^{-\beta}\sin(\beta\pi/2)\right)^2\right\}}{1+(T\omega)^2}\right|_{\omega=\omega_g}} = 1. \tag{8}$$

$$\begin{aligned}\angle G(j\omega)|_{\omega=\omega_g} &= -\tan^{-1}(T\omega) - \tau\omega - \tan^{-1}\left.\left(\frac{K_i\omega^{-\beta}\sin(\beta\pi/2)}{K_p + K_i\omega^{-\beta}\cos(\beta\pi/2)}\right)\right|_{\omega=\omega_g}. \\ &= -\pi + \varphi_m\end{aligned} \tag{9}$$

$$\begin{aligned}|G(j\omega)|_{\omega=\omega_p} &= \sqrt{\left.\frac{K^2\left\{\left(K_p + K_i\omega^{-\beta}\cos(\beta\pi/2)\right)^2 + \left(K_i\omega^{-\beta}\sin(\beta\pi/2)\right)^2\right\}}{1+(T\omega)^2}\right|_{\omega=\omega_p}}. \\ &= 10^{|GM|/20}\end{aligned} \tag{10}$$

$$\angle G(j\omega)|_{\omega=\omega_p} = -\tan^{-1}(T\omega) - \tau\omega - \tan^{-1}\left.\left(\frac{K_i\omega^{-\beta}\sin(\beta\pi/2)}{K_p + K_i\omega^{-\beta}\cos(\beta\pi/2)}\right)\right|_{\omega=\omega_p} = -\pi. \tag{11}$$

Reframing Eqs. (8) and (9), we obtain simpler expressions of controller parameters K_p and K_i in terms of gain crossover frequency and phase margin as:

$$K_p = \pm\frac{\sqrt{1+\left(T\omega_g\right)^2}}{K\sqrt{1+(\tan\varphi_1)^2}} \pm \frac{\sqrt{1+\left(T\omega_g\right)^2}}{K\sqrt{1+(\tan\varphi_1)^2}}\cot\left(\beta\pi/2\right)\tan\varphi_1. \tag{12}$$

$$K_i = \mp\frac{\omega_g^{\beta}\sqrt{1+\left(T\omega_g\right)^2}}{K\sqrt{1+(\tan\varphi_1)^2}}\csc\left(\beta\pi/2\right)\tan\varphi_1. \tag{13}$$

where $\varphi_1 = -\pi + \varphi_m + \tan^{-1}\left(T\omega_g\right) + \tau\omega_g$. Also, another set of expressions for K_p and K_i with respect to phase crossover frequency and its desired gain margin can be obtained by modifying Eqs. (10) and (11) as:

$$K_p = \pm\frac{10^{|\mathrm{GM}|/20}\sqrt{1+\left(T\omega_p\right)^2}}{K\sqrt{1+(\tan\varphi_2)^2}} \pm \frac{10^{|\mathrm{GM}|/20}\sqrt{1+\left(T\omega_p\right)^2}}{K\sqrt{1+(\tan\varphi_2)^2}}\cot\left(\beta\pi/2\right)\tan\varphi_2. \tag{14}$$

$$K_i = \mp\frac{10^{|GM|/20}\omega_p^{\beta}\sqrt{1+\left(T\omega_p\right)^2}}{K\sqrt{1+(\tan\varphi_2)^2}}\csc\left(\beta\pi/2\right)\tan\varphi_2. \tag{15}$$

where $\varphi_2 = -\pi + \tan^{-1}\left(T\omega_p\right) + \tau\omega_p$. Equating Eqs. (12) and (14), we obtain a curve that provides a relationship between β and $10^{|\mathrm{GM}|/20}$. Similarly, another curve is obtained by equating Eqs. (13) and (15). On plotting both the curves, value of β can be determined graphically from the point of intersection of the two curves. Using the intersection point, K_p and K_i can be calculated either using Eqs. (12) and (13) or Eqs. (14) and (15). Once the design of continuous-time FOPI controller is completed, the open-loop response, $G_{\mathrm{OL}}(s)$, is plotted to validate the desired design criteria.

The fractional-order controller requires proper approximation. To this aim, Oustaloup approximation is employed for a frequency interval (ω_b, ω_h). The N^{th} order approximation of $s^{\beta}(0 < \beta < 1)$ is formulated as [15]:

$$s^{\beta} = K'\prod_{i=1}^{N}\frac{s+\omega_i'}{s+\omega_i}. \tag{16}$$

where $\omega_u = \sqrt{\omega_h\omega_b^{-1}}$, $\omega_i = \omega_b\omega_u^{(2i-1+\beta)/N}$, $\omega_i' = \omega_b\omega_u^{(2i-1-\beta)/N}$, and $K' = \omega_h^{\beta}$.

The approximated counterpart $G_{\mathrm{OL}}'(s)$ is plotted together with $G_{\mathrm{OL}}(s)$ for comparison. Likewise, the rationalized FOPI controller is discretized for a known sampling time (Δ) using the Al-Alaoui operator to get $C_D(z)$. The operator is mathematical expressed as given below [18]:

$$s = \frac{8}{\Delta 7}\left(\frac{z-1}{z+1/7}\right). \tag{17}$$

The discretized OLTF is then calculated as $G_D(z)$. The frequency responses of $G_{\mathrm{OL}}(s)$ and $G_D(z)$ are compared from simulation results.

3 Simulations and Results

Considering $\tau = 0.01$ s, respective FOPTD plant is given as below [13]:

$$P(s) = \frac{1}{1+0.4s}e^{-0.01s}. \tag{18}$$

The frequency domain criteria are specified as $\omega_g = 10$ rad/s, $\omega_p = 150$ rad/s, and $\varphi_m = 60°$. On substituting these values in the related equations and plotting the two curves, we obtain $\beta = 0.8706$ at the point of intersection as seen in Fig. 1. Subsequently, values of $K_p = 2.7086$ and $K_i = 19.37$ are computed.

Hence, the designed FOPI controller is given as:

$$C(s) = \left(2.7086 + \frac{19.37}{s^{0.8706}}\right). \tag{19}$$

The OLTF is written as follows:

$$G_{\mathrm{OL}}(s) = P(s) \times C(s) = \left(\frac{1}{1+0.4s}e^{-0.01s}\right) \times \left(2.7086 + \frac{19.37}{s^{0.8706}}\right). \tag{20}$$

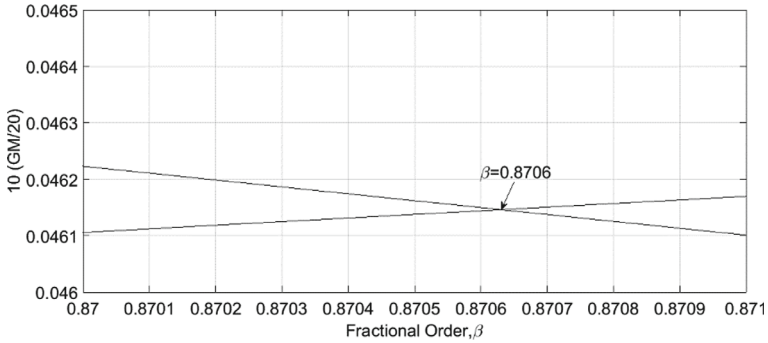

Fig. 1 Plot of β versus $10^{|GM|/20}$

Since Eq. (19) possesses a fractional term $s^{0.8706}$, it undergoes fifth-order ($N = 5$) approximation using Oustaloup method for the interval (0.001 ~ 1000) rad/sec.

$$s^{0.8706} \approx \frac{\begin{array}{c}409.1s^5 + 3.294 \times 10^4 s^4 + 1.574 \times 10^5 s^3 + 4.729 \times 10^4 s^2 \\ + 892.6s + 1\end{array}}{\begin{array}{c}s^5 + 892.6s^4 + 4.729 \times 10^4 s^3 + 1.574 \times 10^5 s^2 \\ + 3.294 \times 10^4 s + 409.1\end{array}}. \tag{21}$$

Therefore, approximated FOPI controller is given as follows:

$$C(s) \approx \frac{\begin{array}{c}1127s^5 + 1.065 \times 10^5 s^4 + 1.342 \times 10^6 s^3 + 3.178 \times 10^6 s^2 \\ + 6.405 \times 10^5 s + 7926\end{array}}{\begin{array}{c}409.1s^5 + 3.294 \times 10^4 s^4 + 1.574 \times 10^5 s^3 + 4.729 \times 10^4 s^2 \\ + 892.6s + 1\end{array}}. \tag{22}$$

The integer-order approximant of $G_{\mathrm{OL}}(s)$ denoted by $G_{\mathrm{OL}}{}'(s)$ is then obtained from above Eq. (21) as follows:

$$G'_{\mathrm{OL}}(s) \approx \frac{\begin{array}{c}1127s^5 + 1.065 \times 10^5 s^4 + 1.342 \times 10^6 s^3 + 3.178 \times 10^6 s^2 \\ +6.405 \times 10^5 s + 7926\end{array}}{\begin{array}{c}1.636s^7 + 299.5s^6 + 1.454 \times 10^4 s^5 + 9.768 \times 10^4 s^4 \\ +1.768 \times 10^5 s^3 + 4.765 \times 10^4 s^2 + 893s + 1\end{array}}. \tag{23}$$

Collectively, both the frequency responses $G_{\mathrm{OL}}(s)$ and $G'_{\mathrm{OL}}(s)$ are plotted and it is prominent from the Bode diagram of Fig. 2 that the desired $\omega_g = 10$ rad/s, $\omega_p = 150$ rad/s, $\varphi_m = (180° - 120°) = 60°$, and a specific GM = 26.7 dB have been attained. This illustrates that the integer-order approximation is properly carried out and successfully satisfies all the desired criteria.

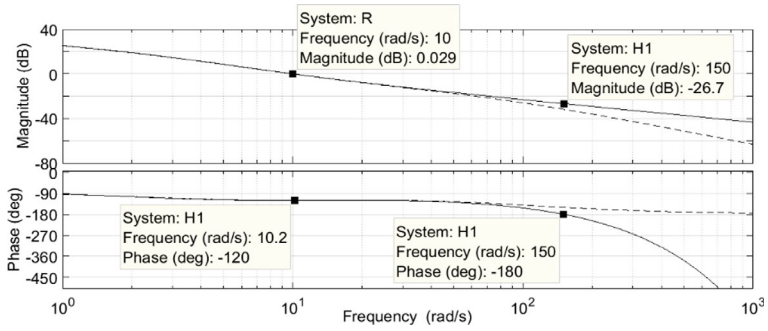

Fig. 2 Plot of $G_{\mathrm{OL}}(s)$ and $G'_{\mathrm{OL}}(s)$ with specified design criteria

Now, the discrete-time realization of the integer-order controller is executed using Al-Alaoui operator given by Eq. (17). For a sampling time $\Delta = 0.007$ s, the $s^{0.8706}$ term is discretized as follows:

$$s^{0.8706} \approx \left(\frac{8}{\Delta 7}\right)^{0.8706} \times \left(\begin{array}{c} 2.633 \times 10^7 z^5 - 4.789 \times 10^7 z^4 + 2.03 \times 10^7 z^3 + 2.472 \times 10^6 z^2 \\ -7.565 \times 10^5 z - 7.851 \times 10^4 \\ \hline 5.848 \times 10^7 z^5 - 9.098 \times 10^7 z^4 + 1.511 \times 10^7 z^3 + 1.596 \times 10^7 z^2 \\ +2.45 \times 10^6 z + 1.102 \times 10^5 \end{array} \right). \tag{24}$$

Using Eq. (24), the discretized FOPI controller is given as below:

$$C_D(z) \approx \left(\begin{array}{c} 7.154 \times 10^9 z^5 - 1.272 \times 10^{10} z^4 + 4.935 \times 10^9 z^3 + 8.746 \times 10^8 z^2 \\ -1.256 \times 10^8 z - 1.582 \times 10^7 \\ \hline 2.223 \times 10^9 z^5 - 4.044 \times 10^9 z^4 + 1.714 \times 10^9 z^3 + 2.088 \times 10^8 z^2 \\ -6.388 \times 10^7 z - 6.629 \times 10^6 \end{array} \right). \tag{25}$$

Subsequently, the respective discrete-time OLTF is computed as given below:

$$G_D(z) \approx \left(\begin{array}{c} 1.718 \times 10^7 z^7 - 2.562 \times 10^7 z^6 + 3.475 \times 10^6 z^5 + 4.862 \times 10^6 z^4 \\ +5.402 \times 10^5 z^3 - 8.128 \times 10^4 z^2 - 1.701 \times 10^4 z - 775.3 \\ \hline 9.317 \times 10^8 z^7 - 3.138 \times 10^9 z^6 + 3.861 \times 10^9 z^5 - 1.968 \times 10^9 z^4 \\ +2.372 \times 10^8 z^3 + 8.735 \times 10^7 z^2 - 1.059 \times 10^7 z - 1.545 \times 10^6 \end{array} \right). \tag{26}$$

The frequency responses of $G_D(z)$ and $G_{OL}(s)$ are plotted for $\Delta = 0.007$ s as shown in Fig. 3. It is observed that magnitude and the phase characteristics of $G_D(z)$ are converging reasonably with the ideal characteristics especially in the mid frequency range. Although there is some amount of deviation near the extreme limits, the phase fitting remains flat around ω_g.

Moreover to establish the robustness condition, frequency response of discretized OLTF is simulated by varying the plant gain up to 700%. It is witnessed in Fig. 4 that there is no change in phase characteristics and a flat phase around gain crossover frequency prevails, thereby verifying the robustness.

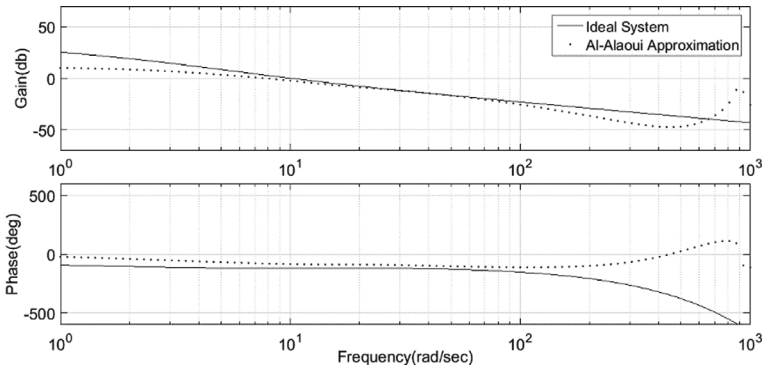

Fig. 3 Plot of $G_{\mathrm{OL}}(s)$ and $G_D(z)$ for $\Delta = 0.007$ s

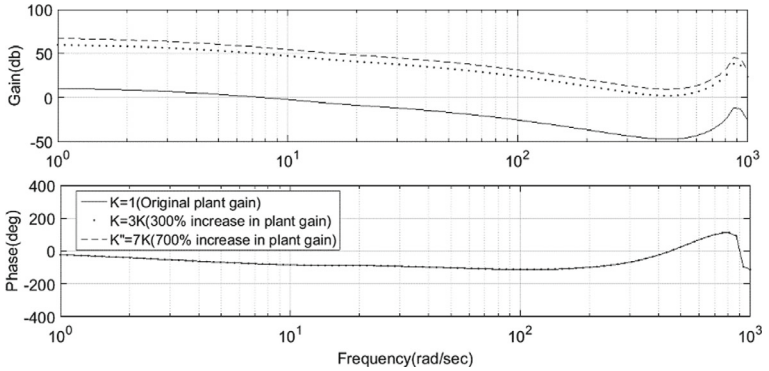

Fig. 4 Plot of $G_D(z)$ for three different plant gains

4 Conclusions

In this work, a discrete-time FOPI controller has been realized for a FOPTD plant. The design procedure is structured into three stages. The initial stage includes tuning of fractional-order controller to provide robustness by considering four design specifications. In the next stage, Oustaloup approximation is employed to obtain its equivalent integer-order controller. The approximated controller then undergoes discretization using Al-Alaoui operator in the final stage. Simulation results depict that the discretized controller almost resembles the ideal system for the mid frequency limit. Also, by varying plant gain, no change in phase characteristics is observed and flat phase prevails around gain crossover frequency indicating robust nature.

References

1. Dinh, T.N., Kamal, S., Pandey, R.K.: Fractional-order system: control theory and applications. Fractal Fractional **7**(48) (2023)
2. Sondhi, S., Hote, Y.V.: Fractional order controller and its applications: A review. In: Proceedings of the IASTED Asian Conference on Modelling, Identification and Control (AsiaMIC 2012), Phuket, Thailand (2012)
3. Rawat, H.K., Goyal, V., Kumar, J.: Comparative performance analysis of fractional-order nonlinear PID controller for NPK model of nuclear reactor. In: 2nd International Conference on Power Electronics AND IoT Applications in Renewable Energy and its Control (PARC), pp. 1–6, Mathura, India (2022)
4. Birs, I., Muresan, C., Nascu, I., Ionescu, C.: A survey of recent advances in fractional order control for time delay systems. IEEE Access **7**, 30951–30965 (2019)
5. Joshi, S.D., Talange, D.B.: Fractional order modeling and control of depth system of AUV-a case study. In: 2nd International Conference on Advances in Computer Science and Engineering Los Angeles, USA (2013)
6. Muresan, C.I., Birs, I., Ionescu, C., Dulf, E.H., De Keyser, R.: A review of recent developments in autotuning methods of fractional order controllers. Fractal Fractional **6**, 37 (2022)
7. Bayat, F.M.: General rules for optimal tuning the controllers with application to first-order plus time delay system. Can. J. Chem. Eng. **90**(6), 1400–1410 (2018)
8. Kumar, P., Chaudhary, S.K.: Stability analysis and fractional order controller design for control system. Int. J. Appl. Eng. Res. **12**(20), 10298–10304 (2017)
9. Chen, P., Luo, Y., Peng, Y., Chen, Y.: Optimal robust fractional order controller synthesis for first order plus time delay systems. ISA Trans. **114**, 136–149 (2021)
10. Ranjbaran, K., Tabatabaei, M.: Fractional order [PI], [PD] and [PI], [PD] controller design using bode's integrals. Int. J. Dyn. Control **6**(1), 200–212 (2018)
11. Yuce, A., Tan, N., Atherton, D.P.: Fractional order PI controller design for time delay systems. IFAC-PapersOnLine **49**(10), 94–99 (2016)
12. Swarnakar, J., Adhikary, B.: Band limited realization of fractional-order proportional integral controller for a class of finite dimensional system. In: Pandian, A., Ntalianis, K., Palanisamy, R. (eds.) Intelligent Computing, Information and Control Systems, ICICCS 2019, Advances in Intelligent Systems and Computing, vol. 1039, pp. 70–77, Springer Cham (2020)
13. Senol, B., Demiroglu, U.: Frequency frame approach on loop shaping of first order plus time delay systems using fractional order PI controller. ISA Trans. **86**, 192–200 (2019)
14. Demiroglu, U., Senol, B.: Frequency frame approach on tuning FOPI controller for TOPTD thermal processes. ISA Transactions (2020)
15. Oustaloup, A., Levron, F., Mathieu, B., Nanot, F.M.: Frequency band complex noninteger differentiator: characterization and synthesis. Trans. Circ. Syst. **47**, 25–39 (2000)
16. Stanislawski, R., Rydel, M., Li, Z.: A new reduced-order implementation of discrete-time fractional-order PID controller. IEEE Access **10**, 17417–17428 (2022)
17. Ogata, K.: Discrete-time control systems. Prentice-Hall, Inc. (1995)
18. Al-Alaoui, M.A.: Simulation and discretization of fractional order systems. In: Proceedings of the 2009 International Conference on Genetic and Evolutionary Methods, GEM, Las Vegas, USA (2009)

Energy Management System for Sustainable Energy Sources Using Hybrid Approaches

Mahesh Palavalasa, Shamik Chatterjee, and R. S. R. Krishnam Naidu

Abstract A growth in interest in the production of electric power from Renewable Energy Sources (RES) can be attributed to the resources of greenhouse emissions from centralised power plants. Even still, there are significant inconsistencies in their findings due to global warming, which is a major issue. This issue is resolved by developing a hybrid source that combines several different types of energy. Utilising an energy management system (EMS) will help meet demand, increase system efficacy and ensure hybrid systems driven by RES which are working to their full potential. This article provides a description of the Improved Tuna Swarm Optimization-based Modified Perturb and Observe (ITSO-MP&O) for Sustainable Energy Sources (Solar, Wind and Battery). This work uses MATLAB/Simulink to create a simulation-based integrated system model. It is based on fundamental conceptual flaws. According to the overall simulation results, the recommended ITSO-MP&O accomplishes a total harmonic distortion of 0.82%.

Keywords Energy management system · Improved tuna swarm optimization · Modified perturb and observe · Sustainable energy sources · Total harmonic distortion

1 Introduction

For the past few years, the mechanisms necessary to monitor, regulate and optimise the use of power are the focus of the most recent difficulties in EMS for smart grids [1]. A number of solutions have been developed recently to monitor RES and

M. Palavalasa (✉) · S. Chatterjee
School of Electronics and Electrical Engineering, Lovely Professional University, Punjab, India
e-mail: palavalasamahesh@gmail.com

R. S. R. Krishnam Naidu
Department of Electrical and Electronics Engineering, N S Raju Institute of Technology, Vishakhapatnam, India

© The Author(s), under exclusive license to Springer Nature Singapore Pte Ltd. 2025

H. P. Singh et al. (eds.), *Recent Developments in Control, Automation and Power Engineering*, Lecture Notes in Electrical Engineering 1303,
https://doi.org/10.1007/978-981-96-0047-2_23

manage data collection employing power control systems in response to the continually rising demand in the business, industry and residential areas [2]. Renewable energy-based substitutes to single-source networks are preferable. RES incorporation attempts to improve the structure and functionality of grid and lower carbon emissions by utilising more renewable energy, storage technologies, as well as other energy resources [3]. Actually, RES is skilled at enhancing the global system in a number of ways, including cost, power quality and capacity utilisation reduction. Energy sources in the past few decades have included solar, tidal, biomass and wave energy [4]. As a result, developments in the usage of sustainable energy systems have rapidly increased in recent decades. RES are additionally seen as a viable option for rural areas' need for electricity. It has been determined that solar and wind systems are the most promising ones. However, atmospheric factors including sun illumination, the outside temperature, air volume and wind velocity, among others, have an impact on the power produced [5].

Additionally, the amount of solar irradiation is lower during overcast conditions and missing at night. Furthermore, the nature of power output from a windmill is highly inconsistent. Most of these issues can be resolved by using a hybrid system, which increases reliability by compensating for one method's limitations with another [6]. A hybrid source is a combination of different sources that function in a coordinated and autonomous manner. Even yet, it becomes crucial to store extra power produced if all energy is to be sourced exclusively from RES [7]. The primary objective is to obtain reliable, sustained source at a certain voltage and frequency. Whenever producing electricity from RES is not feasible, stored energy is typically provided by a battery bank that charges in accordance with the used control system when excess power is generated [8]. A PV-wind combination may be enough to supply renewable energy in a grid-connected system. For a freestanding grid, however, an energy storage device is required to compensate for voltage and frequency variations [9]. The need for energy has grown steadily during the past few years. Modern technologies have predicted that buildings will have a variety of smart and eco-friendly architectural elements. Therefore, there is a need for research into smart grid technologies, a grid being a key component of those technologies. For the efficient, reliable deployment of RES, microgrid construction is essential [10]. The following is a list of the contributions to the study:

- In order to obtain the important duty cycle ratio in this investigation, ITSO-MP&O adjusted the step size. The grid's overvoltage problems are lessened by the higher voltage produced by greater duty cycle ratio.
- The ITSO-MP&O seeks to establish a better EMS in order to satisfy the expectations of an elevated need.
- The converter is switched on in order to manage the backup power sources and generate dependable energy.

Section 2 of this study adds the relevant work-based energy management system (EMS) among sources of renewable energy. The technique and arithmetic formulations utilised in suggested technique are described in Sect. 3. The assessment and

evaluation of the results are revealed in Sect. 4. Lastly, Sect. 5 delivers the research's conclusion.

2 Literature Review

Kavya Santhoshi et al. [11] exhibited artificial neural network (ANN)-based continuous provision of converter and battery in an arrangement that was supplied by a Z source converter and linked to the grid. ANN was used to manage the battery in order to increase its longevity and endurance. Consequently, the converted AC electricity was fed into the grid. The stable reference node's energy was eventually routed to an inverter. In addition, the system's shortcomings include slow tracking, low service standards and a failure to respond quickly to a range of circumstances.

An appropriate controller is included in the united RES-dependent grid that was designed by Padhmanabhaiyappan et al. [12]. The DC-DC was created using the MPPT, a converter through a translation ratio and AWOA utilised it to identify the optimal modification methods to minimise the energy gap among supplier and consuming. An additional capacitor is required by the system's converter in order to get the desired results.

A smart grid built on fractional-order proportional-integral-derivative (FOPID) approaches and a ground-breaking resource system management was developed by Ahmad Aziz et al. [13]. Battery-powered hybrid sources, wind and solar energy are all used in a grid. In order to maximise the quantity of power produced by RES while also improving grid voltage regulation, a sophisticated FOPID approach is being developed. However, the cost of computation increases since the parameters shift so frequently.

Meenakshi et al. devised an efficient energy transfer control approach for PV that incorporates functional and accounting tracking [14]. This paper introduces a realistic architecture for a Modified Flower Pollination Algorithm (MFPA) to improve steadiness. Unfortunately, the results were obtained by self-pollination, that was not the best method for essential reorganisation.

Satish Kumar et al. [15] established an efficient EMS in order to examine the system effectiveness for a modest hybrid supply chain. The primary objective is to supply the system with energy continuously under all operating conditions. Although it was still requested, it was more difficult to discern when the load was continually changing how efficiently RES delivered power.

With the use of MFPA and MP&O technique, Naidu et al. [16] have effectively proven an effective EMS. Reduced scaling factor is used by MFPA to extract more power through the PV panel. Then, it is used to raise step size, initialise more particles and restore the position of the components. In order to generate constant power from the hybrid model, MP&O technique is also utilised to activate the pulses of converter.

3 Proposed Method

A hybrid system combines solar, wind, an inverter, a battery, as well as various extra parts. There are several models of PV-wind combinations that are used in studies to meet load demand. Figure 1 displays the block diagram of suggested model. Its main purpose is to evaluate the data while analysing MPPT in a system of solar cells by different levels of brightness. It provides the necessary alternation for the significant variables. Variations in grid voltage and frequency are minimised by the control technique. The suggested mechanism regulates total power and determines either to deliver or collect reactive power in response to system oscillations.

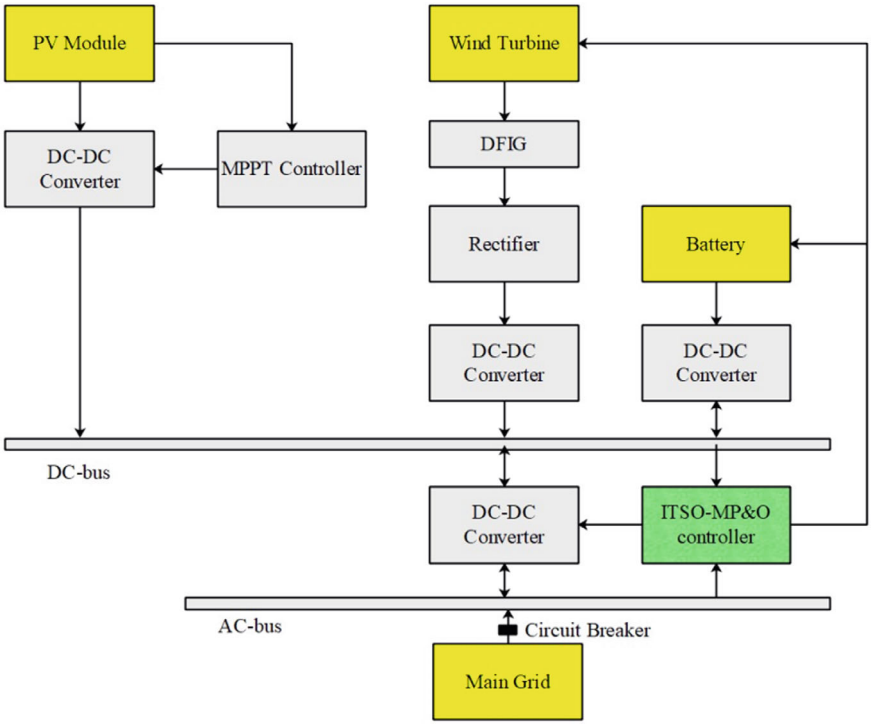

Fig. 1 Block diagram

3.1 Modelling of Sustainable Energy Sources

3.1.1 Photo-Voltaic

Isolated PV does not continuously provide useable electricity; PV systems depend on the weather. Single diodes are recommended for design and quantitative study. Destination, working conditions and rising temperatures are all important variables for PV power [16]. By interconnecting the panels, one may calculate the voltage and current. PV array uses the MPPT technology to raise the MPP.

3.1.2 Wind Energy

The scientific simulation of wind includes the designing of generators and wind turbine forces at work. For simulating, a wind generator with 3 blades and no repair costs was erected. The wind can be applied to determine the amount of power generated by a turbine. The efficiency is non-dimensional as an outcome of the tip-speed quantitative relationship. At a height of 1000 m, the air velocity in the ground's surroundings is supposed to be 14 m per second [17].

3.1.3 Battery

In the unlikely case that the combination system's power is insufficient, the battery is employed to supply load, regulate voltage and save additional energy. Battery size is motivated by humidity, maximum depth of discharge and endurance. It fills once there was a demand for energy generated by the sun and wind that exceeds the amount that is available [18]. The progression of discharge starts each time the load crosses the RES voltage limit.

3.2 Tuna Swarm Optimisation

A carnivorous fish called the tuna inhabits the ocean's surface. Even if a single tuna may swim more quickly, they cannot move as quickly as nimble fish. Therefore, tunas use the tactic of group movement for predation. These animals are renowned for using cunning and successful foraging techniques to locate and catch their prey. Tuna uses two different foraging techniques, including spiral foraging and parabolic foraging [19].

3.2.1 Initialisation

It is the initial phase of the majority of optimisation approaches. In TSO, the standard search space, which is theoretically defined in Eq. (1) as follows, is used to generate the initial inhabitants in a randomised fashion:

$$X_i^{\text{int}} = \text{rand} \times (u_b - l_b) + lb,\ i = 1, 2, \ldots, \text{NP}. \tag{1}$$

where X_i^{int} refers individual at the initial stage and the upper and the lower bounds are characterised as u_b and l_b correspondingly. NP stands for the total population of tuna. The term "rand" refers to the randomised vector, which is dispersed in a uniform space and falls between the values of 0 and 1.

3.2.2 Spiral Foraging

It is difficult for predators to lock their victims whenever a school of little fish changes course to protect them from them. Tuna hunts their prey by forming a spiral. Tuna transmit data to their neighbours after reaching their goal. Equation (2) presents this tuna technique numerically as follows:

$$X_i^{t+1} = \begin{cases} \alpha_1.(X_{\text{best}}^t + \beta.\left|X_{\text{best}}^t - X_i^t\right| + \alpha_2.X_i^t,\ i = 1 \\ \alpha_1.(X_{\text{best}}^t + \beta.\left|X_{\text{best}}^t - X_i^t\right| + \alpha_2.X_{i-1}^t, i = 2, 3, \ldots, \text{NP} \end{cases}. \tag{2}$$

The rate of α_1, α_2, β and l is calculated by means of the Eq. (3–6) as follows:

$$\alpha_1 = a + (1 - a).\frac{t}{t_{\max}}. \tag{3}$$

$$\alpha_2 = (1 - a) - (1 - a).\frac{t}{t_{\max}}. \tag{4}$$

$$\beta = e^{bl}.\cos(2\pi b). \tag{5}$$

$$l = e^{3\cos}(((t_{\max} + 1/t) - 1)\pi). \tag{6}$$

The optimistic individual at current location is characterised as X_{best}^t. The weighted coefficients α_1 and α_2 control the person in both the optimal state and the preceding state, respectively. A is the symbol for the constant that is used to identify the function of the tuna that tracks the upbeat person. The terms t and $t_{\max}$, accordingly, stand for the iteration at the current state and the maximum iterations. b is a representation of the random number, that is dispersed between 0 and 1. The tuna's capacity for exploitation increases as they spiral for food. However, it is unlikely that every fish in the school could be fed. Therefore, a randomised coordinate point is produced in

a spiral search to aid those doing a wider search, as shown in Eq. (7):

$$X_i^{t+1} = \begin{cases} \alpha_1.(X_{\text{rand}}^t + \beta.\left|X_{\text{rand}}^t - X_i^t\right| + \alpha_2.X_i^t,\ i = 1 \\ \alpha_1.(X_{\text{rand}}^t + \beta.\left|X_{\text{rand}}^t - X_i^t\right| + \alpha_2.X_{i-1}^t, i = 2, 3, .\text{NP} \end{cases}. \tag{7}$$

The randomly produced reference point is signified as X_{rand}^t. As a result, as the number of iterations increases, TSO modifies reference points from random to ideal values. Equation (8) shows the finalised solution for the spiral foraging strategy as below:

$$X_i^{t+1} = \begin{cases} \alpha_1.(X_{\text{best}}^t + \beta.\left|X_{\text{best}}^t - X_i^t\right| + \alpha_2.X_i^t,\ i = 1 \\ \alpha_1.(X_{\text{best}}^t + \beta.\left|X_{\text{best}}^t - X_i^t\right| + \alpha_2.X_{i-1}^t,\ i = 2, 3, \ldots, \text{NP, if rand} < \dfrac{t}{t_{\max}} \\ \alpha_1.(X_{\text{rand}}^t + \beta.\left|X_{\text{rand}}^t - X_i^t\right| + \alpha_2.X_i^t,\ i = 1 \\ \alpha_1.(X_{\text{rand}}^t + \beta.\left|X_{\text{rand}}^t - X_i^t\right| + \alpha_2.X_{i-1}^t,\ i = 2, 3, .\text{NP},\ \textit{if rand} \geq \dfrac{t}{t_{\max}} \end{cases}. \tag{8}$$

3.2.3 Parabolic Foraging

Tuna has a parabolic growth pattern and use mutual searching to find food sources. The tuna's two-process had a 50% chance of selection. This action is quantitatively expressed as follows in Eq. (9):

$$X_i^{t+1} = \begin{cases} X_{\text{best}}^t + \text{rand} \times \left(X_{\text{best}}^t - X_i^t\right) + \text{TF} \times p^2 \times \left(X_{\text{best}}^t - X_i^t\right), \text{if rand} < 0.5 \\ \text{TF} \times p^2 \times X_i^t, \text{if rand} \geq 0.5 \end{cases}. \tag{9}$$

The rate of $\rho = \left(1 - \frac{t}{t_{\max}}\right)^{(t/t_{\max})}$ and random number lies between 1 or − 1 which signified as TF. Each person reconstructs a location in search space depending on probability z by randomly choosing two foraging approaches. The people are updated and reviewed during the optimisation process till the ideal value is attained.

Each tuna will alternately use the spiral foraging approach during the iterative process of TSO. According to likely hood z, tuna also produce additional individuals in exploration area. Therefore, when creating new individual positions, TSO will select various methods based on z. All populations are continuously modified during runtime until a specific number of iterations has been reached. The TSO method then returns the ideal person in the population together with their ideal value.

3.2.4 Improved Tuna Swarm Optimization

It is critical to provide a stability among the swarm intelligence optimisation method's exploration capabilities and its own exploration capacity. The weight variables are crucial to the TSO algorithm. The weight factors α_1 and α_2 control how closely tuna individuals follow the most advantageous individual when using the spiral foraging method. This illustrates how the algorithm was optimised. Similar to this, the weight parameter p controls how closely average people follow the ideal individual in the parabolic foraging plan. The degree to which tuna follow the ideal individual is higher while the weight parameter is big, allowing the population as a whole to better explore the entire space. Conventional tuna individuals fail to mimic the ideal individuals when the weight factor is tiny. They will only swim in a limited portion of the area, allowing the common tuna to create a field surrounding it. To bring it up, shifts in weight factors affect the TSO's ability to explore and exploit new areas. It is clear that the linear shifts in the weight parameters α_1 and α_2 are present. The linear increases in the weight parameters α_1 and α_2 do not, nevertheless, accurately reflect the actual optimisation of the method since the TSO optimisation mechanism is so complicated. Many researchers now adapt nonlinear gains to enhance swarm capability and to overcome the shortcomings of linear weights. The nonlinear weight approach has a superior optimisation result than the linear weight strategy, according to numerous trials [20]. As a result, this work introduces two enhanced nonlinear weight variables, α_{1i} and α_{2i}. These are their algebraic models as mentioned in Eqs. (10) and (11):

$$\alpha_{1i}(t) = \alpha_{1\text{ini}} - (\alpha_{1\text{ini}} - \alpha_{1\text{fin}}).\sin\left(\frac{t}{\mu.T_{\text{Max}}}.\pi\right). \tag{10}$$

$$\alpha_{2i}(t) = \alpha_{2\text{ini}} - (\alpha_{2\text{ini}} - \alpha_{2\text{fin}}).\sin\left(\frac{t}{\mu.T_{\text{Max}}}.\pi\right). \tag{11}$$

$\mu = 2$, $\alpha_{1\text{ini}}$ means the initial rate of α_1; $\alpha_{1\text{fin}}$ signifies the final rate of α_1; $\alpha_{1\text{ini}}$ represents the initial rate of α_2; $\alpha_{2\text{fin}}$ refers the final rate of α_2; then associated the improved weight parameters α_{1i} and α_{2i} through the new α_1 and α_2. The improved weight characteristics α_{1i} and α_{2i} can clearly be seen to alter quickly in the early stages, which causes regular tuna fish to closely resemble the ideal person. It improves TSO's ability to explore the entire world. In the late stage, the weight parameters α_{1i} and α_{2i} alter gradually, allowing tuna individuals to explore their surroundings. It improves TSO's capacity to conduct local searches. A brand-new nonlinear weight parameter called p_i is introduced for the spiral foraging method. Here, its mathematical representation is stated in Eq. (12):

$$p_i(t) = p_{\text{ini}} - (p_{\text{ini}} - p_{\text{fin}}).\sin\left(\frac{t}{\mu.T_{\text{Max}}}.\pi\right). \tag{12}$$

Review the differences between the enhanced weight parameter p_i^2 and the baseline weight parameter p^2. A tuna individuals may track its prior individual with greater precision since gained parameter p_i^2 rapidly falls in previous stage. It improves TSO's ability to explore the entire world. In the final iteration, the revised weight parameter p_i^2 drops gradually, allowing tuna to swim to discover their surroundings. It improves TSO's capacity for local exploration.

4 Result and Discussion

The results and computations of the study are validated by MATLAB coding. MATLAB R2020a is used in the development and evaluation of the ITSO-MP&O coupled to HRES. It features an Intel Core i5 processor with 8 GB of RAM and Windows 10 as its software. An analysis of the proposed approach with conventional methods has been done, and outcomes demonstrate that ITSO-MP&O is more effective. Most of the works now in existence have suggested the optimal hybrid system modelling to save costs by taking into account the dependability restrictions. The results achieved showed that as system reliability rises, costs inevitably rise as well. In order to achieve the maximum amount of hybrid systems, it is crucial to select a suitable method with high convergence speed and accuracy. In order to address the aforementioned concerns, ITSO-MP&O is chosen in this study since it is ideal for optimisation problems with discrete variables.

The recommended system is proven to have a mitigating impact during various light radiation using the ITSO-MP&O. Figure 2 shows a Simulink illustration of the proposed model. The following components are present in Fig. 2; they are PV, Wind, Battery, grid, converter, inverter, controller (ITSO-MP&O), scope and other libraries which connecting all the blocks in the Simulink model. The wind energy is produced with the help of wind speed, height and blades rotation. In case of failure in the both the PV and wind, battery source will come into the action. These three processing are controlled by the method name called ITSO-MP&O. The wind and batteries are delivered in their ON/OFF states according to the duty cycle from the MP&O and uninterruptedly changed till the network attains MPP by using ITSO. Using proper step size, the rate of duty cycle could be changed, permitting the PV to benefit from a better position and draw power from the grid. Every step of the modelling approach involves an evaluation of the proposed efficacy. The design was evaluated using a range of situations, configurations of energy sources and user types.

4.1 Voltage and Current of MPPT

The measurements for MPPT are shown in Figs. 3 and 4. The results show that, in terms of MPPT efficacy, the suggested ITSO-MP&O control operates better than the conventional techniques. As seen in the Figures, the recommended ITSO-MP&O

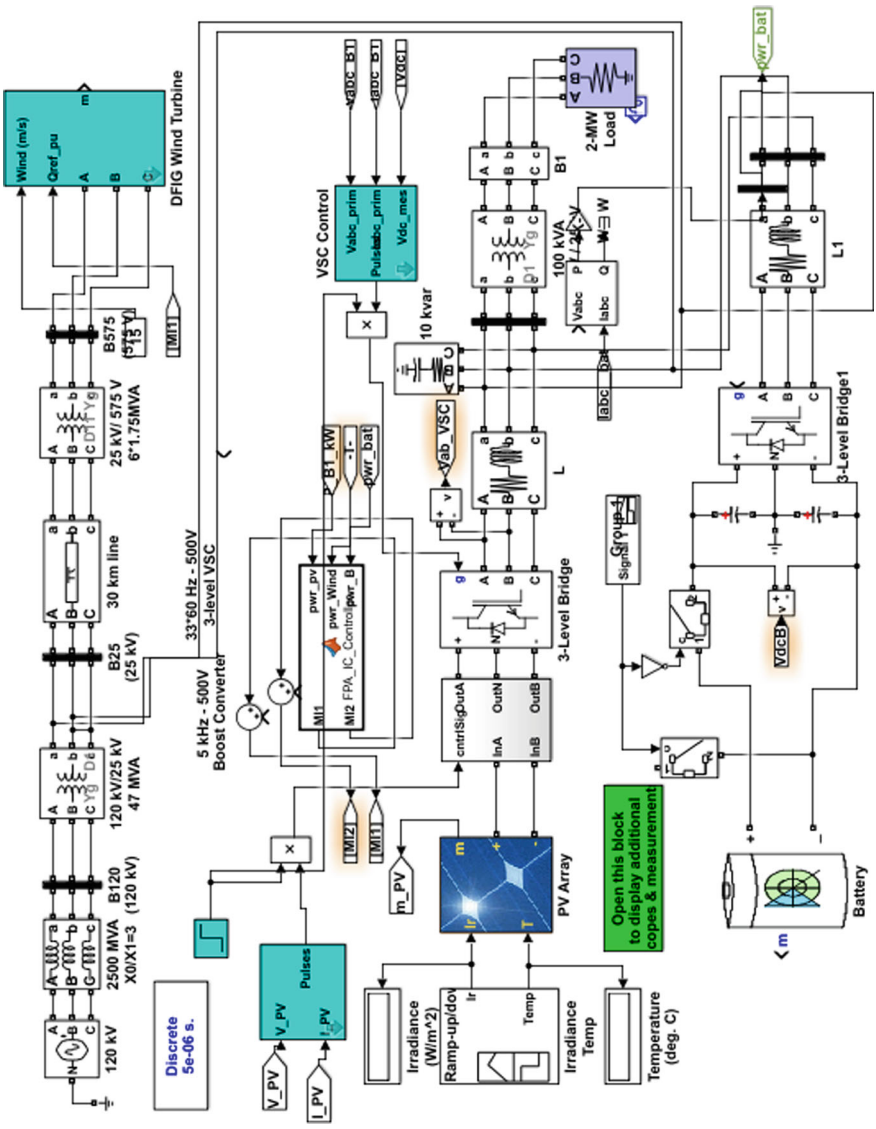

Fig. 2 Representation of proposed method in MATLAB Simulink

Fig. 3 MPPT voltage

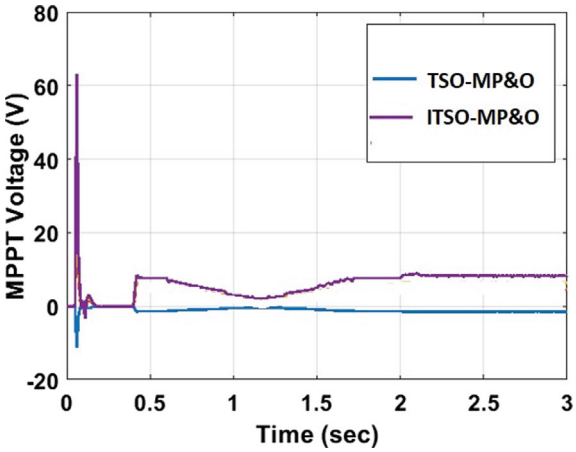

Fig. 4 MPPT current

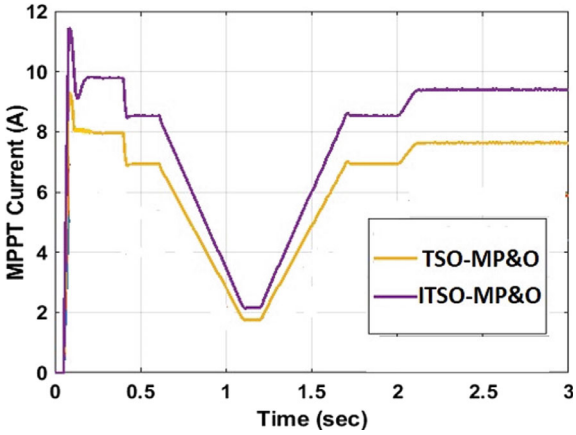

provides outstanding effectiveness in both steady and fluctuating phases. Because the current fluctuates between modes that are continuous and changing, the ITSO-MP&O operates more effectively.

4.2 Grid Voltage and Current

The total grid voltage from RES transmitted via TSO-MP&O is displayed in Fig. 5. The findings show that differences in surroundings have less of an effect on energy output than do modifications in sunlight. More power is supplied initially than is required for the intermediate sun irradiation. On the contrary, less electricity will be

needed than what would be needed for minimal or no brightness. Voltage that might be reached within 1.35 and 1.65 s.

The entire grid current provided to system over 0.9 and 1.4 s, accordingly, is shown in Fig. 6. Through increased grid current, it generates additional energy in a variety of scenarios. Originally, MPP decided to use a TSO-MP&O system. Furthermore, explain how the ITSO-MP&O can be used to handle peak loads with the anticipated RES. The outcomes of the simulation showed that the procedure was both challenging and reliable at the same time. Additionally, the equipment has been utilised to investigate how the operation of HRES with a power supply varies.

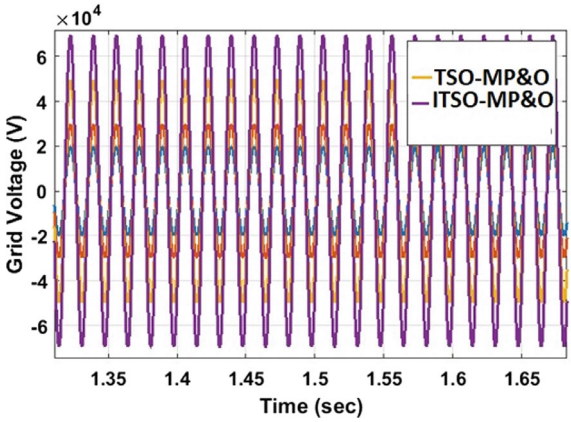

Fig. 5 Grid voltage within 1.35–1.65 s

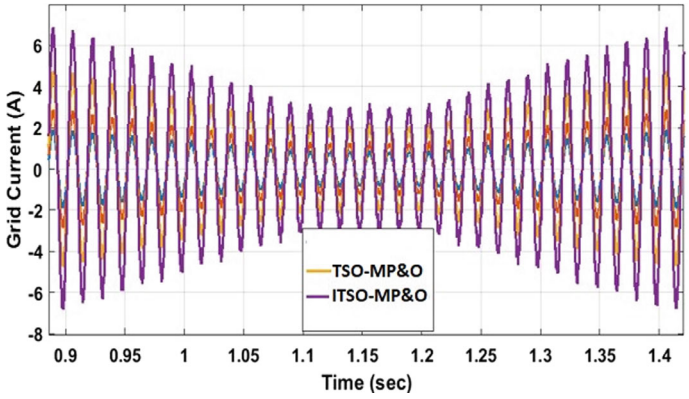

Fig. 6 Grid current within 0.9–1.4 s

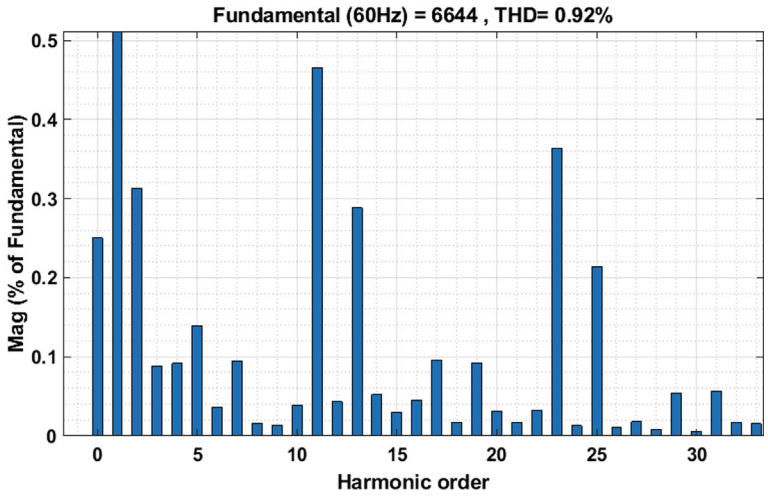

Fig. 7 THD for TSO-MP&O

4.3 Analysis of THD

A THD for different configurations is shown in Figs. 7 and 8, correspondingly. Compared to earlier iterations (TSO-MP&O), THD is 0.82% smaller in the ITSO-MP&O. Capacitors are placed among the power source and the load in the present investigation in order to reduce anomalies in power transmission. ITSO transmission satisfies power needs and enables effective control of the resources (wind and batteries) under fluctuating system loads.

4.4 Comparative Analysis

Because of two main factors, the proposed ITSO-MP&O controller produces more energy. (i) The best battery and wind combination and (ii) the best MPP at various load peaks. Consequently, the results demonstrate that the power grid system's optimal configuration utilising an assortment of hybrid sources makes the recommended approach much superior to the other optimisation methodologies now in use. The efficiency of hybrid sources that make use of ITSO-MP&O is evaluated by contrasting grid-integrated RES installations. The traditional MPPT control is linked to the anticipated ITSO-MP&O [15]. Table 1 compares the various levels of power that HRES produces.

From the Table 1, it clearly displays that ITSO-MP&O surpasses the current MPPT controller [15], albeit it does so only seldom in terms of power generation. Table 2 compares the analysis of THD with the currently used ANN [11] technique.

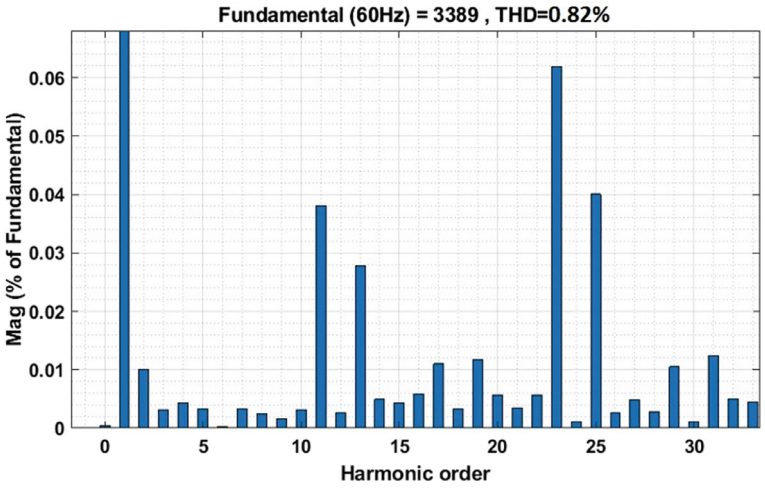

Fig. 8 THD for ITSO-MP&O

Table 1 Evaluation of sustainable sources with existing method

Time (Min)	PV (W)		Wind (W)		Battery (W)	
	MPPT controller [15]	ITSO-MP&O	MPPT controller [15]	ITSO-MP&O	MPPT controller [15]	ITSO-MP&O
0	50	68.12	35	54.15	2	16.15
10	54.26	69.35	42.18	55.62	− 22.2	2.30
20	54.26	71.88	42.18	56.24	− 43.14	0.85
30	54.26	72.45	42.18	57.86	− 43.14	4.45
40	54.26	73.86	42.18	59.34	− 22.17	5.82
50	54.26	75.17	42.18	61.72	2.9	9.11
60	54.26	77.38	42.18	63.18	16.13	10.29
70	54.26	79.44	42.18	64.98	22.24	16.46

Table 2 Investigation of THD

Methods	THD (%)
ANN [11]	1.26
Proposed ITSO-MP&O	0.82

THD is illustrated visually in Fig. 9. As compared to the current ANN [11], which has 1.26% error distortions, the suggested ITSO-MP&O system anticipates 0.82% fewer distortions, so that is a very low amount. The length of time is necessary to complete a specific process. The comparative evaluation of computational time and the existing MFPA-MP&O [16] is tabulated in Table 3.

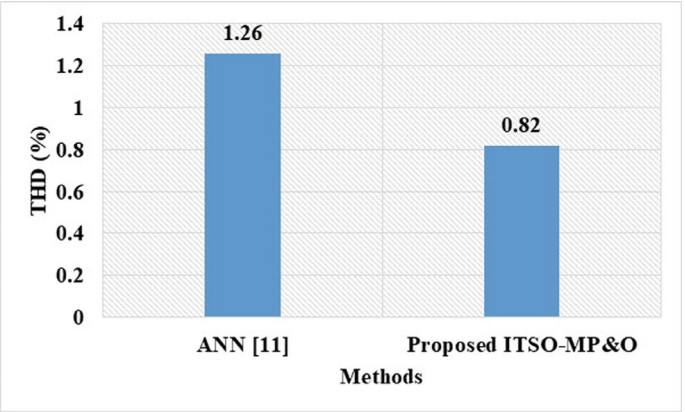

Fig. 9 Comparison of THD

Table 3 Evaluation of computational time

Confidence Level (%)	Computational time (s)	
	MFPA-MP&O [16]	Proposed ITSO-MP&O
90	1.7	1.3
95	1.8	1.5
100	1.9	1.6

To reduce computation time while considering the aforementioned conditions, the appropriate step size is limited to 3–4 kW. Table 3 explicitly shows that, in terms of computing time, the proposed ITSO-MP&O planning surpasses the current MFPA-MP&O planning for system resolution.

5 Conclusion

Due to negative environmental effects and an increase in energy costs associated with the use of traditional energy sources, renewable energy systems are anticipated to become more commonplace in future. RES like solar and wind have the ability to partially address the load problem because they are complementary to one another. Although due to their unpredictable character, such answers are rarely totally reliable when independently studied. Standalone PV and wind farms have been shown to be a more competitively feasible choice in this situation for meeting the energy needs of many remote consumers throughout the entire globe. It provides an understanding of the integrated system's configuration, simulation, sustainable energy sources, optimisation standards, management schemes and technology for optimal sizing. In the current research, the ITSO-MP&O method is used to build an efficient

EMS with the use of RES. The proposed ITSO-MP&O generates a THD of 0.82% and produces more electricity than other current techniques. Future work on this project will analyse alternative RES, such as fuel cells and diesel, to lessen the error distortion in grid-connected models.

References

1. Naderipour, A., Kamyab, H., Klemeš, J.J., Ebrahimi, R., Chelliapan, S., Nowdeh, S.A., Abdullah, A., Marzbali, M.H.: Optimal design of hybrid grid-connected photovoltaic/wind/battery sustainable energy system improving reliability, cost and emission. Energy **257**, 124679 (2022)
2. Wang, J., Xu, X., Wu, L., Huang, Q., Chen, Z., Hu, W.: Risk-averse based optimal operational strategy of grid-connected photovoltaic/wind/battery/diesel hybrid energy system in the electricity/hydrogen markets. Int. J. Hydrogen Energy **48**(12), 4631–4648 (2023)
3. Niveditha, N., Rajan Singaravel, M.M.: Optimal sizing of hybrid PV–wind–battery storage system for net zero energy buildings to reduce grid burden. Appl. Energy **324**, 119713 (2022)
4. Rouholamini, M., Wang, C., Nehrir, H., Hu, X., Hu, Z., Aki, H., Zhao, B., Miao, Z., Strunz, K.: A review of modeling, management, and applications of grid connected Li ion battery storage systems. IEEE Transa Smart Grid (2022)
5. Cholamuthu, P., Irusappan, B., Paramasivam, S.K., Ramu, S.K., Muthusamy, S., Panchal, H., Nuvvula, R.S., Kumar, P.P., Khan, B.: A grid-connected solar PV/wind turbine based hybrid energy system using ANFIS controller for hybrid series active power filter to improve the power quality. Int. Trans. Electr. Energy Syst. **2022** (2022)
6. Rathod, P., Mishra, S.K., Bhuyan, S.K.: Renewable energy generation system connected to micro grid and analysis of energy management: a critical review. Int. J. Power Electron. Drive Syst. **13**(1), 470 (2022)
7. Naidu, R.S.R.K., Palavalasa, M., Chatterjee, S.: Integration of hybrid controller for power quality improvement in photo-voltaic/wind/battery sources. J. Cleaner Prod. **330**, 129914 (2022)
8. Gulzar, M.M., Iqbal, A., Sibtain, D., Khalid, M.: An innovative converterless solar PV control strategy for a grid connected hybrid PV/wind/fuel-cell system coupled with battery energy storage. IEEE Access **11**, 23245–23259 (2023)
9. Raff, R., Golub, V., Knežević, G., Topić, D.: Modeling of the off-grid PV-wind-battery system regarding value of loss of load probability. Energies **15**(3), 795 (2022)
10. Boualem, S., Kraa, O., Benmeddour, M., Kermadi, M., Maamir, M., Cherif, H.: Power management strategy based on Elman neural network for grid-connected photovoltaic-wind-battery hybrid system. Comput. Electr. Eng. **99**, 107823 (2022)
11. Santhoshi, B.K., Mohanasundaram, K., Kumar, L.A.: ANN-based dynamic control and energy management of inverter and battery in a grid-tied hybrid renewable power system fed through switched Z-source converter. Electr. Eng. **103**(5), 2285–2301 (2021)
12. Padhmanabhaiyappan, S., Karthik, R., Ayyar, K.: Optimal utilization of interconnected RESs to microgrid: a hybrid AWO-ANFIS technique. Soft. Comput. **24**, 10493–10513 (2020). https://doi.org/10.1007/s00500-019-04558-3
13. Al Alahmadi, A.A., Belkhier, Y., Ullah, N., Abeida, H., Soliman, M.S., Khraisat, Y.S.H., Alharbi, Y.M.: Hybrid wind/PV/battery energy management-based intelligent non-integer control for smart DC-microgrid of smart university. IEEE Access **9**, 98948–98961 (2021)
14. De, M., Das, G., Mandal, K.K.: An effective energy flow management in grid-connected solar–wind-micro-grid system incorporating economic and environmental generation scheduling using a meta-dynamic approach-based multi-objective flower pollination algorithm. Energy Rep. **7**, 2711–2726 (2021)

15. Kumar, P.S., Chandrasena, R.P.S., Ramu, V., Srinivas, G.N., Babu, K.V.S.: Energy management system for small scale hybrid wind solar battery based microgrid. IEEE Access **8**, 8336–8345 (2020)
16. Jain, A.A., Rabi, B.J., Darly, S.S.: Application of QOCGWO-RFA for maximum power point tracking (MPPT) and power flow management of solar PV generation system. Int. J. Hydrogen Energy **45**, 4122–4136 (2020). https://doi.org/10.1016/j.ijhydene.2019.12.071
17. Nyeche, E.N., Diemuodeke, E.O.: Modelling and optimisation of a hybrid PV-wind turbine-pumped hydro storage energy system for mini-grid application in coastline communities. J. Cleaner Prod. **250**, 119578 (2020). https://doi.org/10.1016/j.jclepro.2019.119578
18. Hamanah, W.M., Abido, M.A., Alhems, L.M.: Optimum sizing of hybrid PV, wind, battery and diesel system using lightning search algorithm. Arab. J. Sci. Eng. **45**, 1871–1883 (2020). https://doi.org/10.1007/s13369-019-04292-w
19. Xie, L., Han, T., Zhou, H., Zhang, Z.R., Han, B., Tang, A.: Tuna swarm optimization: a novel swarm-based metaheuristic algorithm for global optimization. Comput. Intell. Neurosci. 1–22 (2021)
20. Wang, W., Tian, J.: An improved nonlinear tuna swarm optimization algorithm based on circle chaos map and levy flight operator. Electronics **11**(22), 3678 (2022)

ANFIS-Controlled Hybrid Renewable Source System for Optimal Power Sharing

Ravikant, Asha Rani, and Vijander Singh

Abstract As many grid systems are included with renewable sources, optimal utilization of the generated power from these renewable sources has become mandatory. Efficient controllers will stabilize the system with faster response rate making the power utilization from the renewable sources efficient. In this paper, we are considering different sources like solar plant, PMSG wind farm, and battery storage unit. The unpredictable renewable sources, solar plant and wind farm, are connected in parallel with battery storage unit which can store excess power. This excess power stored in battery can later be utilized during deficit renewable power conditions. The renewable sources' maximum power extraction is done using MPPT controllers, and the reference DC link voltage is set by controller of the battery storage unit. A comparative analysis with PI and ANFIS controllers applicable on the converter of battery storage unit is done for optimal power sharing and stabilization of the system. The complete analysis and modeling are carried out in MATLAB software with results represented in plotting graphs.

Keywords PMSG (Permanent magnet synchronous generator) · MPPT (Maximum power point tracking) · PI (Proportional integral) · ANFIS (Adaptive neuro-fuzzy inference system)

Ravikant (✉) · A. Rani · V. Singh
Netaji Subhas University of Technology, Dwarka, New Delhi 110078, India
e-mail: ravishoeran786@gmail.com

A. Rani
e-mail: asha.rani@nsut.ac.in

V. Singh
e-mail: vijaydee@nsut.ac.in

© The Author(s), under exclusive license to Springer Nature Singapore Pte Ltd. 2025

H. P. Singh et al. (eds.), *Recent Developments in Control, Automation and Power Engineering*, Lecture Notes in Electrical Engineering 1303,
https://doi.org/10.1007/978-981-96-0047-2_24

1 Introduction

Power generation using natural sources like solar irradiation and winds in the environment has become a part of electrical grid system which represents renewable power generation [1]. Shifting to renewable power generation has become mandatory as the conventional ways of power generation using coal and diesel as fuel are deteriorating the environment as hazardous gases are produced. Due to this, there are many climatic disasters taking place throughout the globe which is becoming a threat to living being's survival. Therefore, these conventional power generation units are replaced with renewable source power generation units [2]. These sources include solar plants, wind farms, tidal wave power farms, biogas plants, etc. From all these sources, wind farms and solar plants are considered to be the most viable and reliable option for generation of electrical power.

However, these sources (wind farms and solar plants) do not generate stable and continuous power as the climatic parameters (solar irradiation and wind speeds) are not constant. With variation of these parameters, the power and voltage outputs of the solar panels and generators will change. So, it is very difficult to make these sources to work in standalone condition as they might collapse compensating a load with higher capacity than they are generating [3, 4]. It is now important that these sources either need to be operated in parallel to the grid or with any other stable source which can support during change in the power generation of renewable sources [5]. There are many researches done with grid connected in parallel to the renewable sources making it conventional topology. Making these renewable sources to work in standalone mode for remote areas is the novel task to be achieved.

In this paper, we are considering a standalone renewable source system with battery storage unit as the backup device, which can support the load during deficit renewable power generation and also store power during excess renewable power generation [6, 7]. Each source is integrated with different power converters to ensure power generation at stable voltages. The outline diagram of the standalone renewable source system is seen in Fig. 1.

As observed in the above outline diagram, the DC distribution generation is considered to be solar plant which is connected to a DC-DC booster converter (BC) for voltage stabilization. The AC distribution generation is considered to be PMSG (Permanent Magnet Synchronous Generator) wind farm connected to AC-DC converter [8]. PMSG machine is opted as it is the only machine which can generate power without any external power feeding. These two renewable generation units are supported with storage element (battery) connected to bidirectional converter (BDC) which can deliver and absorb power from the DC bus during deficit and excess renewable power conditions [9]. All these converters tend to operate as same DC voltage magnitude to ensure power sharing to the load. For maximum power extraction from renewable sources, converters are operated using MPPT algorithms. At stable DC bus voltage, an inverter is connected for the AC loads to be operated.

The internal modeling of each generation and storage unit is discussed in detail in further Sect. 2 and 3. A comparative analysis with different controllers (PI and

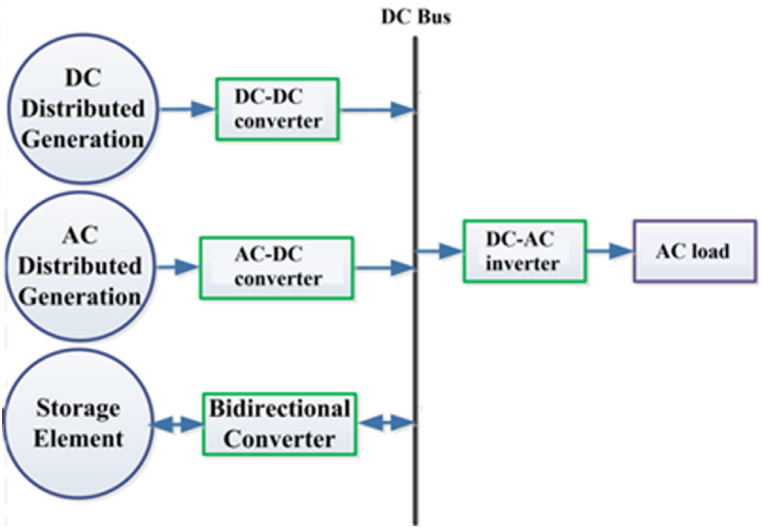

Fig. 1 Standalone renewable source system with battery storage support unit

ANFIS) for the BDC is done using MATLAB Simulink software, and the results are presented in Sect. 4 followed by conclusion and references in Sect. 5.

2 System Configuration

As observed in test system schematic Fig. 1, there are three source modules which include renewable DC source considered as solar plant with multiple series and parallel solar panels connected to DC-DC voltage booster controlled by MPPT algorithm for maximum power extraction [10]. The second renewable source is an AC source considered to be wind farm with PMSG machine connected to rectifier and DC voltage regulator buck–boost converter (BBC) controlled by another MPPT module for maximum power extraction from PMSG. A supporting battery storage module is connected with BDC topology for power storage which can be utilized later during load demand or renewable power failure [11]. The complete circuit structure with connection to AC load through three-phase inverter is shown in Fig. 2.

As can be observed in Fig. 2, both the BC and the BBC have single switch whereas the BDC converter has two switches representing boost switch S1 and buck switch S2. The converters of the renewable sources (solar plant and wind farm) are controlled by individual MPPT control techniques, incremental conductance and Power signal feedback for solar plant and wind farm, respectively [12]. The below is the incremental conductance MPPT flow chart for the solar plant BC (Fig. 3).

The MPPT flow chart starts with measurement of solar panel voltage $V(k)$ and current $I(k)$ which represents present measured values. The change in these values

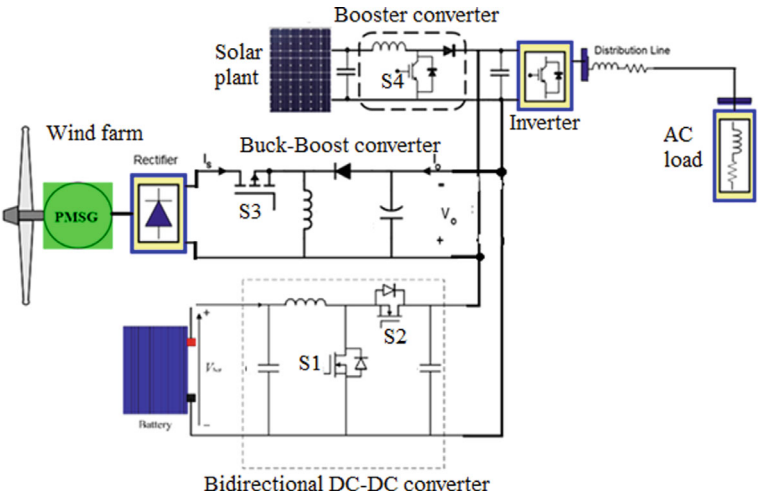

Fig. 2 Test system circuit configuration

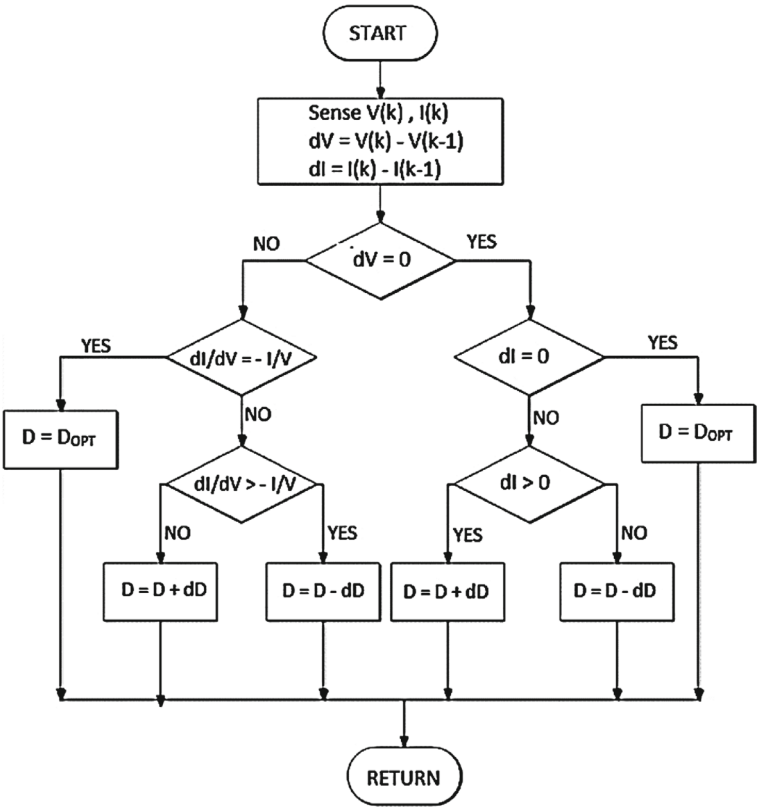

Fig. 3 Incremental conductance MPPT

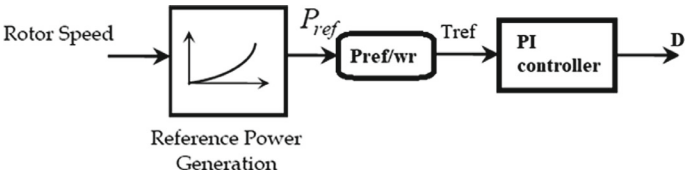

Fig. 4 Power signal feedback MPPT for wind farm

(dV and dI) are generated using past values $V(k-1)$ and $I(k-1)$ of these measured parameters using unit delay [13]. The change in the duty cycle D of the booster switch is given as

$$\begin{aligned} D &= D + dD\left\{\begin{array}{c} If\ dV = 0;\ dI > 0 \\ If\ dV \neq 0;\ \frac{dI}{dV} < -\frac{I}{V} \end{array}\right\} \\ D &= D - dD\left\{\begin{array}{c} If\ dV = 0;\ dI < 0 \\ If\ dV \neq 0;\ \frac{dI}{dV} > -\frac{I}{V} \end{array}\right\}. \end{aligned} \tag{1}$$

The duty cycle D does not change if there is no change in voltage and current parameter which represents no change in solar irradiation. The power signal feedback MPPT for the converter of the wind farm is shown in Fig. 4.

The reference power generation is set of bench mark values of reference power (P_{ref}) generated for a given rotor speed w_r of PMSG machine [14]. The reference torque T_{ref} is given as

$$T_{\text{ref}} = P_{\text{ref}} \big/ w_r. \tag{2}$$

The duty ratio for the switch of the wind farm converter is given as

$$D_{wf} = T_{\text{ref}}\left(K_p + \int K_i.\mathrm{d}t\right). \tag{3}$$

The values of K_p and K_i are tuned until the converter DC voltage is stabilized and maximum power extraction is achieved.

3 Control Structure Design

The renewable source converter's MPPT controller does not have any voltage reference at which the converters have to operate. Therefore, BDC of the battery storage unit is controlled by constant voltage feedback controller [15]. In this controller, a reference voltage value is set by the user as per the requirement of the load connected on the AC side of the inverter. Figure 5 is the constant voltage feedback controller for the given BDC.

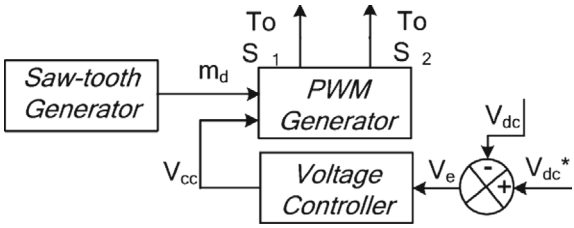

Fig. 5 Constant voltage feedback controller for BDC

The duty ratio V_{cc} for the switches S1 and S2 (which operate alternatively with NOT gate for S2) is generated by a voltage controller. This voltage controller stability will control the DC bus voltage of the complete system, where the other two renewable sources are connected in parallel for power sharing [16]. A basic PI controller is connected considering as conventional voltage controller where the duty ratio for the BDC is given as

$$V_{cc} = \left(V_{dc}^{*} - V_{dc}\right) * (K_p + \int K_i.dt). \tag{4}$$

This conventional PI controller is replaced with ANFIS voltage controller for better control on duty ratio of the BDC [17]. The configuration of the ANFIS controller is done using 'Sugeno' type fuzzy inference system (FIS) [11]. The FIS is configured with one input variable 'E' and one output variable 'D'. The input variable 'E' defines the error of the DC voltage comparison, and the output 'D' variable is the duty ratio for the BDC. The below is the 'Sugeno' FIS model defined using fuzzy tool in MATLAB software [11] (Fig. 6).

The input variable is constrained within a range of -1500 to 1500, while the output variable is limited to a range of -100 to 100. Both the input and output variables are represented using nine membership functions with a 'guass' type shape. The output variable is further discretized into nine constant values, each falling within the $-$ 100 to 100 range. Figure 7a illustrates the input and output membership functions. The modeling approach employed is linear, consisting of nine input membership functions and nine corresponding output membership functions.

The output variable constant mmfs is set with these value NVB $= -$ 100, NB $=$ $-$ 75, NM $= -$ 50, NS $= -$ 25, $Z = 0$, PS $= 25$, PM $= 50$, PB $= 75$, and PVB $=$ 100. To train the FIS using ANFIS tool, training data is required which is taken from

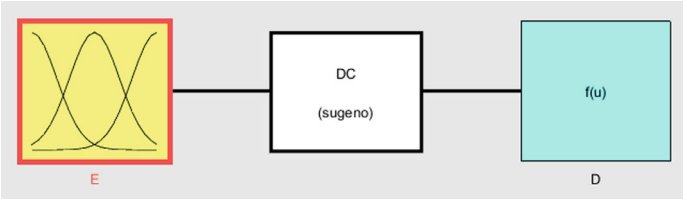

Fig. 6 Sugeno FIS variable definition

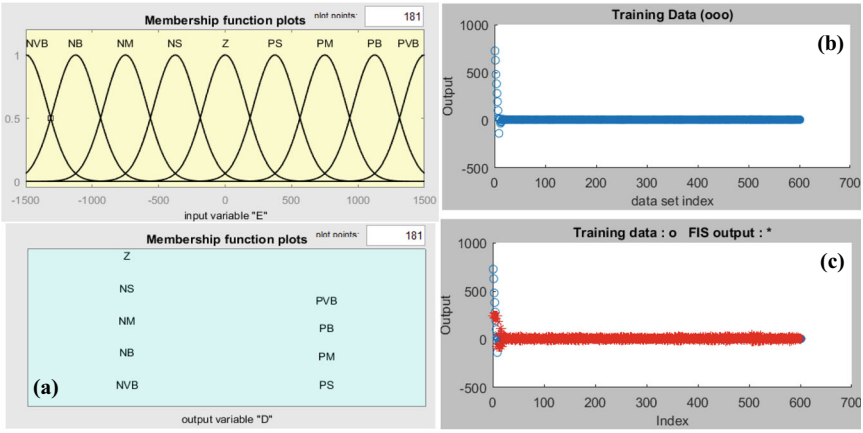

Fig. 7 **a** Input and output membership functions of 'Sugeno' FIS, **b** importing of training data, and **c** imported and trained data of FIS

input and output of PI controller during simulation which is exported to workspace. The trained data is imported to ANFIS training tool from workspace as shown in Fig. 7b [18].

This imported data is used to train the FIS with nine mmfs of input and output variables using 'hybrid' training algorithm [18]. After the training, the imported data and trained data is updated as in Fig. 7c.

This trained FIS will be exported to workspace of MATLAB software which will be taken into fuzzy block of the simulation for generating duty ratio of BDC [18]. The ANFIS voltage regulator modeling for BDC is seen in Fig. 8.

The output duty ratio is limited between two limits using saturation so as to get stabilized DC voltage at the DC bus. The simulation results and analysis of the complete test system with two renewable sources and one battery storage unit with different voltage controllers of BDC are shown in next section.

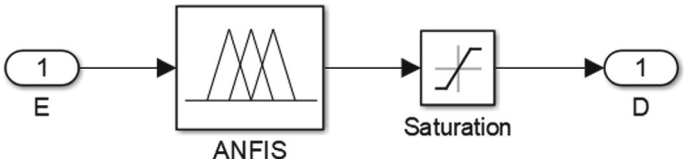

Fig. 8 ANFIS modeling

4 Simulation Results

In order to check the power balance of the renewable sources, the simulation of the test system is run for 1.5 s with different operating conditions. The test system parameters for the simulation are given in Table 1.

With all the above parameters in test, system of standalone hybrid renewable source is modeled and the simulation is run with different conditions. In the total simulation time of 1.5 s, the solar irradiation is changed from 1000 W/m^2 to 500 W/m^2 at 0.5 s and wind speed is changed from 12 m/s to 8 m/s at 1 s. The powers and voltages of all sources and loads are recorded and represented in graphical format with time as reference.

In Fig. 9, solar plant voltage and current with respect to change in solar irradiation are shown. The V_{pv} is recoded at 400 V throughout the simulation and current is changing from 55 to 25A when the solar irradiation is dropped.

In Fig. 10, the wind farm PMSG rotor speed and electromagnetic torque of the machine with respect to change in wind speed are shown.

As per the change in solar irradiation and wind speed of the renewable sources, the changes in characteristics of battery storage unit measuring battery state of charge (SOC), current, and voltage are shown in Fig. 11.

Table 1 Test system parameters

Name of the parameter	Values
PV rating	$V_{mp} = 54.7$ V, $I_{mp} = 5.58$ A, $V_{oc} = 64.2$ V, $I_{sc} = 5.96$ A, Power of one panel = 305 W, $N_p = 10$, $N_s = 7$. $P_{total} = 21$ kW
Wind farm rating	PMSG rating: $P_{wf} = 39$ kW, 560 Vdc, 111 N m, 3000 rpm, $R_s = 0.05\Omega$, $L_s = 0.635$ mH, $\psi = 0.192$ V s, $J = 0.011$ kg m^2, number of pole pairs $P = 4$
Battery rating	Li-ion type. $V_{bat} = 500$ V, Capacity = 200A h
Lb_{pv} (booster inductor of PV unit)	1 mH
Lb_{bat} (booster inductor of battery unit)	161.95 uH
Lb_{wf} (booster inductor of wind farm)	100 uH
Cdc (DC link capacitance)	12000 uF
Vdcref (DC bus voltage reference)	725 V
SPWM parameters	Modulation index (m) = 1, $f = 50$ Hz, switching frequency $f_{sw} = 2$ kHz
All DC-DC converters carrier frequency	$f_c = 5$ kHz
Torque controller gains of wind farm	$K_p = 5$; $K_i = 0.0023$
DC regulator gains of BDC	$K_p = 0.05$; $K_i = 0.0023$
LC filter of inverter	$L_f = 1$ mH; $C_f = 100$ uF
Main AC load	55 kW

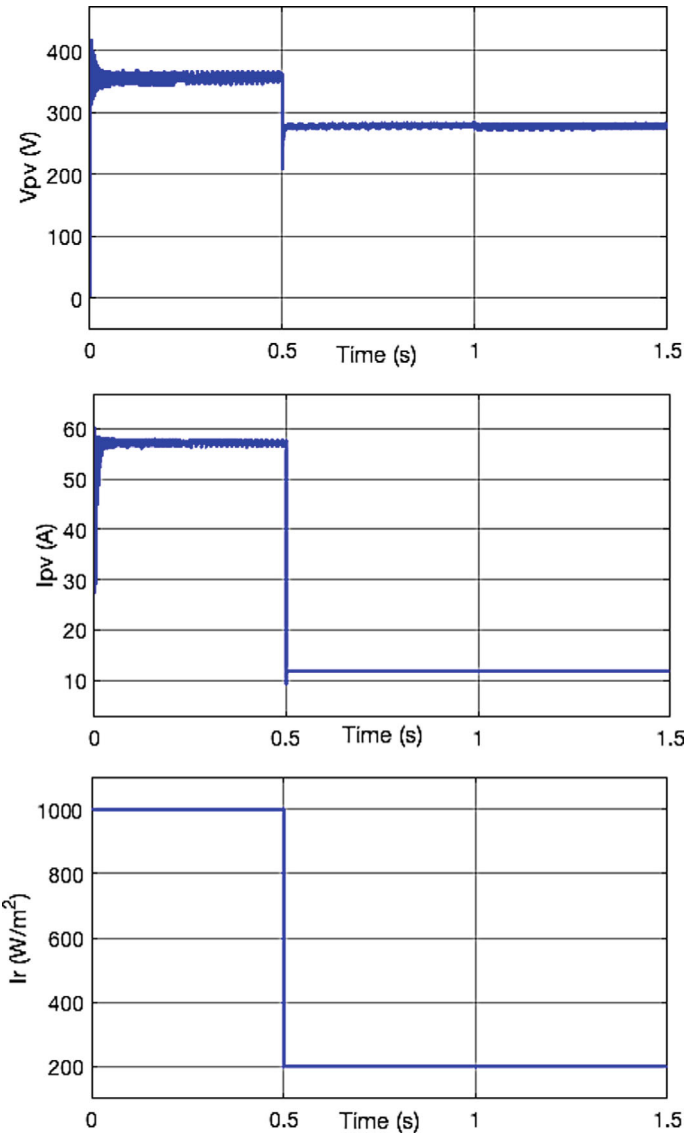

Fig. 9 Solar plant characteristics V_{pv} and I_{pv}

The voltage of the battery is always maintained at 550 V with only change in battery current from 35 to 55 A at 0.5 s and from 55 to 75 A at 1.5 s. The SOC is always dropping as the battery is always discharging because of heavy load demand of 55 kW.

In Fig. 12, the powers of solar plant, battery power, and wind farm power with respect to DC bus voltage set at 750 V are shown. The power of solar plant is dropping

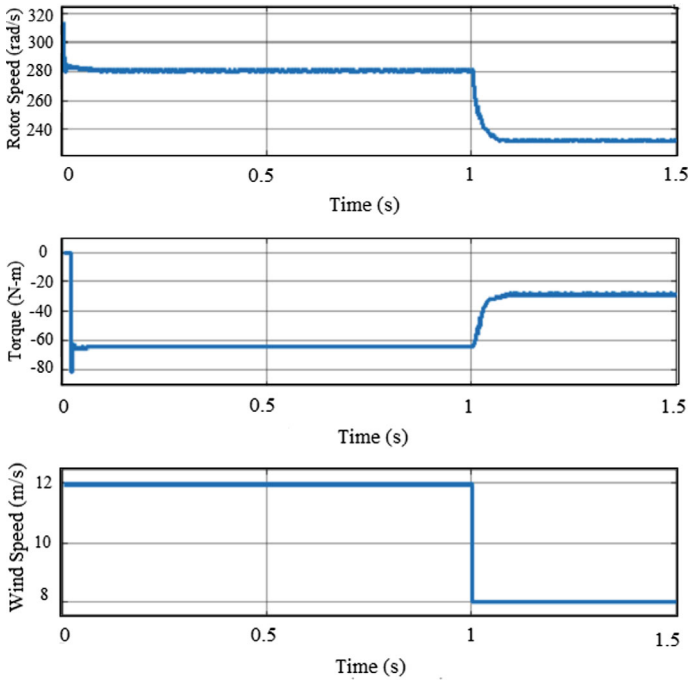

Fig. 10 Wind farm characteristics

from 21 to 10 kW at 0.5 s when the irradiation is dropped. The power of wind farm is dropped from 16 to 7 kW when the wind speed is dropped. As per the change in these renewable powers, the battery power is changed from 19 to 30 kW at 0.5 s and from 30 to 40 kW at 1 s so as to meet the load power demand of 50 kW. The sources' power delivery comparison is given in Table 2.

In Table 2, the inverter three-phase output voltages and currents measured after LC filter feeding the 55 kW load are shown.

In Fig. 13, the active and reactive power graphs of the given load are shown. As observed in Table 2, the power of all the sources is cumulatively generating 57 kW in any condition and compensating the load of 55 kW. The remaining 2 kW is the conversion loss and transmission loss due to different converters in the test system.

The complete test system is run with different voltage controllers (PI and ANFIS) defined as per Sect. 3, and the DC bus voltage is compared. The reference DC bus voltage in the constant voltage feedback controlled is set to 750 V. Different parameters of DC bus voltage measurement with PI and ANFIS controllers are compared and are given in Table 3.

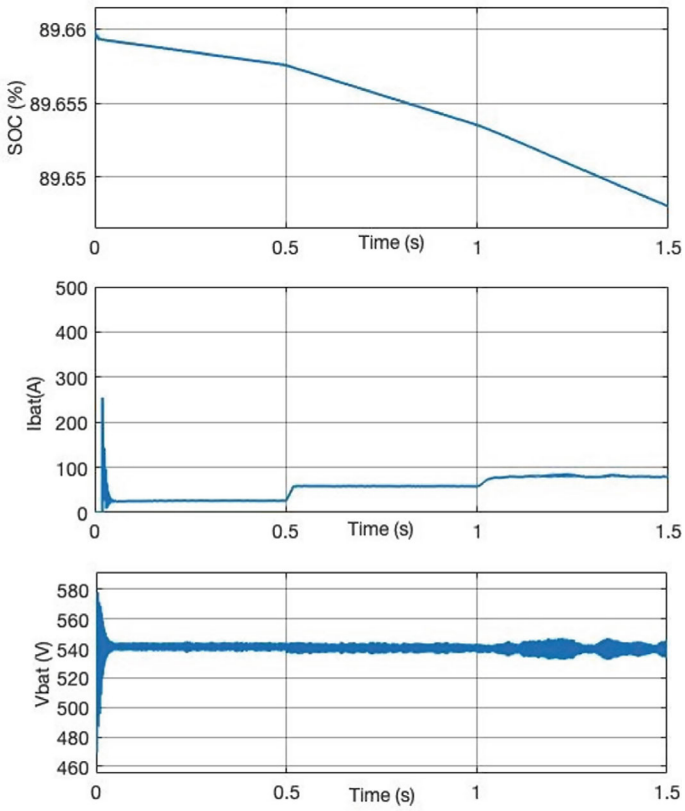

Fig. 11 Battery unit characteristics

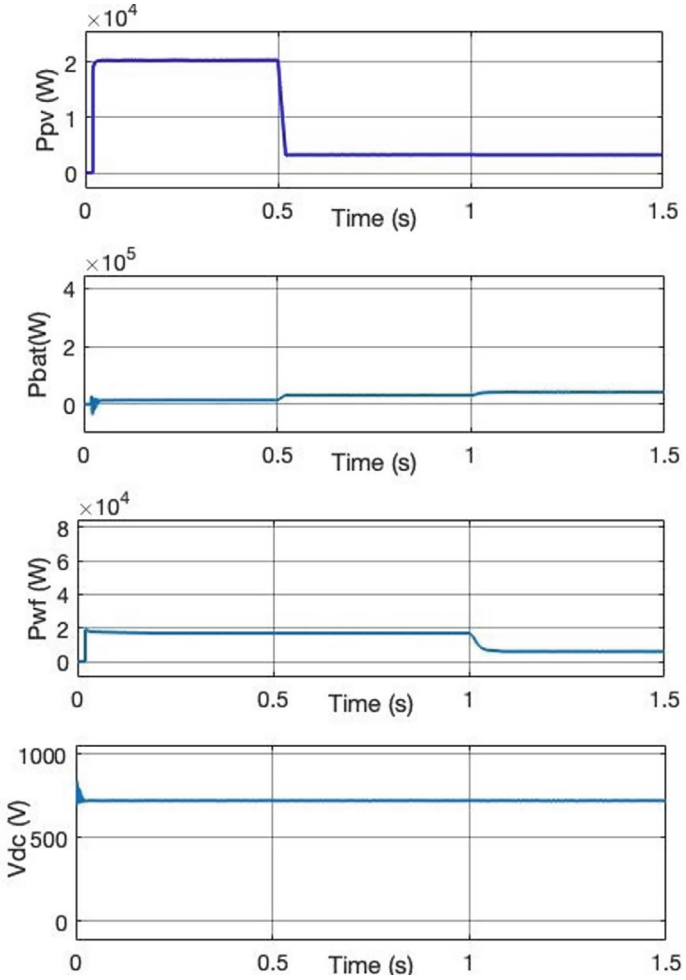

Fig. 12 Powers and DC bus voltage of all sources

Table 2 Power comparison

Power	Value		
	0–0.5 s (kW)	0.5–1 s (kW)	1–1.5 s (kW)
Ppv	21	10	10
Pwf	17	17	7
Pbat	19	30	40
Pload	55	55	55

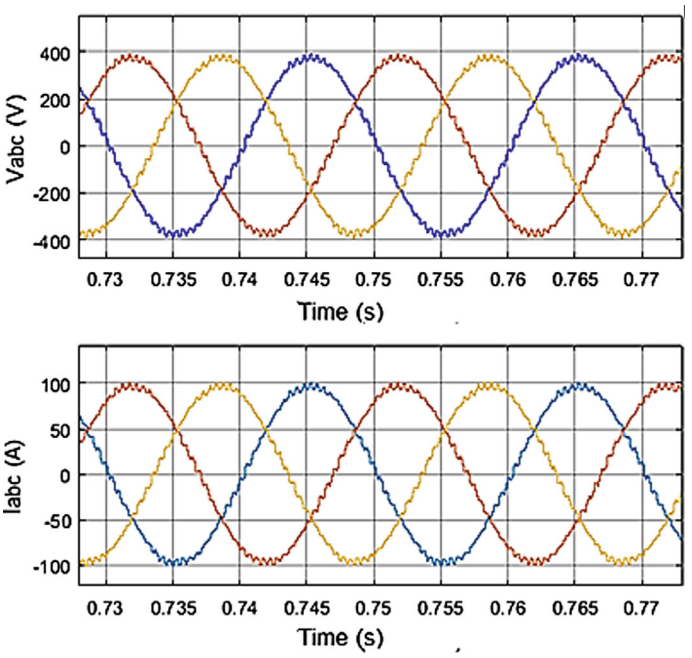

Fig. 13 Three-phase voltages and currents of main AC load

Table 3 DC bus voltage parameter comparison

Parameters	PI	ANFIS
Magnitude	725 V	750 V
Peak	930 V	830 V
Settling time	0.05 s	0.02 s
Ripple	< 1%	< 1%

5 Conclusion

The simulation results of the test system, which incorporates a solar plant, wind farm, and battery storage unit, indicate that these energy sources adequately meet the load demand under various environmental conditions. The battery effectively supports the load during both solar irradiation and different wind speeds in the test system. The DC bus voltage is measured and compared when controlled by two different controllers, PI and ANFIS. Upon analyzing the DC bus voltage parameters, it is evident that the ANFIS controller outperforms the PI controller. Specifically, the ANFIS controller achieves a voltage magnitude of 750 V, whereas the PI controller only reaches 725 V, falling short of the desired reference value generation. Moreover, the peak voltage for the PI controller is 930 V, while the ANFIS controller keeps it at a safer 830 V, reducing potential damage to the load. The crucial parameter,

settling time of the voltage, is significantly better with the ANFIS controller at 0.02 s compared to the PI controller's 0.05 s. Based on these comparisons, it is evident that the test system's DC bus voltage exhibits greater stability, faster settling time, and more accurate magnitude generation when operated with the ANFIS controller. All the valid results and comparison graphs were generated using MATLAB simulation software.

References

1. Jiang, W., Yang, C., Liu, Z., Liang, M., Li, P., Zhou, G.: A hierarchical control structure for distributed energy storage system in DC micro-grid. IEEE Access **7**, 128787–128795 (2019). https://doi.org/10.1109/ACCESS.2019.2939626
2. Zia, M.F., Elbouchikhi, E., Benbouzid, M.E.H.: An energy management system for hybrid energy sources-based stand-alone marine microgrid. IOP Conf. Ser. Earth Environ. Sci. **322**, 012001 (2019)
3. Ma, X., Liu, S., Liu, H., Zhao, S.: The selection of optimal structure for stand-alone micro-grid based on modeling and optimization of distributed generators. IEEE Access **10**, 40642–40660 (2022). https://doi.org/10.1109/ACCESS.2022.3164514
4. Singh, B., Singh, M.K.: Solar PV, PMSG-wind energy conversion system and battery based standalone DC micro-grid system. In: 2022 5th International Conference on Power Electronics and their Applications (ICPEA), Hail, Saudi Arabia, 2022, pp. 1–6. https://doi.org/10.1109/ICPEA51060.2022.9791165
5. Tawil, T.E., Charpentier, J.F., Benbouzid, M.: Sizing and rough optimization of a hybrid renewable-based farm in a stand-alone marine context. Renew. Energy **115**, 1134–1143 (2018)
6. Gopi, P., Lalitha, M.P., Bhanu, S.A.J.: A wind and solar based ac micro grid with optimized power quality for local non-linear loads. In: 2021 International Conference on Technology and Policy in Energy and Electric Power (ICT-PEP), Jakarta, Indonesia, 2021, pp. 296–301. https://doi.org/10.1109/ICT-PEP53949.2021.9600903
7. Zhang, C., Xu, Y., Dong, Z.Y.: Robustly coordinated operation of a multi-energy micro-grid in grid-connected and islanded modes under uncertainties. IEEE Trans. Sustain. Energy **11**(2), 640–651 (2020). https://doi.org/10.1109/TSTE.2019.2900082
8. Haseeb, M., Kazmi, S.A.A., Malik, M.M., Ali, S., Bukhari, S.B.A., Shin, D.R.: Multi objective based framework for energy management of smart micro-grid. IEEE Access **8**, 220302–220319 (2020). https://doi.org/10.1109/ACCESS.2020.3041473
9. Zafar, Shafique, A., Nazir, Z., Zia, M.F.: A comparison of optimization techniques for energy scheduling of hybrid power generation system. In: 2018 IEEE 21st International Multi-Topic Conference (INMIC). IEEE, pp. 1–6 (2018)
10. Mutarraf, M., Terriche, Y., Niazi, K., Vasquez, J., Guerrero, J.: Energy storage systems for shipboard microgrids—a review. Energies **11**(12), 3492 (2018)
11. Baset, D.A., Rezk, H., Hamada, M.: Fuzzy logic control based energy management strategy for renewable energy system. In: 2020 International Youth Conference on Radio Electronics, Electrical and Power Engineering (REEPE), pp. 1–5 (2020). https://doi.org/10.1109/REEPE49198.2020.9059203
12. Chen, C.-I., Chen, Y.-C., Chen, C.-H.: Energy Management between power generation, storage, and consumption for building microgrid. In: 2020 International Symposium on Computer, Consumer and Control (IS3C), pp. 335–338 (2020). https://doi.org/10.1109/IS3C50286.2020.00093
13. Shahid: Smart grid integration of renewable energy systems. In: 7th International Conference on Renewable Energy Research and Applications, Paris, France, 14–17 Oct (2018)

14. Thokar, R.A., Gupta, N., Niazi, K.R., Swarnkar, A., Sharma, S., Meena, N.K.: Optimal integration and management of solar generation and battery storage system in distribution systems under uncertain environment. Int. J. Renew. Energy Res. **10**(1) (2020)
15. Liu, D., Li, C., Jiang, Z., Kong, R., Wu, L., Ma, C.: Integrated power grid management system based on micro service. In: 2020 Eighth International Conference on Advanced Cloud and Big Data (CBD), Taiyuan, China, pp. 37–41 (2020). https://doi.org/10.1109/CBD51900.2020.00016
16. Sinsel, S.R., Riemke, R.L., Hoffmann, V.H.: Challenges and solution technologies for the integration of variable renewable energy sources: a review. Renew. Energy **145**, 2271–2285 (2020)
17. Lingang, Y., Yueliang, C., Caiquan, Z., Qiu, C., Zhihui, X., Zhaohui, S.: Design of power source micro source synchronous grid connected controller. In: 2020 IEEE 4th Information Technology, Networking, Electronic and Automation Control Conference (ITNEC), Chongqing, China, pp. 2336–2340 (2020). https://doi.org/10.1109/ITNEC48623.2020.9085001
18. Ndiaye, Mbaye Ndiaye, E.H., Tankari, M.A., Lefebvre, G., Thiaw, L.: Experimental validation of neuro-fuzzy energy management for a DC electrical micro-network. In: 2022 10th International Conference on Smart Grid (icSmartGrid), Istanbul, Turkey, pp. 102–106 (2022). https://doi.org/10.1109/icSmartGrid55722.2022.9848577

Robust Sliding Mode Controller for Flyback Converter in Continuous Conduction Mode

Mukund Kumar Choudhary, G. L. Pahuja, and Rahul Sharma

Abstract This paper presents a detailed examination of the design and simulation of a robust sliding mode control system for a flyback converter. Sliding mode control is a nonlinear approach aimed at driving the system state onto a specific sliding surface and maintaining it there, independent of uncertainties or disturbances. The paper also explores the working principle of the proposed converter. Furthermore, the paper extensively discusses the modeling of the flyback converter under various conditions, taking into consideration different scenarios to accurately represent its behavior. To achieve sliding mode control, the converter's state space averaged (SSA) model is also thoroughly explained. Finally, the simulation results demonstrate that the output voltage of the fly-back converter remains nearly constant even in the presence of significant changes or disturbances at the input side. This underscores the effectiveness of the sliding mode control technique in ensuring a stable output voltage under varying operational conditions.

Keywords Sliding mode control (SMC) · Sliding surface · Flyback converter · Pulse width modulated signals (PWM)

M. K. Choudhary (✉) · G. L. Pahuja · R. Sharma
National Institute of Technology Kurukshetra, Kurukshetra, India
e-mail: roymukund007@gmail.com

G. L. Pahuja
e-mail: glpahuja@nitkkr.ac.in

R. Sharma
e-mail: rahul0303@nitkkr.ac.in

© The Author(s), under exclusive license to Springer Nature Singapore Pte Ltd. 2025

H. P. Singh et al. (eds.), *Recent Developments in Control, Automation and Power Engineering*, Lecture Notes in Electrical Engineering 1303,
https://doi.org/10.1007/978-981-96-0047-2_25

1 Introduction

In power electronics, flyback converters are a common topology for voltage conversion applications. They are ideal converters for a variety of low- to medium-power applications due to their simplicity, cost-effectiveness, and galvanic isolation compared to other converter topologies, they require fewer components, which lowers their cost and complexity. Flyback converters can also offer galvanic isolation between input and output, assuring electrical safety and enabling a variety of applications that need isolation.

The storage and transfer of energy are the foundations upon which the flyback converter operates. It makes use of a transformer to store energy in the primary winding when the switching transistor is in the "on" state and release it to the load when it is in the "off" state. Flyback action, in which the transformer stores energy in the magnetic field during the "on" state and releases it as a voltage pulse to the secondary side during the "off" state, allows for this energy transfer.

In order to obtain precise and dependable control in the midst of uncertainties and disturbances, sliding mode control is a robust and efficient control approach that is frequently employed in a variety of engineering applications. An overview of sliding mode control [1], its core ideas, and its benefits in solving difficult control issues are given in this introduction. Sliding mode control operates based on the concept of sliding surfaces. A sliding surface is a mathematical construct defined in the state space of a control system. The goal of sliding mode control is to drive the system states onto the sliding surface and keep them there, resulting in robust and precise control.

The robustness of sliding mode control is one of its main benefits. It is made to deal with potential system performance-affecting uncertainties, parameter changes, and outside disruptions. By ensuring that the system's trajectory converges to the sliding surface despite any uncertainties present, sliding mode control accomplishes robustness. The system offers resilience and reliable performance once it is on the sliding surface since it is insensitive to the unpredictable circumstances. The ability of sliding mode control to handle nonlinear systems is another noteworthy feature. Many systems in the real world have nonlinear dynamics, which makes it difficult for linear control [2], approaches to operate satisfactorily in these situations. On the other hand, sliding mode control is ideally adapted to deal with nonlinearities and can successfully stabilize and control nonlinear systems. In sliding mode control, the control action is discontinuous, which means that sudden changes in the control inputs may occur during the control process. Because sliding mode control is discontinuous, it can cause chattering, which is characterized by abrupt changes in control signals. However, a number of strategies have been devised to reduce chattering and guarantee effective control operations.

Numerous industries, including robotics, power electronics, aerospace systems, automotive systems, and many more, have found use for sliding mode control. It is a desirable option for complex control situations where accurate and dependable

control is required due to its robustness, capacity for handling uncertainties, and effectiveness in dealing with nonlinearities.

2 The Flyback Converter Modeling and Working Principle

2.1 Nominal Condition

Fl**y**back converter [3] is as represented in Fig. 1. L_m is equivalent magnetizing inductance of flyback transformer referred to primary side of circuit, V_{in} input voltage to circuit, i_{Lm} magnetizing current, n_1 and n_2 are turns ratio on primary and secondary of transformer, respectively.

The two different modes is observed as per the Mosfet switching action when gate pulse signal given to Mosfet switch, i.e., on state, during on state the diode on secondary side of transformer is in reverse bias mode and energy is stored in primary side of transformer, second state when Mosfet switch is turned off, i.e., off state of flyback converter, diode on the secondary side of converter gets forward and forward bias and stored energy in primary side transformer is supplied to the load resistor and output capacitor. Equivalent circuits for the following two stages are represented in Figs. 2 and 3 respectively.

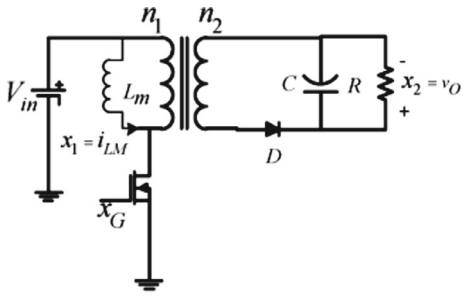

Fig. 1 Flyback converter schematic circuit

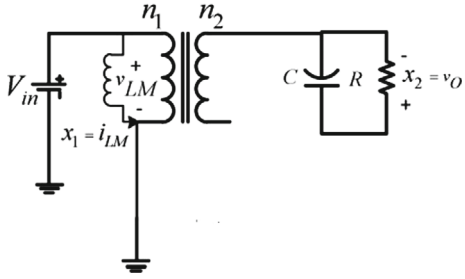

Fig. 2 Flyback converter equivalent circuit during on state

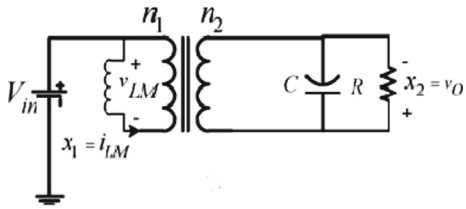

Fig. 3 Flyback converter equivalent circuit during off state

2.2 Steady-State Analysis of Flyback Converter

During on state as equivalent circuit for flyback converter is represented in Fig. 2 the diode is reverse biased and winding on secondary of transformer are open-circuited.

The magnetizing current I_{lm} can be represented as:

$$V_{Lm} = V_{\text{in}} \Rightarrow i_{Lm} = \frac{V_{\text{in}}}{L_m} t + I_1 0 \leq t \leq t_{\text{on}} \tag{1}$$

I_1 inductor current when switch is turned on, at t_{on} (when Mosfet switch turned off)

$$I_2 = \frac{V_{\text{in}}}{L_m} t_{\text{on}} + I_1 \tag{2}$$

When Mosfet switch is turned off the inductor current on the secondary of circuit is as follows

$$\begin{aligned} &V_{Lm} = -\frac{n_1}{n_2} V_o \Rightarrow i_{Lm} = \left(-\frac{n_1}{n_2}\right) \frac{V_o}{L_m} (t - t_{\text{on}}) + I_2 \\ &t_{\text{on}} \leq t \leq T_s \end{aligned} \tag{3}$$

T_s is switching period of converter, d is duty ratio: $d = \frac{t_{\text{on}}}{T_s}$ (Fig. 4).

3 The State Space Averaged (SSA) Model

The flyback converter switching between two structures viz., structure-1 when Mosfet switch ON, structure-2 when Mosfet switch OFF, periodically to study the dynamic behavior of flyback converter state space modeling [4] technique is used.

Let consider V_o and i_{Lm} be state variables

$$X^T = (x_1, x_2) \Rightarrow (i_{Lm}, V_o) \tag{4}$$

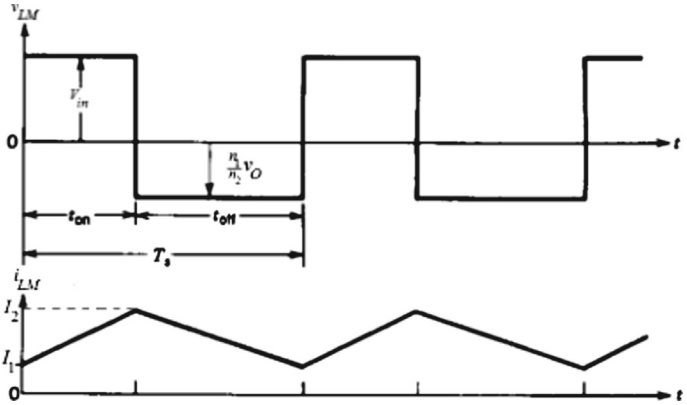

Fig. 4 Steady state voltage and current of boost converter

Figure 2 represents the ON state of flyback converter, state space equation can be calculated as:

$$\dot{X} = A_{\text{on}}X + B_{\text{on}}0 \leq t \leq t_{\text{on}} \tag{5}$$

where A_{on} and B_{on} can be interpreted as

$$A_{\text{on}} = \begin{bmatrix} 0 & 0 \\ 0 & -\frac{1}{\text{RC}} \end{bmatrix}, B_{\text{on}} = \begin{pmatrix} \frac{V_{\text{in}}}{L_m} \\ 0 \end{pmatrix} \tag{6}$$

Figure 3 represents the OFF state of flyback converter, state space equation can be calculated as:

$$\dot{X} = A_{\text{off}}X + B_{\text{off}}t_{\text{on}} \leq t \leq T_s \tag{7}$$

where A_{off} and B_{off} can be interpreted as

$$A_{\text{off}} = \begin{bmatrix} 0 & -\frac{n_1}{n_2}\frac{1}{L_m} \\ \frac{n_1}{n_2}\frac{1}{c} & -\frac{1}{\text{RC}} \end{bmatrix}, B_{\text{off}} = \begin{pmatrix} 0 \\ 0 \end{pmatrix} \tag{8}$$

The state variable will show nonlinear behavior during ON and OFF intervals, although all the input parameters remains constant during each switching cycle. Considering the condition that variation in state variables over one switching cycle is small in comparison with average cycle of state variables then total deviation in state vector over one period T can be formulated as:

$$(A_{\text{on}}X + B_{\text{on}})d + (A_{\text{off}}X + B_{\text{off}})(1 - d) \Rightarrow A_{\text{avg}}X + B_{\text{avg}} \tag{9}$$

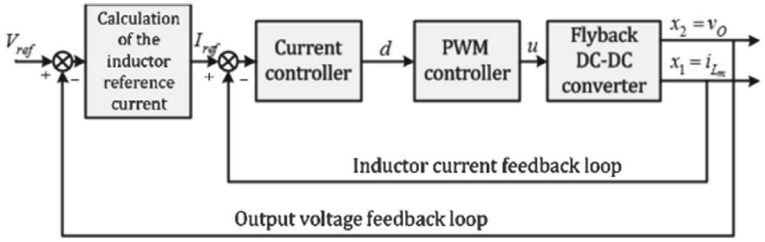

Fig. 5 Inner current outer voltage indirect control of flyback converter

After averaging state space model can be obtained as:

$$\dot{X} = \begin{bmatrix} 0 & -\frac{n_1}{n_2}\frac{1}{L_m}(1-d) \\ \frac{n_1}{n_2}\frac{1}{C}(1-d) & -\frac{1}{\mathrm{RC}} \end{bmatrix} + \begin{bmatrix} \frac{V_{\mathrm{in}}}{L_m}d \\ 0 \end{bmatrix} \tag{10}$$

Transfer functions of the flyback converter

$$i_{Lm} = I_{Lm} + i_{lm} \tag{11}$$

$$v_o = V_o + v_O, D = \Delta + d \tag{12}$$

Equation (10) averaged state space model [5] of the converter yields the following findings when Eq. (11) is substituted (Fig. 5).

If the DC elements are considered final state space matrix:

$$\begin{bmatrix} \dot{i}_{lm} \\ \dot{v}_o \end{bmatrix} = \begin{bmatrix} 0 & -\frac{n_1}{n_2}\frac{1}{L_m}(1-\Delta) \\ \frac{n_1}{n_2}\frac{1}{C}(1-\Delta) & -\frac{1}{\mathrm{RC}} \end{bmatrix} \begin{bmatrix} i_{lm} \\ v_O \end{bmatrix} + \begin{bmatrix} \frac{V_{\mathrm{in}}}{L_m} + \frac{n_1}{n_2}\frac{1}{L_m}v_o \\ 0 \end{bmatrix} d \tag{13}$$

Applying Laplace transformation to the Eq. (13) with zero initial conditions:

$$\begin{bmatrix} \dot{i}_{lm} \\ \dot{v}_o \end{bmatrix} = \mathrm{Inv}\left[\mathrm{SI} - \begin{bmatrix} 0 & -\frac{n_1}{n_2}\frac{1}{L_m}(1-\Delta) \\ \frac{n_1}{n_2}\frac{1}{C}(1-\Delta) & -\frac{1}{\mathrm{RC}} \end{bmatrix} \right] \begin{bmatrix} \frac{V_{\mathrm{in}}}{L_m} + \frac{n_1}{n_2}\frac{1}{L_m}v_o \\ 0 \end{bmatrix} d \tag{14}$$

As system state variables are supposed to be output from control-system perspective, duty cycle, d can be used to regulate the output voltage v_o and inductor current i_{lm} of the flyback converter. Transfer functions can be represented as:

$$H_1(S) = \frac{v_o}{d},\ H_2(S) = \frac{i_{lm}}{d} \tag{15}$$

Considering Eq. (14) transfer function can be obtained as:

$$H_1(S) = \frac{V_{\text{in}}(R - \text{SL}_m \frac{n_1}{n_2} \frac{\Delta}{(1-\Delta)^2}}{S^2 L_m \text{RC}\left(\frac{n_1}{n_2}\right)^2 + \text{SL}_m\left(\frac{n_1}{n_2}\right) + R(1-\Delta)^2} \tag{16}$$

$$H_2(S) = \frac{V_{\text{in}}\left(1 + \Delta + \text{SRC}\frac{\frac{n_1}{n_2}}{1-\Delta}\right))}{S^2 L_m \text{RC}\left(\frac{n_1}{n_2}\right)^2 + \text{SL}_m\left(\frac{n_1}{n_2}\right) + R(1-\Delta)^2} \tag{17}$$

As presence of right half plane zero in Eq. 16 result unstable behavior of flyback converter therefore direct output voltage controlling is difficult, also similar problem is not observed in Eq. (17) so by simply selecting suitable compensating network inductor current can be controlled.

4 Design of Controller Using Sliding Mode Control for Flyback Converter

Consider nonlinear system having origin as its operating point at steady state.

$$\dot{p} = Mp + uNp \tag{18}$$

where M and N are square matrix of order $(n * n)$ having all the real terms. The switching control action can be controlled by, scalar control u, its value can be either 0 and 1. Hence u can be represented as:

$$u = \frac{1}{2}(1 + \text{sgn}S(p)) \tag{19}$$

In above Eq. (19), sgn refers to mathematics signum function, $S(p)$ refers to sliding surface for sliding mode controller design.

$$\text{Case 1 : if} \qquad S(p) > 0 \Rightarrow u = 1 \tag{20}$$

$$\text{Case 2 : if} \qquad S(p) < 0 \Rightarrow u = 0 \tag{21}$$

From Lyapunov function for stability of nonlinear system one of necessary and sufficient condition for state variables to be sliding on sliding surface is

$$\lim S\dot{S} < 0 \tag{22}$$

for smooth sliding of state variables on sliding surface manifold equivalent control u_{eq} is designed by equating derivative of sliding manifold to zero, i.e.,

$$\frac{dS}{dt} = 0 \Rightarrow \left[\frac{\partial S}{\partial p}\right]^T \dot{p} = 0 \tag{23}$$

From Eq. (18) referring the value of $\dot{p}$ and equating in Eq. (23), equivalent control can be found as:

$$u_{\text{eq}} = -\frac{\left[\frac{\partial S}{\partial p}\right]^T Mp}{\left[\frac{\partial S}{\partial p}\right]^T Np} \quad 0 \leq u_{\text{eq}} \leq 1 \tag{24}$$

Selecting inductor current as reference:

$$i_{\text{ref}} = K_P[V_{\text{ref}} - V_o] + K_I \int (V_{\text{ref}} - V_o)\mathrm{d}t \tag{25}$$

4.1 Designing and Selection of Sliding Surface Manifold

Sliding surface manifold [6] is considered to be linear combination of state variables of the system vector.

$$S(p) = \gamma_1 p_1 + \gamma_2 p_2 + \gamma_3 p_3 \tag{26}$$

While designing of sliding manifold the state variables selected must have zero steady-state error response, for same reason the flyback converter output voltage and inductor current to chosen as state variables, i.e., p_1 and p_2 respectively, in fixed frequency control to reduce steady-state error an extra control variable p_3 is introduced. The γ_1, γ_2 and γ_3 are fixed constant gains of systems.

$$\begin{aligned} p_1 &= i_{\text{ref}} - i_{LM}, \; p_2 = V_{\text{ref}} - v_o \\ p_3 &= \int (p_1 + p_2)\mathrm{d}t \end{aligned} \tag{27}$$

4.2 Design of Equivalent Controller for Flyback Converter

Assuming flyback converter to be in continuous conduction mode (CCM) [7] and from Eq. (27) the dynamic characteristic of flyback converter can be formulated

Table 1 Values of fixed constant gains

Gain	Value
K_1	0.15
K_2	0.5
K_3	0.3
K_4	0.5
K_5	300

$$\begin{aligned}
\dot{p}_1 &= \frac{\mathrm{d}(i_{\mathrm{ref}} - i_{LM})}{\mathrm{d}t} \Rightarrow -\frac{K_p}{C} i_C + K_I(V_{\mathrm{ref}} - v_o) - \frac{uV_{\mathrm{in}} - (1-u)\frac{n_1}{n_2} v_o}{L_m} \\
\dot{p}_2 &= \frac{\mathrm{d}(V_{\mathrm{ref}} - v_o)}{\mathrm{d}t} \Rightarrow -\frac{1}{C} i_C \\
\dot{p}_3 &= p_1 + p_2 \Rightarrow \big(K_p + 1\big)(V_{\mathrm{ref}} - v_o) - i_{LM} + K_I \int (V_{\mathrm{ref}} - v_o)\mathrm{d}t
\end{aligned} \tag{28}$$

In above Eqs. (28) u is scalar control function for Mosfet switch.

Case 1: If u is logic 1, resembles switch is in ON state.

Case 2: If u is logic 0, resembles switch is in OFF state.

Equating the Eq. (28) of sliding surface derivative with respect to time as zero, equivalent controller can be obtained (Table 1).

$$u_{\mathrm{eq}} = \frac{1}{V_{\mathrm{in}} + K_2 v_o}\left[K_1(V_{\mathrm{ref}} - v_o) + K_2 v_o + K_3 i_c + K_4 i_{LM} + K_5 \int (V_{\mathrm{ref}} - v_o)\mathrm{d}t \right. \tag{29}$$

where

$$\begin{aligned}
&K_1 = L_m\left[K_I + \frac{\gamma_3}{\gamma_1}(K_P + 1)\right],\ K_2 = \frac{n_1}{n_2},\ K_3 = -L_m\frac{\gamma_3}{\gamma_1},\ K_4 = -\frac{L_m}{C}, \\
&K_5 = L_m\frac{\gamma_3}{\gamma_1}K_I
\end{aligned} \tag{30}$$

5 MATLAB Simulations

See Figs. 6, 7, 8, 9, 10 and 11, Table 2.

As SMC controller designed for flyback converter when output load varies from [10–13 Ω], i.e., 30% increment in output load keeping input voltage 10 V constant, reference voltage as 20 V we observe that time taken to track the output voltage is smooth and designed controller response quickly to any output load variation (Figs. 12, 13 and 14).

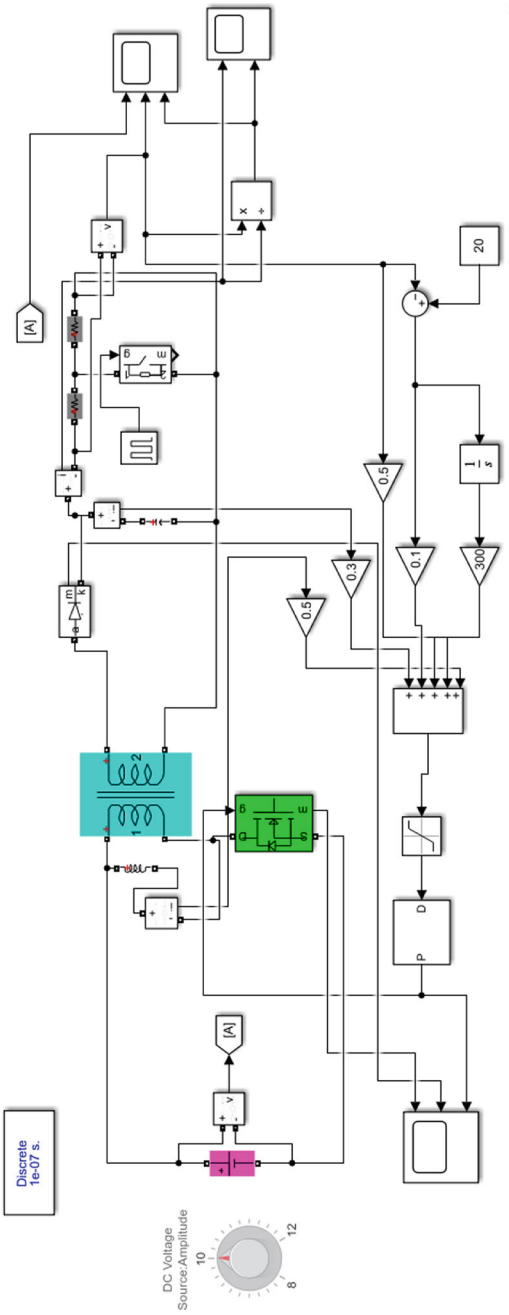

Fig. 6 Flyback converter MATLAB Simulink model

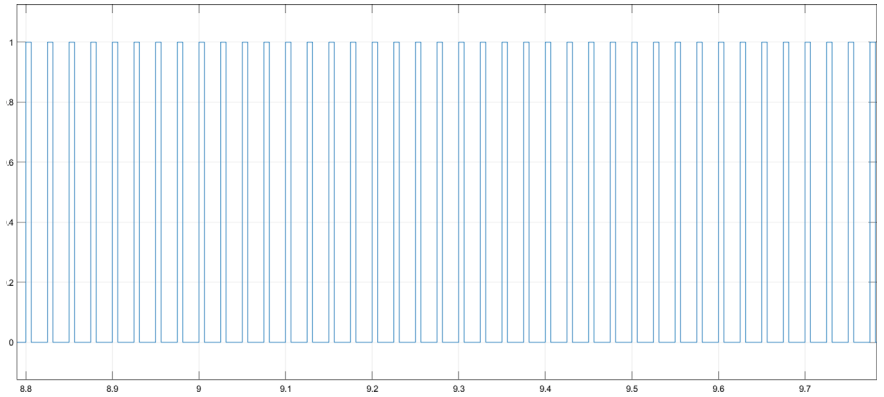

Fig. 7 PWM control signals given to switch ($u = 1$ or $u = 0$)

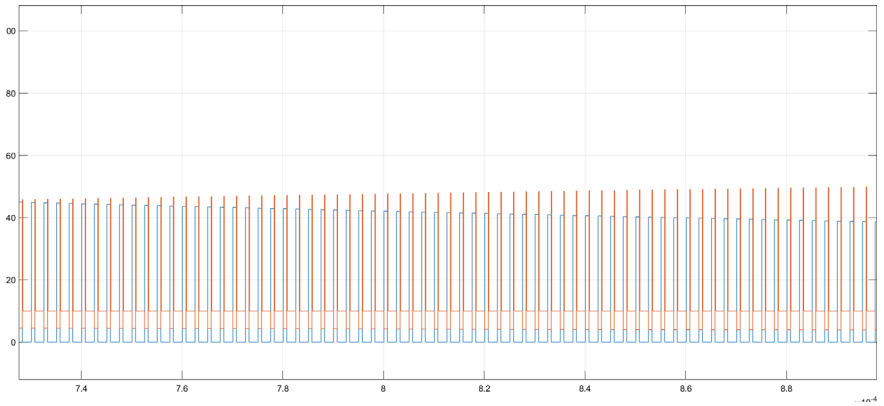

Fig. 8 Spectrum of Mosfet signals

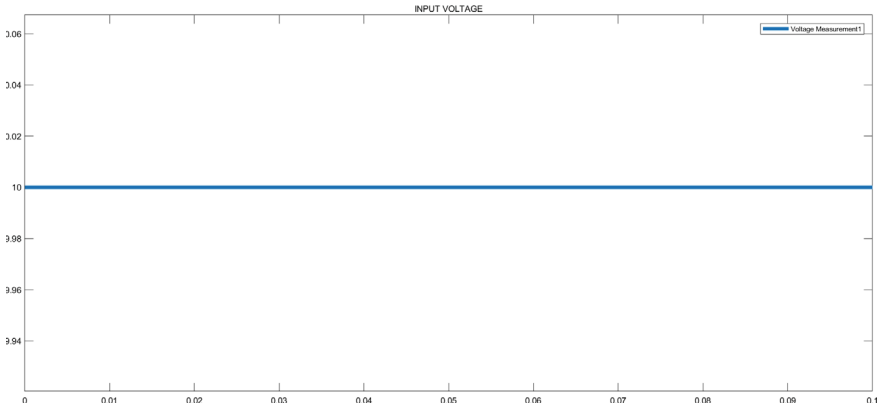

Fig. 9 Input voltage [8] applied to flyback converter

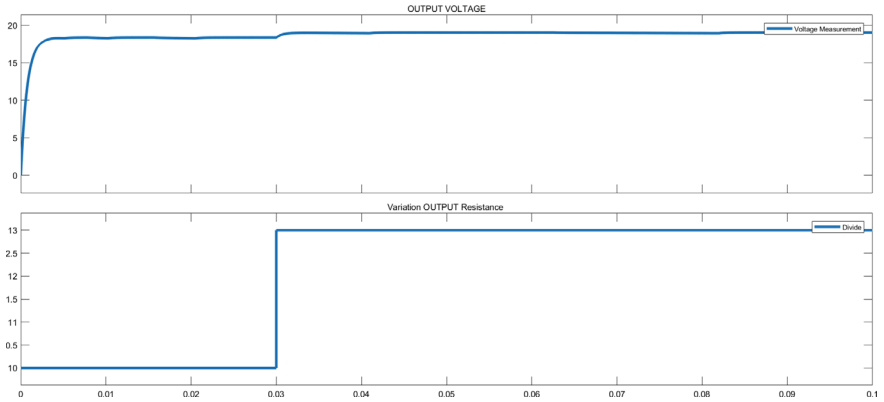

Fig. 10 Output load changes from 10–13 Ω

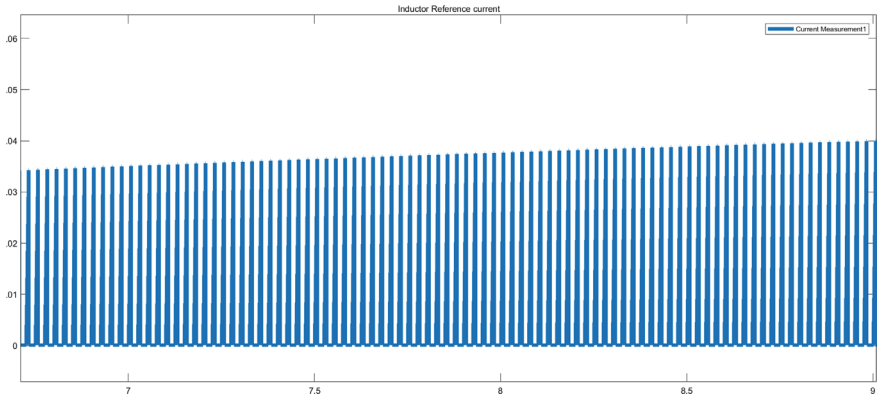

Fig. 11 Inductor reference current

Table 2 Parameters of flyback converter for SMC controller

Parameters of converter	Reference values
Input voltage	10 V
Output reference voltage	20 V
Load resistance	10 Ω
Output filter capacitor	470 micro-farad
Primary winding leakage reactance	100 micro-Henry
Switching frequency	30 kHz
Transformer turns ratio ($N1/N2$)	0.5

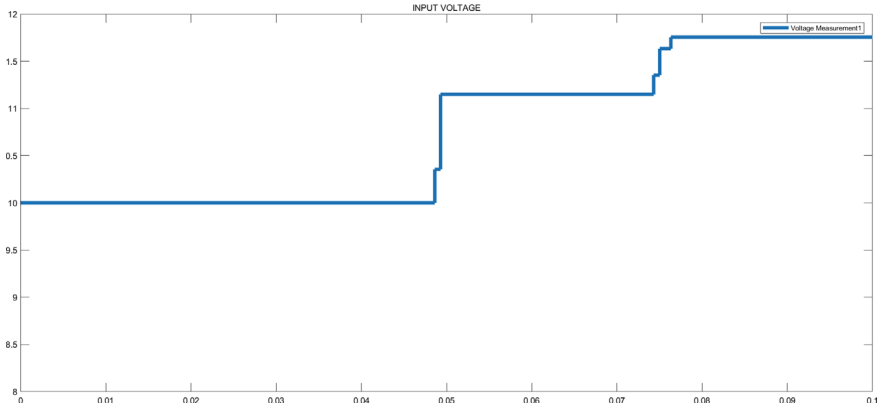

Fig. 12 Input voltage variation from [10 V–11 V–12 V]

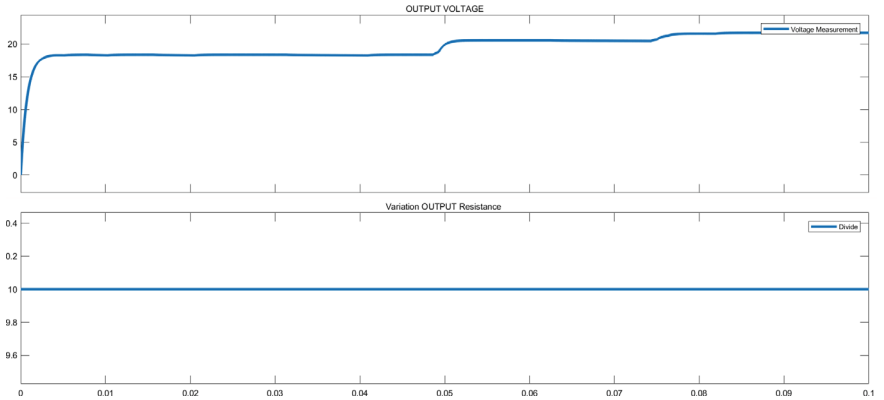

Fig. 13 Simulation result for output voltage and R10ohm

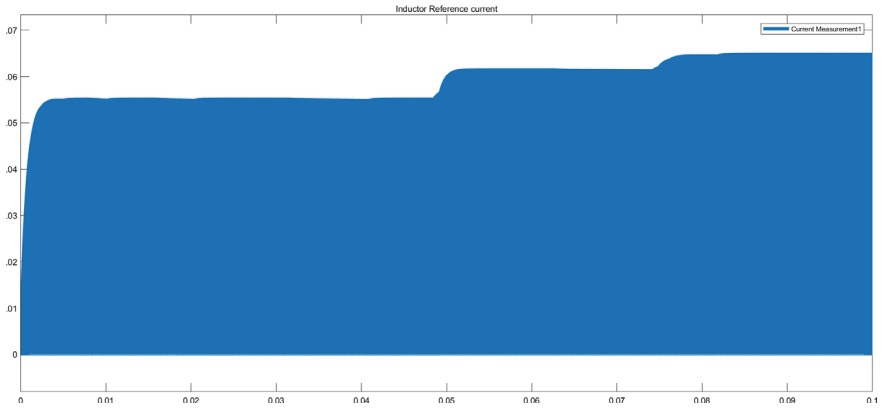

Fig. 14 Inductor reference current

When the input voltage is varied from [10 V–11 V–12 V] keeping output load resistance 10 Ω, we observe that there is slight disturbance that arises in output voltage whenever there is input voltage changes, but it tracks the output voltage quickly and settles down at fast rate (Figs. 15, 16, 17, 18, 19 and 20).

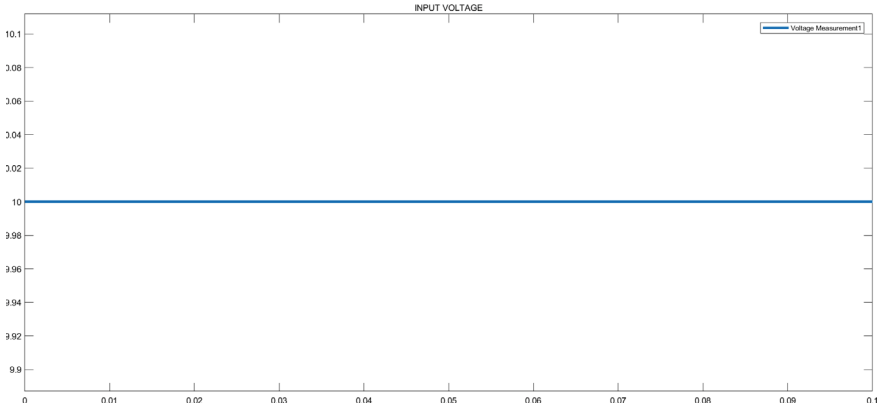

Fig. 15 Input voltage [8] applied to flyback converter

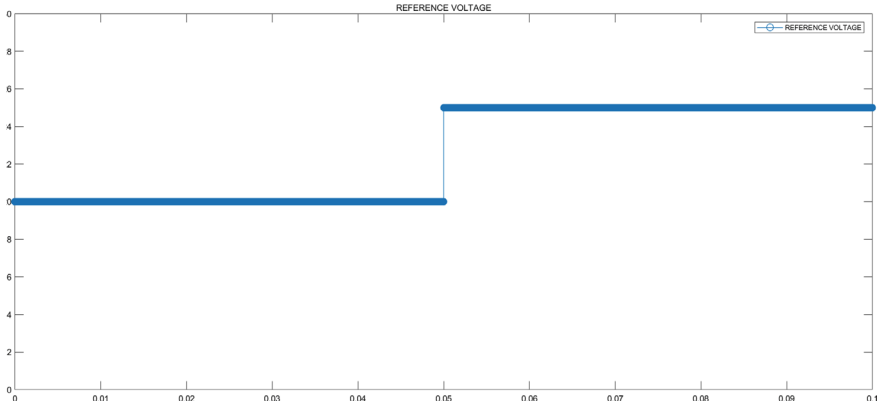

Fig. 16 Variation in reference voltage [20–25 V]

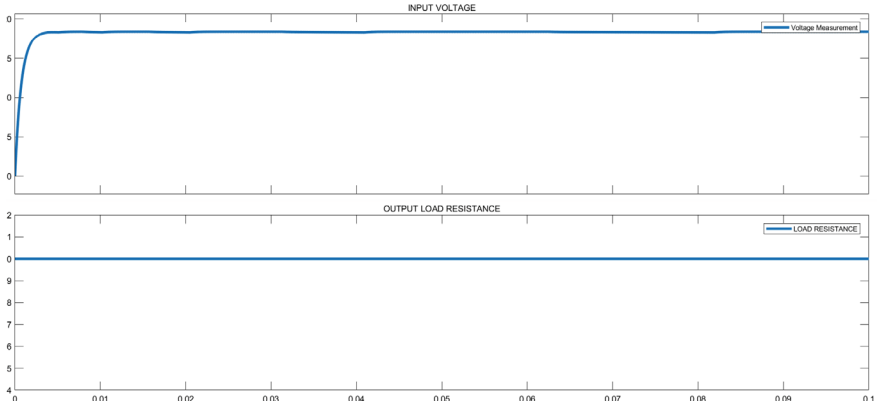

Fig. 17 Result of output voltage and load resistance

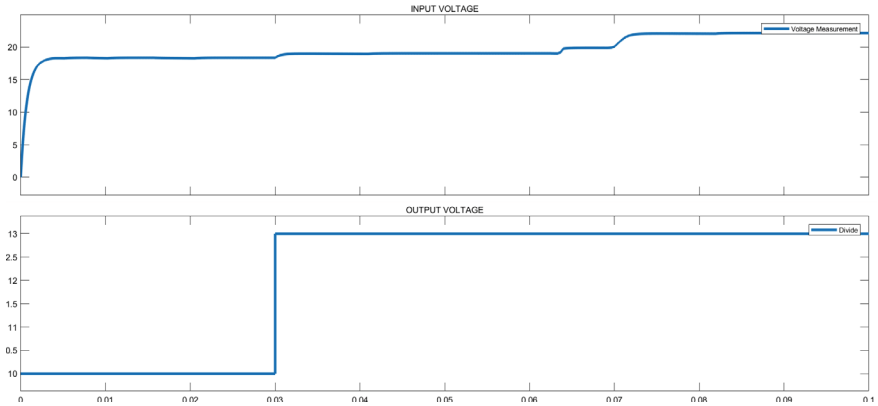

Fig. 18 Variation in output load resistance [10–13 Ω]

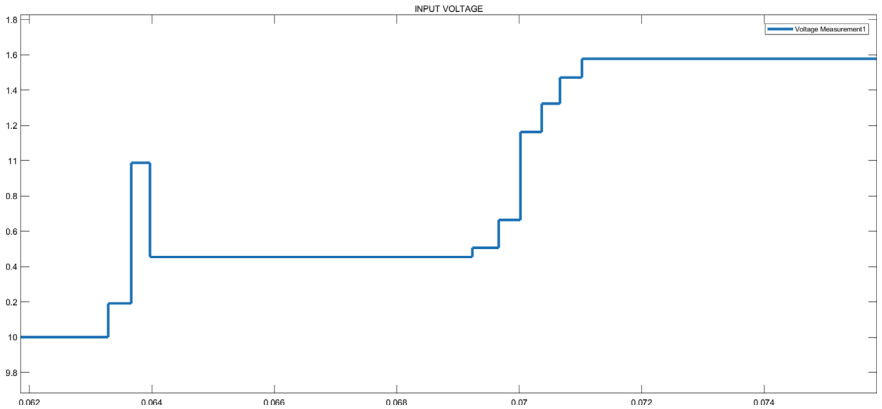

Fig. 19 Variation in input voltage [10 V–11 V–12 V]

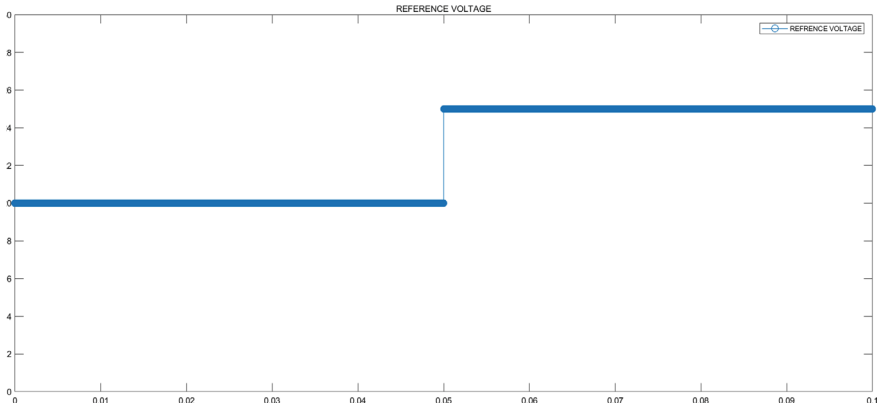

Fig. 20 Variation in reference voltage [20–25 V]

6 Conclusion

From above mathematical modeling and MATLAB Simulation of flyback converter in CCM mode, design sliding mode control, we can conclude that sliding mode control is nonlinear control technique that aims to drive the state variable onto a specific sliding manifold and maintain it on that surface regardless of uncertainties and disturbances. Like we put disturbances by varying input voltage, output load resistance, and reference voltage but still controller manages to track the desired output voltage and inductor current.

The primary objective of SMC is to achieve robustness to uncertainties and disturbances.

Its robustness to uncertainties, insensitivity to parameter variations, and ability to handle nonlinear dynamics make it particularly suitable for systems with complex and uncertain dynamics. SMC has been successfully applied in various control applications, including power electronics, robotics, aerospace systems, and automotive systems.

Sliding mode control (SMC) is a robust control technique that has been widely studied and applied in various engineering fields. While the future scope of work for sliding mode control can vary depending on specific applications and research interests, here are some potential areas of focus:

1. Advanced SMC algorithms: Researchers can explore the development of advanced SMC algorithms that improve control performance, reduce chattering effects, and enhance robustness. This can involve designing novel sliding surfaces, incorporating adaptive techniques, or combining SMC with other control strategies.
2. Nonlinear systems: Sliding mode control has proven effective for linear systems, but its application to nonlinear systems remains an active area of research. Future work can focus on developing sliding mode control approaches tailored for

nonlinear systems, such as adaptive sliding mode control, higher-order sliding mode control, or fractional order sliding mode control.
3. Applications in emerging technologies: Sliding mode control has been successfully applied in various fields, including power electronics, robotics, aerospace, and automotive systems. As emerging technologies such as renewable energy systems, autonomous vehicles, and smart grids continue to advance, there is a need to adapt and optimize sliding mode control techniques for these specific applications.

References

1. Komurcugil, H., Biricik, S., Bayhan, S., Zhang, Z.: Sliding mode control: overview of its applications in power converters. IEEE Ind. Electron. Mag. **15**(1), 40–49 (2021). https://doi.org/10.1109/MIE.2020.2986165
2. Young, K.D., Utkin, V.I., Ozguner, U.: A control engineer's guide to sliding mode control. IEEE Trans. Control Syst. Technol. **7**(3), 328–342 (1999). https://doi.org/10.1109/87.761053
3. Coruh, N., Urgun, S., Erfidan, T.: Design and implementation of flyback converters. In: 2010 5th IEEE Conference on Industrial Electronics and Applications, Taichung, Taiwan, pp. 1189–1193 (2010). https://doi.org/10.1109/ICIEA.2010.5515894
4. Cheng, W., He, X., Xu, S., Sun, W.: Analysis and accurate modeling of a flyback converter on conducted EMI. In: 2015 9th International Conference on Power Electronics and ECCE Asia (ICPE-ECCE Asia), Seoul, Korea (South), pp. 2275–2281 (2015). https://doi.org/10.1109/ICPE.2015.7168103
5. Kleebchampee, W., Bunlaksananusorn, C.: Modeling and control design of a current-mode controlled flyback converter with optocoupler feedback. In: 2005 International Conference on Power Electronics and Drives Systems, Kuala Lumpur, Malaysia, pp. 787–792 (2005). https://doi.org/10.1109/PEDS.2005.1619792
6. Ramos-Paja, C.A., Bastidas-Rodriguez, J.D., Saavedra-Montes, A.J.: Sliding-mode control of a photovoltaic system based on a flyback converter for microinverter applications. Appl. Sci. **12**, 1399 (2022). https://doi.org/10.3390/app12031399
7. Salimi, M., Hajbani, V.: Sliding-mode control of the DC-DC flyback converter in discontinuous conduction mode. In: The 6th Power Electronics, Drive Systems and Technologies Conference (PEDSTC2015), Tehran, Iran, pp. 13–18 (2015). https://doi.org/10.1109/PEDSTC.2015.7093242
8. Baby, Nithya, M.: Sliding mode controlled forward converter. In: 2015 IEEE 9th International Conference on Intelligent Systems and Control (ISCO), Coimbatore, India, pp. 1–4 (2015). https://doi.org/10.1109/ISCO.2015.7282270
9. Seker, M., Zergeroglu, E.: A new sliding mode controller for the DC to DC flyback converter. In: 2011 IEEE International Conference on Automation Science and Engineering, Trieste, Italy, pp. 720–724 (2011). https://doi.org/10.1109/CASE.2011.6042474
10. Yigeng, H., Yu, W.: A robust flyback converter based on high order sliding mode control for fuel cell. In: IECON 2014—40th Annual Conference of the IEEE Industrial Electronics Society, Dallas, TX, USA, pp. 3936–3940 (2014). https://doi.org/10.1109/IECON.2014.7049089
11. Cornea, O., Andreescu, G.D., Patrascu, C.-C., Muntean, N.: HD improvement of a bidirectional flyback inverter by using sliding-mode control. In: 2015 International Aegean Conference on Electrical Machines and Power Electronics (ACEMP), 2015 International Conference on Optimization of Electrical and Electronic Equipment (OPTIM) and 2015 International Symposium on Advanced Electromechanical Motion Systems (ELECTROMOTION), Side, Turkey, pp. 488–493 (2015). https://doi.org/10.1109/OPTIM.2015.7426746

12. Riaz, M., Yasin, A.R., Arshad Uppal, A., Yasin, A.: A novel dynamic integral sliding mode control for power electronic converters. Sci. Progress **104**(4) (2021). https://doi.org/10.1177/00368504211044848
13. Utkin, V.I.: Sliding mode control design principles and applications to electric drives. IEEE Trans. Industr. Electron. **40**(1), 23–36 (1993). https://doi.org/10.1109/41.184818

An Employment of PID Controller-Based Genetic Algorithm for the Load Frequency Control of Two-Area Power System Network

Arun Singh Rana, Omveer Singh, and C. B. Vishwakarma

Abstract The paper presents the load frequency control of two-area power system network using PID controller-based genetic algorithm. The structure of power system network consists of solar photovoltaic (SPV), wind turbine (WT), battery energy (BESS), and conventional source (CS) which are connected with common grid and a connected load. SPV, WT, and BESS have variable generation which lot of fluctuations in generated power and frequency. In order to avoid such fluctuations, closed-loop PID controller is applied and tuning of PID controller is assessed with traditionally and genetic algorithm (GA). It is observed that change in frequency and change in power developed are found to be less with GA in comparison with PID controller and traditional method. Similarly, the settling time to achieve the steady state is found to be reduced with GA in comparison to others.

Keywords SPV · WT · BESS · GA · PID

List of Symbols

T_{12}	Deviation in tie-line power
K_P	Gain of net output
T_p	Time constant of net output
T_s	Time constant of solar PV array
T_w	Time constant of wind turbine
T_b	Time constant of BESS
T_g	Time constant of conventional source
K_p	Proportionality constant of PID controller

A. S. Rana (✉) · O. Singh
Department of Electrical Engineering, Gautam Buddha University, Greater Noida, Uttar Pradesh, India
e-mail: arunrana2k1@gmail.com

C. B. Vishwakarma
Department of Electrical Engineering, HBTU Kanpur, Kanpur, Uttar Pradesh, India

© The Author(s), under exclusive license to Springer Nature Singapore Pte Ltd. 2025

H. P. Singh et al. (eds.), *Recent Developments in Control, Automation and Power Engineering*, Lecture Notes in Electrical Engineering 1303,
https://doi.org/10.1007/978-981-96-0047-2_26

K_i	Integral constant of PID controller
K_d	Derivative constant of PID controller
B	Bias factor of frequency
Δd_s	Wind turbine disturbance
Δd_w	Solar PV disturbance
ΔP_W	Deviation in wind turbine output
ΔP_b	Deviation in BESS output
ΔP_d	Deviation in load disturbance
ΔP_S	Deviation in solar PV array

1 Introduction

In addition to ensuring that power transfers on the tie line connecting the two linked electrical systems remain at the predetermined point, the load frequency control, that is an essential component of the power system, also minimizes frequency variation to zero in the event that a disruption occurs. Modern microgrid power systems incorporate a lot of battery packs and sources of clean energy to reduce energy consumption and increase the efficiency of using energy. Naturally, the power system is also exposed to some disturbance elements that are directly influenced by external factors, such as wind or sun, and this considerably increases the complexity of the LFC. The article's main focus, with regard to communication methods, is LFC in a multi-area interconnected microgrid energy system. In order to counteract frequency deviation caused by a power imbalance, a sliding mode management scheme based on the flexible event-triggered method is proposed. By taken into consideration a three-area power system linked to power from renewable sources and storage of energy, the pertinent LFC model is initially constructed. Secondly, the LFC scheme gains networked supervision. A dynamic trigger mechanism that is capable of dynamically adjusting the event-triggered limit is developed in order to improve the efficiency of data transfer. Next, the network-induced delayed LFC scheme is constructed. Lastly, the Luenberger observer is designed to compute precondition faults and facilitate the construction of sliding surfaces [1–5]. Additional research is available in [6, 7].

It should be taken into account that the processes indicated above frequently assume task state in a continual way, which means that every packet of data is delivered through shared networks of communication with any data updating or processing. However, as mentioned in [8, 9], the control system's update period often has a 2–4 s update interval (sampling interval) in a real-world power system. Such a system only transmits the sampled information when an established threshold criterion is broken. Through the use of time-triggered tested-data control, the duration of sampling can also be prolonged [10, 11]. By applying the Lyapunov theory to an autonomous hybrids electrical system, researchers were able to achieve an extended sampling time [12]. For both a conventional single-area and a multi-area power system that uses wind power, a longer sample duration was designed in order

to reduce the channel's occupation and transmitting the signal. It is being demonstrated that implementing energy storage devices in electrical systems is an effective way to mitigate the impact of electrical breakdowns and variations in load demand on system performance. ESS can respond quickly when electric systems' load frequencies change. Several investigations have been conducted on ESS-powered power systems. Utilizing integrated frequency management and the power store mix modulating of frequency program of the Southern China Power Grid, as demonstrated in [13] can enhance the frequency control performance indices of generators via storage of energy. In [14, 15], linked power systems using supercapacitors are discussed. To attain the LFC index, it is advised to handle supercapacitor charging and discharge using the Buck-Boost architecture and fuzzy control approach. Xie et al. [15] investigated a hybrid system of storing energy consisting of supercapacitors and fuel cell technology that combined artificial neural networks with adaptable control methods to achieve LFC in multi-area interconnected electrical systems. To monitor the max power point for photovoltaic systems, a TSMC for electrical systems has been created [16]. In [17], connection to the grid and wind energy are considered. The LFC of the system with generation constraints is reached by TSMC design. TSMC was developed and improved utilizing an artificial bee colony approach with subsystems incorporating ESS and renewable energy sources of information, which satisfied the LFC control requirements [18]. The optimal control of multi-hydrogen renewable energy system has been discussed in [19], and implementation of performance parameters with power electronics converter has been discussed in [20].

2 Structure of Multi-area System

The components of the network of the power system include a connected load, a common grid, and solar photovoltaic, wind turbine, battery energy, and conventional sources. The structure of integrated system composite of various generating units is shown in Fig. 1. The structure of model of proposed system is referred from Ref. [1]. Generally the disturbance in solar and wind occurs frequently throughout the day. These disturbances or fluctuations also affect the output power which ultimately causes the change in frequency and power. Similar type of fluctuation or deviation in the output will be observed for other generating sources like (BESS and conventional source).

In order to analyze such fluctuations, the generating sources are represented in the form of transfer function. The first-order transfer function is self-sufficient to analyze the effect of disturbance.

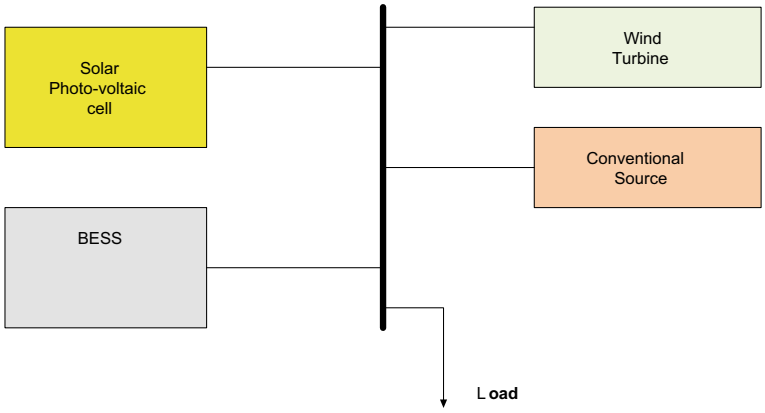

Fig. 1 Structure of the integrated system

3 Transfer Function Model of Two-Area System Based on PID Controller

The multi-area system's function of transfer model is cited in [1]. Equation 1 illustrates how the tie-line power flow between the two electrical system regions is dependent upon changes in the two-area systems' frequencies.

$$\Delta P_{\text{tie}} = \frac{2\pi T_{12}}{s}(\Delta F_1 - \Delta F_2). \tag{1}$$

The difference between various generating units and load is passing through first-order system which gives change in frequency of area 1 as shown in Eq. 2.

$$\left(\Delta P_S + \Delta P_W + \Delta P_b + \Delta P_g - \Delta P_d\right)\frac{K_p}{(1 + sT_P)} = \Delta F_1. \tag{2}$$

The change in solar photovoltaic output depends on the disturbance as mentioned in Eq. 3.

$$\Delta P_s = \frac{1}{1 + sT_s}\Delta d_s. \tag{3}$$

The change in wind turbine output depends on the input disturbance as mentioned in Eq. 4.

$$\Delta P_w = \frac{1}{1 + sT_w}\Delta d_w. \tag{4}$$

The change in BESS output depends on the frequency deviations as mentioned.

$$\Delta P_b = \frac{1}{1 + sT_b} \Delta F_1. \tag{5}$$

The change in area control for a particular area depends on the power deviations and fluctuations in frequency. Ideally, this change in frequency and power must be approached to 0. In general way, ACE depends on change in frequency and power deviations as a linear combination which is mentioned in Eq. 6.

$$\text{ACE} = \beta \Delta F_1 + \Delta P_{\text{tie}}. \tag{6}$$

This ACE passes through PID controller and certain transfer function gain which gives change in power generation of conventional source as shown in Eq. 7.

$$\Delta P_g = \frac{1}{(1 + sT_g)(1 + sT_d)} \left(k_p + \frac{k_i}{s} + sk_d \right) \text{ACE}. \tag{7}$$

The proportionality constant of PID controller is determined randomly on hit and trial basis, and value of proportionality constant is determined as:

$$K_p = 25.6,\ K_i = 32.7,\ K_d = 43.6.$$

It is found that still change in power and frequency is high with the hit and trial method of tuning the PID controller. In order to improve or reduce the change in power and frequency, genetic algorithm is employed and its design aspects will be discussed in the next sections.

The transfer function model of the various generating units for the two-area power system network is shown in Fig. 2. The structure wise modeling of two area system is same with the connection of tie line power.

4 Development of Genetic Algorithm (GA)

Another optimization method to manage or train the transfer function's unknowable parameters is the genetic algorithm. Three steps make up the genetic algorithm: reproduction, crossover, and mutation.

The best strings from the string mate pool's total number will be chosen for reproduction. Following reproduction, crossover is used, in which bits are exchanged between the two best strings. After that, a particular string undergoes mutation, where an arbitrary shift from 1 to 0 or 0 to 1 happens at the specified place. The following essential parameters are needed for genetic algorithm:

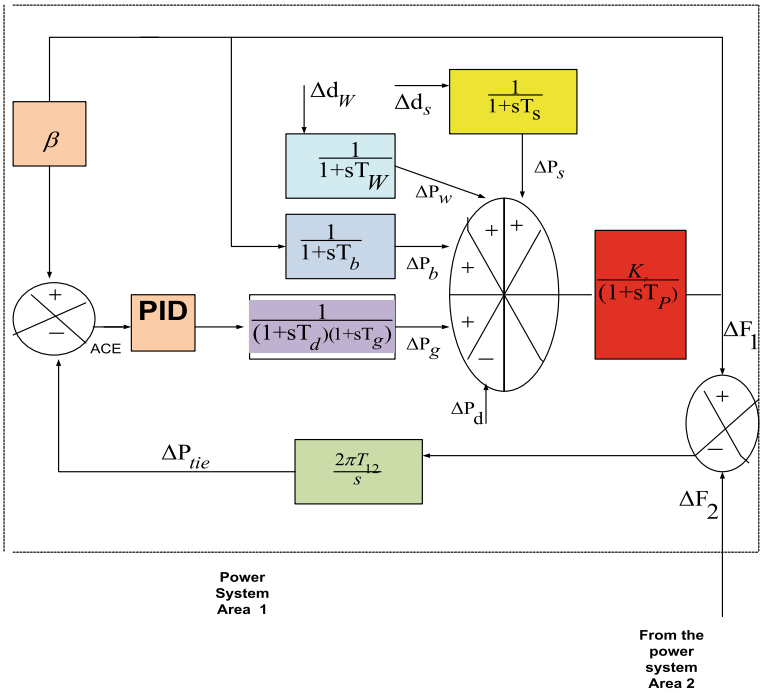

Fig. 2 Transfer function model of the various generating units

Size of the population: 5.
String length: 5.
Crossover of the Probability, $P_c = 0.7$.
Mutation of the Probability, $P_m = 0.06$.

The pertaining value of 'ACE' that belongs to three variables only (K_p, K_i, K_d). These three variables will be determined by Eq. 8:

$$f^r = f^{\min} + \frac{f^{\max} - f^{\min}}{2^l - 1} y^r, \tag{8}$$

where 'r' is iteration, and y^r is length of the binary string.

Equation (9) will be utilized for attaining the new constraint variables:

$$(f^r)_{\text{new}} = \frac{1}{(1 + \frac{\alpha' \varepsilon^r}{f^r})}. \tag{9}$$

Convergence factor $= f^r - (f^r)_{\text{new}}$.

Consider Eq. 7 as objective function as represented in Eq. 9 and trained the parameters using genetic algorithm with the help of reproduction, crossover, and

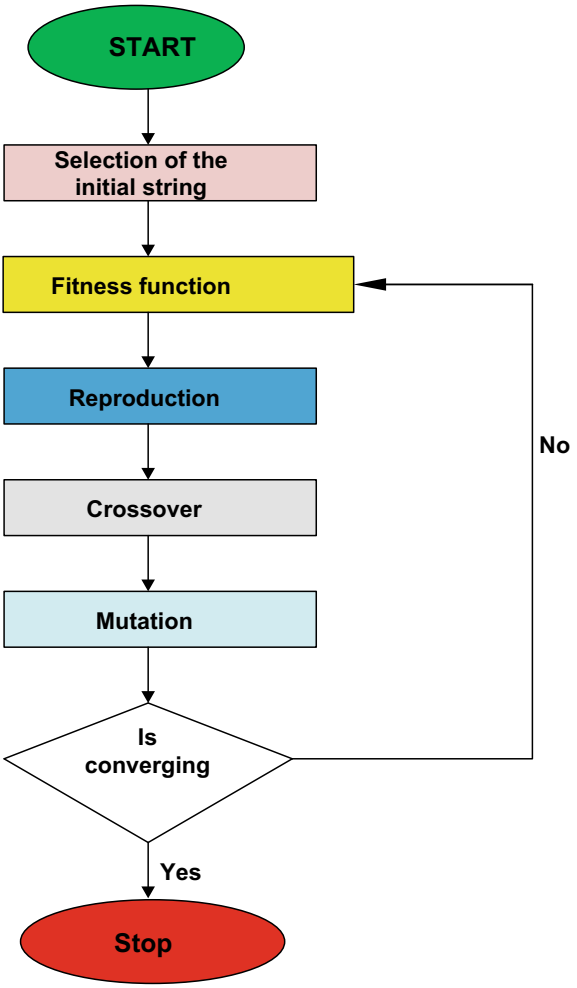

Fig. 3 Steps of genetic algorithm explaining through flowchart

mutation. The selection process of internal parameters has been discussed above along with Eq. 8. The flowchart explaining the genetic algorithm is shown in Fig. 3.

5 Performance Analysis of Frequency Deviation and Power Deviation

See Figs. 4, 5, 6, 7, 8, and 9.

The various characteristics of mechanical power deviation are observed for various disturbances like 1, 2, and 3% disturbance in the load. Similarly, the frequency deviation is also observed for various disturbances like 1, 2, and 3%. Both frequency

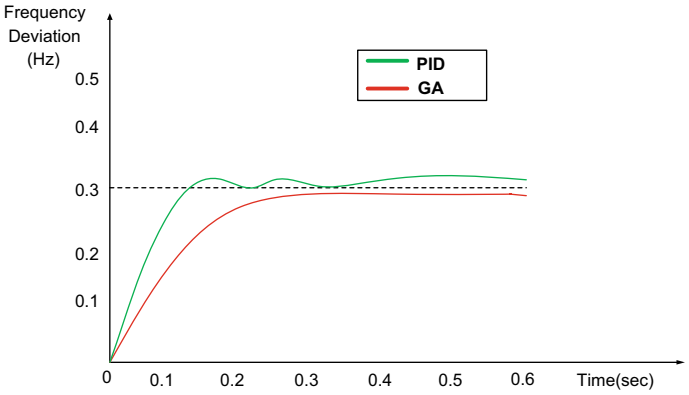

Fig. 4 Frequency deviation (Hz) of two-area system for 1% disturbance

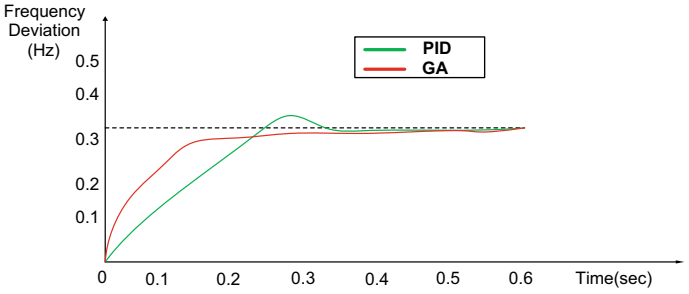

Fig. 5 Frequency deviation (Hz) of two-area system for 2% disturbance

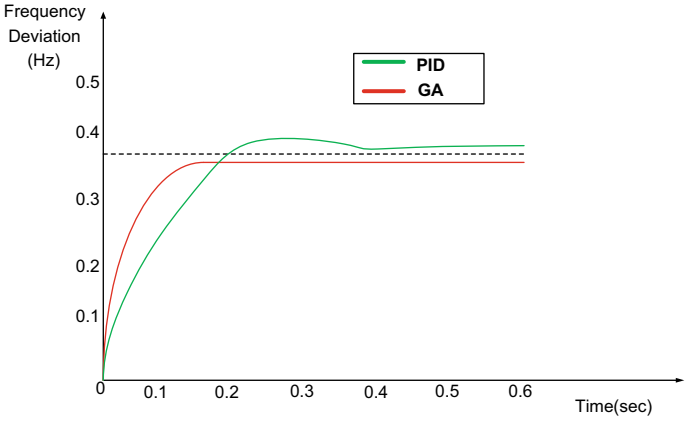

Fig. 6 Frequency deviation (Hz) of two-area system for 3% disturbance

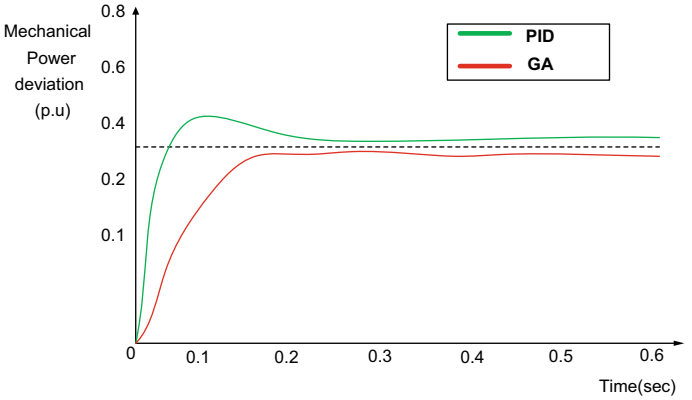

Fig. 7 Mechanical power deviation (Hz) of two-area system for 1% disturbance

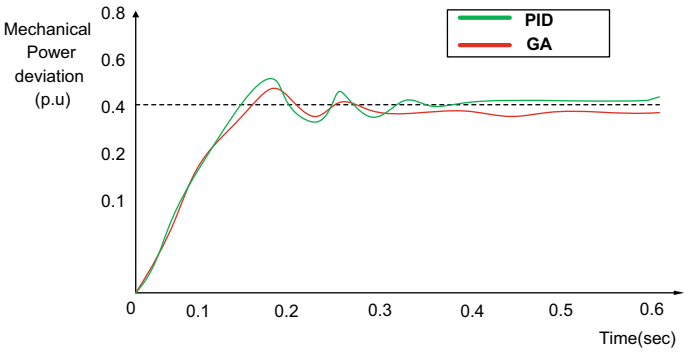

Fig. 8 Mechanical power deviation (Hz) of two-area system for 2% disturbance

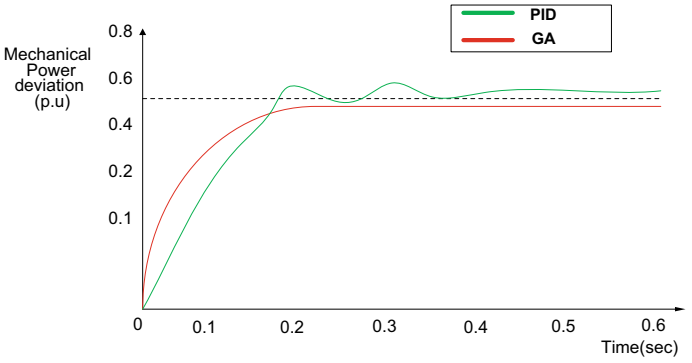

Fig. 9 Mechanical power deviation (Hz) of two-area system for 3% disturbance

deviation and mechanical deviation are analyzed with genetic algorithm and PID controller. The frequency deviation in Hz for various disturbances with PID controller and GA is shown in Table 1, and its graphical analysis is shown in Fig. 10.

Similarly, the mechanical power deviation in *p.u* for various disturbances with PID controller and GA is shown in Table 2, and its graphical analysis is shown in Fig. 11.

The settling time to reach the steady state in frequency deviation with PID controller and genetic algorithm for various disturbances is shown in Table 3, and its graphical comparison is shown in Fig. 12.

From the various characteristics, it is observed that frequency deviation and mechanical power deviation are found to be least with GA in comparison to PID controller for various load disturbances.

Similarly, settling time to attain the steady value of frequency deviations is found to be reduced more with GA in contrast to the PID controller.

Table 1 Frequency deviations for various disturbances

Load disturbance	PID controller	GA
1%	0.32	0.28
2%	0.29	0.27
3%	0.40	0.36

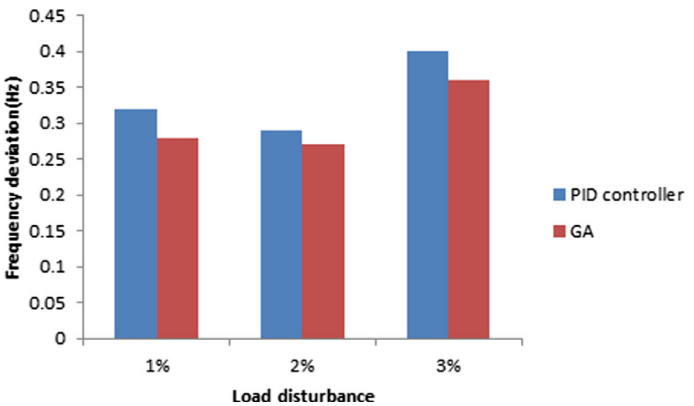

Fig. 10 Frequency deviation (Hz) comparison for various disturbances

Table 2 Mechanical power deviations for various disturbances

Load disturbance	PID controller	GA
1%	0.34	0.28
2%	0.41	0.38
3%	0.52	0.48

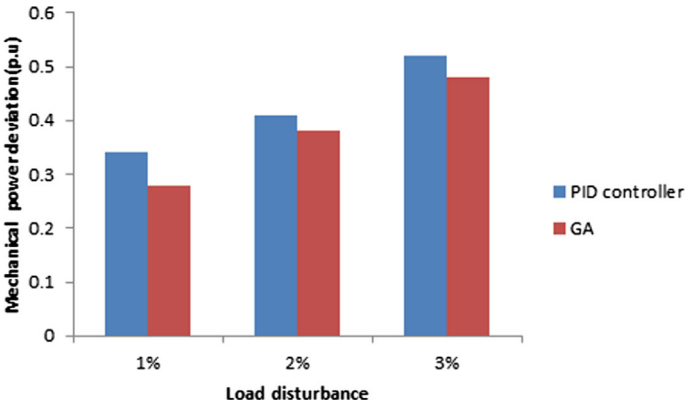

Fig. 11 Mechanical power deviation (*p.u*) comparison for various disturbances

Table 3 Settling time of the frequency deviations for various disturbances

Load disturbance (%)	PID controller	GA
1	0.40	0.30
2	0.35	0.31
3	0.40	0.20

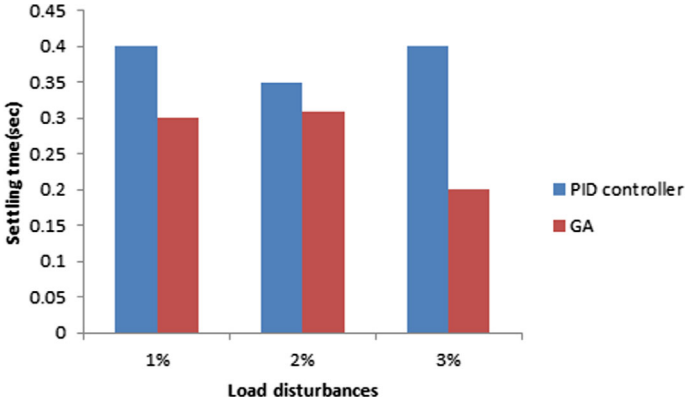

Fig. 12 Settling time of frequency deviation (s) comparison for various disturbances

6 Conclusion

The LFC of a multi-area power system network utilizing a PID controller-based genetic algorithm is presented in the study. The solar photovoltaic (SPV), wind turbine (WT), battery energy (BESS), and conventional source (CS) components of

the power system network are connected to the common grid and a connected load. The variable generation used by SPV, WT, and BESS results in significant variations in the generated power and frequency. Closed-loop PID controllers are used to prevent these fluctuations, and their tuning is evaluated using both conventional and genetic algorithms. When compared to PID controllers and conventional methods, it is shown that GA results in less change in frequency and change in power developed. Similar to this, it is discovered that using GA is faster than other methods for reaching a steady state.

References

1. Li, H., Wang, X., Xiao, J.: Adaptive event-triggered load frequency control for interconnected microgrids by, observer-based sliding mode control. IEEE Access, pp. 68271–68280 (2019)
2. Li, Z., Li, X., Cui, B.: Planar clouds based load frequency control in interconnected power system with renewable energy. IEEE Access **6**, 3645936468 (2018)
3. Xu, Y., Li, C., Wang, Z., Zhang, N., Peng, B.: Load frequency control of a novel renewable energy integrated micro-grid containing pumped hydropower energy storage. IEEE Access **6**, 2906729077 (2018)
4. Zhang, Y., Li, Y.W.: Energy management strategy for supercapacitor in droop-controlled DC microgrid using virtual impedance. IEEE Trans. Power Electron. **32**(4), 27042716 (2017)
5. Chen, C., Cui, M., Wang, X., Zhang, K., Yin, S.: An investigation of coordinated attack on load frequency control. IEEE Access **6**, 3041430423 (2018)
6. Yang, F., He, J., Wang, D.: New stability criteria of delayed load frequency control systems via infinite-series-based inequality. IEEE Trans. Ind. Inf. **14**(1), 231–240 (2018)
7. Jin, L., Zhang, C.K., He, Y., et al.: Delay-dependent stability analysis of multi-area load frequency control with enhanced accuracy and computation efficiency. IEEE Trans. Power Syst. **34**(5), 3687–3696 (2019)
8. Shang-Guan, X.C., He, Y., Zhang, C.K., et al.: Sampled-data based discrete and fast load frequency control for power systems with wind power. Appl. Energy **259**(114202) (2020)
9. Wen, S., Yu, X., Zeng, Z., et al.: Event-triggering load frequency control for multi-area power systems with communication delays. IEEE Trans. Ind. Electron. **63**(2), 1308–1317 (2016)
10. Dahiya, P., Mukhija, P., Saxena, A.R.: Design of sampled data and event-triggered load frequency controller for isolated hybrid power system. Int. J. Electr. Power Energ. Syst. **100**, 331–349 (2018)
11. Peng, C., Li, F.: A survey on recent advances in event-triggered communication and control. Inform. Sci. **457–458**, 113–125 (2018)
12. Liu, X., Zhang, Y., Lee, K.Y.: Coordinated distributed MPC for load frequency control of power system with wind farms. IEEE Trans. Ind. Electron. **64**(6), 5140–5150 (2017)
13. Bagheri, A., Jabbari, A., Mobayen, S.: An intelligent ABC-based terminal sliding mode controller for load-frequency control of islanded micro-grids. Sustain. Cities Soc. **64**(102544) (2021). https://doi.org/10.1016/j.scs.2020.102544
14. Fan, G.D., Liu, S.L., Pei, J.: Load frequency coordinated optimization control of hybrid power generation system consisted of PV, thermal power and energy storage. Proc. CSU-EPSA **32**(12), 134143 (2020)
15. Xie, P.H., Wang, C., Liu, P.H.: Application of joint frequency regulation technology of energy storage and thermal power in China southern power grid. Autom. Electr. Power Syst. **45**(4), 172179 (2021)
16. Ourahou, M., Ayrir, W., EL Hassouni, B., Haddi, A.: Review on smart grid control and reliability in presence of renewable energies: challenges and prospects. Math. Comput. Simul. **167**, 1931 (2020)

17. Liao, K., Xu, Y.: A robust load frequency control scheme for power systems based on second-order sliding mode and extended disturbance observer. IEEE Trans. Ind. Inform. **14**(7), 30763086 (2018)
18. Xu, D., Liu, J., Yan, X.: A novel adaptive neural network constrained control for a multi-area interconnected power system with hybrid energy storage. IEEE Trans. Ind. Electron. **65**(8), 66256634 (2019)
19. Zhang, K., Zhou, B., Or, S.W., Li, C., Chung, C.Y., Voropai, N.I.: Optimal coordinated control of multi-renewable-to-hydrogen production system for hydrogen fueling stations. IEEE Trans. Ind. Appl. **58**(2), 2728–2739 (2022)
20. Lucas, K.E., et al.: Robust control of interconnected power electronic converters to enhance performance in DC distribution systems: a case of study. IEEE Trans. Power Electron. **36**(4), 4851–4863 (2021)

Order Reduction of Linear Dynamic System Using Recursive Pole Array Technique and Pade Approximation

Deepa Kumari, Kirti Pal, and C. B. Vishwakarma

Abstract The article introduces a novel method for enormous scale linear dynamic systems to minimize the single-input and single-output (SISO) order/multi-inputs and multi-outputs (MIMO) systems order. The coefficients of the numerator(s) is/are estimated using the approach of the Pade approximation approach, while the reduced order denominator polyn. has been determined by using recursive pole array technique. The proposed technique assures the stability of the reduced model, if model of origin form of high-order degree is very stable. The method's validity is demonstrated on the few syst. considering from the exist. literature. The graphical and analytical comparison has been done with the help of MATLAB/Simulink.

Keywords Reduction · Pade · Stability · Transf. function · Order

1 Introduction

The modeling of linear and nonlinear complex dynamic systems has a significant role in analysis and design of the control systems. Higher-order differential equations and complex models are realized during the mathematical modeling of the large-scale dynamic systems. These equations are not easy to use to analyze and synthesize the controller design. In order to have good understanding of the system, and to minimize the complexity in terms of hardware implementation and computations, the model order reduction techniques are quite useful.

D. Kumari (✉) · K. Pal
Department of Electrical Engineering, Gautam Buddha University, Gautam Buddha Nagar, Greater Noida, India
e-mail: deepa.bhati93@gmail.com

K. Pal
e-mail: kirti.pal@gbu.ac.in

C. B. Vishwakarma
Department of Electrical Engineering, HBTU, Kanpur, India
e-mail: cvishwakarma@hbtu.ac.in

© The Author(s), under exclusive license to Springer Nature Singapore Pte Ltd. 2025

H. P. Singh et al. (eds.), *Recent Developments in Control, Automation and Power Engineering*, Lecture Notes in Electrical Engineering 1303,
https://doi.org/10.1007/978-981-96-0047-2_27

Previously, many authors suggested several order reduc. techniques in [1–5]. Further, many researchers have suggested mixed methods that could match the response [6–12]. Sinha and Pal suggested clustering techniques based on IDM in which separate clusters of poles and zeroes are formed to get a cluster center [4]. Just the poles are gathered collectively in the literature [5] in order to identify the group's the center, which is then used to calculate the denominator. Additionally, in contrast to [4, 5], Vishwakarma [6] proposed an improved pole cluster technique using IDM that produces an additional prominent cluster center. Abha [13] in her work suggested a method to get a better cluster if more poles are grouped to form a cluster. The suggested approach is a hybrid reduction technique applicable for SISO and MIMO dynamic systems and is known as Recursive Pole Array Technique. By creating an array of pole and identifying the most prominent pole array center, the pole array technique is used in this way to build the poly. deno. of the simplified model. The Pade approx. technique is used for calculating the num. polynomial coefficients. To use of instances from research, the suggested strategy is contrasted with the renowned reduction techniques. The analytical and graphical study is done here to further validate the above proposed method.

2 Statement of Problem

2.1 SISO System

The trans. funct. of SISO system for nth order has been mentioned as

$$G(s) = \frac{N(s)}{D(s)} = \frac{e_0 + e_1 * s + e_2 * s^2 + \ldots + e_{n-1}s^{n-1}}{f_0 + f_1 s + f_2 s^2 + \ldots + f_n s^n}, \tag{1}$$

whereas for e_i, i lies between 0 and $n-1$,andfor f_i; i lies between 0 and n which are constant of scalar. The kth ($k < n$) order reduced transfer function is:

$$G_k(s) = \frac{N_k(s)}{D_k(s)} = \frac{x_0 + x_1 s + x_2 s^2 + \ldots + x_{k-1}s^{k-1}}{y_0 + y_1 s + y_2 s^2 + \ldots + y_k s^k}, \tag{2}$$

where for x_i, i lies between 0 and $k-1$ and for y_i, i lies between 0 and k which are constant of scalar. The kth order model will analyzed in reduced form as mentioned in Eq. (2) and Eq. (1).

2.2 MIMO Systems

Consider the high-order original system of the order 'n' having 'r' number of inputs and 'q' number of outputs, as follows:

$$G(s) = \frac{1}{D(s)} = \begin{bmatrix} x_{11.}(s) & x_{12}(s) & \cdots & x_{1r}(s) \\ x_{21.}(s) & x_{22}(s) & & x_{2r}(s) \\ \vdots\vdots & & \vdots & \vdots \\ x_{q1}(s) & x_{q1}(s) & \cdots & x_{qr}(s) \end{bmatrix}. \tag{3}$$

Consider $G(s) = [g_{ij}(s)]$, in which 'i' lies between 1 and q; 'j' lies between 1 and r which forms $q \times r$ as a transfer matrix. The expression of $g_{ij}(s)$ can be opted as:

$$g_{ij}(s) = \frac{a_{ij}(s)}{D_n(s)} = \frac{a_0 + a_1 * s + a_2 * s^2 + \cdots + a_{n-1}s^{n-1}}{b_0 + b_1 s + b_2 s^2 + \cdots + b_n s^n}.$$

Again 'i' lies between 1 and q; 'j' lies between 1 and r allowing for 'r' inputs and 'q' outputs. The trans. funct. matrix of reduced form of the kth order could be synthesized as

$$R_k(s) = \frac{1}{D_k(s)} = \begin{bmatrix} c_{11.}(s) & c_{12}(s) & \cdots & c_{1r}(s) \\ c_{21.}(s) & c_{22}(s) & & c_{2r}(s) \\ \vdots\vdots & & \vdots & \vdots \\ c_{q1.}(s) & c_{q1}(s) & \cdots & c_{qr}(s) \end{bmatrix}. \tag{4}$$

Assume $[R_k(s)] = [g_{ij}(s)]$, 'i' lies between 1 and q; 'j' lies between 1 and p as $q \times p$ as a transfer matrix. The expression of $g_{ij}(s)$ will be opted as:

$$r_{ij}(s) = \frac{c_{ij}(s)}{D_k(s)} = \frac{c_0 + c_1 s + c_2 s^2 + \ldots + c_{k-1}s^{k-1}}{d_0 + d_1 s + d_2 s^2 + \ldots + d_k s^k}.$$

With the objective to realize the reduced model of order 'k' in the form of Eq. (4), such that it retains the important characteristics of the original system represented by Eq. (3).

3 Method Designing

The proposed method involves the two steps:

Step1: Estimation of the *k*th order reduced denomin.

Cluster centers are determined using the formula, and separate cluster are designed for the real and complex poles. In case of MIMO systems, a common denominator is formulated first.

Case1: Let 'z' be the real poles formed in 1 cluster of the form (p_1, p_2, p_3,…p_z), then cluster center is:

$$p_c = \left\{ \left(\sum_{i=1}^{z} \sqrt{p_i} \right) \div z \right\}^2, \tag{5}$$

where p_c is the required cluster center and it is repeated $(z + 1)$ times.

Case2: Complex conjugate poles form pair occurs in a certain pattern; then the cluster center in complex form is of the form of the $A_c \pm jB_c$,

where

$$A_c = \left\{ \left(\sum_{i=1}^{m} \sqrt{\alpha_i} \right) \div m \right\}^2 \text{and} \, B_c = \left\{ \left(\sum_{i=1}^{m} \sqrt{\beta_i} \right) \div m \right\}^2. \tag{6}$$

For a kth order reduced model to determine the denominator polynomial, a number of cases could happen:

Case1: The denominator for kth order of model of reduced system could be attained, if all the cluster centers are real as:

$$D_k(s) = (s - p_{c1.})(s - p_{c2.}).\ldots.(s - p_{ck.}). \tag{7}$$

Case 2: If the pole cluster center's pairs of the clusters are complex conjugate and $(k - 2)$ clusters are real, then $D_k(s)$ can be obtained as:

$$D_k(s) = (s - p_{c1.}) * (s - p_{c2.}) * \ldots . \left(s - p_{c(k-2).}\right) * \left(s - \overset{\circ}{\underset{c1}{p}}.\right) * \left(s - \overset{*}{\underset{c1}{p}}.\right), \tag{8}$$

where $\overset{\circ}{\underset{c1}{p}}$ and $\overset{*}{\underset{c1}{p}}$ are complex conjugate cluster centers or $\overset{\circ}{\underset{c1}{p}} = Ac + jBc$ and $\overset{*}{\underset{c1}{p}} = A_c - jB_c$

Case 3: If the complex conjugate is all cluster centers, then $D_k(s)$ can be obtained as:

$$D_k(s) = \left(s - \overset{\circ}{\underset{c1}{p}}.\right) * \left(s - \overset{*}{\underset{c1.}{p}}\right) * \left(s - \overset{\circ}{\underset{c2.}{p}}\right) * \left(s - \overset{*}{\underset{c2}{p}}.\right) \ldots \left(s - \overset{\circ}{\underset{\frac{ck}{2}}{p}}\right).\left(s - \overset{*}{\underset{\frac{ck}{2}}{p}}\right). \tag{9}$$

Step 2: The Pade Approximation is Applied to Calculate the *K*th Order Reduced Model's Numerator

$G(s)$ for nth order could be extended in power series at approximately $s = 0$ as

$$G(s) = \frac{\sum_{i=0}^{n-1} e_i s^i}{\sum_{i=0}^{n} f_i s^i} = c_0 + c_1 s + c_2 s^2 + \cdots . \tag{10}$$

In case of MIMO, separately the numerators of the transfer matrix are decreased. $g_{ij}(s)$ for nth order could be extended in power series at approximately $s = 0$ as,

$$g_{ij}(s) = \frac{\sum_{i=0}^{n-1} e_i s^i}{\sum_{i=0}^{n} f_i s^i} = c_0 + c_1 s + c_2 s^2 + \cdots . \tag{11}$$

The power series coefficients are calculated as follows:

$$c_0 = e_0$$

$$c_i = \frac{1}{f_0}\left[e_i - \sum_{j=1}^{i} f_i c_{i-j} \right], \quad i > 0. \tag{12}$$

The kth order model of SISO in reduced form is

$$G_k(s) = \frac{N_k(s)}{D_k(s)} = \frac{\sum_{i=0}^{k-1} a_i s^i}{\sum_{i=0}^{k} b_i s^i}. \tag{13}$$

The kth order model of MIMO in reduced form is

$$r_{ij}(s) = \frac{c_{ij}(s)}{D_k(s)} = \frac{\sum_{i=0}^{k-1} a_i s^i}{\sum_{i=0}^{k} b_i s^i}. \tag{14}$$

$D_k(s)$ is calculated from Eqs. (7)–(9). For $G_k(s)/r_{ij}(s)$ to be Pade approx. of $G(s)/g_{ij}(s)$, we have

$$\begin{aligned} x_0 &= y_0 c_0, \\ x_1 &= y_0 c_1 + y_1 c_0, \\ x_{k-1} &= y_0 c_{k-1} + y_1 c_{k-2} + \cdots + y_{k-1} c_1 + y_k c_0. \end{aligned} \tag{14}$$

The $x_j; j = 0, 1, 2, \ldots, k-1$, is obtained by resolving the aforementioned 'k' eqs. of linearity type.

4 Comparative Analysis Using Various Methods

MATLAB/SIMULINK is utilized for estimating the integral square error (ISE) index to check accuracy and error. The ISE is defined as:

$$\mathbf{ISE} = \int_0^\infty \left[g_{ij}(t) - r_{ij}(t)\right]^2 \mathrm{d}t, \tag{16}$$

where $i = 1$ and 2, $j = 1$ and 2, $g_{ij}(t)$ and $r_{ij}(t)$ are responses of the unit step input of the initial and reduced model for the ith-output and jth-input.

For graphical comparison, step and bode plots have been shown for the original and the reduced model.

5 Instances

Instance 1: Assume a system of 4th order whose transfer function is:

$$G(s) = \frac{24 + 24 * s + 7 * s^2 + s^3}{(s+1) * (s+2) * (s+3) * (s+4)}.$$

The expanded form of transfer function $G(s)$ at $s = 0$ is:

$$G(s) = 1 - 1.0833s + 1.090208s^2 - 1.06643s^3 + \cdots.$$

Using the step 1, two centers of the clusters from poles -1, -2, -3, -4 can be formed from Eq. (3) as:

Pole cluster center is $P_{c1} = -1.1062$.

Pole cluster center is $P_{c2} = -3.1167$.

As a result, Eq. (7) can be used to synthesize denominator $D_2(s)$, which is represented by:

$$D_2(s) = 3.4477 + 4.2229s + s^2.$$

The second order in reduced form can be taken in the form of:

$$G_2(s) = \frac{a_0 + a_1}{3.4477 + 4.2229s + s^2}.$$

Now, using step 2: $a_0 = 3.4477$, $a_1 = 0.4880$.

Finally, the second-order reduced model is:

$$G_2(s) = \frac{3.4477 + 0.4880s}{3.4477 + 4.2229s + s^2}.$$

See Figs. 1, 2 and Table 1.

Instance 2: Consider a fourth-order stable system:

$$G(s) = \frac{2400 + 1800s + 496s^2 + 28s^3}{240 + 360s + 204s^2 + 36s^3 + 2s^4}.$$

The expanded form of transfer function $G(s)$ at $s = 0$ is

$$G(s) = 10 - 7.5s + 4.81667s^2 - 2.2333s^3 + \cdots.$$

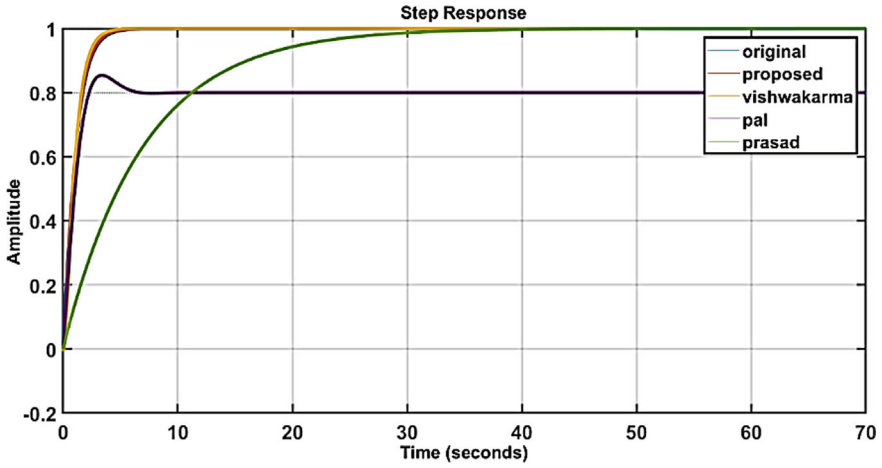

Fig. 1 Compar. of the step respon. for the instance 1

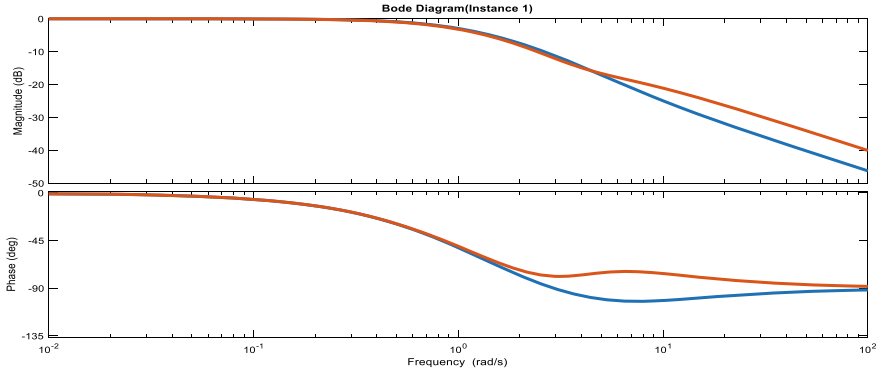

Fig. 2 Bode plot comparison of instance 1

Table 1 Compar. of ISE with the standard methods

Method of reduction	Reduced model	ISE
Proposed method	$\frac{3.4477+0.4880s}{3.4477+4.2229s+s^2}$	0.0007426
Vishwakarma [14]	$\frac{4.5713-0.189762s}{4.5713+4.76187s+s^2}$	0.008014
Pal [15]	$\frac{24+16.0008s}{24+42s+30s^2}$	0.01188
Prasad and Pal [16]	$\frac{34.2465+s}{34.2465+239.8082s+s^2}$	1.893
Davison [17]	$\frac{2-s^2}{2+3s+s^2}$	0.2702
Parthasarathy et al. [18]	$\frac{0.6997+s}{0.6997+1.45771s+s^2}$	0.03419

Poles are -7.8033 and $-1.1967 \pm j0.6934$.
Using step 1, one complex cluster center is calculated:

$$-A_c \pm jB_c = -1.7066 \pm j0.76427.$$

Hence, denominator $D_2(s)$ can be synthesized by utilizing Eq. 7 which is expressed as $D_2(s) = 3.4966 + 3.4132s + s^2$.
Now, using step 2: $a_0 = 34.966$ and $a_1 = 7.9075$.
Finally, the reduced model is:

$$G_2(s) = \frac{34.966 + 7.9075s}{3.4966 + 3.4132s + s^2}.$$

See Figs. 3, 4 and Table 2.
Instance 3: Assume a sixth-order system whose transfer function is:

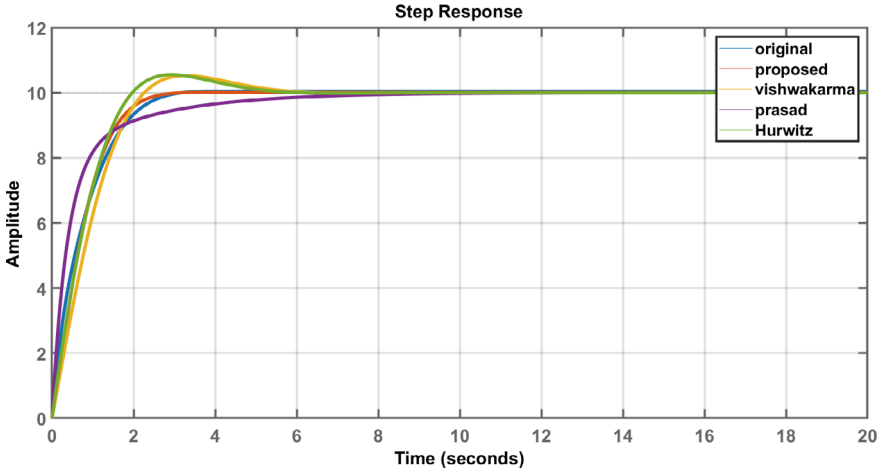

Fig. 3 Compar. of responses of step input for the instance 2

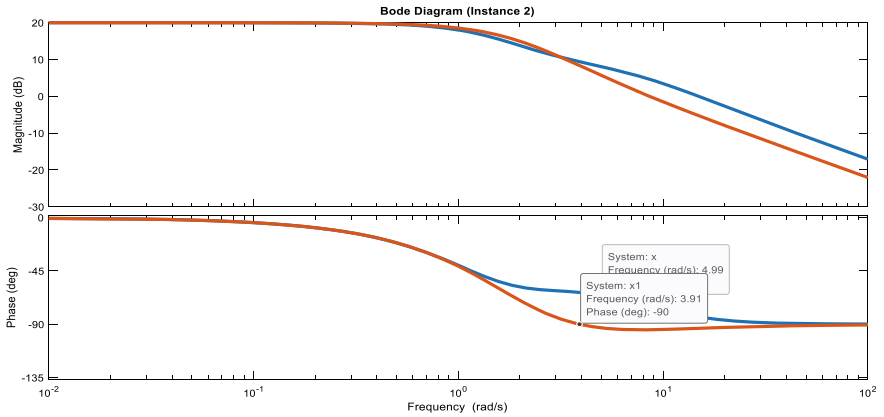

Fig. 4 Bode plot of instance 2

Table 2 Compar. of error using ISE

Methods for reduction	Reduced model	ISE
Proposed method	$\frac{34.966+7.9075s}{3.4966+3.4132s+s^2}$	0.3589
Vishwakarma [14]	$\frac{2400+1371.048s}{240+317.149s+201s^2}$	1.763
Prasad [19]	$\frac{11.90362+22.532255s}{1.190362+3.145997s+s^2}$	2.743
Routh-Hurwitz Array [20]	$\frac{13.043478+9.046283s}{1.3043478+1.701323s+s^2}$	1.208

$$G(s) = \begin{bmatrix} \frac{2*(s+5)}{(s+1)*(s+10)} & \frac{(s+4)}{(s+2)*(s+5)} \\ \frac{(s+10)}{(s+1)*(s+20)} & \frac{(s+6)}{(s+2)*(s+3)} \end{bmatrix} = \frac{1}{D_6(s)} \begin{bmatrix} a_{11}(s) & a_{12}(s) \\ a_{21}(s) & a_{22}(s) \end{bmatrix},$$

where $D_6(s) = 6000 + 13{,}100 * s + 10{,}060 * s^2 + 3491 * s^3 + 571 * s^4 + 41 * s^5 + s^6$.

$a_{11}(s) = 6000 + 7700 * s + 3610 * s^2 + 762 * s^3 + 70 * s^4 + 2 * s^5$.

$a_{12}(s) = 2400 + 4160 * s + 2182 * s^2 + 459 * s^3 + 38 * s^4 + s^5$.

$a_{21}(s) = 3000 + 3700 * s + 1650 * s^2 + 331 * s^3 + 30 * s^4 + s^5$.

$a_{22}(s) = 6000 + 9100 * s + 3660 * s^2 + 601 * s^3 + 42 * s^4 + s^5$.

Here, $D_6(s)$ is the comm. denomin. poly.

The poles are situated at: $-1, -2, -3, -5, -10, -20$.

Using step 1, two centers of the cluster from poles of real form can be formed from Eq. (5) as:

Pole cluster center is $P_{c1} = -1.097803$, $P_{c2} = -5.6066$.

Therefore, common denominator $D_6(s)$ can be synthesized using Eq. (7) and is given by:

$$D_6(s) = 6.154960 + 6.70442s + s^2.$$

The second order in reduced form can be taken:

$$G_2(s) = \frac{1}{6.154960 + 6.70442s + s^2} \begin{bmatrix} 6.154960 + 1.164956s & 2.46198 + 1.5739s \\ 3.07748 + 0.428604s & 6.154960 + 2.580597s \end{bmatrix}.$$

See Figs. 5, 6 and Table 3,

Instance 4: Assume a fourth-order system whose trans. funct. is:

$$G(s) = \begin{bmatrix} \frac{(s+20)}{(s+1)*(s+10)} \\ \frac{(s+10)}{(s+2)*(s+5)} \end{bmatrix} = \frac{1}{D_4(s)} \begin{bmatrix} a_{11}(s) \\ a_{21}(s) \end{bmatrix},$$

where $D_4(s) = 100 + 180s + 97s^2 + 18s^3 + s^4$.

$a_{11}(s) = 200 + 150s + 27s^2 + s^3$.

$a_{12}(s) = 100 + 120s + 21s^2 + s^3$.

Here, $D_4(s)$ is the common part of the denominator of polynomial. The position of system poles is at: − 1, − 2, − 5, and − 10. Two centers in cluster manner from real poles using step 1 can be formed from Eq. (5) as:

Pole cluster center is $P_{c1} = -1.106234$.

Pole cluster center is $P_{c2} = -5.53117$.

Therefore, $D_2(s)$ can be synthesized using Eq. 7 which is expressed as:

$$D_2(s) = 6.118768 + 6.637404s + s^2.$$

The second order in reduced form can be taken as:

$$G_2(s) = \frac{1}{6.118768 + 6.637404s + s^2} \begin{bmatrix} 12.237536 + 0.425395s \\ 6.118768 + 2.9661432s \end{bmatrix}.$$

See Figs. 7, 8 and Table 4.

6 Conclusions

This manuscript has demonstrated a dynamic SISO and MIMO systems for the model order reduc. of linear dynamic system. The estimation of coefficient of both numerator and reduced order denominator has been assessed by using Pade approximation and recursive pole array technique. Various instances from the existing literature of third order and fourth order have been opted to validate the effective of the both pade

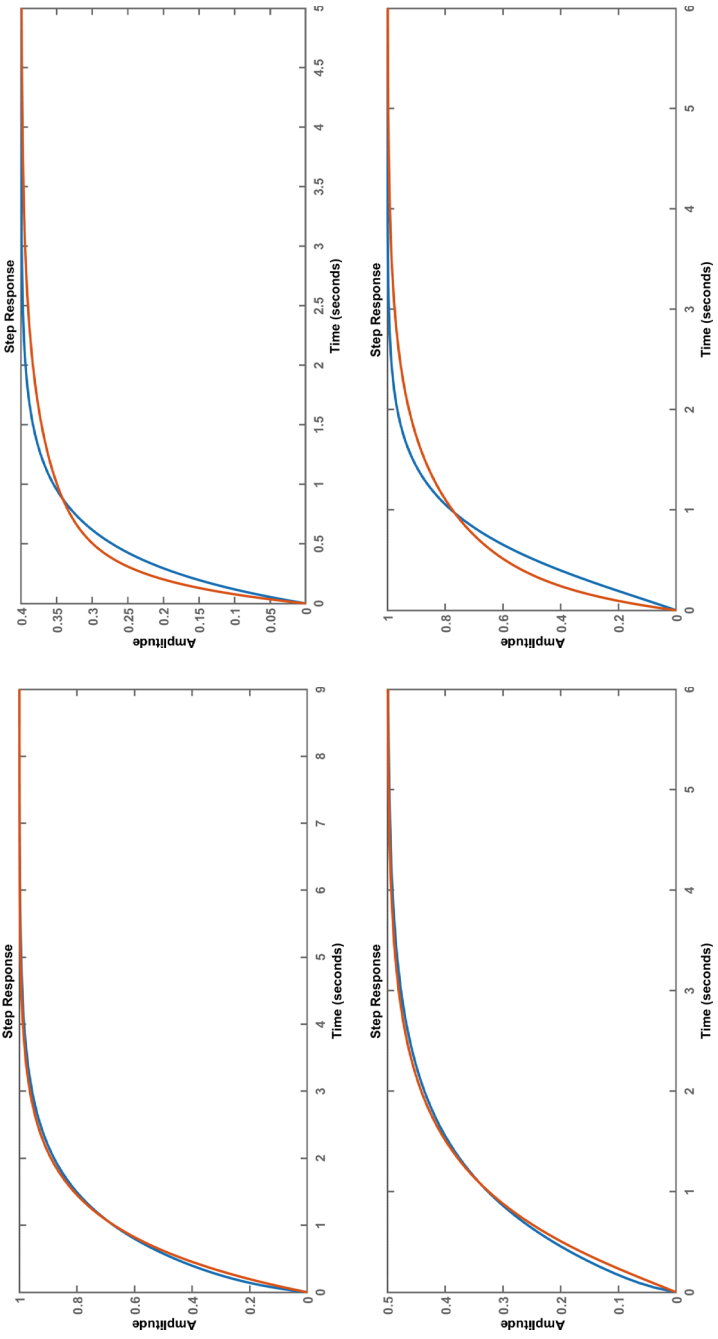

Fig. 5 Step responses comparisons for the instance 3

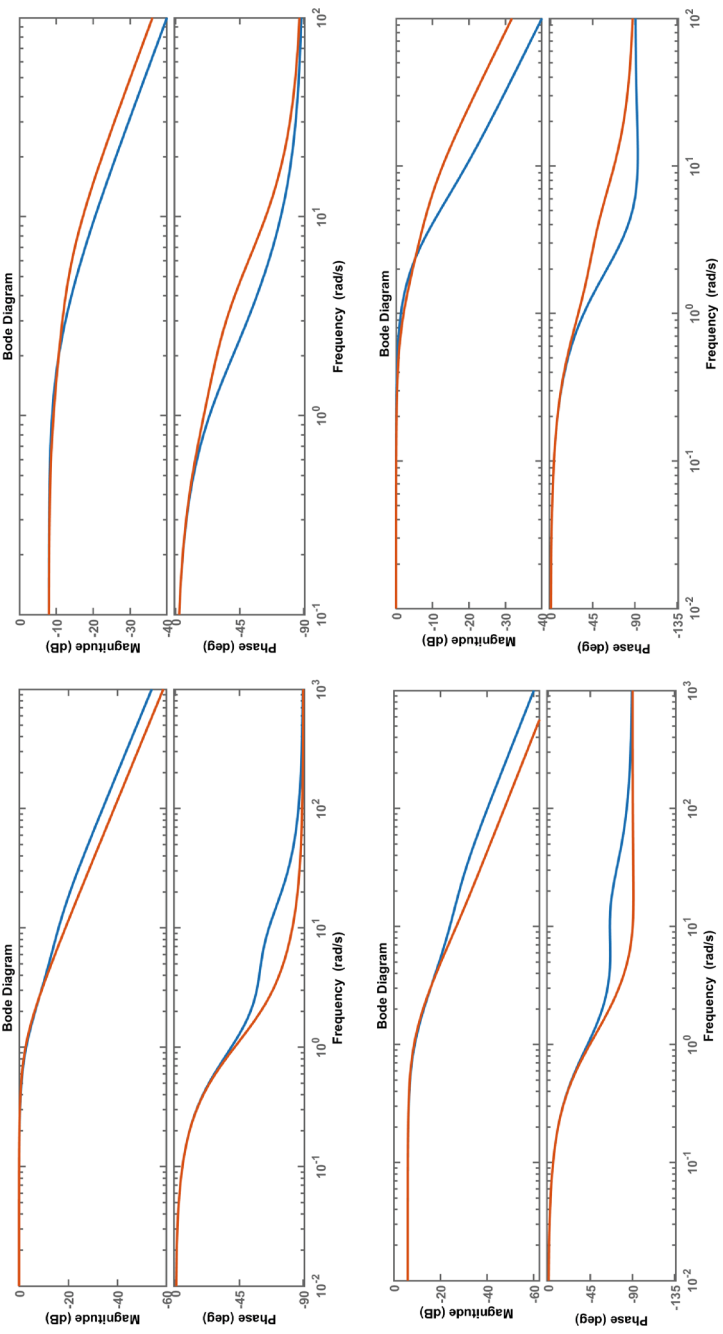

Fig. 6 Bode plot comparison of instance 3

Table 3 Comparison of error using ISE

ISE of the $r_{ij}(s)[i = 1 \text{ and } 2; j = 1 \text{ and } 2]$				
Various methods of reduction	r_{11}	r_{12}	r_{21}	r_{22}
Propo. method	0.001	0.0001	0.0003	0.012
Vishwakarma [14]	0.036	0.0003	0.0103	0.029
Pras et al. [21]	0.031	0.0002	0.2619	0.022
Safo and Chiang [22]	0.591	0.0371	0.0073	1.066
Prasad and Pal [23]	0.137	0.0024	0.0402	0.068

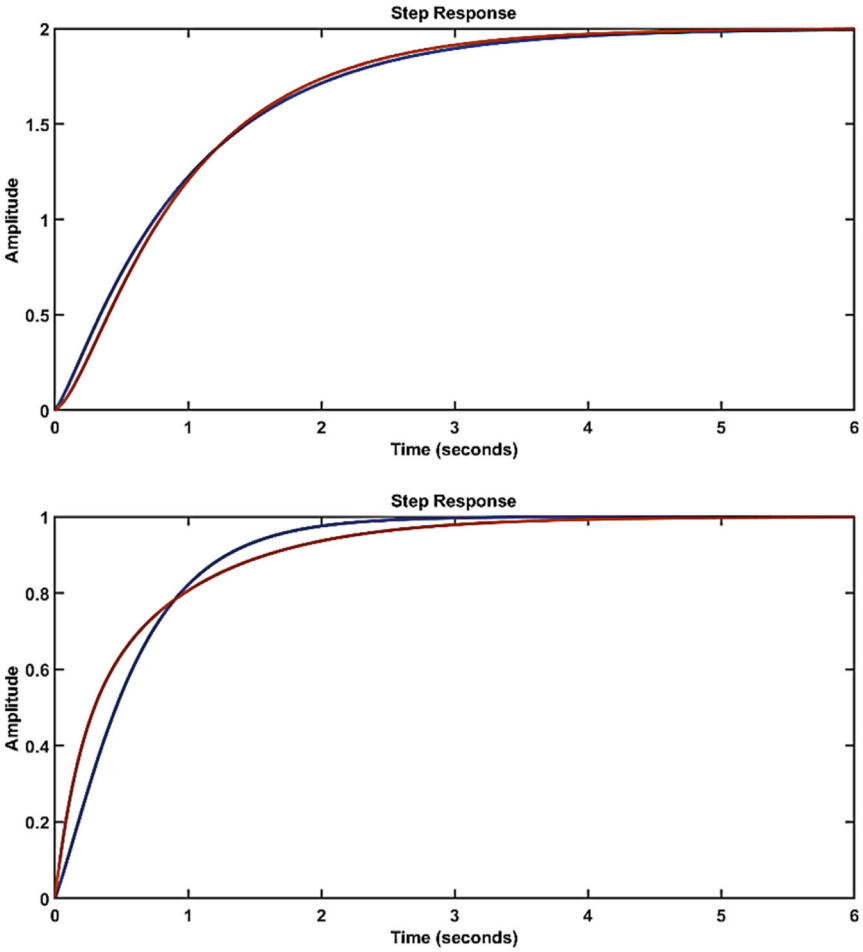

Fig. 7 Comparison of the step responses for the instance 4

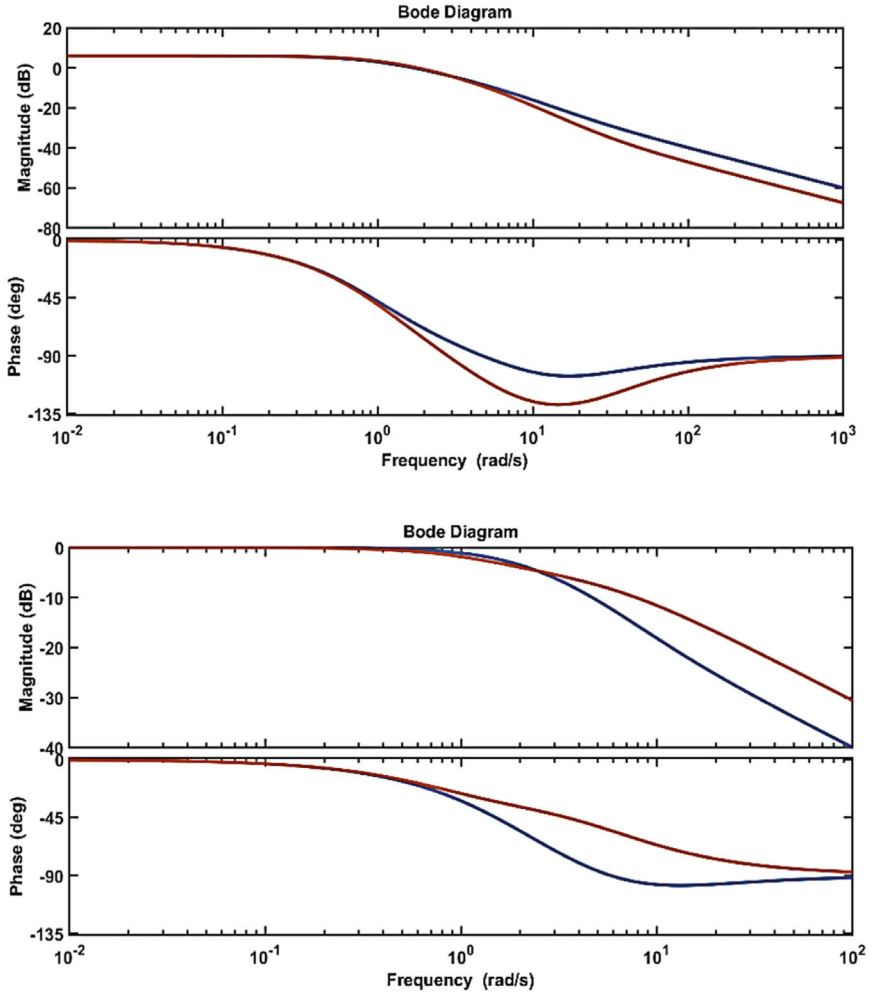

Fig. 8 Bode plot of instance 4

Table 4 Integral square error for instance 4

Method of reduction	r_{11}	r_{21}
Proposed method	0.004937	0.01326
Abha Kumari [24]	0.021436	0.018892
Vishwakarma [14]	0.00930	0.01230

approximation and recursive pole array technique. If the initial model is determined to be stable, the stability of the lower-order model will be verified. The proposed techn. preserves the stability of the model while preventing steady-state inaccuracy between the responses of step input of the orig. larger-order systems and the decreased lower-order systems.

References

1. Mukherjee, S.: Order reduction of linear systems using Eigen spectrum analysis. J. Electr. Eng. **77**, 76–79 (1996)
2. Mittal, K., Prasad, R., Sharma, S.P.: Reduction of linear dynamic systems using an error minimization technique. J. Inst. Engg. India (EL) **84**, 201–206 (2004)
3. Mukherjee, S., Satakshi, Mittal, R.C.: Model order reduction using response-matching technique. J. Franklin Institute (Elsevier) **342**(5), 503–519 (2005)
4. Sinha, K., Pal, J.: Simulation based reduced order modelling using a clustering technique. Comput. Electr. Eng. **16**(3), 159–169 (1990)
5. Pal, J., Sinha, A.K., Sinha, N.K.: Reduced order modelling using pole clustering and time moments matching. J. Inst. Eng. India (EL) **76**, 1–6 (1995)
6. Vishwakarma, C.B.: Order reduction using modified pole clustering and pade approximations. In: World Academy of Science, Engineering and Technology. Int. J. Electr. Comput. Energetic, Electron. Commun. Eng. **5**(8), 998–1002 (2011)
7. Parmar, G., Mukherjee, S., Prasad, R.: System reduction using factor division algorithm and eigen spectrum analysis. Appl. Math. Modelling (Elsevier) **31**(11), 2542–2552 (2007)
8. Shamash, Y.: Linear system reduction using pade approximations to allow retention of dominant poles. Int. J. Control **21**(2), 257–272 (1975)
9. Tiwari, S.K., Kaur, G.: Model reduction by new clustering method and frequency response matching. J. Control Autom. Electr. Syst. **28**, 78–85 (2017)
10. Sharad, K., et al.: Improved reduced order modeling using clustering method with dominant pole retention. IETE J Res. (2018)
11. Prajapati, K., et al.: Reduced order modeling of LTI systems by using Routh approximation and fraction division methods. J. Circ. Syst. Signal Process. (2019)
12. Prajapati, K., Prasad, R.: Order reduction in linear dynamic systems by using the improved balanced realization technique. J. Circ. Syst. Signal Process. (2019)
13. Kumari, A., Vishwakarma, C.B.: A renovated pole clustering technique for model order reduction. In: International Conference on Power Electronics, Control and Automation (ICPECA), pp. 1–6 (2019)
14. Vishwakarma, C.B.: Model order reduction of linear dynamic systems for control systems design. Ph.D Thesis, IIT, Roorkee, India (2009)
15. Pal, J.: Stable reduced order Pade approximants using Routh Hurwitz array. Electron. Lett. **15**(8), 225–226 (1979)
16. Prasad, R., Pal, J.: Stable reduction of linear systems by continued fractions. J. Inst. Eng. (India) **72**, 113–116 (1991)
17. Davison, E.J.: A method for simplifying linear dynamic systems. IEEE Trans. Autom. Control **AC-11**, 93—101 (1966)
18. Parthasarathy, R., Jayasimha, K.N.: System reduction using stability equation method and modified Cauer continued fraction. Proc. IEEE **70**(10), 1234–1236 (1982)
19. Prasad, R., Mittal, A.K., et al.: Linear Model reduction using the advantages of Mihailov criterion and Factor division. J. Inst. Eng. India, IE (I) J.-EL **84**, 7–10 (2003)
20. Krishnamurthy, V., et al.: Model reduction using the routh stability criterion. IEEE Trans. Autom. Control **AC-23**(4), 729–731 (1978)

21. Prasad, R., Pant, A.K., et al.: Multivariable systems approximation using polynomial derivatives. J. Inst. Eng. India, IE(I), J.-EL **76**, 186–188 (1995)
22. Safonov, M.G., Chiang, R.Y.: Model reduction for robust control: a Schur relative error method. Int. J. Adaptive Control Signal Process. **2**, 259–272 (1988)
23. Prasad, R.: Use of continued fraction expansion for stable reduction of linear multivariable systems. J. Inst. Eng. (India), IE(I) J. EL, **72**, 43–47 (1991)
24. Kumari, A., et al.: Order reduction of dynamic systems by using renovated pole clustering technique. In: International Conference on Power Energy, Environment and Intelligent Control (PEEIC), India (2019)

Power Generation from Food and Garden Waste in Educational Institute

Amit Atri, Anita Khosla, and Shashank Gaur

Abstract This paper proposes a biomass-based power generating system in educational campus in Delhi-NCR. Food waste from hostel mess or canteen along with garden wastes like grass and leaves are collected and biogas is obtained from them by the process of anaerobic digestion. This biogas is stored and is used as fuel for biogas genset which produces electricity. The digested slurry obtained from anaerobic digestor finds application as fertilizer which adds to the system's economic value and reduces the cost of biogas to Rs. 1 per kg. Daily approximately 150 kg biomass is available which gives 190 m^3 biogas. The power generating system is simulated on Homer software for determining its stability. On simulation, 4.2 kW biogas powered generator produces 36,792 kWh electric energy annually when working 8760 h. On comparing with conventional coal-based power plants, annually 34,927 kg CO2equivalent emissions are reduced. Such type of system eliminates biodegradable waste, produces energy and is environment friendly.

Keywords Food waste · Garden waste · Anaerobic digestion · Biogas · PLC · Homer

1 Introduction

Growth in industrialization and increase in purchasing power is causing an increase in energy consumption. As per the Ministry of Power, 56.8% of installed electricity generation capacity in India is based on fossil fuels [1]. Coal dominates the power generation scenario in India with 50.7% of the installed capacity that is based on coal and lignite. Conventional power plants are large-scale power plants which are located at large distance from load centers. Transmission of electricity over long distance requires transmission network which causes power loss. Distributed generation involves power generation at or near load centers usually using renewable

A. Atri (✉) · A. Khosla · S. Gaur
Manav Rachna International Institute of Research and Studies, Faridabad 121004, India
e-mail: amitatri85@gmail.com

© The Author(s), under exclusive license to Springer Nature Singapore Pte Ltd. 2025

H. P. Singh et al. (eds.), *Recent Developments in Control, Automation and Power Engineering*, Lecture Notes in Electrical Engineering 1303,
https://doi.org/10.1007/978-981-96-0047-2_28

energy. Limited stocks and environment issues related to usage of fossil fuels have shifted the focus on renewable energy resources.

With increase in urbanization landfill sites are getting loaded beyond capacity. Municipal solid waste (MSW) consists of 40–45% organic matter, 20–30% inert matter, and the rest is recyclable matter [2]. Decomposition of organic waste emits methane which is inflammable and also causes global warming. After segregation of waste, each type of waste is treated in the most efficient manner, like organic matter is suitable for anaerobic digestion, inert matter finds application in construction work, and recyclable material can be reused. Anaerobic digestion of organic matter gives biogas and the digested organic matter is rich in nutrients and can be used as fertilizer. This can reduce the import of fertilizer in India and add to biogas plant's economic value. As per Ministry of Chemicals and Fertilizers [3], in the year 2020–21, India imported 98.28 Lakh Metric Tons (LMT) urea, 48.82 LMT Di-Ammonium Phosphate (DAP), 42.27 LMT Muriate of Potash (MOP), 13.9 LMT nitrogen, phosphorous and potassium (NPK) fertilizers.

Zhang [4] reviewed process of anaerobic digestion, factors affecting biogas production, effect of pretreatment of substrate and co-digestion. Pramanik [5] discussed process parameters involved along with methods for enhancing biogas production, challenges faced and future perspectives. Patel [6] reviewed different researches conducted for obtaining biogas from anaerobic digestion of food waste, garden waste, vegetable waste and bagasse. Biogas production increased on adding cow dung to these wastes. Food waste is biodegradable and high amount of water which makes it suitable for anaerobic digestion. Anaerobic digestion is an effective method for obtaining biogas from food waste. Atri [7] proposed a model for generating electricity using organic waste. Biogas produced by anaerobic digestion was used as a fuel for high temperature fuel cell and the waste heat was used for pretreatment of organic waste which increased the biogas production.

Second section of this paper gives introduction to biogas, process of anaerobic digestion, and factors affecting biogas production. Third section garden and kitchen waste availability in Manav Rachna International Institute of Research and Studies proposes an automated biogas producing system utilizing that waste. In fourth section simulation is done on Homer software for determining economic feasibility of biogas to electricity production system. For generating electricity, food and garden waste is subjected to anaerobic digestion. Process of anaerobic digestion is carried out by an automated digester using programmable logic controller to maximize the biogas production. An economic analysis of the power generating system is done to determine its feasibility.

2 Biogas Production from Food and Garden Waste

Anaerobic digestion is the process of breaking down of complex organic matter into simpler ones by action of microorganisms thereby producing biogas. Biogas consists of methane (40–70%), carbon dioxide (25–40%), and small quantities of nitrogen

Table 1 Properties of biogas

S. No	Property	Value
1	Lower heating value (MJ/kg)	5.5
2	Density (kg/m^3)	0.720
3	Carbon content (%)	2
4	Sulfur content (%)	0

Table 2 Biogas produced from different types of feedstocks

S. No.	Type of biomass	Biogas produced (Nm^3/MT) fresh matter)
1	Tomato residue	101.8 ± 18.7
2	Potato residues	126.8 ± 3.5
3	Vegetable, fruit and legume waste	158.1 ± 18.7
4	Beet pulp	104.5 ± 13.6
5	Grapes and vinasses	150.0 ± 12.1
6	Crop/agriculture residue	± 4.9

and hydrogen with traces of hydrogen sulfite [8]. Properties of biogas as fuel are given in Table 1.

Biogas is having low heating value of 17.99–20.64 MJ/Nm^3. Process of obtaining biogas consists of four stages, i.e., hydrolysis, acidogenesis, acetogenesis and methanogenesis. Main factors affecting biogas production are—type of feedstock, temperature, hydraulic retention time, pH value of slurry, organic loading rate, volatile fatty acids (VFA), C/N ratio, moisture content, etc. [9]. Digested slurry obtained after biogas production is rich in nutrients and can be used as fertilizer for agriculture purposes.

Microorganisms doing anaerobic digestion are most active in two temperature ranges, i.e., thermophilic (40–70 °C) and mesophilic (25–40 °C). Al Mamun [10] found 32–35 °C as the most suitable temperature, below which biogas production starts decreasing. On the other hand [11] stated thermophilic range as more suitable by reducing pathogens and mitigating odor. By insulating the digester the temperature can be maintained efficiently. Animal, plant, industrial, municipal and sewage waste can be used for producing biogas, the amount of biogas obtained from different types of feedstocks is shown in Table 2 [12].

3 Biogas Producing System

System is to be installed in Manav Rachna International Institute of Research and Studies Institute which is spread in 60 acres near south Delhi-Haryana border having coordinates as 28°27′01.0″N and 77°17′08.4″. Satellite image of the institute, i.e., Fig. 1 shows a large area under grass, plants and trees. Institute is having two boys'

hostel with capacity of 446 students and two girls hostel with one in campus and one off campus having total capacity of 359 students. In the hostel mess, food is prepared three times, i.e., breakfast, lunch and dinner. Daily 80 kg of plant waste and 70 kg of food waste is produced which can be utilized for obtaining biogas.

This biomass is mixed with water to attain the required pH value and moisture content. Approximately equal quantity of water is added making total weight of slurry as 300 kg. Taking standard density of slurry as 1030 kg/cu-m [13], operating on 35 °C temperature with hydraulic retention time 30 days.

$$\text{Volume of daily charge } (Vd) = \text{weight of slurry/density}$$
$$Vd = \frac{300}{1030} = 0.291\text{m}^3 \quad (1)$$

$$\text{Volume of digester} = Vd \times \text{retention time} \times 1.1$$
$$= 0.291 \times 30 \times 1.1$$
$$= 9.6\,m^3 \quad (2)$$

As Volume = Π/4 $D2$ H.

For height (H) and diameter (D) ratio equal to 1.5, we get $H = 3.02$ m and $D = 2.01$ m.

Taking reference from Table 2, average 189.68 m^3 biogas is produced which is stored in balloons.

Automated biogas production system is shown in Fig. 2.

Figure 3 shows the ladder logic program for PLC. In the system, M8000 is moisture sensor which senses moisture content in the feedstock (food and garden waste in this case) which is kept in the mixing tank. Analog to digital converter is used and is calibrated at constant (K) value 40 for the desired water content. As the water content is less than the desired level, valve of the water supply connected to the output Y000 is switched on by Mitsubishi's FX1N which is connected to the valve of the water supply. Simultaneously, the mixing motor (Y001) is turned on which

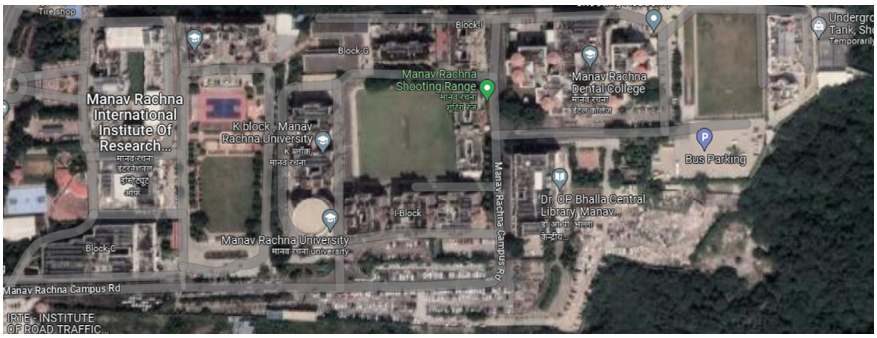

Fig. 1 Satellite image of the institute

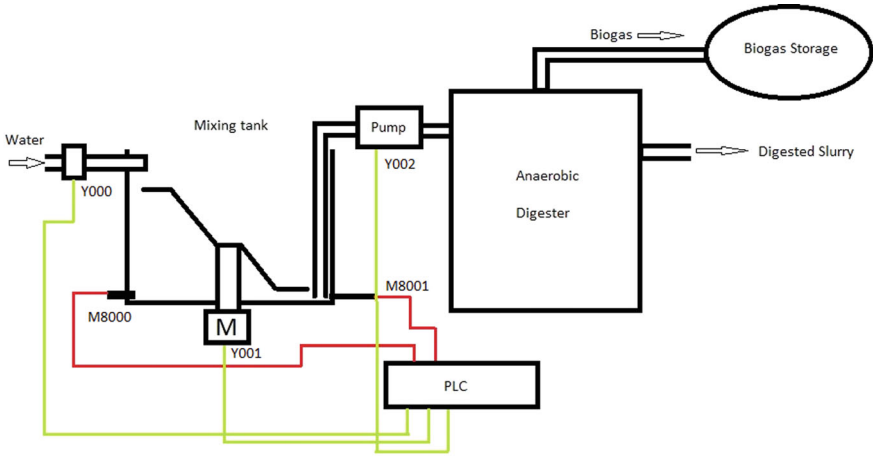

Fig. 2 Automated biogas producing system

cuts and reduces size of the biomass particles. Reduced size of biomass increases its digestibility and so biogas production also increases. As the slurry attains required moisture level, the output M0 is obtained. Water level sensor M8001 senses the presence of slurry, which along with M0 switches the pump Y002 connected which pumps out slurry from mixing tank and feeds it to anaerobic digester; from there biogas and digested slurry is obtained. Biogas is stored in storage balloons and digested slurry is supplied for use in agriculture sector. Digester is built underground so as to minimize the temperature variations.

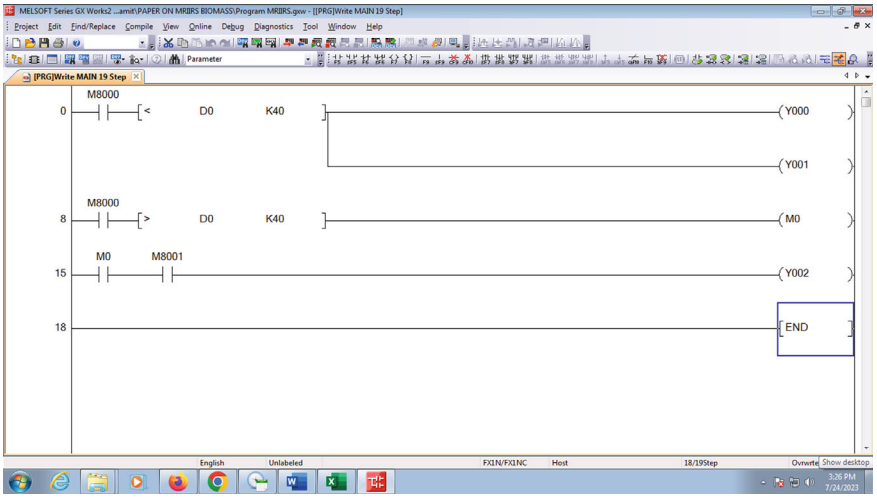

Fig. 3 Ladder logic program

4 Analysis of Costs Involved and Electricity Production

Table 3 indicates the cost of different components involved in the biogas system, on taking reference from company's brochures, e-commerce websites and venders' catalogues.

Taking moisture content as 48% [14] daily 75 kg of digested biomass or fertilizer is available. On selling fertilizer at a rate of Rs. 5 per kg, cost of biogas reduces to Rs. 1 per kg. System is simulated in Homer. Figure 4 shows the grid connected power generation system and Fig. 5 shows monthly energy production.

Table 3 Cost of different components involved in the biogas system

S. No.	Equipment	Cost in Rs.
1	Motor (0.5 HP)	3000
2	Mixing tank	1860
3	Pump	2500
4	Anaerobic digester	130,000
5	Balloons	5000
6	Purification unit	100,000
7	PLC (Mitsubishi's FX1N)	10,000
8	Auxiliary equipment	100,000
9	Biogas genset	12,500/kW

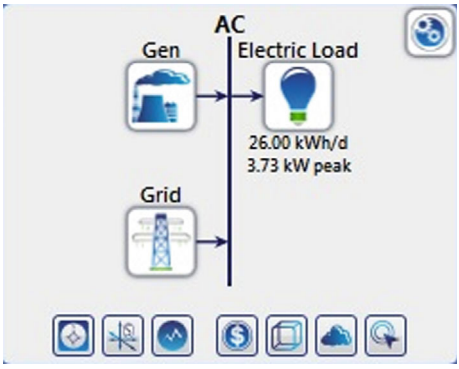

Fig. 4 Grid connected generation system

Fig. 5 Monthly energy production

Gen				
Hours	Production (kWh)	Fuel (kg)	O&M Cost (₹/yr)	Fuel Cost (₹/yr)
8,760	36,792	69,164	1,104	69,164

Fig. 6 Generat or specifications

Cost			
NPC (₹)	COE (₹)	Operating cost (₹/yr)	Initial capital (₹)
₹433,459	₹0.598	₹14,261	₹152,500

Fig. 7 Cost economics for power generating system

Optimal capacity of generator is 4.2 kW and in 8760 h of operation69164 kg biogas is consumed producing 36,792 kWh energy as in Fig. 6.

Net present cost (NPC) of power generation system is Rs. 433,459, running cost is Rs. 14,261 and cost of energy (COE) is Rs. 0.598 as in Fig. 7.

On comparing with conventional coal-based power plants, annually 34,927 kg CO2 equivalent emissions are reduced [15].

5 Conclusion

Biogas is a renewable and clean fuel finding applications in cooking, heating, transportation and power generation. In large educational institutions, a large amount of food waste is produced in at different locations like cafeteria and hostel mess. Garden waste is also produced as a large amount of area is covered by garden and playgrounds. These food, kitchen and garden wastes are suitable raw material for biogas production by the process of anaerobic digestion. Automated biogas production system minimizes the wastage and maximizes overall efficiency. Using 80 kg of plant waste and 70 kg of food waste gives 189.68 m^3 biogas and 75 kg fertilizer. This biogas produces 36,792 kWh electricity annually with cost of energy as Rs. 0.598. This shows the system is economically feasible.

Installation of these automated systems in educational institutions reuses food and garden waste, maximizes biogas production, generates electricity, is environment friendly and the digested biomass is further useful as fertilizer which maintains soil's nutritional value.

References

1. Ministry of Power, Govt. of India. Last accessed 21 July 2023. Available at: https://powermin.gov.in/en/content/power-sector-glance-all-india
2. Atri, A., Khosla, A., Prakash, L.: Power generation using municipal solid waste: a review. Renew. Energy Optim. Plan. Control Proc. ICRTE **2022**, 111–122 (2023)
3. Ministry of Chemicals and Fertilizers, Govt of India. Last accessed 21 July 2023. Available at: https://pib.gov.in/PressReleasePage.aspx?PRID=1810907
4. Zhang, C., Su, H., Baeyens, J., Tan, T.: Reviewing the anaerobic digestion of food waste for biogas production. Renew. Sustain. Energy Rev. **38**, 383–392 (2014)
5. Pramanik, S.K., Suja, F.B., Zain, S.M., Pramanik, B.K.: The anaerobic digestion process of biogas production from food waste: Prospects and constraints. Bioresour. Technol. Rep. **8**, 100310 (2019)
6. Patel, K., Pamnani, A.: Generation of biogas from kitchen waste, bagasse and garden waste. Int. J. Latest Technol. Eng. Manag. Appl. Sci. (IJLTEMAS) **6**, 50–53 (2017)
7. Atri, A., Khosla, A.: Intelligent power generation from anaerobic digestion of municipal solid waste: a case study of Faridabad, India. Int. J. Intell. Syst. Appl. Eng. **11**(10s), 877–887 (2023)
8. Atri, A., Khosla, A.: A case study for analyzing the power generation from wastes. Ambient Sci, pp. 22–25 (2022)
9. Gashaw, A.: Anaerobic co-digestion of biodegradable municipal solid waste with human excreta for biogas production: a review. Am. J. Appl. Chem. **2**(4), 55–62 (2014)
10. Al Mamun, M.R., Torii, S.H.U.I.C.H.I.: Enhancement of production and upgradation of biogas using different techniques-a review. Int. J. Earth. Sci. Eng. **8**(2), 877–892 (2015)
11. Moset, V., Poulsen, M., Wahid, R., Højberg, O., Møller, H.B.: Mesophilic versus thermophilic anaerobic digestion of cattle manure: methane productivity and microbial ecology. Microb. Biotechnol. **8**(5), 787–800 (2015)
12. Tamburini, E., Gaglio, M., Castaldelli, G., Fano, E.A.: Biogas from agri-food and agricultural waste can appreciate agro-ecosystem services: the case study of Emilia Romagna region. Sustainability **12**(20), 8392 (2020)
13. Lima, A., Victor, V.M.: Physical properties of cattle dung. Pharma Int. J. **11**(1), 399–402 (2022)
14. Ezeah, C., Fazakerley, J.A., Roberts, C.L., Cigari, M.I. and Ahmadu, M.D.: Characterisation and compositional analyses of institutional waste in the United Kingdom: a case study of the university of wolverhampton. J. Multidiscip. Eng. Sci. Technol. (JMEST), pp. 3159–0040 (2015)
15. Garg, A., Shukla, P.R., Kankal, B., Mahapatra, D.: CO2 emission in India: trends and management at sectoral, sub-regional and plant levels. Carbon Manag. **8**(2), 111–123 (2017)

Modeling and Performance Analysis of a Model Predictive and Feedback Linearization Controlled UAV Autonomous Quadcopter Drone in 3D Dynamics

Ahsan Kabir Nuhel, Md. Nursari Hasan Sheham, Mir Mohibullah Sazid, Riad Mollik Babu, Hossain Md. Arif Shah, Bishal Saha, and Diva Bhatia

Abstract Autonomous drones are one of the key technological advances of the modern era and have a high impact on delivering different items and military usage. Thanks to its advanced technology, which has made the system faster and safer in all its uses, in this paper, a fully autonomous drone is built using model predictive control (MPC) and feedback linearization controllers. The quadcopter is modeled for its better performance and mobility. The unmanned aerial vehicle (UAV) uses performance control inputs, and the authors also presented preliminary flight experiments in which the UAV was limited to vertical and yaw movements. The performance is tested in a vacuum as well as against the drag force. For a better understanding of the output of the systems, different user-defined trajectories are built to analyze the performance attributes. In order to evaluate the characteristics and capacities of the overall system, the aforementioned systems underwent carefully planned planning, design, and implementation processes. The accompanying visual aids illustrate various scenarios in which a drone successfully monitors and maintains its set reference trajectory.

Keywords UAV · MPC · Trajectory · Motion · Performance · Feedback · Linearization

A. K. Nuhel (✉) · Md. N. H. Sheham · M. Mohibullah Sazid · H. Md. Arif Shah
American International University-Bangladesh, Dhaka, Bangladesh
e-mail: nuhel7050@gmail.com

R. M. Babu
University of Asia Pacific, Dhaka, Bangladesh

B. Saha · D. Bhatia
Vellore Institute of Technology, Vellore, India

© The Author(s), under exclusive license to Springer Nature Singapore Pte Ltd. 2025

H. P. Singh et al. (eds.), *Recent Developments in Control, Automation and Power Engineering*, Lecture Notes in Electrical Engineering 1303,
https://doi.org/10.1007/978-981-96-0047-2_29

1 Introduction

Autonomous drone is revolutionizing for the industrial safety, security, and monitoring. The UAVs can be used in remote places to provide valuable data and security options [1]. Apart from that, UAV is also capable of monitoring large area for identification of potential threats. Alongside, this is being used to supply emergency medicine supply, food delivery, picture, and video recording. The UAVs are also being used by the military to execute hard operation by installing military equipment in the drone which can be controlled remotely [2].

In a drone design, different number of propellers is used. Single propeller design can only use to up down vertically where the two-propeller design is energy-efficient, but it cannot be controlled in precise directions [3]. As a result of that, most the drone uses four-propeller or quadcopter design.

In this paper, the author has designed a quadcopter autonomous drone using MPC controller and feedback linearization controller. It also discussed how the drone is flying in preset location using this control system algorithm. Using different user-defined trajectories of the drone, the performance is analyzed.

The paper is separated into four distinct sections. It began with a discussion of previous research on this topic. In Sect. 3, the methodologies used to construct the system are described, and in Sect. 4, the system's outcome is evaluated. The discussion concluded with an overview of the future potential for enhancing the projects.

2 Literature Review

Philipp Foehn and Dario Brescianini build with the use of learned data abstraction [4], time-optimal trajectory planning, and nonlinear filtering this study introduces a unique system for vision-based, autonomous drone racing. Since the drone has a global map and a drift-compensated state estimate, it can complete the course even if it can't see the gates, and it can also plan a nearly optimal path across the course based on its approximate drone dynamics in real time.

Azade Fotouhi and Ming Ding build a prototype with Internet of Things Applications Capable of Being Piloted Fully Autonomously by Drones [5]. The authors perform a theoretical analysis of the maneuverability of drones in order to shed some insight on the tradeoff that exists between the flying velocity and the steering agility of drones.

Dinh Dung Nguyen and Jozsef Rohacs worked on autonomous flight trajectory system control for drones [6]. In the paper, the defining of routes as well as commanded trajectories with the autonomous execution of defined routes has been suggested. The global positioning system (GPS) serves as a reference, and GIS mapping provides further context for the airspace layout and fixed routes. The application of the concept calls for a number of additional research and solutions, such as

the following of a drone's trajectory (or corridor) by a self-driving trajectory tracking control system.

Rogerio Bonatti and Yanfu Zhang developed a system for aerial filming that is able to make principled tradeoffs between shot smoothness, occlusion, and cinematography guidelines, even when actor predictions are noisy [7]. The authors offer a novel approach using real-time covariant gradient descent, which we use to effectively identify the desired trajectories by optimizing a collection of cost functions. This algorithm allows them to find the trajectories more quickly than previous methods.

3 Methodology

The research focuses on the development and implementation of a sophisticated control system that combines model predictive control techniques with feedback mechanisms to facilitate autonomous flight in a three-dimensional space. By leveraging advanced mathematical models and real-time data processing, this project aims to enhance the drone's stability, maneuverability, and overall performance. The flowchart concerning linear feedback controlling and model predictive controlling are given in Figs. 1 and 2.

3.1 Quadcopter Modeling

The quadcopter exhibits forces and moments that arise from various factors, including the influence of gravity, drag, and thrust generated by its four rotor blades, in addition to external disturbances. The overall thrust is oriented in the negative z-axis within the body frame and is the aggregate of the thrust generated by the four individual motors [8]. In the context of an inertial frame, the aggregate force can be mathematically

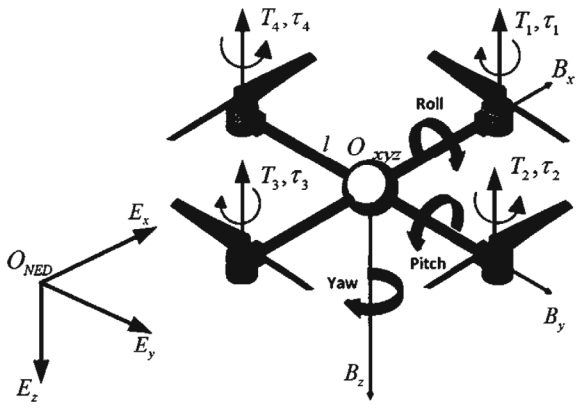

Fig. 1 Dynamics of the quadcopter

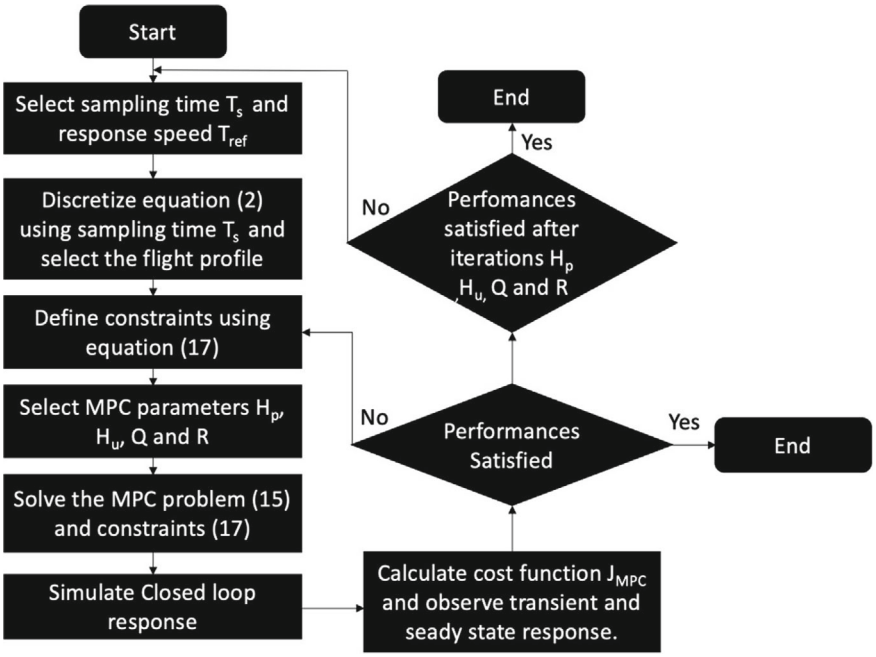

Fig. 2 Flowchart illustrating the design process of model predictive control

represented as:

$$\begin{pmatrix} F_x \\ F_y \\ F_z \end{pmatrix} = -\begin{bmatrix} 0 \\ 0 \\ mg \end{bmatrix} + R_{ib}\begin{bmatrix} 0 \\ 0 \\ \sum_{k=1}^{4} T_k \end{bmatrix} + F_{\text{drag}} + F_{\text{ext}}. \tag{1}$$

Within this particular framework, the symbol g is utilized to represent the gravitational acceleration, while F_{drag} is employed to signify the force that emerges from drag. Additionally, F_{ext} encompasses all external forces, including those that originate from wind. At the most fundamental level, the control input is associated with the command for thrust that is directed toward the four motors. In order to optimize operational efficiency and enhance safety measures, a comprehensive attitude control system is utilized to compute precise thrust commands for individual motors [9]. In contrast, the control inputs encompass the prescribed roll angle ϕ_{cmd}, pitch angle θ_{cmd}, yaw rate $\dot{\psi}_{\text{cmd}}$ cmd, and vertical velocity w_{cmd}. The relationship between the vertical velocity, denoted as w, and a specified vertical velocity command can be characterized by a Laplace transfer function, which can be mathematically represented as follows:

$$W(s) = \frac{k_w}{\tau_w s + 1} W_{\text{cmd}}(s). \tag{2}$$

This implies that the overall thrust at a given time t can be expressed as

$$T(t) = \frac{g + \dot{w}(t)}{\cos\theta(t)\cos\phi(t)} = \frac{g + 1/\tau_w(k_w w_{\text{des}}(t) - w(t))}{\cos\theta(t)\cos\phi(t)}. \tag{3}$$

Second-order systems are used as approximations for the attitude dynamics. The Laplace transfer functions that map commands to attitudes for pitch and roll are stated as

$$\Phi(s) = \frac{k_\phi \omega_\phi^2}{s^2 + 2\xi_\phi \omega_\phi s + \omega_\phi^2} \Phi_{\text{cmd}}(s) \tag{4}$$

$$\Theta(s) = \frac{k_\theta \omega_\theta^2}{s^2 + 2\xi_\theta \omega_\theta s + \omega_\theta^2} \Theta_{\text{cmd}}(s). \tag{5}$$

The rate regulation is represented for the yaw as

$$\Psi(s) = \frac{1}{s} \frac{k_\psi}{\tau_\psi s + 1} \dot{\Psi}_{\text{cmd}}. \tag{6}$$

At this point, the dynamics can be summed up as

$$\begin{aligned} \dot{p}(t) &= v(t) \\ \dot{v}(t) &= a(t) = -g + R_{ib}(t)T(t) - Dv(t) + a_{\text{ext}}(t) \\ \dot{\theta}(t) &= \omega(t) \\ \dot{\omega}(t) &= f_\omega(\omega(t), \theta(t), \theta_{\text{cmd}}(t)) \end{aligned} \tag{7}$$

In this context, the symbol p represents position, v represents velocity, a represents acceleration, θ represents attitude, and ω represents angular acceleration. There exists a total of twelve states and three external disturbances in the system. The function f_ω is defined by Eqs. (4–6). The nonlinearity of this model is evident solely in the velocity derivative, with the input term $R_{ib}T$ being represented as a vector.

3.2 Model Predictive Control

To effectively accomplish the desired objective, it may be impractical to utilize a centralized optimization approach due to the intricate nature of the problem and the multitude of control inputs at play. In the domain of non-convex optimization problems characterized by a high-dimensional vector of variables, the issue of premature convergence to a local minimum is a commonly encountered obstacle [10]. In

addition, the processing unit integrated into the unmanned aerial vehicle (UAV) may face difficulties in achieving the necessary computational capacity to efficiently optimize a wide range of control inputs. However, it is not recommended to exclusively focus on optimizing controls for all unmanned aerial vehicles (UAVs) solely within a ground station. The primary cause of this issue can be attributed to the inherent constraints imposed by the range of communication and the potential ramifications of a communication breakdown. Such a breakdown could lead to the unmanned aerial vehicles (UAVs) being unable to receive crucial control commands, thereby posing a threat to the overall success of the mission.

Therefore, the primary objective of this study is to address a cooperative control issue in which each unmanned aerial vehicle (UAV) aims to optimize its control inputs in order to update its state and minimize a local cost function [11]. The cost function also takes into account the desired states of the other unmanned aerial vehicles (UAVs). It is expected that the achievement of the overall mission objective will be facilitated by the collaborative efforts of each individual unmanned aerial vehicle (UAV), as they adhere to a standardized procedure. The issue of collision avoidance among unmanned aerial vehicles (UAVs) is also being considered.

Given a set of unmanned aerial vehicles (UAVs) denoted as x^i, where $\boldsymbol{i}$ belongs to the set $\{0, \ldots, I-1\}$, the algorithm aims to determine a control input sequence $U_k^i = \left\{u_0^i, u_1^i, \ldots, u_{K-1}^i\right\}$ belonging to the set of real numbers $R^{2\times K}$ for the i th UAV. This control input sequence is intended to solve the optimal control problem described as follows:

$$\begin{aligned}
&\text{minimize } \delta(C\acute{x}_K) + \sum_{k=0}^{K-1} L^i\left(C\overline{x}_k, u_k^i\right),\\
&\text{subject to } x_{k+1}^i = f_d\left(x_k^i, u_k^i\right),\\
&v_{a_{\min}} \le u_{v_k}^i \le v_{a_{\max}}\\
&\phi_{\min} \le u_{\phi_k}^i \le \phi_{\max}\\
&\left|C\left(x_k^i - x_k^j\right)\right| > r_c, \forall j \in \{0, \ldots, I-1\}\backslash\{i\},
\end{aligned} \tag{8}$$

whereas

$$\delta(C\overline{x}_K) = F(Cx_K) - aJ(C_K) \tag{9}$$

and

$$L^i\left(C\overline{x}_k, u_k^i\right) = aJ(C\overline{x}_k) + b\left(u_{v_k}^i - u_{v_{k-1}}^i\right)^2 + c\left(u_{\phi_k}^i - u_{\phi_{k-1}}^i\right)^2 \tag{10}$$

Let us denote the commanded airspeed and roll angle for the i th unmanned aerial vehicle (UAV) in the previous optimization loop as $u_{v_{-1}}^i$ and $u_{\phi_{-1}}^i$, respectively. Furthermore, let $\overline{x}_k = \left[x_{k'}^0 \ldots, x_k^{I-1}\right]$ represent the state vector in the k-th iteration of the optimization loop. The number of horizon steps is represented by K, indicating the planning horizon. Additionally, r_c is used to signify the minimum safe distance between UAVs, which is necessary to prevent collisions. The constant weighting

factors, denoted as a, b, and c, are utilized in conjunction with the matrix $C \in R^{2\times 3}$ to specify that only the north (x) and east (y) positions are extracted from the state vector.

$$C_1 = \begin{bmatrix} 1\ 0\ 0 \\ 0\ 1\ 0 \end{bmatrix} \tag{11}$$

The function J in Eq. (13) denotes the grid search function, which is the cumulative sum of rewards obtained from visited cells. On the other hand, the function F represents the terminal cost (or cost-to-go) function, which quantifies the distance between the terminal position and the unvisited cell that possesses the highest reward.

3.3 Feedback Linearization Control

The primary goal of FL is to transform and express it in the conventional state-space format. By isolating the previous inputs X_d and Y_d, we obtain the subsequent transformation:

. (12)

. (13)

The substitution effectively eliminates the nonlinear components present in Eqs. (12) and (13), resulting in the formation of a linear system characterized by the introduction of new input variables, namely u_1 and u_2. The resultant linear system can be expressed in the following manner:

$$\vec{X} = g\left(r, \theta, \dot{r}, \dot{\theta}, u_1, u_2\right) \tag{14}$$

The linear function g is determined using the method of forward and backward substitution. The state-space form can be utilized to represent the final linear process model.

$$\dot{\acute{X}} = A\acute{X} + BU; \acute{Y} = C\acute{X} \tag{15}$$

The symbol U represents the vector $\left[\, u_1\ u_2 \,\right]^T$. The symbol $\acute{X}$ represents the expression $\left[\, r\ \theta\ \dot{r}\ \theta \,\right]^T$. The output vector $\acute{Y}$ represents the values of r and $\omega = \dot{\theta}$. Matrices $A, B \wedge C$ are designed to guarantee the controllability and observability of the state-space system. To provide a concise overview of the FL process, Fig. 3 illustrates the linearization scheme employed thus far.

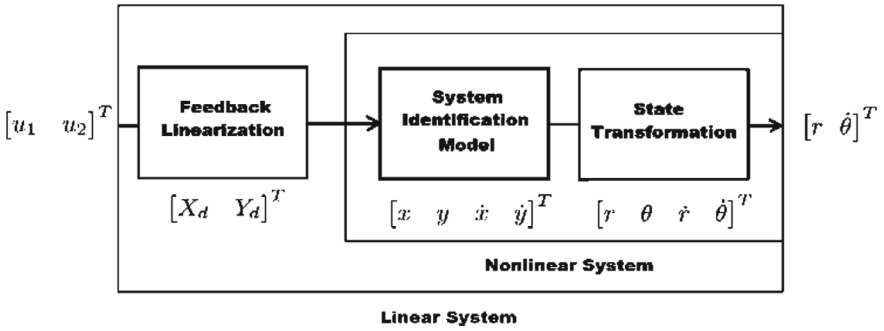

Fig. 3 Overview of system identification, state transformation, and FL

4 Result Analysis

The proposed model was evaluated by considering the influence of air resistance. To simulate real-world conditions, the authors incorporated drag force, which caused tilting of the system. As the unmanned aerial vehicle (UAV) accelerated, the drag force increased in the opposite direction, while maintaining alignment proportionally [12, 13]. Consequently, the rate of forward acceleration diminished over time. The results indicate that higher velocities lead to greater drag, necessitating increased forward force to counteract the escalating drag velocity. Additionally, the UAV exhibited more pronounced downward tilting, resulting in larger horizontal components of the thrust force. Conversely, minimal tilting occurred in the absence of drag force. Furthermore, in a trajectory with a constant radius, the UAV's velocity remained relatively constant. Moreover, a larger radius over time corresponded to a greater centripetal acceleration (Fig. 4).

The analysis of Fig. 5 reveals that the phi angle exhibits a negative trend over time, contributing to centripetal acceleration. In contrast, the theta angle displays a positive trend over time, generating a forward flight force [14]. When the drag force coefficients were increased by a factor of ten, it was observed that the phi angle remained unaffected by the amplified drag force. This outcome can be attributed to the spiral's radius not increasing during the given time period. However, the theta angle experienced a slight impact due to the UAV's pronounced tilting in a specific direction, aiming to counterbalance the excessive drag force by generating a greater horizontal force. Consequently, the UAV exhibited a heightened degree of tilt.

Examining Fig. 6, it becomes apparent that due to the relatively high upward velocity, a significant downward drag force is exerted. As a result, certain points in the graph indicate minimal U1 control input, while all propeller angular velocities (omega values) experience a substantial increase. This behavior is necessary as the UAV requires a substantial thrust to facilitate upward acceleration, thereby compensating for the opposing drag force. Following Fig. 7, from a, there was a substantial amount of fluctuation in following the setpoint by the drone's Yaw motion (where the author kept all reference yaw values equal during one outer loop). On the

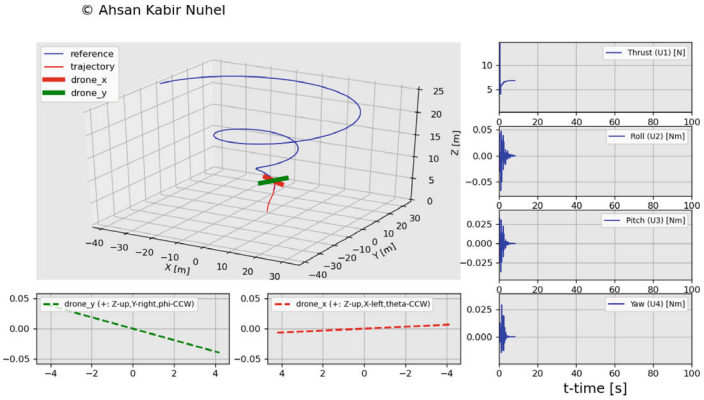

(a) UAV motion with drag force

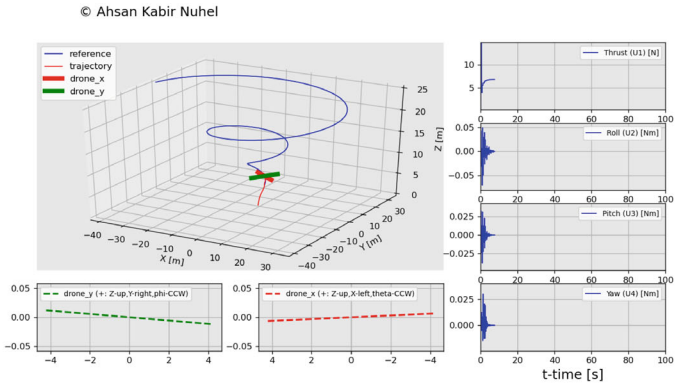

(b) UAV motion in vacuum environment (no drag force)

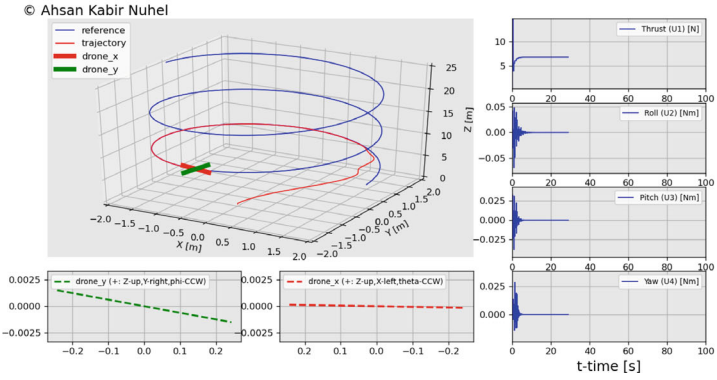

(c) UAV motion in spiral with a constant radius

Fig. 4 UAV motion in different circumstances

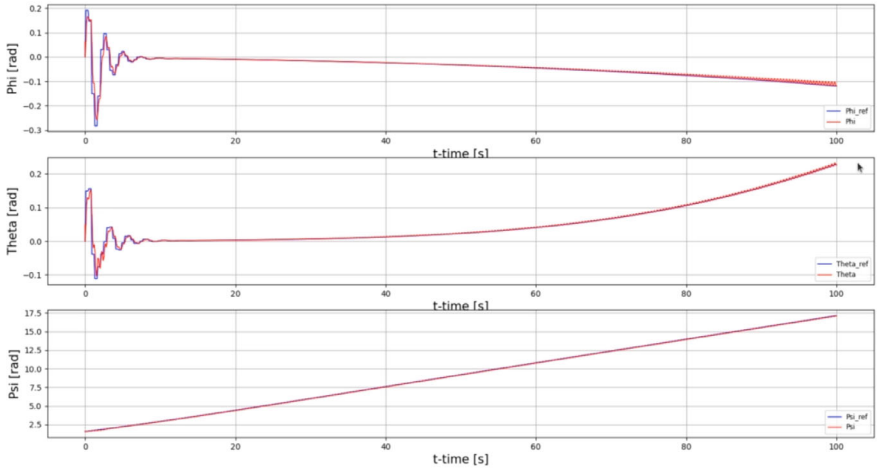

Fig. 5 Performance concerning control input angles

other hand, the yaw trajectory was quite smooth in figure b (where author created a vector containing continuous yaw reference values), resulting in better tracking performance. Authors have used Runge–Kutta method to integrate the plants [15].

The principal investigator of the study developed a range of discrete trajectory models to systematically evaluate the efficacy and efficiency of the comprehensive system under investigation, as delineated in Fig. 8. These meticulously formulated methodologies were meticulously executed to holistically appraise various facets and capabilities inherent in the overarching system. The visual aids presented below offer specific instances wherein an unmanned aerial vehicle (UAV) rigorously monitors

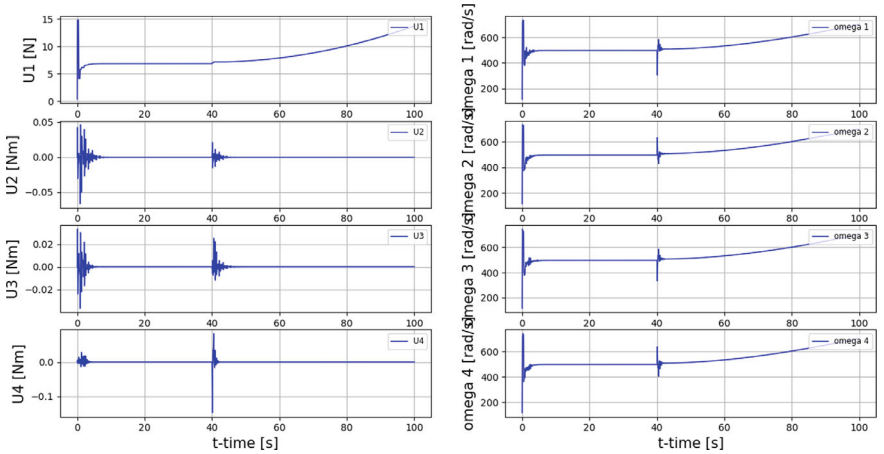

Fig. 6 Performance concerning control inputs

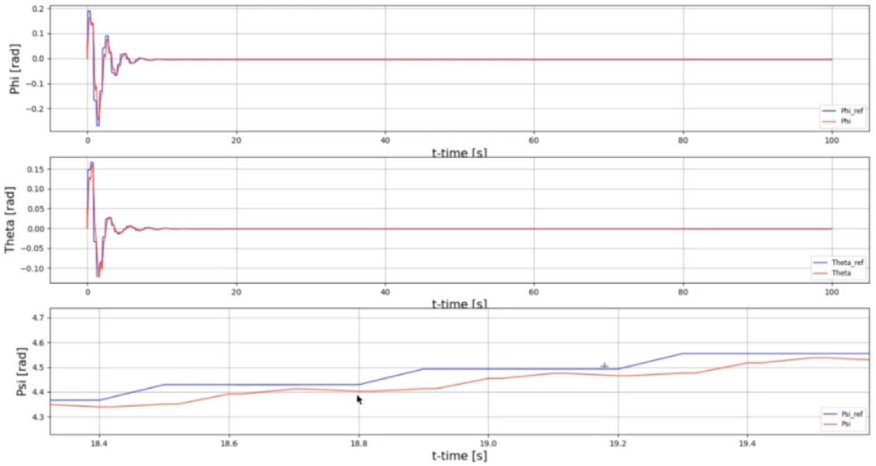

(a)

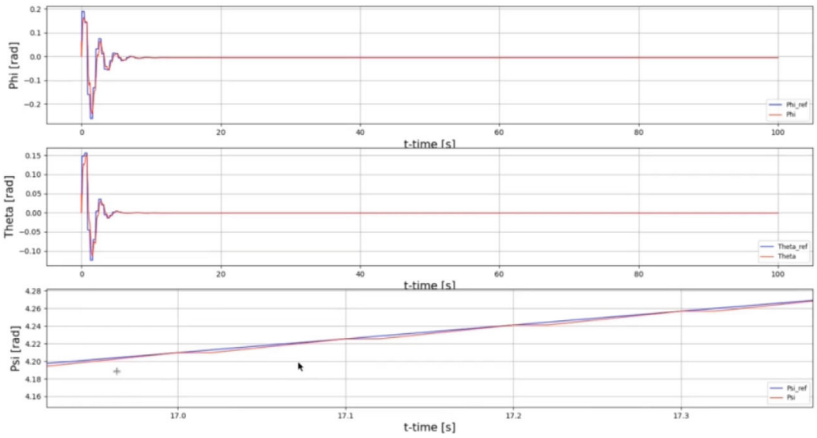

(b)

Fig. 7 Results of the drone yaw motion

and faithfully adheres to its designated reference trajectory. Within the accompanying illustrations, the reference trajectory is distinctly delineated in blue, while the real-time position of the UAV is conspicuously demarcated in red. These visual representations adeptly demonstrate the adept instantiation of control algorithms, thus accentuating the system's inherent capacity to precisely pursue the envisaged trajectory while meticulously upholding the desired positional parameters.

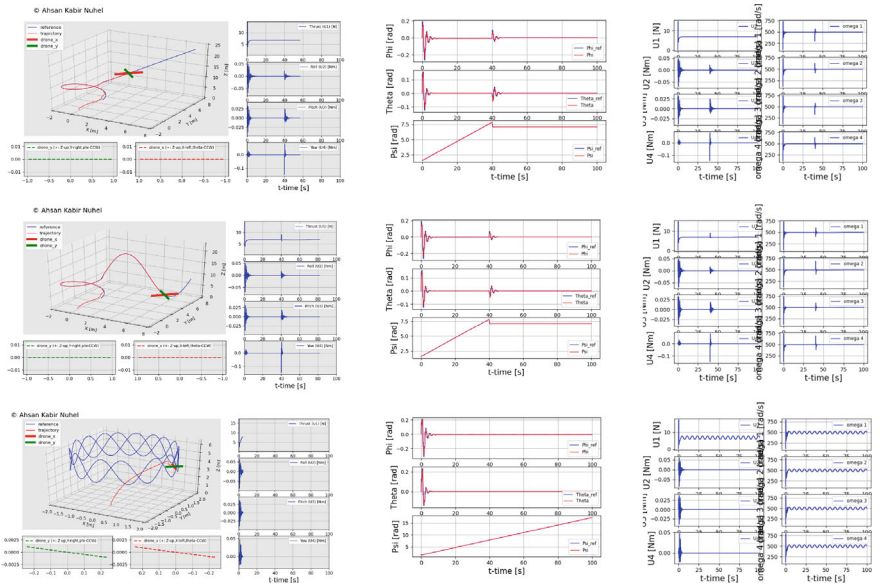

Fig. 8 User-defined different trajectories and UAV's performance attributes

5 Conclusion

Autonomous drone can be useful in multiple purposes. In this paper, the authors designed a four-propeller drone using MPC controller and feedback linearization control. Using the different trajectory, the drone performance is analyzed. This kind of drones can be useful in delivering emergency medicine supply, food delivery monitoring a certain place, and taking important pictures in of human unreachable zones. The drone can be improved by using unsupervised machine learning-based path planning and obstacle avoidance. Reinforcement-based machine learning can also be integrated for more advanced control and automation of the system.

References

1. Maddikunta, P.K.R., Hakak, S., Alazab, M., Bhattacharya, S., Gadekallu, T.R., Khan, W.Z., Pham, Q.-V.: Unmanned aerial vehicles in smart agriculture: Applications, requirements, and challenges. IEEE Sens. J. **21**(16), 17608–17619 (2021)
2. Iqbal, S.: A study on UAV operating system security and future research challenges. In: 2021 IEEE 11th Annual Computing and Communication Workshop and Conference (CCWC), pp. 0759–0765. IEEE (2021)
3. Vechtel, D., Buch, J.-P.: Aspects of yaw control design of an aircraft with distributed electric propulsion. CEAS Aeronaut. J. **13**(4), 847–860 (2022)
4. Foehn, P., Brescianini, D., Kaufmann, E., Cieslewski, T., Gehrig, M., Muglikar, M., Scaramuzza, D.: Alphapilot: Autonomous drone racing. Auton. Robot. **46**(1), 307–320 (2022)

5. Fotouhi, A., Ding, M., Hassan, M.: Understanding autonomous drone maneuverability for internet of things applications. In: 2017 IEEE 18th International Symposium on a World of Wireless, Mobile and Multimedia Networks (WoWMoM), pp. 1–6. IEEE (2017)
6. Nguyen, D.D., Rohacs, J., Rohacs, D.: Autonomous flight trajectory control system for drones in smart city traffic management. ISPRS Int. J. Geo-Inf. **10**(5), 338 (2021)
7. Bonatti, R., Zhang, Y., Choudhury, S., Wang, W., Scherer, S.: Autonomous drone cinematographer: Using artistic principles to create smooth, safe, occlusion-free trajectories for aerial filming. In: Proceedings of the 2018 International Symposium on Experimental Robotics, pp. 119–129. Springer International Publishing (2020)
8. Zhang, Y., Zhu, R., Wu, J., Wang, H.: SimoBot: an underactuated miniature robot driven by a single motor. IEEE/ASME Trans. Mechatron. **27**(6), 5748–5759 (2022)
9. Nuhel, A.K., Sazid, M.M., Bhuiyan, M.N.M., Arif, A.I., Roy, P.H., Islam, M.R.: Developing a self-driving autonomous car using artificial intelligence algorithm. In: 2022 6th International Conference on Electronics, Communication and Aerospace Technology, pp. 1240–1249. IEEE (2022)
10. Shrestha, E., Reddy, C., Wan, H., Zhuang, Y., Vasudevan, R.: Sense, imagine, act: multimodal perception improves model-based reinforcement learning for head-to-head autonomous racing. arXiv preprint arXiv:2305.04750 (2023)
11. Yingxun, W.A.N.G., Zhang, T., Zhihao, C.A.I., Jiang, Z.H.A.O., Kun, W.U.: Multi-UAV coordination control by chaotic grey wolf optimization based distributed MPC with event-triggered strategy. Chin. J. Aeronaut. **33**(11), 2877–2897 (2020)
12. Hightower, B.J., Wijnings, P.W.A., Scholte, R., Ingersoll, R., Chin, D.D., Nguyen, J., Shorr, D., Lentink, D.: How oscillating aerodynamic forces explain the timbre of the hummingbird's hum and other animals in flapping flight. Elife **10**, e63107 (2021)
13. Nuhel, A.K., Sazid, M.M., Bhuiyan, M.N.M., Arif, A.I.: Designing and performance-analysis of a 3 DOF robotic manipulator arm and its higher order integration for 7 DOF robotic arm. In: 2022 4th International Conference on Sustainable Technologies for Industry 4.0 (STI), pp. 1–6. IEEE (2022)
14. Swain, P.K., Dora, S.P.: Experimental and numerical investigation of wing–wing interaction and its effect on aerodynamic force of a robotic dragonfly during hovering and forward flight. Arch. Appl. Mech. **91**(5), 2039–2052 (2021)
15. Song, Y., Steinweg, M., Kaufmann, E., Scaramuzza, D.: Autonomous drone racing with deep reinforcement learning. In: 2021 IEEE/RSJ International Conference on Intelligent Robots and Systems (IROS), Prague, Czech Republic, pp. 1205–1212 (2021)

GA Optimization Methods for Charging of Electric Vehicles by Scheduling the Load of Home Appliances

Madhavi Nerkar, Aniruddha Mukherjee, and Bhanu Pratap Soni

Abstract Modern and challenging alternatives to traditional vehicles are electric vehicles (EVs). With low operating costs and the ability to utilize renewable energy sources, they offer environmental benefits. The increasing adoption of electric vehicles has given rise to challenges concerning efficient charging infrastructure and load management. This research paper focuses on the application of GA optimization to address the issue of EV charging by creating a schedule for the usage of home appliances. The objective is to optimize the charging process by considering the electricity demand of both EVs and home appliances, all while minimizing overall energy costs and maximizing user satisfaction. The paper provides an overview of GA optimization techniques and their relevance in EV charging scenarios. It also discusses the integration of load scheduling for home appliances and presents the advantages, challenges, and potential future research directions in this field.

Keywords Electric vehicle · Sustainability · Energy management · Genetic algorithm · Optimization · V2G · Charging

1 Introduction

In recent years, the popularity of electric vehicles (EVs) has surged, driven by their environmental advantages and advancements in battery technology. This surge in EV adoption has led to an increased demand for efficient charging infrastructure to support the growing number of EVs on the road. However, the simultaneous charging of multiple EVs, coupled with the energy consumption of home appliances, poses challenges for the electricity grid and necessitates effective load management strategies.

M. Nerkar · A. Mukherjee
Department of EEE, University of Engineering and Management, Jaipur, India

B. P. Soni (✉)
School of Electrical and Electronics Engineering, Fiji National University, Suva, Fiji
e-mail: bpsoni.ee@gmail.com

© The Author(s), under exclusive license to Springer Nature Singapore Pte Ltd. 2025

H. P. Singh et al. (eds.), *Recent Developments in Control, Automation and Power Engineering*, Lecture Notes in Electrical Engineering 1303,
https://doi.org/10.1007/978-981-96-0047-2_30

The electrical infrastructure may experience a substantial burden due to the uncontrolled charging of these vehicles. Over the past several years, extensive research has been conducted on the critical and complex issue of EV charge scheduling. This research encompasses the most recent advancements in the field of smart grid scheduling algorithms for EV charging. For real-time charging, certain heuristic and meta-heuristic algorithms are taken into consideration. Various EV scheduling methods have been developed based on GA and Intelligent Scatter Search (GA and ISS), Particle Swarm Optimization (PSO), and Reinforcement Learning (RL) algorithms, with objectives ranging from power loss minimization, energy cost reduction, to peak load alleviation [12, 20].

The hierarchical structure of our survey, which primarily centers around the environment for EV charge scheduling, is illustrated in Fig. 1. This environment encompasses the pricing rules formulated by utility companies and the optimization tools, along with the optimization objectives required to formulate an optimal EV charging plan. This is aimed at formulating an optimal charging schedule. The primary emphasis of this study revolves around achieving the most efficient scheduled EV charging within the context of Real-Time Pricing (RTP), Critical Peak Pricing (CPP), and Time-of-Use (ToU) dynamic energy pricing schemes [18]. The objectives and optimization methodologies utilized to achieve these goals are integrated into an ideal timetable for electric vehicle charging [3].

Various optimization approaches [17, 19] for EV charging have been explored. GA optimization methods offer numerous advantages for EV charging and load scheduling scenarios due to their capacity to handle intricate, nonlinear, and dynamic optimization problems. Additionally, they possess a global search capability, which permits them to explore an extensive range of potential solutions, ultimately leading to optimal or near-optimal outcomes. Their adaptability to manage both continuous and discrete variables makes them versatile for optimizing various parameters in EV charging and load scheduling.

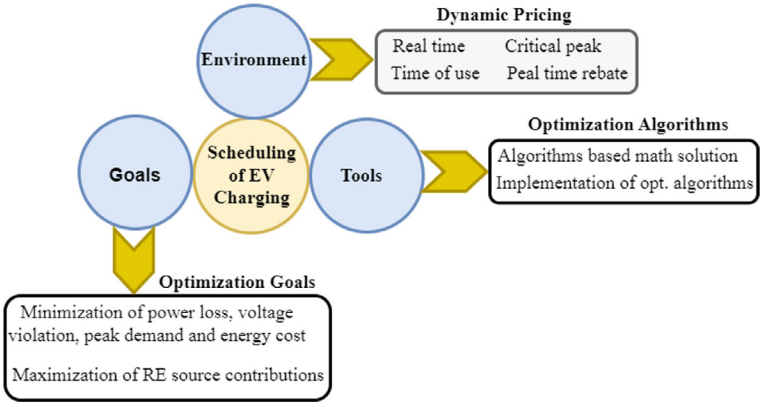

Fig. 1 Scheduling's of EV charging

2 Literature Review

Integrating home appliance load scheduling with EV charging optimization can further optimize the energy consumption. For instance, Sayad et al. [5] proposed a hybrid GA approach that optimizes both EV charging and home appliance load scheduling. Their study demonstrated improved energy efficiency and reduced charging costs [24]. In some cases, EV charging optimization involves multiple objectives, such as cost minimization, load balancing, and user satisfaction. GA-based multi-objective optimization approaches can address these objectives simultaneously. For example, [11, 20] proposed a multi-objective GA optimization approach for EV charging and home appliance scheduling, considering cost, grid congestion, and user preferences.

An intelligent optimization strategy using GA for EV charging and household appliance operation is given in [21], and the approach incorporated demand response and user satisfaction considerations. The results indicated significant reductions in energy costs and peak demand, highlighting the benefits of GA optimization in achieving efficient and user central energy management. The study developed a multi-objective optimization model for EV charging scheduling in [2, 10], aiming to minimize energy costs, balance loads, and consider user preferences. It achieved an optimal trade-off among these objectives, resulting in improved energy cost savings and reduced charging time. The researchers utilized a GA to solve the multi-objective optimization problem.

The study proposed [6], a GA-based charging algorithm that considered the charging demand of EVs and the power consumption of home appliances. The study successfully achieved load balancing, reduced charging costs, and optimized the charging process [13, 23]. It developed a genetic algorithm (GA)-based solver to optimize the charging schedule based on both charging demand and the power consumption of home appliances. By incorporating load constraints and user preferences into the objective function, the research addressed the coordination of electric vehicle (EV) charging with home appliance load scheduling through GA optimization. The findings demonstrated the effectiveness of the proposed algorithm in achieving load balance and reducing costs.

3 Problem Statement

Optimal time selection of EV charging in load scheduling of home is a crucial aspect that requires careful consideration. Here are some common problems associated with this issue,

- Peak demand management [9]
- Load balancing [16]
- User preference consideration [15].

These are the problems associated with the optimal time selection of EV charging in load scheduling of home. Hence in this paper, we consider GA optimization which

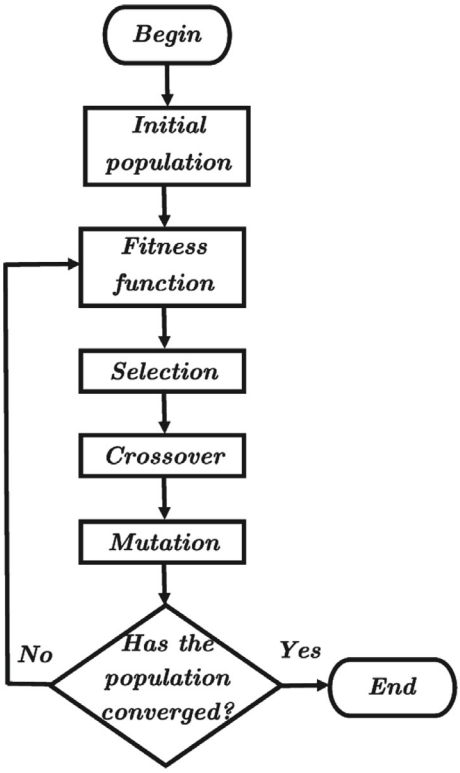

Fig. 2 GA block diagram

can be employed for the optimal time selection of EV charging in load scheduling of home. These methods utilize the principles of natural selection, genetic variation, and evolution to find near-optimal solutions. GA-based optimization methods have shown promise in providing efficient solutions for EV charging and load scheduling [18]. GA optimization is a heuristic search algorithm inspired by the principles of natural evolution and genetics. Figure 2 represents the block diagram of GA working.

A population of possible solutions is gathered, their fitness is evaluated, and genetic operators including selection, crossover, and mutation are used to help the population expand and become better through the years.

4 System Model and Methodology

4.1 Optimization of EV Scheduling

The optimal load position of EV charging at home refers to determining the most efficient and advantageous location for charging electric vehicles within a residential

setting. Optimal charging station placement considering the electrical infrastructure capacity and charging demand. Their results in [7] indicated the importance of optimal load position for efficient energy distribution. A mathematical model for optimal EV charger location selection and their study [8] considered factors such as charging demand, electrical infrastructure capacity, and cost optimization. The results demonstrated the significance of load position optimization in minimizing costs and maximizing energy distribution efficiency.

The primary goal of an optimization of EV scheduling is to optimize energy consumption, increase energy efficiency, and reduce energy costs while ensuring user comfort and convenience. GA can be applied to optimize the load position of EV charging at home. These algorithms consider factors such as charging demand, electrical infrastructure capacity, cost optimization, and grid constraints. GA optimization methods aim to find the most suitable load positions that minimize energy losses, voltage drops, and infrastructure costs while meeting charging requirements [1, 4, 14]. Scheduling for EV charging in connection with time-of-use pricing. Here, the objective function is to charge at the most affordable rate, with the number of charging piles and the instantaneous power of the stations functioning as constraints [22].

4.2 Proposed Method

The goal of the proposed GA optimization approach is to find an optimal or near-optimal solution that balances the charging requirements of EVs, the operation of home appliances, and the overall energy cost and grid constraints. It has the following objectives: to find optimal position of EV charging by scheduling the load of home appliances by considering the variables, objective, constraints, and GA optimization steps. The research paper aims to provide a comprehensive solution to the problem of charging EVs by scheduling the load of home appliances.

In this paper,the provided data represents a list of home appliances along with their scheduling details, including the start time, end time, duration, and costs. Additionally, there is an entry for an electric vehicle (EV) charging schedule.

The load scheduling data of smart home given in Table 1 is crucial for optimizing energy consumption and distribution. This data derived the daily load consumption of home appliances along with EV. By intelligently timing the operation of appliances and devices, home owners can enhance energy efficiency, manage peak loads, integrate renewable sources, and align consumption with user preferences. The above data represents a list of home appliances and their corresponding scheduling details for load scheduling. Table 2 gives description of the different tariff intervals and corresponding unit prices in $.

Overall, the data provides specific scheduling details for a range of home appliances and an electric vehicle, including their operational time intervals, duration, and cost factors. This information is essential for developing load scheduling algorithms

Table 1 Sample data of load scheduling for home

Appliances	Start time	End time	Duration	Cost factor (C)
TV	10:30:00 AM	2:00:00 PM	2	0.13
Washing machine	12:00:00 AM	11:30:00 PM	10	1.5
Vacuum cleaner	12:00:00 AM	11:30:00 PM	6	0.3
Halogen lamp	8:00:00 PM	11:30:00 PM	1	0.5
Stove	7:00:00 AM	11:00:00 AM	2	3
Computer	8:00:00 AM	11:30:00 PM	6	2
Microwave	7:00:00 AM	11:00:00 AM	1	1
Lights	6:00:00 PM	11:30:00 PM	5	0.5
Lights	5:00:00 AM	9:00:00 AM	3	0.5
Pool Pump	11:00:00 AM	3:00:00 PM	1	2
Refrigerator	12:00:00 AM	11:30:00 PM	23	0.5
Laptop	8:00:00 AM	11:30:00 PM	4	0.3
Printer	8:00:00 AM	11:30:00 PM	4	0.3
AC1	12:00:00 PM	4:00:00 PM	4	1.5
AC2	7:00:00 PM	11:30:00 PM	4	1.5
Rice cooker	6:00:00 AM	6:00:00 PM	12	0.5
Blender	6:00:00 AM	12:00:00 PM	2	0.3
Mixer	6:00:00 AM	12:00:00 PM	2	0.3
Water heater	5:00:00 AM	8:00:00 PM	12	1.5
Hair dryer	5:00:00 AM	10:00:00 AM	4	0.5
EV	12:00:00 AM	5:00:00 PM	5	4

Table 2 Tariff intervals

Intervals	Start time	End time	Prices P_j
Off peak 1	12:00:00 AM	6:00:00 AM	0.4
Peak 2	6:00:00 AM	10:00:00 AM	1
Standard	10:00:00 AM	3:00:00 PM	0.6
Peak 2	3:00:00 PM	9:00:00 PM	1
Off peak 2	9:00:00 PM	12:00:00 AM	0.4

that aim to optimize the overall energy consumption and cost efficiency of the system. Minimization of electricity costs: The system aims to minimize the electricity costs associated with the operation of smart home appliances.

4.3 Objective Function

The minimum total cost T_{cost} is defined as the objective function to be minimized:

$$T_{\text{cost}} = \sum_{i=1}^{N} \sum_{j=1}^{M} \left[\frac{1}{2} \left(\sum_{t=1}^{P} S_{ij}(t) \right) \times P_j \times C_i \right], \tag{1}$$

where T_{cost} represents the total cost of energy consumption to be minimized. Its summation of the cost is calculated for each appliance and time interval. N is the number of appliances. P is the number of time intervals (i.e., $P = 48$). M is the number of tariff intervals (i.e., $P = 5$). $S_{ij}(t)$ represents the energy consumption of appliance i during time interval t of tariff interval j. P_j is the price of electricity for tariff interval j. C_i is the cost factor for appliance i.

It's the target to reduce the value of T_{cost}, which corresponds to minimizing the total cost of energy consumption calculated by using Eq. 1, thereby achieving cost optimization in the load scheduling problem.

The load scheduling system aims to optimize the operation of home appliances in order to reduce the overall cost of energy consumption while considering tariff intervals and appliance specific costs. The system utilizes a GA optimization approach to find the optimal scheduling solution.

The system provides an automated approach to optimize the scheduling of home appliances, considering tariff intervals, appliance costs, and the objective of cost minimization. By utilizing the GA optimization technique, it searches for the best scheduling solution and enables efficient utilization of energy resources.

5 Experimental Result and Analysis

The GA implementation optimizes electric vehicle (EV) charging and home appliance schedules in a smart home. It uses chromosomes to represent schedules, applies selection, crossover, and mutation operations to evolve solutions, and evaluates fitness based on energy efficiency, cost reduction, and user preferences. The algorithm aims to find the best schedule by iterative generating generations of schedules until termination conditions are met. This approach enhances energy management and convenience in a smart home environment.

The proposed GA-based scheduling method for EV charging considering the electricity demand of home appliances. The GA algorithm aimed to reduce peak demand, improve user satisfaction, and minimize overall energy costs. The optimization model integrated home appliance load constraints and user preferences into the objective function. As a result, the objective of optimization may be stated as to

- **Energy Cost Reduction** The algorithm aimed to minimize energy costs by optimizing the charging and home appliance load scheduling.

- **Charging Time Optimization** The algorithm aimed to reduce the charging time for EVs by considering their charging demand and available time slots.
- **User Satisfaction** The algorithm considered user preferences, such as preferred departure times or charging time windows, to increase user satisfaction and convenience.

Figure 3 illustrates the optimized EV scheduling during the morning hours, given that the minimum load occurs in both the morning and evening periods throughout the day. In contrast, Fig. 4 depicts the initial load curve without the use of GA, resulting in a less favorable fitness position for minimum load. Conversely, Fig. 5 demonstrates the optimal load curve achieved through the application of GA, leading to the best fitness position for minimum load. In GA, the determination of the best and worst fitness relies on parameters such as the number of generations, population size, mutation rate, and crossover rate. However, during program execution, the system randomly selects parents and offspring, leading to fluctuations in the best and worst fitness values over time.

Further investigation, as presented in Table 3, could concentrate on comprehending the underlying factors that contribute to the observed trends and evaluating the computational efficiency of the GA across varying population sizes. Moreover, it will be essential to account for the specific objectives and constraints inherent to the optimization problem, as this will be pivotal in gauging the practical significance of these findings within real-world scenarios. Across different population sizes, the best

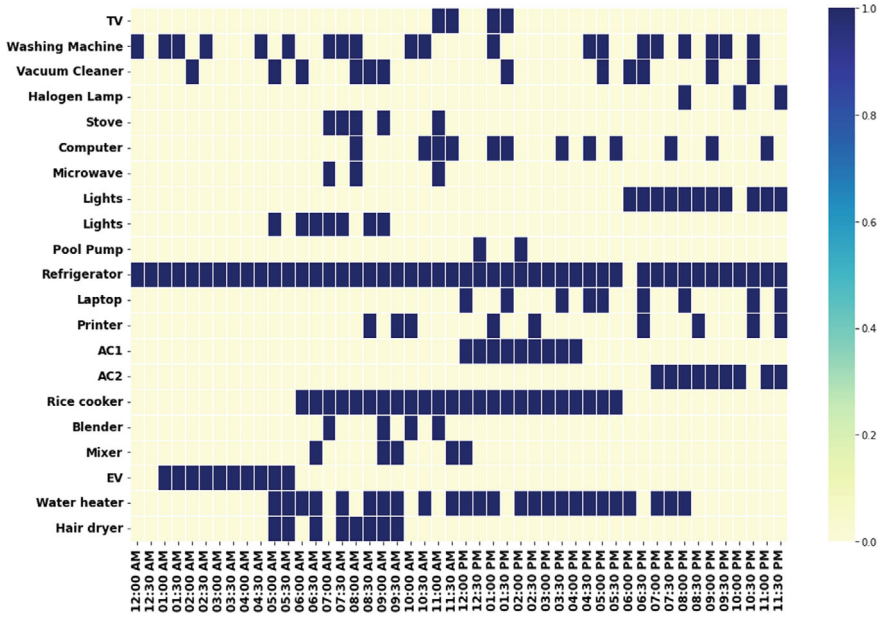

Fig. 3 Scheduling's of EV charging

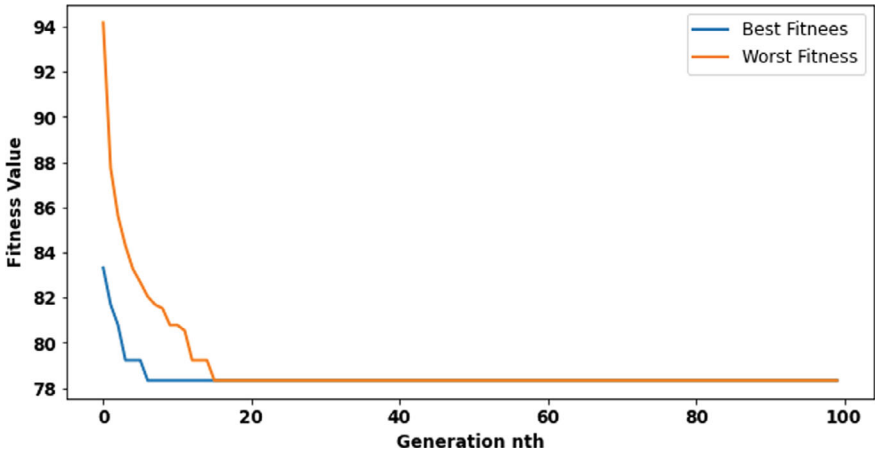

Fig. 4 Fitness curves

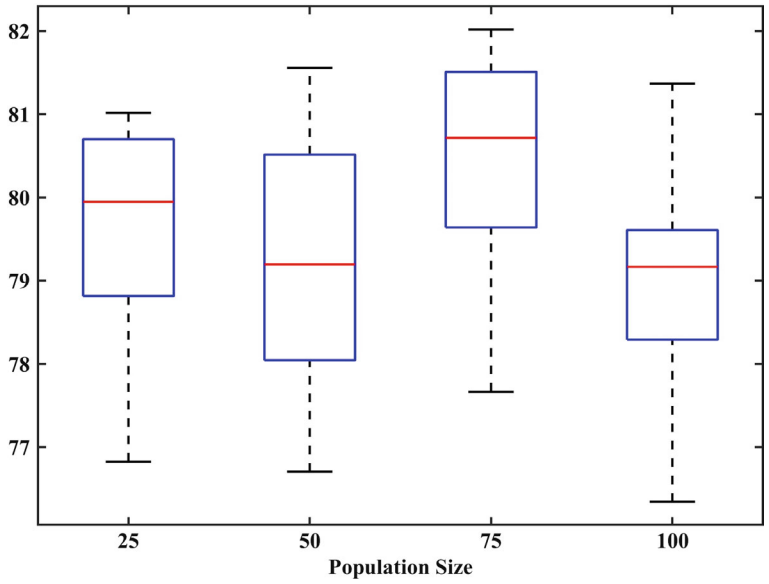

Fig. 5 Box plot analysis

objective values exhibit a remarkable similarity, underscoring the consistent quality of solutions generated by the GA. Notably, a population size of 75 stands out, boasting the highest "Best Value" and "Average Value." This suggests a well-balanced trade-off between exploration and exploitation. However, it's worth noting that this particular population size also displays the highest variance, indicating a sensitivity to initial conditions.

Table 3 GA optimization results (20 times run)

Number of population	Min cost	Max cost	Mean	Variance
25	76.825	81.01	79.666	1.532
50	76.705	81.55	79.338	1.679
75	77.665	82.01	80.398	2.152
100	76.344	81.36	79.1	1.392

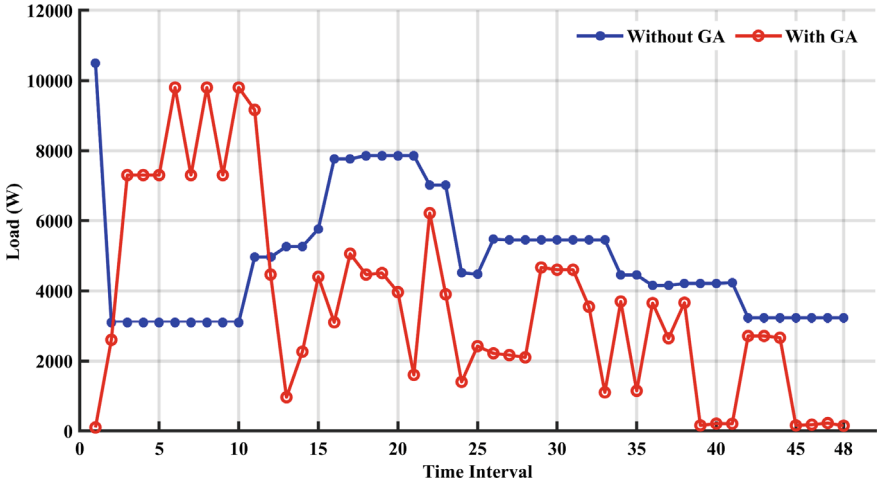

Fig. 6 Power consumption (load profile) 24 h

Table 3 presents the results of GA optimization across varying population sizes. The box plot showcasing the GA results in response to changes in population size can be found in Fig. 5. This data illustrates the performance of GA in identifying optimal solutions for EV scheduling under different population sizes. Notably, population size displays the highest variance, indicating sensitivity to initial conditions. This insight emphasizes how GA functions in locating optimal EV scheduling solutions while adapting to diverse population sizes.

The GA effectively employed key genetic operators, including crossover, mutation, and selection, to generate innovative solutions and enhance population fitness. Through iterative development of the population, the GA algorithm systematically adjusted appliance scheduling across various time slots to minimize the objective function. A more favorable solution for electric vehicle charging is evidenced in Fig. 6, underscoring the efficacy of the GA approach.

6 Conclusion

In this paper, the analysis focused on GA optimization methods for EV charging and load scheduling in the context of home appliances. The research paper emphasizes that GA optimization methods play a significant role in enabling optimal time selection of EV charging in load scheduling of home appliances, leading to improved energy management, cost savings, and enhanced user experiences. The optimal load position of EV load scheduling at home, highlighting the importance of coordination between EV charging and home appliances, considering TOU pricing.

Future research can focus on integrating renewable energy sources, considering vehicle-to-grid (V2G) capabilities, and exploring advanced GA and other metaheuristic optimization techniques and their variants.

References

1. Abdullah-Al-Nahid, S., Khan, T.A., Taseen, M.A., Jamal, T., Aziz, T.: A novel consumer-friendly electric vehicle charging scheme with vehicle to grid provision supported by genetic algorithm based optimization. J. Energy Storage **50**, 104655 (2022)
2. Alshammari, N.F., Samy, M.M., Barakat, S.: Comprehensive analysis of multi-objective optimization algorithms for sustainable hybrid electric vehicle charging systems. Mathematics **11**(7), 1741 (2023)
3. Amin, A., Tareen, W.U.K., Usman, M., Ali, H., Bari, I., Horan, B., Mekhilef, S., Asif, M., Ahmed, S., Mahmood, A.: A review of optimal charging strategy for electric vehicles under dynamic pricing schemes in the distribution charging network. Sustainability **12**(23), 10160 (2020)
4. Efthymiou, D., Chrysostomou, K., Morfoulaki, M., Aifantopoulou, G.: Electric vehicles charging infrastructure location: a genetic algorithm approach. Eur. Transp. Res. Rev. **9**(2), 1–9 (2017)
5. El Sayed, F.T., Amer, G.M., Fayez, H.M.: Scheduling home appliances with integration of hybrid energy sources using intelligent algorithms. Ain Shams Eng. J. **13**(4), 101676 (2022)
6. Elmehdi, M., Abdelilah, M.: Genetic algorithm for optimal charge scheduling of electric vehicle fleet. In: Proceedings of the 2nd International Conference on Networking, Information Systems and Security, pp. 1–7 (2019)
7. Goli, P., Jasthi, K., Gampa, S.R., Das, D., Shireen, W., Siano, P., Guerrero, J.M.: Electric vehicle charging load allocation at residential locations utilizing the energy savings gained by optimal network reconductoring. Smart Cities **5**(1), 177–205 (2022)
8. Jia, Z., Li, J., Zhang, X.P., Zhang, R.: Review on optimization of forecasting and coordination strategies for electric vehicle charging. J. Mod. Power Syst. Clean Energy (2022)
9. Jones, C.B., Vining, W., Lave, M., Haines, T., Neuman, C., Bennett, J., Scoffield, D.R.: Impact of electric vehicle customer response to time-of-use rates on distribution power grids. Energy Reports **8**, 8225–8235 (2022)
10. Kumar, S., Singh, R.: Advanced speed control of an automated guided vehicle. In: Proceeding of the International Multi-conference of Engineers and computer scientists, vol. 2 (2011)
11. Kwon, Y., Kim, T., Baek, K., Kim, J.: Multi-objective optimization of home appliances and electric vehicle considering customer's benefits and offsite shared photovoltaic curtailment. Energies **13**(11), 2852 (2020)
12. Nerkar, M., Mukherjee, A., Soni, B.P.: A review on optimization scheduling methods of charging and discharging of EV. In: AIP Conference Proceedings, vol. 2452. AIP Publishing (2022)

13. Pande, A.S., Soni, B.P., Bhadane, K.V.: Classification and review of electric circuit models for electric vehicle batteries. Int. J. Electr. Hybrid Veh. **15**(2), 107–126 (2023)
14. Pande, A.S., Soni, B.P., Bhadane, K.V.: Electrical models for EV's batteries: an overview and mathematical design of RC network. J. Inst. Eng. (India) Ser. B **104**(2), 533–547 (2023)
15. Piamvilai, N., Sirisumrannukul, S.: Optimal scheduling of movable electric vehicle loads using generation of charging event matrices, queuing management, and genetic algorithm. Energies **15**(10), 3827 (2022)
16. Ravi, S.S., Aziz, M.: Utilization of electric vehicles for vehicle-to-grid services: Progress and perspectives. Energies **15**(2), 589 (2022)
17. Saxena, A., Soni, B.P., Gupta, V.: Minimax approximation synthesis in PSS design by embedding gravitational search algorithm. In: 2014 IEEE International Conference on Advanced Communications, Control and Computing Technologies, pp. 929–934. IEEE (2014)
18. Sharma, A.K., Saxena, A., Soni, B.P., Palwaliya, D.K.: Supervised learning based demand response simulator with RTP and PTR in context of smart grid. In: 2022 IEEE International Conference on Power Electronics, Smart Grid, and Renewable Energy (PESGRE), pp. 1–5. IEEE (2022)
19. Soni, B.P., Saxena, A., Gupta, V.: A minimax polynomial approximation objective function approach for optimal design of power system stabilizer by embedding particle swarm optimization. TELKOMNIKA Indones. J. Electr. Eng. **14**(2), 191–198 (2015)
20. Soni, B.P., Saxena, A., Gupta, V.: Support vector machine based approach for accurate contingency ranking in power system. In: 2015 Annual IEEE India Conference (INDICON), pp. 1–5. IEEE (2015)
21. Tutkun, N., Burgio, A., Jasinski, M., Leonowicz, Z., Jasinska, E.: Intelligent scheduling of smart home appliances based on demand response considering the cost and peak-to-average ratio in residential homes. Energies **14**(24), 8510 (2021)
22. Wu, J., Su, H., Meng, J., Lin, M.: Electric vehicle charging scheduling considering infrastructure constraints. Energy **278**, 127806 (2023)
23. Yeh, Y.C., Tsai, M.S.: Development of a genetic algorithm based electric vehicle charging coordination on distribution networks. In: 2015 IEEE Congress on Evolutionary Computation (CEC), pp. 283–290. IEEE (2015)
24. Zhou, K., Cheng, L., Lu, X., Wen, L.: Scheduling model of electric vehicles charging considering inconvenience and dynamic electricity prices. Appl. Energy **276**, 115455 (2020)

Design of Type Compensators Using *K*-factor Method

Adnan Mukhtar and Arghya Chakravarty

Abstract This chapter addresses a proper step-by-step mathematical procedure for implementing and designing the Type-2/3 compensators using the *K*-factor method that has not been previously described in any literature. This method offers a methodical and effective means of adjusting the *K*-factor and getting suitable values for compensator design. Synthesis of feedback compensators with any desired crossover frequency and phase margin is feasible using a few algebraic equations and the presented methodology. Type-2 compensators boost system damping to enhance closed-loop response, whereas Type-3 compensators insert a pole at the origin to eliminate steady-state error. This chapter examines the origin, use, advantages, disadvantages, and applications of the *K*-factor technique in the context of compensator design.

Keywords Bode plot · Compensator design · Crossover frequency · Geometric mean · *K*-factor · Phase boost · Significant pole–zero · Type-2/3 compensators

Nomenclatures

K_{2C}	Type-2 compensator gain
K_{3C}	Type-3 compensator gain
ω_{2P}	Type-2 compensator pole frequency
ω_{2Z}	Type-2 compensator zero frequency
ω_{2C}	Type-2 compensator crossover frequency
$G_{2C}(s)$	Type-2 compensator transfer function
ω_{3P}	Type-3 compensator pole frequency
ω_{3Z}	Type-3 compensator zero frequency

A. Mukhtar (✉) · A. Chakravarty
SRM University, Mangalagiri, Guntur, Andhra Pradesh 522502, India
e-mail: adnan_mukhtar@srmap.edu.in

A. Chakravarty
e-mail: arghya.c@srmap.edu.in

© The Author(s), under exclusive license to Springer Nature Singapore Pte Ltd. 2025

H. P. Singh et al. (eds.), *Recent Developments in Control, Automation and Power Engineering*, Lecture Notes in Electrical Engineering 1303,
https://doi.org/10.1007/978-981-96-0047-2_31

ω_{3C}	Type-3 compensator crossover frequency
$G_{3C}(s)$	Type-3 compensator transfer function
ϕ_{B2}	Phase boost for Type-2 compensator
ϕ_{B3}	Phase boost for Type-3 compensator
K	Separation factor
PM	Phase margin

1 Introduction

Feedback loop stability analysis has always involved some trial and error. It was still difficult to start with a desired outcome and then determine the specific circuit values required to achieve that outcome, even though computer modeling and computer-aided design made it very simple to analyze the effects of a specific design [1]. Many designers simply consider stable or unstable conditions when considering control system feedback loop adjustment. In fact, for any given loop crossover frequency and phase margin [2], there is an optimal error compensator transfer function. The maximum gain below crossover and the lowest gain above crossover represent the ideal design's characteristics. To obtain optimal performance, a certain pole–zero location must be used. Without using trial and error, this pole–zero positioning and the resulting system component values can be found. Additionally, there is an ideal phase margin or loop bandwidth for each given open-loop crossover frequency [2, 3]. The performance of a feedback control loop can be enhanced using simple, effective, and easy-to-use techniques. These methods can be applied to any form of single or multiple-loop system and will produce the best results without the traditional trial-and-error method. Two new ideas are presented: the idea of phase boost as the key variable in loop stability, and the idea of the K-factor as a practical way to define both phase boost and the contours of the Bode gain curve.

To achieve the desired system performance in the world of control systems, compensator design is crucial. To alter the dynamics of control systems and improve their stability, transient response, and error characteristics, compensators are used [4–9]. Two standardized feedback compensators that satisfy the needs of each known loop are presented in this chapter. Type-2 and Type-3 compensators are two commonly utilized compensator types, and each one has distinct benefits for enhancing system behavior. The purpose of Type-2 compensators is to increase the closed-loop system's damping, which enhances stability margins and decreases sensitivity to shocks. The insertion of a pole at the origin, on the other hand, distinguishes Type-3 compensators and effectively eliminates steady-state error for step inputs. Both types of compensators are essential when designing reliable control systems that adhere to strict performance specifications. With the use of a few straightforward algebraic equations, these compensators allow the control engineer to choose a desired outcome, such as a particular loop phase margin (PM) or crossover frequency ($\omega_{2C/3C}$), and then determine the component values required to arrive at these results.

The K-factor method has become a potent and adaptable tool for creating Type-2 and Type-3 compensators. To obtain desired system characteristics, including settling time, overshoot, and steady-state error, this method includes modifying the *K*-factor. Engineers may efficiently customize the compensator to meet certain control objectives by adjusting the *K*-factor, making it a popular option in a variety of control system applications. With the *K*-factor method, the design of Type-2 and Type-3 compensators will be thoroughly examined in this chapter. The main goal is to understand the fundamental ideas behind the *K*-factor approach and how it works in practice for designing compensators. By understanding and applying this powerful technique, engineers can successfully enhance control systems to meet tight performance criteria and address practical challenges in a range of applications.

2 *K*-factor Technique

The term "*k*" is a measurement of the spacing between the insignificant pole and significant zero; as a result, it is often referred to as a separation factor. The *K*-factor technique is a way of designing a compensator that requires adding the *K*-factor as a parameter. The compensators can be designed using the *K*-factor technique if the following information is known:

a) System Model: A mathematical simulation of the system or plant we want to manage. This model provides details about the system's transfer function, state-space representation, or any other appropriate form, and it represents the dynamics of the system.
b) Control Objectives: Control goals that are clear and well-defined, such as desirable closed-loop performance, stability margins, disturbance rejection, noise attenuation, or any other requirements that the compensator must achieve.
c) Compensator Structure: The kind of compensator structure to be utilized (such as PID, Type-2, Type-3, or another kind of cutting-edge control structure). Type-2 and Type-3 compensators frequently employ the *K*-factor approach, but other control schemes can also make use of it.
d) Frequency Response Analysis: The knowledge of the required closed-loop frequency response as well as the open-loop system's frequency response characteristics. This aids in modifying the behavior of the compensator and the influence of the *K*-factor on the control system.
e) *K*-factor Tuning Methods: The understanding of various tuning techniques or optimization algorithms to determine the right *K*-factor value that satisfies the design requirements and control goals. Trial-and-error, pole–zero placement, optimization algorithms, and frequency domain analysis are some examples of these techniques.

The frequency response of the system is typically used to build compensators using the *k*-factor technique, with the basic specifications loop phase margin (PM) or crossover frequency ($\omega_{2C/3C}$) [10]. The crossover frequency is the geometric mean

of zero and pole frequencies [1, 11]. The phase margin PM and crossover frequency can be obtained by plotting the bode plot of the transfer function representing the plant or system.

3 Compensator Design

The compensator design is a crucial aspect of control systems, and its importance cannot be overstated since it is crucial in ensuring favorable dynamic performance and stable regulation of a control system. A well-designed compensator plays a pivotal role in achieving desired system performance, stability, and robustness. Sufficient phase margin and gain margin are required for a control loop to function successfully [10, 11]. For this reason, having a design process that can handle both design factors is crucial. This chapter develops a methodical design technique for Type-2 and Type-3 compensators that makes it simple for the designer to take phase margin and gain margin into account and modify the compensator until the design requirement is met. The design of Type-2 and Type-3 compensators involves determining the constant gains K_{2C} and K_{3C} and determining the location of the significant zeros (ω_{2Z}, ω_{3Z}) and insignificant poles ($\omega_{2P,}$ ω_{3P}). These parameters are involved, therefore choosing the right ones to satisfy the phase margin and gain margin could be exceedingly difficult and time-consuming.

A design approach is presented below that is relatively easy to use, simply using the crossover frequency and phase margin to "tune" the compensators.

3.1 Type-2 Compensator

The Type-2 compensator consists of one significant zero, and two poles (one at the origin and the other insignificant pole somewhere in between) [2]. The Type-2 compensator belongs to the category of lead-type compensators featuring a pole at the origin. Designers employ this type of compensator to give the control loop a phase boost. As a result, this compensator delivers a maximum phase boost of 90° [7, 10, 12] while ensuring zero steady-state error. The maximal phase boost of the compensator is known to occur at a frequency equal to the geometric mean of the frequencies of the insignificant pole and the significant zero. This type of compensator is often designed by setting the necessary loop crossover frequency to the geometric mean of the significant zero and insignificant pole. This method can yield the highest phase margin possible from a given compensator. It does not, however, account for the gain margin, another crucial loop component.Despite the non-minimum phase issue faced by the control systems, when combined with a cascaded Type-2 compensator, it demonstrates improved closed-loop performance. By appropriately tuning this compensator, the control system can achieve faster responses, minimal overshoots, and zero steady-state error.

3.1.1 Mathematical Modeling

Type-2 compensator is a lead compensator with an additional pole at the origin [4–6, 8, 9, 13]. This compensator offers a maximum phase boost of 90° [3, 10] while maintaining zero steady-state error. This lead compensator has a significant zero and insignificant pole. Mathematically, the compensator is expressed as follows:

$$G_{2C}(s) = k_{2C}\left(1 + \frac{s}{\omega_{2Z}}\right) \Big/ s\left(1 + \frac{s}{\omega_{2P}}\right) \tag{1}$$

The argument of (1) at $s = j\omega_{2C}$ is written as follows:

$$\phi_{B2} = \tan^{-1}\left(\frac{\omega_{2C}}{\omega_{2Z}}\right) \Big/ \tan^{-1}\left(\frac{\omega_{2C}}{\omega_{2P}}\right) \tag{2}$$

where ϕ_{2C} is the $\arg[G_{2C}(s)]$ or phase boost and ω_{2C} is the crossover frequency or frequency at which maximum boost occurs.

$$\phi_{B2} = \tan^{-1}\left(\frac{\omega_{2C}}{\omega_{2Z}}\right) - \tan^{-1}\left(\frac{\omega_{2C}}{\omega_{2P}}\right) \tag{3}$$

Differentiating (3) w.r.t ω_{2C}

$$\phi'_{B2} = \frac{1}{\omega_{2Z}\left[1 + \frac{\omega_{2C}}{\omega_{2Z}}\right]^2} - \frac{1}{\omega_{2P}\left[1 + \frac{\omega_{2C}}{\omega_{2P}}\right]^2} = 0 \tag{4}$$

$$\frac{1}{\omega_{2Z}\left[1 + \frac{\omega_{2C}}{\omega_{2Z}}\right]^2} = \frac{1}{\omega_{2P}\left[1 + \frac{\omega_{2C}}{\omega_{2P}}\right]^2} \tag{5}$$

$$\frac{1}{\omega_{2Z}\left(\omega_{2Z}^2 + \omega_{2C}^2\right)/\omega_{2Z}^2} = \frac{1}{\omega_{2P}\left(\omega_{2P}^2 + \omega_{2C}^2\right)/\omega_{2P}^2} \tag{6}$$

$$\frac{\omega_{2Z}}{\left(\omega_{2Z}^2 + \omega_{2C}^2\right)} = \frac{\omega_{2P}}{\left(\omega_{2P}^2 + \omega_{2C}^2\right)} \tag{7}$$

$$\omega_{2Z}\left(\omega_{2P}^2 + \omega_{2C}^2\right) = \omega_{2P}\left(\omega_{2Z}^2 + \omega_{2C}^2\right) \tag{8}$$

$$\omega_{2Z}\omega_{2P}^2 + \omega_{2Z}\omega_{2C}^2 = \omega_{2P}\omega_{2Z}^2 + \omega_{2P}\omega_{2C}^2 \tag{9}$$

$$\omega_{2Z}\omega_{2C}^2 - \omega_{2P}\omega_{2C}^2 = \omega_{2P}\omega_{2Z}^2 - \omega_{2Z}\omega_{2P}^2 \tag{10}$$

$$(\omega_{2Z} - \omega_{2P})\omega_{2C}^2 = \omega_{2P}\omega_{2Z}(\omega_{2Z} - \omega_{2P}) \tag{11}$$

$$\omega_{2C}^2 = \omega_{2P}\omega_{2Z} \tag{12}$$

$$\omega_{2C} = \sqrt{\omega_{2P}\omega_{2Z}} \tag{13}$$

The highest phase boost occurs precisely at this frequency, and this frequency is the geometric mean of the pole and zero frequencies [1].

3.1.2 Derivation of *K*-factor

The *K*-factor is designed as a support tool for compensator synthesis. It is defined as the square root of the ratio between the insignificant pole and the significant zero frequencies in Type-2 compensators [1].

$$K = \sqrt{\frac{\omega_{2P}}{\omega_{2Z}}} \tag{14}$$

From (12), $\omega_{2C}^2/\omega_{2P} = \omega_{2Z}$ and $\omega_{2C}^2/\omega_{2Z} = \omega_{2P}$

$$K = \sqrt{\frac{\omega_{2P}}{\omega_{2C}^2/\omega_{2P}}} \tag{15}$$

$$K = \sqrt{\frac{\omega_{2P}^2}{\omega_{2C}^2}} \tag{16}$$

$$\mathrm{K} = \sqrt{\left(\frac{\omega_{2\mathrm{P}}}{\omega_{2\mathrm{C}}}\right)^2} \tag{17}$$

$$k = \frac{\omega_{2P}}{\omega_{2C}} \tag{18}$$

$$\omega_{2P} = K\omega_{2C} \tag{19}$$

$$K = \sqrt{\frac{\omega_{2C}^2/\omega_{2Z}}{\omega_{2Z}}} \tag{20}$$

$$K = \sqrt{\frac{\omega_{2C}^2}{\omega_{2Z}^2}} \tag{21}$$

$$K = \sqrt{\left(\frac{\omega_{2C}}{\omega_{2Z}}\right)^2} \tag{22}$$

$$k = \frac{\omega_{2C}}{\omega_{2Z}} \tag{23}$$

$$\omega_{2Z} = \frac{\omega_{2C}}{K} \tag{24}$$

$$\phi_{B2} = \tan^{-1}(K) - \tan^{-1}\left(\frac{1}{K}\right) \tag{25}$$

From trigonometric identity [11]

$$\tan^{-1}(K) + \tan^{-1}(1/K) = 90^\circ \tag{26}$$

$$\tan^{-1}(1/K) = 90^\circ - \tan^{-1}(K) \tag{27}$$

Substituting the value of (27) in (25).

$$\phi_{B2} = \tan^{-1}(K) - [90^\circ - \tan^{-1}(K)] \tag{28}$$

$$\phi_{B2} = \tan^{-1}(K) - 90^\circ + \tan^{-1}(K) \tag{29}$$

$$\phi_{B2} = 2\tan^{-1}(K) - 90^\circ \tag{30}$$

$$2\tan^{-1}(K) = \phi_{B2} + 90^\circ \tag{31}$$

$$\tan^{-1}(K) = \frac{\phi_{B2}}{2} + 45^\circ \tag{32}$$

$$K = \tan(\frac{\phi_{B2}}{2} + 45^\circ) \tag{33}$$

The Bode diagram for this compensator is shown in Fig. 1.

3.2 Type-3 Compensator

The Type-3 compensator consists of two significant zero, three poles (one at the origin and the other two insignificant poles somewhere in between) [11]. The Type-3 compensator belongs to the category of lead–lead-type compensators featuring a pole at the origin [4–6, 8, 9, 13]. Designers employ this type of compensator to give the control loop a phase boost. As a result, this compensator delivers a maximum phase boost of 180° [10], while ensuring zero steady-state error. The maximal phase boost of the compensator is known to occur at a frequency equal to

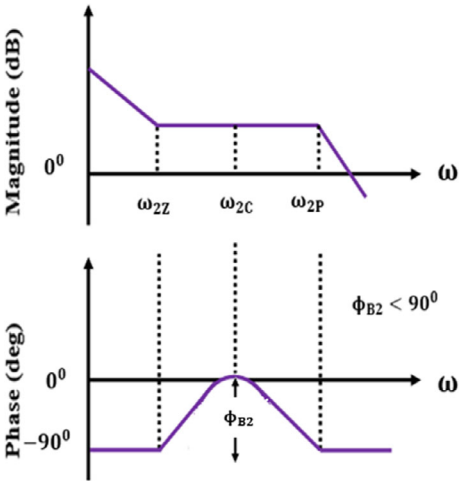

Fig. 1 Bode plot for Type-2 compensator

the geometric mean of the double frequency of the insignificant pole and the double frequency of significant zero. This type of compensator is often designed by setting the necessary loop crossover frequency to the geometric mean of the significant zeros and insignificant poles [1]. This method can yield the highest phase margin possible from a given compensator. It does not, however, account for the gain margin, another crucial loop component.

There are circumstances where the phase lag can exceed 180^0, even if the maximum phase from a Type-2 compensator at any frequency is at most zero degrees. For this reason, in cases when the Type-2 compensator is not sufficient to supply the phase margin required to keep the loop stable, a Type-3 compensator is needed. Despite the non-minimum phase issue faced by the control systems, when combined with a cascaded Type-3 compensator, it demonstrates improved closed-loop performance. By appropriately tuning this controller, the system can achieve faster responses, minimal overshoots, and zero steady-state error.

3.2.1 Mathematical Modeling

Type-3 compensator is a lead–lead compensator with an additional pole at the origin. This compensator offers a maximum phase boost of 180° [10, 12] while maintaining zero steady-state error. This lead–lead compensator has two significant zeroes two insignificant poles and one pole at the origin. Mathematically, the controller is expressed as follows:

$$G_{3C}(s) = k_{3C}\left(1 + \frac{s}{\omega_{3Z}}\right)^2 \Big/ s\left(1 + \frac{s}{\omega_{3P}}\right)^2 \tag{34}$$

The argument of (34) at $s = j\omega_{3C}$ is written as follows:

$$\phi_{B3} = 2\tan^{-1}\left(\frac{\omega_{3C}}{\omega_{3Z}}\right) \Big/ 2\tan^{-1}\left(\frac{\omega_{3C}}{\omega_{3P}}\right) \tag{35}$$

$$\phi_{B3} = 2\tan^{-1}\left(\frac{\omega_{3C}}{\omega_{3Z}}\right) - 2\tan^{-1}\left(\frac{\omega_{3C}}{\omega_{3P}}\right) \tag{36}$$

Differentiating (36) w.r.t ω_{3C}

$$\phi'_{B3} = \frac{2}{\omega_{2Z}\left[1 + \frac{\omega_{3C}}{\omega_{3Z}}\right]^2} - \frac{2}{\omega_{2P}\left[1 + \frac{\omega_{3C}}{\omega_{3P}}\right]^2} = 0 \tag{37}$$

$$\frac{2}{\omega_{2Z}\left[1 + \frac{\omega_{3C}}{\omega_{3Z}}\right]^2} = \frac{2}{\omega_{2P}\left[1 + \frac{\omega_{3C}}{\omega_{3P}}\right]^2} \tag{38}$$

$$\frac{2}{\omega_{2Z}\left(\omega_{3Z}^2 + \omega_{3C}^2\right)/\omega_{3Z}^2} = \frac{2}{\omega_{3P}\left(\omega_{3P}^2 + \omega_{3C}^2\right)/\omega_{3P}^2} \tag{39}$$

$$\frac{2\omega_{3Z}}{\left(\omega_{3Z}^2 + \omega_{3C}^2\right)} = \frac{2\omega_{3P}}{\left(\omega_{3P}^2 + \omega_{3C}^2\right)} \tag{40}$$

$$\omega_{3Z}\left(\omega_{3P}^2 + \omega_{3C}^2\right) = \omega_{3P}\left(\omega_{3Z}^2 + \omega_{3C}^2\right) \tag{41}$$

$$\omega_{3Z}\omega_{2P}^2 + \omega_{3Z}\omega_{3C}^2 = \omega_{3P}\omega_{3Z}^2 + \omega_{3P}\omega_{3C}^2 \tag{42}$$

$$\omega_{3Z}\omega_{3C}^2 - \omega_{3P}\omega_{3C}^2 = \omega_{3P}\omega_{3Z}^2 - \omega_{3Z}\omega_{3P}^2 \tag{43}$$

$$(\omega_{3Z} - \omega_{3P})\omega_{3C}^2 = \omega_{3P}\omega_{3Z}(\omega_{3Z} - \omega_{3P}) \tag{44}$$

$$\omega_{3C}^2 = \omega_{3P}\omega_{3Z} \tag{45}$$

$$\omega_{3C} = \sqrt{\omega_{3P}\omega_{3Z}} \tag{46}$$

The highest phase boost occurs precisely at this frequency, and this frequency is the geometric mean of the double pole and double zero frequencies [1].

3.2.2 Derivation of *K*-factor

The *K*-factor is designed as a support tool for compensator synthesis. It is defined as the ratio of the double insignificant pole to the double significant zero frequencies in

Type-3 compensators [1].

$$K = \frac{\omega_{3P}}{\omega_{3Z}} \tag{47}$$

From (45), $\omega_{3C}^2/\omega_{3P} = \omega_{3Z}$ and $\omega_{3C}^2/\omega_{3Z} = \omega_{3P}$

$$K = \frac{\omega_{3P}}{\omega_{3C}^2/\omega_{3P}} \tag{48}$$

$$K = \left(\frac{\omega_{3P}}{\omega_{3C}}\right)^2 \tag{49}$$

$$\sqrt{K} = \frac{\omega_{3P}}{\omega_{3C}} \tag{50}$$

$$\omega_{3P} = \sqrt{K}\omega_{3C} \tag{51}$$

$$K = \frac{\omega_{3C}^2/\omega_{3Z}}{\omega_{3Z}} \tag{52}$$

$$K = \left(\frac{\omega_{3C}}{\omega_{3Z}}\right)^2 \tag{53}$$

$$\sqrt{K} = \frac{\omega_{3C}}{\omega_{3Z}} \tag{54}$$

$$\omega_{3Z} = \frac{\omega_{3C}}{\sqrt{K}} \tag{55}$$

$$\phi_{B3} = 2[\tan^{-1}\left(\sqrt{K}\right) - \tan^{-1}\left(\frac{1}{\sqrt{K}}\right)] \tag{56}$$

From trigonometric identity

$$\tan^{-1}\left(\sqrt{K}\right) + \tan^{-1}\left(1/\sqrt{K}\right) = \pi/2 \tag{57}$$

$$\tan^{-1}\left(\frac{1}{\sqrt{K}}\right) = \frac{\pi}{2} - \tan^{-1}\left(\sqrt{K}\right) \tag{58}$$

Substituting the value of (58) in (56)

$$\phi_{B3} = 2\{\tan^{-1}\left(\sqrt{K}\right) - [\frac{\pi}{2} - \tan^{-1}\left(\sqrt{K}\right)]\} \tag{59}$$

$$\phi_{B3} = 2\{\tan^{-1}\left(\sqrt{K}\right) - \frac{\pi}{2} + \tan^{-1}\left(\sqrt{K}\right)\} \tag{60}$$

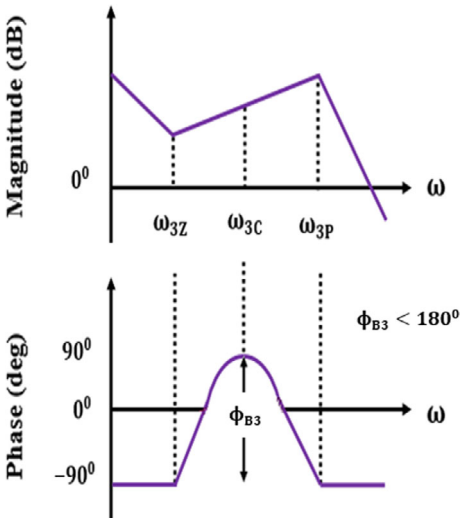

Fig. 2 Bode plot for Type-3 compensator

$$\phi_{B3} = 2\{2\tan^{-1}\left(\sqrt{K}\right) - \frac{\pi}{2}\} \tag{61}$$

$$\phi_{B3} = 4\tan^{-1}\left(\sqrt{K}\right) - \pi\} \tag{62}$$

$$4\tan^{-1}\left(\sqrt{K}\right) = \phi_{B3} + \pi \tag{63}$$

$$\tan^{-1}\left(\sqrt{K}\right) = \frac{\phi_{B3}}{4} + \frac{\pi}{4} \tag{64}$$

$$\sqrt{K} = \tan(\frac{\phi_{B3}}{4} + \frac{\pi}{4}) \tag{65}$$

The Bode diagram for this compensator is shown in Fig. 2.

4 Comparison with Other Compensator Design

In control systems engineering, the *K*-factor approach to compensator design is just one technique among many. Every design approach has advantages, disadvantages, and particular application domains. Let's contrast the *K*-factor approach with a few other popular techniques for compensator design:

1. PID Control: Proportional–integral–derivative (PID) control is a commonly employed compensator design technique. For many control applications, it offers good performance and is easy to install. PID control modifies the control action

according to the error, the integral of the error, and rate of change of the error using three terms: proportional, integral, and derivative. Although PID control works well for simple control tasks, the K-factor approach may be a better fit for handling complex system dynamics and uncertainties.

2. State-Space Control: A cutting-edge and potent compensator design method that models the control system in state-space form is called state-space control. Control loops with multiple inputs and outputs can be designed by engineers, which makes it appropriate for intricate multivariable systems. State-space control offers a strict framework for stability and performance analysis and can handle both linear and nonlinear systems. However, in comparison with the K-factor technique, it can necessitate more intensive modeling work.
3. Frequency Domain Methods: The Bode plot analysis and Nyquist stability criterion are two examples of frequency domain methods, which are traditional control techniques that evaluate the performance of control systems based on frequency response. These techniques are useful for studying system behavior in the frequency domain and for stability research. Since the K-factor approach takes frequency response into account when designing compensators, it can be seen as an extension of existing techniques.
4. Optimal Control: Optimal control strategies aim to identify the control inputs that maximize a performance indicator, such as lowering energy consumption or raising system efficiency. These methods use optimization algorithms to determine the optimal course of action. The K-factor approach prioritizes stability and robust performance above the direct optimization of a specific performance measure.

Comparison Summary: The K-factor approach provides a balance between conventional and modern control techniques due to its adaptability. It is effective for both uncertain linear and nonlinear systems. PID control is well-liked and easy to use for basic control tasks, yet its performance and robustness may not match that of the K-factor method. State-space control is useful for complex multivariable systems, although it may need more modeling effort. The investigation of frequency response and stability carried out using the frequency domain methods and the K-factor methodology is identical. While stability and resilience are given priority in the K-factor approach, optimum control aims to enhance performance.

The requirements, complexity of the control system, and trade-offs between robustness, performance, and implementation ease are taken into consideration when deciding on the compensator design strategy. Engineers often mix multiple approaches or use advanced control techniques to effectively satisfy the specific requirements of the control application.

5 Advantages of the *K*-factor Technique

The *K*-factor technique is a common choice among engineers and researchers for compensator design since it is favored in control systems for multiple reasons. The following are some of the main benefits of the *K*-factor method:

1. Simplicity and Ease of Implementation: The *K*-factor approach is comparatively easy to comprehend and use. It entails adding or changing a single gain parameter (*K*-factor) to change the plant transfer function. Because of its simplicity, engineers with different degrees of experience can use it, facilitating rapid design iterations and prototyping.
2. Versatility: Numerous control systems can benefit from the flexibility and applicability of the *K*-factor technique. It is appropriate for a wide range of engineering applications, from industrial processes and communication systems to mechanical and electrical systems, as it may be used in both discrete-time and continuous-time systems.
3. Stability and Robustness: By methodically adjusting the system's poles and zeros, the *K*-factor technique helps designers attain the necessary closed-loop resilience and stability. Engineers can enhance the system's reaction to uncertainties and shocks, guaranteeing steady and dependable performance, by carefully choosing the *K*-factor.
4. Intuitive Interpretation: Engineers can intuitively understand how the *K*-factor parameter affects the compensator's gain and how it affects system performance. During the design process, this interpretive simplicity promotes efficient decision-making and improves design comprehension.
5. Fast Design Iterations: Rapid design iterations are possible using the *K*-factor method because of its simplicity and directness. Once the desired performance parameters are fulfilled, engineers can fine-tune the design by quickly adjusting the *K*-factor and monitoring its effect on system behavior.
6. Minimal Computational Complexity: The calculations involved in the *K*-factor method are rather simple, especially when compared to some other compensator design methods that call for intricate computations or iterative algorithms. Therefore, even with limited processing resources, it can be effectively applied in real-time control applications.

6 Disadvantages of the *K*-factor Technique

The *K*-factor method has some drawbacks and restrictions, despite being a useful tool for building compensators and enhancing control system performance. Here are some of the main problems with the *K*-factor approach:

1. Requires Deep System Knowledge: The *K*-factor method primarily depends on a detailed comprehension of the dynamics and properties of the system. To properly select acceptable *K*-values, engineers need to have a thorough understanding of

the system. When working with complicated or poorly understood systems, this requirement might provide a serious obstacle.
2. Not Always Intuitive: It may take some trial and error and not always be intuitive to choose K-values. To obtain the intended system performance, engineers may need to make a few tweaks, which can be time- and resource-consuming.
3. Lack of Optimization: The K-factor approach is not by definition an optimization strategy. Although it enables engineers to modify system behavior, it might not always find the best answer for a certain combination of performance requirements. Various optimization techniques might need to be used independently.
4. Complex Systems Require Approximations: To properly use the K-factor method, approximations or simplifications may be required when the system is extremely complex or has many poles and zeros. The control system design may have flaws because of these approximations.

7 Applications

Numerous engineering fields have applications for the K-factor technique, particularly in control system design and analysis. Some significant applications of the K-factor technique are aerospace control system design, power electronic systems, renewable energy systems, and more.

7.1 Aerospace Control Design

Aerospace control system design is a significant and difficult endeavor because of the stringent safety regulations and high-performance requirements. In aeronautical control systems, the K-factor technique is a useful tool for achieving strong disturbance rejection, precise tracking, and stability. The K-factor technique is specifically used in the following three aircraft control systems:

1. Aircraft Flight Control Systems
2. Spacecraft Attitude Control Systems
3. Unmanned Aerial Vehicles (UAVs) and Drones

The K-factor methodology offers a methodical and efficient way to design compensators in all these aerospace applications, guaranteeing accuracy, stability, and reliable performance. The application of the K-factor technique is beneficial in the design and development of aerospace control systems due to its capacity to manage uncertainties, adjust to various operating situations, and accomplish performance goals. Nevertheless, it's crucial to remember that to satisfy the exacting standards of the aircraft sector, aerospace control systems frequently need extra safety precautions, redundancy, and rigorous testing and validation. Using the K-factor technique can be a useful part of this thorough design process.

7.2 Power Electronic Systems

Power electronics systems, where precise control and stability are essential for effective and dependable operation, might also benefit from the application of the *K*-factor approach. Power electronics systems are widely employed in many different applications, including power converters, voltage regulators, renewable energy systems, and motor drives. The *K*-factor technique can be applied to power electronics systems compensator design in the following ways:

(1) Motor Drives
(2) Voltage Regulators
(3) Renewable Energy Systems
(4) Power Factor Correction (PFC)
(5) Current and Voltage control

The utilization of the *K*-factor method in power electronics systems presents various benefits, such as enhanced performance, resilience, and consistency. Through the application of the *K*-factor approach, compensators may be designed by engineers to efficiently regulate power electronic circuits, guaranteeing dependable and effective performance in a range of applications. Nonetheless, throughout the design phase, it is crucial to consider the unique needs and features of the power electronics system in addition to the difficulties posed by high-power components, switching noise, and thermal control. Furthermore, to prevent component damage and guarantee dependable operation, power electronics systems must carefully evaluate safety and protection measures.

8 Conclusion

When designing the type compensators, the *K*-factor approach is an effective tool that provides fine control over systems performance. It is a useful tool in control system engineering because it enables engineers to precisely adjust gain, poles, and zeros to satisfy certain requirements. However, a thorough understanding of control theory and system characteristics is necessary for successful implementation. The *K*-factor method can be effectively used to create highly optimized and effective control systems. For designing Type-2 and Type-3 compensators, the *K*-factor technique offers a potent and simple method. Control engineers can create reliable and effective control systems with better noise rejection, disturbance attenuation, and transient response characteristics by modifying the *K*-factor. The approach is a useful tool for creating high-performance control systems because of how straightforward it is to use. For a successful implementation, proper system modeling and identification are still crucial. The *K*-factor technique continues to be crucial in creating complex control systems that satisfy the dynamic demands of diverse industries as technology develops.

References

1. Venable, H.D.: The *K*-factor: A new mathematical tool for stability analysis and synthesis. In: 1983 Proceedings of the Powercon, vol. 10, pp. 1–12, San Diego. California (1983)
2. Cao, L.: Design Type II compensation in a systematic way. Power Manag. Des. Line, 1–9 (2012)
3. Rana, N., Ghosh, A., Banerjee, S.: A comparative closed-loop performances of a DC-DC switched-mode boost converter with classical and PSO-based optimized type-II/III controllers. Int. J. Power Electron. **11**(1), 74–101 (2020)
4. Saurav, S., Ghosh, A.: Design and analysis of PID, Type II and Type III controllers for Fourth Order Boost Converter. In: 2021 7th International Conference on Electrical Energy Systems (ICEES), Chennai, India, pp. 323–328 (2021)
5. Rana, N., Ghosh, A., Banerjee, S.: Design and implementation of an improved tri-state boost converter with optimal Type-III controller. Int. J. Power Electron. **10**(3), 236–265 (2019)
6. Ghosh, A., Banerjee, S.: A comparison between classical and advanced controllers for a boost converter. In: 2018 IEEE International Conference on Power Electronics, Drives and Energy Systems (PEDES), Chennai, India, pp. 1–6 (2018)
7. Haribabu, D., Vangari, A., Sakamuri, J.N.: Dynamics of voltage source converter in a grid-connected solar photovoltaic system. In: 2015 International Conference on Industrial Instrumentation and Control (ICIC), Pune, India, pp. 360–365 (2015)
8. Ghosh, A., Banerjee, S.: Design and implementation of Type-II compensator in DC-DC switch-mode step-up power supply. In: Proceedings of the 2015 Third International Conference on Computer, Communication, Control, and Information Technology (C3IT), Hooghly, India, pp. 1–5 (2015)
9. Ghosh, A., Banerjee, S.: Design of Type-III controller for dc-dc switch-mode boost converter. In: 2014 6th IEEE Power India International Conference (PIICON), Delhi, India, pp. 1–6 (2014)
10. Fernández, C., Lázaro, A., Zumel, P., Valdivia, V., Martínez, C., Barrado, A.: Design space boundaries of linear compensators applying the *k*-factor method. In: 2013 Twenty-Eighth Annual IEEE Applied Power Electronics Conference and Exposition (APEC), pp. 2706–2711 (2013)
11. Cao, L.: Design Type III compensator design for power converters. Power Electron. Technol., 20–25 (2011)
12. Lee, S.W.: Demystifying Type II and Type III compensators using Op-Amp and OTA for DC/DC Converters. Power Manag. Appl. Rep., 1–15 (2014)
13. Banerjee, S., Ghosh, A., Rana, N.: An improved interleaved boost converter with PSO-based optimal Type-III controller. IEEE J. Emerg. Sel. Top. Power Electron. **5**(1), 323–337 (2017)

Placement and Sizing of Distributed Generation Using MELGWO Algorithm in Distribution Networks

Priyanka Maurya and Prabhakar Tiwari

Abstract The demand for electricity continues to grow, distributed generation (DG) offers a viable solution to meet this increasing energy need. DG involves generating electricity on a small scale and placing it directly into the local power grid or where it's needed. Determining the most advantageous location and appropriate capacity for DG is of utmost importance in improving the voltage stability of the power system, minimizing real power losses (RPL), and maximizing annual cost savings. Optimally situating DG within the distribution system can lead to positive results, including an improved voltage profile and reduced line losses. This paper employs a grey wolf optimizer with memory, evolutionary, and local search technique (MELGWO) to effectively allocate and size distributed generation within distributed networks. The algorithm's performance is evaluated using test systems comprising 15- and 85-bus systems. The outcomes validate that the method works well in finding the right places and sizes for DGs.

Keywords Distributed generation · Metaheuristic algorithm · Loss minimization · Voltage profile improvement · Optimal allocation

1 Introduction

Currently, there is a substantial surge in the demand for electrical power. Nevertheless, the existing power generation capacity is inadequate to meet this increasing demand, necessitating the incorporation of supplementary or contingency power sources into the distribution system (DS). This leads to a need for additional power sources. The efficiency of the DS declines as a result of decreased voltage levels and elevated losses within the system. The integration of DG into the electric power system is one option that offers numerous benefits, including reduction in losses, savings during peak

P. Maurya (✉) · P. Tiwari
Department of Electrical Engineering, Madan Mohan Malaviya University of Technology, Gorakhpur, India
e-mail: priya456maurya@gmail.com

© The Author(s), under exclusive license to Springer Nature Singapore Pte Ltd. 2025

H. P. Singh et al. (eds.), *Recent Developments in Control, Automation and Power Engineering*, Lecture Notes in Electrical Engineering 1303,
https://doi.org/10.1007/978-981-96-0047-2_32

times, improvement in voltage profiles, and improvement in the electrical system's dependability and stability.

Optimizing the placement of DG units within a DS using the hybrid grey wolf optimizer algorithm (HGWO) to minimize power loss and improve the network's voltage magnitude [1]. The sine–cosine algorithm (SCA) has been proposed to determine the best position and capacity of DGs in order to achieve optimal outcomes [2]. The approach for optimum allocation based on the Ant Colony Search Algorithm (ACSA) has been presented in [3]. The elephant herding optimization algorithm (EHO) has been recommended to ascertain the ideal DG sizing in DSs, aiming for enhancements in voltage profile, stability, loss reduction, and economic advantages [4]. A whale optimization algorithm (WOA) for identifying the most suitable DG unit sizes [5]. A proposed approach employs the Ant Lion Optimization (ALO) algorithm for determining the ideal DG unit sizes. This algorithm draws inspiration from the distinctive hunting behaviour of ant lions [6]. An introduced hybrid algorithm merges the Power Loss Index (PLI) with the Genetic Algorithm (GA). The Index Vector Method (IVM) approach has been combined with the Artificial Bee Colony (ABC) optimization algorithm for determining the optimal size of DG units [7]. A Particle Swarm Optimization (PSO) approach is utilized to achieve optimal DG allocation and enhance the voltage profile [8]. An approach based on the Bat algorithm has been proposed in the study [9]. An approach utilizing PSO to optimize the sizing and positioning of DG units has been presented in [10]. The ABC optimization algorithm is employed in conjunction with the IVM and PLI approaches to identify appropriate placements for DGs and shunt capacitors [11]. The Coulomb–Franklin's algorithm (CFA) is utilized to identify the optimal size and placement of DG units and capacitor banks (CB) in the system [12]. A method called ant colony optimization (ACO) has been suggested [13]. A quasi-oppositional forensic-based investigation (QOFBI) approach [14] An African vulture optimization (AVO) algorithm has been proposed as an approach [15].

The key contribution of this paper is outlined below:

- This paper solves the difficult challenge of optimizing the placement of distributed generation units on a radial power distribution network using a metaheuristic technique known as the MELGWO algorithm.
- This paper optimizes the placements and sizes of DG units, which leads to RPL decreases, and there is an improvement in bus voltages, resulting in maximizing the annual economic loss (AEL) savings.

2 Problem Statement

A key objective of DG issues is to ascertain the best size and optimal location that minimizes real power losses (RPL), improves voltage magnitude in the system, and increases annual economic loss savings. The cumulative total real power loss (P_{TRloss}) is computed by summing up the real power losses across all branches within the Radial Distribution System (RDS), expressed as [12]:

$$P_{TRloss} = \sum_{k=1}^{j-l} P_{loss(k,k+1)} \tag{1}$$

2.1 Objective Function

The primary key goal is to achieve the minimum value of the total real power loss within the system, which is defined as follows:

$$F = \text{minimum } (P_{\text{TRloss}}) \tag{2}$$

2.2 Bus Voltage Constraint

The voltage profile at every bus is subject to limitations imposed by:

$$0.95 \leq V_j\,(p.u.) \leq 1.05 \tag{3}$$

The voltage on each bus needs to remain within specified limits, where the voltage thresholds are set at 0.95 per unit (p.u.) for minimum and 1.05 per unit (p.u.) for maximum, respectively.

2.3 Real Power Constraint

The actual power introduced injected by the DG units at the j^{th} bus ($P_{DG,j}$) is constrained by:

$$P_{DG,j}^{\min} \leq P_{DG,j} \leq P_{DG,j}^{\max} \tag{4}$$

where $P_{dg,j}^{k}$ and $P_{dg,j}^{k}$ are the lowest and highest capacities of the DG units in kW, respectively. The capacity of the DG unit has a major effect on the system's performance. If the size is larger than the optimal size, network losses increase; similarly, if the DG size is smaller than the ideal size, system losses also rise. As a result, installing the DG unit at its optimal size is essential to achieving the best system performance [10].

2.4 Power Factor Constraint

The operational power factor ($pf_{DG,j}$) of the DG unit must stay within the specified limits [1].

$$pf_{DG,j}^{\min} \leq pf_{DG,j} \leq pf_{DG,j}^{\max} \tag{5}$$

where $\text{pf}_{DG,j}^{\min}$ and $\text{pf}_{DG,j}^{\max}$ are the lesser and greater restrictions of pf of DG unit, respectively.

3 Grey Wolf Optimizer

The GWO algorithm derives its inspiration from the social leadership and hunting tactics observed in the natural behaviour of grey wolves, wherein three prominent wolves, α, β, and δ, guide the remaining ω wolves towards potential areas, mirroring the stages of encircling, hunting, and prey attack during wolf hunting [1]. The modelling of the grey wolves' encircling behaviour towards their prey can be represented through the following equations, as demonstrated in Eqs. (6) and (7).

$$D = \left|k \times Z_p(t) - Z(t)\right| \tag{6}$$

$$Z(t+1) = Z_P(t) - l \times D \tag{7}$$

In Eqs. (6) and (7), Z_P signifies the prey's location, while Z represents the vector and it shows where a grey wolf is located. The parameter t denotes the ongoing repetition. The coefficient vectors, k and l, are determined through calculations based on Eqs. (8) and (9).

$$l = 2 \times l \times e_1 - b(t) \tag{8}$$

$$k = 2 \times e_2 \tag{9}$$

In Eqs. (8) and (9), the vectors e_1 and e_2 are generated randomly within the range [0, 1]. The elements of the vector follow a linear decrease from 2 to 0 as iterations progress, in accordance with the equation expressed as Eq. (10) [16].

$$b(t) = 2 - (2 \times t)/Max\ Iter \tag{10}$$

In the hunting behaviour of wolves, considering the assumption that α, β, and δ wolves possess more precise information about the prey's whereabouts, the remaining wolves ω are compelled to emulate their lead. To this end, the subsequent equations

are employed.

$$Z(t+1) = Z_{j1}(t) + Z_{j2}(t) + Z_{j3}(t)/3 \tag{11}$$

In the attacking process, the cessation of the hunting process occurs as the prey's movement halts, signalling the commencement of the wolves' attack phase. This transition is mathematically governed by the gradual reduction of the value of the parameter $b(t)$ throughout the iterations, effectively managing the interplay between exploration and exploitation. This dynamic is precisely captured by Eq. (10). During this phase, wolves undergo a transition by altering their positions to assume random locations lying between their present position and the position of the prey.

4 GWO with Memory, Evolutionary Operator, and Local Search (MELGWO)

Solving the DG allocation challenge involves discrete decisions because of the specific bus numbers and DG unit capacities involved. Additionally, the problem is not straightforward due to the nonlinear power balance constraint. To make searching for such complex solutions more effective, a previous study [1] proposed GWO with memory, an evolutionary operator, and local search algorithms. Based on the GWO algorithm, this approach takes cues from grey wolves' leadership and hunting tactics. Four distinct wolf types (α, β, δ, and ω) model leadership roles. There are three main phases to the hunting procedure: seeking prey, encircling it, and launching an attack. The MELGWO algorithm enhances the GWO algorithm by integrating three components: memory for past solutions, improved evolutionary methods, and a more effective local search technique.

4.1 Memory

The memory feature enables the wolves to store their best positions in memory vector (M) and utilize this information to update their current positions using the equation.

$$X(t+1) = (\delta_1 + e_1).(\delta_2 + e_2).(\delta_3 + e_3) \tag{12}$$

where δ and e represent the random values ranging from 0 to 1.

4.2 Evolutionary Operator

The evolutionary operators comprise crossover and mutation, applied to the wolves to boost population diversity and prevent premature convergence. The crossover operator is used on X and M to create a new position I, as described by the following Eq. (13) .

$$I(t+1) = \begin{cases} X_i(t+1), & \gamma_n < 0.5 \\ M_i(t+1), & \gamma_n < 0.5 \end{cases} \tag{13}$$

where γ_n represents a generated in a unpredictable approach value between 0 and 1. The mutation operator is employed on I to generate a new position V, as determined by the following Eq. (14).

$$V(t+1) = X(t+1) + \gamma_p(U_i - L_i) \tag{14}$$

γ_p represents a randomly generated value between 0 and 1, and U_i and L_i indicate the search space's the top and bottom bounds. Indicate the search space's the top and bottom bounds.

4.3 Local Search

The stochastic local search technique involves introducing random perturbations to the wolves. This improves their local search capabilities and helps them break free from local optima. This process generates a new position S by employing Eq. (15).

$$S(t+1) = V_j(t+1) + \gamma_f(W_j - V_j(t+1)) \tag{15}$$

γ_f represents a randomly generated value ranging from 0 to 1, and W_j stands for a randomly selected number within the search space. The flowchart diagram illustrating the implementation process for MELGWO is presented in Fig. 1.

5 Result and Discussion

The effectiveness of the GWO with memory, evolutionary operator, and local search (MELGWO) in solving the DG planning problem is assessed through simulations on various test systems, which include the 15-bus and 85-bus distribution networks, incorporating both Type I and Type II DG units. The MELGWO algorithm is utilized to determine the ideal capacities of the DG units to minimize power losses, improve voltage profiles, and maximize annual energy cost savings.

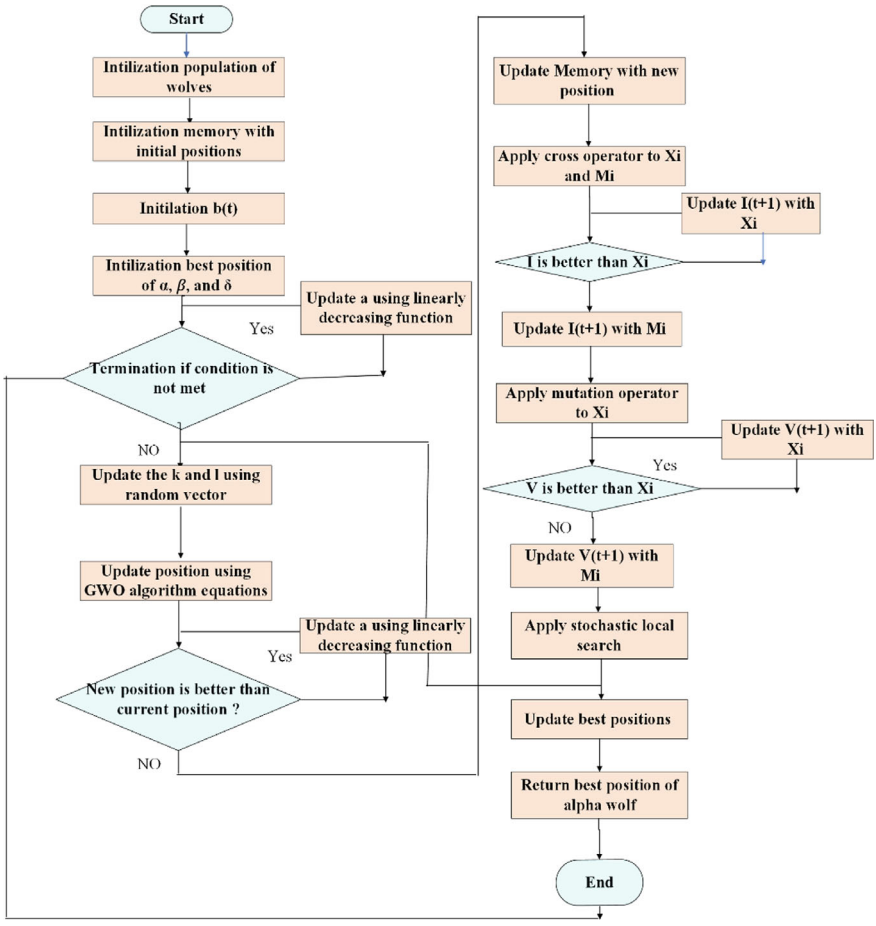

Fig. 1 Implementation process for MELGWO

5.1 15-Bus System

Figure 2 depicts the single-line schematic of the 15-bus system. The system operates with total active and reactive loads of 1226.4 kW and 1251.2 kVAr, respectively [6]. In the absence of DG, the real losses are recorded as 61.794 kW and their corresponding values, respectively. Before implementing DG units, the minimum voltage observed was 0.94452.

Table 1 presents the RPL, AEL, and minimum voltage magnitudes after different types of DGs are installed. In the 15-bus system, the best location for DG placement is identified as bus 3. For Type II DG, the voltage magnitude is greater at a pf of 0.7. Similar losses are reduced as compared to other DG types when operating at 0.7 lagging pf, as shown in Table 1. The maximum reduction in power loss from the base

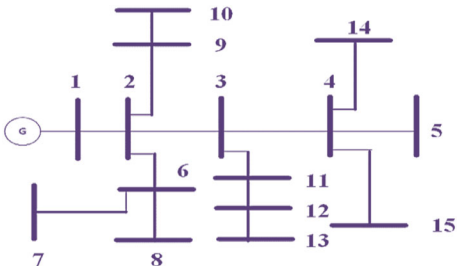

Fig. 2 15-bus system

case value of 61.794 kW to 15.03 kW is shown in Fig. 4. This is because Type II DG supplies both real and reactive power at a lagging pf. Similarly, the savings in costs have experienced significant increases, reaching percentages of 75.67% specifically for Type II DG operating at a pf of 0.7 as shown in Fig. 3. The voltage profile of the 15-bus system is shown in Fig. 5, showcasing the impact of different types of DG installations with base cases. Fig. 5 indicates that the most significant enhancement in voltage profile is achieved by the Type II DG operating at a pf of 0.7 lagging.

Table 1 Simulation outcomes for 15-bus system

Parameters	Base Case	With Type I DG (kW)	With Type II DG (kVA) at 0.7 lagging pf
Location	–	3	3
DG size	–	1022	1295.7
RPL (kW)	61.794	37.863	15.03
% Power loss	–	38.72	75.67
AEL ($)	4974.2	3047.8	1209.8
% Saving	–	38.72	75.67
V_{min} (p.u.)	0.94452	0.9672	0.97842

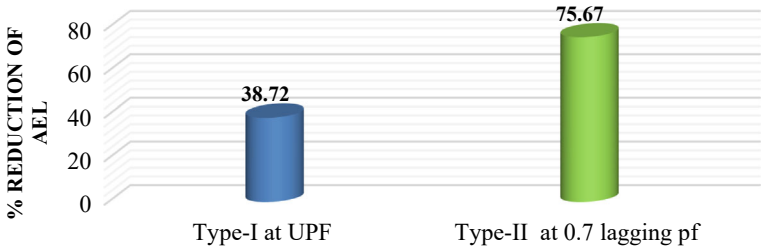

Fig. 3 % AEL saving

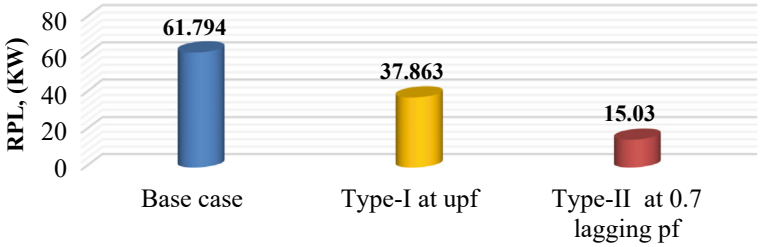

Fig. 4 RPL reduction

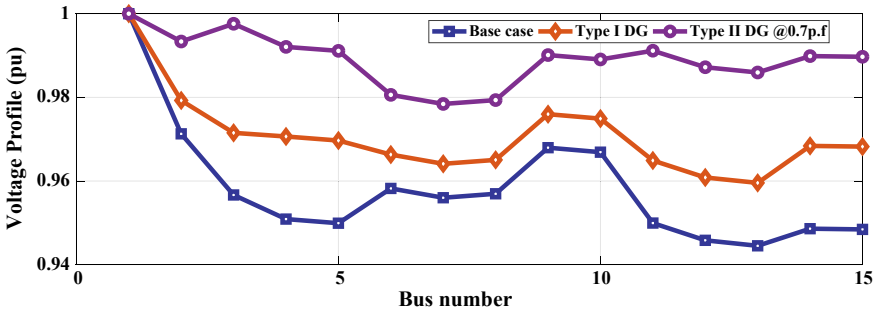

Fig. 5 Voltage profile 15-bus system

5.2 85-Bus System

Figure 6 depicts the schematic diagram of the 85-bus system. This system operates with total active and reactive loads of 2514.3 kW and 2565.1 kVAr, respectively. Without any DG units, the real power losses are 299.31 kW. The lowest voltage measured before incorporating DG units is 0.873890.

Table 2 presents the simulation outcomes for Type I DG units in all three scenarios. When compared to the base case scenario, the actual power loss drops from 299.31 kW to 167.44 kW with the inclusion of 1 DG unit, with 2 DG units, the RPL reduces to 148.49 kW and 141.63 kW when 3 DG units are employed. Similarly, the annual economic loss is reduced to 44.05% for a single DG unit, 50.39% for two DG units, and 52.68% for three DG units.

Similarly, Table 3 represents the simulation outcomes for Type II DG units at 0.708 lagging pf across all three cases. In comparison with the base case, the RPL has been lowered to 60.509 kW from its base case value of 299.31 kW within the 1 DG unit, 27.598 kW within the 2 DG unit, and 15.695 kW when 3 DG units are installed. Moreover, the annual economic loss savings are increased to 79.78% for one DG unit, 90.77% for two DG units, and 94.75% for three DG units. All the simulation results show that Type II at 0.708 lagging pf for the installation of three DG units results in the most significant decrease in power loss and maximizes the

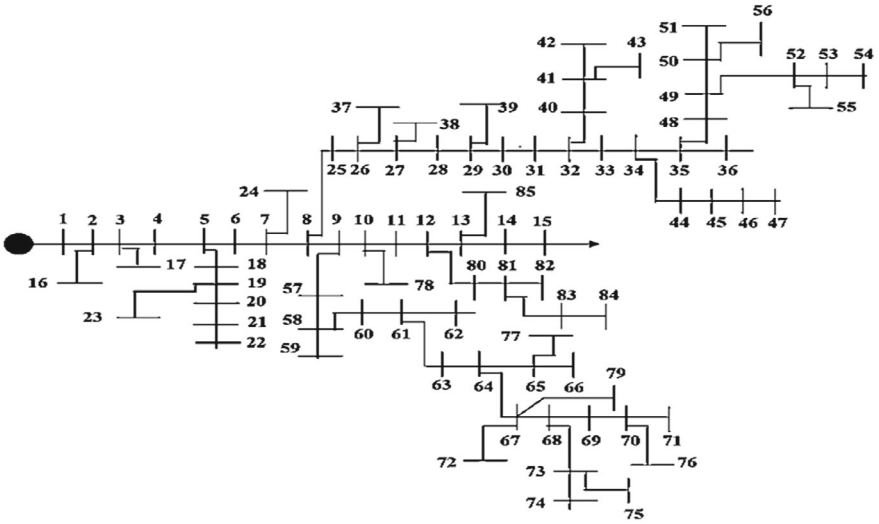

Fig. 6 85-bus system

Table 2 Outcomes for Type I DG units for 85-bus system

Parameters	Base Case	One DG unit	Two DG unit	Three DG unit
Location	–	8	9,34	8, 34, 68
DG size (kW)	–	2222	664, 1580.2	455.5, 622.8, 1188.7
RPL (kW)	299.31	167.44	148.49	141.63
% Power loss	–	44.05%	50.39%	52.68%
AEL ($)	24,093	13,478	11,953	11,400
% Saving	–	44.05	50.39	52.68
V_{min} (pu)	0.87389	0.92713	0.94616	0.95204

cost savings in terms of annual economic loss (AEL) which is shown in Figs. 7 and 8.

Figure 9 shows voltage profiles for the 85-bus system, both incorporating and not incorporating several kinds of DGs. The diagram clearly indicates that the Type II Distributed Generator (DG), operating at an optimal pf of 0.708, improves the voltage profile to a significant extent.

Table 3 Results for Type II DG units at 0.708 lagging pf for 85-bus system

Parameters	Base case	One DG unit	Two DG unit	Three DG unit
Location	–	8	34, 9	10, 34, 67
DG size (KVAr)	–	3092.2	864.4, 2148.4	965.7, 813.7, 1053.8
RPL (kW)	299.31	60.509	27.598	15.695
% Power loss	–	79.78%	90.77%	94.75%
AEL ($)	24,093	4871.1	2221.5	1263.4
% Saving	–	79.78	90.77	94.75
V_{min} (p.u.)	0.87389	0.96139	0.97804	0.9901

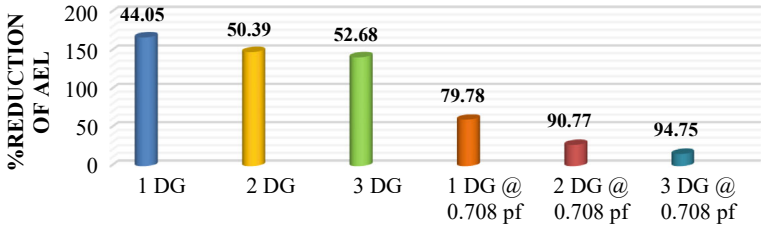

Fig. 7 % AEL reduction for 85-bus system

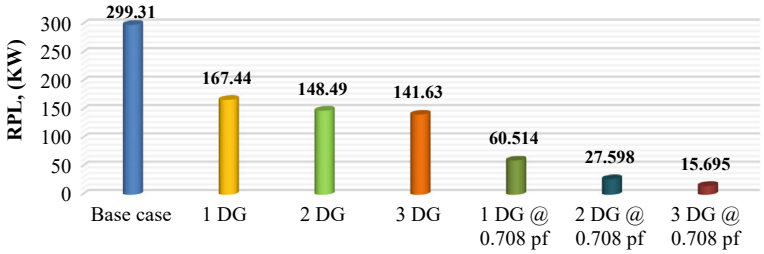

Fig. 8 RPL reduction for 85-bus system

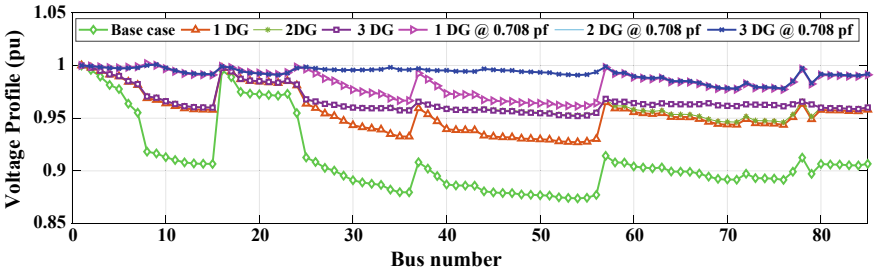

Fig. 9 Voltage profile for 85-bus system

6 Conclusion, Future Scope, and Limitations

This paper uses the GWO with memory, an evolutionary and local search technique, which is a new metaheuristic approach (MELGWO). Finding the ideal location and size for DG units is the main key goal of this paper, with the objectives of reducing RPL, enhancing voltage magnitude across the system, and maximizing annual economic cost savings. The method applies to 15-bus and 85-bus systems. The main conclusion of this work is listed below:

- The most significant results are observed for the Type II DG when operated at an optimal pf of 0.7 and 0.708 within both the 15-bus and 85-bus systems.
- For 15-bus systems, the maximum reduction in power loss is 15.03 kW when one DG unit is placed, and similarly, the maximum percentage annual economic savings is 75.67%. For 85-bus systems, the maximum reduction in power loss is 15.695 kW when three DG units are placed, and similarly, the maximum percentage annual economic savings is 94.75%. This is because it has the capacity to generate combined reactive and active power.
- The simulation results show that incorporating DG units has a positive impact on voltage profiles, effectively reduces power losses, and maximizes annual economic loss savings.

6.1 Future Scope and Limitations

- Hybrid optimization techniques can be employed for optimal planning of DG with reactive power-compensating devices.
- This paper doesn't consider uncertainties, such as fluctuations in load demand or renewable energy generation, when determining the best location and size for DG units.

References

1. Sanjay, R., Jayabarathi, T., Raghunathan, T., Ramesh, V., Mithulananthan, N.: Optimal allocation of distributed generation using hybrid grey Wolf optimizer. IEEE Access. **5**, 14807–14818 (2017). https://doi.org/10.1109/ACCESS.2017.2726586
2. Ang, S., Leeton, U., Chayakulkeeree K., Kulworawanichpong, T.: Sine cosine algorithm for optimal placement and sizing of distributed generation in radial distribution network. GMSARN Int. J. (2018)
3. Lakshmi, M.G.V.N., Laxmi, A.J., Reddy, M.S.V.: Optimal Allocation and sizing of distributed generation in distribution network using ant colony search algorithm (2014)
4. Prasad, C.H., Subbaramaiah, K., Sujatha, P.: Cost–benefit analysis for optimal DG placement in distribution systems by using elephant herding optimization algorithm. Renew. Wind Water Sol. **6** (2019). https://doi.org/10.1186/s40807-019-0056-9

5. Dinakara Prasad Reddy, P., Veera Reddy, V.C., Gowri Manohar, T.: Optimal renewable resources placement in distribution networks by combined power loss index and whale optimization algorithms. J. Electr. Syst. Inf. Technol. **5**, 175–191 (2018). https://doi.org/10.1016/j.jesit.2017.05.006
6. Dinakara Prasasd Reddy, P., Veera Reddy, V.C., Gowri Manohar, T.: Ant Lion optimization algorithm for optimal sizing of renewable energy resources for loss reduction in distribution systems. J. Electr. Syst. Inf. Technol. **5**, 663–680 (2018). https://doi.org/10.1016/j.jesit.2017.06.001
7. Rakesh, R., VenkataPapana, P., Keerthi, S.: A hybrid algorithm for optimal allocation of DG in radial distribution system. In: 2017 IEEE Region 10 Symposium (TENSYMP), (2017)
8. Singh, A., Shrestha, A., Phuyal, S., Adhikary, B., Papadakis, A.: Particle swarm optimization approach for distributed generation allocation planning for voltage profile improvement. IEEE (2016)
9. Salkuti, S.R.: Optimal Allocation of DG and D-STATCOM in a distribution system using evolutionary based bat algorithm. Int. J. Adv. Comput. Sci. Appl. **12**, 360–365 (2021). https://doi.org/10.14569/IJACSA.2021.0120445
10. Prakash, P.: Optimal DG allocation using particle swarm optimization. In: Proceedings—International Conference on Artificial Intelligence and Smart Systems, ICAIS 2021 (pp. 940–944). Institute of Electrical and Electronics Engineers Inc. (2021). https://doi.org/10.1109/ICAIS50930.2021.9395798
11. Dixit, M., Kundu, P., Jariwala, H.R.: Incorporation of distributed generation and shunt capacitor in radial distribution system for techno-economic benefits. Eng. Sci. Technol., Int. Journal. **20**, 482–493 (2017). https://doi.org/10.1016/j.jestch.2017.01.003
12. Tiwari, V., Dubey, H.M., Pandit, M.: Assessment of optimal size and location of DG/CB in distribution systems using coulomb–Franklin's Algorithm. J. Inst. Eng. (India) Ser. B. **103**, 1885–1908 (2022). https://doi.org/10.1007/s40031-022-00811-w
13. Godha, N.R., Bapat, V.N., Korachagaon, I.: Ant colony optimization technique for integrating renewable DG in distribution system with techno-economic objectives. Evol. Syst. **13**, 485–498 (2022). https://doi.org/10.1007/s12530-021-09416-y
14. Malika, B.K., Pattanaik, V., Sahu, B.K., Rout, P.K.: Quasi-oppositional forensic-based investigation for Optimal DG selection for power loss minimization. Process. Integr. Optim. Sustain. **7**, 73–106 (2023). https://doi.org/10.1007/s41660-022-00277-9
15. Biswal, S.R., Shankar, G.: Optimal deployment and sizing of distributed generations and capacitor banks in radial distribution system using African Vultures optimization algorithm. In: AIP Conference Proceedings. American Institute of Physics Inc. (2022). https://doi.org/10.1063/5.0115143
16. Miao, Z., Yuan, X., Zhou, F., Qiu, X., Song, Y., Chen, K.: Grey wolf optimizer with an enhanced hierarchy and its application to the wireless sensor network coverage optimization problem. Appl. Soft Comput. (2020)

Stability Preservation Technique for Order Reduction of *z*-Domain Interval Structure

Shweta Kumari and Amit Kumar Choudhary

Abstract Decades passed, since the technique for reduction of higher order to lower-order transfer function is under development. With new methods evolving, a breakthrough was for interval systems. Considering the approximation and stability of the system here discussed is a stability preservation method for order reduction of discrete interval system. Examples are used to justify the development of the proposed method through comparisons with the existing order reduction techniques.

Keywords Interval arithmetic · Stability preservation method · Reduction technique · Error

1 Introduction

During the last couple of decades, numerous methods for order reduction were developed to approximate higher-order transfer functions to their lower-order representative both for *s*-domain and *z*-domain systems. In view of the advantages of digital systems over analog ones, handling a discrete system model is consistent and consequently of interest for order reduction.

Today, most practical systems, such as cold rolling mills, continuously stirred tank reactors, oblique aircraft, and electric motors, are of uncertain settings because of the uncertainties arising from disturbances like model dynamics, parameter variation, sensor noises, actuator constraints, etc. Hence, the investigation of stability and transients of interval systems has attracted the attention of many researchers.

Like the existing arithmetic rules for definite numerical, there are also rules for interval systems [1]. Kharitonov's theorem [2] is useful to study the stability of interval systems. With the pioneering of interval arithmetic, Bandyopadhyay et al. proposed the order reduction of the interval system [3]. Later, many more methodologies were developed for the interval system in the continuous time domain [4–15].

S. Kumari · A. K. Choudhary (✉)
Department of Electrical Engineering, BIT Sindri, Dhanbad, Jharkhand 828123, India
e-mail: amit.ee@bitsindri.ac.in

© The Author(s), under exclusive license to Springer Nature Singapore Pte Ltd. 2025

H. P. Singh et al. (eds.), *Recent Developments in Control, Automation and Power Engineering*, Lecture Notes in Electrical Engineering 1303,
https://doi.org/10.1007/978-981-96-0047-2_33

This raised the demand among the researchers for reduction of order of interval systems in the z- domain. Thus, to date to the author's literature survey, only limited resources or methodologies are available in discrete domains [16–29]. This seems to be the motive for the authors to offer a new methodology for order reduction of discrete-time interval systems using the stability preservation method. During the literature survey, the authors encountered the usage of a Routh-like table directly for the discrete-time domain [30, 31]. This forms the base for employing the Routh-like table in this proposed methodology. Apart from this, a vast list of order reduction methodologies via Routh Approximation is also available in the literature [32, 33].

The organization of the paper is a way to have a brief introduction with a literature survey in Sect. 1 followed by preliminaries about the interval arithmetic in Sect. 2. Section 3 elaborates on the proposed methodology. Further, Sect. 4 opens an arena for validation and justification of the proposed methodology through exhaustive examples. Lastly, the conclusion Sect. 5 emerges with a better and simpler algorithm with an attempt to have a stable reduced system. The proposed methodology will be an accumulation of the literature on z-domain interval systems.

2 Preliminaries

Higher-order z-domain interval system transfer function can be considered as (1) where n is the order of the system.

$$T_n(z) = \frac{\left[N_{n-1}^-, N_{n-1}^+\right]z^{n-1} + \left[N_{n-2}^-, N_{n-2}^+\right]z^{n-2} + \ldots. + \left[N_0^-, N_0^+\right]}{\left[D_n^-, D_n^+\right]z^n + \left[D_{n-1}^-, D_{n-1}^+\right]z^{n-1} + \ldots.. + \left[D_0^-, D_0^+\right]} = \frac{N_n(z)}{D_n(z)}. \quad (1)$$

The desired reduced order transfer function is considered as (2) where $k < n$ and k are the order of the reduced system.

$$R_k(z) = \frac{\left[n_{k-1}^-, n_{k-1}^+\right]z^{k-1} + \left[n_{k-2}^-, n_{k-2}^+\right]z^{k-2} + \ldots.. + \left[n_0^-, n_0^+\right]}{\left[d_k^-, d_k^+\right]z^k + \left[d_{k-1}^-, d_{k-1}^+\right]z^{k-1} + \ldots.. + \left[d_0^-, d_0^+\right]} = \frac{N_k(z)}{D_k(z)}. \quad (2)$$

To have an insight toward the interval arithmetic calculation, let [*a, b*] and [*c, d*] be two intervals where *a, c* are minimum and *b, d* are maximum entries in the individual intervals. Similar, to the arithmetic rules of definite numerical, interval arithmetic also exists as described below [1].

$$\text{Addition}: \ [a, b] + [c, d] = [a + c, b + d], \quad (3)$$

$$\text{Subtraction}: \ [a, b] - [c, d] = [a - d, b - c], \quad (4)$$

$$\text{Multiplication}: \ [a,b] \times [c,d] = [\text{Min}(ac, ad, bc, bd), \text{Max}(ac, ad, bc, bd)], \tag{5}$$

$$\text{Division}: \ \frac{[a,b]}{[c,d]} = [a,b] \times \left[\frac{1}{d}, \frac{1}{c}\right]. \tag{6}$$

3 Proposed Method

Algorithm proposed in this manuscript can be discussed with the consideration of higher-order interval system and the resulting reduced model of the transfer function as stated in (1) and (2). As stated in [30], a *Routh-like* table is used directly for the considered z-domain system (1).

The *Routh*-like array for the numerator and denominator interval polynomials of (1) is shown in Tables 1 and 2, respectively. The first consecutive rows of each table comprises odd quantities (*i.e., first, third, fifth,* etc.) and the additional row the even coefficients (*i.e., second, fourth, sixth,* etc.) (Table 1).

Table 1 Numerator array

$[N_{n-1}^-, N_{n-1}^+]$	$[N_{n-3}^-, N_{n-3}^+]$	$[N_{n-5}^-, N_{n-5}^+]$
$[N_{n-2}^-, N_{n-2}^+]$	$[N_{n-4}^-, N_{n-4}^+]$	$[N_{n-6}^-, N_{n-6}^+]$
$[N_{3,1}^-, N_{3,1}^+]$	$[N_{3,2}^-, N_{3,2}^+]$	
$[N_{4,1}^-, N_{4,1}^+]$	$[N_{4,2}^-, N_{4,2}^+]$	
$[N_{n-2,1}^-, N_{n-2,1}^+]$	$[N_{n-2,2}^-, N_{n-2,2}^+]$	
$[N_{n-1,1}^-, N_{n-1,1}^+]$	$[N_{n-1,2}^-, N_{n-1,2}^+]$	
$[N_{n,1}^-, N_{n,1}^+]$		

Table 2 Denominator array

$[D_n^-, D_n^+]$	$[D_{n-2}^-, D_{n-2}^+]$	$[D_{n-4}^-, D_{n-4}^+]$
$[D_{n-1}^-, D_{n-1}^+]$	$[D_{n-3}^-, D_{n-3}^+]$	$[D_{n-5}^-, D_{n-5}^+]$
$[D_{3,1}^-, D_{3,1}^+]$	$[D_{3,2}^-, D_{3,2}^+]$	
$[D_{4,1}^-, D_{4,1}^+]$	$[D_{4,2}^-, D_{4,2}^+]$	
$[D_{n-2,1}^-, D_{n-2,1}^+]$	$[D_{n-2,2}^-, D_{n-2,2}^+]$	
$[D_{n-1,1}^-, D_{n-1,1}^+]$	$[D_{n-1,2}^-, D_{n-1,2}^+]$	
$[D_{n,1}^-, D_{n,1}^+]$		

Further, rows of the tables are accomplished in the predictable way by calculating the coefficients by the procedures described below where $i \geq 3$ and $1 \leq j \leq \left(n-1+\frac{3}{2}\right)$. For numerator,

$$\left[N_{i,j}^{-}, N_{i,j}^{+}\right] = \frac{\begin{array}{c}\left[N_{i-2,j+1}^{-}, N_{i-2,j+1}^{+}\right]\left[N_{i-1,1}^{-}, N_{i-1,1}^{+}\right] \\ -\left[N_{i-2,j}^{-}, N_{i-2,j}^{+}\right]\left[N_{i-1,j+1}^{-}, N_{i-1,j+1}^{+}\right]\end{array}}{\left[N_{i-1,1}^{-}, N_{i-1,1}^{+}\right]}. \tag{7}$$

Similarly for denominator

$$\left[D_{i,j}^{-}, D_{i,j}^{+}\right] = \frac{\begin{array}{c}\left[D_{i-2,j+1}^{-}, D_{i-2,j+1}^{+}\right]\left[D_{i-1,1}^{-}, D_{i-1,1}^{+}\right] \\ -\left[D_{i-2,j}^{-}, D_{i-2,j}^{+}\right]\left[D_{i-1,j+1}^{-}, D_{i-1,j+1}^{+}\right]\end{array}}{\left[D_{i-1,1}^{-}, D_{i-1,1}^{+}\right]}. \tag{8}$$

See Table 2.

Once the Routh-like tables are computed for the numerator and denominator, respectively, the desired reduced order polynomials will be formed as $N_k(z)$ and $D_k(z)$ accordingly by considering the $(n+1-k)$ th and $(n+2-k)$ th rows for numerator and $(n+1-k)$ th and $(n+2-k)$ th denominator of the above two tables as depicted below:

$$\begin{aligned} N_k(z) = &\left[N_{n+1-k,1}^{-}, N_{n+1-k,1}^{+}\right]z^{k-1} + \left[N_{n+2-k,1}^{-}, N_{n+2-k,1}^{+}\right]z^{k-2} \\ &+ \left[N_{n+1-k,2}^{-}, N_{n+1-k,2}^{+}\right]z^{k-3} + \ldots, \end{aligned} \tag{9}$$

$$\begin{aligned} D_k(z) = &\left[D_{n+1-k,1}^{-}, D_{n+1-k,1}^{+}\right]z^{k} + \left[D_{n+2-k,1}^{-}, D_{n+2-k,1}^{+}\right]z^{k-1} \\ &+ \left[D_{n+1-k,2}^{-}, D_{n+1-k,2}^{+}\right]z^{k-2} + \ldots. \end{aligned} \tag{10}$$

Further, the reduced model is depicted as

$$R_k(z) = \frac{\begin{array}{l}\left[N_{n+1-k,1}^{-}, N_{n+1-k,1}^{+}\right]z^{k-1} \\ +\left[N_{n+2-k,1}^{-}, N_{n+2-k,1}^{+}\right]z^{k-2} + \cdots\end{array}}{\begin{array}{l}\left[D_{n+1-k,1}^{-}, D_{n+1-k,1}^{+}\right]z^{k} \\ +\left[D_{n+2-k,1}^{-}, D_{n+2-k,1}^{+}\right]z^{k-1} + \cdots\end{array}} = \frac{N_k(z)}{D_k(z)}. \tag{11}$$

The obtained Eq. (11), $R_k(z)$, is the desired reduced order system (2).

Any proposed methodology should be verified and validated for its existence and further applications. Thus, to verify the proposed methodology, integral square error is computed, and to validate, exhaustive examples are used in the next section.

Square error is considered to be the suitable tool for performance analysis in continuous time domain. Here, it is considered with a modification toward discrete-time systems as the weighted error sum expressed as:

$$J = \sum_{k=0}^{\infty} \left[y_n(k) - y_m(k) \right]^2, \tag{12}$$

where $y_n(k)$ and $y_m(k)$ represent the step responses of the original $T_n(z)$ system and reduced $R_k(z)$ model, respectively.

Weighted error sums allow the determination of the sum of the squares of the errors between the unit step responses of the higher-order system and the lower-order model over a fixed interval of time. The advantage of this is it is less sensitive to the relative importance of the individual error terms, and by summing the squares of the errors, it gives more weight to larger errors, allowing for a more accurate overall performance of the reduced order model. This makes it a good valid tool for comparison when the goal is simply to minimize the overall error magnitude, rather than focusing on specific types of errors.

Ideally, minimum J assures for an estimated model of the higher-order system. As the paper reflects interval system, two separate transfer functions, (i) with lone lower limits and (ii) with solitary upper limits, account for calculating the error. Thus, the deliberate J under two error columns lower and upper limits make the investigation and assessment informal with the acknowledged procedures.

In addition, step response of the unique system and reduced models also authenticate the projected algorithm.

4 Illustrative Examples

This section attempt to validate the proposed algorithm with few exhaustive examples through their comparison to the exiting techniques.

Example 1: Consider a third-order system described by the transfer function available in literature [16, 17, 28, 33].

$$T_3(z) = \frac{[1, 2]z^2 + [3, 4]z + [8, 10]}{[6, 6]z^3 + [9, 9.5]z^2 + [4.9, 5]z + [0.8, 0.85]}. \tag{13}$$

As proposed in the methodology, the Routh-like tables and their respective computation are performed here for both the numerator and denominators polynomials, respectively (Tables 3 and 4).

From above arrays, the second-order reduced model, numerator and denominator polynomials are obtained as

$$N_2(z) = [3, 4]z + [8, 10], \tag{14}$$

Table 3 Numerator array

z^2	[1,2]	[8,10]
z^1	[3,4]	
z^0	[8,10]	

Table 4 Denominator array

z^3	[6,6]	[4.9,5]
z^2	[9,9.5]	[0.8,0.85]
z^1	[4.105,4.744]	
z^0	[0.8,0.85]	

$$D_2(z) = [9, 9.5]z^2 + [4.105, 4.744]z + [0.8, 0.85]. \tag{15}$$

Combining both the polynomials derives the reduced second-order model $R_2(z)$ as (16):

$$R_2(z) = \frac{[3, 4]z + [8, 10]}{[9, 9.5]z^2 + [4.105, 4.744]z + [0.8, 0.85]}. \tag{16}$$

The reduced second-order model $R_2(z)$ as obtained by Bandyopadhyay et al. [16] is:

$$R_2(z) = \frac{[0.8845, 0.9] + [0.5921, 0.6055]z}{[0.1437, 0.3805] + [0.8041, 1.2465]z + [1, 1]z^2}. \tag{17}$$

The reduced model $R_2(z)$ as obtained by Singh and Chandra [17] is (18):

$$R_2(z) = \frac{[1.0743, 1.2703] + [0.4023, 0.2349]z}{[0.1437, 0.3805] + [0.8041, 1.2465]z + [1, 1]z^2}. \tag{18}$$

The model $R_2(z)$ $\gamma - \delta$ approximation method [28] is (19)

$$R_2(z) = \frac{[-1.328, 1]z + [3.522, 5.85]}{[6.89, 8.14]z^2 + [3.94, 5.44]z + [0.55, 1.8]}. \tag{19}$$

The second-order reduced model $R_2(z)$ by Routh approximation method [33] is computed as (20):

$$R_2(z) = \frac{[-10, 12]z + [20, 42]}{[40, 48.84]z^2 + [28.1, 30.9]z + [5.76, 14.60]}. \tag{20}$$

The unit step response of original and reduced second order of the above presented models is shown in Fig. 1 (*lower limit*) and Fig. 2 (*upper limit*).

Also, the comparison between their weighted error sums is tabulated in Table 5.

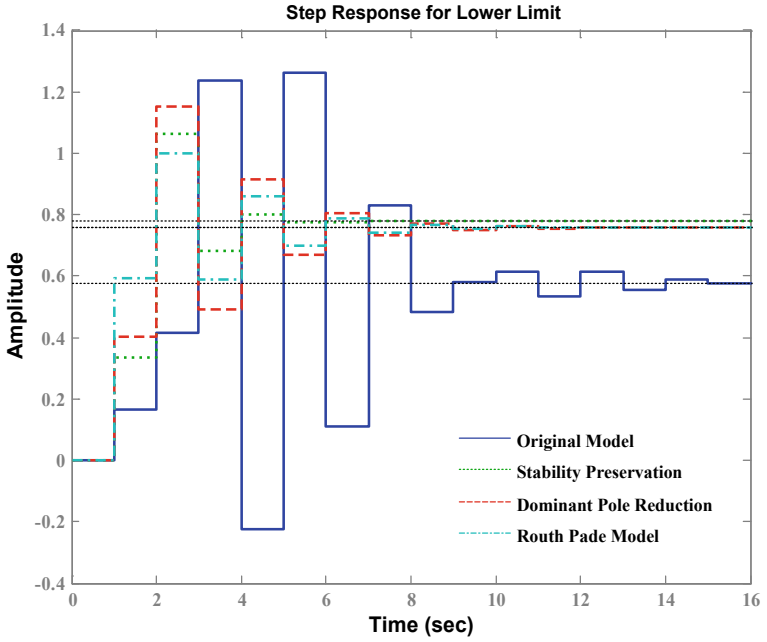

Fig. 1 Step responses of the lower limit

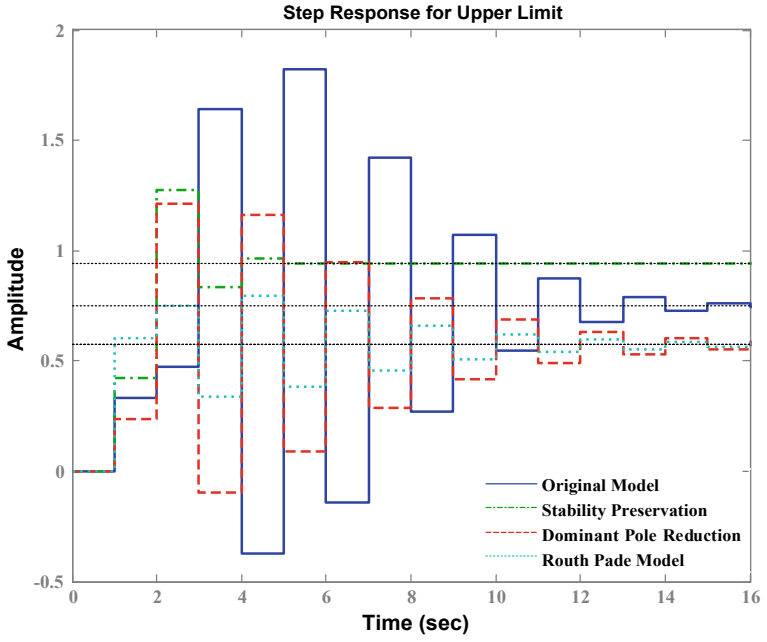

Fig. 2 Step responses of the upper limit

Table 5 Comparison between the weighted error sums

Methods	Weighted error sum	
	Lower limit	Upper limit
Proposed method	0.027778	0.007695
Routh pade method [16]	0.180994	0.074075
Dominant pole reduction [17]	0.055523	0.009689
$\gamma - \delta$ approximation method [28]	0.129175	0.044303
Routh approximation method [33]	0.173611	0.007680

Example 2. Consider a fourth-order system described by the transfer function.

$$T_4(z) = \frac{[12, 14]z^3 + [220, 240]z^2 + [800, 900]z + [1100, 1200]}{[1, 1.2]z^4 + [16, 18]z^3 + [90, 100]z^2 + [160, 180] + [110, 120]}. \quad (21)$$

The reduced third-order model $R_3(z)$ by proposed method is given as:

$$R_3(z) = \frac{[220, 240]z^2 + [663.33, 921.818]z + [1100, 1200]}{[16, 18]z^3 + [68, 102.5]z^2 + [160, 180]z + [110, 120]}. \quad (22)$$

The model $R_3(z)$ as obtained by differentiation method [29] is (22):

$$R_3(z) = \frac{[40, 63]z^2 + [800, 900]z + [1100, 1200]}{[4, 4.5]z^3 + [45, 50]z^2 + [120, 135]z + [110, 120]}. \quad (23)$$

The comparison between the weighted error sums is tabulated in Table 6.

As observed from the two examples, the proposed algorithm justifies for its satisfactorily establishment. Further examples are to validate the proposed algorithm on the practical available higher-order discrete-time interval systems.

Example 3. Consider the automatic voltage regulator system available form [25].

$$T_5(z) = \frac{\begin{array}{c}[0.95, 1.05]z^4 + [11.10, 12.27]z^3 + [11.56, 112.78]z^2 \\ +[1.76, 1.95]z + [0.031, 0.03]\end{array}}{\begin{array}{c}[168.22, 185.93]z^5 + [-473.21, -428.14]z^4 + [349.91, 386.74]z^3 \\ +[-94.12, 85.15]z^2 + [-4.07, -3.68]z + [-1.24, -1.13]\end{array}}. \quad (24)$$

Table 6 Comparison between the weighted error sums

Methods	Weighted error sum	
	Lower limit	Upper limit
Proposed method	3.062500	2.777778
Differentiation Tech [29]	4.000000	5.444444

Table 7 Comparison between the weighted error sums

Methods	Weighted error sum	
	Lower limit	Upper limit
Proposed method	0.000042	0.028201
Arithmetic operator [25]	0.007303	0.014698

The reduced second-order model $R_2(z)$ by proposed method is obtained as

$$R_2(z) = \frac{[0.142, 23.56]z + [0.031, 0.03]}{[-164.862, 135.73]z^2 + [-8.53, 10.36]z + [-1.24, -1.13]}. \quad (25)$$

The reduced model $R_2(z)$ by using arithmetic operator [25] is:

$$R_2(z) = \frac{[-3740.8, 5834]z + [-5674.2, 3936]}{[-41060, 45979]z^2 + [-121011, 111415]z + [-71886, 76564]}. \quad (26)$$

Weighted error sum of the above reduced models is depicted in Table 7.

Example 4. Consider another available discrete-time interval system as:

$$T_8(z) = \frac{\begin{array}{l}[1.6484, 1.7156]z^7 + [1.0937, 1.1383]z^6 + [-0.2142, -0.2058]z^5 \\ +[0.1490, 0.1550]z^4 + [-0.5263, -0.5057]z^3 + [-0.2672, -0.2568]z^2 \\ +[0.0431, 0.0449]z + [-0.0061, -0.0059]\end{array}}{\begin{array}{l}[23.52, 24.48]z^8 + [-1.7156, -1.6484]z^7 + [-1.1383, -1.0937]z^6 \\ +[0.2058, 0.2142]z^5 + [-0.1550, -0.1490]z^4 + [0.5057, 0.5263]z^3 \\ +[0.2568, 0.2672]z^2 + [-0.0449, -0.0431]z + [0.0059, 0.0061]\end{array}}. \quad (27)$$

The reduced model $R_2(z)$ computed by the proposed method is given as:

$$R_2(z) = \frac{[-0.8521, 0.4904]z + [-0.0061, -0.0059]}{[-7.9515, 11.2269]z^2 + [-0.1349, 0.1905]z + [0.0059, 0.0061]}. \quad (28)$$

See Table 8.

Table 8 Computed weighted error sums

Methods	Weighted error sum	
	Lower limit	Upper limit
Proposed method	0.001375	0.000697

5 Conclusions

The attempt to propose a new methodology for z-domain interval system is accomplished in this paper. The methodology emerges as a easy method for reduction of the transfer function, with an assurance to sustain the stability of the system. Stability preservation method or Routh-based stability criterion is applied here for both numerator and denominator. Moreover, there has been a continuous practice to develop an algorithm that would conceptually be simple with improved consequences as associated to prevailing approaches.

References

1. Hansen, E.: Interval arithmetic in matrix computations. Part I, SIAM J. Numerical Anal. **2**, 308–320 (1965)
2. Kharitonov, V.L.: Asymptotic stability of an equilibrium position of a family of systems of linear Differential equations. Differentsial'nye Uravneniya **14**, 2086–2088 (1978)
3. Bandyopadhyay, B., Upadhye, A., Ismail, O.: γ-δ Routh approximations for interval systems. IEEE Trans. Autom. Control **42**(8), 1127–1130 (1997)
4. Bandyopadhyay, B., Ismail, O., Gorez, R.: Routh-Pade approximation for interval systems. IEEE Trans. Autom. Control **39**(12), 2454–2456 (1994)
5. Singh, V.P., Chandra, D.: Routh-approximation based model reduction using series expansion of interval systems. In Proceedings of ICPCES 2010—International Conference on Power, Control and Embedded Systems, pp. 1–4 (2010)
6. Choudhary, A.K., Nagar, S.K.: Application of various order reduction methodologies over power system components. IFAC-PapersOnLine, Elsevier, pp. 185–190 (2015)
7. Mangipudi, S.K., Begum, G.: Model order reduction of linear time interval system using stability equation method and a soft computing technique. Adv. Electr. Electron. Eng. **14**(2), 153–161 (2016)
8. Tanwar, N.S., Bhatt, R., Parmar, G.: Order reduction of interval systems using Big bang Big crunch and Routh approximation. In: Proceedings of 1st IEEE International Conference on Power Electronics, Intelligent Control and Energy Systems, ICPEICES (2016)
9. Singh, C.N., Kumar, D., Samuel, P.: Order reduction of interval systems using direct truncation and stability equation method. In: Proceedings of International Conference on Advances in Mechanical, Industrial, Automation and Management Systems, AMIAMS-2017 363–368 (2017)
10. Potturu, S.R., Prasad, R.: Reduction of interval systems using Kharitonov's polynomials and their derivatives. In: Proceedings of 6th International Conference on Computer Applications in Electrical —Recent Advances, CERA-2017, pp. 445–449 (2018)
11. Singh, C.N., Kumar, D., Samuel, P., Sachan, A.: Model reduction of continuous-time interval systems using Eigen spectrum analysis. In: Proceedings of 2nd IEEE International Conference on Power Electronics, Intelligent Control and Energy Systems, ICPEICES-2018, pp. 1103–1108 (2018)
12. Potturu, S.R., Prasad, R.: Order reduction of interval systems using Kharitonov's theorem and stability equation method. In: Proceedings of the American Control Conference, pp. 6224–6229 (2018)
13. Potturu, S.R., Prasad, R.: Model order reduction of LTI interval systems using differentiation method based on Kharitonov's theorem. IETE J. Res. **68**(3), 2079–2095 (2019)
14. Deveerasetty, K.K., Nagar, S.K.: Model order reduction of interval systems using an arithmetic operation. Int. J. Syst. Sci. **51**(5), 886–902 (2020)

15. Meena, V.P., Singh, V.P., Barik, L.: Kharitonov polynomial-based order reduction of continuous interval systems. Circ. Syst. Signal Process **41**(2), 743–761 (2022)
16. Ismail, O., Bandyopadhyay, B., Gorez, R.: Discrete interval system reduction using Padé approximation to allow retention of dominant poles. IEEE Trans. Circ. Syst.-I: Fundamental Theory Appl. **44**(11):1075–1078 (1997)
17. Singh, V.P., Chandra, D.: Model reduction of discrete interval system using dominant poles retention and direct series expansion method. In: Proceedings of the 5th International Power Engineering and Optimization Conference (PEOCO-2011), Shah Alam, Selangor, Malaysia, pp. 27–30 (2011)
18. Choudhary, A.K., Nagar, S.K.: Direct truncation method for order reduction of discrete interval system. In: Proceedings of Annual IEEE India Conference, INDICON-2013 (2013)
19. Sharma, M.K., Kumar, D.: Modified $\gamma - \delta$ Routh approximation method for order reduction of discrete interval systems. In: Proceedings of the 10th Asian Control Conference (ASCC), Kota Kinabalu, Malaysia, pp. 1–5
20. Choudhary, A.K., Nagar, S.K.: Revisiting approximation techniques to reduce order of interval system. IFAC-PapersOnLine **49**(1), 241–246 (2016)
21. Chandel, A., Sharma, M.K., Parashar, D.: Mixed algorithm for large scale uncertain discrete interval models. In: Proceedings of the IEEE Uttar Pradesh Section International Conference on Electrical, Computer and Electronics Engineering, UPCON-2016, pp. 400–403 (2017)
22. Choudhary, A.K., Nagar, S.K.: Novel arrangement of Routh array for order reduction of z-domain uncertain system. Syst. Sci. Control Eng. **5**(1), 232–242 (2017)
23. Choudhary, A.K., Nagar, S.K.: Model order reduction of discrete-time interval systems by differentiation calculus. Autom. Control. Comput. Sci. **52**(5), 402–411 (2018)
24. Choudhary, A.K., Nagar, S.K.: Model order reduction of discrete-time interval system based on Mikhailov stability criterion. Int. J. Dyn. Control **6**(4), 1558–1566 (2018)
25. Choudhary, A.K., Nagar, S.K.: Order reduction in z-domain for interval system using an arithmetic operator. Circ. Syst. Signal Process **38**(3), 1023–1038 (2019)
26. Padhy, A.P., Singh, V., Singh, V.P.: Stable approximation of discrete interval systems. Circ. Syst. Signal Process **40**(10), 5204–5219 (2021). https://doi.org/10.1007/s00034-021-01714-9
27. Meena, V.P., Yadav, U.K., Singh, V.P., Khan, B.: Model order diminution of discrete interval systems using Kharitonov polynomials. IEEE Access **10**, 66722–66733 (2022)
28. Choudhary, A.K., Nagar, S.K.: Gamma delta approximation for reduction of discrete interval system. In: Proceedings of International Conference on Advances in Recent Technologies in Electrical and Electronics (ARTEE), pp. 91–4 (2013)
29. Pappa, N., Babu, T.: Biased model reduction of discrete interval system by differentiation technique. In: Proceedings of 2008 Annual IEEE India Conference, Kanpur, India, pp. 258–261 (2008)
30. Shamash, Y., Feinmesser, D.: Reduction of discrete time systems using a modified Routh array. Int. J. Syst. Sci. **9**(1), 53–64 (1978)
31. Bandyopadhyay, B., Kande, T.M., Srisailm, M.C.: Routh type approximation for discrete system. In: Proceedings of the IEEE International Symposium on Circuits and Systems, vol. 3, pp. 2899–2902 (1988)
32. Choudhary, A.K., Nagar, S.K.: Order reduction techniques via Routh approximation: a critical survey. IETE J. Res. **65**(3), 365–379 (2018)
33. Parashar, D., Sharma, M.K., Chandel, A.: Model reduction of discrete interval systems by Routh approximation method. In: Proceedings of 2015 IEEE Recent Advances in Intelligent Computational Systems (RAICS), Trivandrum, India, pp. 290–293 (2015)

Pregnancy, Postpartum Hemorrhage Management System Using IoT

Amit Kumar Singh, M. Kavin, M. Thamaraiselvan, M. Periyasamy, M. Kiruthik Rosan, and Pyare Mohan Tiwari

Abstract This work aims to develop an Internet of Things (IoT)-based system for managing postpartum hemorrhage (PPH) in resource-poor countries to reduce maternal mortality rates. The researchers developed an IoT hardware device and a mobile application to monitor and manage PPH. The system incorporates real-time sensors to measure blood loss and critical parameters, such as oxygen saturation (SpO_2) and heart rate. The collected data is transmitted to critical care units using IoT technology. Blood loss is measured using an ultrasonic sensor, and the system has shown 95% accuracy in monitoring SpO_2 and heart rate for healthy individuals. The patient's blood loss was simulated using a local red fluid. The developed IoT-based PPH management system provides real-time monitoring and is cost-effective. It enables physicians to estimate blood loss accurately and administer appropriate fluid replacement, thereby reducing maternal mortality rates associated with PPH. The system is also suitable for home-based management to a certain extent. Continuously monitoring critical parameters during delivery helps reduce mortality rates during and immediately after pregnancy. The proposed design is particularly useful in low-resource settings, making it a valuable tool for PPH management in resource-poor countries.

Keywords PPH management · Blood loss · SpO2 · Heart rate · IoT

A. K. Singh (✉)
Department of Biomedical Engineering, Vignan's Foundation for Science, Technology and Research, Guntur, India
e-mail: amitsingh6711@gmail.com

M. Kavin · M. Thamaraiselvan · M. Periyasamy · M. K. Rosan
Department of Biomedical Engineering, VSB Engineering College, Karur, India

P. M. Tiwari
Department of Electrical and Electronics Engineering, Amity University, Noida, India

© The Author(s), under exclusive license to Springer Nature Singapore Pte Ltd. 2025

H. P. Singh et al. (eds.), *Recent Developments in Control, Automation and Power Engineering*, Lecture Notes in Electrical Engineering 1303,
https://doi.org/10.1007/978-981-96-0047-2_34

1 Introduction

PPH is commonly known when there is a blood loss of greater than 500 ml within 24 h after a baby's birth, while unembellished PPH is defined as blood loss exceeding 1000 ml within the equivalent timeframe. PPH affects nearly 2% of world women during the labor process [1]. Due to PPH, different symptoms like dizziness, feeling faint, and blurred images occur. According to R. Saxena et al., PPH accounts for one-third of all maternal deaths, making it the world's leading cause of maternal mortality. It is also the cause of 60% of maternal deaths in developing countries. Most of these deaths happen in the third stage of the labor process, which occurs within 4 h of delivery [2]. Therefore, there is a requirement for quick identification of risk for PPH in patients. Therefore, the routine active management of the third labor stage and blood loss assessment is essential [3].

PPH spread is about 1–10% among pregnant women. The PPH is classified into two categories based on time. The first is primary PPH, which happens within the first 24 h after childbirth. The second one is secondary or late PPH, which occurs from 12 to 24 weeks after postpartum [4]. There are four reasons for PPH: thrombin, tone, trauma, and tissue, also known as the four T's in the medical field [5].

The common causes of PPH are uterine atony, thrombin, uterine trauma, and retained placental tissue. In uterine atony, the uterus becomes soft and weak, and the uterus muscles do not contract enough to clamp the placental blood vessels to stop the blood. In retained placental tissue, the placenta does not separate from the uterine wall; thus, the uterus loses its ability to contract, which leads to blood flow. For uterine trauma, the vagina, cervix, uterus, and perineum got damaged due to external equipment like forceps and others while extracting the baby from the mother's womb. Finally, in the case of thrombin, coagulation or eclampsia conditions can affect the body's blood clotting ability and thus lead to blood loss even for a tiny bleed [6].

There are many symptoms in the mother that show the PPH sign. The most common one is obstinate, extreme bleeding even after childbirth. There are many other symptoms, like a drop in blood pressure (BP), dizziness, blurred vision, increased heart rate, clammy skin, nausea, pelvic pain, and a change in the SpO_2 values [7]. So, the patient or the caretaker must be very cautious about the conditions even after delivery. Sometimes, the symptoms do not occur even after the patient is discharged from the hospital [8]. The most common diagnostic method for PPH is the visual and physical examination, the patient's health history, and laboratory tests. One can also find the PPH condition based on the mother's blood loss amount calculation by weighing the blood-soaked pads or cotton from the delivery time or even after the delivery. Other methods of PPH diagnosis are measuring the pulse rate (PR), SpO_2, BP, and red blood cell (RBC) count, and ultrasound of the uterus and other related organs of the body [5].

Evensen et al. have shown different treatment methods that can be used on an emergency base in terms of medical terms [9]. The first step is to stop the blood loss from the source of the bleeding as early as possible. The next step is to provide additional units of blood to the patient. So based on the conditions, both methods

can also be used simultaneously. Other methods to stop blood loss include uterine massage, medication to stimulate the contraction of the uterus, removing retained placental tissues, repairing lacerations, packing the uterus with sterile gauze, and catheter to put pressure on the uterine and uterine artery embolization. In some cases, laparotomy can also be performed [9]. Cunningham et al. have developed a device that uses uterine compression techniques to stop blood flow [10].

The absence of diagnosis, treatment approaches, and medicine for active management of the third stage are the causes of the high prevalence of PPH in developing countries. Other factors include inexperienced caregivers, a shortage of blood transfusion and anesthesia supplies, and operational capacities.

There were a few research papers on PubMed and ResearchGate about developing a digital device for PPH management that can be used even as a point of care technology (POCT). One research paper published in 2019 by D. D. Tekela et al. shows the development of the digital postpartum hemorrhage management device. In this work, the blood loss after the delivery system was integrated with a fluid delivery, and the patient's vital signs were also monitored. The designed method captures and quantifies total blood loss after delivery. The mother's heart rate and blood pressure are constantly monitored by the software system. These vital sign values are used with the measured blood loss to calculate the amount of IV fluid that must be supplied to the mother. The suggested gadget passed the accuracy, cost-effectiveness, and ease-of-use tests with 91.28% accuracy [11]. Many current technology-based detections for bleeding use pantograph, gravimetric, bag collector, under buttock, specialty mat, and scoring measurement to detect early bleeding [12]. Shanti et al. have used IoT to monitor the vital parameters of expectant women in resource-poor countries [13]. Sarhaddi et al. have shown different methods to monitor pregnant women, but none shows PPH monitoring [14]. Most developed methods are either unaffordable for resource-poor countries, time-consuming, or cannot provide data in real time and hence cannot be used for home-based remote monitoring. Real-time monitoring is needed in emergencies. That is why our proposed system included the PR measurement instead of the blood pressure measurement. The device interface is there with the IoT system. Then, the data is sent to medical personnel in real time. Our prime focus is maintaining the cost below a limit with improved accuracy of vital parameter measurements. So, in the proposed system, we measure the mother's PR, blood flow rate, total bold loss, and SpO_2. The prime focus is to develop a system that can be used even by a non-trained person. SpO_2 is used instead of RBC count measurement as it requires laboratory set-up. For similar reasons, BP measurement is not included in our work. So, in the future, we may introduce this parameter in our work.

2 Methods

2.1 Development of PPH System

The functional blocks of the prototype system are shown in Fig. 1. The system consists of different components chosen based on their requirements and advantages over other sensors and components. The jar is used to measure the total blood loss, and the ultrasonic sensor is placed to measure the jar's liquid level in the specified time to calculate the total loss of blood and also help calculate the mother's blood flow rate. The ultrasonic sensor was used as it has some advantages over the other methods, like non-contact measurement applications with highly viscous fluids that match our work requirements; for the measurement of the PR and SpO_2, the MAX30100-integrated chip from Maxim Integrated Company was used. It is based on the finger plethysmography technique and uses the infrared light-emitting diode as a source and the photodetector to measure the PR and SpO_2. The technique is reliable, and the sensor comes as a calibrated module. The Hall effect sensor measured the blood flow rate, and the part number was YF-S201 [11]. The advantage of this sensor is that the Hall effect gives the contactless measurement of the fluid flow. There is a solenoid valve to empty the collection jar, a 16 * 2 LCD [11] for data display, 5 and 12 V DC power supplies, and a 4 * 4 keypad to input patient information. The ultrasonic sensor module is based on the ultrasonic principle, and the part number is HCSR04 [11]. The system has the advantages of a non-contact method and saves money and time due to the self-calibrated module used for the sensors.

The 8-bit PIC16F877A microcontroller from the microchip was used to control and monitor the PPH system. The controller is quite popular, is easy to use, and has sufficient input/output ports to develop the PPH system. The microcontroller also contains the serial protocol for the data transmission to the IoT module. The part number used for the IoT module is ESP 8266-12E [15]. The IoT module is responsible for the remote transmission of sensor data to the medical staff in real time.

2.2 The Procedure of the IoT-Based Control System

The procedure for using the developed IoT system is shown in Fig. 2. First, the user has to install all the sensors on the patient, put the mechanism to collect the blood from the patient, and attach it to the collection jar. Then, on the system, check for leaks in any part. After that, the sensors' data goes to the microcontroller unit, which sends it to the LCD. It also sends the data to the IoT, reaching the healthcare personal smart mobile app and displaying all the parameters to the doctor/medical staff.

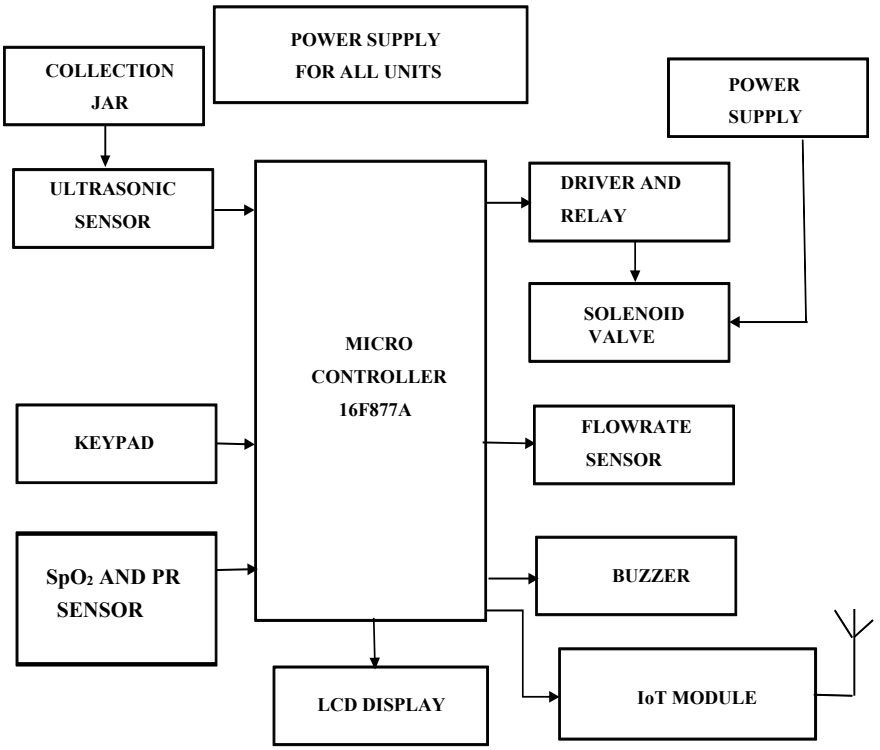

Fig. 1 Block diagram of microcontroller-based PPH prototype

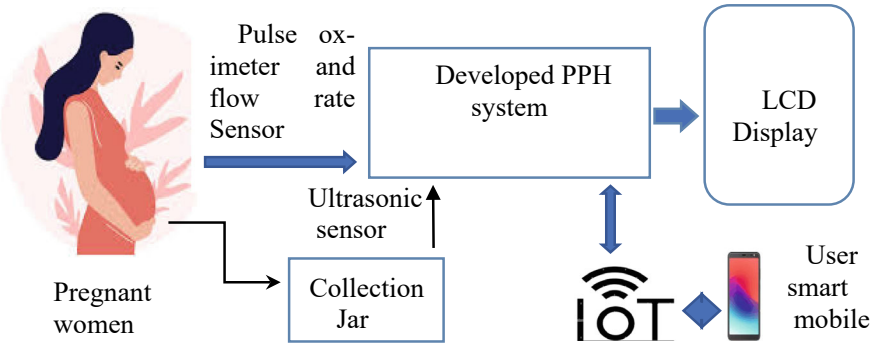

Fig. 2 Block diagram of procedure for PPH patient

2.3 *Flowchart of the Program Used in the PPH System*

The flow chart of the C-code written in Arduino IDE [16] is shown in Fig. 3. First, the microcontroller is initialized, and then, it initializes all the sensors and the relays attached to the system along with the initial IoT module. Next, the sensors sense the patient-related parameters. Then, after proper signal conditioning, it goes to the LCD for proper display. Now, the microcontroller checks for the SpO_2, PR, blood flow rate, and total blood loss values. The system also continuously monitors the women's health status using real-time sensors after delivery, such as SpO_2 and heartbeat.

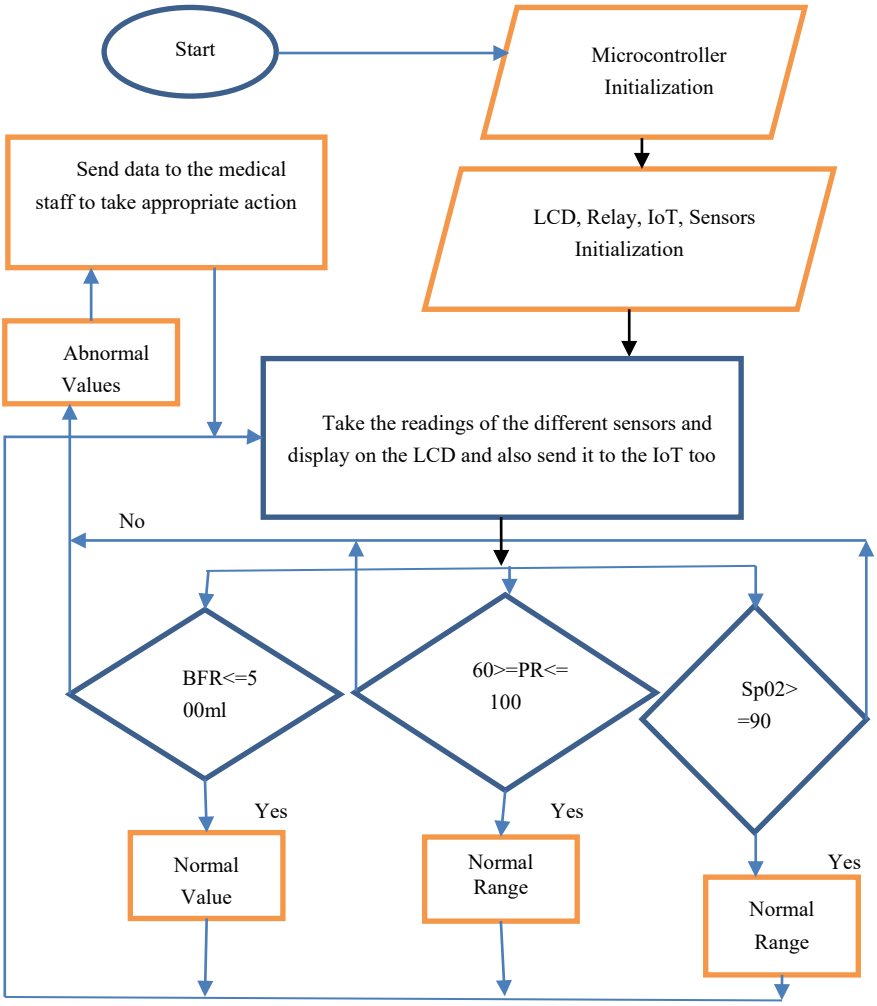

Fig. 3 Flowchart for program of PPH system

Once any health parameter goes abnormal, the system automatically sends a message to the medical staff to give a trip to the woman. So, if any parameter is outside the specified range, as shown in the flow chart, the microcontroller triggers the attached buzzer. At the same time, it sends real-time data to the smart mobile user via the IoT module. The collection and measurement of blood loss can provide the command to the system via a keypad to compensate for the mother's blood loss. The IV fluid need is estimated using vital sign readings and measured blood loss. The system's status, such as vital signs, excessive blood loss, and flow rate of the IV fluid, is updated on the web page via IoT for easy access from anywhere in the world. Figure 4 shows the values of the different sensors on the smartphone app using the IoT application. A free platform named ThingSpeak application was used to develop the app for the Android-based smart mobile [17]. The app shows different sensor values, like ultrasonic sensor readings for the bold level in the jar, the blood flow rate, SpO_2, and the PR. The app also shows the last keypad values used by the user.

The website for the system was developed in a hypertext markup language, and the server was provided from the ThingSpeak/college website. We have used HTML language to design the web pages for our program. The website is simple, and the user can open it on their mobile/laptop/computer using the web browser application on their systems. Then, the user must enter the user's name and password to use the application. Finally, the entered data is displayed on the website. The snapshot of the website page taken on the smart mobile is shown in Fig. 4. It shows the sensors' data and GPS location. After using it, the user closes the application. The website's data is refreshed every 10 s in real time on the web browser and stored in the Excel sheet.

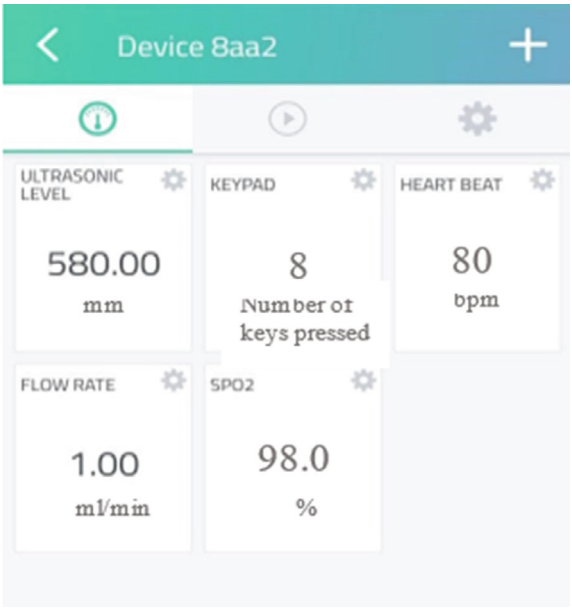

Fig. 4 App snapshot displays different parameters of mother in real time on user's smart mobile

3 Results

This paper presents a potential device for flow rate measurement in real time. Nearly all the sensors used are in self-calibration mode. An ultrasonic sensor is used for blood measurement purposes. The doctor's or nurse's lengthy ethical clearance process is required for system installation; hence, the device is not tested on maternity women. Also, getting the patient is difficult, so we tested the system using red liquid to simulate the blood. The consent form was signed by the healthy individual as per the ICMR guidelines. The SpO_2 and the PR are calculated for healthy students. The data for 10 people was collected in a one-day symposium held in the college. The age of the subject is between 18 and 22 years. The Dr Trust Signature Series Finger Tip Pulse Oximeter [18] was used to correlate the developed system's measured SpO_2 and PR value to the standard device. Table 1 shows the values of the data collected from the ten healthy persons aged 18–22 years. The developed device shows a maximum error of $\pm$ 4% compared to the standard device and can be used for clinical purposes when commercialized. The real-time data was sent to the user's smart mobile, and the IoT-based system provides several advantages. The sensors' data was then sent to the smart mobile app using the Internet, and Fig. 4 shows different data in real time to the end-user app. The data was also stored on the cloud server. The developed prototype is shown in Fig. 5. The device is also simple and cost-effective, making it useful for resource scare country settings.

Table 1 Readings were collected from ten healthy subjects to measure SpO_2 and PR and compare them to standard device

S. No.	Standard instrument (Dr Trust Signature Series Finger Tip Pulse Oximeter)		Data from the developed device		Percentage error from the standard instrument for SpO_2 (% error)	Percentage error from the standard instrument for PR (% error)
	SpO_2 (%)	PR (BPM)	SpO_2 (%)	PR (BPM)		
1	99	80	97	78	2.0	2.5
2	98	85	96	81	2.0	4.7
3	97	90	98	93	− 1.0	− 3.3
4	98	88	98	88	0.0	0.0
5	96	84	97	86	− 1.0	− 2.3
6	95	89	98	92	− 3.1	− 3.3
7	98	75	96	72	2.0	4
8	96	70	99	73	− 3.1	− 4.2
9	97	85	96	88	1.0	− 3.5
10	98	82	98	84	0.0	− 2.4

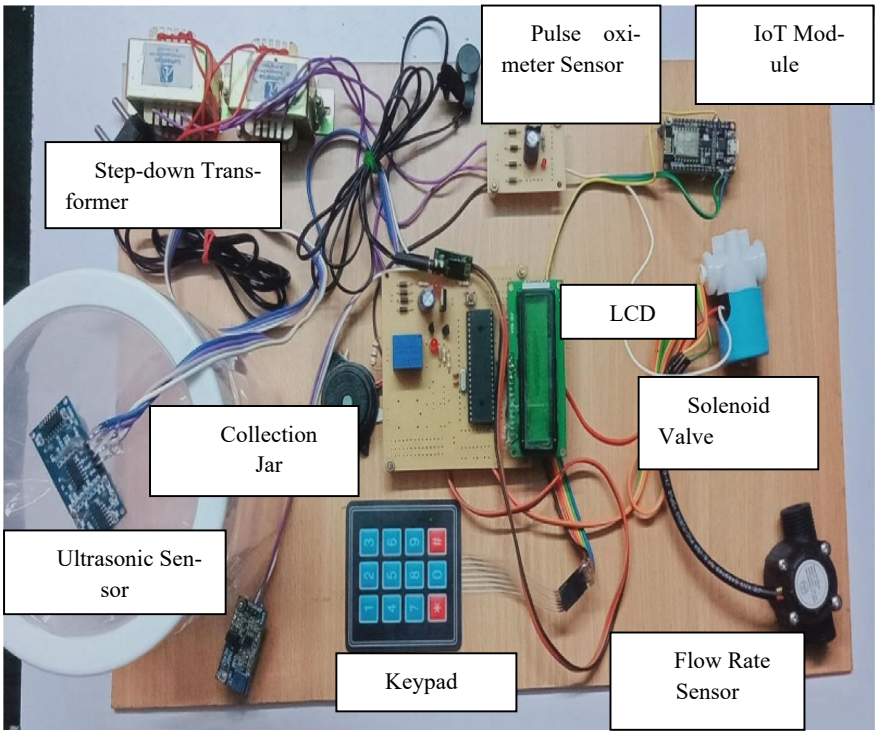

Fig. 5 Photo of developed real-time PPH prototype

4 Conclusion

The effective management of PPH is necessary to prevent complications arising during PPH conditions of the mothers. The presented digitalized PPH management device is helpful for physicians as a decision support system. It monitors vital signs to assess the quantity of blood loss and the patient's awareness. After additional testing and iterations, the developed prototype provides 95.88% accuracy. The proposed method favors low-resource settings and situations where expertise and means are scarce.

The developed device helped the patients even after the delivery. It concludes with a comprehensive postpartum visit no later than 12 weeks after delivery. Postpartum maternal health care impacts the fitness of both mothers and their children; however, it is not adequately provided for or emphasized in national guidelines or country-wide health goals worldwide. Recommendations for promoting maternal health include organizing postpartum maternal health, comparing and reforming the system of routine postpartum fitness care, encouraging a circle of relatives guide, providing guide organizations, designing long-term instructional programs, and conducting

research on postpartum maternal fitness. In addition, the timing of the complete postpartum visit needs to be individualized and patient-centered. The developed device in the future can also be tested on real-time patients and developed commercially for a bright and affordable future for human society.

The device will help the rural population, in the case of PPH patients, to be monitored for the condition at their homes while unable to meet/reach the hospital after the PPH condition. This method can help reduce the mortality rate in rural areas, and we also tried to reduce the cost of this developed system and provide IoT functionality that is more affordable for developing countries. The device was not tested for real-time PPH patients as it is challenging to get the patient and time-consuming to get ethical approval. But, we have tested the instrument on the red solution available from the local market for calibrating the sensors. The proposed design is suitable for low-resource settings countries. This happens because the developed cost is around 100 $ for the components used. It enables doctors to accurately estimate blood loss and deliver fluid. It aids in the reduction of maternal mortality due to PPH.

Acknowledgements We thank VSB Engineering College, Karur, for providing the infrastructure support for making the prototype.

References

1. Department of Reproductive Health and Research W: WHO recommendations for the prevention and treatment of postpartum haemorrhage (2012)
2. Saxena, R.: Postpartum hemorrhage. In: Evidence Based Color Atlas of Obstetrics and Gynecology Diagnosis and Management, pp. 270–275 (2013)
3. Bienstock, J.L., Eke, A.C., NAH.: Postpartum hemorrhage. New Engl. J. Med. 1635–1645 (2021). https://doi.org/10.1056/NEJMra1513247
4. Neary, C., Naheed, S., McLernon, D.J., Black, M.: Predicting risk of postpartum haemorrhage: a systematic review. BJOG An. Int. J. Obstet. Gynaecol. **128**, 46–53 (2021). https://doi.org/10.1111/1471-0528.16379
5. Postpartum Hemorrhage: Causes, Risks, Diagnosis and Treatment. https://my.clevelandclinic.org/health/diseases/22228-postpartum-hemorrhage. Accessed 7 Jul 2022
6. Carroli, G., Cuesta, C., Abalos, E., Gulmezoglu, A.M.: Epidemiology of postpartum haemorrhage: a systematic review. Best Pract. Res. Clin. Obstet. Gynaecol. **22**, 999–1012 (2008). https://doi.org/10.1016/j.bpobgyn.2008.08.004
7. Almutairi, W.M.: Literature review: Physiological management for preventing postpartum hemorrhage. Healthc **9** (2021). https://doi.org/10.3390/healthcare9060658
8. Sheldon, W.R., Blum, J., Vogel, J.P., et al.: Postpartum haemorrhage management, risks, and maternal outcomes: findings from the World Health Organization Multicountry Survey on Maternal and Newborn Health. BJOG **121**(Suppl), 5–13 (2014). https://doi.org/10.1111/1471-0528.12636
9. Evensen, A., Anderson, J.M., Fontaine, P.: Postpartum hemorrhage: prevention and treatment. Am. Fam. Physician **95**, 442–449 (2017)
10. Cunningham, C., Watt, P., Aflaifel, N., et al.: PPH butterfly: a novel device to treat postpartum haemorrhage through uterine compression. BMJ Innov. **3**, 45–54 (2017). https://doi.org/10.1136/bmjinnov-2016-000144

11. Tekela, D.D., Asmare, A.G., Gebremariam, B.M., et al.: Digital postpartum hemorrhage management device (DPHMD). BMC Pregnancy Childbirth **19**, 1–6 (2019). https://doi.org/10.1186/s12884-019-2601-3
12. Safitri, T., Respatiningrum, R., Aminin, F.: Modern technology to diagnose early postpartum hemorrhage in island areas : a systematic review. Int. J. Soc. Sci. **1**, 865–874 (2022). https://doi.org/10.53625/ijss.v1i5.2429
13. Shanthi, G., AAR, AN: Iot-Based monitoring system for expectant women. Int J. Sci. Res. Eng. Manage. **07**:1–6 (2023). https://doi.org/10.55041/ijsrem18180
14. Sarhaddi, F., Azimi, I., Labbaf, S., et al.: Long-term IoT-based maternal monitoring: system design and evaluation. Sensors **21**, 1–21 (2021)
15. Ktron E of: ESP8266 ESP-12E WiFi Module—2.4 Ghz. In: KTRON India. https://www.ktron.in/product/esp8266-esp-12e-wifi-module/ (2022). Accessed 7 Jul 2022
16. Software|Arduino. https://www.arduino.cc/en/software. Accessed 7 July 2022
17. Cayenne Features—Developer|myDevices.com. https://developers.mydevices.com/cayenne/features/. Accessed 21 June 2022
18. Dr Trust USA Professional Series Finger Tip Pulse Oximeter 2022. https://drtrust.in/collections/dr-trust-pulse-oximeters/products/dr-trust-usa-professional-series-finger-tip-pulse-oximeter-with-audio-visual-alarm-and-respiratory-index. Accessed 7 July 2022

Analyzing the Link Lifetime and Doppler Shift Between Connected Vehicles in VANET

Vishvendra Pal Singh Nagar and Anil Kumar Sagar

Abstract The highly dynamic new technology known as Vehicular Ad Hoc Networks (VANETs) supports wireless communication between hybrid vehicles. Wireless sensor networks' (WSNs) technology is used by hybrid cars for a range of tasks, including real-time data gathering, monitoring, control, and sharing that data for remote monitoring and system diagnostics. Hybrid vehicles may interface with infrastructure via Intelligent Transport System (ITS) to receive real-time traffic, road, and weather information. Depending on the road's specifications, a vehicle's mobility speed may vary. Certain VANET characteristics, such as dynamic vehicle speed, vehicle mobility in terms of movement, network density, etc., make wireless communication challenging to maintain the connectivity of dynamic wireless network. As speed is one of the factors that leads to a rapid change in topology, this paper examines and analyzes the effects of speed and mobility on the performance of wireless communication protocols. The findings show that raising a vehicle's speed has an adverse impact on the connection of the network, with a negative correlation between speed and wireless network link lifetime.

Keywords Vehicle to vehicle · Link lifetime · Doppler shift · DSDV · OFDM · Hybrid vehicles

1 Introduction

Vehicular Ad Hoc Networks (VANETs) are the most advance approach for wireless communication in modern transport ecosystem. These network models are largely used in the context of Intelligent Transportation Systems (ITSs) to improve safety

V. P. S. Nagar (✉)
Department of Computer Science and Engineering, Sharda University, Greater Noida, India
e-mail: vishvendra.nagar@gmail.com

A. K. Sagar (✉)
Sharda School of Engineering and Technology (SSET), Sharda University, Greater Noida, India
e-mail: aksagar22@gmail.com

© The Author(s), under exclusive license to Springer Nature Singapore Pte Ltd. 2025

H. P. Singh et al. (eds.), *Recent Developments in Control, Automation and Power Engineering*, Lecture Notes in Electrical Engineering 1303,
https://doi.org/10.1007/978-981-96-0047-2_35

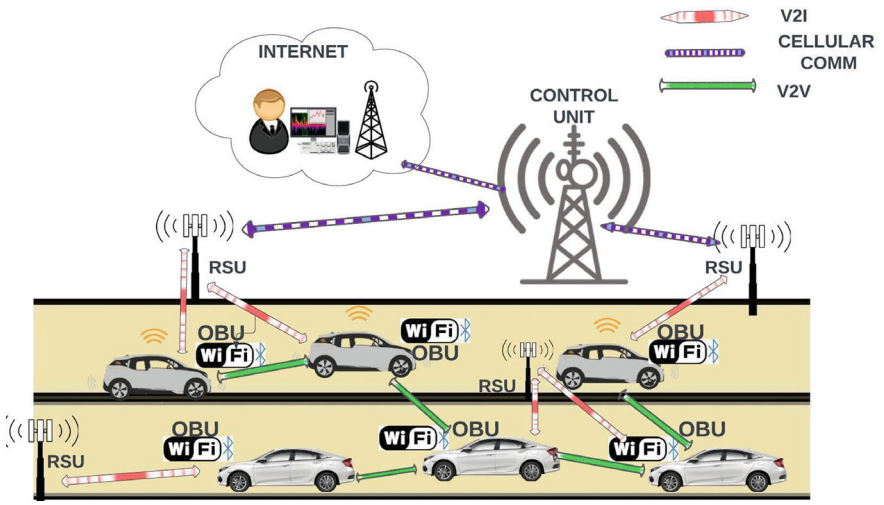

Fig. 1 VANET network communication

on road, traffic, and travel management and provide various infotainment services to drivers and passengers. These models provide the ability to establish easy wireless communication among dynamic and static vehicles. VANET further divided into two basic models (I) vehicle-to-vehicle (V2V) communication (ii) vehicle-to-infrastructure communication (V2I). Certain characteristic of VANET makes the wireless communication difficult to publish data such as dynamic speed of vehicle, mobility of the vehicle in terms of movement, and density of network. This paper is to study and analyze the effects of speed and mobility on wireless communication protocol performance, as the speed is one of the variables that trigger the rapid topology change [1]. The networking and communication framework for VNAET is based on mobile networking and computing, in which vehicles act as nodes that lack infrastructure, are dynamic in nature, have a dynamic network topology, and are highly mobile. *"Vehicle-to-Vehicle (V2V)"* and *"Vehicle-to-Infrastructure (V2I)"* communications are the types of VANET communication [2]. Vehicle-to-vehicle networking (V2V) may make use of any kind of wireless networking technology like Long-Term Evolution (LTE) [3], Global System for Mobile Communication (GSM), Global Positioning System (GPS), etc. (Fig. 1).

2 Shortened Link Lifetimes

The performance of Destination-Sequenced Distance Vector (DSDV) protocol can be considerably impacted by the velocity at which vehicles are moving in a Vehicular Ad hoc Network (VANET) [4]. DSDV is a proactive routing protocol that updates routing tables on a regular basis or when the network topology changes at all nodes. Routing

tables are maintained by DSDV using recurrent updates. The network architecture can vary quickly in high-speed situations when vehicles are continually moving and swiftly altering their places. The routing tables may undergo frequent updates and modifications as a result, which could raise control overhead and use up important network resources. After topology modifications, DSDV needs time for routing tables to converge. High-speed traffic can lead to more frequent network changes, which could result in longer convergence times because routes need to be updated and recalculated more frequently. For DSDV to preserve accurate routing data, links between nodes must be stable to guarantee that services and information are accessible and available when they are needed [5]. Due to the rapid movement of vehicles into and out of each other's communication range, high-speed vehicles can result in shorter-lasting relationships. This may lead to more frequent route invalidations and link breaks. The duration of communication link or connection between two devices or nodes remains active and dependable, which is referred to as the link lifespan. Link lifetime is a crucial parameter that is employed in wireless communication networks, such as Vehicular Ad Hoc Networks (VANETs), to evaluate the stability and reliability of connections between mobile or stationary nodes [6]. Estimating how long a communication link between two nodes will be active before it is likely to be disrupted or broken owing to factors like distance [7], interference, and mobility is the process of calculating the link lifespan in a wireless network, such as a Vehicular Ad hoc Network (VANET). For routing protocols, the link lifespan is a crucial parameter because it determines how frequently routes need to be changed. Here is a formula for calculating link lifetime that has been condensed and explained:

Transmission range (R): The maximum distance at which a signal can be reliably transmitted and received between two dynamic nodes.
Relative Speed (S) is the speed at which two nodes are moving in relation to one another.
Relative Speed = |Velocity of Object 1 − Velocity of Object 2|.
Link Lifetime = (2 * Packet Transmission Time)/(Relative Speed).
LL = (2 * Packet Transmission Time)/(Relative Speed) + (Transmission Range)/(Relative Speed).

An increase in relative speed leads to a decrease in link lifetime. This is because the two vehicles are moving away from each other, which reduces the amount of time that they have to communicate (Tables 1 and 2).

The graph in Fig. 2 enables us to compare the velocity of two vehicles, Car 1 (shown as the blue line) and Car 2, as they move over a range of 0.2–2 km. Although Car 1 accelerates more quickly than Car 2 at first, both cars see a similar linear increase in speed as they travel farther. Both vehicles appear to follow a linear trajectory, with Car 1 regularly outpacing Car 2. It appears that the speed of both cars has a linear relationship with distance, indicating that their velocities are changing steadily. Both vehicles pick up speed as the distance widens, but Car 1 consistently travels faster than Car 2 across the whole range. The graph compares the speeds of two cars across a variety of distances and demonstrates that Car 1 consistently travels farther than Car 2.

Table 1 Parameters for two vehicles

Parameter	Vehicle-1	Vehicle-2
Initial speed	0 m/s	0 m/s
Initial distance	0	100Mtr
Acceleration rate	4 km/h	3.5 km/h
Total distance covered	2 km	2 km
Transmission range	300 m	300 m
Transmission rate	4 mbps	4 mbps
Data size	1000 bits	1000 bits
Interval	200 m	200 m

Table 2 Comparison of relative speed and link lifetime of vehicles

Distance (km)	Speed car 1 (km/h)	Speed car 2 (km/h)	Relative speed (km/h)	Packet transmission time (min)	Link lifetime (min)
0.2	13.3	10.7	2.6	0.00025	0.77
0.4	26.7	21.4	5.3	0.00025	0.57
0.6	40	32.1	7.9	0.00025	0.38
0.8	53.3	42.8	10.5	0.00025	0.25
1	66.7	53.5	13.2	0.00025	0.14
1.2	80	64.2	15.8	0.00025	0.08
1.4	93.3	74.9	18.4	0.00025	0.06
1.6	106.7	85.6	21	0.00025	0.05
1.8	120	96.3	23.7	0.00025	0.04
2	133.3	107	26.3	0.00025	0.03

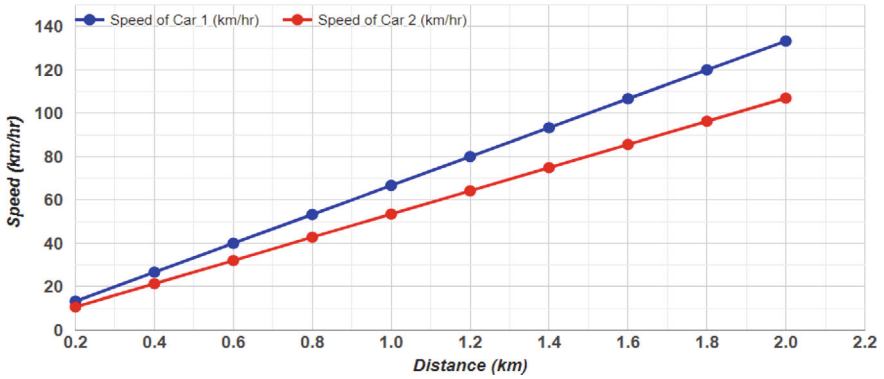

Fig. 2 Comparison of speed between vehicles

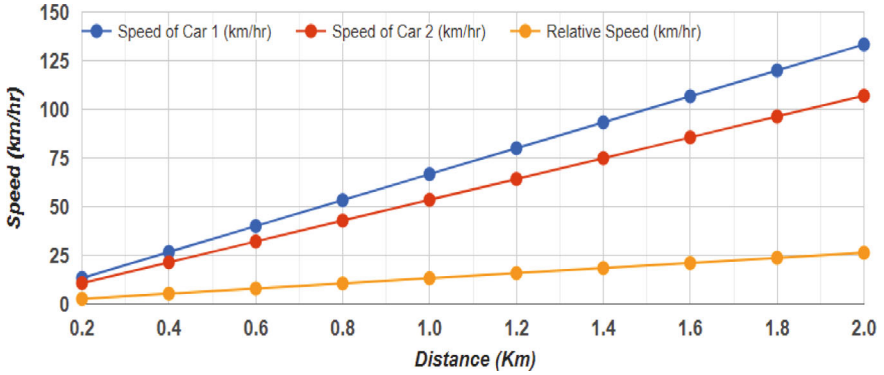

Fig. 3 Comparison of relative speed among connected vehicles

The "Relative Speed of Vehicles" chart in Fig. 3 graphically illustrates information on the velocities of two vehicles. Speed of Car 1 (km/h): This line on the graph shows how fast Car 1 is moving over time. Car 1 accelerates gradually from a starting speed of 13.3 km/h. Speed of Car 2 (km/h): This line displays Car 2's speed over time. The acceleration of Car 2 is slightly slower than that of Car 1 and it begins at a speed of 10.7 km/h. The third line displays the relative speed between Cars 1 and 2 in kilometers per hour. It is calculated as the difference in speeds between Cars 1 and 2 at each instant in time. Starting at 2.6 km/h, this line steadily picks up speed.

The line graph in Fig. 4 illustrates the relationship between different parameters, including the link lifetime, relative speed, and distance between Cars 1 and 2. The corresponding values for each parameter are plotted on the *y*-axis as the *x*-axis distance rises. The title of the graph alludes to a trend that has been noticed: as relative speed rises, link lifetime falls. The graph shows how the speeds of Cars 1 and 2 fluctuate as the distance between them grows. Additionally, the two cars' relative speeds are estimated and shown. The same graphic also displays the link lifetime (in seconds). The chart makes it simple to spot patterns and trends by allowing users to compare how these factors vary as distance rises.

3 OFDM and the Doppler Effect

Connected vehicles communicate with one another via a variety of wireless technologies, including radio waves and light rays. These waves are subject to the Doppler Effect, just like any other sort of wave [8]. Doppler shift is impacted by the speed changes of linked cars. The apparent shift in frequency of a wave caused by an observer moving away from the wave source is known as the Doppler Effect. The relative speed of the two vehicles affects how much Doppler shift there is. The Doppler shift will be greater the faster the two cars are approaching one another.

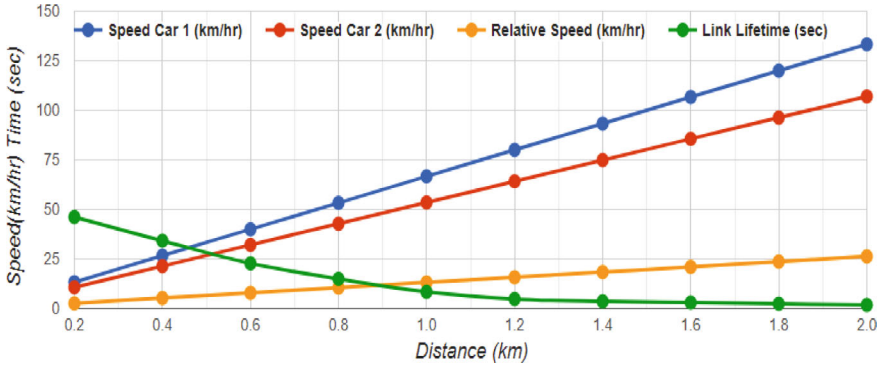

Fig. 4 Comparison of link lifetime with relative speed

Doppler shift can affect the Vehicular Ad Hoc Network (VANET) protocols, particularly in situations when fast-moving automobiles are involved. The frequency of a signal seems to vary due to relative motion between the source of the signal and the observer in a phenomenon known as Doppler shift. This relative motion in VANETs happens as the cars get closer to or farther away from one another. The frequency of the signal that a vehicle receives changes as a result of Doppler shift. Communication protocols that depend on a specific frequency range may become less accurate as a result of this frequency shift.

$$f' = f(c - vs/c + vr).$$

f' is the observed frequency (shifted frequency).
f is the emitted or transmitted frequency.
c is the speed of light (approximately $3 \times 1083 \times 108$ m per second).
vr is the relative velocity between the source and the receiver.
vs is the speed of sound.

Doppler shift can affect Wi-Fi transmission, especially in situations where moving devices, such mobile phones, laptops, or automobiles with Wi-Fi technology, are involved. Similar to other wireless communication systems like cellular networks or satellite communications, the Doppler shift in Wi-Fi operates on a similar theoretical foundation.

The Orthogonal Frequency Division Multiplexing (OFDM) protocols used by Dedicated Short-Range Communications (DSRC) have a 10 MHz bandwidth [9]. A maximum data rate of 27 Mbps can be sent with this technique. There are some variations between this method and the 802.11 a method of OFDM. The resulting data rate additionally applies quadratic maximum 27 Mbps half of data of 54 Mbps from 802.11a because the DSRC's capacity is only half that of 802.11a.

To account for the Doppler Effect, which led to the Spread of Doppler in the frequency domain, the lifespan of the symbols on DSRC is double that of 802.11's.

An OFDM symbol on DSRC has duration of 8 s, but that over Wi-Fi is 4 s. Wi-Fi users' portability and mobility are rather sluggish. This means that, in contrast to DSRC technology in particular VANET, the Doppler Effect can be disregarded. Table 3 shows the comparison between DSRC, 802.11p, 802.11a protocols. Modulation-type Binary-Phase Shift Keying (BPSK), Quadrature-Phase Shift Keying (QPSK), and Quadrature Amplitude Modulation (QAM) are common in all.

Table 4 compares several modulation techniques, coding rates, and data rates in a Vehicular Ad Hoc Network (VANET) for both the 20–10 MHz bandwidths. The amount of bits that each symbol or subcarrier for each configuration represents is shown in the "Bits Per Symbol and Subcarrier" column.

This graph (Fig. 5) displays information on several modulation schemes and the relevant data rates for those schemes at various coding rates and bandwidths. Effectively comparing the data rates of several modulation schemes at various coding

Table 3 Comparison between DSRC, 802.11p, and 802.11a

Parameter	DSRC	802.11p	802.11a
Rate of information data	3–27 Mbps	6–54 Mbps	6–54 Mbps
Type of modulation	BPSK, QPSK	BPSK, QPSK	BPSK, QPSK
	16 QAM	16 QAM	16 QAM
	64 QAM	64 QAM	64 QAM
Rate of coding	1/2, 1/3, 3/4	1/2, 1/3, 3/4	1/2, 1/3, 3/4
Subcarrier count	52 (48 + 4)	52 (48 + 4)	Typically 52 (48 + 4)
OFDM symbol length	8 µs	4 µs	4 µs
Time of guard	1.6 µs	0.8 µs	0.8 µs
Period for FFT	6.4 µs	3.2 µs	3.2 µs
Duration of preamble	32 µs	16 µs	16 µs
Bandwidth	10 MHz	10 MHz	20 MHz
Frequency for subcarrier	0.156 MHz	0.156 MHz	0.3125 MHz

Table 4 Data rates and modulation in VANET

Modulation scheme	Coding rate	Data rate (20 MHz) (Mbps)	Data rate (10 MHz) (Mbps)	Bits/symbol and subcarrier
BPSK	1/2	3	6	0.5
	3/4	4.5	9	0.75
QPSK	1/2	6	12	1
	3/4	9	18	1.5
16-QAM	1/2	12	24	2
	3/4	18	36	3
64-QAM	2/3	24	48	4
	3/4	27	54	4.5

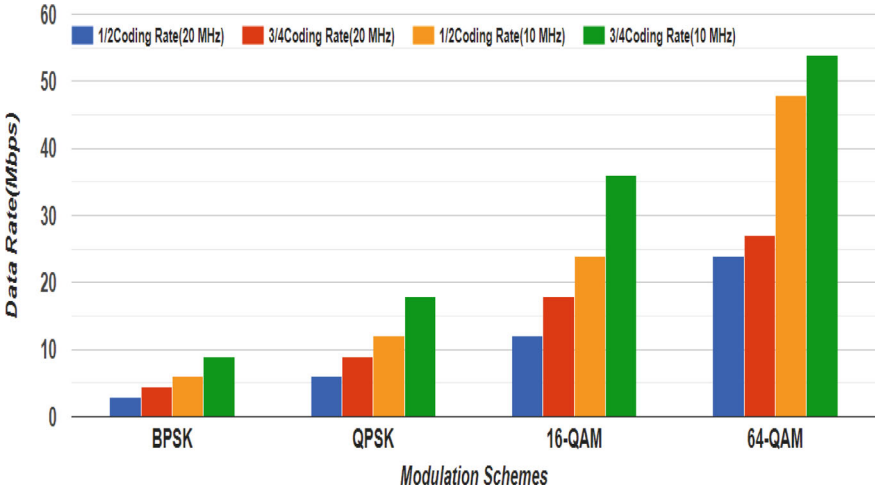

Fig. 5 Comparison for data rates using various modulation schemes in VANET

rates (1/2 and 3/4) and bandwidths (20–10 MHz) is the chart. It makes it simple to visually compare how various modulation schemes fare in terms of data rate under various conditions. Readability and comprehension are improved by the bold, appropriately sized axis labels, and legend text. Overall, the graph gives a clear and illuminating illustration of how data rate variances dependent on modulation schemes, coding rates, and bandwidths might vary.

Digital modulation for VANET includes BPSK, QPSK, 16- and 64-QAM, and convolution code at rates of 1/2 and 3/4 [10]. It generates varied data rates up to 54 Mbps for the bandwidth of 10 MHz at each modulation point and coding rate. The amount of bits per symbol needed increases with increasing data rate generation. As shown in Table 2, it takes 4.5 bits per symbol to achieve the level of 64 QAM modulations at a coding rate of 34, which is the most common number of bits per symbol employed.

Table 3 summarizes the three scenarios and their respective modulation schemes, coding rates, and data rates for both 20–10 MHz bandwidths in a VANET. The choice of scenario depends on the specific communication requirements and environmental conditions in the VANET (Table 5).

Table 5 Various scenarios to adopt modulation

Scenario	Modulation scheme	Coding rate	Data rate (20 MHz)	Data rate (10 MHz)
High data rate requirement	64-QAM	3/4	24 Mbps	12 Mbps
Robust communication	QPSK	1/2	6 Mbps	3 Mbps
Balanced approach	16-QAM	3/4	18 Mbps	9 Mbps

4 Conclusion

This study looks at how vehicle speed and mobility affect network connectivity by affecting the link lifetime and the Doppler Effect, which both have an impact on how well VANET protocols perform. The calculations were done, and the performance differences among wireless protocols were provided based on the link lifetime prediction formula. Results reveal that when vehicle speed increases, network throughput and link lifetime ratio drop, indicating deterioration in the performance of the wireless network protocol, whereas link lifespan and Doppler shift rise as vehicle speed increases. Communication that uses real-time data to improve road safety between hybrid vehicles and other vehicles is a crucial component of the VANET ecosystem.

References

1. Yudistira, B.G.K., Anggoro, R., Shiddiqi, A.M.: Addition of neighbors in the number of VANETS node factors: DSR-PNT performance study. J. Wirel. Mob. Netw. Ubiquitous Comput. Dependable Appl. **13**(4), 196–210 (2022)
2. Lu, R., Lin, X., Liang, X., Sheen, X.: A dynamic privacy-preserving key management scheme for location-based services in VANETs. IEEE Trans. Intell. Transp. Syst. **13**, 127–139 (2012)
3. Chauhan, M., Rakesh, N.: Comprehensive assessment of resource allocation techniques for leading V2V network technologies. In: 2023 International Conference on Computational Intelligence and Sustainable Engineering Solutions (CISES), pp. 855–861. IEEE (2023)
4. Ema, R.R., Ahmed, M.F., Ahmed, M.H., Islam, T.: Effect of number of nodes and speed of nodes on performance of DSDV, AODV, AOMDV, DSR and GPSR routing protocols in VANET. In: 2019 10th International Conference on Computing, Communication and Networking Technologies (ICCCNT), pp. 1–6. IEEE (2019)
5. Singh, R., Kathuria, K., Sagar, A.K.: December. Secure routing protocols for wireless sensor networks. In: 2018 4th International Conference on Computing Communication and Automation (ICCCA), pp. 1–5. IEEE (2018)
6. Bohacek, S., Ilic, A., Sridhara, V.: On the predictability of link lifetimes in urban MANETs. In: Third International Symposium on Modeling and Optimization in Mobile, Ad Hoc, and Wireless Networks (WiOpt'05), pp. 209–218. IEEE (2005)
7. Sagar, A.K., Lobiyal, D.K.: A multi-objective optimization approach for lifetime and coverage problem in wireless sensor network. In: Intelligent Computing, Networking, and Informatics: Proceedings of the International Conference on Advanced Computing, Networking, and Informatics, India, June 2013, pp. 343–350. Springer India (2014)

8. Pamungkas, W., Suryani, T.: Doppler effect in VANET technology on high user's mobility. In: 2018 International Conference on Information and Communications Technology (ICOIACT), pp. 899–904. IEEE (2018)
9. Rayamajhi, A., Biron, Z.A., Merco, R., Pisu, P., Westall, J.M., Martin, J.: The impact of dedicated short range communication on cooperative adaptive cruise control. In: 2018 IEEE International Conference on Communications (ICC), pp. 1–7. IEEE (2018)
10. Abdelgader, A.M., Lenan, W.: The physical layer of the IEEE 802.11 p WAVE communication standard: the specifications and challenges. In: Proceedings of the World Congress on Engineering and Computer Science, vol. 2, pp. 22–24 (2014)

Comparative Analysis of Short-Term Load Forecasting Techniques: Conventional Deep Learning Models Versus Proposed LSTM with Attention Layers

Ravi Shekhar Tiwari, D. Lakshmi, Pragya Jha, Shubh Sharma, Neelu Nagpal, and Pierlugi Siano

Abstract This research article explores a comparison of both conventional deep learning models and proposed a LSTM model equipped with attention layers for the short-term load forecasting (STLF). The study evaluates the accuracy and efficiency of both models using the power system data of Delhi city, India. The forecasts with the proposed LSTM model with attention layers outperform the conventional time-series models results better accuracy with a 1.9% Mean Squared Error (MSE) which is lower as compared to 2.35% for the best-performing conventional model. The proposed model also exhibits better interpretability, as the attention mechanism allows for the identification of significant input features that contribute to the forecasting performance. The proposed model is a promising technique for STLF in real-time applications. Overall, the study highlights the potential of using LSTM model with attention layers for accurate and efficient STLF in power systems.

Keywords Short-term load forecasting · Deep learning · Recurrent neural networks · Gated recurrent units · Long short-term memory with attention

R. S. Tiwari
IIT Patna, Bihar 801106, India

D. Lakshmi
VIT Bhopal University, Sehore, Madhya Pradesh 466114, India

P. Jha (✉) · S. Sharma · N. Nagpal
Maharaja Agrasen Institute of Technology, Delhi 110086, India
e-mail: pragya.jha077@gmail.com

N. Nagpal
e-mail: nagpalneelu1971@ieee.org

P. Siano
University of Salerano, 84084 Fisciano, Italy
e-mail: psiano@unisa.it

© The Author(s), under exclusive license to Springer Nature Singapore Pte Ltd. 2025

H. P. Singh et al. (eds.), *Recent Developments in Control, Automation and Power Engineering*, Lecture Notes in Electrical Engineering 1303,
https://doi.org/10.1007/978-981-96-0047-2_36

1 Introduction

Forecasting electricity demand is vital for effective power system operation and planning. Precision in predicting STLF is important to manage supply and demand balance, enhancing system efficiency, and ensuring a dependable and steady power supply [1]. Recently, diverse models, such as statistical, classical machine learning (ML), deep learning (DL), and ensemble learning (EL), have been documented for their performance in STLF [2]. Among these reported techniques, particularly Artificial Neural Networks (ANNs), have demonstrated encouraging outcomes in predicting short-term load, as indicated by the findings in a study by Khwaja in 2020 [3]. The traditional ANN models encounter the issue of vanishing gradient, restricting their capacity to grasp long-term dependence within time-series data. In response to this concern, LSTM models have been suggested and have showcased excellent performance across diverse time-series forecasting assignments, as evidenced by studies conducted by Haque in 2022 and Farsi in 2021 [4, 5]. Additionally, attention mechanisms have been introduced to long short-term memory (LSTM) models to improve interpretability and capture feature importance [6]. However, there are few studies that compare the performance of conventional DL models and LSTM models with attention layers for short-term load forecasting [7, 8]. A trend of many hybrid models such as LSTM-RNN [4], new ensemble model, SELNet [9], integrated CNN and LSTM [10], and many more have been reported for accurate prediction of STLF. Hamad and Abdulrahman [11] the study uses techniques such as LSTM and Gated Recurrent Units (GRU) neural networks using weather data, weekend and weekday data, and the Kurdistan regional electrical load data. One hot encoding is carried out to label weekend and weekday data.

The objective of this research is to assess the predictive precision and efficiency of traditional time-series models with the proposed LSTM model with attention layers. The performance evaluation is carried out using real-world data from a power system in Delhi metropolitan, India. The study also aims to investigate the interpretability of the proposed LSTM model with attention layers and its potential for real-time applications.

The key points of the research are as below:

- LSTM with an attention model is proposed to forecast the STLF of a metropolitan city.
- Forecasting the pattern of electricity demand in a city with high population density, varying climates, urbanization, industrial setups, cultural diversity, and a floating population in the absence of complete and comprehensive standards.
- The report includes a review comparing the proposed method with several cutting-edge approaches, demonstrating its superior performance in STLF results. The precision and reliability of the outcomes are notable, even in the absence of complex feature engineering.

Section 1 provides an introduction and overview of the research, followed by Sect. 2, which outlines the proposed LSTM model with attention layers. Section 3

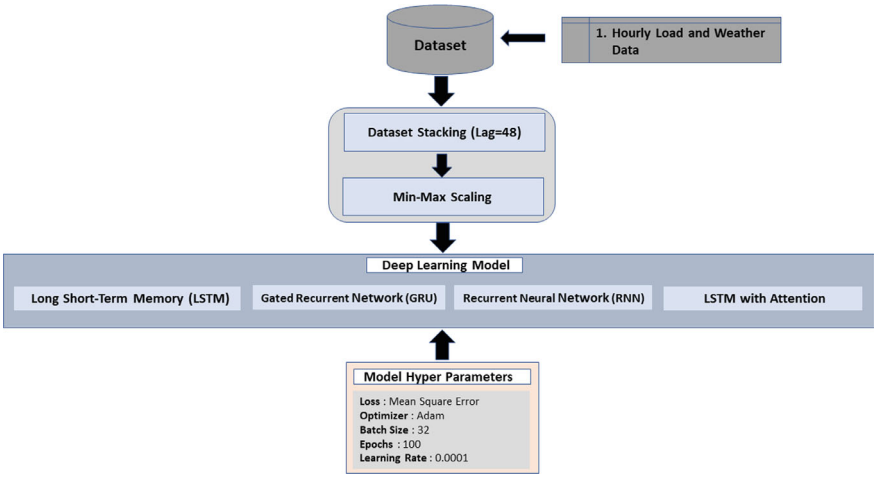

Fig. 1 Proposed architecture of the experimentation

discusses the data used for the model, while Sect. 4 presents the methodology employed. Section 5 unveils the experimental configuration and key findings from the comparative analysis. Finally, Sect. 6 interprets the proposed model and its potential for real-time applications, concluding with a discussion on the future scope of this research.

2 Proposed STLF Models

Figure 1 represents the different forecasting DL models adopted to predict the hour-to-hour load demand of Delhi city based on the weather, load, and calendar data as discussed below. In this study, four different types of models are proposed for load forecasting using the collected data. The time-series models include Recurrent Neural Networks (RNNs), LSTM, GRU, and LSTM with attention. The architectures of these models were chosen based on their proven effectiveness in time-series forecasting tasks.

3 Dataset

The dataset consists of hourly measurements of load (MW) and weather data, including minimum temperature, maximum temperature, and humidity at two different intervals, from 01/01/2017 to 31/12/ 2019. The dataset was split into the three data in parts of 8:1:1. These sets are used for training, validation, and testing of

model. Table 1 displays the number of records in each of the three sets. The dataset was not shuffled and was preprocessed after being split into three sets.

(i) **Dataset Preprocessing**

The dataset is a time-series nature; hence, we employed two different preprocessing techniques to configure the DL models.

(ii) **Dataset Stacking: Lag = 48**

The counts of previous time steps used for input to make a prediction for the next time step are termed as lag. RNN or its derivative models such as LSTM or GRU takes a sequence of input data over time and processes it to predict output at each time step. As the model progresses through each time step, it takes into account the present input value along with the preceding output value, which then serves as the input for the subsequent time step. By incorporating this previous output value into the current time step's computation, the LSTM can maintain some memory of the past and potentially improve its prediction accuracy. The number of previous time steps, or lags, that are used as input to the LSTM is determined by the window size of the time-series data. Finding the appropriate window size can help the model capture more complex patterns and dependencies in the data, but it also increases the computational complexity and training time. In this proposed methodology, we have used 48-time step values as the lag.

(iii) **Min–Max Scaling**

This method is employed in data preprocessing to transform numeric features, adjusting them to a consistent range of values, commonly between 0 and 1. The procedure includes subtracting the minimum value of the feature from all values and subsequently dividing by the feature's range (i.e., the gap between the maximum and minimum values). The resultant values are then adjusted to fit within the 0–1 range. This scaling method is useful when the features in a dataset have vastly different ranges, and we want to ensure that they are equally important in the analysis. We have scaled the data after stacking the data with a lag of 48.

$$x_{\text{scaled}} = x - \frac{x_{\min}}{x_{\max}} - x_{\min}. \tag{1}$$

Table 1 Selected data distribution and model parameters for the sequence prediction parameter values

Set name	Data points	Count % age	Hyperparameters	Value
Train set	20,985	80%	Loss	Mean square error
Validation set	2623	10%	Optimizer	Adam
Test set	2623	10%	Batch size	32
Total	26,231	100%	Epochs	100
			Learning rate	0.00001
			Lag	48

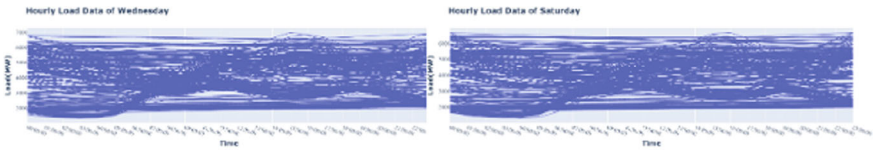

(a) Wednesday Load Consumption. (b) Load Consumption.

Fig. 2 Load consumption for weekday and weekend trends in the Delhi NCR region

(iv) **Analysis of Load Consumption on a Daily Basis**

In this study, the hourly pattern of energy consumption by the population of the Delhi NCR Region on each day of the week is analyzed. Due to space constraints, only Wednesday and Saturday hourly trends of load patterns are depicted in Fig. 2. The trend shows a consistent decrease in consumption from midnight to 6:00 AM on almost all days, followed by an increase until noon, and then sustained at a similar level until 11:59 PM.

4 Methodology

The proposed methods were trained using the training dataset, and the hyperparameters were optimized using the validation dataset (refer Table 1).

The training of model is exercised through the algorithm of back propagation. MSE loss function is minimized by using Adam optimizer. The same hyperparameters, as indicated in Table 1, are consistently applied across all four categories of DL models for time-series analysis for the hourly load forecast. Hypothesis testing is done to evaluate the statistical significance of the outcomes. The outcomes are significant with the p-value below 0.05 (in terms of statistic). Based on the results of the evaluation metrics and statistical analysis, the best model was selected for load forecasting. Figure 1 shows the design and implementation of an experimental architecture for load forecasting.

RNN Model

The loss versus epochs are shown in Fig. 3a. Train, validation, and test loss converge to the loss value of 0.05 from the 75th epoch. Figure 3b shows that there are no sequence dependencies. However, certain factors contribute to the occurrence of the most significant residual errors, primarily attributed to fluctuations in seasonality.

GRU Model

The loss versus epochs are shown in Fig. 3c where train, validation, and test losses converge to the loss value of 0.05 from the 75th epoch. Figure 3d shows that there are no sequence dependencies. However, certain factors contribute to the occurrence of the most significant residual errors, primarily attributed to fluctuations in seasonality.

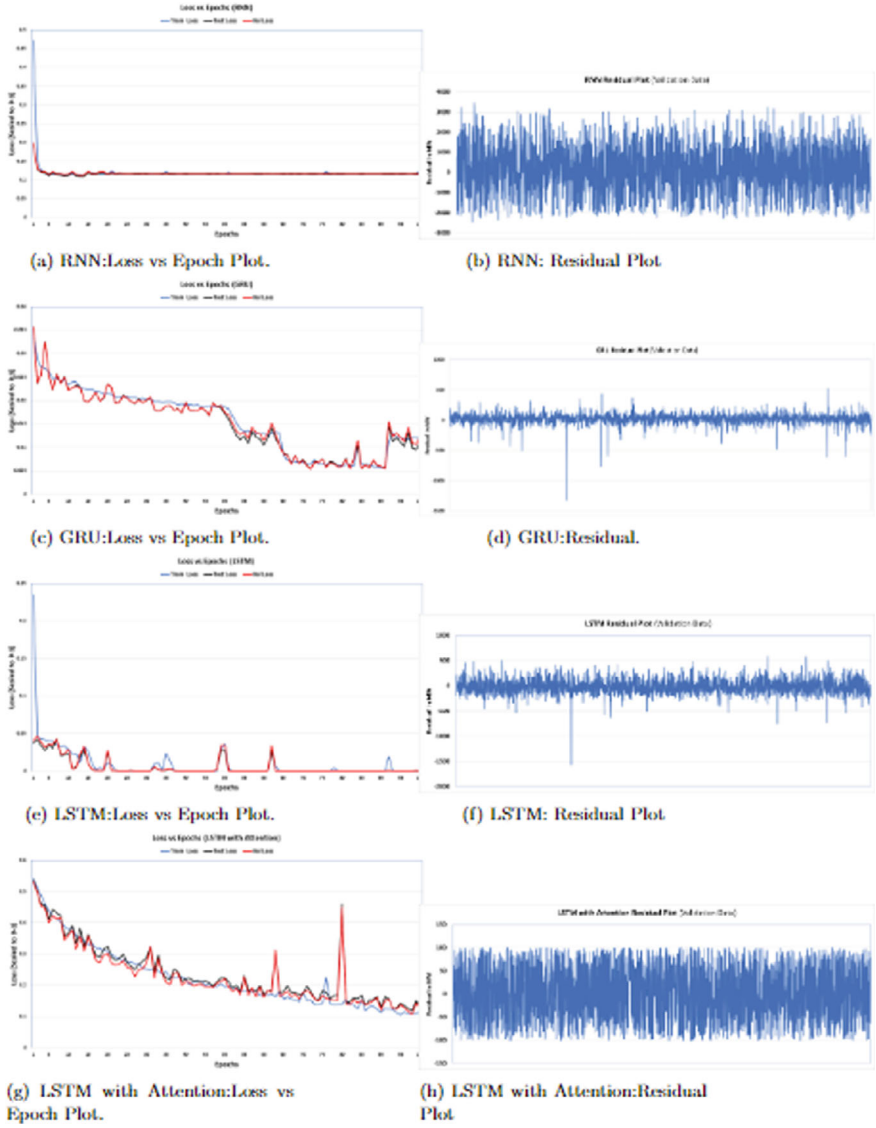

Fig. 3 Performance analysis of four proposed forecasting models

LSTM Model

The LSTM model, a variant of RNN model, is featuring a series of hidden layers linked by memory cells. Nevertheless, the LSTM boasts a more intricate architecture that encompasses three gates: input, output, and forget to empower LSTM to

selectively retain or discard information within the memory cell, contingent on its significance for the ongoing prediction task.

The loss versus epochs are shown in Fig. 3e where it is observed that train, validation, and test losses converge to near zero from the 65th epoch. Figure 3f shows that there are no sequence dependencies. However, certain factors contribute to the occurrence of the most significant residual errors, primarily attributed to fluctuations in seasonality.

LSTM Model with Attention

This version is useful for tasks that involve processing sequential data and the LSTM with attention model configuration is presented in Table 2.

With attention mechanism, a model is capable to concentrate on specific segments of an input sequence during prediction. Within the realm of LSTM, attention serves to assign significance weights to different time steps within the input sequence. LSTM with attention is a combination of LSTM and attention mechanisms. With the use of LSTM, the input sequence is processed to generate a series of hidden states followed by the utilization of attention to target on the major parts of the input series at the time of forecasting. In this proposed methodology, we have used attention methodology with the LSTM. We have applied attention between the weather features set and the load. Dot-product attention is a type of attention mechanism used in machine learning that computes the correlation among a query and key vectors by taking

Table 2 LSTM with attention model configuration

Layer (L)	Output shape	Parameter	Connected to
Input L1	[(None,48,1)]	0	[]
Input L2	[(None,48,5)]	0	[]
LSTM L1	(None,48,128)	66,560	[Input L1]
LSTM L2	(None,48,128)	68,608	[Input L2]
LSTM L3	(None,64)	49,408	[LSTM L1]
LSTM L4	(None,64)	49,408	[LSTM L1]
Dense L1_1	(None,64)	4160	[LSTM L3]
Dense L1_2	(None,64)	4160	[LSTM L4]
Dense L1_3	(None,64)	4160	[Dense L1_1]
Dense L1_4	(None,64)	4160	[Dense L1_2]
Attention layer	(None,64)	49,408	[DenseL1_4,Dense L1_3]
Dense L1	(None,100)	6500	[]
Dense L2	(None,75)	7575	[Dense L1]
Dense L3	(None,6)	456	[Dense L2]
Total parameter		2,65,155	
Trainable parameters		2,65,155	
Non-trainable parameters		0	

their dot product. This mechanism is often used in neural machine translation and language modeling tasks.

If a set of query vectors Q is known then in terms of set of K and V, the attention scores are computed as follows:

$$\text{Attention}\,(Q,\ K) = \text{softmax}\left(Q * \frac{K^T}{\sqrt{d_k}}\right). \tag{1}$$

For Q, each row corresponds to a query vector; V is termed as value vector, K refers as a matrix with dimension d_k, where each row corresponds to a key vector. In (1), K^T is divided by $\sqrt{d_k}$. This is done for scaling this dot product so that it does not result a large value. The attention scores are used to compute a weighted sum of the value vectors:

$$\text{Attention}(Q, K, V) = \text{Attention}(Q, K).V, \tag{2}$$

where V is the matrix of value vectors, where each row corresponds to a value vector. The resulting output is the weighted sum of the value vectors for each query:

$$\text{Output} \ = \ \text{Attention}(Q, K, V). \tag{3}$$

The attention mechanism facilitates the LSTM to target on various segments of the input sequence when delivering an output. Keeping one input sequence, keys and values are typically derived, while the query vector is derived from a different source, such as a decoder state in a sequence-to-sequence model. The dot-product attention mechanism has the advantage of being computationally efficient, as it can be efficiently implemented using matrix multiplication. It also has the property that the magnitude of the attention scores is controlled by the dimensionality of the key vectors, which can help to stabilize the attention mechanism during training. The loss versus epochs are shown in Fig. 3g. Train, validation, and test losses converge to the loss value of 0.05 from the 75th epoch. Since LSTM models capture long-term dependencies in sequential data, it's essential to examine the residual plots for any signs of sequence dependencies. Figure 3h shows that there are no sequence dependencies. Due to the attention mechanism, there are no most significant residual errors, primarily attributed to fluctuations in seasonality.

5 Results and Discussion

The entire simulation experimentation is carried out using TensorFlow with Python 3.9 platform, Numpy, and Sklearn. This section focuses on analyzing the results obtained from the experiments conducted on four different models: RNN, GRU, LSTM, and LSTM with attention. The comparative analysis is carried out by examining the loss versus epochs plot and the residual plots. These visualizations provide

important inferences for the performance analysis of each model. The loss versus epochs plot illustrates the correlation among the loss function and training epochs' counts. It serves as an indicator of how well the models are learning and converging toward an optimal solution. By comparing the loss trends of the four models, we can identify which architecture performs better in terms of minimizing the loss function. This analysis helps in determining the model's overall accuracy and ability to generalize.

In addition to the loss versus epochs plot, the residual plots are examined to gain a deeper understanding of the model's predictive capabilities. Residual plots display the disparities between the forecast of target variable and its true values. By evaluating the residuals, we can assess how well the models understand the data by capturing their underlying patterns and trends. This analysis allows us to identify any systematic biases or errors in the predictions made by each model. By considering both the loss versus epochs plot and the residual plots, we can make informed comparisons among the RNN, GRU, LSTM, and LSTM with attention models. The corresponding results of the four-model trained are shown in Fig. 3.

As we have trained the models and the model metrics are shown in the form of graphs. All trained models have same quantity of output nodes and input features from the dataset of hourly load and weather dated from 01/01/2017 to 31/12/ 2019. The model is forecasting all the input features by considering the previous 48 lag values. Therefore, we cannot be assured that if the model's loss is low, its forecasting will be accurate. This is because our interest lies in predicting the next load by considering the area's weather conditions, while the model's loss metric is based on all six features, calculated using the Mean Squared Error. Some of the output nodes will be deviating heavily while some of the nodes will be deviating slightly, for calculating the loss value after each of the iteration the model is taking account of all the features present in the dataset including those we are not interested to forecast. Hence, the loss of the models is aggregated mean square error for all the features not only the forecasting variable. So we have plotted the residual values of each of the models, and experimentally, we found that LSTM with attention has less residual values compared to other models.

6 Conclusion

This paper has presented a comparative analysis of STLF techniques, focusing on conventional time-series models and a proposed LSTM model with attention layers. By evaluating the accuracy and efficiency of proposed models using real-world data from a power system in Delhi, the study has provided valuable insights. LSTM with attention offers numerous benefits compared to the basic LSTM sequence-to-sequence model. These include enhanced capability in managing lengthy sequences and improved output quality. The findings clearly show that the proposed LSTM

model with attention layers outperforms traditional DL models in terms of forecasting accuracy. With a lower MSE of 1.9% compared to 2.35% for the best-performing conventional model, the LSTM model proves to be more reliable and precise. Moreover, the proposed LSTM model with attention layers offers improved interpretability. The attention mechanism incorporated within the model allows for the identification of significant input features that contribute to the forecasting performance. This enhanced interpretability enables a deeper understanding of the factors influencing load forecasting outcomes, aiding decision-making processes in power systems. Although the proposed LSTM model has a slightly longer training time compared to the conventional models, it exhibits promising potential for real-time applications of STLF. The combination of high accuracy, interpretability, and reasonable training time makes it a viable and effective technique for forecasting load demands in power systems.

References

1. Cecati, C., Kolbusz, J., Różycki, P., Siano, P., Wilamowski, B.M.: A novel RBF training algorithm for short-term electric load forecasting and comparative studies. IEEE Trans. Industr. Electron. **62**(10), 6519–6529 (2015)
2. Lee, E., Rhee, W.: Individualized short-term electric load forecasting with deep neural network based transfer learning and meta learning. IEEE Access **9**, 15413–15425 (2021)
3. Khwaja, A.S., Anpalagan, A., Naeem, M., Venkatesh, B.: Joint bagged-boosted artificial neural networks: using ensemble machine learning to improve short-term electricity load forecasting. Electric Power Syst. Res. **179**, 106080 (2020)
4. Haque, A., Rahman, S.: Short-term electrical load forecasting through the heuristic configuration of regularized deep neural network. Appl. Soft Comput. **122**, 108877 (2022)
5. Farsi, B., Amayri, M., Bouguila, N., Eicker, U.: On short-term load forecasting using machine learning techniques and a novel parallel deep LSTM-CNN approach. IEEE Access **9**, 31191–31212 (2021)
6. Khetarpal, P., Nagpal, N., Siano, P., Al-Numay, M.: Power quality disturbance signal segmentation and classification based on modified BI-LSTM with double attention mechanism. Authorea (2023). https://doi.org/10.22541/au.167865037.70684326/v1
7. Lin, J., Ma, J., Zhu, J., Cui, Y.: Short-term load forecasting based on LSTM networks considering attention mechanism. Int. J. Electr. Power Energy Syst. **137**, 107818 (2022)
8. Zang, H., Xu, R., Cheng, L., Ding, T., Liu, L., Wei, Z., Sun, G.: Residential load forecasting based on LSTM fusing self-attention mechanism with pooling. Energy **229**, 120682 (2021)
9. Shen, Y., Ma, Y., Deng, S., Huang, C.J., Kuo, P.H.: An ensemble model based on deep learning and data preprocessing for short-term electrical load forecasting. Sustainability **13**(4), 1694 (2021)
10. Rafi, S.H., Deeba, S.R., Hossain, E.: A short-term load forecasting method using integrated CNN and LSTM network. IEEE Access **9**, 32436–32448 (2021)
11. Hamad, Z., Abdulrahman, I.: Deep learning-based load forecasting considering data reshaping using MATLAB\Simulink. Int. J. Energy Environ. Eng. **13**(2), 853–869 (2022)

Colourization of Greyscale Images Using GAN with ResNet as the Backbone

Shikhar Gaur, Md Salman, Anshu Khurana, and Seema Kalonia

Abstract Over the past years, automatic image colouring processes have generated considerable interest in several applications, including the restoration of old or damaged images we aim to achieve a comprehensive and adaptable colourization process by leveraging a combination of architectural components. Specifically, we employ a CGAN augmented with ResNets and U-Net architectures, incorporating the leaky ReLU activation function within a GAN framework. This approach offers improved performance, particularly in scenarios involving highly processed or thematically specialized photographs.

Keywords Deep learning · Image colourization · Generative adversarial network (GAN) · U-Net · Convolutional layers · Generator · Discriminator · ResNet-18 · Tanh · Leaky ReLU

1 Introduction

Greyscale picture automatic colourization has long been a topic of active machine learning research. This is a result of its many uses, which include colouring and colour restoration for animation. We shall discuss a colouring technique in this manuscript using generative adversarial networks (GANs). Early in the new millennium, models of grey painting started to appear.

S. Gaur (✉) · Md Salman · A. Khurana · S. Kalonia
Department of Information and Technology, Maharaja Agrasen Institute of Technology, Delhi, India
e-mail: shikhar9901@gmail.com

© The Author(s), under exclusive license to Springer Nature Singapore Pte Ltd. 2025

H. P. Singh et al. (eds.), *Recent Developments in Control, Automation and Power Engineering*, Lecture Notes in Electrical Engineering 1303,
https://doi.org/10.1007/978-981-96-0047-2_37

1.1 Generative Adversarial Network (GAN)

Generator and discriminator models in GANs work together to learn how to solve the issue. In this configuration, the generator model creates a 2-channel image from a greyscale image (a 1-channel photo) as its input. Both channels are for *and *b, respectively. To decide if this resulting 3-channel image is true or untrue, the discriminator joins the input greyscale image to these two created channels. In order for the discriminator to identify real photos as such (3-channel images in the Lab colour space), it is also necessary to expose it to real images.

The layered perceptron model is utilized by both the discriminator and generator designs. Since colourization is a subset of image modification problems, convolutional neural networks (CNNs) are used as both generators and discriminators (Figs. 1 and 2).

2 Literature Survey

In 2002, Welsh [2] projected a method that used texture fusion to colourize photos. To colourize a greyscale image, brightness and quality data from a colour image already in existence were compared to the greyscale image. However, because this proposed approach was a forward issue, all of the solutions were deterministic.

An alternative version of the colouring problem was put up by Levin et al. [3] in 2005. In this calculation, the inverse approach of constructing a cost function is applied, whereby a pixel's divergence from the weighted average of its neighbouring pixels is penalized. The approach was less than ideal because both of the suggested ways still needed a lot of user input.

By contrasting the colour difference between the created convolutional neural network and the GAN, a colourization technique was suggested. In addition to

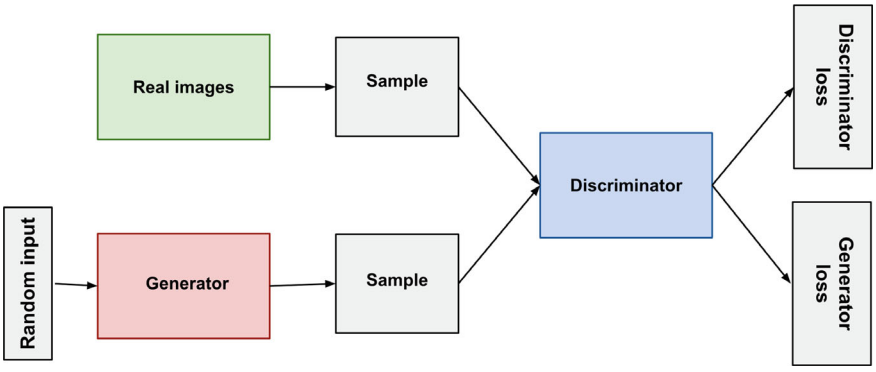

Fig. 1 Generative adversarial network architecture [1]

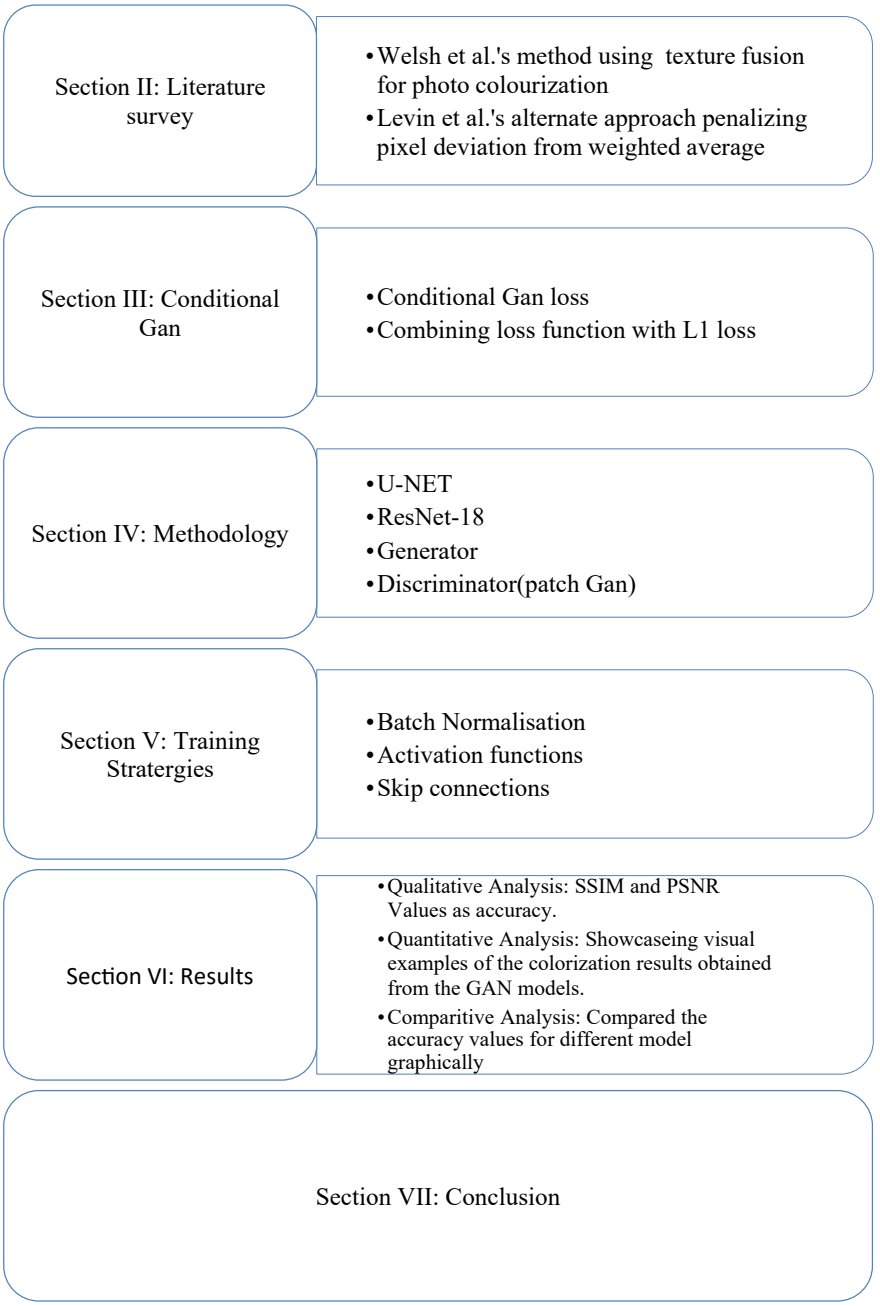

Fig. 2 Proposed Conditional GAN Architecture for Image Colorization

learning a mapping from the input image to the output, the model in the study also learns a loss function to train this mapping. Their method was successful in resolving erroneous issues including colourizing pictures and compositing photos in placemark maps and boundary maps.

By generalizing the high-resolution image colouring process and suggesting a learning strategy that considerably accelerates and stabilizes the process, we hope to further our approach.

One new type of generative models (GANs) is the generative adversarial network [4]. A GAN is composed of two small networks called generators and discriminators. A generator's purpose is to create an output that cannot be identified. The discriminant task entails categorizing samples in accordance with either the original distribution of the data or the generator's model distribution. Until the generator consistently provides results that the discriminator is unable to classify, both subnets are trained simultaneously.

In 2022, Zayd [5] noted that the outcomes were consistently superior to those of U-Net and DenseNet as well as other CNN designs. For instance, ResNet18 with skip connections was shown to generate more accurate and aesthetically beautiful colourized images than alternative designs in a study by Hsu in (2019), with a higher SSIM score for the generated images.

3 Conditional GAN

Randomly produced noise data is used is the input for the generator in a standard GAN [4]. The auto-colorization problem, however, cannot be solved using this strategy because it uses a greyscale image as its input rather than noise. A GAN variation known as conditional generative adversarial networks was used to tackle this issue.

Consider the following: y is the intended two-channel output of the generator (which may also represent the two-colour channels of the original image), z is the generator's noise input, and x is the greyscale image. Additionally, D is a discriminator, and G is a generator model. The conditional GAN loss is then:

$$\mathscr{L}_{L1}(G) = E_{(}x, y, z)\big[\|y - G(x, z)\|_1\big] \tag{1}$$

To improve the model's accuracy and give the process more control, we combine the L1 loss, commonly known as mean absolute error, with this loss function.

$$G^* = \arg\min_G \max_D \mathscr{L}_{\text{cGAN}}(G, D) + \lambda \mathscr{L}_{L1}(G) \tag{2}$$

The development model is still discovering how to colourize the image, [6] so most of the time it stays conservative and uses colours like "grey" and "browni." However, if you're unsure which colour is better, take the average and apply it. Apply the L1 regularization term to constrain color prediction errors while preserving spatial

coherence in adversarial training. The L1 loss is as much as feasible reduced by that colour. The total loss function is therefore:

$$\mathscr{L}_{\text{cGAN}}(G, D) = E_x, y\big[\log D(x, y)\big] + E_x, y\big[\log(1 - D(x, G(x, z))\big] \quad (3)$$

4 Methodology

An output to high-dimensional input conversion image-to-image transformation problem is image colourization. When the input and output structures are extremely similar, this can be likened to a pixel-wise regression problem. In addition to generating an output matching the input's spatial dimensions, this requires the network to provide colour information for every pixel in the supplied image that is greyscale. We provide a comprehensive convolutional model architecture that extends the regression loss as a baseline by employing adversarial meshes. In this case, the colour space $L * a * b *$ is used to complete the colourization task. This is possible because the remaining two channels can fully encode the colour information since a dedicated channel in the $L * a * b *$ colour space is used to represent photos brightness. As a consequence, it avoids jarring shifts in brightness and colour caused by slight differences in intensity levels, such as those present in RGB.

4.1 U-Net

A straight mapping from the grey—scale field to the colour image space must be discovered by the base model. Low-level information cannot, however, reach the network because of a blockage in the encoder-decoder architecture [6]. This issue is fixed by combining the reduced path's objects with the enlarged network path's up-sampled output. In both greyscale and colour images, this results in the raised edge location being shared across the input and output. U-Net is the name of this architecture.

Encoding and decoding units are proportionately placed lin the U-Net design. The constriction path consists of a eaky ReLU activation function with a slope of 0.2 and 4×4 convolution layers with stride 2 for down-sampling, followed by batch normalization. The stations are doubled after an operation is finished. Each unit in the path is comprised of the ReLU activation algorithm, batch normalization, and an up-sampling 4×4 inverted convolution operation with stride 2. Feature maps from the contracting path's encoder layers are concatenated with the corresponding decoder layers' outputs via skip connections to preserve spatial details during upsampling. The pooling layer, which is a 1×1 convolution is the network's final layer, or cross station parametric. For the top layer, we employ the hyperbolic tangent function. In the $L * a * b *$ colour space there are three channels in the output layer (Fig. 3).

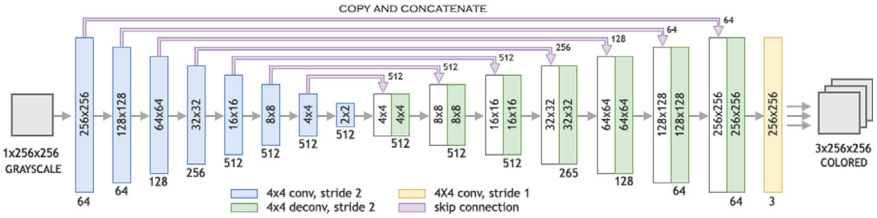

Fig. 3 U-Net architecture [7]

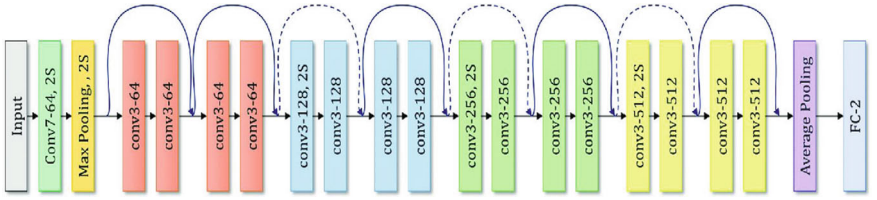

Fig. 4 ResNet architecture [8]

4.2 ResNet-18

In this work, we use ResNet-18 with an up-sampling architecture with batch normalization and ReLU activation function [5]. We use predetermined techniques such as arbitrary resizing, cropping, and horizontal flips to generalize our model. The BGR image must first be converted to the lab colour space before the channel can be deployed. Figure [3] illustrates this distinction. As shown, the two images are split into bright, red-green, and blue-yellow, respectively. The model enters the *L* channel and estimates values for channels *a* and *b*. The estimated *a* and *b*, respectively, are compared with the original *a* and *b*, respectively, to determine similarity. To obtain the output image, we merge the original *L* channel with the predictions for *a* and *b* (Fig. 4).

4.3 Generator

The generator's encoding and decoding components use the same architecture as U-Net. The narrowing route consists of one by one convolution that makes up the network's last layer, and 4 × 4 convolution layers with a stride of 2 for down-sampling. Each procedure is followed by two stations [9]. Every unit in the route consists of a 4 × 4 transposed convolutional layer that uses stride 2 for up-sampling, batch normalization, an activation map from the narrowing path for a mirrored layer, and a ReLU activation function at the end. Finally, the ReLU activation function. A 1 × 1 bridge makes up the network's final layer station dynamic pooling layer,

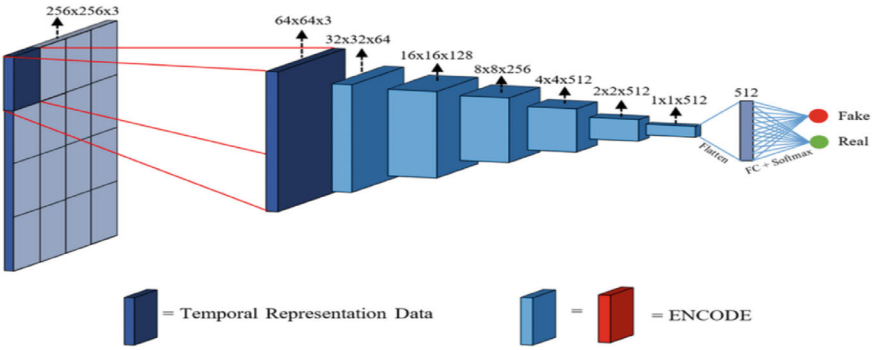

Fig. 5 Patch-GAN [2]

which is similar to convolution. We use a hyperbolic tangent function for the final layer.

4.4 Discriminator (Patch-GAN)

In this case, we utilize the patch-GAN architecture with a U-Net-like constricting path. A series of 4×4 stride 2 convolutional layers increase the number of channels by two after each down-sampling [9]. Following each convolutional layer is batch normalization, which comprises leaky-ReLU activation with a slope of only 0.2. Irrespective of input is legitimate or fake, a sigmoid function is executed after the final layer return probabilities for 70×70 patches (Fig. 5).

5 Training Strategies

We employ the Adam optimizer with weights from [10] to train our model. We utilized a discriminator and a generator we manually reduced the training rate by at least ten percent each time the loss function started to level off, starting with an initial learning rate of 2×10^{-4}. Following the guidelines, we selected hyperparameter as our $\lambda = 100$. This will force the generator to produce an image that resembles the ground truth.

- Batch normalization

A really deep neural network type of training called batch normalization, the signals are normalized to a layer in mini-batches. Consequently, there is a notable decrease in the quantity of training epochs needed to build a deep network and stabilization of cognitive development.

- Activation function leaky ReLU

Leaky rectified linear unit, or leaky ReLU, is a type of activation function style that is based on ReLU but has a slight negative slope rather than a flat slope for values. Prior to training, gradient coefficients are established. In other words, they are not acquired through training.

- One-sided label smoothing

Label smoothing is an approach that provides smoothed labels to a discriminator network. This means that instead of marking each example as 1 (true) or 0 (false), you can use decimal values like 0.9 (true), 0.7(true), 0.1 (false), or 0.3(false).

- Activation function Tanh

Tanh can be thought of as an improved logistic sigmoid. The range of the tanh function is (− 1 to 1). Tanh also has a sigmoidal form with an s shape. The benefit of this is that the tanh graph will show the negative inputs as highly negative and the zero inputs as mapped close to zero.

- Skip connections

When more layers with particular activation functions are added to neural networks, the gradients of the loss function approach zero, making the network difficult to train. ResNet18's fundamental idea is to stack the remaining skip blocks together. In order to maintain the gradient, we employ an identity function.

6 Results

The result of the model after training the GAN. Comparing the picture provided to the Resnet-18 model, U-Net (Tanh as activation function) model and U-Net (leaky ReLU) we can notice that a faultless combination of colourization.

The results demonstrate that ResNet18 works better than competing algorithms and generates colour images with higher SSIM ratings. This shows that ResNet18 produces more accurate and lovely colour rendering because it is better at grasping the fundamental structure and characteristics of input greyscale images.

The study's findings have important implications for image colourization because they suggest that ResNet18, rather than U-Net with either leaky or Tanh ReLU activation, may be a more suitable neural network architecture for this task. This might aid in raising the calibre of colourized images used in applications like video improvement, artistic rendering, and photo restoration. To further enhance the performance of ResNet18, additional study may be required to investigate the possible advantages of various neural network topologies for this task as well as to optimize the training procedure and hyperparameters.

We have seen that there are some cases of incorrect staining. Images with high jitter are often tinted green maybe this happens because of the model that typically

turns green anytime it detects a region of high volatility pixel intensity value due the vast amount of green-coloured images in the training sample. In pictures with a clear sky, the hue is very obvious. Where the sky is brightly coloured, there is an odd blue-to-bright-yellow hue gradation.

- ResNet18 (Leaky ReLU activation) Results

  See Figs. 6, 7, 8 and 9.

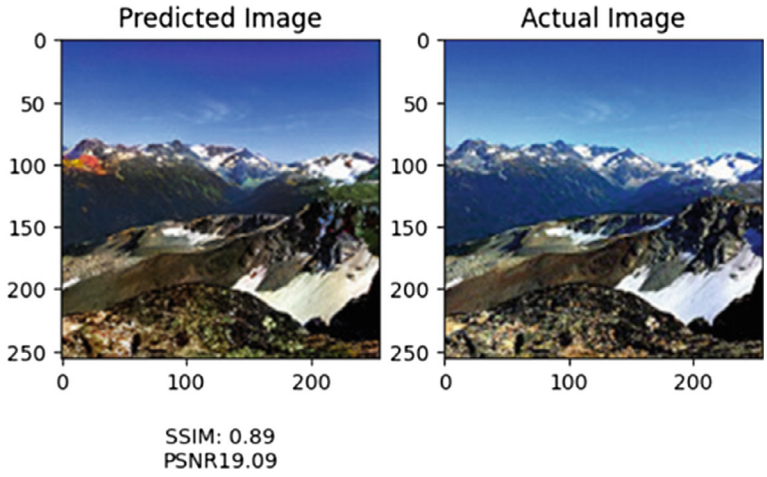

Fig. 6 Actual versus model: image comparison (SSIM, PSNR)

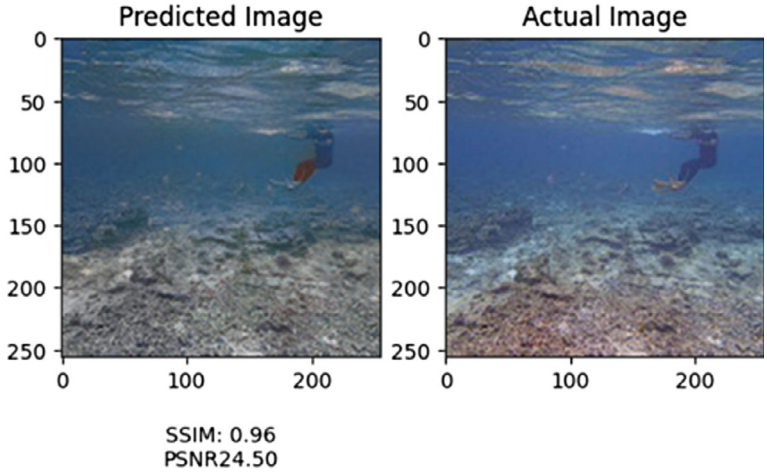

Fig. 7 Actual versus model: image comparison (SSIM, PSNR)

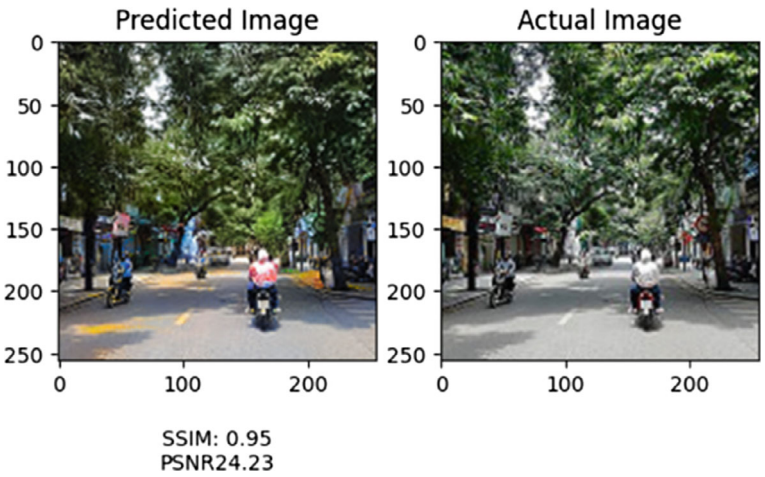

Fig. 8 Actual versus model: image comparison (SSIM, PSNR)

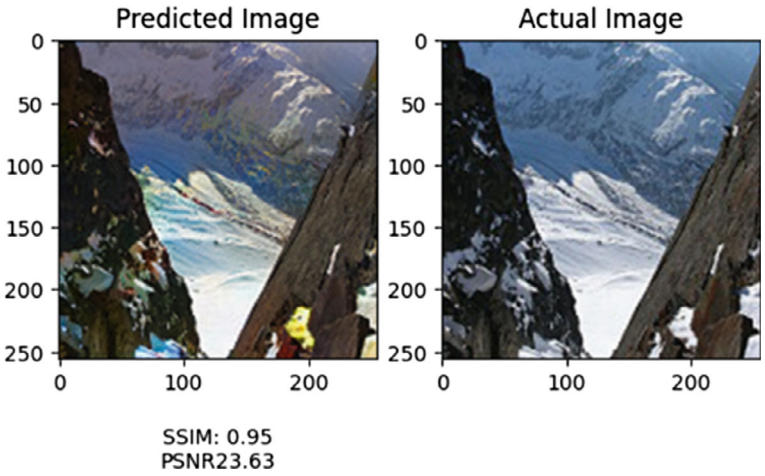

Fig. 9 Actual versus model: image comparison (SSIM, PSNR)

- U-Net (Tanh activation) Results

  Figs. 10, 11, 12 and 13.

- U-Net (Leaky ReLU activation) Results

  See Figs. 14, 15, 16 and 17.

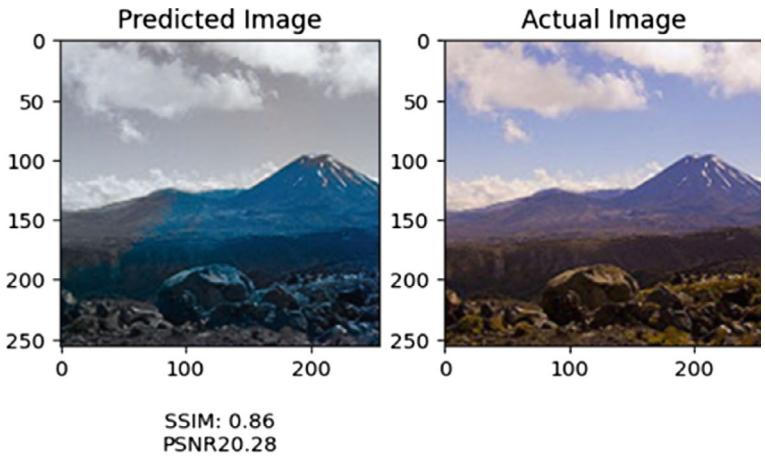

Fig. 10 Actual versus model: image comparison (SSIM, PSNR)

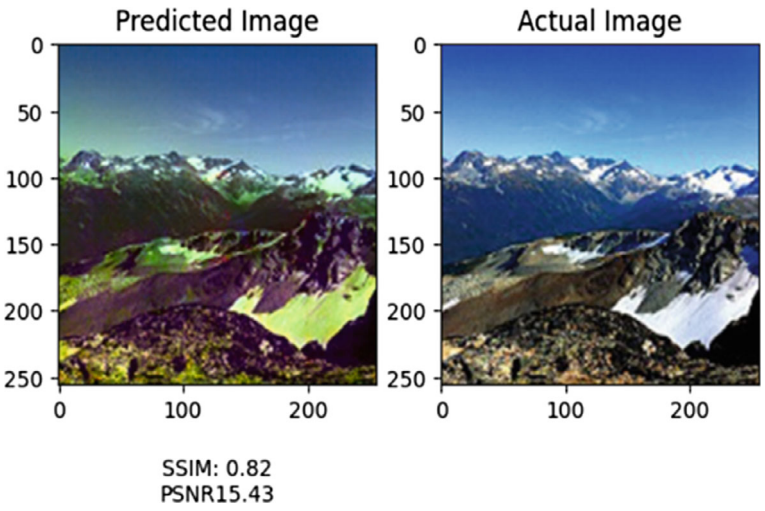

Fig. 11 Actual versus model: image comparison (SSIM, PSNR)

- ResNet18 (Tanh activation) Results

See Figs. 18, 19, 20, 21, 22 and 23.

ResNet18 with leaky ReLU received the greatest PSNR and SSIM score of 22.8 and 0.93 based on the obtained PSNR and SSIM values, indicating superior preservation of image quality compared to the other models.

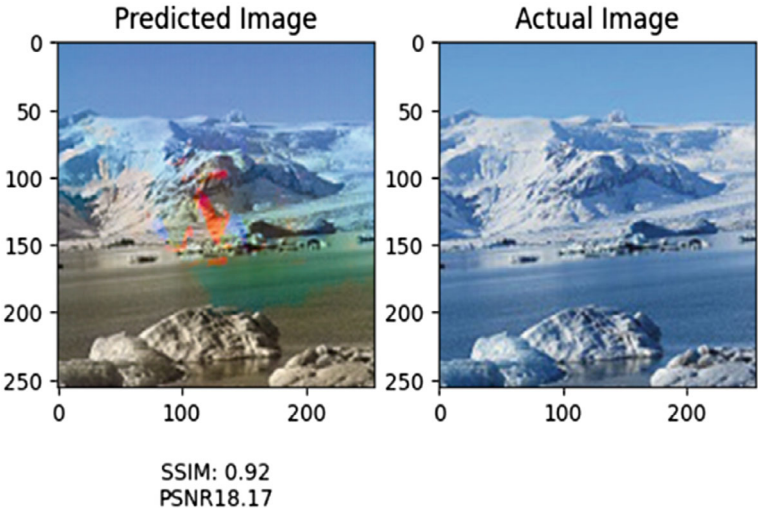

Fig. 12 Actual versus model: image comparison (SSIM, PSNR)

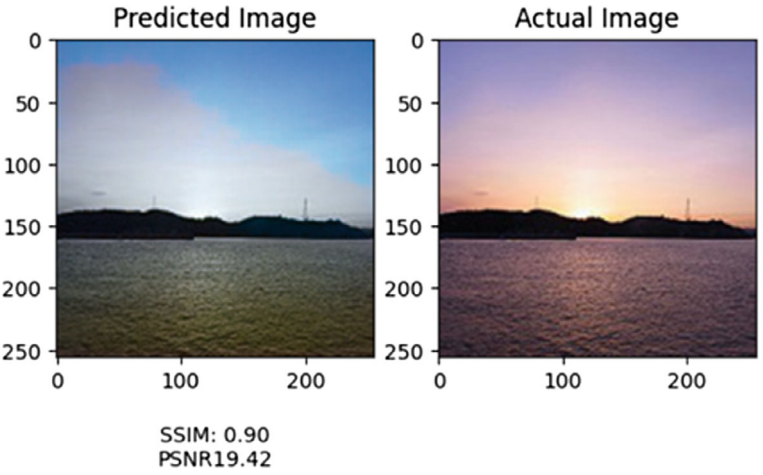

Fig. 13 Actual versus model: image comparison (SSIM, PSNR)

The advantage of ResNet18 with leaky ReLU in terms of structural similarity (SSIM) and image quality preservation (PSNR) is further supported by these findings. The increased PSNR value indicates that ResNet18 with a leaky ReLU was able to produce colourized images with less distortion and greater integrity to the original image.

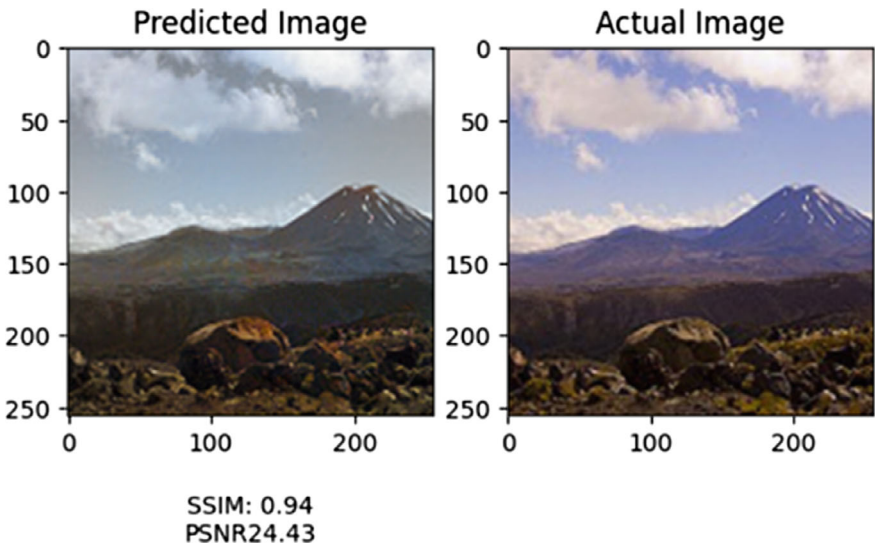

Fig. 14 Actual versus model: image comparison (SSIM, PSNR)

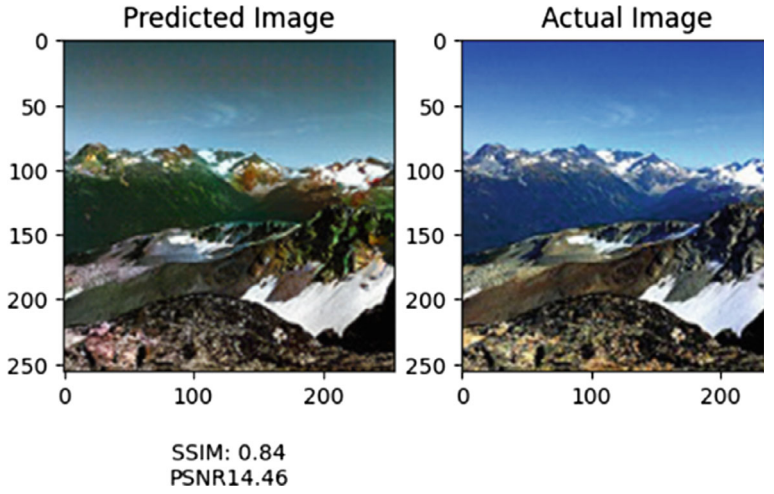

Fig. 15 Actual versus model: image comparison (SSIM, PSNR)

In conclusion, ResNet18 with leaky ReLU outperformed U-Net with Tanh activation, ResNet18 with Tanh activation, and U-Net with leaky ReLU activation in terms of structural similarity and image quality preservation, making it a more useful model for the task of image colourization.

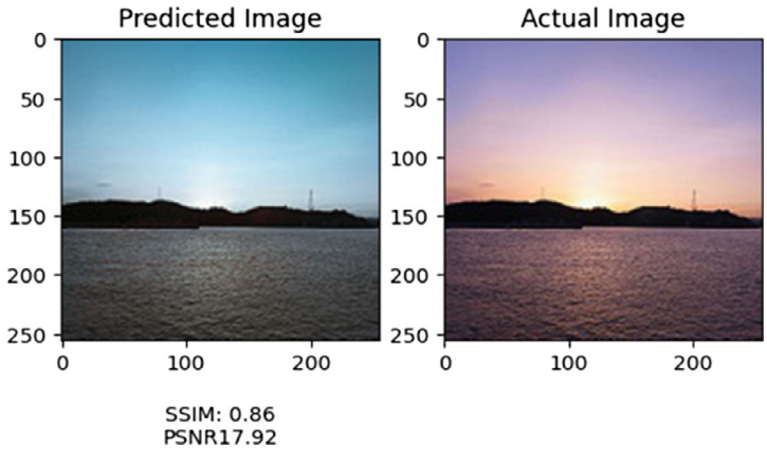

Fig. 16 Actual versus model: image comparison (SSIM, PSNR)

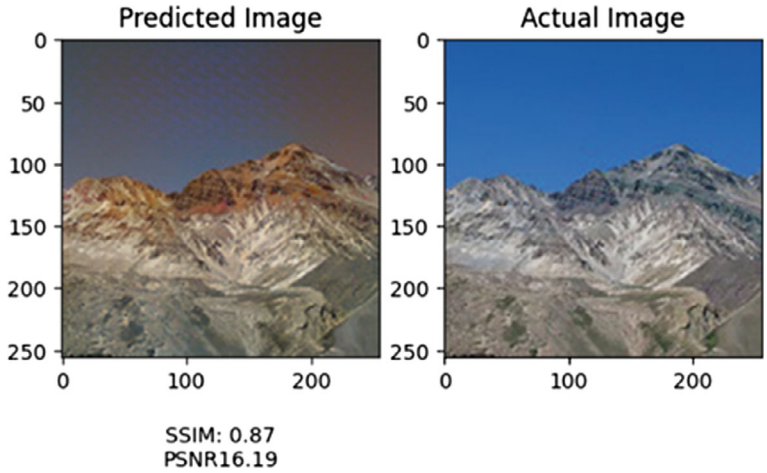

Fig. 17 Actual versus model: image comparison (SSIM, PSNR)

7 Conclusions

The results of this study's comparison of the effectiveness of four distinct neural network designs for image colourization were assessed using the SSIM metric. According to the study, ResNet18 was able to capture the underlying features and structures of the input greyscale images with the highest level of colourized image quality.

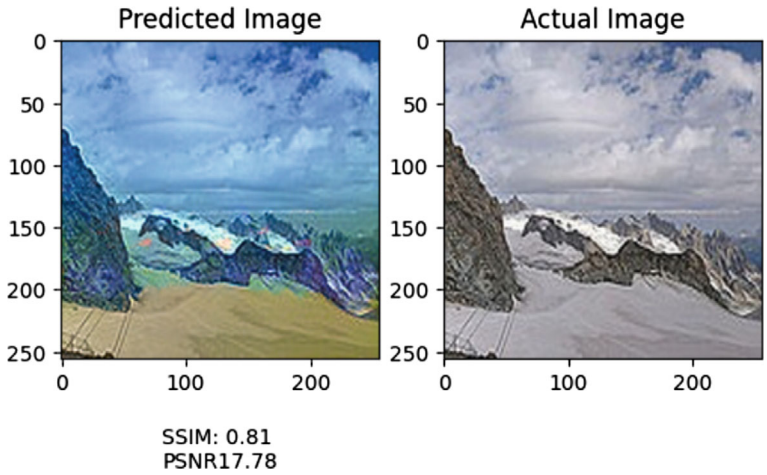

Fig. 18 Actual versus model: image comparison (SSIM, PSNR)

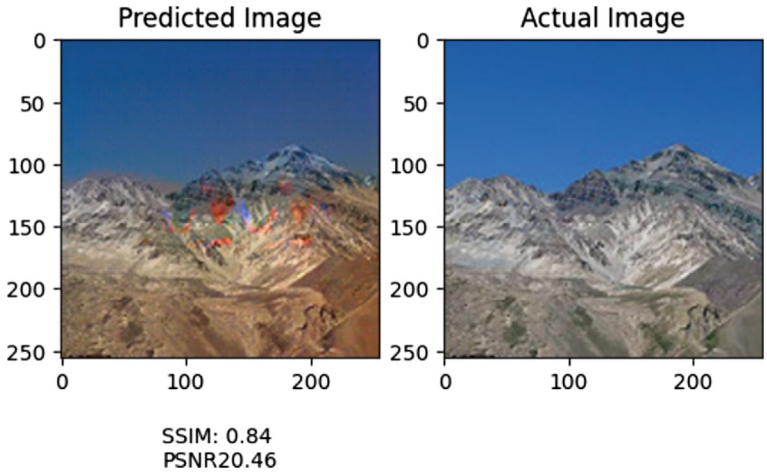

Fig. 19 Actual versus model: image comparison (SSIM, PSNR)

The importance of these findings stems from the fact that image colourization is a crucial process with multiple real-world applications in industries including photography, film restoration, and creative rendering. Images' visual appeal and historical significance can be increased with accurate and efficient colourization, increasing their viewer accessibility and educational value.

Compared to U-Net with either Tanh or leaky ReLU activation, the findings of this study imply that ResNet18 may be a more suitable neural network architecture for image colourization. To fully understand the possible advantages of various neural network topologies, more research is required and to optimize the training process and

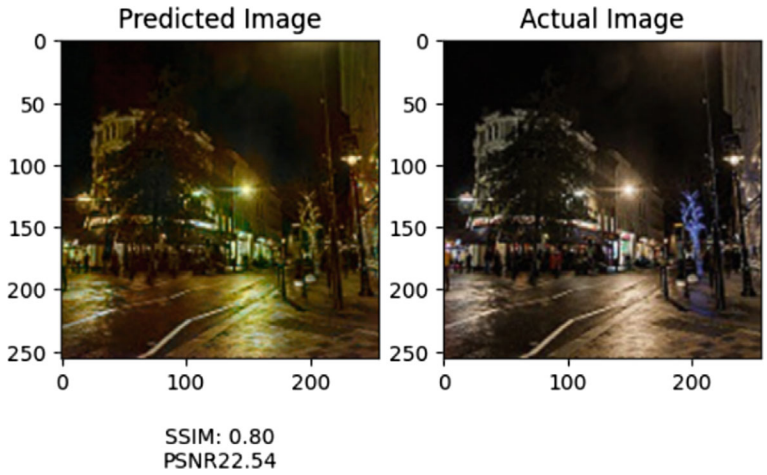

Fig. 20 Actual versus model: image comparison (SSIM, PSNR)

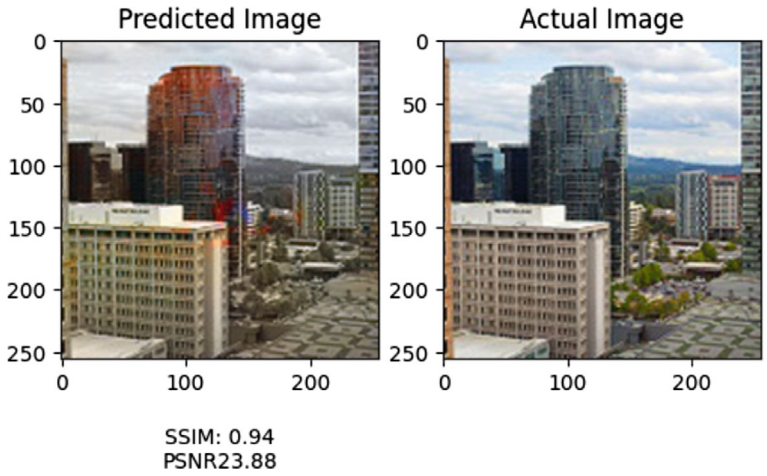

Fig. 21 Actual versus model: image comparison (SSIM, PSNR)

hyperparameters in order to further improve the performance of ResNet18. Overall, this study adds to our knowledge of the advantages and disadvantages of various neural network designs for colourization of images and offers information that may be utilized to create colourization models that are more effective and efficient in the future.

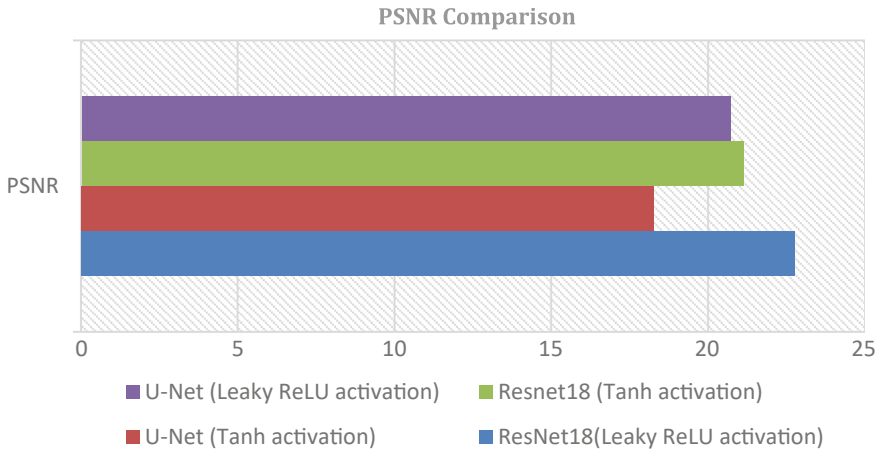

Fig. 22 Comparison among PSNR values of different GAN models

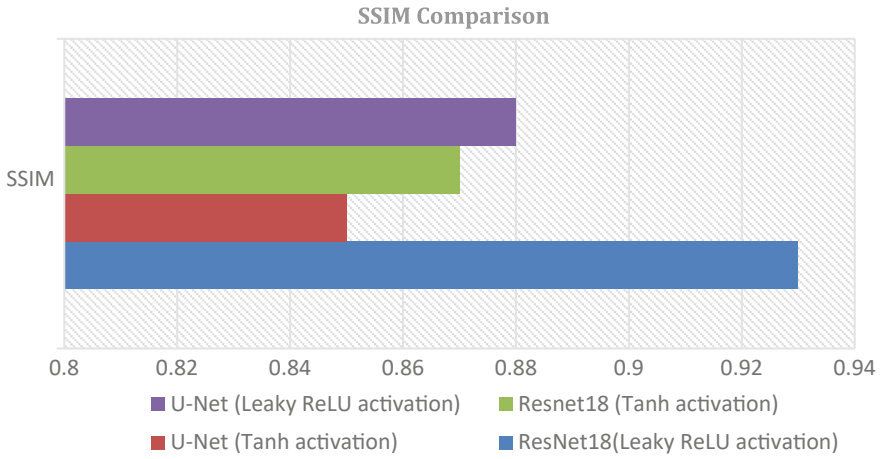

Fig. 23 Comparison among SSIM values of different GAN models

Acknowledgements We would like to thank everyone who assisted me with this project in advance. We truly thank you. Dr. Anshu Khurana and Ms. Seems Kalonia, our project mentors, for their invaluable support and direction. Their inspiration and advice were crucial to the project's success. Without their really helpful recommendations and agreeable demeanour, we could not have finished this assignment. We would also like to thank the teachers for their thoughtful support and cooperation all the way through the lifecycle.

References

1. A diagram of generative adversarial network [Diagram]. Google for Developers https://developers.google.com/machine-learning/gan/gan_structure
2. Ganokratanaa, T., Aramvith, S., Sebe, N.: Unsupervised anomaly detection and localization based on deep spatiotemporal translation network. IEEE Access **8**, 50312–50329 (2020)
3. Levin, L.A., Venkatesan, R.: An average case NP-complete graph colouring problem. Comb. Probab. Comput. **27**(5), 808–828 (2018)
4. Mirza, M., Osindero, S.: Conditional generative adversarial nets. arXiv preprint arXiv:1411.1784. Phillip Isola Jun-Yan Zhu Tinghui Zhou Alexei A. Efros Berkeley AI Research (BAIR) Laboratory, UC Berkeley, Image-to-Image Translation with Conditional Adversarial Networks (2014)
5. Zayd, M.H., Yudistira, N., Wihandika, R.C.: Image colorization using U-Net with skip connections and fusion layer on landscape images. arXiv preprint arXiv:2205.12867 (2022)
6. Zhang, S., Zhu, C., Sin, J.K., Mok, P.K.: A novel ultrathin elevated channel low-temperature poly-Si TFT. IEEE Electron Device Lett. **20**(11), 569–571 (1999)
7. Hwang, J., Zhou, Y.: Image colorization with deep convolutional neural networks. In Stanford University, Tech. Rep (2016)
8. Kundu, R., Das, R., Geem, Z.W., Han, G.T., Sarkar, R.: Pneumonia detection in chest X-ray images using an ensemble of deep learning models. PloS one **16**(9), e0256630 (2021)
9. Anwar, S., Tahir, M., Li, C., Mian, A., Khan, F.S., Muzaffar, A.W.: Image colorization: a survey and dataset. arXiv preprint arXiv:2008.10774 (2020)
10. Zhang, R., Zhu, J.Y., Isola, P., Geng, X., Lin, A. S., Yu, T., Efros, A.A.: Real-time user-guided image colorization with learned deep priors. arXiv preprint arXiv:1705.02999 (2017)
11. Dhir, R., Ashok, M., Gite, S.: An overview of advances in image colorization using computer vision and deep learning techniques. Rev. Comput. Eng. Res. **7**(2), 86–95 (2020)
12. Huang, S., Jin, X., Jiang, Q., Liu, L.: Deep learning for image colorization: current and future prospects. Eng. Appl. Artif. Intell. **114**, 105006 (2022)
13. Kiani, K., Hematpour, R., Rastgoo, R.: Automatic grayscale image colorization using a deep hybrid model. J. AI Data Mining **9**(3), 321–328 (2021)
14. Nazeri, K., Ng, E., Ebrahimi, M.: Image colorization using generative adversarial networks. In: International Conference on Articulated Motion and Deformable Objects, pp. 85–94. Springer, Cham (2018)
15. Simonyan, K., Zisserman, A.: Very deep convolutional networks for large-scale image recognition. arXiv preprint arXiv:1409.1556 (2014)
16. Welsh, T., Ashikhmin, M., Mueller, K.: Transferring color to greyscale images. In: Proceedings of the 29th Annual Conference on Computer Graphics and Interactive Techniques, pp. 277–280 (2002)
17. Jam, J., Kendrick, C., Drouard, V., Walker, K., Hsu, G.S., Yap, M.H.: Symmetric skip connection Wasserstein GAN for high-resolution facial image inpainting. arXiv preprint arXiv:2001.03725 (2020)

Development of Electrical Power Train for Conversion of Motorcycle with an Internal Combustion (IC) Engine to an Electric Bike

Sachin Chavhan and Mahesh Kumbhar

Abstract The global transportation sector is facing numerous challenges, including increase in carbon emissions, air pollution, and dependence on fossil fuels. In response, the emergence and rapid growth of electric vehicles (EVs) have garnered significant attention as a sustainable transportation solution. While going for the new electric vehicles, the old internal combustion (IC) engine-driven vehicles are being scrapped. Instead of scrapping these vehicles, a transformation approach can be adopted to convert them into electric vehicles. This paper focuses on the conversion of IC engine bike into electric bike as a retrofitting approach to transform conventional two-wheelers into eco-friendly e-bike. The key work involved in the conversion process include the removal of the IC engine and related parts, designing and selection of electrical system components and assembling. The system designing, component selection procedure including function of each element is discussed in this paper. From the end result, it can be concluded that the conversion of a conventional bike into an electric bike is a much cheaper option than buying a new bike. Also operational efficiency of the converted electric bike is significantly higher than the conventional.

Keywords Electric bike · BLDC motor · Controller · E-bike calculations · Battery requirements

S. Chavhan (✉)
Shivaji University, Kolhapur, Walchand College of Engineering, Sangli, Maharashtra, India
e-mail: sachin.chavhan22@gmail.com

M. Kumbhar
Department of Electronics and Telecommunication Engineering, RIT, Islampur, Maharashtra, India
e-mail: mahesh.kumbhar@ritindia.edu

© The Author(s), under exclusive license to Springer Nature Singapore Pte Ltd. 2025

H. P. Singh et al. (eds.), *Recent Developments in Control, Automation and Power Engineering*, Lecture Notes in Electrical Engineering 1303,
https://doi.org/10.1007/978-981-96-0047-2_38

1 Introduction

Transportation plays a crucial role in the functioning of society, enabling economic activities, facilitating social interactions, and connecting people and places. The conventional transportation is based on fossil fuels, and the consumption of which generates huge carbon footprints. The electric vehicle can significantly reduce emission of greenhouse gases and make the transportation eco-friendly [1]. Electric two-wheeler bikes are gaining popularity on account of convenience and cheaper traveling cost for local transportation. To develop an electric bike, electrical engineering domain and mechanical engineering domain need proper addressing. The electrical part includes motor, speed controller, and battery whereas mechanical parts include frame and fabrication [2]. In designing electrical parts, the designer has to make a proper choice of motor speed and power ratings, battery ratings, and suitable speed controller [3]. The mechanical part involves selection of material to be used for fabrication, frame (chassis) design, design of steering, suspension, and brakes [4]. An electric bike is characterized by its top speed and travel range in single charging of the battery. The features of solar-based charging, closed-loop speed control, etc., add to the performance of the bike [5].

While opting for electric bikes, the conventional IC engine bike may not be completely scrapped. Rather, retrofitting [6] is possible to transform an IC engine bike into an electric bike. To perform this alteration, the IC engine drivetrain is to be replaced by electric drivetrain. Even a conventional wheelchair is converted into an electric quad bike to assist physically challenged persons [7]. For an electric tricycle, a motor can be added with appropriate speed controller and battery to assist the human in propelling. The conventional bicycles can thus cover more distance without subjecting the rider to paddling stress [8] and provide a comfortable and enjoyable ride. An electric bike frame should be designed with an objective to get a comfortable ride with maximum efficiency and minimum cost. Finite element analysis tools are applied in designing bike frame to achieve higher efficiency [9]. The electric bike is often added with battery energy management systems and battery thermal management systems to optimize battery performance. Renewable energy-based battery charging further improved the travel range [10].

As this paper focuses on conversion of IC engine bike into electric bike, the conventional powertrain component needs replacement with electric powertrain. For this conversion, the electric powertrain components need to be designed or calculated accordingly. The most important calculation is for the power rating of the electric motor. The motor power rating calculation is based on the total tractive force [11].

Hub motor, mid drive motor, and friction drive motor are the common types of motors for electric bikes. A hub motor is the most popular one. It is located within the hub of the wheel. It provides direct power to the wheels and hence smooth riding experience. While choosing a motor for an electric bike, the factors considered are—load requirements, terrain, compatibility with bike frame, desired speed, and budget. A review of different types of AC and DC motors is discussed in [12] with working principle, operational requirements, features, and shortfalls. Induction

motor and brushless DC (BLDC) motor are identified as best suitable motor for electric powertrain [13]. The multi-criteria analysis [14, 15] considering torque ripple, noise level, efficiency, cost, size, dependability, fault tolerance, overload capacity, power density, wide speed range, and control simplicity has shown that the switched reluctance motor (SRM), induction motor, and BLDC motor standouts among all the motor. A detailed comparison of traction motors for various electric vehicles is presented in [16]. The trends suggest that the manufacturers are looking forward to the axial flux PMDC motor and use of rare earth permanent magnet material for reducing torque ripples. The SRMs are only suitable for lower power ratings of electric bikes [17]. The BLDC motor is the unanimous choice of many researchers for propulsion of electric vehicles on account of high power density [18], high efficiency, torque-speed characteristics, and cost. A comparative study [19] of in-runner (hub type) and outrunner (mid drive mount) BLDC motor suggests that a designer has to make a choice on the basis of torque requirements and frame structure. Commonly, in runners BLDC motors are preferred by the designers.

The performance of electric bikes often depends on the battery used. The performance of batteries for electric vehicle application is characterized by energy density, weight, lifespan, lifecycles, charging time compatibility, and capacity. Earliest electric vehicle used a lead acid battery which was substituted with nickel cadmium (NICD) battery and nickel metal hydride (NIMH) battery. Sodium-ion batteries are still in the research and development phase, and commercial availability is relatively limited compared to lithium-ion batteries. The latest versions come with lithium-ion (Li ion) or lithium polymer (LiPO) batteries [20]. The lithium-ion battery is constructed as a battery pack consisting of a series and parallel combination of large no. of cells. Any inconsistency in either of connected cells results in reduced battery life. Battery assessment techniques [21] and testing strategies are useful in isolating such underperforming cells. Disposal of such cells leads to massive environmental pollution; hence, recycling of lithium-ion batteries helps in protecting the environment [22]. While making the choice of battery rating, the travel range of the vehicle and motor ratings are considered [23]. The sophisticated systems consist of a battery energy management system (BEMS) and battery thermal management system (BTMS) for battery management in electric vehicles. The BEMS covers battery charging and protection whereas BTMS is responsible for maintaining the battery temperature [24, 25]. Recently, super-capacitors and ultra-capacitors have been introduced for battery management [26].

The interface between energy storage battery and motor is accomplished through a motor controller also called an electric bike (e-bike) controller. Its prime function is power conversion. For BLDC motors, a three-phase inverter is constructed to provide the required signal to set the motor into rotation. The e-bike control unit takes reference from throttle and brakes and accordingly adjusts the speed of the motor [27]. The recent e-bike controller also integrates accessories like headlamps, pass sensors, tilt sensor, Bluetooth devices, and many more [28]. The speed control of BLDC motor is done with PWM control in open-loop [29] and closed-loop control with feedback of speed sensor [30]. The advanced control techniques in the form of field-oriented control (FOC) and direct torque control (DTC) are also being implemented

Fig. 1 Photograph of bike under consideration

in e-bike controllers for BLDC motors [31]. Some researchers are still working on improving the performance of speed control by modifying these techniques, applying optimization techniques and modifying the inverter drive.

For the desired features of the electric bike, a proper selection of BLDC motor ratings (speed and power), battery capacity (voltage and ampere-hour), and motor controller is desired. The calculations and selection of these components for converting conventional IC engine bike into electric bike are subsequently discussed.

2 IC Engine Bike Under Consideration

For experimentation purposes, a 1992 model 'Kinetic Luna' is considered. Kinetic Luna had a 50 cc two-stroke petrol engine making power of 2.2 BHP and 4.2 Nm torque. Luna was a common bike for transportation in rural and urban areas of India in 1980 and 90s. Figure1 shows the photograph of the bike in IC engine form. From this bike, the engine, carburetor, paddle assist, chain, and rear wheels are removed. These components formed a mechanical powertrain for the bike. For conversion into electric bike, these components are replaced with BLDC hub motor, BLDC motor controller, and lithium-ion battery.

3 Electric Bike Component Calculations

The main component for calculation is motor ratings. The motor rating is dependent on total force or power required to set the bike into motion [11]. The important considerations to be noted for calculation of driving components of electric bike are mentioned in Table 1.

Table 1 Parameters considered for electric bike calculations

Parameter	Value
Raider weight	80 kg
Speed of vehicle (V)	30 KM/Hr
Coefficient of rolling resistance (μ)	0.015
Gravitational acceleration	9.81 M/S^2
Air density (ρ)	1.25 kg/M^3
Weight of bike	40 kg
Front area (A)	0.5 M^2
Drag coefficient (Cd)	0.3–0.7
Slope angle (θ)	30°
Radius of the wheel (r)	0.2032 m
Acceleration (a)	0.833 m/s^2

The total traction force of electric bike is,

$$F_T = F_R + F_{\text{ad}} + F_{\text{slope}} + Ma + \frac{A}{r^2} \tag{1}$$

where

F_T = traction force,
F_R = Rolling resistance,
F_{ad} = Air drag,
F_{slope} = Hill climbing force,
M = Mass,
a = Acceleration,
r = Radius of the wheel.

The rolling resistance is calculated as

$$F_R = \mu Mg \cos\theta \tag{2}$$

$$F_R = 0.015 \times 120 \times \cos(30) = 1.55N$$

The air drag force is,

$$F_{\text{ad}} = \frac{\rho C_d A V^2}{2} \tag{3}$$

$$F_{\text{ad}} = \frac{1.25 \times 0.3 \times 0.5 \times 8.33^2}{2} = 6.50\,N$$

The climbing force is,

$$F_{\text{slope}} = Mg \sin\theta \tag{4}$$

$$F_{\text{slope}} = 120 \times \sin(30) = 60N$$

Acceleration force is,

$$F_a = Ma \tag{5}$$

$$F_a = \frac{120}{9.81} \times 0.833 = 10.18$$

and

$$\frac{A}{r^2} = \frac{0.5}{0.2032^2} = 12.10N$$

Therefore the total traction force is,

$$F_T = 90.33N$$

The torque required for motor is,

$$torque(\tau) = F_T r \sin\theta = 90.33 \times 0.2032 \times \sin(30) = 9.17\,\text{Nm}$$

The power rating of the motor is calculated from torque as

$$P = \frac{\tau.n}{9.5488} \tag{6}$$

and

$$P = \frac{9.17 \times 392}{9.5488} = 376W$$

The required speed of the hub motor is calculated by considering the wheel specification as follows:

The diameter (d) of wheel is 0.4064 M.

The circumference of wheel = π.d = 1.276 M.

Hence in one rotation of the wheel, the vehicle travels a distance of 1.276 M. Thus, for a traveling distance of 30 KM (30,000 M), the number of rotations of the wheel required is = 23,511. These many rotations are required in one hour to attain a speed of 30 KM/Hr. Thus, the required RPM of motor is,

$$RPM = \frac{23511}{60} = 391.84$$

Hence, for the construction of electric bike a brushless DC motor (a standard motor available in market) with following specifications is selected and the photograph of the same is shown in Fig. 2a. This is later fitted on the wheel rim with the help of spokes. The assembly of this with tube and type completes the rear wheel of the e-bike as seen in Fig. 2b.

$$\text{Power} = 350\ \text{W},\ \text{Voltage} = 36\ \text{V},\ \text{and Speed} = 400\ \text{RPM}$$

The developed vehicle is expected to reach 30 KM/Hr speed and travel 75 KM range in single charge of battery; hence, a lithium-ion battery is selected with voltage rating of 36 V and 30 Ah current capacity. Photograph of the selected battery is shown in Fig. 3. For battery charging, ENTROX 36 V, 10 A, 350 W lithium-ion battery charger is used. The time taken to charge the battery is 3 Hrs. The charger has efficiency of 90%. Hence for full charging of 36 V, 30 Ah battery, the total electrical energy is,

$$\text{EE} = \text{v} \times \text{i} \times \text{t} = 1080\ \text{Watt Hr}$$

With efficiency of 90%, energy sourced by the supply is,

$$E\ \text{supply} = {}^{\text{EE}}/_{0.9} = 1200\ \text{Watt Hr}$$

(a) (b)

Fig. 2 **a** Photograph of BLDC hub motor. **b** Rear wheel assembly

Fig. 3 36 V, 30 Ah lithium-ion battery

$= 1.2$ units of electricity.

For commercial electrical supply, the electricity bill (inclusive of all taxes and charges) is Rs. 20/- per unit.

Hence, cost of single charging is $20 \times 1.2 =$ Rs. 24/-.

The running cost = cost of charging / travel range = Rs. 0.32/KM.

While the same bike was running on petrol, the running cost with mileage of 40 KMPL was Rs. 2.5/KM. considering the cost of petrol to be Rs. 100/Ltr.

For driving the BLDC motor, an electric bike controller is chosen. For a 350 W brushless dc motor, this motor controller operates in the 36 to 48 V operating voltage range at a maximum current of 15 A. It has add-ons for the motor, the accelerator, the brake, the battery, battery charging, the brake light, and the power lock. The photograph of the BLDC motor controller is shown in Fig. 4, and those of accelerator throttle and brake level are shown in Figs. 5 and 6, respectively.

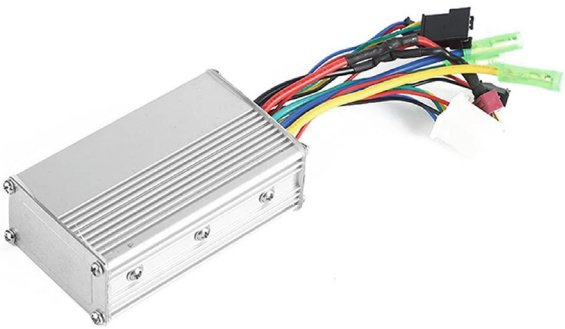

Fig. 4 BLDC motor controller

Fig. 5 Accelerator throttle

Fig. 6 Brakes

Table 2 Component specifications

Items	Ratings
BLDC hub motor	350 W, 36 V, 400 RPM
Battery (lithium-ion)	36 V, 30 Ah
Throttle and brake lever	HALL effect sensor-based throttle and brake switch integrated
Controller	SNA 350 W BLDC motor controller
Battery charger	ENTROX 36 V, 10 A, 350 W lithium-ion battery charger

Table 2 provides the summary of specifications of components chosen for converting conventional IC engine bike into e-bike. Photographs of developed electric bike are shown in Fig. 7.

Fig. 7 Photograph of developed bike

4 Conclusion

Electric bikes are the preferred choice of the users for short range travels. In the process of conversion of an IC engine bike into an electric bike, the engine, carburetor-throttle, and petrol fuel storage tank are, respectively, replaced by the BLDC motor, speed controller, and battery storage system. The conversion process is a lot cheaper than buying a new electric bike. With electric vehicles, not just air pollution but noise pollution is also significantly reduced. The permanent magnet brushless DC motor offers greater efficiency, longevity, better torque-speed characteristics, and almost noise-free operation; hence, the developed bike runs silently. By converting the conventional IG engine-based bike to electric bike, the operation cost, i.e., traveling cost, can be reduced from Rs. 2.5 per km to Rs. 0.32 per km. Thus, the conversion of conventional bikes into electric bikes results in pollution-free and cost-effective traveling.

References

1. Keseev, V., Mihaylov, G., Ivanova, E., Iliev, T.:Competitiveness of electric vehicles. In: 2016 12th IEEE International Symposium on Electronics and Telecommunications (ISETC), Timisoara, Romania, pp. 3–6. https://doi.org/10.1109/ISETC.2016.7781043
2. Dimitrov, V.:Overview of the ways to design an electric bicycle. In: 2018 IX National Conference with International Participation (ELECTRONICA), Sofia, Bulgaria, pp. 1–4. https://doi.org/10.1109/ELECTRONICA.2018.8439456

3. Keseev, V.P.: Electric bicycle design experiences and riding costs. In: 2020 7th International Conference on Energy Efficiency and Agricultural Engineering (EE&AE), Ruse, Bulgaria, pp. 1–4. https://doi.org/10.1109/EEAE49144.2020.9279070
4. Reddy, N.P.K., Prasanth, K.V.S.S.V.: Next generation electric bike E-bike. In: 2017 IEEE International Conference on Power, Control, Signals and Instrumentation Engineering (ICPCSI), Chennai, India, pp. 2280–2085. https://doi.org/10.1109/ICPCSI.2017.8392123
5. Gomathi, S., Gnanaraj, F.F., Faridhabanu, M.R., Vengadapathiraj, M., Kamalakannan, R., Arthy, M.: Design and parameter selection of E-Vehicle. In: 2022 International Conference on Computer, Power and Communications (ICCPC), Chennai, India, pp. 349–354. https://doi.org/10.1109/ICCPC55978.2022.10072127
6. Kumar, N.A., Joseph, A.S.:Retrofitting of conventional two-wheelers to electric two-wheelers. In: 2021 13th IEEE PES Asia Pacific Power & Energy Engineering Conference (APPEEC), Thiruvananthapuram, India, pp. 1–8. https://doi.org/10.1109/APPEEC50844.2021.9687799
7. Sujitha, S., Kumar Reddy, M.R., Harshitha, R.: Design and fabrication of quad bike for physically challenged person. In: 2022 International Conference on Smart Generation Computing, Communication and Networking (SMART GENCON), Bangalore, India, pp. 1–4. https://doi.org/10.1109/SMARTGENCON56628.2022.10084305
8. Orr, T., Robertson, N., Hill, J., McAllister, K., Hoopes, C., Jaafar, I.:Design, analysis, and manufacturing of a novel electrically-assisted human powered vehicle. In: 2022 Intermountain Engineering, Technology and Computing (IETC), Orem, UT, USA, pp. 1–6. https://doi.org/10.1109/IETC54973.2022.9796891
9. Mitesh, M.T., Manish, K.B., Kuldeep, M.S., Darshan, H.P., Chirag, D.A.: Design & development of e-bike—a review. Icon. Res. Eng. J. **1**(5) (2017)
10. Rahul, B.G., Parth, C.P., Farhan, T.D., Azlankhan, A.P., Viranchi, S.: Review for design and development of electric bike. Int. J. Sci. Res. Develop. **5**(09), 889–893 (2017)
11. Prakruti, J.N.: Design and control of light weight electric vehicle. Int. J. Adv. Eng. Res. Develop. **2**(4), 527–536 (2015)
12. Tahir, A.Z., Ahmadu, A.G., Maruf, A.A.: Review of motors for electric vehicles. J. Sci. Res. Rep. **24**(6), 1–6 (2019); Article no. JSRR.50678
13. Aliasand, A.E., Josh, F.T.: Selection of motor for an electric vehicle: a review. Mater. Today Proceed. **24**, 1804–1815 (2020)
14. Dimitrios, R., Stavros, D.K., Dimitrios, D.P., George, V., Konstantinos, G.A., Christos-Spyridon, K.: Comparative review of motor technologies for electric vehicles powered by a hybrid energy storage system based on multi-criteria analysis. MDPI J. Energ. **16**(2555) (2023)
15. Hicham, E.H., Mourad, Z., Ahmed, C., Oussama, L., Nasr, G.: A multi-criteria analysis and trends of electric motors for electric vehicles. MDPI World Electric Veh. J. **13**(65) (2022)
16. Krings, A., Monissen, C.: Review and trends in electric traction motors for battery electric and hybrid vehicles. In: 2020 International Conference on Electrical Machines (ICEM), Gothenburg, Sweden, pp. 1807–1813 (2020). https://doi.org/10.1109/ICEM49940.2020.9270946
17. Inte, R.A., Jurca, F.N.:A novel synchronous reluctance motor with outer rotor for an electric bike. In: 2016 International Conference and Exposition on Electrical and Power Engineering (EPE), Iasi, Romania, pp. 213–218 (2016). https://doi.org/10.1109/ICEPE.2016.7781335
18. Sudha, B., Anusha, V., Sachin, S.: A review: high power density motors for electric vehicles. J. Phys. Conferen. Series 1706 (2020)
19. Chlebosz, W., Ombach, G., Junak, J.: Comparison of permanent magnet brushless motor with outer and inner rotor used in e-bike. In: The XIX International Conference on Electrical Machines—ICEM 2010, Rome, Italy, pp. 1–5 (2010). https://doi.org/10.1109/ICELMACH.2010.5608000
20. Chian, T.Y., Wei, W.L.J., Ze, E.L.M., Ren, L.Z., Ping, Y.E., Abu Bakar*, N.Z., Faizal, M., Sivakumar, S.: A review on recent progress of batteries for electric vehicles. Int. J. Appl. Eng. Res. ISSN 0973–4562 **14**(24), 4441–4461 (2019)

21. Weidong, C., Jun, L., Zhaohua, Y., Gen, L.: A review of lithium ion battery for electric vehicle applications and beyond. In: 10th International Conference on Applied Energy (ICAE 2018), pp. 22–25 (2018)
22. Pražanová, A., Knap, V., Stroe, D.I.: Literature review, recycling of lithium-ion batteries from electric vehicles, part i: recycling technology. MDPI J. Energ. **15**(1086) (2022)
23. Mahajan, A., Adhav, S., Anvekar, A.: Design fabrication of e-bicycle and comparative analysis of lead acid battery and lithium ion battery. JETIR **7**(12) (2020)
24. Farisi, S.A., Ajie, G.S., Setyawati, R.B., Stulasti, K.N.R., Azinuddin, Y.R., Sudian, D.A.P.B., Nurfi, R.A., Sulistiyawan, S., (Kiwi) Aliwarga, H.A., Suci, W.G.: Increasing electric bicycle performance using lithium ferro phosphate batteries with a battery management system. J. Energ. Storagetechnol. Appl. **2**(1), 30–37 (2022)
25. Kailong, L., Kang, L., Qiao, P., Cheng, Z.: A brief review on key technologies in the battery management system of electric vehicles. Front. Mech. Eng.**14**(1), 47–64 (2019)
26. Sousa, D.M., Costa Branco, P.J., Dente, J.A.: Electric bicycle using batteries and supercapacitors. In: 2007 European Conference on Power Electronics and Applications, Aalborg, Denmark, pp. 1–10 (2007). https://doi.org/10.1109/EPE.2007.4417425
27. Cheng, J., Lu, C., Zhang, G., Wu, C., Huang, Y.:Research and design of electric vehicle controller based on brushless DC motor. In: 2017 36th Chinese Control Conference (CCC), Dalian, China, pp. 10132–10136 (2017). https://doi.org/10.23919/ChiCC.2017.8028971
28. Dumitrache, F., Carp, M.C., Pana, G.:E-bike electronic control unit. In: 2016 IEEE 22nd International Symposium for Design and Technology in Electronic Packaging (SIITME), Oradea, Romania, pp. 248–251 (2016). https://doi.org/10.1109/SIITME.2016.7777288
29. Faruque, K.F.I., Nawshin, N., Bhuiyan, M.F., Uddin, M.R., Hasan, M., Salim, K.M.: Design and development of BLDC controller and its implementation on e-bike. In: 2018 International Conference on Recent Innovations in Electrical, Electronics & Communication Engineering (ICRIEECE), Bhubaneswar, India, pp. 1461–1465 (2018). https://doi.org/10.1109/ICRIEECE44171.2018.9008597
30. Purnata, H., Yusuf, M., Riyanto, S.D.: Closed loop system BLDC motor for electric-bike. In: 2020 International Conference on Applied Science and Technology (iCAST), Padang, Indonesia, pp. 422–428 (2020). https://doi.org/10.1109/iCAST51016.2020.9557642
31. Mohanraj, D., et al.: A Review of BLDC motor: state of art, advanced control techniques, and applications. IEEE Access **10**, 54833–54869 (2022). https://doi.org/10.1109/ACCESS.2022.3175011

Belief Reliability Evaluation of F-18 LLF System by Disjoint Method

Roopshi Gupta and G. L. Pahuja

Abstract A new reliability metric called belief reliability takes both aleatory and epistemic uncertainty into consideration. Conventional system belief reliability theory depends on a complicated formula for belief reliability that is challenging to understand and apply in practical systems having random and uncertain components**.** To resolve these issues, an efficient method, i.e. disjoint method, is proposed that generates a very smaller number of terms in comparison with conventional decomposition method for belief reliability evaluation of a practical system. Benchmark problem, i.e. F-18 LLF system, helps to quantify the findings and validate the outcomes.

Keywords Belief reliability · Disjoint method · Decomposition method

1 Introduction

Reliability [1–3] is one of the system's most important characteristics. It tells about a system's or component's capacity to carry out an essential task for a specific amount of time under defined operational conditions. A system's reliability is very significant because it is the way in which we can determine how reliable the system is and what are the chances that the system might fail when it is in operation? Therefore, it is crucial to evaluate a product's reliability before putting it to use in order to reduce the danger of failure.

There are numerous ways to determine a system's reliability, but as our systems become more complicated over time, their level of uncertainty is also increasing. The

R. Gupta (✉) · G. L. Pahuja
Department of Electrical Engineering, NIT Kurukshetra, Kurukshetra, Haryana, India
e-mail: Roopshigupta8@gmail.com

G. L. Pahuja
e-mail: glpahuja@nitkkr.ac.in

© The Author(s), under exclusive license to Springer Nature Singapore Pte Ltd. 2025

H. P. Singh et al. (eds.), *Recent Developments in Control, Automation and Power Engineering*, Lecture Notes in Electrical Engineering 1303,
https://doi.org/10.1007/978-981-96-0047-2_39

traditional approaches for determining system reliability have thus become inadequate and less trustworthy, requiring the development of a method that can evaluate the system's randomness and uncertainty.

There are uncertain and random components, which has recently been noted in the literature. Probability theory [4] has dealt with uncertainty, and recently, reliability analysis has taken into account randomness concerns in terms of epistemic probability. [5]. Therefore, the idea of belief reliability [6, 7] is developed to determine the reliability of system that contain both uncertainty and randomness.

First of all, reliability engineers cannot comprehend the formula. Second, because we have to calculate every possible combination of the component states and perform multiple comparisons, the computational complexity [8] for using this method seems excessively high. As a result, in this work, we develop a novel belief reliability analysis technique known as the disjoint method to enhance the effectiveness and efficiency of the formula.

As the decomposition method [9, 10] creates unnecessary, failing components' and system functionality, in this paper disjoint method has been proposed which overcomes the limitation of decomposition method by generating only success components' system function.

In the 2nd section, decomposition method in addition to belief reliability evaluation for series configuration and parallel–series configuration system and its limitation is defined.

In the 3rd section, disjoint method is mentioned in this quick summary of basic reliability rules in Table 1 and comparison between reliability and belief reliability evaluation rules has been proposed.

4th section includes detailed algorithm disjoint method [11], i.e. the old decomposition method's step count has been reduced, and a new disjoint method has been created as well as results of both methods are compared which may be accounted for rounding off error.

Table 1 Reliability operation

Operation on element	Reliability evaluation
X ∩ Y	E1*E2
$\bar{X}$ ∪ Y	1 − (E1*E2)
X	E1
Y	E2
$\bar{X}$	1 − E1
$\bar{Y}$	1 − E2
$\bar{X} \cap \bar{Y}$	(1 − E1)*(1 − E2)
$\bar{X} \cup \bar{Y}$	(1 − ((1 − E1)*(1 − E2)))
$X \cup \bar{Y}$	1 − (E1*(1 − E2))
$\bar{X} \cup Y$	1 − ((1 − E1)*E2)
$X \cap \bar{Y}$	E1*(1 − E2)
$\bar{X} \cap \bar{Y}$	(1 − E1)*E2

Table 2 Comparison of results by both method

Belief reliability of system by Decomposition method	Belief reliability of system by Disjoint method
0.9725	0.9717

5th section includes results, i.e. belief reliability of system by decomposition method as well as disjoint method numerically. Results by both methods are compared further in Table 2.

2 Belief Reliability Analysis of a System

2.1 Decomposition Method

An approach used in system reliability analysis to evaluate the reliability of complex systems is the decomposition method and sometimes signifies to as the series–parallel method or the cut set method [12]. It involves dividing down a larger system into smaller subsystems and evaluating each subsystem's reliability [13, 14] using series and parallel combinations, thus helpful for analysing large and complex systems.

Such systems are handled by the method that has been described. We will first go over some basic ideas with a brief example to help clarify this approach. There is an algorithm for computer-based belief reliability analysis of complex uncertain random systems.

Let us consider the following: an uncertain random system with series configuration, $R_{B,u}^{(P)}(t)$ m random components with belief reliabilities as (t), u = 1, 2,..,x and n uncertain components with belief reliabilities $R_{B,v}^{(U)}(t)$ v = 1, 2,.., y.

Consequently, the system might be reduced to a segment that contains uncertainty and randomness, failure times for random components are j1, j2,..., ja and for the uncertain components are i1, i2,..., ib, and the system having belief reliability, such as $R_{B,S}(t)$, can be computed as:

$$\begin{aligned} R_{B,S}(t) &= R_{B,u}^{(P)}(t) \cdot R_{B,v}^{(U)}(t) \\ &= P_r\left\{\Lambda_{u=1}^{x} i_u > t\right\}.M\left\{\Lambda_{v=1}^{y} i_v > t\right\} \\ &= P_r\left\{\cap_{u=1}^{x}(j_u > t)\right\} \cdot M\left\{\cap_{v=1}^{y}(i_v > t)\right\} \\ &= \Pi_{u=1}^{x} R_{B,u}^{(P)}(t).\Lambda_{v=1}^{y} R_{B,v}^{(U)}(t) \end{aligned} \tag{1}$$

Parallel–series configuration system:

$$\begin{aligned} R_{B,S}(t) &= R_{B,u}^{(P)}(t) \cdot R_{B,v}^{(U)}(t) \\ &= P_r\left\{\Lambda_{u=1}^{x} i_u > t\right\}.M\left\{\Lambda_{v=1}^{y} i_v > t\right\} \end{aligned}$$

$$= 1 - P_r\left\{\Lambda_{u=1}^{x}(i_u \le t)\right\} \cdot \left(1 - M\left\{\Lambda_{v=1}^{y} i_v \le t\right\}\right)$$
$$= 1 - P_r\left\{\cap_{u=1}^{x}(j_u \le t)\right\} \cdot \left(1 - M\left\{\cap_{v=1}^{y} i_v \le t\right\}\right)$$
$$= \left(1 - \Pi_{u=1}^{x} R_{B,u}^{(P)}(t)\right). \vee_{v=1}^{y} R_{B,v}^{(U)}(t) \quad (2)$$

2.2 *Decomposition Method Limitations*

Decomposition method in F-18 LLF (see Fig. 1) system generates sixty-four success expressions, while only eight success terms are produced by the disjoint method. We can conclude that the disjoint method is a quick and effective way to analyse the belief reliability of any system.

3 Disjoint Method

The disjoint approach [11, 15] is a technique used in the discipline of reliability engineering to calculate the reliability of a system made up of a number of interdependent components or subsystems. The approach makes the assumption that a system only fails when all of its parts or subsystems fail simultaneously.

The individual reliabilities of the components or subsystems and their interdependencies must be known in order to implement the disjoint technique. Fault trees or other equivalent techniques can be used to model the interdependencies.

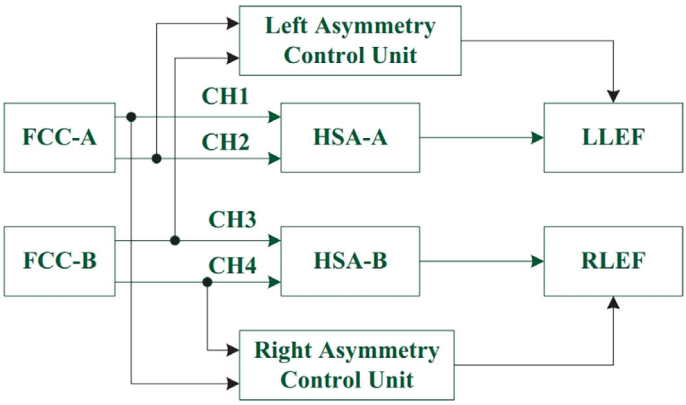

Fig. 1 F-18 LLF system

It is essential to remember that the disjoint technique assumes independence between the parts or subsystems, which means that the failure of one part has no bearing on the likelihood of failure of the others.

3.1 Basic Rules

The theory put forth in this work is a combination rule that transfers the fundamental conviction with X and Y as two elements.

Let us consider reliability of an element X as E1 and Y as E2.

3.2 Comparison Between Reliability and Belief Reliability Rules

Let us consider reliability of element X and Y as E1 and E2 whereas belief reliability as BR1 and BR2, respectively.

To calculate complement of one element

For reliability evaluation, it will be $\overline{E1}$ and $\overline{E2}$.

Similarly for belief reliability evaluation, it will be $\overline{BE1}$ and $\overline{BE2}$.

For elements in series

For reliability calculation, we do a product between reliabilities, for example if element X and Y are in series; then, overall system reliability will be given as

$$Rs = E1 * E2 \tag{3}$$

For belief reliability calculation, we perform min operation between belief reliabilities of elements. Overall system belief reliability will be given as,

$$R_{BS} = \min(BE1 \wedge BE2) \tag{4}$$

For elements in parallel

For reliability calculation, we do dot product between one minus the reliabilities of elements. Overall system reliability will be given as,

$$\text{Rs} = 1 - ((1 - \text{E1}) * (1 - \text{E2})). \tag{5}$$

For belief reliability calculation, we perform max operation between belief reliabilities of elements. Overall belief reliability of system is given as,

$$R_{BS} = \max (\text{BE1 V BE2}). \quad (6)$$

4 Proposed Algorithm

Algorithm 1 Assume path sets to be known.

Algorithm 2 Assume all components mutually exclusive.

Algorithm 3 Find disjoint product of reliabilities of aleatory as well as epistemic components by expanding path sets along previous path set [16].

Rules for finding success terms.
Rule 1- $\overline{1 \cup 2} = \overline{1} * \overline{2}$, 1 and 2 components aleatory.
Rule 2- $\overline{1 \cup 2} = \min (\overline{1} \Lambda \overline{2})$, 1 and 2 components epistemic.
Rule 3- $\overline{1 \cup 23} = \min (\overline{1} \Lambda \max (\overline{2} \cup \overline{3}))$, 1 and 2 components epistemic.
Rule 4- Find overall system belief reliability by adding all disjoint success terms.
Components of Rotorcraft system are defined below as.
FCC—Flight control computer.
CH—Channel.
HSA—Hydraulic servo-actuator.
LLEF—Left leading edge flap.
RLEF—Right leading edge flap (Fig. 2).
In above RBD, components 1, 2, and 7 are aleatory components while rest are epistemic components.
E1 = 0.9688, E2 = 0.9200, BE3 = 0.9500, BE4 = 0.9000, BE5 = 0.8000, BE6 = 0.8800, E7 = 0.9600, BE8 = 0.9700, BE9 = 0.9500.
Reliability of a system has been calculated as:
All possible paths from source to destination are evaluated as
P1 = 1.
P2 = 2.
P3 = 3.
P4 = 56.
P5 = 89.
P6 = 59.
P7 = 86.
P8 = 4576.
Then, disjoints corresponding to each path will be calculated as
P1disj = 1.
P2disj = $2|\overline{1} = 2$ V $\overline{1}$.
P3disj = $3|\overline{1 \cup 2} = 3\ \overline{12}$.
P4disj = $56|\overline{1 \cup 2 \cup 3} = (5\ \Lambda\ 6\ \Lambda\ \overline{3})\overline{12}$.
P5disj = $89|\overline{1 \cup 2 \cup 3 \cup 56} = (8\ \Lambda\ 9\ \Lambda\ \overline{3}$ V $(\overline{5} \cup \overline{6}))\overline{52}$.
P6disj = $59|\overline{1 \cup 2 \cup 3 \cup 56 \cup 89} = (5\ \Lambda\ 9\ \Lambda\ \overline{3}\ \Lambda\ \overline{6}\ \Lambda\ \overline{8})\ \overline{12}$.

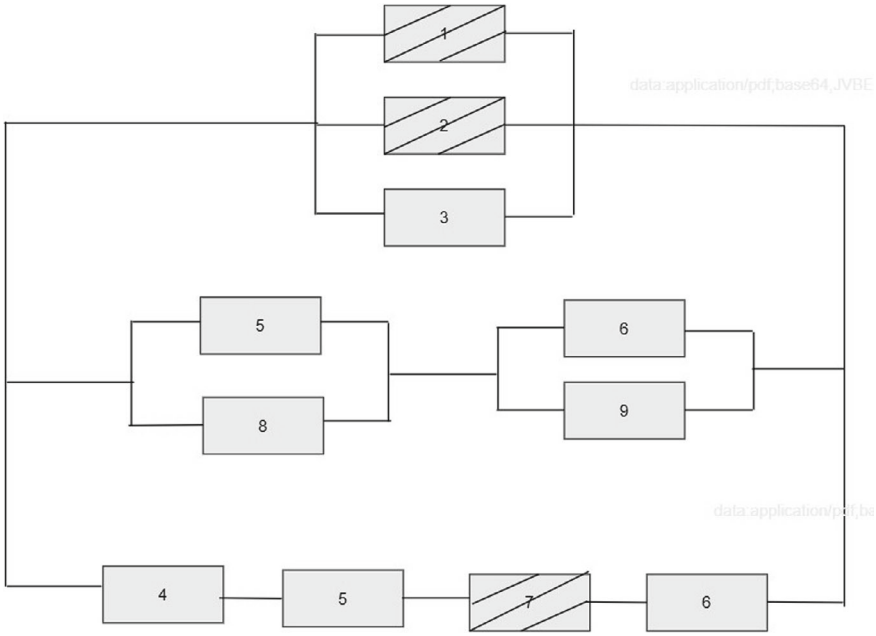

Fig. 2 RBD of above F-18 LLF system

P7disj = $86|\overline{1 \cup 2 \cup 3 \cup 56 \cup 89 \cup 59} = (8\ \Lambda\ 6\ \Lambda\ V\ \overline{3}\ \Lambda\ \overline{9}\ \Lambda\ \overline{5})\overline{12}$.
P8disj = $4576|\overline{1 \cup 2 \cup 3 \cup 56 \cup 89 \cup 59 \cup 86} = (4\ \Lambda\ 5\ \Lambda\ 6\ \Lambda\ \overline{8}\ \Lambda\ \overline{9}\ \Lambda\ \overline{3})\ \overline{1}\ \overline{2}\ \overline{7}$.
Overall belief reliability of F-18 LLF system is calculated as,

$$R_{BS} = 1 + (2\,\overline{1}) + (3\overline{1}\,2) + (5\Lambda\,6\Lambda\,\overline{3})\overline{1}\overline{2} + (8\Lambda 9\Lambda\overline{3}\mathrm{V}(\overline{5} \cup \overline{6}))\overline{1}\overline{2} + (5\Lambda 9\Lambda\overline{3}\Lambda\overline{6}\Lambda\overline{8})\overline{1}\overline{2} + (8\Lambda 6\Lambda\mathrm{V}\overline{3}\Lambda\overline{1}\overline{9}\Lambda\overline{5})\overline{1}\overline{2} + (4\Lambda 5\Lambda 6\Lambda\overline{8}\Lambda\overline{9}\Lambda\overline{3})\overline{1}\overline{2}\overline{7}$$

$$R_{BS} = 0.9688 + (0.9200 * 0.0312) + (0.9500 * 0.0312 * 0.08) + (0.05 * 0.0024)\ (0.05 * 0.0024) + (0.005 * 0.0024) + (0.005 * 0.0024) + (0.003 * 0.0023).$$

$$R_{BS} = 0.9688 + 0.0287 + 0.00237 + 0.00012 + 0.00012 + 0.00012 + 6.9 * 10^{-5}$$

$$R_{BS} = 0.9717$$

F-18 LLF [17] control system's reliability is $R_{BS} = 0.9717$.

5 Results

The disjoint method is significantly more efficient than the decomposition method because it contains eight terms instead of the sixty-four in the decomposition method for the belief reliability expression. While solving F-18 LLF system's belief reliability through decomposition method, belief reliability of whole system is evaluated as 0.9725. Thus, both by comparing disjoint method with decomposition method, disjoint method also gives accurate result as obtained by decomposition method. Further results are compared in Table 2. Given below, disjoint method used for belief reliability evaluation yields negligible error of 0.0008, which may be accounted for rounding off error.

6 Conclusion

The limitations of the decomposition method for calculating belief reliability have been determined in this paper. The disjoint method of the F-18 LLF system, a novel approach to evaluating belief reliability, has been presented. This method reduces the drawbacks of the decomposition method. The easy disjoint approach only produces non-cancelling terms in the expression for belief reliability. Additionally, compared to the decomposition method, the number of non-cancelling terms in the belief reliability expression is extremely small. The practical F-18 LLF system, a benchmark problem in reliability literature, has been used to test both approaches.

References

1. Ebeling, C.E.: An introduction to reliability and maintainability engineering. McGraw-Hill, New York, NY, USA (2004)
2. Balaguruswamy, E.: Reliability engineering. New Delhi, India: McGraw-Hill Education(India) Private Limited (1984)
3. Jipeng, W., Qingyuan, Z., Yuanzhu, Z., Xiaomei, S.: Reliability analysis and health management of the radar range based on belief reliability theory. In: *2022 4th International Conference on System Reliability and Safety Engineering (SRSE), Guangzhou, China*, pp. 278–283 (2022). https://doi.org/10.1109/SRSE56746.2022.10067838.
4. Flage, R., Baraldi, P., Zio, E., Aven, T.: Probability and possibility-based representations of uncertainty in fault tree analysis. Risk Anal. **33**(1), 121–133 (2013)
5. Beer, M., Ferson, S., Kreinovich, V.: Imprecise probabilities in engineering analyses. Mech. Syst. Signal Process. **37**(1–2), 4–29 (2013)
6. Barlow, R.E., Proschan, F.: Mathematical theory of reliability. Wiley, New York NY, USA (1964)
7. Zeng, Z., Wen, M., Kang, R.: Belief reliability: a new metrics for products' reliability. Fuzzy Optim. Decis. Making **12**(1), 15–27 (2013)
8. Martin, L.S.: *Reliablity of Computer Systems and Networks*. John Wiley & Sons Inc. New York, NY, USA (2002)

9. Zhang, Q., Kang, R., Wen, M.: Decomposition method for belief reliability analysis of complex uncertain random systems. IEEE Trans. **7**, 132711132719 (2019)
10. Qingyuan, Z., Rui, K., Meilin, W.: Decomposition method for belief reliability analysis of complex uncertain random systems. J Artic (2019)
11. Locks, M.O.: A minimizing algorithm for sum of disjoint products. IEEE Trans. Rel. **36**(4), 445–453 (1987)
12. Jasman, G.B., Kai ,O.S.: A new technique in minimal path and cutset evaluation. IEEE Trans. Reliabil. **34**, 136–143 (1985)
13. Smith, C.O.: Introduction to reliability in design. McGraw Hill, New York
14. Lewis, E.E.: Introduction to reliability engineering. John Wiley and Sons, New York
15. Tripathy, P.K., Dash, R.K., Tripathy, C.R.: A self-generating disjoint minimal cutset method for evaluating the reliability of interconnection networks. In: *2010 International Conference on Signal Processing and Communications (SPCOM)*, Bangalore, India, pp. 1–5 (2010). https://doi.org/10.1109/SPCOM.2010.5560528
16. Satyanarayana, A., Prabhakar, A.: New topological formula and rapid algorithm for reliability analysis of complex networks. IEEE Trans. On Rel. **27**(2), 82100 (1968)
17. Zeng, Z., Kang, R., Wen, M., Zio, E.: Uncertainty theory as a basis for belief reliability. Inf. Sci. **429**, 26–36 (2018)
18. Liu, Z., Yang, S., Yang, M., Kang, R.: Software belief reliability growth model based on uncertain differential equation. IEEE Trans. Reliab. **71**(2), 775–787 (2022). https://doi.org/10.1109/TR.2022.3154770
19. Hao, X., Ying, C., Yujia, W., Rui, K.: Belief reliability analysis of electrical performance based on analog behavior modelling. In: *2021 Global Reliability and Prognostics and Health Management (PHM-Nanjing), Nanjing, China*, pp. 1–4 (2021). https://doi.org/10.1109/PHM-Nanjing52125.2021.9612655

Author Index

A
Abhik Kumar, 143
Abhishek, 179
Aditya Kumar Singh, 55
Adnan Mukhtar, 369
Amit Atri, 335
Amit Kumar Choudhary, 399
Amit Kumar Goel, 11
Amit Kumar Singh, 411
Anil Kumar Sagar, 423
Aniruddha Mukherjee, 357
Anirudh Anand, 129
Anirudh Nawani, 1
Anita Khosla, 335
Ankit Gupta, 179
Anshu Khurana, 443
Anurag Verma, 11
Anu Tonk, 113
Arghya Chakravarty, 369
Arif Shah, Hossain Md., 343
Arun Singh Rana, 305
Aryan Thakur, 205
Asha Rani, 271
Ashish Mani, 219
Asmita Rajawat, 79

B
Babu, Riad Mollik, 343
Bhanita Adhikary, 243
Bharat Bhushan Naib, 11
Bhatia, Diva, 343

C
Chaudhary Indra Kumar, 67

D
Deepa Kumari, 319
Devraj Gautam, 205
Dipin Garg, 33

E
Eshaan Yadav, 67

F
Faiza Mushtaq, 93

G
Gaurav Kaushal, 179

H
Harpreet Singh Bedi, 93

I
Ishita Kanotra, 55

J
Jaspal Singh, 219
Javed Dhillon, 1
Jaydeep Swarnakar, 243
Jayesh Kumar, 105

© The Editor(s) (if applicable) and The Author(s), under exclusive license to Springer Nature Singapore Pte Ltd. 2025

H. P. Singh et al. (eds.), *Recent Developments in Control, Automation and Power Engineering*, Lecture Notes in Electrical Engineering 1303,
https://doi.org/10.1007/978-981-96-0047-2

Jyoti Ohri, 191

K
Kajal Rani, 55
Kavin, M., 411
Kirti Pal, 319
Kiruthik Rosan, M., 411
Krishnam Naidu, R. S. R., 253
Kushagra M. Agrawal, 79

L
Lakshmi, D., 433
Lokesh, 179
Lubna Siddiqui, 219

M
Madhavi Nerkar, 357
Mahesh Kumbhar, 461
Mahesh Palavalasa, 253
Manikandan, S., 23
Maria Manuel Vianny, 23
Mir Mohibullah Sazid, 343
Mukund Kumar Choudhary, 287

N
Nagireddy Ranga Rao, 1
Neelofer Afzal, 113
Neelu Nagpal, 433
Neha Goel, 11
Nuhel, Ahsan Kabir, 343

O
Omveer Singh, 231, 305

P
Pahuja, G. L., 287, 473
Palak Girdhar, 33
Periyasamy, M., 411
Prabhakar Tiwari, 385
Pradeep Kumar, 165
Pragya Jha, 433
Pritish Sharma, 191
Priyanka Maurya, 385
Pyare Mohan Tiwari, 411

R
Raghav Tola, 79
Rahul Sharma, 287
Rajat Bhardwaj, 23
Ram Bhushan Singh, 1
Ravikant, 271
Ravi Shekhar Tiwari, 433
Rayguru, M. M., 143
Rohit Sharma, 33
Rohit Singla, 129
Roopshi Gupta, 473

S
Sachin Chavhan, 461
Sachin Gangwar, 11
Sagnik Ghosh, 155
Saha, Bishal, 343
Salman Md, 443
Sandeep Bhatia, 11, 205
Seema Kalonia, 443
Seikh Atif Aslam, 105
Shamik Chatterjee, 253
Shashank Gaur, 335
Sheham, Md. Nursari Hasan, 343
Shelly Vadhera, 45
Shikhar Gaur, 443
Shipra Saraswat, 55
Shivam, 155
Shreya Chaudhary, 231
Shubh Sharma, 433
Shweta Kumari, 399
Siano, Pierlugi, 433
Soni, Bhanu Pratap, 357
Sourav Kumar Singh, 105
Subhash Yadav, 179
Sudarshan K. Valluru, 143
Surender Kumar, 205
Suresh Kumar Sudabattula, 105

T
Tanooj Sreesailam, 1
Thamaraiselvan, M., 411

U
Udit Mittal, 179
Utsab Bhattacharya, 165

V
Vaibhav Sharma, 33
Vandana Khanna, 113
Vijander Singh, 271
Vikas Kumar Badhan, 45

Vikrant Sharma, 23
Virender, 23
Vishvendra Pal Singh Nagar, 423
Vishwakarma, C. B., 305, 319
Vivek Bhardwaj, 23